Understanding composition-property-phase relations in high Fe_2O_3 Hanford waste glasses

James David Eales

A thesis submitted as partial fulfilment of the requirements of

Sheffield Hallam University

for the degree of Doctor of Philosophy

November 2023

Candidate Declaration

1. I have not been enrolled for another award of the University, or other academic or professional organisation, whilst undertaking my research degree.
2. None of the material contained in the thesis has been used in any other submission for an academic award.
3. I am aware of and understand the University's policy on plagiarism and certify that this thesis is my own work. The use of all published or other sources of material consulted have been properly and fully acknowledged.
4. The work undertaken towards the thesis has been conducted in accordance with the SHU Principles of Integrity in Research and the SHU Research Ethics Policy.
5. The word count of the thesis is 50,024.

Name	James David Eales
Date	3rd November 2023
Award	PhD
Research Institute	Materials and Engineering Research Institute
Director(s) of Studies	Prof. Paul Bingham

This thesis is dedicated to my late mother, Vicky Whiffen.

Acknowledgements

Firstly, I would like to thank my supervisory team, Prof. Paul Bingham and Dr. Anthony Bell. Their support and guidance over the years have truly helped my professional development in ways I could not have predicted at the start of my studies. I would like to thank the wider research group members both past and present, especially Jess Rigby, Katrina Skerratt-Love, Alex Scrimshire, & Alex Stone. Each and every one of you went above and beyond to help me in some way, and I am grateful to have worked around you all.

In 2019, I spent two months at the Pacific Northwest National Laboratory's Applied Science Laboratory. I would like to Tongan "Tony" Jin, Brian Riley, Saehwa Chong, Derek Cutforth, and Derek Dixon for an incredible work experience. I'd also like to thank Albert Kruger, Wendy Chun, and Brenda Weisner for making such an unforgettable experience possible.

Throughout the project, a lot of data was generated in external facilities. I'd like to thank Ben Spencer and Marek Nikiel of the University of Manchester for the acquisition and support during the processing of the XPS data. For the acquisition of the boron K-edge XANES data, I would like to thank Steffano Nanaronne, Angelo Giglia, and Nicola Mahne at the BEAR beamline at the Elettra Synchrotron, Trieste Italy. At the ESRF in Grenoble, France, I would like to thank Paul Thompson and Laurence Bouchenoire for their help in acquiring the Fe K-edge XANES data.

My family deserve endless praise for their support during my studies. Special mentions go out to my siblings, Jack and Jordanna, for their unique ability to make light of everything, and my grandparents (especially my wonderfully clever Grandma) for their words of support and encouragement. As a family, we rallied together to deal with the painful loss of my mother, who would have been over the moon to see me finish this. I truly could not have done this without you all.

Lastly, I would like to acknowledge the unwavering support of my loving fiancé Hollie. I would not be the person I am today without her unconditional encouragement and constant reminders that life exists beyond academia. I consider myself a lucky man to have such positive influence in my life.

Publications & Conferences

Publications

Eales, J. D., Bell, A. M. T., Cutforth, D. A., Kruger, A. A., & Bingham, P. A., Structural changes in borosilicate glasses as a function of Fe_2O_3 content: A multi-technique approach, *J. Non-Cryst. Solids*, **622**, 2023, 122664.

Conference Presentations (Oral)

Eales, J. D., Bell, A. M. T., Cutforth, D. A., Kruger, A. A., & Bingham, P. A., "Structural changes in borosilicate glasses as a function of Fe_2O_3 content: A multi-technique approach", Society of Glass Technology Annual Meeting, Cambridge, UK, September 2023.

Eales, J. D., Fox, K. M., Kruger, A. A., Goel, A., Guillen, D. P., McCloy, J. S., Vienna, J. D., Aminorroaya-Yamini, S., & Bingham, P. A., Thermal, chemical, and phase property changes in Hanford analogue glasses with varying Fe_2O_3 contents, Physics of Non-Crystalline Solids, Canterbury, UK, June 2022.

Eales, J. D., Fox, K. M., Kruger, A. A., Goel, A., Guillen, D. P., McCloy, J. S., Vienna, J. D., Aminorroaya-Yamini, S., & Bingham, P. A., Understanding composition-property-phase relations in high-Fe_2O_3 Hanford waste glasses, Joint International Centre for Theoretical Physics (ICTP) and International Atomic Energy Authority (IAEA) Summer School, Trieste, Italy, 2019.

Eales, J. D., Fox, K. M., Kruger, A. A., Goel, A., Guillen, D. P., McCloy, J. S., Vienna, J. D., Aminorroaya-Yamini, S., & Bingham, P. A., Understanding composition-property-phase relations in high-Fe_2O_3 Hanford waste glasses, International Commission on Glass' 4th Winter School, Wuhan, China, November 2018.

Conference Presentations (Poster)

Eales, J. D., Bell, A. M. T., Cutforth, D. A., Kruger, A. A., & Bingham, P. A., "Structural changes in borosilicate glasses as a function of Fe_2O_3 content: A multi-technique approach", 3rd SUMGlass Summer School, Nimes, France, September 2023.

Eales, J. D., Rigby, J. C., Scrimshire, A., Fox, K. M., Kruger, A. A., Goel, A., Guillen, D. P., McCloy, J. S., Vienna, J. D., Aminorroaya-Yamini, S., & Bingham, P. A., Understanding composition-property-phase relations in high-Fe_2O_3 Hanford waste glasses, International Conference of the Applications of the Mössbauer Effect, Croatia, September 2021. (Presented Remotely).

Eales, J. D., Fox, K. M., Kruger, A. A., Goel, A., Guillen, D. P., McCloy, J. S., Vienna, J. D., Aminorroaya-Yamini, S., & Bingham, P. A., Understanding composition-property-phase relations in high-Fe_2O_3 Hanford waste glasses, STEM for Britain, Parliamentary Poster Event for Early-Career Researchers, London, UK, March 2019.

Abstract

To support the vitrification efforts at the US Hanford site, three borosilicate glasses were designed and incrementally doped on a pro-rata basis with Fe_2O_3 from 0 – 14 mol%. The first series was an Na-borosilicate glass, the second introduced CaO, Al_2O_3, and Li_2O into the composition, while the third was derived from a high-Fe waste glass composition (known as HLW Ng-Fe2). These three glass sample series were used to investigate how Fe_2O_3 integrates into borosilicate glass networks of varying complexity.

^{57}Fe Mössbauer and Fe K-edge XANES spectroscopies were used to describe the iron chemistry across all three glass series, while B K-edge XANES, Raman, Si 2p & B 1s spectroscopies were used to describe the glass network. The iron was demonstrated to exist entirely as Fe^{3+} in all samples, while the coordination of the Fe^{3+} was shown to be predominantly tetrahedral, with some evidence of higher-coordinated units. The silicate sub-network was shown to be more affected by the increasing Fe_2O_3 contents in the simplest glass series, but in more complex series, the borate sub-network was shown to be affected more by increasing Fe_2O_3 content. The boron coordination, as determined by B K-edge XANES spectroscopy, showed no substantial changes as a function of increasing Fe_2O_3 content. Complex tetrahedral avoidance hierarchies and mixed modifier effects were presented as hypotheses to explain these network effects.

The Hanford analogue series was selected for further research on the glass properties. The glasses were split into two sub series – the “Laboratory Produced” and the “Canister Centreline Cooled” series. The latter samples were heat treated to represent the slow cooling in the HLW steel canisters to be used at the Hanford Waste Treatment Plants (WTPs). The glass transition temperature, phase abundances (as measured by Rietveld refinement of XRD patterns), and 7-day chemical durability were studied. It was found that there are very few deviations between the two sub-series in glass transition temperature and chemical durability, but the heat-treated series showed a greater abundance of crystalline phases. All properties were consistent with limits set by the glass reference material (DWPF-EA glass) in literature. However, further work is required to confirm this as no reference material was studied alongside these samples.

Table of Contents

List of Figures

List of Tables

Disclaimer on Laboratory Work

This project spanned a time period from 2018 through to 2023 when this thesis was ultimately submitted. During this time, the COVID-19 global pandemic occurred, starting in 2020, with social-distancing measures in effect well into 2022. These measures, combined with the use of sub-contracted work, resulted in some of the lab work being done externally by other individuals, at the direction of the author. In all cases, the sample preparation and the associated data analysis/interpretation was done by the author with guidance and input from the individuals who carried out the lab work. Below is a list of these individuals, to whom the author once again offers their thanks:

University of Manchester – Ben Spencer, and Marek Nikiel carried out the X-ray Photoelectron Spectroscopy Measurements in 2020.

European Synchrotron Radiation Facility – Beamline BM28: Paul Thompson carried out the iron (Fe) K-edge X-ray Absorption Spectroscopy experiments in 2021.

Elettra Synchrotron – BEAR Beamline: Angelo Giglia and Nicola Mahne carried out the boron (B) K-edge X-ray Absorption Spectroscopy experiments in 2021.

Glass Technology Service: Specific technician not known – X-ray Fluorescence analysis of the samples in 2021. This work was sub-contracted as the in-house XRF spectrometer at Sheffield Hallam University was out-of-order and therefore unavailable for use.

University of Sheffield: Shania Laming carried out the Induced Coupled Plasma – Optical Emission Spectroscopy analysis on the leachates from the PCT-B experiments in 2022. This work was sub-contracted rather than due to the COVID-19 pandemic.

Sheffield Assay Office – Belen Morales carried out the boron (B) and lithium (Li) Induced Coupled Plasma – Optical Emission Spectroscopy measurements for compositional analysis in 2022. This work was sub-contracted rather than due to the COVID-19 pandemic.

Chapter 1 – The Hanford Site

1.1 History of the Hanford site

When considering the approach to this project, the background of the larger project needs to be appreciated. The Hanford site (**Fig. 1.1**) was commissioned in 1943 by the US army to generate weapons-grade materials for nuclear weapons as part of the Manhattan project. The site was selected for the proximity to the Columbia River, dry climate, and sparse population. The Columbia River was used to provide cooling water for the reactors [1,2]. As it was only one of seventeen large sites commissioned to aid in producing nuclear weapons, it had three well defined tasks. Firstly, it had to receive the mined uranium and manufacture it into fuel for the reactors. Secondly, it had to produce plutonium from the uranium fuel. Lastly, it had to extract and refine the plutonium so that it could be forwarded to the next site for further production towards weaponization [1,2].

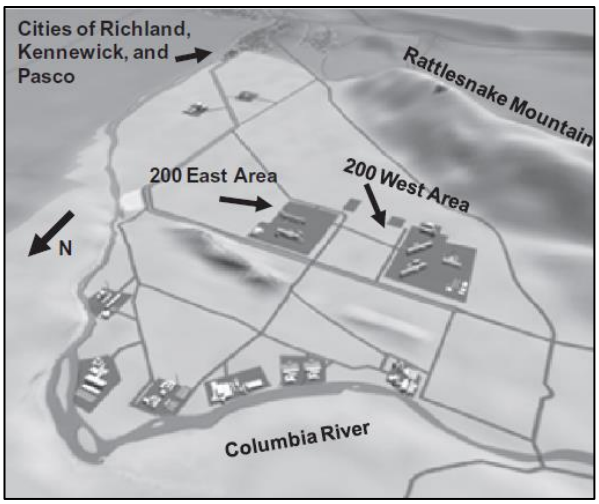

Figure 1.1: *Site map of the Hanford site [1]. The reactors lined the Columbia River.*

The mined uranium was enriched and processed into metal fuel slugs in the southern-most part of the Hanford site, known as the "300 Area". The reactors were located along the northern most part of the Hanford site along the banks of the Columbia River, known as the "100 Area". The plutonium and uranium extraction plants were shared across the east and west parts of the "200 Area" [1,2].

The first reactors were operational in 1944 and contributed the materials for both the world's first nuclear explosion at the Alamogordo site in New Mexico, known as "Trinity" and the plutonium nuclear bomb known as the "Fat Man" dropped over Nagasaki, Japan. During the lifetime of the Hanford site, nine nuclear reactors were built and operational

by 1963 [2] with the reactors contributing to the generation of 65% of the total amount of plutonium generated by US government reactors [1]. Of the plutonium generated, approximately 81% was weapons-grade plutonium with the remaining 19% being fuel-grade plutonium (**Figs. 1.2 & 1.3**) [1]. Fuel-grade plutonium is defined as having between 80 – 93 wt% plutonium-249 [3], with weapons-grade plutonium having greater than 93 wt% plutonium-249 [3].

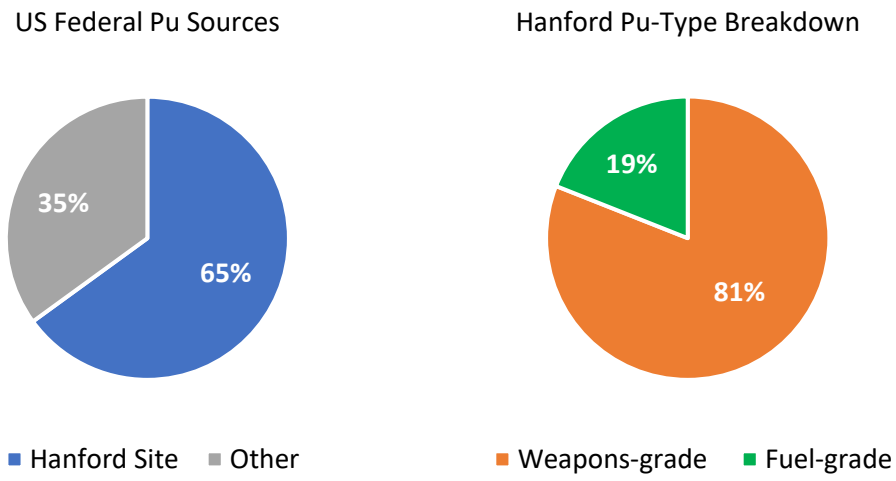

Figures 1.2 & 1.3: *Pie charts illustrating the extent and nature of the plutonium generation at the Hanford site.*

Fuel-grade plutonium production did not come into effect until 1963, and from 1971 until 1981 all plutonium produced at the Hanford site was fuel-grade plutonium. Weapons grade plutonium was produced again from 1982 until all plutonium production ceased at Hanford in 1986 [1,2].

1.2 Nuclear Fuel Cycle

The Hanford site used uranium fuel to generate both the weapons grade plutonium and for the energy grade plutonium. The fissile uranium itself arrived at the site in the form of enriched metal tubes from other federal sites, such as the Fernald Feed Materials Production Centre, in Fernald Ohio [1]. These tubes were then assembled into a reactor-ready state at the facilities in the "300 area" at Hanford. The plutonium-239 was produced from neutron capture of uranium-238 (non-fissile) with the high energy neutrons being provided by the fission reaction of U-235 taking place in the reactor [1,2,4]. The method is outlined in Equations 1.1 – 1.3 [4].

$$U_{238}^{92} + n_1 \rightarrow U_{239}^{92} \quad \text{(Eq. 1.1)}$$

$$U_{239}^{92} \rightarrow Np_{239}^{93} + \beta^- \quad \text{(Eq. 1.2)}$$

$$Np_{239}^{93} \rightarrow Pu_{239}^{94} + \beta^- \quad \text{(Eq. 1.3)}$$

However, this reaction did not occur in isolation. U-238 can also undergo alpha decay (see **Fig. 1.4** for more information on the decay of U-238 [5]), while the fission reaction of the fissile U-235 has several potential daughter nuclei, some of which with long half-lives (see **Table 1.1** for details [6]). While the neutron capture reaction produces the desirable Pu-239 needed for weapons production, a vast array of "waste components" are also produced in the overall process.

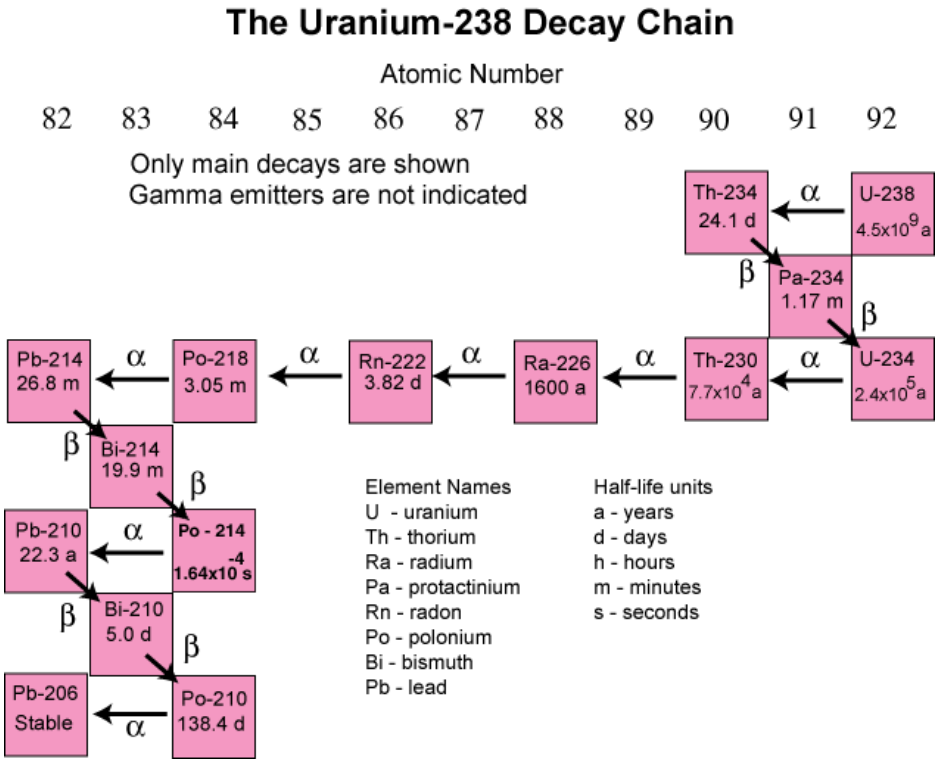

Figure 1.4: *The decay path of Uranium-238. Diagram made by the US Geological Survey (USGS) [5].*

Table 1.1: The radionuclides produced in U-235 fission with a half-life longer than 1 year. Recreated from table 21.1 in reference [6].

Daughter Nucleus	Thermal Fission Yield (%)	Half-Life (Years)
Selenium-79	0.0443	$<6.5 \times 10^4$
Krypton-85	1.318	10.72
Rubidium-87	2.558	4.8×10^{10}
Strontium-90	5.772	28.5
Zirconium-93	6.375	1.5×10^6
Technetium-99	6.074	2.13×10^5
Palladium-107	0.147	6.5×10^6
Tin-126	0.0536	$\sim 1 \times 10^5$
Iodine-129	0.757	1.57×10^7
Caesium-135	6.536	3.0×10^6
Caesium-137	6.536	30.0
Samarium-151	0.4196	90
Europium-155	0.0320	4.96

Once the reactions in the reactors have taken place, the Pu-bearing mixed metal slugs are then transferred on the extraction plants whereby the plutonium-239 is then extracted, while the remaining fission products are held for a period of time before being transferred to waste tanks [1,2,7,8]. The cooling water is also held until the temperature decreases before being pumped back into the Columbia river [1,2,7,8].

1.3 Extraction Plants

As well as the nine reactors active during the active lifetime of the Hanford site, there were five reprocessing plants at the site and a finishing plant. The names of the reactors/plants and their respective lifetimes can be seen in **Tables 1.2 & 1.3** [1,2].

Table 1.2: The list of reactors at the Hanford site during the operational lifetime.

Reactor Name	Years Active
B	1944 – 1968
D	1944 – 1967
F	1945 – 1965
H	1949 – 1965
DR (D Replacement)	1950 – 1964
C	1952 – 1969
KE (K Plant East)	1954 – 1970
KW (K Plant West)	1954 – 1971
N	1962 – 1987

Table 1.3: The list of processing facilities at the Hanford site during the operational lifetime.

Plant Name	Reprocessing Technique	Years Active
T	Bismuth Phosphate	1944 – 1956
B	Bismuth Phosphate	1944 – 1956
REDOX	REDOX	1952 – 1967
U	Uranium Recovery	1952 - 1958
REDOX	PUREX	1956 – 1972, 1982 - 1990
Z	Plutonium Finishing	1949 - 1989

1.3.1 Bismuth Phosphate Process

Across the five reprocessing plants, multiple plutonium and uranium extraction processes were utilised. The first process was the “Bismuth Phosphate Batch Processing” process which started initially in the T-Plant, before being used in the B-Plant [1,2,8,9]. The major disadvantages of this process were – it could not extract uranium from the spent fuel, which meant no fuel recycling could be done, it was inefficient (process was not continuous), and it produced large quantities of radioactive waste [1,2,9,10]. A patent filed by Thompson & Seaborg [11] describes the general bismuth phosphate batch process used at the Hanford site to precipitate the Pu-239 (described as “element 94”) from irradiated uranium. The process involves changing the plutonium oxidation state so that the solubility of the Pu-bearing chemicals is in opposition to the solubility of the remaining elements, such as U, Np, and any fission products within the solution, so that the Pu-

bearing materials can be separated and further processed for either weaponization or fuel purposes. The mixture of irradiated Pu-bearing uranium is first dissolved in nitric acid to create uranyl nitrate hexahydrate ($UO_2(NO_3)_2 \cdot 6H_2O$) solution. Bismuth phosphate is added to the irradiated solution, along with reducing agents to precipitate the plutonium out of the mix in an insoluble plutonium phosphate compound, while the control of the pH of the mixture along with the use of "controlling agents", typically sulphates in the form of sulphuric acid, ensure that the uranium and other fission products remain soluble in the mix and do not interfere with the reduction of the plutonium [11]. The insoluble Pu-bearing phases are removed from the mixture. The reducing agents of choice tended to be ferrous-based (Fe(II)), particularly ferrous sulphamate, ferrous nitrate, and ferrous ammonium sulphate as well as other reducing agents such as hydrogen peroxide and hydrazine [11]. This resulted in increased quantities of sulphates and other sulphur bearing chemicals, nitrates, and ferric compounds (with the 'ferrous' oxidising to 'ferric' (Fe^{3+}) in the reactions with the Pu) being introduced to the waste [9, 11]. This waste was then transferred to the steel sub-terranean storage tank farms for interim storage. **Fig. 1.5** shows a flow diagram of this process (recreated from ref [9]).

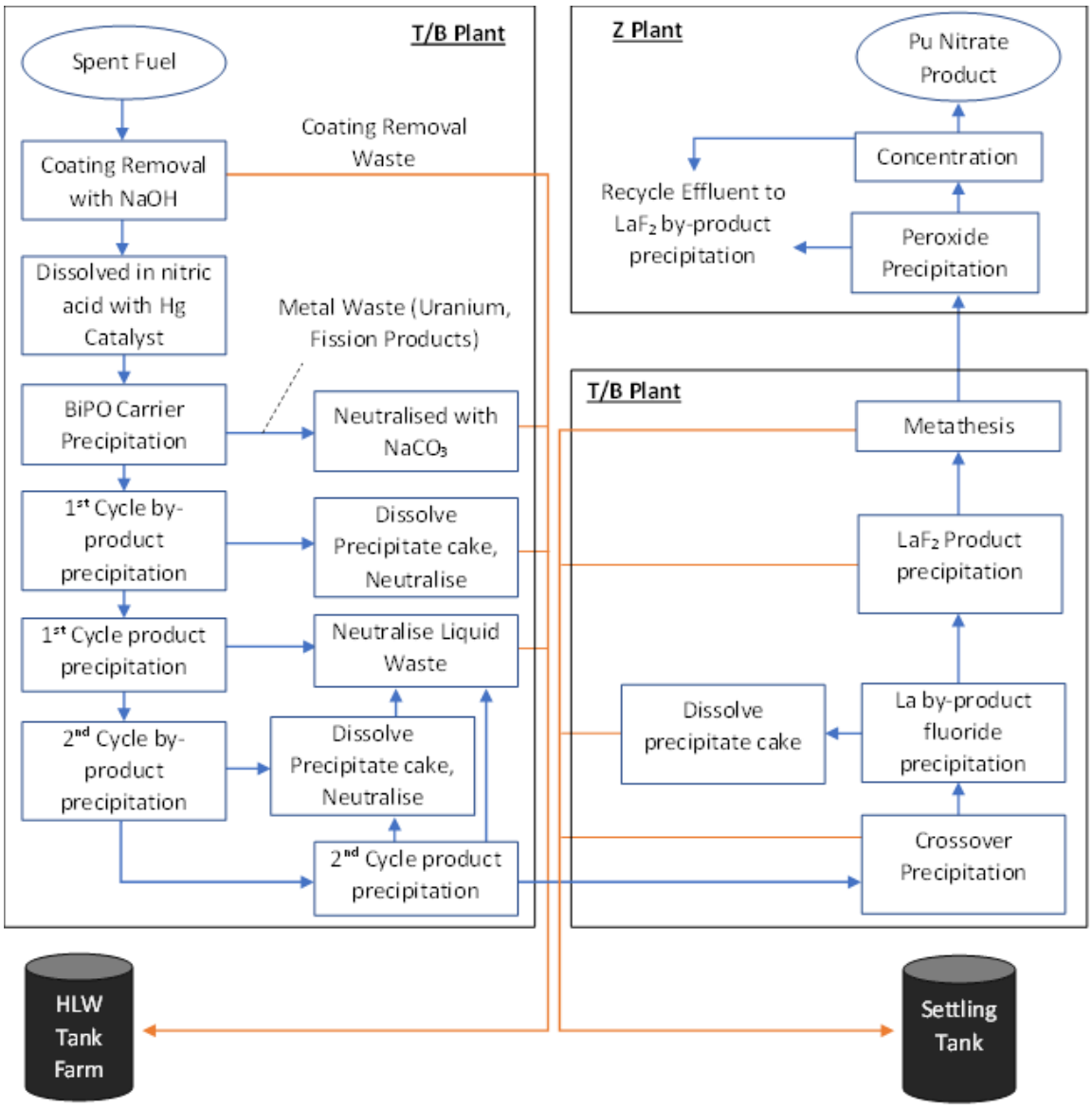

Figure 1.5: *The flowsheet of the Bismuth Phosphate process from the T/B plants through to the Z plant [9].*

1.3.2 REDOX

The REDOX (**Red**uction **Ox**idation) process was introduced in 1952 as an improved method of plutonium extraction was carried out at the REDOX plant and the first of two main continuous process methods used at Hanford [1,2,8,9]. A patent filed by Seaborg [11] describes the method to specifically remove plutonium (also described as "element 94") from irradiated uranium. It uses ethers such as organic hexone (aka methyl isobutyl ketone, MIBK) and aluminium nitrate ($Al(NO_3)_3$) salts to extract both plutonium and uranium in continuous process, which increased the process efficiency. Similarly to the bismuth phosphate method, the process oxidises and reduces the Pu and U components to extract the desirable target element by removing the phase that is immiscible in the

ether. The reducing agent of choice for this method is sulphur dioxide (SO_2), though ferric chemicals were also used in this process. While this method increased the efficiency of the Pu extraction from the bismuth phosphate, the disadvantages to this process were that some of the ethers were explosive, which complicated recycling and disposal of process wastes [9,10]. Waste chemicals include ammonium nitrate (a known oxidiser), hexone (known to be flammable), and sodium dichromate (a known oxidiser), amongst a variety of nitrate, sulphate, and ferrous bearing chemicals [9, 10, 11].

Furthermore, the use of hexone lead to complications of containing radioactive ruthenium, which was not readily extracted by hexone. The ruthenium would volatilise as RuO_4 gas, which required the installation of specific caustic scrubbers to prevent the release of ruthenium into the environment [9].

1.3.3 PUREX

The PUREX (**P**lutonium and **Ur**anium **Ex**traction) process further upgraded on the REDOX process. It was first used at the Savannah River site before being employed in the PUREX plant at Hanford [1,2,9,10]. Nitric acid (HNO_3) and tri-butyl phosphate, TBP, with an evaporation process to extract the purified Pu-239. The general chemical processes in the PUREX process are summarised by Herbst *et al.* [14] by 6 main steps:

1). Dissolution of the solid nuclear fuels into a liquid feed.

2). Solvent extraction cycles utilising liquid-liquid separation of Pu or U products by alternating the oxidation state of the target product, making it immiscible in one liquid phase but not the other.

3). Recycling of organic phases.

4). Extraction of recycling of the TBT solvent.

5). Treatment of waste effluent.

6). Purification of the plutonium products.

Initially, ferrous sulphamate was used at PUREX plant as the reducing agent of choice [13], but it was replaced by hydrazine in later uses. Globally, ferrous reducing agents are no longer used in this process [14] in favour of hydrazine. Waste chemicals from this process include TBT, kerosene, ammonium nitrate, and ammonium fluoride.

The ruthenium volatilisation issue which arose from the REDOX process was addressed by using a split scrubbing system that uses a scrub system with higher acidity and temperatures to favour Ru decontamination from the solution. If use in isolation, this would promote zirconium extraction along with the desired products, which is not ideal [9]. A second scrubbing system was used in parallel with lower temperatures and acidity to facilitate Zr decontamination from the solution [9, 14].

1.3.4 Uranium Extraction

The uranium extraction process was process that took place in the U plant between 1952 – 1958 [1,2,9]. As the name suggests, the process involved extraction of uranium from the tank wastes. However, this was not done with goal of fuel reprocessing but more with a goal to remove uranium from the waste so that it could be recycled used in other national programs that required uranium. The plant itself used a modified PUREX process, in which U-bearing sludge was sluiced from the waste tanks and pumped into the plant. Once in the plant, the sludge was centrifuged to separate the liquid from the solid U-bearing waste before being extracted, finished, and ultimately moved on from the site [1,2,9].

1.3.5 Plutonium Finishing

The plutonium finishing plant, or Z plant (named for being the last plant in the Hanford process) was the plant that refined the extracted plutonium into the final finished product before being sent to the next site in the process. The finished project varied from purified plutonium pucks to Pu-metal fabrications for both weapons and fuel grade plutonium purposes [1,2,9].

1.4 Tank Farms

Throughout the lifetime of the site, there were vast quantities of waste generated by the multiple processes utilised at the various steps in the wider process. The most toxic and radioactive of the waste, was stored in tank farms across the site. Initially the tanks were single-shelled steel tanks constructed in groups to meet the demand of the supplied waste. The tanks were buried as deep as 50 ft (15.24 m) below the surface with approximately 6ft (1.83 m) from the top of the tank to the ground surface. **Table 1.4** details the periods of the initial single-shell tank (SST) constructions [1,2,9,15].

Table 1.4: The construction periods of the Hanford waste tanks including both single-shell tanks and double-shell tanks.

Years	No. of Tanks	Farm ID
1943 - 1944	64	B, T, C, U
1946 – 1949	42	BX, TX, BY
1950 – 1955	39	S, TY, SX, A
1963 - 1964	4	AX

Initially, these tanks were expected to store mixed phase waste, which included a supernatant liquid, mixed liquid/solid sludge, and precipitated saltcake phase. The expected lifetime of these tanks was 10 – 20 years [1,2,7,9], by which point better storage methods would have been developed. This was reinforced by the designed methods in which to transfer waste across tank farms by way of underground pipes and diversion boxes.

Some of single shelled tanks and associated systems began to show signs of leakage, and by 1980, 67 out of 149 SSTs were designated as at least “suspected leakers” as defined by the methods outlined in the Waste Storage Tank Status and Leak Detection Criteria report [16]. To counter this, between 1968 and 1986, 28 double-shelled tanks (DST) were designed and built with the intention of storing the liquid waste across several of the tank farms [1,2,9]. The liquid waste was pumped from the single tanks into the double-shelled tanks to minimise the risk of further leakages from the aged single-shelled tanks. The double-shelled tanks have an expected lifetime of 25 – 50 years, meaning most are well within or beyond the expected lifetime originally the tanks were designed for [1,2,9]. **Fig 1.6** shows an overview of the layout of the tank farms.

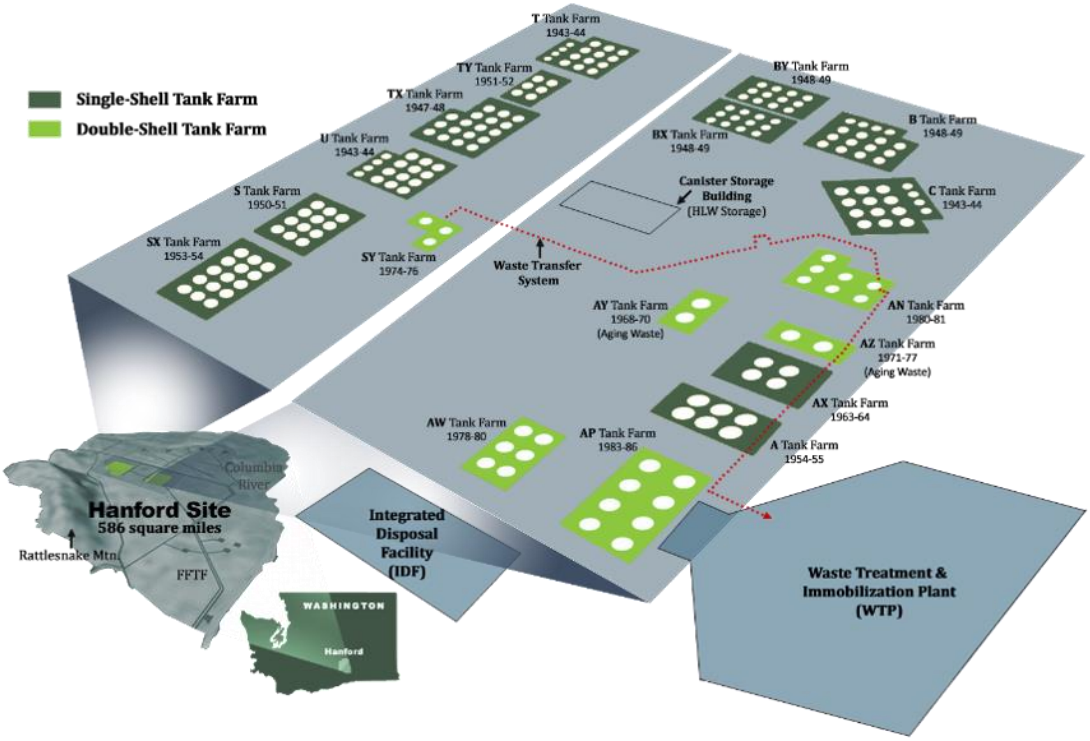

Figure 1.6: *An overview of the layout of the tank farms. Image credit to Washington River Protection Solutions [17].*

1.4.1 Tank Farms A & AX

Tank Farm A consists of six 1,000,000 gallon SSTs designed to store boiling, irradiated waste from the PUREX plant. Of the six tanks, three are designated as "suspected leakers". The farm was constructed in 1955 but wasn't fully utilised until 1956 [8,15,18].

The tanks were first filled with organic wash waste (OWW) and HLW supernate from the PUREX plant 1956. The waste achieved temperatures of over 100 ^{o}C which caused surges of pressure within some of the tanks that resulted in steam released from the tank farm stacks. Air lift circulators were retroactively installed to mitigate pressure build ups from the hot PUREX waste [8,18]. Throughout the lifetime of tanks, waste was also transferred from C-farm tanks between 1965 and 1966, with supernatant being transferred back to the C-farm tanks between 1972 and 1976 [8,18].

Tank farm AX consists of four 1,000,000-gallon SSTs also designed to store boiling, irradiated waste from the PUREX plant, however, some tanks were assigned to receive waste from the B plant caesium ion exchange processes between 1969 – 1972 [8,15,18].

Of the A-farm tanks, A-104, A-105, and AX-104 were found to be leakers. A-104 was found to have leaked PUREX supernatant sludge (PSS) waste, while A-105 was found to have leaked either PSS, or B Plant ion exchange (IX) waste [18]. AX-104 was found to

have leaked, but the nature of the leak is at present indeterminate. Initial reporting suggested that the tank had leaked PSS, but the concentrations of radionuclides found around the tank were inconsistent of this type of waste [18].

1.4.2 Tank Farm B, BX, & BY

B Farm was constructed to receive plutonium purification cycle waste (sometimes referred to as "224 Waste") from the B plant. The farm consists of twelve 530,000-gallon single shell tanks in which 7 are suspected to have leaked [8,15,19].

The BX farm consists of twelve 530,000-gallon tanks in four separate 3-tank cascade chains built in proximity to the B farm to receive waste from the B plant [8,15,20]. The BX farm was built to support the B Farm in receiving waste from the B plant. Of the twelve tanks, BX-101, BX-102, BX-108, BX-110, and BX-111 were all designated as either confirmed or suspected leakers that require further assessment [20].

Similar to the BX farm, the BY farm consists of twelve 758,000 tanks in four separate 3-tank cascade, situated north of the BX farm, it initially served as a bank-up farm for the BX tanks in receiving wastes from the B plant, which was achieved by maintaining a connection to the northern most tanks in the BX farm [8,15,21]. After being constructed Between 1948 and 1949, the BY farm initially received metal waste and TBT waste from the B Plant. From 1955 to 1958 the tanks were emptied to receive waste from Cs and Sr recovery processes that took place at the U plant. The storage of metal waste and first cycle decontamination waste meant that fission products as well as uranium and low levels of plutonium were also stored in this tank farm at some point during the active life [15, 21].

BY-103 and BY-108 were designated as confirmed leakers, while BY-105, BY-106, BY-107, BY-108 was initially designated as leakers, but have since been recommended for re-examination [21].

1.4.3 Tank Farm C

Tank farm C consisted of twelve 530,000-gallon SSTs (known as the 100-series) and four 55,000-gallon SSTs (known as the 200 series), that were initially built to take the waste from the bismuth-phosphate extraction processes which took place at the nearby B Plant [8,15,22]. Of these tanks, 3 of the 100-series tanks were designated the "assumed leaker" status and all 4 four of the 200-series tanks were designated as "assumed leakers" [22].

C farm tanks began service in 1946 with various wastes from the B Plant. Between 1952 and 1953 this waste was removed from these tanks, and they were re-used to store tri-butyl phosphate waste from the U Plant in 1953. These three tanks were then used as part of the "in farm scavenging" program [8] where wastes were transferred between the tanks and a recovery vault for precipitation of strontium and caesium using ferrocyanide [8,22]. The supernatant was sent back to C farm tanks so that the solid waste could precipitate out before the liquid was "cribbed". This took place until 1958. In 1960 the tanks began receiving wastes from the PUREX plant until 1962 when the waste was transferred to the B farm, and subsequent wastes were stored in B farm tanks. Between 1963 and 1965, the C tank farms began receiving PUREX HLW supernatant (PSN) from A farm tanks to prepare the A tanks for sludge sluicing [22].

Of the C Farm tanks, C-101 C-110 have been designated as "Confirmed Leakers", with C-101 having leaked PUREX supernatant waste and C-110 having leaked CSR (Cs Recovery) waste. Tank C-111 had been previously designated a "suspected leaker" but it was determined that the loss of waste within the tank could be accounted for by evaporation losses [22]. For C-105 it was determined that a leak of PUREX supernatant had occurred, but the nature of the leak is still being investigated and therefore C-105 remains a "suspected *leaker"* [22].

1.4.4 Tank Farm S & SX

The S farm consists of 12 750,000-gallon SSTs and was originally designed to receive hot condensate waste from the REDOX plant. The farm is arranged in a 3-tank cascade series. After initially receiving REDOX waste from the REDOX plant, the S farm then received some ion exchange waste from the U farm in 1974. From 1974 the S farm received evaporator wastes and evaporator bottom wastes until 1977 [8,15].

The SX farm consists of 15 1,000,000-gallon SSTs in five sets of 3-tank cascades. Of the 15 tanks, 10 of them have been designated a "suspected leaker". The SX tanks were designed to take HLW from the REDOX plant between 1955 – 1956 [8,15,23]. After this time, the farm utilised the cascades for internal transfers of various REDOX waste types, (boiling waste, evaporator bottom waste) and ion exchange waste from the caesium-recovery campaign at the B-plant. From 1975, the SX farm received evaporator waste supernatant from the S farm and then began receiving more evaporator waste [23].

Of the two SST S farms, all the leakers reside in the SX farm. SX-104 was designated as having “questionable integrity” (and consequently described as a “suspected leaker”) but following an assessment in 2010, it was found that the tank integrity was “sound” and that inventory losses are unlikely to have occurred due to a leak [23]. In the same assessment, it was found that SX-110 also lacked evidence to suggest that it had leaked waste, with a recommendation that a specific assessment done on the SX-110 tank. SX-107 – 109, and SX-111 – 115 leaked REDOX waste, and in the case of SX-112, also leaked some ion exchange waste [23]. Tank S-104 was initially classed as an “assumed leaker”, however, following a reassessment in 2011, it was determined the loss of inventory was due to overflow or an inlet pipe issue, and the tank itself was classed as “sound” [24].

1.4.5 Tank Farm T, TX, TY

The T farm was built to receive “224 waste” from the B plant. It consists of 4 55,000-gallon SSTs and 12 530,000-gallon SSTs. The farm was built between 1943 – 1944 [15]. The larger SSTs initially received second-cycle waste from bismuth phosphate process done at the T plant, however, they also received the aforementioned “224 waste” from the B plant. The smaller SSTs received “224 waste” from the B plant for the majority of their work life [8,15,25,26].

The TX farm consists of 18 750,000-gallon SSTs which were built between 1947 – 1948. The tank initially supported the T farm and received waste from the T and B plants. From 1952, the tank farm received waste from the U plant as well as waste from the bismuth phosphate process used at the T and B plants [8,25].

The TY farm was initially built to receive wastes from the nearby T plant, which utilised the bismuth phosphate process. It consists of 6 750,000-gallon SSTs built between 1951 and 1952. Initially, the farm received treated ferrocyanide-bearing waste from 1954 until 1956 [15,25,27]. From 1954 through to 1966, the tanks also received first cycle decontamination waste; both from the T plant. From 1959 the TY tanks also received TBP waste from the U plant, and from 1967 the tanks received REDOX waste. Both waste-types continued to be received at this farm until 1974 [27]. Tanks T-101, T-103, and T-106 were all designated as leakers, with the likely waste originating from the B plant [25,26]. Tanks TX-105, TX-110, and tanks TX-113 – TX-117 were all confirmed as leakers with waste likely being TBP waste from the B plant [25]. Some of leaks likely occurred during the transfer and cascading between tanks. Tanks TY-101, TY-103, TY-

105, and TY-106 also likely leaked TBP waste both from the tanks and potentially from the connecting pipes during waste transfers [25,27].

1.4.6 Tank Farm U

The U-tank farm was constructed between 1943 - 1944 and consisted of 12 530,000-gallon and 4 53,000-gallon single-shell tanks. The farm was initially built to receive bismuth phosphate waste from the nearby B and T plants, however, it also received REDOX waste, evaporator waste, and bottom wastes [15,24].

Of the 16 tanks, four have been designated as leakers, with tank U-104 suspected to have leaked bismuth phosphate waste, tanks U-110 and U-112 suspected to have leaked REDOX waste, and tank U-101 leaking an unspecified waste type [24,28].

1.4.7 Double Shell Tanks

The double shell tank (DST) farms were purpose-built to aid the ageing single shell tank farms described in sections 1.4.1 – 1.4.6. The double layer was included to provide extra protection against leaks with intrinsic leak detection systems to further enhance this [1,2,29,30]. A simple illustration of the differences between the single shell tanks and the double shell tanks can be seen in **Fig. 1.7**.

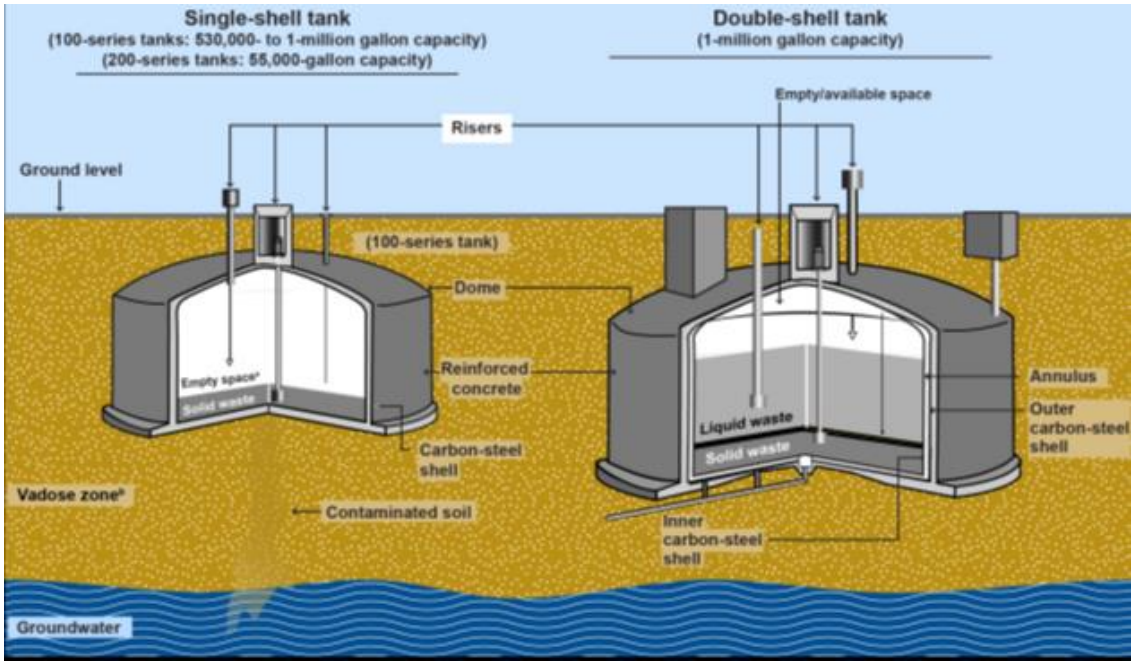

Figure 1.7: *An overview of the differences between a single shell, and double shell tank (Image sourced from reference [31]).*

The primary support offered by the DST farms to the SST farms was the ability to receive drainable liquid waste that otherwise would be stored in SSTs to provide stability to waste

containment within the farms. To date, all drainable liquids have been transferred from SSTs to DSTs [1,2]. An example would be the AY-102 DST, which was built as part of the AY tank farm to assist in receiving hot PUREX waste. AY-102 initially received hot waste from Tank A-104, while also receiving stored liquids from other A farm tanks. It also received condensates from all A farm SSTs and waste from the B plant [29]. Primarily, the DSTs received liquid wastes as these were most likely to leak and allow radionuclides to mobilise into the environment. However, liquid wastes often had solid particles within, and the DSTs do contain solid waste settled in the bottom of the tanks [29].

As of 2012, tank AY-102 was designated as a "suspected leaker" after large quantities of potassium were detected outside of the single shell in 2007 [29]. The AY-102 DST was the first DST constructed and issues with the design were found during and post-construction. It is suspected that these difficulties, coupled with the high heat of the waste lead to corrosive damage to the containment and resulted in a leak [29]. It is noted that subsequent DSTs, including AY-101, are monitored using the lessons learned from AY-102 and as such remain classified as "sound" [30].

1.5 Current Clean-Up Plans

1.5.1 Legal Mandate

In 1976 the Resource Conservation and Recovery Act (RCRA) was passed [1,32], which was followed in 1980 by the Comprehensive Environmental Response, Compensation, and Liability Act (CERCLA) [1,33]. These laws initially were the primary laws that were brought in to govern the new drive to clean up the Hanford site. This set the foundation for the Hanford Federal Facility Agreement and Consent Order, which is commonly referred to as the "Tri-Party Agreement", as it involves an agreement between the Washington State Department of Ecology, the Environmental Protection Agency (EPA), and the US Department of Energy (US DoE) [1,34]. This agreement has enshrined the clean-up of the Hanford site into a legal mandate and will ensure that the combined parties are constantly working towards defined objectives and goals with the ultimate objective of remediating the Hanford site.

1.5.2 Early Research

A comprehensive study carried out by McElroy et al. [35] called the 'Waste Solidification Engineering Prototypes (WSEP)' research at Hanford, investigated various solidification techniques designed by multiple national laboratories in the US. The main processes

investigated were ‘Fluidized Bed Calcination’ developed by the Idaho Chemical Processing Plant [35], ‘Pot Calcination’ developed by Oak Ridge National Laboratory [35], ‘Spray Solidification’ developed by Battelle-Northwest [35], and ‘Phosphate Glass Solidification’, developed by Brookhaven National Laboratory [35]. The study showed that all could solidify the waste apart from the phosphate glass, which was shown to devitrify as a result of the slow cooling of the initial process.

The original phosphate glass pilot was designed to demonstrate the process over a continuous basis using simulated reactor waste that originated from 57 tonnes of uranium in reprocessed fuel [36]. The phosphate glasses were made by mixing simulated PUREX waste and H_3PO_4 at 1200°C, and showed good resistance to environmental degradation [36]. However, there were some issues with the glasses including an incident that involved the concentrated mixture overflowing when the platinum melter was held at 1100°C to 1200°C, whilst another issue was when excessive foaming in the denitrator-evaporator caused by the presence of dibutyl phosphate from the PUREX waste [36].

A subsequent study carried out for the Savannah River Laboratory by Kelley in 1975 [37] studied borosilicate glasses as suitable solid matrix in which to immobilise the waste. It was found that it could dissolve a wide range of components, with a high waste loading capability (up to 40 wt%), with low base leachability of radionuclides. The final borosilicate waste form was also found to retain durable phases despite partial devitrification after prolonged exposure to high temperatures (~600ºC) [37]. Jantzen (1986) [38] then applied a systems-based approach to selecting a suitable glass matrix in which to vitrify the radioactive waste stored in the US. Multiple glass matrices including phosphate, high-silicate aluminosilicate, and borosilicate glasses were investigated for their waste-loading, processability, durability, and thermal stability properties. It was determined that borosilicate glass was the most suited to vitrify the diverse and complex US waste, while also maintaining high theoretical durability and low leachability for the foreseeable future [38]. Borosilicate glass was then successfully used at the Defence Waste Processing Facility (DWPF) to vitrify the legacy defence high level waste stored at the Savannah River Site from 1994, where glass frit was added to waste in a joule heated ceramic melter. The success of the DWPF fed into the decision to vitrify the stored waste at the Hanford site into borosilicate glass also using a joule heated ceramic melter [39].

1.5.3 Current Plans

Despite the success of the DWPF, it was decided that there needed to be specific modifications to process used at the Savannah River Site to make it more applicable to the complexities of the Hanford site. The first major change is substituting the use of glass frit added to waste, for adding the raw glass forming chemicals (GFCs) to the waste feed prior to being fed into the melter [40]. This is primarily to allow increased levels of control over how much of the GFCs will be needed as a function of the composition of the waste, which is a crucial aspect considering the complexities of the wastes as a result of the details outline sections 1.3 & 1.4 [40]. This allows for easier optimisation of waste loading of varied wastes. Another key difference is the "direct feed" approach to vitrification, which involves minimal-to-no pre-treatment [40]. A study by Matlack *et al*. [40] showed that while the waste would potentially be processed faster if the waste was pre-treated before vitrification, the benefits are far outweighed by the risks and extra waste generated by using an extra step. It was shown that the pre-treatment did not affect the volume of glass produced and therefore pre-treatment of the waste showed no clear advantage over the direct-feed approach [40]. In this process, the waste slurry will be mixed with the GFCs immediately prior to entering the melter. Once mixed the slurry will be poured onto a bath of molten glass, creating a foam layer on the melt surface, known as the "Cold Cap" [41]. The "Cold Cap" plays host to a wide range of chemical reactions that have unique consequences of melter performance, such as the ability to improve retention of volatiles [41], while also potentially inhibiting heat transfer and limiting waste feed rates [42-44]. Due to varying degrees of positive and negative effects the cold cap has, it has been the subject of a wide variety of studies to better understand the role it plays in the melt process. This includes attempts at modelling the thermal profile of the cold cap [45-49], attempting to better understand the foaming behaviour and the links to multi-valent waste species [50-52], and some of physical properties of the cold cap itself [50,53-56], all in an attempt to better optimise the influence the cold cap has on the melt process.

The melter technology to be employed at the Waste Treatment and Immobilisation Plants (WTP) at the Hanford site, are joule-heated ceramic melters with Monofrax K3 high-chromia refractory (see **Fig. 1.8**).

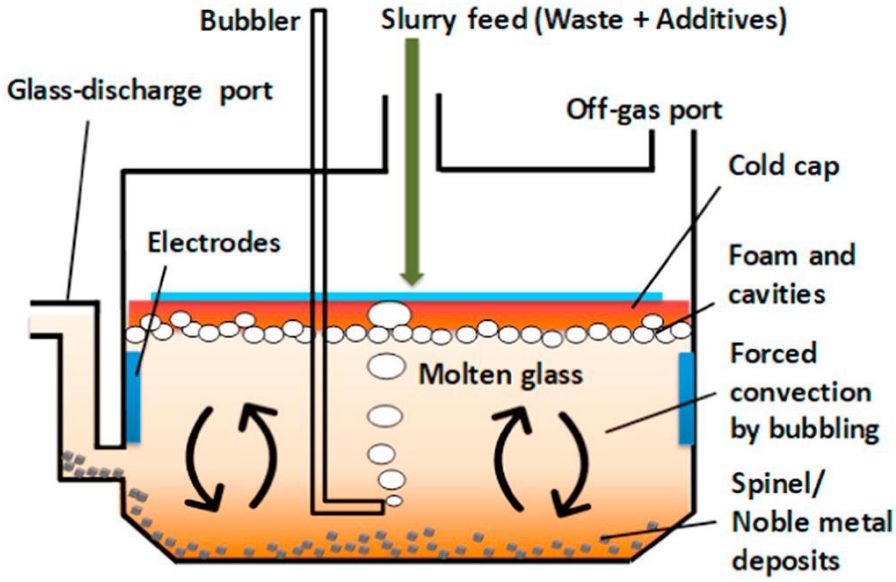

Figure 1.8: *A simple diagram of the expected melter system to be employed at the Hanford WTPs (Image source from ref [57]).*

The melter uses bubble agitation to force convection currents and encourage homogenisation within the melter. The slurry feed is added to the melter at a comparable rate to the homogenised melt being discharged through the port, to maintain a continuous process. As well researching cold-caps influence on processibility, research has gone into researching refractory corrosion of the Monofrax K3 [58]. The high-chromia nature of the Monofrax K3 [58], has raised concerns over spinel crystallisation (see Chapter 1.5.4 for more information on why spinel crystals are a cause for significant concern around waste vitrification). The initial research investigated dimension loss using standardised methods, however, these methods do not describe the thermodynamic/kinetic/chemical mechanisms that govern the corrosion reactions [59]. It has been established that the Monofrax K3 exhibits increased corrosion in the presence of alkali and alkaline earth metals, whereas components like alumina and silica inhibit corrosion in Monofrax K3 [60,61].

1.5.4 Limiting Factors

With the vast array of potential waste components, coupled with radioactive decay heat and a slow canister cooling, crystalline phases stabilising within the waste form is inevitable. However, controlling which crystal phases stabilise and how much, has been the focus of considerable studies in US waste vitrification research. The two major concerns are spinel crystallisation and nepheline crystallisation. The general formula for spinel crystals is $A^{2+}B^{3+}{}_2O_4$, where A and B sites can be occupied by a variety of elements,

including transition metals. Nepheline crystals are aluminosilicate crystals with the general formula of $(Na,K)AlSiO_4$ that can include tetrahedral Fe^{3+} in the Al sites.

The interests in spinel crystals are primarily due to the risk spinel phases pose to glass melters [62-68]. Spinel crystals can accumulate within the melter systems, particularly in the pouring spouts, as a result of the temperature decrease from the furnace chamber to the pouring spout [67], which can result in clogging and obstruction of the pouring spout. This can lead to significant shortening of melter lifetimes if not adequately accounted for. Jantzen & Brown [64] found that the octahedral site preference energy (OSPE) order for the formation of spinel crystals in complex nuclear waste glasses is $Ni^{2+} \approx Fe^{2+} > Mg^{2+} > Mn^{2+}$. Further research has investigated the specific joule heated ceramic melter to be employed at Hanford [68], which used silicon oil and magnetite (spinel: Fe_3O_4) crystals to simulate flow tests in pouring mechanisms. It was found that on a particular riser, there was significant crystalline accumulation with a bend on the riser. However, the test repeatability was an issue as the accumulation did not reset, and further tests showed less accumulation build up on top of the previous build up. The research into understanding the spinel crystallisation within waste forms at both the DWPF and the expected wastes at Hanford have allowed the development of spinel tolerance models for the Hanford process [69-75]. The vast majority of the research aimed to assess the acceptable levels of spinel crystallisation found in the final waste form as a function of theoretical spinel agglomeration within the melter and pouring spouts.

Unlike spinel crystals, nepheline crystals provide a set of challenges to the wasteform itself, rather than the melt process. Nepheline crystals are aluminosilicate crystals that reduce the chemical durability of the final waste form by removing alumina and silica from the glass. Significant research has gone into understanding the formation of these crystals within the context of Hanford wastes, as they pose a significant limiting factor on the waste loading capabilities [76-91]. Nepheline crystals typically form in wasteforms that are alumina rich, and silica-poor [76], which poses a significant waste loading challenges for high-alumina wastes if the nepheline discriminator [82] used at the DWPF was to be used at the Hanford WVP (36 wt.% waste loading at DWPF [81] versus < 18 wt.% expected at the WVP [82]). To aid with the waste loading optimisation for the high-Al Hanford wastes, McCloy *et al*. [79] aimed to expand the nepheline discriminator model by looking at the optical basicity of expected waste forms. It was found that at low optical basicity values (OB < 0.55 – 0.57) that nepheline stabilisation was supressed. The low

OB values could be achieved by increasing acidic components such as B_2O_3 and decreasing in alkali and alkaline earth components, allowing for more optimised waste loading of high alumina wastes by controlling the GFCs added to the melt. This further illustrates the importance of the switch from glass frit employed at the DWPF to the addition of GFCs prior to melting to be employed at the Hanford WVP.

Alumina, silica, and boric oxide are not the only components that have an influence on the formation of nepheline [79]. Ahmadzadeh et al. [85] studied nepheline-based glasses and investigated the role of iron in the formation of nepheline in glasses by substituting the Al_2O_3 for Fe_2O_3. It was found that in low abundances of Fe, that tetrahedral Fe3+ could substitute into as much as 37% of the tetrahedral Al sites, however in higher abundances, the iron would preferentially form magnetite or hematite phases. Further work by Jantzen & Brown [77] showed that waste glasses with less than 50 wt.% SiO_2 may also result in nepheline crystallisation with the potential of tetrahedral Fe^{3+} occupying a site in the nepheline structure.

One solution to mitigate secondary phase stabilisation and accumulation of said phases, is to increase the temperature of the melt, as suggested by Marra *et al*. [75]. However, there are several components that are likely to volatise at higher temperatures. Gin *et al*. [92] provided a good review on the solubility of radioisotopes such as the volatile radioactive halides (Cl-36, and I-129), technetium, and caesium. It was found that a variety of factors, including the starting phase of the radioisotope and the oxidation state greatly influence the retention factor, R. It was also noted that components such as noble metals (e.g. Pd) are largely insoluble and will precipitate as alloys or oxides in the melter [92]. For the Hanford site, Langowski *et al*. [93] studied the volatility of technetium through the use of rhenium surrogate, to study Tc volatilisation in low-level waste (LLW, now referred to as LAW). Through the studies, it was shown that even at lab scale experiments, the volatilisation of Tc and Re will occur at temperatures as low as 900 ºC, which is 250 ºC cooler than the expected operational temperatures of the Hanford melters. The precursor materials of the Re bearing “waste” component was found to be a key parameter is volatilisation. Ammonium perrhenate (NH_4ReO_4) raw materials were found to lose as much as 97% of the Re to volatilisation, however, other materials, such as caesium perrhenate ($CeReO_4$), were found to lose as much as 36% of the Re to volatilisation [93]. Matlack *et al*. [94] aimed to improve the technetium retention in LAW waste melts. The study found that nitrate wastes were promoting the volatilisation of

technetium and other volatiles, and that ferrous oxalate (FeC_2O_4) as an additive was found to improve the retention of volatiles by using the nitrate components as an oxidiser to form ferric iron in the waste [94]. Volatilisation remains a concern for the Hanford site, with species such as Cs, Tc, and I having volatile isotopes. Further work is still being done to better understand the volatilisation of radioisotopes and what can be done to prevent the release of the volatile radioisotopes.

1.6 Summary

Throughout the lifetime of the Hanford site, there was vast amounts of radioactive waste produced at the Hanford site, with the most problematic wastes being stored in steel tanks that have exceeded their expected lifetimes. These wastes are highly complex due to the various extractions processes employed across the Hanford site, as well as the mixing of wastes in the form of transferring wastes between tanks for space management and recovery processes, such as the Cs-recovery and U-recovery.

The legal mandate to remediate the Hanford site was officially recognised in 1989 when the Hanford Federal Facility Agreement and Consent Order, which is commonly referred to as the "Tri-Party Agreement", was agreed between the US Department of Energy, the Washington state Department of Ecology, and the Environmental Protection Agency. The early research into how to process the waste so that the radionuclides were immobilised and the waste could be easily managed, focussed on vitrification into a stable glass matrix, with borosilicate and phosphate glasses emerging as early candidates. Borosilicate glass was ultimately chosen for low melting temperature, ability to dissolve a wide range of waste components, being highly resistant to dissolution, while also being far less corrosive to the melters than phosphate glasses. Borosilicate glass was used successfully at the DWPF facility in the Savannah River Site, with lessons learned from this success applied to the Hanford site. The Hanford waste and the methods to be applied at the Hanford site, however, remain unique and a lot of research has been done, and continues to be done on how the complexities of the waste will affect the long term stabilisation of the waste, while also maintaining as good a cost effectiveness and risk management strategy as possible.

In the present day, the large-scale vitrification program has yet to fully commence. The direct feed low-activity waste (DFLAW) plant is currently undergoing commissioning prior to full scale start up (as of December 2022 [95]) with the high-level waste plant set to follow on a decade later [96]. A lot of the research continues to focus on the limiting

factors that are pertinent to the complex Hanford wastes, such as the secondary phase stabilisation as a function of high levels of alumina and transition metals in wastes, better understanding the thermal and chemical profile of the “cold cap” and understanding the trickier elements to vitrify such as the volatiles.

This research will focus on the iron within the Hanford wastes, specifically how high concentrations of iron oxide will affect the final waste forms when the vitrification begins in earnest. As has been discussed in Chapters 1.3, iron has primarily been introduced into the waste through the use of ferrous based reducing agents in the plutonium and uranium extraction processes utilised during the active lifetime of the Hanford site [9-11,14]. With the waste set to be vitrified into borosilicate glass for long term disposal, the effects of high concentrations of iron must be better understood. Studies around the expected Hanford waste forms, show that iron has been linked with spinel [64] and nepheline crystallisation [77,85], as well as being linked to retention of certain volatile components during the melt process, and it also has a mixed influence on the chemical durability [97-99]. Thereforeee, there is a clear need to better understand how high concentrations of iron influence the network and associated properties of borosilicate glasses, so that high-Fe waste can be vitrified and stored in as efficient manner as possible.

1.7 References

[1] Gephart, R. E., Hanford: A conversation about nuclear waste and cleanup, Battelle Press, Columbus, OH, USA, 2003.

[2] Gephart, R. E., A short history of waste management at the Hanford site, *Phys. Chem. Earth*, **35**, 2010; pp 298-306.

[3] NO SPECIFIED AUTHOR, Nonproliferation and arms control assessment of weapons-usable fissile material storage and excess plutonium disposition alternatives, United States Department of Energy, *DOE/NN-0007*, 1997.

[4] Zheng, X. J., Deng, B. Q., Ou, W., & Gou, F., Conversion of U-238 and Th-232 using a fusion neutron source, *World J. Nucl. Sci. Tech.*, **4**, 2014; pp 222-227.

[5] United States Geological Survey, *Uranium*, 2022. (URL: https://pubs.usgs.gov/of/2004/1050/PalosVerdesRn.htm#uranium.htm Accessed at: November 2022)

[6] Choppin, G. R., Liljenzin, J.-O., & Rydberg, J., Chapter 21 - The Nuclear Fuel Cycle, in 'Radiochemistry and Nuclear Chemistry 4th Ed.', Academic Press, Amsterdam, Netherlands, 2013.

[7] Peterson, R. A. Buck, E. C., Chun, J., Daniel, R. C., Herting, D. L., Ilton, E. S., Lumetta, G. J., & Clark, S. B., Review of the scientific understanding of radioactive waste at the U.S. DOE Hanford site, *Environ. Sci. Technol.*, **52**, 2018; pp 381-396.

[8] Agnew, S. F., Boyer, J., Corbin, R. A., Duran, T. A., FitzPatrick, J. R., Jurgensen, K. A., Ortiz, T. P., & Young, B. L., Hanford tank chemical and radionuclide inventories: HDW Model Rev. 4., Los Alamos National Laboratory. *LA-UR-96-3860*, 1997.

[9] Marceau, T. E., Harvey, D. W., Stapp, D. C., Cannon, S. D., Conway, C. A., Deford, D. H., Freer, B. J., Gerber, M. S., Keating, J. K., Noonan, C. F., & Weisskopf, G., Hanford Site Historic District: History of the Plutonium Production facilities 1943 – 1990, Battelle Press, Columbus, OH, USA, 2003.

[10] Gray, L. W., Holliday, K. S., Murray, A., Thompson, M., Thorp, D. T., Yarbro, S., & Venetz, T. J., Separation of plutonium from irradiated fuels and targets, Lawrence Livermore National Laboratory, *LLNL-TR-677668*, 2015.

[11] Thompson, S. G., & Seaborg, G. T., Bismuth phosphate process for the separation of plutonium from aqueous solutions, US2785951A, United States Patent and Trademark Office (USPTO), 1944.

[12] Seaborg, G. T., Extraction method for separating uranium, plutonium, and fission products from compositions containing same, US2811415A, United States Patent and Trademark Office (USPTO), 1957.

[13] Irish, E. R., Description of the PUREX plant process, Hanford Atomic Products Operation General Electric Company, *HW-60116*, 1959.

[14] Herbst, R. S., Baron, P., & Nilsson, M., Chapter 6: Standard and advanced separation: PUREX processes for nuclear fuel reprocessing, in 'Advanced Separation Techniques for Nuclear Fuel Reprocessing and Radioactive Waste Treatment' Ed. By Nash, K. L. & Lumetta, G. J., Woodhead Publishing, Cambridge, UK, 2011.

[15] Anderson, J. D., A history of the 200 Area tank farms, Westinghouse Hanford Company, *WHC-MR-0132*, 1990.

[16] NO SPECIFIED AUTHOR, Tank Leak Assessment Process: Technical Background, Rev. 0, Lockheed Martin Hanford Corp., *HNF-3747*, 1998.

[17] United States Department of Energy, Photos of Tank Farms, 2021. (URL: https://www.hanford.gov/tocpmm/page.cfm/WhoWeAre/PhotosofTankFarms Accessed at: March 2023)

[18] Johnson, M. E., Hanford A and AX-Farm leak assessments report: 241-A-103, 241-A-104, 241-A-105, 241-AX-102, 241-AX-104 and unplanned waste releases, CH2MHill Hanford Group Inc., *RRP-ENV-37956 Revision 1*, 2008.

[19] NO SPECIFIED AUTHOR, Evaluations of tanks 241-B-203 and 241-B-204 level data and in-tank video inspections, Washington River Protection Solutions, *RPP-RPT-55265 Revision 0*, (No Year Specified, report indicates no older than 2013).

[20] Field, J. G., Fort, L. A., & Wood, M., Hanford BX-Farm leak assessments report, Washington River Protection Solutions, *RPP-RPT-47562 Revision 0*, 2011.

[21] Field, J. G., Barton, J. M., Hedel, B. N., Fort, L. A., & Wood, M., Hanford BY-Farm leak assessments report, Washington River Protection Solutions, *RPP-RPT-43704 Revision 0*, 2011.

[22] Field, J. G., & Johnson, M. E., Hanford C-Farm leak assessments report: 241-C-101, 241-C-110, 241-C-111, 241-C-105 and unplanned waste releases, CH2MHill Hanford Group Inc., *RPP-ENV-33418 Revision 1*, 2008.

[23] Johnson, M. E., & Field, J. G., Hanford SX-Farm leak assessments report, Washington River Protection Solutions, *RPP-ENV-39658 Revision 0*, 2010.

[24] Field, J. G., Single-shell tank farm leak inventory assessments summary, Washington River Protection Solutions, *RPP-RPT-61279 Revision 0*, 2019.

[25] Jones, T. E., Simpson, B. C., Wood, M. I., & Corbin, R. A., Preliminary inventory estimates for single-shell tank leaks in T, TX, and TY tank farms, CH2MHILL Hanford Group Inc., *RPP-7218 Revision 0*, 2000.

[26] NO AUTHOR SPECIFIED, Evaluations of tanks 241-T-203 and 241-T-204 level data and in-tank video inspections, Washington River Protection Solutions, *RPP-RPT-55264 Revision 0*, (No Year Specified, report indicates no older than 2012).

[27] Field, J. G., Hedel, B., & Wood, M., Hanford TY-farm leak assessments report, Washington River Protection Solutions, *RPP-RPT-42296 Revision 0*, 2010.

[28] Um, W., Wang, Z., Serne, R. J., Williams, B. D., Brown, C. F., Dodge, C. J., & Francis, A. J., Uranium phases in contaminated sediments below Hanford's U tank farm, *Environ. Sci. Technol.*, **43**, 2009; pp 4280-4286.

[29] Engeman, J. K., Girardot, C. L., Harlow, D. G., & Rosenkrance, C. L., Tank 241-AY-102 leak assessment report, Washington River Protection Solutions, *RPP-ASMT-53793 Revision 0*, 2012.

[30] Barnes, T. J., & Gunter, J. R., 241-AY-101 tank construction extent of condition review for tank integrity, Washington River Protection Solutions, *RPP-RPT-54817 Revision 0*, 2013.

[31] NO SPECIFIED AUTHOR, Hanford cleanup: DOE's efforts to close tank farms would benefit from clearer legal authorities and communication, United States Government Accountability Office, *GAO-21-73*, 2021.

[32] United States Environmental Protection Agency, *Summary of the Resource Conservation and Recovery Act*, Updated 12/09/2022. (Accessed at: https://www.epa.gov/laws-regulations/summary-resource-conservation-and-recovery-act)

[33] United States Environmental Protection Agency, *Summary of the Comprehensive Environmental Response, Compensation, and Liability Act (Superfund)*, Updated 12/09/2022. (Accessed at: https://www.epa.gov/laws-regulations/summary-comprehensive-environmental-response-compensation-and-liability-act).

[34] United States Department of Energy, *Tri-Party Agreement*, Updated 20/12/2022. (Accessed at: https://www.hanford.gov/page.cfm/TriParty).

[35] McElroy, J. L., Schneider, K. J., Hartley, J. N., Mendel, J. E., Richardson, G. L., McKee, R. W., & Blasewitz, A. G., Waste solidification program summary report volume 11: Evaluation of WSEP high level waste solidification processes, Battelle Pacific Northwest Laboratories, *BNWL-1667*, 1972.

[36] Tuthill, E. J., Weth, G. G., Emma, L. C., Strickland, G., & Hatch, L. P., Phosphate glass process for disposal of high level radioactive wastes, *Ind. Eng. Chem. Proc. Des. Dev.*, **6**, 1967; pp 314-321.

[37] Kelley, J. A., Evaluation of glass as a matrix for solidification of Savannah River plant waste, E. I. du Pont de Nemours & Company, Savannah River Laboratory, *DP-1397*, 1975.

[38] Jantzen, C. M., Systems approach to nuclear waste glass development, *J. Non-Cryst. Solids*, **84**, 1985; pp 215-225.

[39] Metcalfe, B. L., & Donald, I. W., Chapter 25: Management of radioactive waste (RAW) from nuclear weapons programmes, in 'Radioactive Waste Management and Contaminated Site Clean-Up: Processes, Technologies and International Experience' Ed. By Lee, W. E., Ojovan, M. I., & Jantzen, C. M., Woodhead Publishing, Cambridge, UK, 2013.

[40] Matlack, K. S., Pegg, I., Kot, W. K., & Joseph, I., Support for HLW direct deed - Phase 2, Vitreous State Laboratory, *VSL-15R3440-1*, 2015.

[41] Tan, S., Chapter 26: Glass-based stabilization/solidification of radioactive waste, in 'Low Carbon Stabilization and Solidification of Hazardous Wastes' Ed. By Tsang, D. & Wang, L., Elsevier, Amsterdam, Netherlands, 2022.

[42] Blair, H. T., & Lukacs, J. M., Investigation of foaming during nuclear defense-waste solidification by electric melting, Pacific Northwest Laboratory, *PNL-3552*, 1980.

[43] Lee, S.-M., Hrma, P., Pokorný, R., Klouzek, J., VanderVeer, B. J., Dixon, D. R., Luksic, S. A., Rodriguez, C. P., Chun, J., Schweiger, M. J., & Kruger, A. A., Effect of melter feed foaming on heat flux to the cold cap, *J. Nucl. Mater.*, **496**, 2017; pp 54-65.

[44] Lee, S.-M., Hrma, P., Pokorný, R., Klouzek, J., Eaton, W. C., & Kruger, A. A., Glass production rate in electric furnaces for radioactive waste vitrification, *J. Am. Ceram. Soc.*, **102**, 2019; pp 5828-5842.

[45] Pokorny, R., & Hrma, P., Model for the conversion of nuclear waste melter feed to glass, *J. Nucl. Mater.*, **445**, 2014; pp 190-199.

[46] Pokorny, R., Hilliard, Z. J., Dixon, D. R., Schweiger, M. J., Guillen, D. P., Kruger, A. A., & Hrma, P., One-dimensional cold cap model for melters with bubblers, *J. Am. Ceram. Soc.*, **98**, 2015; pp 3112-3118.

[47] Dixon, D. R., Schweiger, M. J., Riley, B. J., Pokorny, R., & Hrma, P., Temperature distribution within a cold cap during nuclear waste vitrification, *Environ. Sci. Technol.*, **49**, 2015; pp 8856-8863.

[48] Guillen, D. P., Abboud, A. W., Pokorny, R., Eaton, W. C., Dixon, D. Fox, K., & Kruger, A. A., Development of a validation approach for an integrated waste glass melter model, *Nucl. Technol.*, **203**, 2018; pp 244-260.

[49] Hrma, P., Pokorny, R., Lee, S.-M., & Kruger, A. A., Heat transfer from glass melt to cold cap: Melting rate correlation equation, *Int. J. Appl. Glass Sci.*, **10**, 2019; pp 143-150.

[50] Rigby, J. C., Dixon, D. R., Cutforth, D. A., Marcial, J., Kloužek, J., Pokorný, R., Kruger, A. A., Scrimshire, A., Bell, A. M. T., & Bingham, P. A., Melting behaviour of simulated radioactive waste as functions of different redox iron-bearing raw materials, *J. Nucl. Mater*., **569**, 2022.

[51] Beerkens, R. D. C., & van der Schaaf, J., Gas release and foam formation during melting and fining of glass, *J. Am. Ceram. Soc.*, **89**, 2006; pp 24-35.

[52] Goldman, D. S., Melt foaming, foam stability and redox in nuclear waste vitrification, *J. Non-Cryst. Solids*, **84**, 1986; pp 292-298.

[53] Jin, T., Chun, J., Dixon, D. R., Kim, D.-S., Crum, J. V., Bonham, C. C., VanderVeer, B. J., Rodriguez, C. P., Weese, B. L., Schweiger, M. J., Kruger, A. A., & Hrma, P., Melter feed viscosity during conversion to glass: Comparison between low-activity waste and high-level waste feeds, *J. Am. Ceram. Soc.*, **101**, 2018; pp 1880-1891.

[54] McCarthy, B. P., George J. L., Dixon, D. R., Wheeler, M., Cutforth, D. A., Hrma, P., Linn, D., Chun, J., Hujova, M., Kruger, A. A., & Pokorny, R., Rheology of simulated radioactive waste slurry and cold cap during vitrification, *J. Am. Ceram. Soc.*, **101**, 2018; pp 5020-5029.

[55] Hilliard, Z., & Hrma, P., A method for determining bulk density, material density, and porosity of melter feed during nuclear waste vitrification, *J. Am. Ceram. Soc.*, **99**, 2016; pp 98-105.

[56] Harris, W. H., Guillen, D. P., Kloužek, J., Pokorný, R., Yano, T., Lee, S,-M., Schweiger, M. J., & Hrma, P., X-ray tomography of feed-to-glass transition of simulated borosilicate waste glasses, *J. Am. Ceram. Soc.*, **100**, 2017; pp 3883-3894.

[57] Goel, A., McCloy, J. S., Pokorný, R., & Kruger, A. A., Challenges with vitrification of Hanford High-Level Waste (HLW) to borosilicate glass – An overview, *J. Non-Cryst. Solids: X*, **4**, 2019.

[58] Selkregg, K., Fusion cast refractories: Roles of containment, *Am. Ceram. Soc. Bull.*, **97**, 2018; pp 21-28.

[59] Muller, I. S., Pegg, I. L., Chaudhuri, M., Gilbo, K., & Joseph, I., Final Report: K-3 Refractory Corrosion and Sulfate Solubility Model Enhancement, Vitreous State Laboratory, *VSL-18R4360-1 Rev. 0*, 2018.

[60] Jantzen, C. M., Imrich, K. J., Picket, J. B., & Brown, K. G., High chrome refractory characterization: Part I. Impact of melt reduction/oxidation on the corrosion mechanism, *Int. J. Appl. Glass Sci.*, **6**, 2015; pp 137-157.

[61] Jantzen, C. M., Imrich, K. J., Picket, J. B., & Brown, K. G., High chrome refractory characterization: Part II. Accumulation of spinel corrosion deposits in radioactive waste glass melters, *Int. J. Appl. Glass Sci.*, **6**, 2015; pp 158-171.

[62] Vienna, J. D., Hrma, P., Crum, J. V., & Mika, M., Liquidus temperature-composition model for multi-component glasses in the Fe, Cr, Ni, and Mn spinel primary phase field, *J. Non-Cryst. Solids*, **292**, 2001; pp 1-24.

[63] Jiricka, M., Hrma, P., & Vienna, J. D., The effect of composition on spinel crystals equilibrium in low-silica high-level waste glasses, *J. Non-Cryst. Solids*, **319**, 2003; pp 280-288.

[64] Jantzen, C. M., & Brown, K. G., Predicting the spinel-nepheline liquidus for application to nuclear waste glass processing. Part I: Primary phase analysis, liquidus measurement, and quasicrystalline approach, *J. Am. Ceram. Soc.*, **90**, 2007; pp 1866-1879.

[65] Hrma, P., Crystallization during processing of nuclear waste glass, *J. Non-Cryst. Solids*, **356**, 2010; pp 3019-3025.

[66] Fox, K. M., Crystallization in High Level Waste (HLW) Glass Melters: Operational Experience from the Savannah River Site, Savannah River National Laboratory, *SRNL-STI-2013-00724*, 2014.

[67] Hrma, P., Riley, B. J., Crum, J. V., & Matyas, J., The effect of high-level waste glass composition on spinel liquidus temperature, *J. Non-Cryst. Solids*, **384**, 2014; pp 32-40.

[68] Fox, K. M., & Fowley, M. D., Crystal Accumulation in the Hanford Waste Treatment Plant High Level Waste Melter: Summary of 2017 Experiments, Savannah River National Laboratory, *SRNL-STI-2017-00730 Revision 0*, 2018.

[69] Matyáš, J., Crum, J., Vienna, J., Arrigoni, A., Schaible, M., Tate, R., & Rodriguez, C., Development of crystal-tolerant high-level waste glasses, Pacific Northwest National Laboratory, *PNNL-20072*, 2010.

[70] Kim, D.-S., Schweiger, M. J., Rodriguez, C. P., Lepry, W. C., Lang, J. B., Crum, J. V., Vienna, J. D., Johnson, F., Marra, J. C., & Peeler, D. K., Formulation and characterization of waste glass with varying processing temperatures, Pacific Northwest National Laboratory, *PNNL-20774*, 2011.

[71] Matyáš, J., Huckleberry, A. R., Rodriguez, C. P., Lang, J. B., Owen, A. T., & Kruger, A. A., Crystal-tolerant glass approach for mitigation of crystal accumulation in continuous melters processing radioactive waste, Office of River Protection, *ORP-52717*, 2013.

[72] Matyáš, J., Schaible, M. J., & Vienna, J., Determination of Stokes Shape Factor for Single Particles and Agglomerates, *Ceram. Trans.*, **227**, 2011; pp 195-202.

[73] Vienna, J. D., Skorski, D. C., Kim, D.-S., & Matyas, J., Glass property models and constraints for estimating the glass to be produced at Hanford by implementing current advanced glass formulation efforts, Pacific Northwest National Laboratory, *PNNL-22631 Rev. 1*, 2013.

[74] Matyáš, J., Vienna, J. D., Peeler, D. K., Fox, K. M., Herman, C. C., & Kruger, A. A., Road map for development of crystal-tolerant high level waste glasses, Pacific Northwest National Laboratory, *PNNL-23363*, 2014.

[75] Marra, J. C., & Kim, D.-S., Towards increased waste loading in high level waste glasses: developing a better understanding of crystallization behavior, *Proc. Mater. Sci.*, **7**, 2014; pp 87-92.

[76] Li, H., Hrma, P., Vienna, J. D., Qian, M., Su, Y., & Smith, D. E., Effects of Al_2O_3, B_2O_3, Na_2O, and SiO_2 on nepheline formation in borosilicate glasses: Chemical and physical correlations, *J. Non-Cryst. Solids*, **331**, 2003; pp 202-216.

[77] Jantzen, C. M., & Brown, K. G., Predicting the spinel-nepheline liquidus for application to nuclear waste glass processing. Part II: Quasicrystalline freezing point depression model, *J. Am. Ceram. Soc*., **90**, 2007; pp 1880-1891.

[78] Fox, K. M., Edwards, T. B., & Peeler, D. K., Control of nepheline crystallization in nuclear waste glass, *Int. J. Appl. Ceram. Technol.*, **5**, 2008; pp 666-673.

[79] McCloy, J. S., Schweiger, M. J., Rodriguez, C. P., & Vienna, J. D., Nepheline crystallization in nuclear waste glasses: Progress toward acceptance of high-alumina formulations, *Int. J. Appl. Glass Sci.*, **2**, 2011; pp 201-214.

[80] Rodriguez, C. P., McCloy, J. S., Schweiger, M. J., Crum, J. V. & Winschell, A., Optical Basicity and Nepheline Crystallization in High Alumina Glasses, Pacific Northwest National Laboratory, *PNNL-20184*, 2011.

[81] Pareizs, J. M., Sludge batch 7b qualification activities with SRS tank farm sludge, Savannah River National Laboratory, *SRNL-STI-2011-00548 Revision 0*, 2011.

[82] Vienna, J. D., Kim, D.-S., Schweiger, M. J., Piepel, G. F., & Kruger, A. A., Glass Formulation and Testing for U.S. High-Level Tank Wastes Project 17210 Year 1 Status Report: October 15, 2014, Pacific Northwest National Laboratory, *PNNL-SA-84872*, 2014.

[83] Marcial, J., Crum, J., Neill, O., & McCloy, J., Nepheline structural and chemical dependence on melt composition, *Am. Mineral.*, **101**, 2016; pp 266-276.

[84] Fox, K. M., Edwards, T. B., & McClane, D. L., Chemical composition analysis and product consistency tests supporting refinement of the nepheline model for the high aluminum Hanford glass composition region, Savannah River National Laboratory, *SRNL-STI-2016-00028 Revision 0*, 2016.

[85] Ahmadzadeh, M., Marcial, J., & McCloy, J., Crystallization of iron-containing sodium aluminosilicate glasses in the $NaAlSiO_4$-$NaFeSiO_4$ join, *J. Geophys. Res. Solid Earth*, **122**, 2017;

[86] Vienna, J. D., Kroll, J. O., Hrma, P. R., Lang, J. B., & Crum, J. V., Submixture model to predict nepheline precipitation in waste glasses, *Int. J. Appl. Glass Sci.*, **8**, 2017; pp 143-157.

[87] Deshkar, A., Ahmadzadeh, M., Scrimshire, A., Han, E., Bingham, P. A., Guillen, D., McCloy, J., & Goel, A., Crystallization behavior of iron- and boron-containing nepheline ($Na_2O{\cdot}Al_2O_3{\cdot}2SiO_2$) based model high-level nuclear waste glasses, *J. Am. Ceram. Soc.*, **102**, 2018;

[88] Ahmadzadeh, M., Olds, T. A., Scrimshire, A., Bingham, P. A., McCloy, J. S., Structure and properties of $Na_5FeSi_4O_{12}$ crystallized from $5Na_2O–Fe_2O_3–8SiO_2$ glass, *Acta. Cryst.*, **C74**, 2018; pp 1595-1602.

[89] Marcial, J., Kabel, J., Saleh, M., Washton, N., Shaharyar, Y., Goel, A., & McCloy, J. S., Structural dependence of crystallization in glasses along the nepheline ($NaAlSiO_4$) - eucryptite ($LiAlSiO_4$) join, *J. Am. Ceram. Soc.*, **101**, 2018; pp 2840-2855.

[90] McClane, D. L., Amoroso, J. W., Fox, K. M., & Kruger, A. A., Nepheline crystallization behavior in simulated high-level waste glasses, *J. Non-Cryst. Solids*, **505**, 2019; pp 215-224.

[91] Amoroso, J. W., McClane, D. L., & Fox, K. M., Nucleation and crystal growth behavior of nepheline in simulated high-level waste glasses, Savannah River National Laboratory, *SRNL-STI-2017-00517 Revision 0*, 2017.

[92] Gin, S., Jollivet, P., Tribet, M., Peuget, S., & Schuller, S., Radionuclides containment in nuclear glasses: An overview, *Radiochim. Acta*, **105**, 2017; pp 927-959.

[93] Langowski, M. H., Darab, J. G., & Smith, P. A., Volatility literature of chlorine, iodine, cesium, strontium, technetium, and rhenium; Technetium and rhenium volatility testing, Pacific Northwest National Laboratory, *PNNL-11052*, 1996.

[94] Matlack, K. S., Pegg, I. L., D'Angelo, N., Bardkci, T., Muller, I., Callow, R. A., & Joseph, I., Improving technetium retention in Hanford LAW glass - Phase 2, Vitreous State Laboratory, *VSL-11R2260-1*, 2011.

[95] United States Department of Energy, *Direct-Feed Low-Activity Waste Program*, 2022. (URL: https://www.hanford.gov/files.cfm/DFLAW_Fact_Sheet_Dec2022.pdf Accessed at: January 2023).

[96] United States Department of Energy, *Waste Treatment and Immobilization Plant*, 2022. (URL: https://www.hanford.gov/files.cfm/WTP_Fact_Sheet_Nov2022.pdf Accessed at: January 2023).

[97] Cunnane, J. C., Bates, J. K., Bradley, C. R., Buck, E. C., Ebert, W. L., Feng, X., Mazer, J. J., Wronkiewicz, D. J., Sproull, J., McGraill, B. P., & Altenhofen, M. K., High-Level Waste Borosilicate Glass: A Compendium of Corrosion Characteristics, Volume II, US DoE Office of Waste Management, 1994.

[98] Nogues, J. L., & Hench, L. L., Effect of Fe_2O_3/ZnO on two glass compositions for solidification of Swedish nuclear wastes, *Mat. Res. Soc. Symp. Proc.*, **11**, 1982; pp 273-278.

[99] Van Iseghem, P., Timmermans, W., & De Batist, R., Corrosion behavior of TRUW base and reference glasses, *Mat. Res. Soc. Symp. Proc.*, **26**, 1984; pp 527-534.

Chapter 2 – Project Overview

This PhD project will aim to characterise the property, composition, phase properties of glass waste forms expected from the vitrification of high-Fe Hanford wastes. As mentioned in Chapter 1, there are expected wastes within the Hanford site that will be high in Fe-bearing oxides and compounds due to the use of ferrous and ferric based chemicals in the plutonium and uranium extraction processes. Iron has also been linked to numerous limiting factors, such as secondary phase crystallisation and chemical durability. This research aims to research the influence iron has on the borosilicate glass network and the associated properties. With iron being the element of interest, the various properties will be investigated as a function of varying the iron oxide contents within the glass to establish whether and how these properties vary, to further understand the influence of the iron oxide on the final glass waste form. To address this, some questions must be answered by literature: What is a glass? How has iron oxide been used in glasses historically? How has glass been used to vitrify radioactive wastes? How does iron within the glass impact this?

2.1 Glass Science Overview

2.1.1 What is a glass?

Another element to consider is the nature of glass. The term “glass structure” is a misnomer as it implies there is a well-defined system in which the network will form, as is the case with crystal structures. Crystalline structures have well defined bond angles, lengths, and types to create a single unit that repeats isometrically. Glass is amorphous and does not have well defined bond angles which creates an infinitely non-repeating network that forms the vitreous material (**Fig. 2.1**) [1].

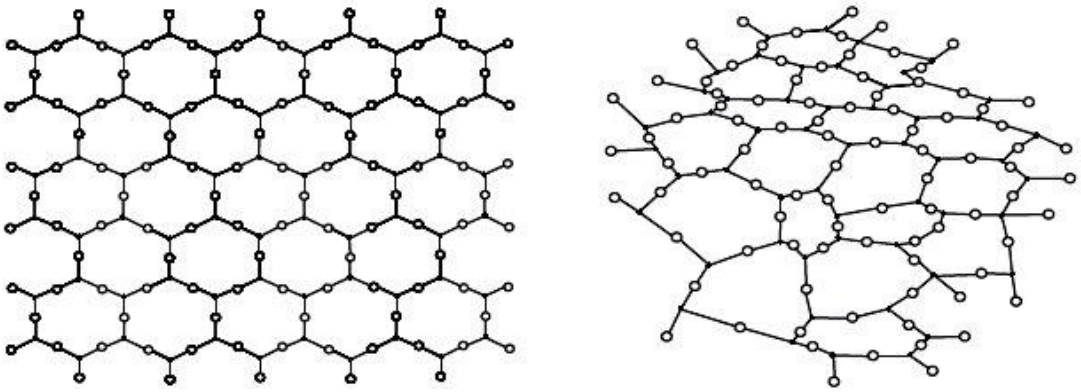

Figure 2.1: *Crystalline structure of quartz (left) and amorphous structure of fused quartz (right) [1].*

Ojovan *et al*. [2] summed up glass as being an amorphous solid below the glass transition temperature (T_g), with T_g being the temperature above which the solid glass will being forming liquid phases. Ojovan and Lee [3] also noted that glasses below the T_g may resemble a liquid in terms of the presence of configurons (network breaking bonds). However, below T_g there is no percolation of bonds and the configurons are largely isolated, but above T_g the configurons tend to percolate into clusters.

The other aspect to glass formation is cooling rate of a material, widely described as the kinetics of glass formation. Avrami published a series of papers [4-6] on the kinetics of phase changes, which began by studying the kinetics of crystal aggregation and showing that for any substance there is a range of temperature and concentration of "germ" nuclei (better known as the "seed" nuclei from which the secondary phase will grow from) in which the kinetics of phase change are equal [4]. This theory was further developed to include considerations of shape and volume of the secondary phase [5], and further so to consider the densities and distributions of the "germ nuclei" (which was then changed to "nucleus" or "grain" depending on the cluster size) [6]. Ulhmann specifically studied the kinetics of glass formation [7]. Uhlmann showed that for a glass to form, there needs to be a sufficient cooling rate and a sufficiently high viscosity. Time-Temperature-Transformation curves can be used to extract critical information to predict how likely a molecule will form a glass [7].

Shelby [8] provided a succinct summary of the kinetic theory for glass formation to show that for any material, it is not a question of "if a material can form a glass", it is a question

of "how fast must a material be cooled to form a glass" [8]. For a glass, the general TTT curve can be seen in **Fig 2.2**.

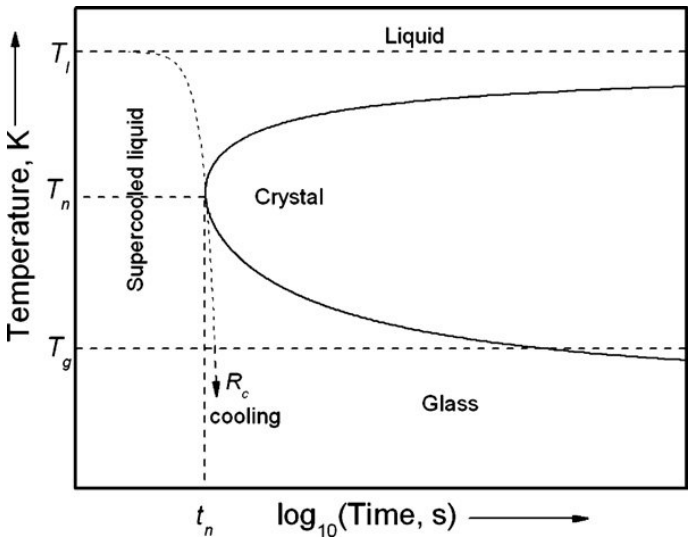

Figure 2.2: *The general TTT curve for a glass [9]. This will vary with material type.*

The TTT curve shows a general view of what the kinetic theory of glass formation for a material looks like. Below T_g the material is a solid, above T_l (referred to as the liquidus temperature) the material is a homogenous liquid melt. For material to form a glass, it must be cooled in such a time that the Time-Temperature line does not pass through the crystal region. Should it do so, secondary crystalline phases will nucleate and grow within this region and the resulting material will have at least two phases [8].

2.1.2 Glass Formation

The structural theory of glass formation focusses more on the composition of the glass, rather than the nature of the melt and kinetics. Zachariasen [10] published the most widely known papers on the nature of glass structure. He used Pauling's coordination number and edge sharing rules [11] to create four fundamental rules for oxides to be considered glass formers:

1) An oxygen atom is linked to not more than two cations.

2) The number of oxygens surrounding the cations must be small (Coordination Number (CN) ≤ 4).

3) The oxygen polyhedra share corners with each other, not edges or faces.

4) At least three corners in each polyhedron must be shared (for the network to be 3-dimensional) [10].

The definitions for the coordination number rule and corner sharing rule were derived from using Linus Pauling's radius ratio rule and the face sharing rule (Equation 2.1) [11].

$$r_c / r_a \leq 0.414 \quad \text{(Eq. 2.1)}$$

r_c = Atomic Radius of the Cation

r_a = Atomic Radius of the anion

Zachariasen stated that a glass network consists of corner sharing trigonal or tetrahedral units in non-repeating isometrical fashion, owing to variations in bond angle and length from crystalline analogues [10]. This was termed the "Random Network Theory" despite Zachariasen himself, never referring to glass networks as "Random".

Further work was investigated by Stanworth, employing another of one Pauling's equations to document the nature of network forming bonds [12] (Equation 2.2) [11], and Sun investigating bond strength of glass network forming bonds [13]. Stanworth noted that glass network forming bonds had a fractional ionic character of approximately 50%, noting the bonds were a hybridisation of covalent and ionic bonding. It was noted that purely ionic bonds had enough freedom to organise into orthodox crystalline configurations, whereas purely covalent bonds do not have the freedom to have significantly varied bond angles or lengths and would be forced to form to a crystalline network. To satisfy the glass formation rules, glass forming bonds must have some degree of covalent and ionic character to them. Sun noted that the network forming bonds had far higher single bond strengths than glass modifying bonds [13].

$$\text{Fractional ionic bond character} = \text{Exp}(-0.25*(\Delta X_e)^2) \quad \text{(Eq. 2.2)}$$

ΔX_e = Difference in electronegativity between the cation and anion

Network modifiers are oxides which do not satisfy Zachariasen's rules for coordination numbers and edge sharing [10]. Stanworth noted that network modifier bonds had much higher fractional ionic character than network forming bonds [12], while Sun noted that the single bond strength of modifier bonds were far lower than former bonds [13]. From this we can say that where network formers form high energy bonds, network modifiers form weaker, ionic bonds. Network intermediates are components that can exist as both within the glass, including simultaneously.

Building on the established "Random Network Theory" put forth by Zachariasen, Greaves published a similarly famous paper which proposed the "Modified Random Network" Theory [14], which is visually represented in **Fig. 2.3**.

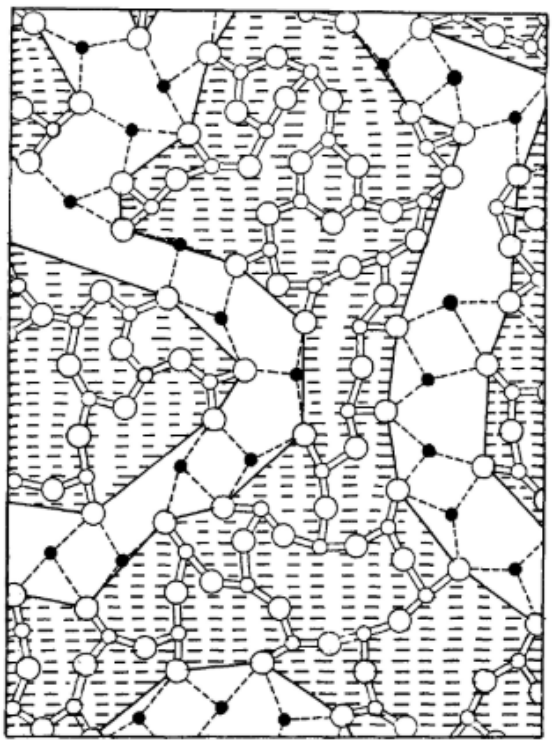

Figure 2.3: *The visual representation of the modified random network theory. The description is directly quoted from the paper [14]: "A modified random network (MRN) for a "2-dimensional" oxide glass. The nominal composition is $M_2O_3(G_2O_3)_2$, where M's are modifying cations and G's are network forming cations. Covalent bonds are shown by the solid lines and ionic bonds by the dotted lines. The shaded regions are defined by the boundary disclinations which run through the G-O (non-bridging) bonds. These highlight the percolation channels of M_2O_3 that run through the network."*

The theory was proposed on the basis of extensive Extended X-ray Absorption – Fine Structure (EXAFS) spectroscopic studies that demonstrated that while there are deviations in the bond lengths, the deviations are finite and therefore there is likely some form of short-range order in the bond arrangements in glass. EXAFS studies were done on silicon thin films, sodium silicate glass, calcium silicate glass, mineral glasses, and Fe^{3+} bearing glasses, with the data reviewed. The studies showed that there were clear environments for the network forming and modifying cations, which somewhat contradicted early assumptions on what network modifiers were and the nature of their interactions with non-bridging oxygens. Initially it was thought that the non-bridging

oxygens simply did not bond any further and that network modifiers essentially acted as interstitial charge compensators [8] (see **Fig. 2.3**). This cannot be true, if there are measurable environments for the modifier cations that can be linked to non-bridging oxygens, which is exactly what was shown by Greaves [14]. Therefore the MRN theory presents the notion that there must be some resolvable short-range and even medium-range order within a glass network, even if the network lacks the clarity and predictability of a "unit cell" used in crystallography.

2.2 Silicate, Borate, and Borosilicate Glass

2.2.1 Overview

Borosilicate glass is an oxide glass matrix in which the primary glass forming oxides are silica (SiO_2) and boric oxide (B_2O_3). As a family of glass, it has found widespread commercial importance for its resistance to thermal shock, high chemical durability and favourable processing temperatures, which has led to widespread use in the culinary industry as well as use as labware. The most commonly recognisable brand being Pyrex glass [8].

2.2.2 Silicate Glasses

To understand borosilicate glasses, it is prudent to introduce to initial silicate and borate glass matrices as they are, before discussing the combined matrix. Silicate glasses are the simplest glass matrix, owing to the fact that silica in glass will exist solely as Si^{4+} tetrahedra. Fused quartz (sometimes referred to as fused silica) is a type of glass that consists solely of silica tetrahedra. It is a highly durable material [8], however, it requires very hot temperatures to produce [15]. Thereforeee, most commercial silica glasses are fluxed with alkali, or alkaline earth metal oxides to reduce the melting temperature. In the case of float glass, silica is fluxed with both alkali and alkaline earth metal oxides, specifically sodium oxide and calcium oxide to give rise to the name soda-lime-silica (SLS) glass. As mentioned in section 2.1.2, glass components can be categorized as either glass network formers, glass network modifiers, and glass network intermediates. Silica is perhaps the most fundamental of glass formers, while alkali and alkaline earth metal oxides are glass network modifiers. A network modifier will depolymerise a glass network, by interacting with oxygens within the silica tetrahedra and preventing them from bridging the silica tetrahedra to one another. From here, the oxygen anions in a glass network can be described as either "bridging", or "non-bridging" oxygens, with the former existing in glass forming bonds that bridge between network forming cations,

while the latter do not. This introduces the notion of "Q speciation" of silica tetrahedra, whereby the number of bridging oxygens on a silica tetrahedra will dictate the Q^n number. For example, in fused quartz glass, every oxygen will form network forming bonds between the network forming silica. For each tetrahedron, there will be four bridging oxygens and therefore is a Q^4 species of silica. In a binary soda-silica glass, there will be oxygens that are non-bridging and for each non-bridging oxygen, the Q number decreases. See **Fig 2.4** for an illustration of this.

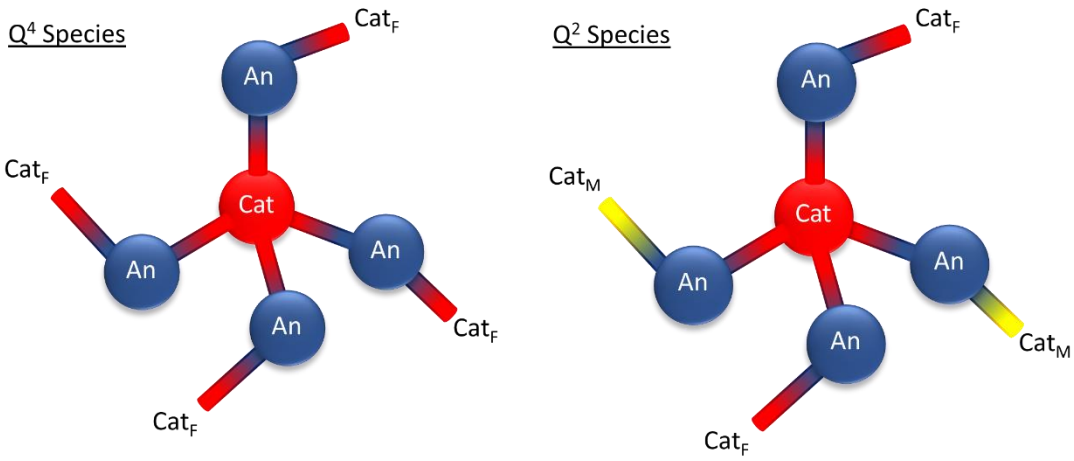

Figure 2.4: *A diagram of both a Q^4 and a Q^2 species tetrahedron. Cat_F denotes a network forming cation, while Cat_M denotes a network modifying cation.*

Given the relative differences in bond characteristics between glass former and glass modifier bonds, and how these may influence the glass properties, it is important to be able to characterise the Q speciation within silicate glasses. Two techniques in particular have proven useful in this endeavour; ^{29}Si Nuclear Magnetic Resonance (NMR) [16-19] and Raman [18,20-29] spectroscopies. In ^{29}Si NMR, the Q-speciation is elucidated by peak fitting the signal with multiple gaussian or Lorentzian peaks to describe the relative abundance of each Q-species.

Raman spectroscopy utilises a similar approach, whereby a specific region of a Raman spectrum of a silicate glass (typically between 900 – 1200 cm^{-1}) is fit with several peaks (peak function type is a debated topic in glass [20,22,28], see Chapter 6 for more detail) to determine the relative abundance of respective Q-species within the glass. An example of this work can be seen in a study by Bancroft *et al*. [28] which studied binary alkali silicates.

However, caution must be used when using Raman spectroscopy as it is not target-element specific like ^{29}Si NMR. So while it is used very successfully for binary silicate glass systems, it has limitations in trinary systems and beyond, due to convolution in the target region.

2.2.3 Borate Glass

Borate glass is glass that is primarily made of vitreous B_2O_3. Borate glasses have very low melting points and low chemical durability, so the uses of borate glasses are somewhat niche compared to silicate glasses. Wright *et al*. [30] compiled a detailed review on the differences between silicate and borate glasses, ranging from vitreous B_2O_3 and fused quartz, through to glasses doped with monovalent modifiers (i.e. alkali metals) and compared the differences between the two.

Vitreous B_2O_3 is a borate glass that is 100% B_2O_3. The network largely consists of trigonal BO_3 units (boron has an oxidation state of B^{3+}, unlike Si^{4+}, so it cannot form tetrahedral units without charge compensation), that connect in a variety of metaborate structures (see **Fig 2.5**).

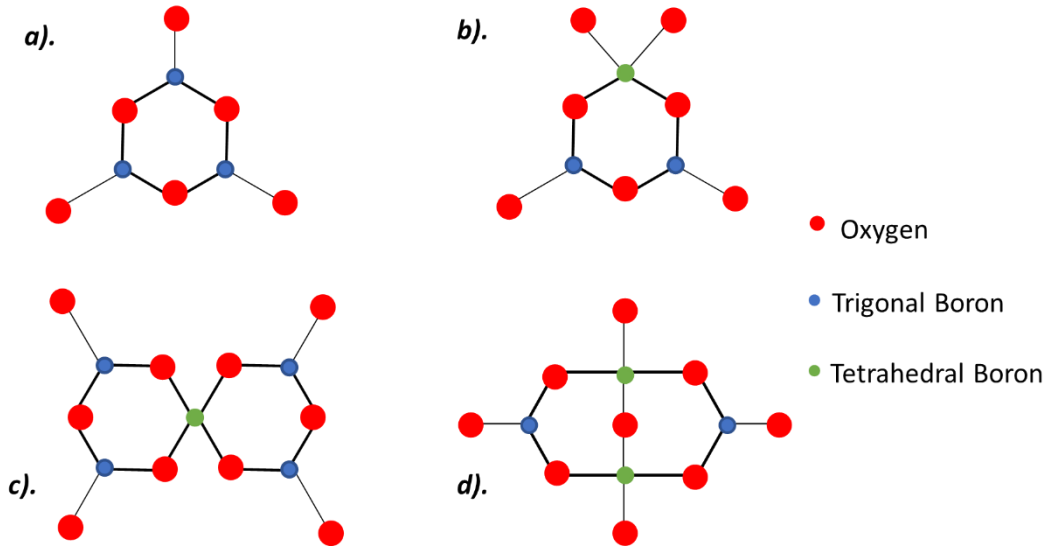

Figure 2.5: *Four examples of metaborate structures; a). boroxol group. b). diborate group. c). pentaborate group. d). diborate group. Recreated from Wright et al. [30].*

The introduction of monovalent modifiers introduces a conversion of some trigonal BO_3 into tetrahedral BO_4^-, but up to a point. Beyond a certain concentration of monovalent ions converting the trigonal borate to tetrahedral borate groups, the monovalent ions convert some of the bridging oxygens within the borate network into non-bridging

oxygens. This is illustrated in **Fig 2.6.** and is colloquially named the "Borate Anomaly" as the exact mechanisms that govern this behaviour are still unclear.

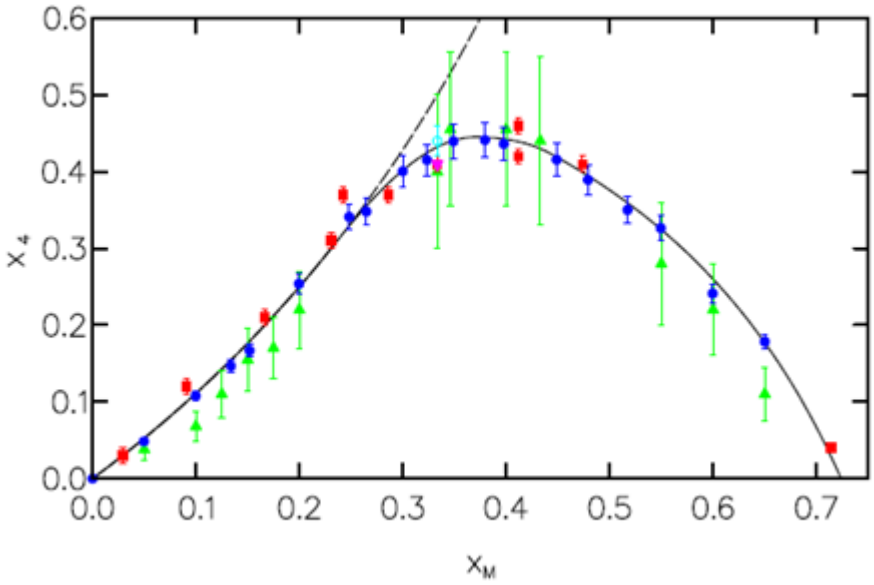

Figure 2.6: *A graph showing the fraction of* $^{[4]}B$ *(*X_4*) against the modifier fraction (*X_M*) where the modifier is* Li_2O*. Graph is sourced from Wright et al. [30], blue data points are from Jellison et al. [31], red data points are from Kroeker and co-workers [32,33], green data points are from Bray & O'Keefe [34], cyan data points are from Cormier et al. [35] and purple data points are from Ratai et al. [36].*

This anomaly manifests itself in the glass properties. Duffy [37] noted that as you increase the alkali content within borate glasses, the basicity of the glass does not increase as a result of the formation of BO_4^-, which is counterintuitive on the face of it. In the case of Li_2O the basicity even decreases as alkali metals are added. In both cases, a high concentration of alkali metal contents, the basicity does begin to increase eventually. According to the calculations used by Duffy [37], this largely due to the high value basicity moderating parameter attributable to $^{[4]}B$, meaning as the alkali metal contents increase, the fraction of $^{[4]}B$ increases (to a point) resulting in a "cancelling out" effect on the overall basicity [37].

This non-linear behaviour for borate glasses will be considered repeatedly throughout this research.

2.2.4 Applications in Nuclear Waste Immobilisation

As mentioned in Chapter 1.5.2, borosilicate glass has shown a great range of desirable qualities that resulted in borosilicate glass being the wasteform of choice for the radioactive waste clean-up efforts at the Savannah River and Hanford sites [38]. Variations of borosilicate glass have been used in nuclear waste immobilisation programs in many countries across the world. It is said that borosilicate glass was first identified as suitable for the vitrification of radioactive waste at the Massachusetts Institute of Technology (MIT) when aluminosilicate glasses were fluxed with B_2O_3 to pour at lower temperatures [38]. The French developed a batch process at the PIVER ("Pilote Verre" translates to "Pilot Glass") but was replaced by the continuous process at the AVM ("Atelier de Vitrification de Marcoule" translates to "Marcoule Vitrification Workshop") due to the increase in demands brought on by increase in production of nuclear waste [38]. The United Kingdom initially also used a batch process, known as the "Harvest batch vitrification" process, but adopted a continuous process inspired by the French AVM. The Full Scale Inactive Facility (FSIF) was constructed in the 1983 operated by British Nuclear Fuels Ltd. and Sellafield to develop a HLW vitrification for UK wastes. This culminated in the construction of the Waste Vitrification Plant (WVP) in 1991, which consists of two parallel calcine-melter combined processes. This has been used to process highly active liquor waste stored on site [38].

Ojovan *et al*. provide a great visual aid (**Fig. 2.7**) [2] as to why borosilicate glass has remained a strong medium for the immobilisation of nuclear waste – the borosilicate glass matrix is capable of dissolving a wide range of multivalent species, making it ideal for complex waste forms [2].

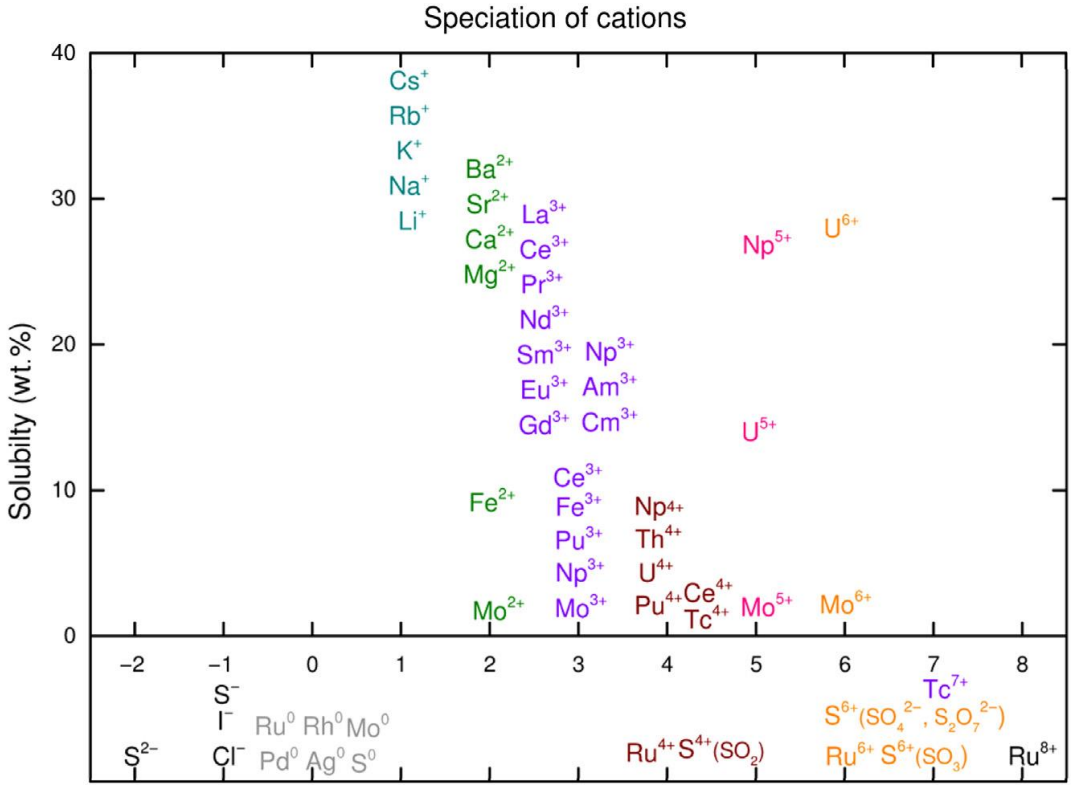

Figure 2.7: *A visual representation of the solubility of species as a function of oxidation state (Found in ref [2], original credit to Sophie Schuller, CEA, France).*

While commercial borosilicate glasses have shown high levels of chemical durability (consider the primary uses of Pyrex and Vycor), non-radioactive waste simulant boroaluminosilicate glasses have shown high levels of durability [39], as measured by a variety of tests, such as the product consistency test (PCT) [40]. While these lab-scale tests provide an insight into comparative chemical durability, there are legitimate questions around how accurate these tests will be in predicting how waste forms behave over humanly inconceivable timescales [41]. However, using such standardised tests to compare potential waste forms against one another, consistently show that borosilicate glasses are amongst the more durable [42]. As mentioned in Chapter 1.5.2, borosilicate glasses are also far less corrosive to the melters, making them an ideal matrix for a continuous vitrification process.

2.2.5 Magic Angle Spinning – Nuclear Magnetic Resonance (MAS-NMR) Spectroscopic Studies on Borosilicate Glass

This project will cover a wide range of spectroscopic studies, each will have a review of the key literature available for that spectroscopic technique. For reasons that will be elaborated upon later in the thesis, nuclear magnetic resonance spectroscopy was not one such technique employed in this research, however, it remains a key technique that has

greatly contributed to wider understanding of what a borosilicate glass is. As such, a brief review of key NMR literature is deemed necessary to introduce an understanding of the borosilicate glass network.

Nuclear magnetic resonance has been used to describe the short-range order around target nuclei in solid materials, including glasses. The introduction of magic angle spinning (MAS) NMR allowed for far greater peak resolution and the ability to resolve different environments for the same target nuclei [43]. Without spinning the sample, the spectra will contain broad featureless peaks that result from the presence of anisotropic spin interactions (from interactions such as chemical shielding). If the correct spin rates and angle are selected, the anisotropic spin interactions can be averaged out and the broad featureless peak can be resolved into well-defined peaks with minimal presence of side bands from quadrupole interactions [43]. However, while the removal of side bands is desirable, if the side bands are well resolved from the main peak, these bands can also provide useful information [43].

While boron only has a single oxidation state, it can form two distinct oxide groups; a charge neutral trigonal group ($^{[3]}$B) and a charge compensated tetrahedral group ($^{[4]}$B). This has led to a large body of research with the aim of developing a model for how a borosilicate network forms, initially culminating in the Yun-Bray-Dell-Xiao model (commonly referred to as the Yun & Bray model) for sodium borosilicate glass [44-46]. This model was developed after extensive ^{11}B nuclear magnetic resonance (NMR) spectroscopy was performed on many glasses with varied SiO_2 : B_2O_3 ratios (referred to as *K* values) and Na_2O : B_2O_3 ratios (referred to as *R* values), with the ratios calculated using molar percent (mol.%). The model predicts that at low *R* values ($R < 0.5$), all of the sodium is used to form $^{[4]}$B groups within the glass, essentially behaving like a binary borate glass [46]. When $0.5 \leq R \leq R_{MAX}$ (where R_{MAX} is the maximum R value in which the maximum amount of $^{[4]}$B forms), borosilicate groups such as reedmergnerite (formula: $½(Na_2O \cdot B_2O_3 \cdot 8SiO_2)$ are formed [46]. At $R_{MAX} \leq R$, the sodium begins to form NBOs on both the silica and the boron, first on the silica, then on the borate groups with a point reached where this will occur across different borate and borosilicate units simultaneously [46].

While there are limitations to the Yun-Bray-Dell-Xiao model (referred to as the YBDX model from here onwards), it has provided a good first order starting point for other

borosilicate like systems. For example, Du and Stebbins [47] presented a modified version of the same model for boroaluminosilicates. The research showed that $^{[4]}$Al and $^{[4]}$B had very similar mixing distributions within the network, and given the YBDX model could predict the amount of $^{[4]}$B within a composition, Du and Stebbins derived modified *R* and *K* constants to incorporate Al_2O_3 into the model using ^{27}Al and ^{17}O NMR studies [47]. This work was initially inspired by an assumption made by YBDX that says that the boron does not mix with the silica beyond the reedmergnerite unit stated in the papers [48-50]. Work by Wang and Stebbins [48], showed by using ^{17}O NMR that trigonal boron does mix with silica in borosilicate glasses. This work also suggested that a $^{[4]}$B avoidance rule, similar to avoidance rule for alumina proposed by Lowenstein [51], was likely in moderate amounts of modifiers within the borosilicate glass (the research studied sodium and potassium borosilicate glass) [48]. Du and Stebbins developed this further studying sodium borosilicate glasses using ^{11}B and ^{17}O NMR spectroscopy. It was shown that $^{[3]}$B rings tend to bond more with borate groups, non-ring $^{[3]}$B tends to be more randomly bonded within the borate and silicate groups, and tetrahedral $^{[4]}$B tends to bond more silicate groups [49]. A further study by Du and Stebbins showed that this mixing is consistent in potassium borosilicate glasses but lithium borosilicate glasses show a greater tendency to phase separate, with $^{[3]}$B rings agglomerating together with the non-ring $^{[3]}$B converted to $^{[3]}$B rings which reduced the mixing between borate and silicate groups [50].

Möncke et al. further investigated the nature of the borosilicate glass network using NMR [52]. One of the principal points of interest in the research was the avoidance rule referenced in the older models [49,51]. The research by Möncke *et al*. [52] used the existence of crystalline borosilicate analogues, such as danburite, as evidence that a $^{[4]}$B avoidance rule does not necessarily explain the borate and silicate mixing patterns. The research showed that a tetrahedral borate group with all non-bridging oxygens will bond in metaborate structures. It was also noted that in annealed glasses, there was less cross linkage between the $^{[4]}$B groups and the silicate groups than the quenched glasses, and that the majority of the B-O-Si bonds occurred between $^{[3]}$B and the silicate groups [52]. This effect was alluded to in an earlier body of work by Möncke *et al*. [53], which noted a similar decrease in the $^{[4]}$B-O-Si linkages in the annealed samples when compared to the quenched samples. Venkatachalam *et al*. [54] looked into the borosilicate network through in situ ^{29}Si and ^{11}B NMR studies [54], it was found that that above the glass transition temperature (T_g) for the borosilicate glasses studied, there was a phase

separation into borate-rich, and silicate-rich phases which included the crystallisation of binary alkali-silicates [54].

Tanaka *et al.* [55] investigated the link between optical basicity and $^{[4]}$B fraction as measured by ^{11}B NMR data for borosilicate and aluminoborosilicate glasses with both alkali and alkaline earth metals within the matrix [55]. It was found that some correlation could be found between the two in borosilicate glasses, the nature of the correlation was unclear with regards to differences of correlation factor between glasses richer in either alkali or alkaline earth modifiers. It was found with aluminoborosilicates, the two properties did not correlate well, and further investigations were needed [55]. Wu and Stebbins [56] further investigated the effect of cation field strength on $^{[4]}$B fraction within aluminoborosilicates with systematically varied concentrations of CaO and Na_2O [56]. It was found that the CaO had dramatically different effects on the network than that of Na_2O. Increased CaO concentrations resulted in lower $^{[4]}$B fractions and also manifested in an increase $^{[5]}$Al fractions, leading to the suggestion that CaO is far less likely to act as a charge compensator than Na_2O [56].

From this selection of studies, trying to elucidate and predict the nature of a borosilicate glass network is not a straightforward task. NMR is a powerful tool in being able to describe short-medium range ordering within glass and yet there is still no singular model or body of work that has provided a one-size-fits-all predictive model for borosilicate glass. Research such as that work done by Lu *et al.* [57] collated a wide variety of models and datasets to develop a machine learning approach to predicting $^{[4]}$B fractions in borosilicate glasses. It is noted that the models developed showed promise in the ability to predict $^{[4]}$B fraction but it is noted that the variances in processes, such as sample preparation and measurement conditions, that make these predictions harder to verify experimentally [57].

2.3 Iron Oxide in glass

2.3.1 Overview

Iron oxide in glass is not a new topic of research. It is used in commercial glass as a colouring agent [58, 59] and has been used to improve the processability of glass [60]. Iron oxide within oxide glasses acts as a glass network intermediate, meaning that it can both polymerise and depolymerise the glass network and consequentially, will influence the glass properties in different ways. Iron can also exist in multivalent and multi-coordinated species with glasses, with the preferential valency and structure being

dependent on a variety of factors, such as glass matrix, wider composition, melt environments, and abundance of the iron itself [61]. This makes it incredibly difficult to predict how the iron will exist within a given glass matrix and how it will influence the glass properties. Many studies have been done to elucidate the nature of iron oxide within glass across a variety of glass matrices, including silicate [62-80], phosphate [81-102], and borosilicate glasses [103-122].

2.3.2 Silicate Glass

Silicate glasses are one of the better glass matrices to use when studying multi-valent, multi-coordination component such as a transition metal like iron. Silicate glass consists of silicate tetrahedral groups that are fluxed with modifier components. The silicon will almost always be four-coordinated with a valency of 4+. Montenero *et al*. [62] studied the behaviour of iron silicate glasses using optical absorption, and electron paramagnetic resonance (EPR) spectroscopies. It was shown that Fe^{3+} behaves more like glass network former and forms tetrahedral groups, whereas the Fe^{2+} behaves more like a glass network modifier and forms octahedral groups. It was also shown that there are interactions between Fe^{3+} and Fe^{2+} in the form of clusters [62]. Bingham *et al*. [63] looked into iron clustering in silicate glasses, in which it was shown that for low abundances of iron oxide (1-3 mol%) that the iron forms Fe(II)-O-Fe^{3+} and Fe^{3+}-O-Fe^{3+} clusters as measured by Mössbauer spectroscopy, and that total abundance of iron oxide does not influence the redox ratios of the iron [63]. Virgo and Mysen [64] studied oxidised and reduced iron silicate glasses using ^{57}Fe Mössbauer spectroscopy. The Fe^{2+}-O-Fe^{3+} clustering effect was seen, with the reduced glasses being noted for being dominated by Fe-rich spinel-like phases with a similar stoichiometry as magnetite (Fe_3O_4), as well as isolated (i.e. not clustered in iron rich units) Fe^{2+} and Fe^{3+} ions [64].

Mekki *et al*. [65] used X-ray photoelectron spectroscopy to investigate the silicate network as a function of increasing the Fe_2O_3 within the glass at the expense of SiO_2. It was shown that while there is both ferrous and ferric iron within the silicate network, if nothing is done to force the oxidation state of the iron during melting, then Fe^{3+} will become the dominant species at higher iron oxide contents. This work also suggested that tetrahedral Fe^{3+} behaves as a glass network modifier by forming non-bridging oxygens, according to the measured O 1s signal. However, this conclusion was reflected in measurements of the physical properties of the glass. A further refinement of the fits suggest that Si-O-Fe bonds would still form glass forming bonds, but with a higher ionic

character than Si-O-Si bonds. This higher ionic character manifests as lower binding energies of the O 1s signal and was incorrectly interpreted as the formation of non-bridging oxygens [65]. Holland *et al*. [66] built on this work by using Mössbauer spectroscopy and neutron diffraction as well as XPS. The research showed that iron exists in predominantly tetrahedral Fe^{3+} and that the Fe-O bond lengths decreases as the Fe_2O_3 contents within the glass increases [66]. Bingham *et al*. [67] investigated the stabilisation of tetrahedral Fe^{3+} in alkali and alkaline earth doped silicate glasses. For Fe^{3+} to be tetrahedral, it must have a charge compensator for the excess negative charge from the oxygen anions. It was shown using optical absorption spectroscopy that alkali cations do this, and the ability to do so is linearly related to the increase in ionic radius and decrease in cation field strength. Alkaline earth cations inhibit the stabilisation of tetrahedral Fe^{3+} linearly by the same criteria. These relationships were described as "selective" [67]. Volotinen *et al.* [68] also used optical absorption spectroscopy to study the sites of Fe^{2+} and Fe^{3+} in silicate glasses. It was shown that Fe^{2+} will prefer to form octahedral sites, while Fe^{3+} will form both octahedral and tetrahedral sites. With the inclusion of ceria (CeO_2), the Fe^{3+} forms more tetrahedral units than octahedral [68]. Jackson *et al*. [69] carried out a comprehensive multi-spectroscopic study on Fe^{2+} environments in silicate melts, in which Fe *K*-edge X-ray absorption near-edge structure (XANES), extended X-ray absorption – fine structure (EXAFS), and ^{57}Fe Mössbauer spectroscopies, as well as ultraviolet – visible – near infrared (UV-Vis-NIR) and magnetic circular dichroism (MCD) spectroscopies. The XANES, EXAFS, and Mössbauer spectroscopies showed the Fe^{2+} to exist in coordinated structures that ranged from 4 – 5.2 oxygens. This was confirmed by the UV-Vis-NIR and MCD spectroscopies which showed 3 distinct sites, two of which were 5-coordinated, the remaining site being 4-coordinated [69]. Vercamer *et al.* [70] carried out a similar, albeit less comprehensive, study for Fe^{3+} in silicate glasses using UV-Vis-NIR absorption and EPR spectroscopies on iron-doped alkaline earth silicate glasses. It was shown that Fe^{3+} in calcium silicate glasses had a tendency to form tetrahedral and 5-coordinated groups which included isolated Fe^{3+} sites. Magnesium promoted the formation of tetrahedral Fe^{3+} and also promoted more clustering of iron sites and fewer isolated iron sites [70]. Bingham *et al*. [71] used XANES and EXAFS to further study Fe^{3+} ions in silicate glasses and show further evidence of the selective behaviour of alkali and alkaline earth moderators. CeO_2 was used to fully oxidise the Fe into Fe^{3+}, and the EXAFS showed that the coordination number of the Fe^{3+} increases from 4.0 (±0.4) to 6.2 (±0.9) with decreasing ionic radii of the alkali / alkaline earth cation,

which was matched by a corresponding increase in bond length from 1.87 (±0.01) to 1.92 (±0.01) Å [71]. Wright *et al*. [72] used neutron diffraction and ^{29}Si magic angle spinning (MAS) NMR, as well as Mössbauer and optical absorption spectroscopies to further describe the Fe^{3+} and Fe^{2+} sites within sodium calcium silicate glasses. It was shown that the iron predominantly exists as glass network polymerising tetrahedra, with network modifying Fe^{2+} and Fe^{3+} octahedra present. It was noted that the presence of Fe^{2+} and Fe^{3+} 5-coordinated modifiers could not be ruled out [72]. Kim *et al*. [73] used ^{29}Si and ^{17}O NMR spectroscopy to describe the changes in the silicate network as function of swapping the Na_2O for Fe_2O_3 in a sodium silicate glass, ranging from 0 – 22.3 wt.% Fe_2O_3. Despite the spectral features broadening due to the paramagnetic qualities of iron (a typically problematic obstacle in using NMR spectroscopy on Fe-bearing samples), the ^{29}Si NMR spectra showed an increase in more polymerised silicate bands with increasing Fe_2O_3 contents. This was matched by the ^{17}O NMR spectra which showed well-resolved bridging oxygen and non-bridging oxygen signals, which showed a decrease in the NBO signal as the Fe_2O_3 increased [73].

There are many more studies on iron-bearing silicate glasses [74-80], but the overarching understanding is that iron can and does form structural units with Fe^{2+} and Fe^{3+} oxidation states within the silicate glass network. The exact nature of the structural units depends on the wider composition, with each unit behaving as either a network modifier, or a network former, thus evidencing the glass network intermediate behaviour of iron within glass.

2.3.3 Phosphate Glass

Phosphate glasses, alongside borosilicate glasses, have been considered as a matrix in which to vitrify complex radioactive waste. However, due to the corrosivity of the melt, and poor chemical durability relative to borosilicate glasses, many countries have opted against using phosphate glasses [2,38]. However, plenty of research investigated how iron integrates within a phosphate glass network, and this section will look to review some of the key literature around iron in phosphate glasses. Lin *et al*. [81] used EXAFS and Mössbauer spectroscopies to describe the iron chemistry within phosphate glasses. It was shown that there is both Fe^{2+} and Fe^{3+} octahedral sites within the network as well as tetrahedral Fe^{3+}, with the iron typically having a lower coordination number than crystalline analogues [81]. Moguš-Milanković *et al*. [82] studied the crystallisation of iron phosphate glasses using X-ray diffraction (XRD), neutron diffraction, and Raman

spectroscopy. The nature of the crystallisation depends on the wider composition of the glass, as well as relative abundance of Fe^{2+} and Fe^{3+} and it was noted that as the Fe_2O_3 increased within the glass, the Fe^{3+} abundance would increase [82]. Ray *et al*. [83] studied the effect of melt time and temperature on iron valency within phosphate glasses and how this subsequently affected the dissolution rate. Melt times were shown to be inconsequential on the iron valency, but higher melt temperatures promoted more Fe^{2+} formation. This phenomenon is not limited to iron, with Leister and Ehrst [84] observing this trend in Fe- and V-bearing silicate glasses. The driving factor behind this is due to the increased oxygen diffusion and lower viscosity of the glass melts [84]. The dissolution rates of these glasses were independent of iron valency as both Fe^{2+} and Fe^{3+} form Fe-O-P bonds that are more resistant to hydration than the P-O-P bonds that are replaced [83]. However, while the introduction of Fe into the phosphate network increases the chemical durability, glass formation becomes increasingly difficult with secondary phases more likely to crystallise [83]. but did decrease as the amount of iron within the glass increased [83]. Similar tendencies were shown in a study by Karabulut *et al*. [85], which studied the inclusion of radioactive waste components into an iron-phosphate glass network as studied by XPS and Mössbauer spectroscopy. The iron chemistry and the wider phosphate network were largely unaffected by the inclusion of Cs, U, and Bi with a corresponding lack of effect seen on the glass properties, which further supported phosphate glasses as a strong candidate to vitrify radioactive wastes [85]. Day *et al*. [86] investigated the chemical durability of iron-phosphate glasses. Iron was shown to increase the chemical durability of simulated phosphate waste forms by integrating within a pyrophosphate (P_2O_7) network (essentially made by two phosphate tetrahedra bonding together) and replacing some of the P-O-P bonds, with more hydration resistant Fe-O-P bonds [86].

Bingham *et al*. [87] carried out a comprehensive study on the effects modifier cations have on the iron phosphate network and associated properties. Raman and Mössbauer spectroscopies, DTA, and PCT-B were carried out to determine the impacts to the glass network, iron chemistry, thermal stability, and chemical durability respectively. It was found that that while monovalent alkali components had negative impacts on the chemical durability and demonstrated a depolymerising effect on the network, the chemical durability remained high in comparison to a borosilicate surrogate waste form. Divalent ions increased the already high chemical durability and increased the thermal stability of the network. Interestingly, the effects on the glass chemistry were seemingly non-linear.

The Fe^{2+} abundance increases with modifier content up to intermediate levels on modifier ions, before decreasing or exhibiting a plateau. Mössbauer spectroscopy confirmed that the average coordination appeared constant which contradicted the theory that the iron coordination changes were behind the non-linear effects on glass chemistry. Bingham *et al*. hypothesised that the iron redox chemistry in the iron-phosphate system must be in part governed by the thermal stability of the system, rather than exclusively the composition of the system [87]. Karabulut *et al*. [88] used Mössbauer and EXAFS spectroscopies to investigate the Fe^{2+} sites in iron phosphate glasses. The Mössbauer spectra indicated that the Fe^{2+} occupied a single site, whereas Fe^{3+} occupied two sites. As the melt conditions were altered to favour Fe^{2+}, it increased the Fe^{2+} at the expense of one particular Fe^{3+} site, rather than both sites proportionally. The EXAFS showed that the average coordination for both Fe^{2+} and Fe^{3+} sites ranged between 4 – 5, indicating a mix of both tetrahedral and octahedral sites for both oxidation states [88].

Many more studies into iron phosphate glasses within the context of nuclear waste have been carried out [89-97], as well as further studies into the effects the wider property changes as a result of compositional changes to the iron phosphate glass [98-103]. In all cases, the iron will exist in mixed Fe^{2+} and Fe^{3+} octahedral sites with more Fe^{2+} being favoured at higher melting temperatures and Fe^{3+} favoured at higher iron contents within the glass. The iron will typically substitute itself into the phosphate network independently of other components, allowing for a consistent network suited for uses such as radioactive waste immobilisation.

2.3.4 Borosilicate Glass

As mentioned in above in section 2.2, borosilicate glass is a silicate glass fluxed with boron and modifier cations such as sodium. The study of iron oxide within a borosilicate glass network is complicated by the fact that the boron can also occupy multiple coordination borate and metaborate groups, with non-linear relationships with other glass forming or modifying cations.

Magini *et al*. [104] used wide-angle X-ray diffraction to show that at lower concentrations of Fe_2O_3 within borosilicate glasses, the iron exists as tetrahedral Fe^{3+}, with an Fe-rich crystalline phase forming at higher Fe-contents [104]. Lichieri *et al*. [105] followed up this work, using Fe *K*-edge EXAFS spectroscopy to describe the iron chemistry within alkali borosilicate glasses. It showed that Fe^{3+} is the dominant valency in alkali-borosilicate glasses, with predominant tetrahedral units. However, as the iron oxide

contents increased, there was increasing evidence that some of the Fe^{3+} formed octahedral units [105]. Agostinelli *et al*. [106] used XPS and Auger electron spectroscopy to describe the iron chemistry in borosilicate glasses. It was shown that as well as forming Fe^{2+} and Fe^{3+} units, it also preferentially bonded to the silicate network, forming iron silicate phases, while also forming iron rich phases that became precursors for Fe-rich crystalline phases [106]. This was seen primarily in the binding energy changes in the O 1s and O *KLL* Auger electrons. Taragin and Eisenstein [107] used ^{57}Fe Mössbauer spectroscopy to describe the iron chemistry in complex borosilicate glasses with Fe_3O_4 added to the glass under reducing conditions (carbon powder was added to the batch prior to melting). Despite the reducing conditions, the Mössbauer data showed significant quantities of Fe^{3+} (exact numbers not stated) with the Fe^{3+} increasing with increasing Fe_3O_4 contents within the glass. It also showed that the Fe^{3+} existed predominantly as tetrahedral units with evidence of octahedral units, with the former acting as a network former and the latter acting as a network modifier. Fe^{2+} showed similar structural units, however, the spectral features (including a broad linewidth) suggest that Fe^{2+} would still act as network modifier in this glass system [107].

Musić *et al*. [108] used a multi-spectroscopic study to describe how iron integrates within borosilicate glass systems. ^{57}Fe Mössbauer spectroscopy showed that the Fe exists predominantly as Fe^{3+} with parameters that suggest the iron is mostly tetrahedral with some qualitative evidence of octahedral iron. The tetrahedral Fe^{3+} is then hypothesised to polymerise the borosilicate network, with the silicate network polymerisation evidenced using IR and Raman spectroscopies. However, the vibrational spectroscopy did note a destruction of diborate groups and the formation of boroxol rings, further suggesting the iron oxide preferentially bonds into the silicate network [108]. Cochain *et al*. [109] carried out a comprehensive multi-spectroscopic study on the effects that iron oxide contents and redox have on a sodium borosilicate glass network. Raman, ^{57}Fe Mössbauer, and boron *K*-edge XANES spectroscopies were used to quantify the iron chemistry and the nature of any changes to the silicate and borate groups within the glass network. The Mössbauer spectra confirmed the desired redox values for the iron (which was also in agreement with wet chemical analysis), and showed that the Fe^{3+} predominantly exists in tetrahedral units with evidence of higher coordinated Fe^{3+}, while the Fe^{2+} exists in octahedral units. The boron *K*-edge XANES spectra showed the iron redox or content did not influence the boron coordination within the glass, and that the glass series had a constant $^{[4]}B$ fraction

0.74 which was in agreement with predictions made by the YBDX model [44-46]. The research also suggests that Fe^{3+}, by way of changing borate bands in the Raman spectra as function of changing Fe^{3+} contents, influences the medium range order around the borate groups. It is suggested that the Fe^{3+} units are being preferentially charge compensated over some of the $^{[4]}B$ units [109].

Ciżman *et al*. [110] also carried out a comprehensive multi-spectroscopic study on iron within borosilicate glass. As well as using ^{57}Fe Mössbauer and IR spectroscopies, X-ray diffraction, transmission electron microscopy (TEM), and dynamic impedance spectroscopy (DIS) was used to describe how iron integrates within a borosilicate glass network and how this influences electrical properties of the glass. The Mössbauer spectra showed that both Fe^{3+} and Fe^{2+} exists in tetrahedral and octahedral groups, while also exhibiting some magnetic ordering in heat treated samples. XRD confirmed the presence of hematite (Fe_2O_3) and magnetite (Fe_3O_4) which explained the sextet present in the Mössbauer spectra [110]. Ratep and Kashif [111] studied the effects of substituting Fe_2O_3 for CuO in lithium borosilicate glass using XPS, IR, and Mössbauer spectroscopies. The Fe in low abundances exist entirely as Fe^{3+}, suggesting that the CuO may potentially oxidise the iron, further supported by the presence of Fe^{2+} when the CuO has been fully substituted out of the glass. Furthermore, the FTIR spectra suggests that the Fe^{3+} groups bonded to $^{[3]}B$ groups rather than the $^{[4]}B$ tetrahedral groups [111].

Wright *et al*. [112] used neutron diffraction to study the Fe^{3+} and Fe^{2+} environments in sodium borosilicate glasses. It was shown that the majority of the iron exists as Fe^{3+} in mixed tetrahedral and octahedral groups, with a small amount of octahedral Fe^{2+}. The tetrahedral Fe^{3+} bond into the silicate network, the negative charge compensated by sodium ions. The octahedral Fe^{3+} preferentially bonds into the borate network via the trigonal borate groups to form non-stoichiometric $FeBO_4$ groups (the lack of stoichiometry comes from the inclusion of Fe^{2+} into the groups) [112]. Glazkova *et al*. [113] studied borosilicate waste simulant glasses using ^{57}Fe Mössbauer spectroscopy and FTIR spectroscopy, and it was shown that while the iron is predominantly Fe^{3+}, it exists in octahedral units rather than tetrahedral units, assigned based on the quadrupole split values for the Fe^{3+} doublet in the Mössbauer [113] (more information on this and the ambiguity of using quadrupole split values for coordination can be found in Chapter 4). Stefanovsky *et al*. [114] studied high-Fe non-active waste glasses expected at the Savannah River Site. Fe *K*-edge XANES and EXAFS spectroscopies were used to show

that the iron exists predominantly as Fe^{3+} tetrahedral units with some Fe^{2+}. The Fe^{3+} tetrahedra was said to be distorted but the bond lengths and coordination numbers calculated using the Fourier transformed EXAFS data confirmed the Fe^{3+} tetrahedra [114].

Many other studies looked into the structural impacts iron oxide has on a borosilicate network [115-120] but in most studies, there are some emerging trends. The first main trend is that the iron exists predominantly as Fe^{3+}, even in when melted in reducing conditions [107]. The Fe^{3+} in most cases will form tetrahedral units with some evidence of octahedral units in certain compositions and melt conditions. Fe^{2+} is typically in octahedral units, and only really appears in low abundances, or when then melt conditions and raw materials have been tailored to produce Fe^{2+} within the glass [109,112]. Amongst these trends, the tetrahedral Fe^{3+} tends to form network forming bonds within the silicate sub-network while octahedral Fe^{2+} and Fe^{3+} tends to bond with trigonal boron in the borate sub-network [111,112].

2.3.5 Radioactive Waste Glass

As outlined in section 2.3.2 and 2.3.3, borosilicate glass and phosphate glasses have emerged as two strong candidates for the immobilisation of radioactive waste, with borosilicate glasses being the preferred matrix for many countries [2,38]. Iron phosphate glasses make a particularly strong candidate matrix owing to its ability to incorporate wide array of components into the network with minimal effects on the properties, while maintaining a high chemical durability, while also melting at lower temperatures [83, 85-87,89-97]. While borosilicate glasses also have a high chemical durability and can incorporate a wide range of waste components, they have also been seen to be less corrosive to melters and maintain high thermal stability [2,38-40,121]. Section 2.3.4 reviewed how iron integrates into a borosilicate glass network, including comments on the iron chemistry within certain types of borosilicate glass, and the associated effects on the borosilicate network. This section will look to discuss how iron oxide effects key properties relating to borosilicate radioactive waste glasses.

Yanagisawa & Sakai [122] studied the influence iron oxide has on the chemical durability of borosilicate glasses. It was shown that iron oxide improves the chemical durability by reducing the leach rate of glass components in hydrothermal conditions. It was suggested that this is an effect of the ferric (Fe^{3+}) ions acting as a glass network intermediate, and the ability to form a durable alteration layer. However, this was at the time of publishing

just a hypothesis that was recommended for further study [122]. This hypothesis was seen in future studies, such as the study carried out by Cassingham *et al*. [123]. This study investigated UK-based HLW MW glasses with the Fe_2O_3 content ranged from 0 – 20 wt.%. Mössbauer spectroscopy confirmed that the iron was entirely Fe^{3+} in tetrahedral coordination, while DTA showed minimal impact to the glass transition temperature, evidencing a lack of influence on thermal stability of the glass. PCT-B over 7, 14, and 28 days showed that the addition of Fe_2O_3 reduced the leach rates of key glass components such as the Si, B, and Na. At longer timescales, the dissolution rate increases over time with high concentrations of Fe_2O_3 (>10 wt%), whereas at mid-to-low concentrations of Fe_2O_3 (0 - 10 wt.%) the dissolution rate does not increase significantly over 28 days. This was attributed to the polymerising effect tetrahedral Fe^{3+} has on the borosilicate glass network with the additional polymerisation strengthening the overall network against dissolution via hydration [123]. A similar effect was observed by Konon *et al*. [124] in a study on porous glasses. Samples with octahedrally coordinated Fe^{3+} were more susceptible to dissolution with the goal of forming porous glasses, yet glasses with tetrahedral Fe^{3+} were far less susceptible to dissolution [124]. Yang *et al*. [125] used computer modelling to determine the nature of substituting Al_2O_3 for Fe_2O_3 in terms of coordination and effect on glass properties of lithium silicate glasses. The iron was said to exist predominantly as Fe^{3+} which polymerised the glass network in a similar manner to the Al^{3+} being removed from the glass. However, glass transition temperature was shown to decrease as the Fe_2O_3 was substituted in, suggesting a decrease in glass stability [125]. This was not seen in the study by Cassingham *et al*. [123], which added Fe_2O_3 in a pro-rata basis into borosilicate radioactive waste surrogate. It is likely that the effects on glass transition temperature in the study by Yang *et al.* [125] are more to do with replacement of Al–O bonds with Fe–O bonds, with the former being higher energy and therefore harder to break down than Fe–O bonds [125,126], rather than a comment on the Fe-O bonds themselves. High Fe_2O_3 contents within glasses have been linked to the nucleation of Fe-bearing crystalline phases as a result of iron clustering [63,64,124]. Romero *et al*. [127] demonstrated this in glass ceramics by showing different concentrations of iron developing slightly different crystalline phases in an aluminosilicate glass system. At lower Fe_2O_3 contents (< 9 wt% Fe_2O_3), the Fe^{3+} ions formed a zinc-iron spinel phase known as franklinite ($ZnFe_2O_4$). Increasing the Fe_2O_3 contents ($9 < Fe_2O_3 < 22$ wt%), results in some Fe^{3+} ions crystallise as hematite (Fe_2O_3), with franklinite still present. Above 22 wt% Fe_2O_3 within the glass, all crystalline Fe^{3+}

ions crystallise as hematite [127]. Mary *et al*. [128] studied the effects of adding Fe_2O_3 to bismuth borate glasses, which were known for having a low melting point. The iron was found to exist entirely as Fe^{3+} in primarily tetrahedral units. The addition of Fe_2O_3 was shown to increase the glass transition temperature of the bismuth borate glasses linearly from 0 – 30 mol% Fe_2O_3, with a further increase from 30 – 40 mol%, but at a lower rate [128].

While the studies by Yang *et al*. [125], Romero *et al*. [127], and Mary *et al*. [128] did not explicitly study radioactive waste glasses, the conclusions from their studies are no less pertinent to studying iron-bearing waste glasses. Understanding that Fe-O bonds are weaker than Si-O and Al-O bonds and could manifest in a reduction in glass transition temperature [125,126], is useful to consider in borosilicate glasses, as well as understanding that Fe^{3+} ions within alternative (relative to Fe-rich radioactive waste glasses) silicate glass networks can crystalise to form spinel and other Fe-rich phases [127], which evidences how common a phenomenon it is. This is a key consideration when looking into iron within Hanford waste glasses, covered in the next section.

2.3.6 Iron and Expected Hanford Waste Glasses

Given the use of ferrous compounds as reducing agents in some of the extraction processes employed at the Hanford site, there are some waste streams that will contain significant quantities of mixed iron-bearing compounds (see Chapter 1.4 for more information). This has led to a significant amount research, particularly around the crystallisation of spinel and nepheline crystals [129-158], as well as how the iron chemistry behaves within the "Cold Cap" within the melter [159-174] (See Chapter 1.5.3 for more information). This section will cover some specifics into how iron oxide has factored into this research.

Primarily, the key areas of research of iron oxide in Hanford waste glasses have centred around the formation of secondary phases. Research by Ahmadzadeh *et al*. [152] has found that iron will preferentially form iron oxide phases (such as Fe_2O_3, Fe_3O_4, and other Fe-bearing spinels), but tetrahedral Fe^{3+} can substitute for the tetrahedral Al^{3+} within the nepheline crystals (up to a fraction of 0.37 Fe-substitution). Further research showed that at high iron concentrations, when substituted in at the expense of Al_2O_3, the iron will preferentially behave as a glass network former, rather than form a secondary phase [152]. Deshkar *et al*. [154] showed that in glasses specifically designed as ideal for the formation of nepheline, where the Al_2O_3 and Fe_2O_3 were substituted for one another, that even after

heat treatment, the Fe ions that crystallise will preferentially crystallise into hematite and magnetite, rather than nepheline (which still formed, but formed with no Fe substitution). It was also shown that there is an iron-rich layer that forms in spinel-bearing glasses that is theorised to have a detrimental impact on the chemical durability [154]. McClane *et al*. [157] noted that in glasses that crystallised nepheline, also crystallised another phase analogous to an Fe-bearing spinel phase, $Li_{0.50}Mn_{0.25}Fe_{2.25}O_4$ [157]. It all cases, while iron can substitute into nepheline via the Al tetrahedra, it is far more likely to crystallise into spinel crystals, or other Fe-bearing crystalline phases such as hematite.

Vienna *et al*. [130] studied the effect spinel forming glass components, such as Ni, Mn, Cr, and Fe effect the liquidus temperature (T_L). The liquidus temperature is the temperature above which the glass melt is fully liquid (see section 2.1.1). It was found that there is a link between the bond characteristics of a component and its relative influence on the liquidus temperature which allowed for a refined model to be able to predict the liquidus temperature of a glass, and by extension predict the spinel crystallisation within a given waste melt [130]. Jantzen and Brown [132] studied spinel crystals and the octahedral site preference energies for spinel crystals and found that Fe^{2+} was more likely to form spinel crystals than Fe^{3+} (which is important to note, as most iron in borosilicate glass is Fe^{3+}) [132]. A follow up study by Jantzen and Brown [144] showed that the wider aspects of the glass network will influence the Fe-based crystallisation, such as the polymerisation of the network. At low polymerisation, spinel and pyroxene ($M2_1\ M1_1\ MT_2\ O_6$, where M2 is a distorted 6-8 coordinated site, and M2 and MT are tetrahedral sites [144]) crystals are able to stabilise within the melt. As the glass network polymerisation increases, the pyroxene and spinel crystals are less likely to crystalise within the melt [144]. McCloy *et al*. [159] studied nepheline formation using simplified glasses that contained Fe_2O_3 as one of the constituent oxides. Using Mössbauer and XRD, it was shown that while the aluminosilicate nepheline crystal formed, and the Fe was almost entirely Fe^{3+}, Fe-rich spinel phases still crystallised despite the absence of Fe^{2+} [159], which is more likely form a spinel phase [132,144].

Rigby *et al*. [169] studied the effects on the melting behaviour of a high-Fe simulated Hanford waste as a function of different Fe-bearing raw materials. It was found that the nature of the iron-bearing raw material had little bearing on the final waste form, but the chemical reactions within the "cold cap" (See Chapter 1.5.3 for more details) were significantly different for ferrous raw materials when compared to ferric raw materials.

The ferrous raw materials, particularly ferrous oxalate ($FeC_2O_4 \cdot 2H_2O$). The ferrous raw materials exhibited a reduction in foaming within the cold cap [169], with "foaming" being a melt property linked to the reduction in melt rate in this type of melter set up [161-163]. These conclusions supported a much earlier study done by Goldman [148], where the ratios of ferric/ferrous iron within a melt was used as an indicator of how much foam was able to stabilise in the melt [171].

Balasubramanya *et al*. [176] studied modifier cations in high-Fe waste simulant glasses. It was shown that that increasing optical basicity and cation field strength by varying the Na_2O with Li_2O or CaO, resulted in widespread changes within the glass network, including increasing the Fe^{2+} (relative to the Fe^{tot}), decreasing the $^{[4]}B$ in favour of $^{[3]}B$, increasing the coordination of the Al units, and increasing the non-bridging oxygens within the glass network. These changes resulted in Fe-rich spinel crystals and hematite being more prevalent in the glasses in the study, as well as the spodumene ($LiAlSi_2O_6$) and calcium rich crystals forming in the glass [176]. These conclusions are in line with the selective behaviour of modifier cations theory presented by Bingham *et al*. [68], discussed in Chapter 2.3.2. Rodriguez *et al*. [177] studied the thermal properties of a range of simulated Hanford simulant glasses, including a high-Fe HLW waste glass (HLW-Ng-Fe2). The thermal properties of the high-Fe Hanford HLW glass showed that it was consistent with the other HLW waste glasses studied in trends and patterns. This suggests that the Fe itself has no significant impact to thermal properties relative to other components such as silica and borate groups, which will have a significant impact on the thermal properties [177]. The same HLW glass formulation came from a study by Matlack *et al*. [178], which aimed to increase the melt rate of high-Fe HLW waste glasses by changing the glass formulation and increasing the waste loading. This was carried out using the same constraints as previous studies, which are that the glass must melt at 1150 ^oC and must have less than 1 wt% spinel crystals at 950 ^oC. HLW-Ng-Fe2 passed the initial crucible/lab made trials and showed significant increase in processing rate after the melter tests, increasing the processing rate between 56 - 59 %, with an increase in waste loading from 37.1 to 42.0 wt% [178]. Matlack *et al*. followed up this study with another looking at the effects of the form of iron (essentially, the starting chemical/mineral prior to melting) on melt rate [179]. The study used the HLW-Ng-Fe2 glass formulation, with 5 different raw materials for the iron oxide within the glass; iron hydroxide ($Fe(OH)_3$), goethite (FeOOH), magnetite (Fe_3O_4), hematite (Fe_2O_3), and a slurry mix of hematite and

magnetite (named NOAH after the company who supplied it for the study). It was found that the melt rate was influenced by the change in raw material, in the following order:

$Fe(OH)_3 < FeOOH < Fe_3O_4 < Fe_2O_3 < NOAH$ [178]

Interestingly, the most viscous of the melts was the melt that used $Fe(OH)_3$, with the least viscous being the NOAH mix. This relationship is inversely proportional to similar studies on the high-Al wastes [179]. The iron raw material was not shown to affect the off-gas emissions during the melting [180].

2.4 The Research Project

2.4.1 Overview

Based on all the information covered so far in this chapter, studying the complexities of iron oxide within a complex waste form will be a challenge, but a necessary challenge in order to support the clean-up efforts of the Hanford site. Iron within oxide glasses have shown to behave in a variety of manners depending on the wider glass composition, with subsequently unique effects on glass properties. The key research questions this thesis aims to address are as follows:

1). How does Fe_2O_3 integrate within a complex borosilicate glass network?

2). How does high concentrations of Fe_2O_3 within the glass, affect the wider glass network?

3). How do these changes to the glass network affect key properties specific to the Hanford site?

In order to address these questions, this research will be split into two main studies: a structural study, and a property study. The structural study will use three borosilicate glass matrices (including a Hanford analogue series), each doped with hematite (Fe_2O_3) in a pro-rata basis with the aim of comparing the results across all three series to generate a thorough understanding of structural impacts as a function of increasing Fe_2O_3 contents. The property study will focus solely on the Hanford analogue series.

2.4.2 Glass Selection – Simple Borosilicate

Three series of borosilicate glasses have been selected for this research. The first series is a simple sodium borosilicate which will be incrementally doped with iron(III) oxide (Fe_2O_3) in a pro-rata basis. The base composition was derived from glass composition

data from a compendium of Hanford HLW glasses provided by the Pacific Northwest National Laboratory [181], with a series of simplifications. They are as follows:

1) The group 1 & 2 components were represented by sodium oxide.
2) Components in low abundance (< 1.0 wt.%) were omitted.
3) All transition metal components were represented by iron(III) oxide.
4) Sulphur dioxide and other non-metal components were omitted.
5) Alumina (Al_2O_3) was omitted.

The purpose of this glass was to use a highly simplified borosilicate glass that contained similar compositional parameters (e.g. similar B_2O_3 / SiO_2 ratio) as expected Hanford waste glasses, while also having a composition that could be easily compared to a wider range of existing literature on Fe-doped borosilicate glasses. It is accepted that the simplifications render this composition unrecognisable from the glasses expected at the Hanford site and as such, this will only be used in structural studies section of this research. This sample series will be incrementally doped from 0 – 14 mol% Fe_2O_3 in a pro-rata basis. These samples are labelled as the "SCFe" series (**S**implified **C**omposition – **Fe** doped), with each sample in this series as "SCFeXXX.X", where the XXX.X is the nominal mol% value of the Fe_2O_3 doped into the sample. For example, "SCFe001.0" describes the 1 mol% Fe_2O_3 doped sample in the simple borosilicate series.

2.4.3 Glass Selection – Complex Borosilicate

The more complex borosilicate glass aimed to introduce more common glass forming chemicals into the series. The glass was derived using the same rules at the simple borosilicate glass series, but with some adjustments. They are as follows:

1) CaO was included – all group 2 oxides are represented by CaO.
2) Li_2O was included – Na_2O now represents all group 1 oxides except Li_2O.
3) Al_2O_3 was included.

The result was a 6-component glass, that rose to 7 components with the inclusion of iron(III) oxide. This glass series still contains the same, or at the very least, comparable B_2O_3 / SiO_2 ratio at the simple series. However, there is the introduction of a group 2 oxide and lithium oxide, both of which behave differently to sodium oxide within an oxide glass. Alumina was also included as this will be a common component in a lot of a of glass formulations, not just those expected in Hanford HLW's. Given that it also a glass network intermediate that forms charge compensated tetrahedral groups, it would be

interesting to note any interactions (if any) with iron chemistry. This glass series will be incrementally doped with Fe_2O_3 from 0 – 10 mol% in a pro rata basis. These samples are labelled as the "CCFe" series (**C**omplex **C**omposition – **Fe** doped), with each sample in this series as "CCFeXXX.X", where the XXX.X is the nominal mol% value of the Fe_2O_3 doped into the sample.

2.4.4 Glass Selection – Hanford Analogue

Due to the variety of wastes expected to be vitrified at the Hanford WVP, and the adjustments to the glass matrix to account for the various complexities (see Chapter 1 for details), picking a single waste simulant may not provide the fullest picture of what to expect at the Hanford site. However, for the purpose of this project, a single high-iron analogue was selected for the abundance of established research available for to compare data generated in this research to. The glass selected is the HLW-Ng-Fe2 glass, studied by Matlack *et al*. [177,176], Rodriguez *et al*. [175], and Rigby *et al*. [168]. This glass was selected to vitrify high-Fe wastes from the C-106 tank (see Chapter 1.4.3 for more information on C-Tank waste). This glass series will be the most comparable glass to the expected waste forms at the Hanford WVP. The expected SiO_2 / B_2O_3 ratio will be comparable to that of the SCFe and CCFe sample series, which should allow some inter series comparison, despite the Hanford analogue composition being the most complex. This series will be doped with Fe_2O_3 from 0 – 10 mol% in a pro-rata basis. These samples are labelled as the "HAFe" series (**H**anford **A**nalogue – **Fe** doped), with each sample in this series as "HAFeXXX.X", where the XXX.X is the nominal mol% value of the Fe_2O_3 doped into the sample.

2.4.5 Structural Studies

The glass structure was investigated using a multi-spectroscopic approach (similar to multi-spectroscopic studies mentioned in Chapter 2.3.1 – 2.3.4, for example, references [66,69,108,109]), to analyse the iron chemistry within the glass, but also the chemistry of the wider glass components, such as the borate and silicate groups. ^{57}Fe Mössbauer spectroscopy was used across all samples to provide information of the oxidation state of the iron within the glass. This was supported by Fe *K*-edge X-ray absorption – near edge structure (XANES) spectroscopy in describing the iron chemistry. Boron *K*-edge XANES was used to characterise the fraction of $^{[4]}$B within the SCFe and CCFe sample series, with X-ray photoelectron spectroscopy (XPS) used to describe the boron, silicon, and oxygen bonding within the same sample series. The HAFe series was not measured using

experiments B *K*-edge XANES and XPS for reasons that are elaborated upon in Chapters 3, 5, & 6. Raman spectroscopy was performed on all glasses to allow qualitative analysis of the borosilicate network.

The results are presented as a function of Fe_2O_3 contents within the respective series. The conclusions will be compared across the series to see how much of the spectroscopic changes can be attributed to the iron, and how the complexity of the wider glass matrix influence the changes.

2.4.6 Property Studies

The properties of the Hanford analogue series are important for describing how the waste form may behave with high-Fe glasses. The properties of interest are glass transition temperature (T_g), chemical durability, and secondary phase stabilisation. Differential thermal analysis (DTA) was performed to measure the glass transition temperature, 7-day product consistency test – method B (PCT-B), was carried out to characterise the chemical durability, and X-ray diffraction with Rietveld refinement was used to characterise the secondary phases that may stabilise in the Hanford analogue glasses. The data generated in both study streams was used to provide an insight as to how high concentrations of Fe_2O_3 integrates within a complex borosilicate glass network and how this in turn influences the glass properties.

2.5 References

[1] Khudiar A. I., & Khan Z. H., Laser-induced effects: On metal chalcogenide thin films, LAP LAMBERT Academic Publishing GmbH & Co, Saarbrucken, Germany, 2016.

[2] Ojovan, M. I., Lee, W. E., & Kalmykov, S. N., Chapter 19: Immobilisation of Radioactive Wastes in Glass, An Introduction to Nuclear Waste Immobilisation 3rd Edition, Elsevier Publishing, Amsterdam, Netherlands, 2019.

[3] Ojovan, M. I., & Lee. W. I., Topologically disordered systems at the glass transition, *J. Phys.: Condens. Matter*, **18**, 2006; pp 11507–11520.

[4] Avrami, M., Kinetics of Phase Change I. General Theory, *Chem. Phys.*, **7**, 1939; pp 1103-1112.

[5] Avrami, M., Kinetics of Phase Change II. Transformation-time relations for random distribution of nuclei, *Chem. Phys.*, **8**, 1940; pp 212-224.

[6] Avrami, M., Kinetics of Phase Change III. Granulation, phase change, and microstructure, *Chem. Phys.*, **9**, 1941; pp 177-184.

[7] Uhlmann, D. R., A kinetic treatment of glass transition, *J. Non-Cryst. Solids*, **7**, 1972; pp 337-348.

[8] Shelby, J. E., Introduction to Glass Science and Technology 2nd Edition, The Royal Society of Chemistry, Cambridge, UK, 2005.

[9] Long, Z., Xie, G., Wei, H., Su, X., Peng, J., Zhang, P., & Inoue, A., On the new criterion to assess the glass-forming ability of metallic alloys, *Mater. Sci. Eng. A*, **509**, 2009; pp 23–30.

[10] Zachariasen, W. H., The atomic arrangement in glass, *J. Am. Chem. Soc.*, **54**, 1932; pp 3841-3851.

[11] Pauling, L., The principles determining the structure of complex ionic crystals, *J. Am. Chem. Soc.*, **51**, 1929; pp 1010-1026.

[12] Stanworth, J. E., Oxide glass formation from the melt, *J. Am. Ceram. Soc.*, **54**, 1971; pp 61-63.

[13] Sun K.-H., Fundamental condition of glass formation, *J. Am. Ceram. Soc.*, **30**, 1947; pp 277-281.

[14] Greaves, G. N., EXAFS and the structure of glass, *J. Non-Cryst. Solids*, **71**, 1985; pp 203-217.

[15] Sakka, S., & MacKenzie, J. D., Relation between apparent glass transition temperature and liquidus temperature for inorganic glasses, *J. Non-Cryst. Solids*, **6**, 1971; pp 145-162.

[16] Olivier, L., Yuan, X., Cormack, A. N., & Jäger, C., Combined ^{29}Si double quantum NMR and MD simulation studies of network connectivities of binary $Na_2O \cdot SiO_2$ glasses: New prospects and problems, *J. Non-Cryst. Solids*, **293-295**, 2001; pp 53-66.

[17] Sen, S., & Youngman, R. E., NMR study of Q-speciation and connectivity in K_2O-SiO_2 glasses with high silica content, *J. Non-Cryst. Solids*, **331**, 2003; pp 100-107.

[18] Le Losq, C., Neuville, D. R., Florian, P., Henderson, G. S., & Massiot, D., The role of Al^{3+} on rheology and structural changes in sodium silicate and aluminosilicate glasses and melts, *Geochim. Cosmochim. Acta*, **126**, 2014; pp 495-517.

[19] Limbach, R., Karlsson, S., Scannell, G., Mathew, R., Edén, M., & Wondraczek, L., The effect of TiO_2 on the structure of Na_2O-CaO-SiO_2 glasses and its implications for thermal and mechanical properties, *J. Non-Cryst. Solids*, **471**, 2017; pp 6-18.

[20] Mysen, B. O., Finger, L. W., Virgo, D., & Seifert, F. A., Curve-fitting of Raman spectra of silicate glasses, *Am. Mineral.*, **67**, 1982; pp 686-695.

[21] Matson, D. W., Sharma, S. K., & Philpotts, J. A., The structure of high-silica alkali-silicate glasses. A Raman spectroscopic investigation, *J. Non-Cryst. Solids*, **58**, 1983; pp 323-352.

[22] Kamitsos, E. I., & Risen, W. E., Vibrational spectra of single and mixed alkali pentasilicate glasses, *J. Non-Cryst. Solids*, **65**, 1984; pp 333-354.

[23] Fukumi, K., Hayakawa, J., & Komiyama, T., Intensity of Raman band in silicate glasses, *J. Non-Cryst. Solids*, **119**, 1990; pp 297-302.

[24] Parkinson, B. G., Holland, D., Smith, M. E., Larson, C., Doer, J., Affagiato, M., Feller, S. A., Howes, A. P., & Scales, C. R., Quantitative measurement of Q^3 species in silicate and borosilicate glasses using Raman spectroscopy, *J. Non-Cryst. Solids*, **354**, 2008; pp 1936-1942.

[25] Malfait, W. J., & Halter, W. E., Structural relaxation in silicate glasses and melts: High-temperature Raman spectroscopy, *Phys. Rev. B*, **77**, 2008.

[26] Hehlen, B., & Neuville, D. R., Raman response of network modifier cations in alumino-silicate glasses, *J. Phys. Chem.*, **119**, 2015; pp 4093-4098.

[27] Koroleva, O. N., The structure of lithium silicate melts revealed by high-temperature Raman spectroscopy, *Spectrosc. Lett.*, **50**, 2017; pp 257-264.

[28] Bancroft, G. M., Nesbitt, H. W., Henderson, G. S., O'Shaughnessy, C., Withers, A. C., & Neuville, D. R., Lorentzian dominated lineshapes and linewidths for Raman symmetric stretch peaks (800–1200 cm^{-1}) in Q^n (n = 1–3) species of alkali silicate glasses/melts, *J. Non-Cryst. Solids*, **484**, 2018; pp 72-83.

[29] O'Shaughnessy, C., Henderson, G. S., Nesbitt, H. W., Bancroft, G. M., & Neuville, D. R., The influence of modifier cations on the Raman stretching modes of Q^n species in alkali silicate glasses, *J. Am. Ceram. Soc.*, 2020; pp 1-11.

[30] Wright, A. C., Dalba, G., Rocca, F., & Vedishcheva, N. M., Borate versus silicate glasses: Why are they so different?, *Phys. Chem. Glasses: Eur. J. Glass Sci. Technol. B*, **51**, 2010; pp 233-265.

[31] Jellison, G. E., Feller, S. A., & Bray, P. J., A re-examination of the fraction of 4-coordinated boron atoms in the lithium borate glass system, *Phys. Chem. Glasses*, **19**, 1978; pp 52-53.

[32] Kroeker, S., Aguiar, P. M., Cerquiera, A., Okoro, J., Clarida, W., Doerr, J., Olesiuk, M., Ongie, G., Affatigato, M., & Feller, S. F., Alkali dependence of tetrahedral boron in alkali borate glasses, *Phys. Chem. Glasses: Eur. J. Glass Sci. Technol. B*, **47**, 2006; pp 393-396.

[33] Aguiar, P. M., & Kroeker, S., Boron speciation and non-bridging oxygens in high-alkali borate glasses, *J. Non-Cryst. Solids*, **353**, 2007; pp 1834-1839.

[34] Bray, P. J., & O'Keefe, J. G., Nuclear magnetic resonance investigations of structure of alkali borate glasses, *Phys. Chem. Glasses*, **4**, 1963; pp 37-46.

[35] Cormier, L., Calas, G., & Beuneu, B., Structure of single and mixed alkali Li–Rb borate glasses by neutron diffraction, *J. Non-Cryst. Solids*, **353**, 2007; pp 1779-1784.

[36] Ratai, E., Chan, J. C. C., & Eckert, H., Local coordination and spatial distribution of cations in mixed-alkali borate glasses, *Phys. Chem. Chem. Phys.*, **4**, 2002; pp 3198-3208.

[37] Duffy, J. A., How does adding alkali oxide to a borate glass decrease its basicity?, *Phys. Chem. Glasses: Eur. J. Glass Sci. Technol. B*, **49**, 2008; pp 202-206.

[38] Jantzen, C. M., Chapter 6: Historical development of glass and ceramic waste forms for high level radioactive wastes, in Handbook of Advanced Radioactive Waste Conditioning Technologies, Ed. By Ojovan, M. I., Woodhead Publishing, Cambridge, UK, 2011.

[39] Plodinec, M. J., Borosilicate glasses for nuclear waste imobilisation, *Glass Technol.*, **41**, 2000; pp 186-192.

[40] ASTM Standard C1285, 2021, "Standard Test Methods for Determining Chemical Durability of Nuclear, Hazardous, and Mixed Waste Glasses and Multiphase Glass Ceramics: The Product Consistency Test (PCT)" ASTM International, West Conshohocken, PA, 2021, DOI: 10.1520/C1285-21, www.astm.org.

[41] Gin, S., Open scientific questions about nuclear glass corrosion, *Proc. Mater. Sci.*, **7**, 2014; pp 163-171.

[42] Jantzen, C. M., Systems approach to nuclear waste glass development, *J. Non-Cryst. Solids*, **84**, 1986; pp 215-225.

[43] Kroeker, S., Chapter 8: Nuclear magnetic resonance spectroscopy of glasses, in Modern Glass Characterisation, Edited by Affatigo, M., John Wiley & Sons Ltd., Hoboken, NJ, USA, 2015.

[44] Yun, Y. H., & Bray, P. J., Nuclear magnetic resonance studies of the glasses in the system Na_2O-B_2O_3-SiO_2, *J. Non-Cryst. Solids*, **27**, 1978; pp 363-380.

[45] Yun, Y. H., Feller, S., & Bray, P. J., Correction and addendum to "Nuclear magnetic resonance studies of the glasses in the system Na_2O-B_2O_3-SiO_2", *J. Non-Cryst. Solids*, **33**, 1979, pp 273-277.

[46] Dell, W. J., Bray, P. J., & Xiao, S. Z., ^{11}B NMR studies and structural modelling of Na_2O-B_2O_3-SiO_2 glasses of high soda content, *J. Non-Cryst. Solids*, **58**, 1983; pp 1-21.

[47] Du, L.-S., & Stebbins, J. F., Network connectivity in aluminoborosilicate glasses: A high-resolution ^{11}B, ^{27}Al and ^{17}O NMR study, *J. Non-Cryst. Solids*, **351**, 2005; pp 3508-3520.

[48] Wang, S., & Stebbins, J. F., Multiple-quantum magic-angle spinning ^{17}O NMR studies of borate, borosilicate, and boroaluminate glasses, *J. Am. Ceram. Soc.*, **82**, 1999; pp 1519-1528.

[49] Du, L.-S., & Stebbins, J. F., Nature of silicon-boron mixing in sodium borosilicate glasses: A high-resolution ^{11}B and ^{17}O NMR study, *J. Phys. Chem. B*, **107**, 2003; pp 10063-10076.

[50] Du, L.-S., & Stebbins, J. F., Solid-state NMR study of metastable immiscibility in alkali borosilicate glasses, *J. Non-Cryst. Solids*, **315**, 2003; pp 239-255.

[51] Lowentstein, W., The distribution of aluminum in the tetrahedra of silicates and aluminates, *Am. Mineral.*, **92**, 1952; pp 92-96.

[52] Möncke, D., Tricot, G., Winterstein-Beckmann, A., Wondrazek, L., & Kamitsos, E. I., On the connectivity of borate tetrahedra in borate and borosilicate glasses, *Phys. Chem. Glasses: Eur. J. Glass Sci. Technol. B*, **56**, 2015; pp 203-211.

[53] Möncke, D., Ehrt, D., Eckert, H., & Mertens, V., Influence of melting and annealing conditions on the structure of borosilicate glasses, *Phys. Chem. Glasses*, **44**, 2003; pp 113-116.

[54] Venkatachalam, S., Schröder, C., Wegner, S., & van Wüllen, L., The structure of a borosilicate and phosphosilicate glasses and its evolution at temperatures above the glass transition temperature: Lessons from in situ MAS NMR, *Phys. Chem. Glasses: Eur. J. Glass Sci. Technol. B*, **55**, 2014; pp 280-287.

[55] Tanaka, Y., Benino, Y., Nanba, T., Sakida, S., & Muira, Y., Correlation between basicity and coordination structure in borosilicate glasses, *Phys. Chem. Glasses: Eur. J. Glass Sci. Technol. B*, **50**, 2009; pp 289–293.

[56] Wu, J., & Stebbins, J. F., Effects of cation field strength on the structure of aluminoborosilicate glasses: High-resolution ^{11}B, ^{27}Al and ^{23}Na MAS NMR, *J. Non-Cryst. Solids*, **355**, 2009; pp 556-562.

[57] Lu, X., Deng, Lu, Du, J., & Vienna, J. D., Predicting boron coordination in multicomponent borate and borosilicate glasses using analytical models and machine learning, *J. Non-Cryst. Solids*, **533**, 2021.

[58] Hostetter, J. C., & Roberts, H. S., Note on the dissociation of ferric oxide dissolved in glass and its relation to the color of iron-bearing glasses. *J. Am. Ceram. Soc.*, **4**, 1921.

[59] Lyle, A. K., & Sharp, D. E., Colour Changes in flint glass. *J. Am. Ceram. Soc.*, **8**, (1933).

[60] Shute, R. L., & Badger, A. E., Effects of iron oxide on melting of glass. *J. Am. Ceram. Soc.*, **25**, (1942).

[61] Darby-Dyar, M., A review of Mossbauer data on inorganic glasses: the effects of composition on iron valency and coordination, *Am. Mineral.*, **70**, (1985).

[62] Montenero, A., Friggeri, M., Giori, D. C., Belkhiria, N., & Pye, L. D., Iron-soda-silica glasses: Preparation, properties, structure, *J. Non-Cryst. Solids*, **84**, 1986; pp 45-60.

[63] Bingham, P. A., Parker, J. M., Searle, T., Williams, J. M., & Fyles, K., Redox and clustering of iron in silicate glasses. *J. Non-Cryst. Solids*, **253**, 1999; pp 203-209.

[64] Virgo, D., & Mysen, B. O., The structural state of iron in oxidized vs. reduced glasses at 1 atm: A ^{57}Fe Mössbauer study, *Phys. Chem. Miner.*, **12**, 1985; pp 65-76.

[65] Mekki, A., Holland, D., McConville, C. F., & Salim, M., An XPS study of iron sodium silicate glass surfaces, *J. Non-Cryst. Solids*, **208**, 1996; pp 267-276.

[66] Holland, D., Mekki, A., Gee, I. A., McConville, C. F., Johnson, J. A., Johnson, C. E., Appleyard, P., & Thomas, M., Structure of sodium iron silicate glass - a multi-technique approach, *J. Non-Cryst. Solids*, **253**, 1999; pp 192-202.

[67] Bingham, P. A., Parker, J. M., Searle, T. M., & Smith, I., Local structure and medium range ordering of tetrahedrally coordinated Fe^{3+} ions in alkali-alkaline earth-silica glasses, *J. Non-Cryst. Solids*, **353**, 2007; pp 2479-2494.

[68] Volotinen, T. T., Parker, J. M., & Bingham, P. A., Concentrations and site partitioning of Fe^{2+} and Fe^{3+} ions in a soda-lime-silica glass obtained by optical absorbance spectroscopy, *Phys. Chem. Glasses: Eur. J. Glass Sci. Technol. B*, **49**, 2008; pp 258-270.

[69] Jackson, W. E., Farges, F., Yeager, M., Mabrouk, P. A., Rossano, S., Waychunas, G. A., Solomon, E. I., & Brown Jr., G. E., Multi-spectroscopic study of Fe(II) in silicate glasses: Implications for the coordination environment of Fe(II) in silicate melts, *Geochim. Cosmochim. Acta*, **69**, 2005; pp 4315-4332.

[70] Vercamer, V., Lelong, G., Hijiya, H., Kondo, Y., Galoisy, L., & Calas, G., Diluted Fe^{3+} in silicate glasses: Structural effects of Fe-redox state and matrix composition. An optical absorption and X-band/Q-band EPR study, *J. Non-Cryst. Solids*, **428**, 2015; pp 138-145.

[71] Bingham, P. A., Hannant, O. M., Reeves-McLaren, N., Stennett, M. C., & Hand, R. J., Selective behaviour of dilute Fe^{3+} ions in silicate glasses: An Fe K-edge EXAFS and XANES study, *J. Non-Cryst. Solids*, **387**, 2014; pp 47-56.

[72] Wright, A. C., Clarke, S. J., Howard, C. K., Bingham, P. A., Forder, S. D., Holland, D., Martlew, D., & Fischer, H. E., The environment of Fe^{2+}/Fe^{3+} cations in a soda-lime-silica glass, *Phys. Chem. Glasses: Eur. J. Glass Sci. Technol. B*, **55**, 2014; pp 243-252.

[73] Kim, H.-I., Sur, J. C., & Lee, S. K., Effect of iron content on the structure and disorder of iron-bearing sodium silicate glasses: A high-resolution ^{29}Si and ^{17}O solid-state NMR study, *Geochim. Cosmochim. Acta*, **173**, 2016; pp 160-180.

[74] Waychunas, G. A., Apted, M. J., & Brown Jr., G. E., X-ray K-edge absorption spectra of Fe minerals and model compounds: Near-edge structure, *Phys. Chem. Minerals*, **10**, 1983; pp 1-9.

[75] Kukkadapu, R. K., Li, H., Smith, G. L., Crum, J. D., Jeoung, J.-S., Poisl, W. H., & Weinberg, M. C., Mössbauer and optical spectroscopic study of temperature and redox effects on iron local environments in a Fe-doped (0.5 mol% Fe_2O_3) $18Na_2O$ - $72SiO_2$ glass, *J. Non-Cryst. Solids*, **317**, 2003; pp 301-318.

[76] Magnien, V., Neuville, D. R., Cormier, L., Roux, J., Hazemann, J.-L., Pinet, O., & Richet, P., Kinetics of iron redox reactions in silicate liquids: A high-temperature X-ray absorption and Raman spectroscopy study, *J. Nucl. Mater.*, **352**, 2006; pp 190-195.

[77] Harizanova, R., Keding, R., Völksch, G., & Rüssel, C., Effect of the thermal history on the conductivity in the system $Na_2O/CaO/SiO_2/Fe_2O_3$, *Phys. Chem. Glasses: Eur. J. Glass Sci. Technol. B*, **49**, 2008; pp 177-181.

[78] Carl, R., Gerlach, S., & Rüssel, C., UV-visible-near infrared spectroscopy of alkali lime aluminosilicate glasses doped with iron, *Phys. Chem. Glasses: Eur. J. Glass Sci. Technol. B*, **52**, 2011; pp 53-58.

[79] Sharharyar, Y., Cheng, J. Y., Han, E., Maron, A., Weaver, J., Marcial, J., McCloy, J. S., & Goel, A., Elucidating the effect of iron speciation (Fe^{2+}/Fe^{3+}) on crystallization kinetics of sodium aluminosilicate glasses, *J. Am. Ceram. Soc.*, **99**, 2016; pp 2306 – 2315.

[80] Alderman, O. L. G., Wilding, M. C., Tamalonis, A., Sendlebach, S., Heald, S., Benmore, C. J., Johnson, C. E., Johnson, J. A., Hah, H.-Y., & Weber, J. K. R., Iron K-edge X-ray absorption near-edge structure spectroscopy of aerodynamically levitated silicate melts and glasses, *Chem. Geol.*, **453**, 2017; pp 169-185.

[81] Lin, Y., Zhang, Y., Huang, W., Lu, K., & Zhao, Y., Structural study of iron in phosphate glasses, *J. Non-Cryst. Solids*, **112**, 1989; pp 136-141.

[82] Moguš-Milanković, A., Rajič, M., Drašner, A., Trojko, R., & Day, D., Crystallization of iron phosphate glasses, *Phys. Chem. Glasses*, **39**, 1998; pp 70-75.

[83] Ray, C. S., Fang, X., Karabulut, M., Marasinghe, G. K., & Day, D. E., Effect of melting temperature and time on iron valence and crystallization of iron phosphate glasses, *J. Non-Cryst. Solids*, **249**, 1999; pp 1-16.

[84] Leister, M., & Ehrt, D., The influence of high melting temperatures on the influence of polyvalent ions in silicate glasses, *Glass Sci. Technol. Glasstech. Ber.*, **73**, 2000; pp 194-203.

[85] Karabulut, M., Marasinghe, G. K., Ray, C. S., Day, D. E., Ozturk, O., & Waddill, G. D., X-ray photoelectron and Mossbauer spectroscopic studies of iron phosphate glasses containing U, Cs and Bi, *J. Non-Cryst. Solids*, **249**, 1999; pp 106-116.

[86] Day, D. E., Wu, Z., Ray, C. S., & Hrma, P., Chemically durable iron phosphate glass wasteforms, *J. Non-Cryst. Solids*, **241**, 1998; pp 1-12.

[87] Bingham, P. A., Hand, R. J., Hannant, O. M., Forder, S. D., & Kilcoyne, S. H., Effects of modifier additions on the thermal properties, chemical durability, oxidation state and structure of iron phosphate glasses, *J. Non-Cryst. Solids*, **355**, 2009; pp 1526-1538.

[88] Karabulut, M., Marasinghe, G. K., Ray, C. S., Day, D. E., Waddill, G. D., Booth, C. H., Allen, P. G., Bucher, J. J., Caulder, D. L., & Shuh, D. K., An investigation of the local iron environment in iron phosphate glasses having different Fe(II) concentrations, *J. Non-Cryst. Solids*, **306**, 2002; pp 182-192.

[89] Metcalfe, B. L., Fong, S. K., & Donald, I. W., Preparation, thermal characterisation and chemical durability of calcium iron phosphate glasses, *Glass Technol*., **46**, 2005; pp 130-133.

[90] Bingham, P. A., Forder, S. D., Hand, R. J., & Lavaysierre, A., Mössbauer studies of phosphate glasses for the immobilisation of toxic and nuclear wastes, *Hyperfine Interact.*, **165**, 2005; pp 135-140.

[91] Karabulut, M., Yuce, B., Bozgodan, O., Ertap, H., & Mammadov, G. M., Effect of boron addition on the structure and properties of iron phosphate glasses, *J. Non-Cryst. Solids*, **357**, 2011; pp 1455-1462.

[92] Gobbo, J. P., Inertization of small-scale chemical wastes using iron phosphate glass, *Quim. Nova*, **37**, 2014; pp 1058-1062.

[93] Takebe, H., Kitamura, N., Amamoto, I., Kobayashi, H., Tsuzuki, T., & Mitamura, N., Composition optimisation of iron phosphate-based glasses for radioactive sludge, *Phys. Chem. Glasses: Eur. J. Glass Sci. Technol. B*, **57**, 2016; pp 213-217.

[94] Joseph, K., Stennett, M. C., Hyatt, N. C., Asuvathraman, R., Dube, C. L., Gandy, A. S., Kutty, K. V. G., Jolley, K., Rao, P. R. V., & Smith, R., Iron phosphate glasses: Bulk properties and atomic scale structure, *J. Nucl. Mater.*, **494**, 2017; pp 342-353.

[95] Bai, J., Hsu, J., Brow, R. K., Kim, C.-W., Szabo, J., & Zervos, A., Structure and properties of Mo-Fe-phosphate glasses, *Phys. Chem. Glasses: Eur. J. Glass Sci. Technol. B*, **60**, 2019; pp 62-69.

[96] Brow, R. K., Kim, C. W., & Reis, S. T., Iron polyphosphate glasses for waste immobilization, *Int. J. Appl. Glass Sci.*, **11**, 2020; pp 4-14.

[97] Dutta, D. P., Roy, M, Mishra, R. K., Meena, S. S., Yadav, A., Kaushik, C. P., & Tyagi, A. K., Structural investigations on Mo, Cs and Ba ions-loaded iron phosphate glass for nuclear waste storage application, *J. Alloys Compd.*, **850**, 2021.

[98] Jermoumi, T., Hafid, M., & Toreis, N., Density, thermal, and FTIR analysis of (50-x)BaO. xFe_2O_3 .$50P_2O_5$ glasses, *Phys. Chem. Glasses*, **43**, 2002; pp 129-161.

[99] Šantić, A., Moguš-Milanković, A., Furić, K., Bermanec, V., Kim, C. W., & Day, D. E., Structural properties of Cr_2O_3-Fe_2O_3-P_2O_5 glasses, Part I, *J. Non-Cryst. Solids*, **353**, 2007; pp 1070-1077.

[100] Liu, H., Yang, R., Wang, Y., & Liu, S., Influence of alumina additions on the physical and chemical properties of lithium-iron-phosphate glasses, *Phys. Procedia*, **48**, 2013; pp 17-22.

[101] Aragón, M. J., Vidal-Abarca, C., Lavela, P., & Tirado, J. L., High reversible sodium insertion into iron substituted $Na_{1+x}Ti_{2-x}Fe_x(PO_4)_3$, *J. Power Sources*, **252**, 2014; pp 208-213.

[102] Li, X., Lu, A., & Yang, H., Structure of ZnO-Fe_2O_3-P_2O_5 glasses probed by Raman and IR spectroscopy, *J. Non-Cryst. Solids*, **384**, 2014; pp 21-27.

[103] Garbarczyk, J. E., Pietrzak, T. K., Wasiucionek, M., Kaleta, A., Dorau, A., & Nowiński, J. L., High electronic conductivity in nanostructured materials based on lithium-iron-vanadate-phosphate glasses, *Solid State Ion.*, **272**, 2015; pp 53-59.

[104] Magini, M., Sedda, A. F., Lichieri, G., Paschina, G., Piccaluga, G., Pinna, G., & Cocco, G., On the coordination of iron ions in sodium borosilicate glasses. I. A wide angle X-ray diffraction investigation, *J. Non-Cryst. Solids,* **65**, 1984; pp 145-159.

[105] Licheri, G., Paschina, G., Piccaluga, G., Pinna, G., Magini, M., & Cocco, G., On the coordination of iron ions in sodium borosilicate glasses: III. An EXAFS investigation, *J. Non-Cryst. Solids*, **72**, 1985; pp 211-220.

[106] Agostinelli, E., Fiorani, D., & Paparazzo, E., XPS studies of iron sodium borosilicate glasses, *J. Non-Cryst. Solids*, **95** & **96**, 1987; pp 373-379.

[107] Taragin, M. F., & Eisenstein, J. C., Mössbauer effect in some complex borosilicate glasses, *J. Non-Cryst. Solids*, **3**, 1970; pp 311-316.

[108] Musić, S., Furić, K., Bajs, Z., & Mohaček, V., Spectroscopic characterization of alkali borosilicate glasses containing iron ions, *J. Mater. Sci.*, **27**, 1992; pp 5269-5275.

[109] Cochain, B., Neuville, D. R., Henderson, G. S., McCammon, C. A., Pinet, O., & Richet, P., Effects of the iron content and redox state on the structure of sodium borosilicate glasses: A Raman, Mössbauer and boron *K*-edge XANES spectroscopy study, *J. Am. Ceram. Soc.*, **95**, 2012; pp 962-971.

[110] Ciżman, A., Rysiakiewicz-Pasek, E., Antropova, T., Krupiński, M., Pshenko, O. A., & Zarzycki, A., Effect of the iron content on the structure and electrical properties of sodium borosilicate glasses: XRD, TEM, Mössbauer, FTIR and DIS spectroscopy study, *J. Non-Cryst. Solids*, **531**, 2020.

[111] Ratep, A., & Kashif, I., X-ray photoelectron, FTIR, and Mössbauer spectroscopy studied the effect of Fe_2O_3/CuO substitution on structural and electrical properties of lithium borosilicate glasses, *J. Mater. Sci: Mater. Electron.*, **32**, 2021; pp 12340-12347.

[112] Wright, A. C., Sinclair, R. N., Shaw, J. L., Haworth, R., Bingham, P. A., Forder, S. D., Holland, D., Scales, C. R., Cuello, G. J., & Vedishcheva, N. M., The environment of

Fe^{3+}/Fe^{2+} cations in a sodium borosilicate glass, *Phys. Chem. Glasses: Eur. J. Glass Sci. Technol. B*, **58**, 2017; pp 78-91.

[113] Glazkova, Y. S., Kalmykov, S. N., Presnykov, I. A., Stefanovsky, O. I., & Stefanovsky, S. V., The structural state of iron in multicomponent aluminum iron borosilicate glass depending on their composition and synthesis conditions, *Glass Phys. Chem.*, **41**, 2015; pp 367–377.

[114] Stefanovsky, S. V., Fox, K. M., Marra, J. C., Shiryaev, A. A., & Zubavichus, Y. V., Structural features of high-Fe_2O_3 and high Al_2O_3/Fe_2O_3 SRS HLW glasses, *Phys. Chem. Glasses: Eur. J. Glass Sci. Technol. B*, **53**, 2012; pp 158–166.

[115] Kaewkhao, J., Siriprom, W., Insiripong, S., Ratana, T., Ratana, T., Kedkaew, C., & Limsuwan, P., Structural and magnetic properties of glass doped with iron oxide, *J. Phys. Conf. Proc.*, **266**, 2011; pp 1-6.

[116] El-Domrawi, G., Hassan, A. M., Ramadan, R., & El-Jadal, S., Nuclear magnetic resonance and FTIR structural studies on borosilicate glasses containing iron oxide, *New J. Glass Ceram.*, **6**, 2016; pp 47-56.

[117] Ciżman, A., Rysiakiewicz-Pasek, E., Krupiński, M., Konon, M., Antropova, T., & Marszałek, M., The effect of Fe on the structure and electrical conductivity of sodium borosilicate glasses, *Phys. Chem. Chem. Phys.*, **19**, 2017; pp 23318—23324.

[118] Meikhail, M. S., & Abdelghany, A. M., Structure and electrical properties of iron borosilicate glasses, *Silicon*, **9**, 2017; pp 895–900.

[119] Rysiakiewicz-Pasek, E., Ciżman, A., Konon, M., & Antropova, T., The influence of iron on structure and electrical properties of sodium borosilicate glasses, *AIP Conf. Proc.*, **2308**, 2020.

[120] Konon, M., Polyakova, I., Stolyar, S., Simonenko, N., Simonenko, T., Zolotov, N., Semenova, E., & Antropova, T., Mössbauer spectroscopy, XRPD, and SEM study of iron containing Na_2O-B_2O_3-SiO_2 glasses, *J. Am. Ceram. Soc.*, **104**, 2021; pp 3149–3157.

[121] Kelley, J. A., Evaluation of Glass as a Matrix for Solidification of Savannah River Plant Waste, *DP-1397*, E I Du Pont de Nemours and Company Savannah River Laboratory, 1975.

[122] Yanagisawa, F., & Sakai, H. Effect of iron and potassium contents in simulated borosilicate glass on its leaching behaviors at hydrothermal conditions, *Geochem. J.*, **21**, 1987; pp 209-217.

[123] Cassingham, N. J., Bingham, P. A., Hand, R. J. & Forder, S. D., Property modification of a high level nuclear waste borosilicate glass through the addition of Fe_2O_3, *Glass Technol.: Eur. J. Glass Sci. Technol. A*, **49**, 2008; pp 21-26.

[124] Konon, M., Antropova, T., Zolotov, N., Simonenko, T., Simonenko, N., Brazovskaya, E., Kreisber, V., & Polyakova, I., Chemical durability of the iron-containing sodium borosilicate glasses, *J. Non-Cryst. Solids*, **584**, 2022.

[125] Yang, Z., Wang, B., & Cormack, A. N., The local structure of Fe in Li(Al, Fe)Si_2O_6 glasses from molecular dynamics simulations, *J. Non-Cryst. Solids*, **444**, 2016; pp 16-22.

[126] Dietzel, A., Die kationenfeldstärken und ihre beziehungen zu entglasungsvorgängen, zur verbindungsbildung und zu den schmelzpunkten von silicate, *Ber. Bunsenges. Phys. Chem.*, **42**, 1942; pp 9-23.

[127] Romero, M., Rincón, J. M., & Acosta, A., Effect of iron oxide content on the crystallisation of a diopside glass–ceramic glaze, *J. Eur. Ceram. Soc.*, **22**, 2002; pp 883–890.

[128] Mary, N., Rebours, M., Castel, E., Vaishnav, S., Deng, W., Bell, A. M. T., Clegg, F., Allsopp, B. L., Scrimshire, A., & Bingham, P. A., Enhanced thermal stability of high-bismuth borate glasses by addition of iron, *J. Non-Cryst. Solids*, **500**, 2018; pp 149-157.

[129] Vienna, J. D., Hrma, P., Crum, J. V., & Mika, M., Liquidus temperature-composition model for multi-component glasses in the Fe, Cr, Ni, and Mn spinel primary phase field, *J. Non-Cryst. Solids*, **292**, 2001; pp 1-24.

[130] Jiricka, M., Hrma, P., & Vienna, J. D., The effect of composition on spinel crystals equilibrium in low-silica high-level waste glasses, *J. Non-Cryst. Solids*, **319**, 2003; pp 280-288.

[131] Jantzen, C. M., & Brown, K. G., Predicting the spinel-nepheline liquidus for application to nuclear waste glass processing. Part I: Primary phase analysis, liquidus measurement, and quasicrystalline approach, *J. Am. Ceram. Soc.*, **90**, 2007; pp 1866-1879.

[132] Hrma, P., Crystallization during processing of nuclear waste glass, *J. Non-Cryst. Solids*, **356**, 2010; pp 3019-3025.

[133] Fox, K. M., Crystallization in High Level Waste (HLW) Glass Melters: Operational Experience from the Savannah River Site, Savannah River National Laboratory, *SRNL-STI-2013-00724*, 2014.

[134] Hrma, P., Riley, B. J., Crum, J. V., & Matyáš, J., The effect of high-level waste glass composition on spinel liquidus temperature, *J. Non-Cryst. Solids*, **384**, 2014; pp 32-40.

[135] Fox, K. M., & Fowley, M. D., Crystal Accumulation in the Hanford Waste Treatment Plant High Level Waste Melter: Summary of 2017 Experiments, Savannah River National Laboratory, *SRNL-STI-2017-00730 Revision 0*, 2018.

[136] Matyáš, J., Crum, J., Vienna, J. D., Arrigoni, A., Schaible, M., Tate, R., & Rodriguez, C., Development of crystal-tolerant high-level waste glasses, Pacific Northwest National Laboratory, *PNNL-20072*, 2010.

[137] Kim, D.-S., Crum, J. V., Schweiger, M. J., Vienna, J. D., Rodriguez, C. P., Johnson, F. C., Lepry, W. C., Marra, J. C., Lang, J. B., & Peeler, D. K., Formulation and characterization of waste glass with varying processing temperatures, Pacific Northwest National Laboratory, *PNNL-20774*, 2011.

[138] Matyáš, J., Huckleberry, A. R., Rodriguez, C. P., Lang, J. B., Owen, A. T., & Kruger, A. A., Crystal-tolerant glass approach for mitigation of crystal accumulation in continuous melters processing radioactive waste, Office of River Protection, *ORP-52717*, 2013.

[139] Matyáš, J., Schaible, M. J., & Vienna, J. D., Determination of Stokes Shape Factor for Single Particles and Agglomerates, *Ceram. Trans.*, **227**, 2011; pp 195-202.

[140] Vienna, J. D., Kim, D.-S., Kruger, A. A., & Matyáš, J., Glass property models and constraints for estimating the glass to be produced at Hanford by implementing current advanced glass formulation efforts, Pacific Northwest National Laboratory, *PNNL-22631 Rev. 1*, 2013.

[141] Matyáš, J., Vienna, J. D., Peeler, D. K., Fox, K. M., Herman, C. C., & Kruger, A. A., Road map for development of crystal-tolerant high level waste glasses, Pacific Northwest National Laboratory, *PNNL-23363*, 2014.

[142] Marra, J. C., & Kim, D.-S., Towards increased waste loading in high level waste glasses: developing a better understanding of crystallization behavior, *Proc. Mater. Sci.*, **7**, 2014; pp 87-92.

[143] Li, H., Hrma, P., Vienna, J. D., Qian, M., Su, Y., & Smith, D. E., Effects of Al_2O_3, B_2O_3, Na_2O, and SiO_2 on nepheline formation in borosilicate glasses: Chemical and physical correlations, *J. Non-Cryst. Solids*, **331**, 2003; pp 202-216.

[144] Jantzen, C. M., & Brown, K. G., Predicting the spinel-nepheline liquidus for application to nuclear waste glass processing. Part II: Quasicrystalline freezing point depression model, *J. Am. Ceram. Soc*., **90**, 2007; pp 1880-1891.

[145] Fox, K. M., Edwards, T. B., & Peeler, D. K., Control of nepheline crystallization in nuclear waste glass, *Int. J. Appl. Ceram. Technol.*, **5**, 2008; pp 666-673.

[146] McCloy, J. S., Schweiger, M. J., & Rodriguez, C. P., & Vienna, J. D., Nepheline crystallization in nuclear waste glasses: Progress toward acceptance of high-alumina formulations, *Int. J. Appl. Glass Sci.*, **2**, 2011; pp 201-214.

[147] Rodriguez, C. P., McCloy, J. S., Schweiger, M. J., Crum, J. V., & Winschell, A., Optical Basicity and Nepheline Crystallization in High Alumina Glasses, Pacific Northwest National Laboratory, *PNNL-20184*, 2011.

[148] Pareizs, J. M., Sludge batch 7b qualification activities with SRS tank farm sludge, Savannah River National Laboratory, *SRNL-STI-2011-00548 Revision 0*, 2011.

[149] Vienna, J. D., Kim, D.-S., Schweiger, M. J., Piepel, G. F., & Kruger, A. A., Glass Formulation and Testing for U.S. High-Level Tank Wastes Project 17210 Year 1 Status Report: October 15, 2014, Pacific Northwest National Laboratory, *PNNL-SA-84872*, 2014.

[150] Marcial, J., Crum, J. V., Neill, O., & McCloy, J., Nepheline structural and chemical dependence on melt composition, *Am. Mineral.*, **101**, 2016; pp 266-276.

[151] Fox, K. M., Edwards, T. B., & McClane, D. L., Chemical composition analysis and product consistency tests supporting refinement of the nepheline model for the high aluminum Hanford glass composition region, Savannah River National Laboratory, *SRNL-STI-2016-00028 Revision 0*, 2016.

[152] Ahmadzadeh, M., Marcial, J., & McCloy, J., Crystallization of iron-containing sodium aluminosilicate glasses in the $NaAlSiO_4$-$NaFeSiO_4$ join, *J. Geophys. Res. Solid Earth*, **122**, 2017; pp 2504-2524.

[153] Vienna, J. D., Kroll, J. O., Hrma, P. R., Lang, J. B., & Crum, J. V., Submixture model to predict nepheline precipitation in waste glasses, *Int. J. Appl. Glass Sci.*, **8**, 2017; pp 143-157.

[154] Deshkar, A., Ahmadzadeh, M., Scrimshire, A., Han, E., Bingham, P. A., Guillen, D., McCloy, J., & Goel, A., Crystallization behavior of iron- and boron-containing nepheline ($Na_2O{\cdot}Al_2O_3{\cdot}2SiO_2$) based model high-level nuclear waste glasses, *J. Am. Ceram. Soc.*, **102**, 2018;

[155] Ahmadzadeh, M., Olds, T. A., Scrimshire, A., Bingham, P. A., & McCloy, J. S., Structure and properties of $Na_5FeSi_4O_{12}$ crystallized from $5Na_2O–Fe_2O_3–8SiO_2$ glass, *Acta. Cryst.*, **C74**, 2018; pp 1595-1602.

[156] Marcial, J., Kabel, J., Saleh, M., Washton, N., Shaharyar, Y., Goel, A., & McCloy, J. S., Structural dependence of crystallization in glasses along the nepheline ($NaAlSiO_4$) - eucryptite ($LiAlSiO_4$) join, *J. Am. Ceram. Soc.*, **101**, 2018; pp 2840-2855.

[157] McClane, D. L., Amoroso, J. W., Fox, K. M., & Kruger, A. A., Nepheline crystallization behavior in simulated high-level waste glasses, *J. Non-Cryst. Solids*, **505**, 2019; pp 215-224.

[158] Amoroso, J. W., McClane, D. L., & Fox, K. M., Nucleation and crystal growth behavior of nepheline in simulated high-level waste glasses, Savannah River National Laboratory, *SRNL-STI-2017-00517 Revision 0*, 2017.

[159] McCloy, J. S., Washton, N., Gassman, P., Marcial, J., Weaver, J., & Kukkadapu, R., Nepheline crystallization in boron-rich alumino-silicate glasses as investigated by multi-nuclear NMR, Raman, & Mössbauer spectroscopies, *J. Non-Cryst. Solids*, **409**, 2015; pp 149-165.

[160] Tan, S., Chapter 26: Glass-based stabilization/solidification of radioactive waste, in 'Low Carbon Stabilization and Solidification of Hazardous Wastes' Ed. By Tsang, D. & Wang, L., Elsevier, Amsterdam, Netherlands, 2022.

[161] Blair, H. T., & Lukacs, J. M., Investigation of foaming during nuclear defense-waste solidification by electric melting, Pacific Northwest Laboratory, *PNL-3552*, 1980.

[162] Lee, S.-M., Hrma, P., Pokorny, R., Klouzek, J., VanderVeer, B. J., Dixon, D. R., Luksic, S. A., Rodriguez, C. P., Chun, J., Schweiger, M. J., & Kruger, A. A., Effect of melter feed foaming on heat flux to the cold cap, *J. Nucl. Mater.*, **496**, 2017; pp 54-65.

[163] Lee, S.-M., Hrma, P., Pokorny, R., Klouzek, J., Eaton, W. C., & Kruger, A. A., Glass production rate in electric furnaces for radioactive waste vitrification, *J. Am. Ceram. Soc.*, **102**, 2019; pp 5828-5842.

[164] Pokorny, R., & Hrma, P., Model for the conversion of nuclear waste melter feed to glass, *J. Nucl. Mater.*, **445**, 2014; pp 190-199.

[165] Pokorny, R., Hilliard, Z. J., Dixon, D. R., Schweiger, M. J., Guillen, D. P., Kruger, A. A., & Hrma, P., One-dimensional cold cap model for melters with bubblers, *J. Am. Ceram. Soc.*, **98**, 2015; pp 3112-3118.

[166] Dixon, D. R., Schweiger, M. J., Riley, B. J., Pokorny, R., & Hrma, P., Temperature distribution within a cold cap during nuclear waste vitrification, *Environ. Sci. Technol.*, **49**, 2015; pp 8856-8863.

[167] Guillen, D. P, Abboud, A. W., Pokorny, R., Eaton, W. C., Dixon, D., Fox, K., & Kruger, A. A., Development of a validation approach for an integrated waste glass melter model, *Nucl. Technol.*, **203**, 2018; pp 244-260.

[168] Hrma, P., Pokorny, R., Lee, S.-M., & Kruger, A. A., Heat transfer from glass melt to cold cap: Melting rate correlation equation, *Int. J. Appl. Glass Sci.*, **10**, 2019; pp 143-150.

[169] Rigby, J. C., Dixon, D. R., Cutforth, D. A., Marcial, J., Kloužek, J., Pokorný, R., Kruger, A. A., Scrimshire, A., Bell, A. M. T., & Bingham, P. A., Melting behaviour of

simulated radioactive waste as functions of different redox iron-bearing raw materials, *J. Nucl. Mater*., **569**, 2022.

[170] Beerkens, R. D. C., & van der Schaaf, J., Gas release and foam formation during melting and fining of glass, *J. Am. Ceram. Soc.*, **89**, 2006; pp 24-35.

[171] Goldman, D. S., Melt foaming, foam stability and redox in nuclear waste vitrification, *J. Non-Cryst. Solids*, **84**, 1986; pp 292-298.

[172] Jin, T., Chun, J., Dixon, D. R., Kim, D.-S., Crum, J. V., Bonham, C. C., Vanderveer, B. J., Rodriguez, C. P., Weese, B. L., Schweiger, M. J., Kruger, A. A., & Hrma, P., Melter feed viscosity during conversion to glass: Comparison between low-activity waste and high-level waste feeds, *J. Am. Ceram. Soc.*, **101**, 2018; pp 1880-1891.

[173] McCarthy, B. P., George, J. L., Dixon, D. R., Wheeler, M., Cutforth, D. A., Hrma, P., Linn, D., Chun, J., Hujova, M., Kruger, A. A., & Pokorny, R., Rheology of simulated radioactive waste slurry and cold cap during vitrification, *J. Am. Ceram. Soc.*, **101**, 2018; pp 5020-5029.

[174] Hilliard, Z., & Hrma, P., A method for determining bulk density, material density, and porosity of melter feed during nuclear waste vitrification, *J. Am. Ceram. Soc.*, **99**, 2016; pp 98-105.

[175] Harris, W. H., Guillen, D. P., Klouzek, J., Pokorny, R., Yano, T., Lee, S.-M., Schweiger, M. J., & Hrma, P., X-ray tomography of feed-to-glass transition of simulated borosilicate waste glasses, *J. Am. Ceram. Soc.*, **100**, 2017; pp 3883-3894.

[176] Balasubramanya, N., Sun, Z., Ahmadzadeh, M., Kamali, S., Neuville, D. R., McCloy, J. S., & Goel, A., Impact of non-framework cation mixing on the structure and crystallization behavior of model high-level waste glasses, *J. Am. Ceram. Soc*., **105**, 2022; pp 3967-3985.

[177] Rodriguez, C. P., Chun, J., Crum, J. V., Canfield, N. L., Rönnebro, E. C. E., Vienna, J. D., & Kruger, A. A., Thermal properties of simulated Hanford waste glasses, *J. Am. Ceram. Soc.*, **100**, 2017; pp 2533-2542.

[178] Matlack, K. S., Gan, H., Chaudhuri, M., Kot, W., & Pegg, I. L., Melter throughput enhancements for high-iron HLW, Office of River Protection, *ORP-54002*, 2012.

[179] Matlack, K. S., Viragh, C., Kot, W. K., Pegg, I. L., & Joseph, I., Effect of the form of iron on HLW melt rate, Vitreous State Laboratory, *VSL-15R3430-1*, 2015.

[180] Matlack, K. S., Bardacki, T., Chaudhuri, M., Gan, H., Gong, W., Kot, W., Pegg, I. L., Joseph, I., & Kruger, A. A., Melt rate enhancement for high aluminum HLW glass formulations, Vitreous State Laboratory, *VSL-08R1360-1*, 2008.

[181] Bingham, P. A., Kim, D.-S., *Personal Communication*, Email correspondence between Bingham, P. A. and Kim, D.-S. dated January 2013, shared with the author (with appropriate permission) on 3rd of October 2018.

Chapter 3 – Glasses to be Studied and Methodology

3.1 Making the Glass

As mentioned in Chapter 2, three series of borosilicate glasses were generated for this research. All three series of glasses were made by creating batches of dry raw materials (Raw materials detailed in **Table 3.1a** & **3.1b**) and mixing these raw materials in a sealed plastic batch bag, by rotating the batch in a figure-of-8 pattern until mixed as homogeneously as possible, as judged by the batch colour being homogeneous by eye. This typically took approximately 10-15 minutes per batch. Prior to batching, most chemicals were dried at 110 ºC in a box oven for at least 16 hours to remove any bonded water from the hygroscopic chemicals. The boric acid (H_3BO_3) was not dried as it loses bonded water below 100 ºC, while the diammonium phosphate ($(NH_4)_2HPO_4$) and lead oxide (PbO) could not be dried prior to batching due to COSHH (Control of Substances Hazardous to Health) constraints. The batches were made to produce a theoretical glass yield of 75 g, which produced batch masses between 80 – 100 g, depending on the composition.

Table 3.1a: The list of target glass oxides and the associated raw materials used to generate them.

Target Oxide	Raw Material	Target Oxide	Raw Material	Target Oxide	Raw Material
Al_2O_3	$Al(OH)_3$	Li_2O	Li_2CO_3	SO_3	Na_2SO_4
B_2O_3	H_3BO_3	MgO	$MgCO_3$	SiO_2	Purified Sand
CaO	$CaCO_3$	MnO_2	MnO_2	SrO	$SrCO_3$
CeO_2	CeO_2	Na_2O	Na_2CO_3	ZnO	ZnO
Cr_2O_3	Cr_2O_3	NiO	NiO	ZrO_2	$Zr(OH)_4$
Fe_2O_3	Fe_2O_3	P_2O_5	$(NH_4)_2HPO_4$		
La_2O_3	$La(OH)_3$	PbO	PbO		

Table 3.1b: The list of raw materials, the purity as given by the supplier, and the supplier.

Raw Material	Purity	Supplier
$Al(OH)_3$	Lab/Reagent Grade	Acros Organics
H_3BO_3	99.99 %	ReAgent
$CaCO_3$	Lab/Reagent Grade	Alfa Aesar
CeO_2	99.99 %	Sigma – Aldrich
Cr_2O_3	98+ %	Alfa Aesar
Fe_2O_3	≥ 96 %	Sigma – Aldrich
$La(OH)_3$	99.95 %	Alfa Aesar
Li_2CO_3	99 %	Acros Organics
$MgCO_3$	Lab/Reagent Grade	Better Equipped
MnO_2	≥ 99 %	Sigma – Aldrich
Na_2CO_3	Lab/Reagent Grade	Better Equipped
NiO	99.99 %	Sigma – Aldrich
$(NH_4)_2HPO_4$	≥ 98 %	Acros Organics
PbO	Lab/Reagent Grade	Sigma – Aldrich
Na_2SO_4	> 99 %	Fisher Scientific
Purified Sand	Lab/Reagent Grade	Better Equipped
$SrCO_3$	Lab/ Reagent Grade	Alfa Aesar
ZnO	≥ 99 %	Sigma – Aldrich
$Zr(OH)_4$	> 97 %	Sigma – Aldrich

"Lab/Reagent Grade" as stated by the supplier, no value for purity given for these chemicals.

The powdered batches were then loaded into Pt/Rh crucibles, which have an approximate volume of 150 ml, and placed in a box furnace at 1150 ºC for 1 hour before being poured and air quenched (The nominal oxide compositions for all three series can be seen in **Table 3.3 - 3.6**). The quenched glass was then turned into a frit in a tungsten carbide mill before being reloaded into the Pt/Rh crucible. This crucible was then reloaded into the furnace at 1150 ºC for a further hour before being poured into cast iron moulds and then transferred to an annealing furnace at 470 ºC for an hour, where the furnace programs ends and the furnace along with the glass is then allowed to cool in free fall towards room temperature. **Figs 3.1 – 3.3** show images of glass fragments made in this manner. The annealing temperature was initially derived from a trial-and-error approach, using the Sciglass online database to provide initial estimates, which could only be considered estimates, owing to a lack of exact compositional matches between database values and glasses studied in this research. These estimates were tested on smaller scale melts where the successful annealing temperature produced annealed glass that was free from cracks and was X-ray amorphous.

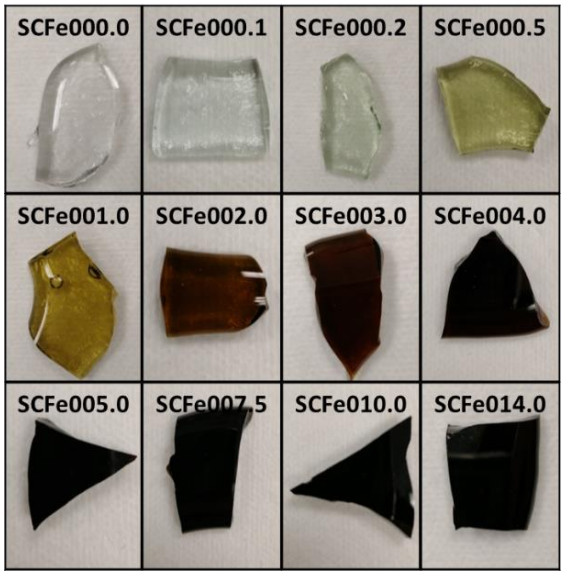

Figure 3.1: *Glass fragments from the SCFe series.*

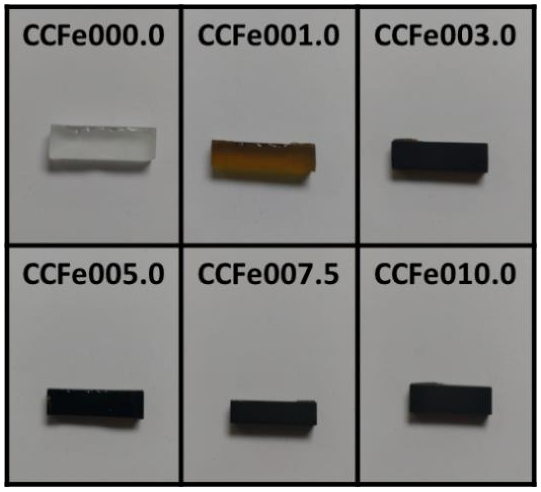

Figure 3.2: *Glass fragments of the CCFe series.*

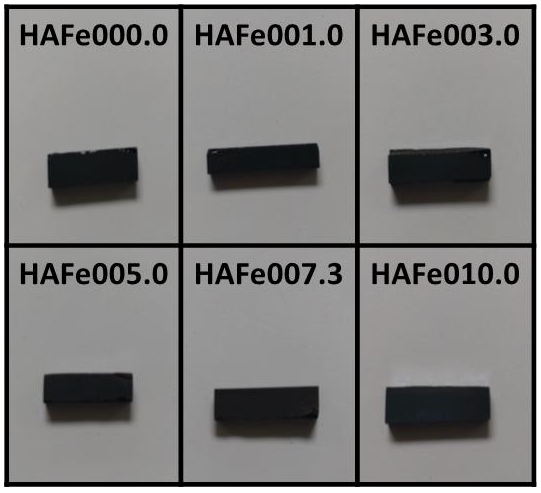

Figure 3.3: *Glass fragments of the HAFe series.*

The method employed to make the samples was selected to be a close representation of how lab-scale glass samples are made at the Pacific Northwest National Laboratory (PNNL) and other affiliated institutes working on Hanford-centric projects [example refs 1-5]. The colour change in the SCFe and CCFe are indicative of the increasing iron oxide contents within the glass. This is not seen in the HAFe series, as there are a number of transition metals present in the iron-free and low-iron samples, rendering all glasses in the series opaque. After making the glass, the composition was verified, and the glasses were checked to ensure they were fully amorphous or whether any secondary crystalline phases stabilised.

3.2 Compositional Analysis

3.2.1 X-ray Fluorescence

To analyse the composition of the glasses, two techniques were used in combination. The first is X-ray Fluorescence (XRF), which relies on using secondary X-rays that are emitted by samples after it is bombarded by high energy X-rays or gamma rays. The incident X-rays cause inner core electrons to excite into higher energy orbitals (or to be ionised altogether), causing the electron configuration to become unstable. To correct this, other electrons relax to the inner core orbital, and this relaxation process produces a measurable X-ray photon known as a fluorescence photon [6]. The process is visually represented in **Fig. 3.4**.

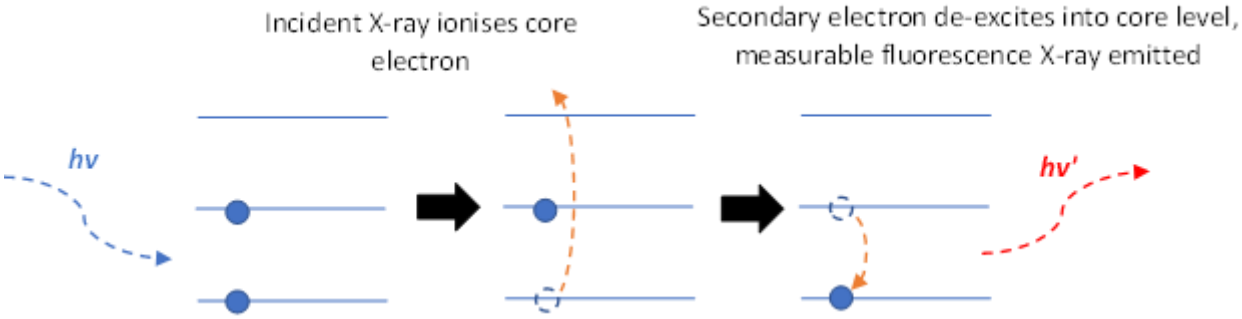

Figure 3.4: *A schematic of how measurable fluorescence X-rays are generated in XRF analysis.*

Combinations of specific energy fluorescence X-rays are used to describe the elements present by comparing the measured signals with known standards or databases of previous studies. The relative intensities are used to describe the amount of a given element within a given sample [6]. Most XRF machines are unable to measure light elements, typically most measurement devices cannot measure elements lighter than

fluorine, and while there are some than can measure elements as light as boron, no instrument can measure elements lighter than beryllium. The limiting factor in these cases tend to be the low energy / high wavelength of the lighter samples, as well as the fluorescence yield of the lighter elements reaching as low as 0.01 [6]. Furthermore, there are two primary modes of XRF measurements – energy dispersive XRF (EDXRF) spectroscopy and wavelength dispersive XRF (WDXRF) spectroscopy. Wavelength dispersive XRF spectroscopy uses diffraction to disperse the different wavelengths of fluorescence radiation from the sample. The dispersed wavelengths can be discretely measured allowing for high degrees of specificity at relatively lighter elements [6]. Energy dispersive XRF spectroscopy, uses a semi-conductor that converts incident photons to electrical current proportional to the photon energy [6]. The simpler set up allows for EDXRF spectrometers to be portable in some cases, allowing for rapid analysis of materials that cannot be conventionally prepared for WDXRF spectroscopy. The lack of wavelength dispersion allows for more elements to be detected simultaneously; however, the resolution is comparatively poor for the lighter elements and the analysis is often not quantitative, unlike the analysis provided by WDXRF [6]. In this research, XRF is used for quantitative compositional analysis of the samples, and thereforeee WDXRF spectroscopy was used in this research.

X-ray fluorescence spectrometers have four base components [6]:

1). An excitation source that provides the exciting X-rays.

2). A sample presentation system that exposes the samples to the exciting X-rays.

3). A photon detection system that detects the characteristic radiation from the source.

4). A data collection system that allows the sample to be characterised based on the detected radiation.

A visual representation of this set up can be seen in **Fig 3.5**.

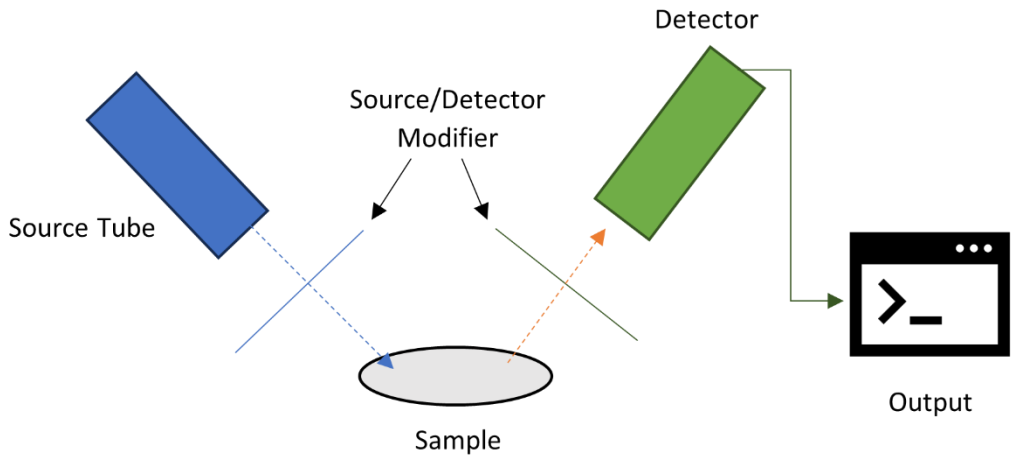

Figure 3.5: *A schematic representation of a XRF spectrometer set up [6].*

The reality of XRF spectrometers is a lot more complex. There are different types of source tubes, which include different anode materials that will impact the range of elements and X-ray lines that can be investigated. There are different sample chambers, detector types, and signal analyser set ups, all with their own strengths and weaknesses [6]. However, the primary focus for this technique in this research was the sample itself.

Due to the nature of this set up, and the fundamental principles of fluorescence, sample preparation is key for XRF. Sample homogeneity, sample density, and surface roughness will all influence how much fluorescence is detected for each component and thus, how accurate the final analysis is for the sample. Falcone et al. [7] in 2002 outlined the "fused bead" sample preparation method employed when measuring glasses and carbonate minerals. It involves the dilution of the sample into a lithium tetraborate ($Li_2B_4O_7$) flux, which is then heated to 1065 ºC and poured into a mould to create a flat glass bead for measurement. This is particularly useful for samples that are of an irregular shape (e.g. powders). Bell et al. [8] then studied how this method might affect the more volatile constituents within feldspar minerals and a silicate glass, such as sulphur, iodine, and sodium, by varying the melt times of the fused bead. It was found that while sodium volatilisation during the fused bead making process was not an issue, the sulphur and iodine volatilisation was significant. In both cases, the longer the melt times, the greater the deviation in composition from the published certified reference material (CRM) values. It was found that for the float-glass CRM, the lower melting time still produced a viable fused bead and returned compositional values in good agreement with the published CRM values. This method, however, is unsuitable for measurements where

boron is a desired measured value, as the fused bead flux being boron-based, renders the sample's intrinsic boron content to be unmeasurable.

X-ray Fluorescence, alongside the fused bead method, has been used to a high degree of success when being used to analyses glass [9-15] and glass raw materials [10 & 14]. The glasses can range from simple soda-lime-silica glasses [9 & 11], to highly complex radioactive waste simulants [12 & 15].

3.2.2 Induced Coupled Plasma – Mass Spectroscopy (ICP-MS)

The other technique to be used in combination with XRF to provide the chemical analysis of the glass is ICP-MS. ICP-MS is capable of quantifying most elements including the light elements, such as boron and lithium, that most XRF spectrometers cannot measure [16]. It relies on samples being diluted into a liquid medium to then be converted into ions using argon plasma. The ions are then detected directly using a mass spectrometer. The mass-to-charge ratio is used to identify elements, while the intensity of the respective ion beam is used to quantify the amount of a given element [16]. A visual representation of the effect is given in **Fig. 3.6**.

Figure 3.6: *A visual representation of how ICP-MS process generates data.*

There are many different various ICP chemical analysis including optical emission spectroscopy (ICP-OES), which instead measures the light emissions as the sample is being converted to ions. The main advantage that ICP-MS has over the OES counterpart is that the mass spectroscopy has far lower limits of detection compared to the limits of OES. The operational limits of OES tend to be around masses that correspond to argon, due to the use of argon plasma, however, this is rarely a problem when measuring glass samples [16].

ICP-MS has been used to measure lighter elements or low-abundance elements in a variety of glasses, including ion-conducting glass materials [17, 18], silicate glasses [19], UK radioactive wastes [20], and US radioactive wastes [1, 21, 22]. It is also used more

widely across the Hanford site, with uses in both glass characterisation [1, 21, 22] and tank waste characterisation [23].

3.2.3 Glass Compositional Analysis

For the glasses made in this study, the lithium oxide and boron oxide were measured using ICP-MS. The other oxides were measured using XRF, with the exception of SO_3.

For the X-ray Fluorescence, samples were prepared by mixing ~1 g of glass powder with ~ 10 g of $Li_2B_4O_7$ flux doped with 0.5% LiI anti-cracking agent in a platinum crucible. The mixture was melted in a platinum crucible in a LeNeo automatic fusion system at 1065 °C for 21 minutes and 45 seconds, and then poured a platinum mould and cooled forming a homogenous fused bead. The samples were analysed by Glass Technology Services (GTS) using the Glass OXI program [24]. The measurement errors were provided by GTS to be ± 2 % relative to the measured abundance.

For the ICP-MS, powdered samples weighing 500 ± 1 mg were added to an acid mixture ($4HNO_3 + 3HF + 2HCl + 2H_2O$) and extracted using an Anton Paar microwave digestion system. After digestion, 2 trials of the sample were diluted to 50 ml with a third trial spiked with a known quantity of Li (in applicable samples only) and B. The third sample was used to calculate the recovery factor. All trials were measured using a Perkin Elmer Nexion-1000 ICP - Mass Spectrometer with a calibration method by the Sheffield Assay Office. The recovery factor was applied to refine the measurement after subtracting the acid blanks. The recovery factor involved adding in a known amount of an internal standard prior to measurement, and determining how much of the known amount was detected in the measurement. This factor is then applied to the components of interest. The Sheffield Assay Office provided the measurement errors as ± 2.7 % for boron and ± 3.8 % for lithium. These errors are relative to the measured abundance.

The glass compositions are given in **Tables 3.3 – 3.6**. The ICP-MS gave the boron and lithium values as elemental boron and elemental lithium in weight percent. These were converted to oxide percent on the assumption that all of the measured boron exists as B_2O_3 within the glass, and all of the measured lithium exists as Li_2O. The calculations for this are detailed in **Table 3.2** and Equation 3.1 below:

Table 3.2: The element and molecule relative atomic masses (RAM and RMM values) used to calculate the element fraction of the oxides. This was then used to calculate the measured weight percent of the respective oxides in given glasses.

Oxide	Target Element Relative Atomic Mass (RAM)	Molecule Relative Molecular Mass (RMM)	Element fraction
Li_2O	6.941	29.881	0.465
B_2O_3	10.811	69.620	0.311

Element Weight Percent / Element Fraction = Molecule Weight Percent (Eq. 3.1)

The calculated weight percent values for all measured samples were then combined with the weight percent values returned by the OXI program for XRF analysis and the nominal values for SO_3 in the HAFe series, to provide overall compositions for all samples. These were then converted from weight percent into molar percent and recorded in **Tables 3.3 – 3.6**, with the nominal data included for comparison. The errors for all measured samples were propagated through all calculations using the partial derivative method.

Table 3.3: The analysed and nominal oxide compositions of the SCFe series samples.

Sample ID	Oxide Composition (mol%)							
	SiO_2		B_2O_3		Na_2O		Fe_2O_3	
	Nominal	Analysed*	Nominal	Analysed*	Nominal	Analysed*	Nominal	Analysed*
SCFe000.0	55.81	56.88 (± 3.01)	16.28	16.53 (± 1.18)	27.91	26.60 (± 1.41)	0.00	0.00 (± 0.00)
SCFe000.1	55.76	56.85 (± 3.07)	16.26	16.28**	27.88	26.67 (± 1.44)	0.10	0.19 (± 0.01)
SCFe000.2	55.70	56.72 (± 3.04)	16.25	16.27**	27.85	26.72 (± 1.43)	0.20	0.29 (± 0.02)
SCFe000.5	55.53	56.80 (± 3.17)	16.20	16.22**	27.77	26.37 (± 1.47)	0.50	0.61 (± 0.03)
SCFe001.0	55.26	54.93 (± 1.56)	16.12	16.32 (± 0.62)	27.63	27.69 (± 0.79)	1.00	1.06 (± 0.03)
SCFe002.0	54.70	54.80 (± 1.51)	15.95	15.96**	27.35	27.21 (± 0.75)	2.00	2.03 (± 0.06)
SCFe003.0	54.14	54.18 (± 1.43)	15.79	16.01 (± 0.54)	27.07	26.72 (± 0.70)	3.00	3.09 (± 0.08)
SCFe004.0	53.58	53.89 (± 1.39)	15.63	15.64**	26.79	26.41 (± 0.68)	4.00	4.06 (± 0.10)
SCFe005.0	53.02	52.78 (± 1.38)	15.47	16.21 (± 0.57)	26.51	25.88 (± 0.68)	5.00	5.14 (± 0.13)
SCFe007.5	51.63	51.58 (± 1.36)	15.06	15.62 (± 0.53)	25.81	25.19 (± 0.66)	7.50	7.61 (± 0.20)
SCFe010.0	50.23	50.04 (± 1.28)	14.65	15.47 (± 0.54)	25.12	24.38 (± 0.63)	10.00	10.10 (± 0.26)
SCFe014.0	48.00	48.59 (± 1.25)	14.00	14.02**	24.00	23.28 (±0.60)	14.00	14.11 (± 0.36)

** B_2O_3 analysed using ICP-MS, everything else analysed using XRF*
*** Nominal values used in calculating normalised mol%*

Table 3.4: The nominal and analysed oxide compositions of the CCFe series samples.

Sample ID	Oxide Composition (mol%)													
	SiO_2		B_2O_3		Na_2O		CaO		Li_2O		Al_2O_3		Fe_2O_3	
	Nominal	Analysed*	Nominal	Analysed*	Nominal	Analysed*	Nominal	Analysed*	Nominal	Analysed*	Nominal	Analysed*	Nominal	Analysed*
CCFe000.0	44.12	46.18 (± 1.12)	12.84	13.02 (± 0.43)	22.01	23.26 (± 0.56)	5.36	5.32 (± 0.13)	8.23	4.74 (± 0.22)	7.45	7.48 (± 0.18)	0.00	0.00 (± 0.00)
CCFe001.0	43.68	44.57 (± 1.08)	12.71	13.52 (± 0.44)	21.79	22.49 (± 0.54)	5.30	5.50 (± 0.13)	8.15	5.37 (± 0.25)	7.37	7.37 (± 0.18)	1.00	1.19 (± 0.03)
CCFe003.0	42.79	47.11 (± 1.14)	12.45	8.69 (± 0.28)	21.35	23.65 (± 0.57)	5.20	5.88 (± 0.14)	7.99	3.55 (± 0.16)	7.22	7.72 (± 0.19)	3.00	3.39 (± 0.08)
CCFe005.0	41.91	44.03 (± 1.01)	12.20	12.68 (± 0.39)	20.91	21.24 (± 0.49)	5.09	5.26 (± 0.12)	7.82	4.57 (± 0.20)	7.07	7.11 (± 0.16)	5.00	5.12 (± 0.12)
CCFe007.5	40.81	42.03 (± 1.05)	11.86	12.05 (± 0.41)	20.36	20.86 (± 0.52)	4.96	5.14 (± 0.13)	7.62	5.14 (± 0.24)	6.89	6.93 (± 0.17)	7.50	7.86 (± 0.20)
CCFe010.0	39.71	42.91 (± 1.00)	11.55	11.79(± 0.37)	19.81	19.77 (± 0.46)	4.82	4.84 (± 0.11)	7.41	3.49 (± 0.16)	6.70	6.89 (± 0.16)	10.00	10.30 (± 0.24)

Table 3.5: The nominal oxide compositions of the HAFe series samples.

Sample ID	Nominal Oxide Composition (mol%)																	
	Al_2O_3	B_2O_3	CaO	CeO_2	Cr_2O_3	Fe_2O_3	La_2O_3	Li_2O	MgO	MnO_2	Na_2O	NiO	P_2O_5	PbO	SO_3	SiO_2	SrO	ZnO	ZrO_2
HAFe000.0	4.25	15.35	0.72	0.05	0.12	0.00	0.01	4.03	0.31	3.53	16.59	0.49	0.35	0.22	0.21	52.89	0.15	0.03	0.71
HAFe001.0	4.20	15.20	0.71	0.05	0.12	1.00	0.01	3.99	0.31	3.49	16.42	0.48	0.35	0.22	0.21	52.36	0.14	0.03	0.70
HAFe003.0	4.12	14.89	0.70	0.05	0.12	3.00	0.01	3.91	0.30	3.42	16.09	0.47	0.34	0.21	0.20	51.30	0.14	0.03	0.69
HAFe005.0	4.03	14.58	0.68	0.05	0.12	5.00	0.01	3.83	0.30	3.35	15.76	0.46	0.34	0.21	0.20	50.24	0.14	0.03	0.67
HAFe007.1	3.94	14.26	0.67	0.05	0.12	7.13	0.01	3.74	0.29	3.28	15.96	0.45	0.33	0.20	0.19	49.12	0.14	0.03	0.66
HAFe010.0	3.82	13.82	0.65	0.05	0.11	10.00	0.01	3.62	0.28	3.18	14.93	0.44	0.32	0.20	0.19	47.60	0.13	0.03	0.64

Table 3.6: The analysed oxide compositions of the HAFe series samples.

Sample ID	Analysed Oxide Composition (mol%)*																	
	Al_2O_3	B_2O_3	CaO	CeO_2	Cr_2O_3	Fe_2O_3	La_2O_3	Li_2O	MgO	MnO_2	Na_2O	NiO	P_2O_5	PbO	SO_3	SiO_2	SrO	ZnO	ZrO_2
HAFe000.0	3.87 (± 0.08)	16.03 (± 0.44)	0.76 (± 0.02)	0.05 (± <0.01)	0.13 (± <0.01)	0.00 (± 0.00)	0.00 (± 0.00)	3.36 (± 0.13)	0.40 (± 0.01)	3.59 (± 0.07)	16.95 (± 0.35)	0.51 (± 0.01)	0.34 (± 0.01)	0.22 (± <0.01)	0.27**	52.56 (± 0.01)	0.13 (± <0.01)	0.00 (± 0.00)	0.82 (± 0.02)
HAFe001.0	4.46 (± 0.09)	12.48 (± 0.36)	0.70 (± 0.01)	0.00 (± 0.00)	0.14 (± <0.01)	1.07 (± 0.02)	0.00 (± 0.00)	3.07 (± 0.12)	0.00 (± 0.00)	4.58 (± 0.10)	17.14 (± 0.37)	0.51 (± 0.01)	0.35 (± 0.01)	0.24 (± 0.01)	0.29**	53.86 (± 0.01)	0.14 (± <0.01)	0.16 (± 0.00)	0.81 (± 0.02)
HAFe003.0	4.32 (± 0.09)	12.81 (± 0.37)	0.73 (± 0.02)	0.00 (± 0.00)	0.15 (± <0.01)	3.15 (± 0.07)	0.03 (± <0.01)	3.14 (± 0.13)	0.45 (± 0.01)	3.59 (± 0.08)	16.39 (± 0.35)	0.52 (± 0.01)	0.36 (± 0.01)	0.23 (± <0.01)	0.29**	52.76 (± 0.01)	0.13 (± <0.01)	0.13 (± 0.00)	0.78 (± 0.02)
HAFe005.0	3.99 (± 0.08)	15.27 (± 0.42)	0.62 (± 0.01)	0.00 (± 0.00)	0.13 (± <0.01)	4.91 (± 0.10)	0.00 (± 0.00)	3.46 (± 0.13)	0.00 (± 0.00)	4.19 (± 0.09)	15.06 (± 0.31)	0.48 (± 0.01)	0.33 (± 0.01)	0.22 (± <0.01)	0.29**	50.13 (± 0.01)	0.20 (± <0.01)	0.00 (± 0.00)	0.71 (± 0.01)
HAFe007.1	4.99 (± 0.10)	11.52 (± 0.31)	0.84 (± 0.02)	0.00 (± 0.00)	0.13 (± <0.01)	8.58 (± 0.17)	0.00 (± 0.00)	2.48 (± 0.09)	0.65 (± 0.01)	3.47 (± 0.07)	12.53 (± 0.25)	0.47 (± 0.01)	0.34 (± 0.01)	0.23 (± <0.01)	0.30**	52.78 (± 0.01)	0.12 (± <0.01)	0.00 (± 0.00)	0.58 (± 0.01)
HAFe010.0	3.82 (± 0.08)	14.25 (± 0.40)	0.58 (± 0.01)	0.00 (± 0.00)	0.17 (± <0.01)	10.92 (± 0.23)	0.00 (± 0.00)	3.31 (± 0.13)	0.00 (± 0.00)	4.20 (± 0.09)	13.94 (± 0.29)	0.57 (± 0.01)	0.29 (± 0.01)	0.19 (± <0.01)	0.32**	46.63 (± 0.01)	0.12 (± <0.01)	0.00 (± 0.00)	0.68 (± 0.01)

***** *Lithium and Boron were analysed using ICP-MS, the rest were analysed using XRF*

****** *Nominal values used in calculating normalised mol%*

The analysed compositions seen in **Tables 3.3 – 3.6** are all broadly comparable to the nominal values intended for each composition with few exceptions. One notable exception can be seen in Table 2, where the analysed B_2O_3 and Li_2O_3 concentrations are significantly lower than the corresponding nominal concentrations in the CCFe003.0 sample. Table 3.6 shows several low-abundance oxides such as CeO_2 and La_2O_3 were not detectable in the sample, this is attributed to the detectable limits of the XRF spectrophotometer, and it is assumed that these oxides are present in the sample.

3.3 Initial Property Characterisation

3.3.1 Density

Density of the glass samples is measured using the Archimedes principle due to the irregular shape of the glass fragments. The Archimedes equation can be seen in Equation 3.2.

$$\rho_m = \frac{m_{air}}{m_{air} - m_{water}} \rho_w \qquad \text{(Eq. 3.2)}$$

Where ρ_m is the density of the object, ρ_w is the temperature dependant density of water, m_{air} is the mass in open air, and m_{water} is the object mass submerged in water. The masses were measured using KERN YBD-03 precision balance. 400 ml of deionised water was used. The temperature of the water was 20 °C, measured using a glass mercury thermometer, which corresponded to ρ_w = 0.998203 g cm^{-3}. For each sample, three separate fragments of glass were measured, and the corresponding densities were averaged with standard error calculated from the repeat measurements. The densities are given **in Table 3.7**.

Table 3.7: The measured densities of the samples.

Sample ID	Density (g cm^{-3})	Sample ID	Density (g cm^{-3})
SCFe000.0	2.519 (± 0.008)	CCFe000.0	2.494 (± 0.003)
SCFe000.1	2.520 (± 0.005)	CCFe001.0	2.534 (± 0.003)
SCFe000.2	2.518 (± 0.001)	CCFe003.0	2.554 (± 0.013)
SCFe000.5	2.521 (± 0.001)	CCFe005.0	2.595 (± 0.011)
SCFe001.0	2.534 (± 0.003)	CCFe007.3	2.653 (± 0.011)
SCFe002.0	2.558 (± 0.009)	CCFe010.0	2.699 (± 0.009)
SCFe003.0	2.582 (± 0.005)	HAFe000.0	2.607 (± 0.016)
SCFe004.0	2.584 (± 0.003)	HAFe001.0	2.614 (± 0.014)
SCFe005.0	2.607 (± 0.001)	HAFe003.0	2.646 (± 0.010)
SCFe007.5	2.655 (± 0.003)	HAFe005.0	2.685 (± 0.004)
SCFe010.0	2.688 (± 0.004)	HAFe007.3	2.694 (± 0.002)
SCFe014.0	2.750 (± 0.002)	HAFe010.0	2.731 (± 0.014)

Table 3.7 shows that the density increases as the iron oxide contents increases, the density of the glass increases, which is to be expected as Fe_2O_3 has a much higher density than all three iron-free glasses (ρ_{Fe2O3} = 5.25 g cm^{-3} [25]).

3.3.2 X-ray Diffraction (XRD)

X-ray diffraction (XRD) utilises Bragg's law to determine the d-spacing in crystalline materials. The d-spacing combined with the intensity of the Bragg peaks can be matched against available databases to identify crystalline phases and their associated structures [26]. The Bragg's law equation (Equation 3.3) can be seen below:

$$n\lambda = 2d\ Sin\theta \qquad \text{(Eq. 3.3)}$$

Where λ is the wavelength of the incident photon, d is the distance between slits in the diffracting medium, in the context of crystals it will be the d-spacing, and θ is the angle of diffraction. The application of Bragg's law is represented by a simple diagram in **Fig. 3.7**.

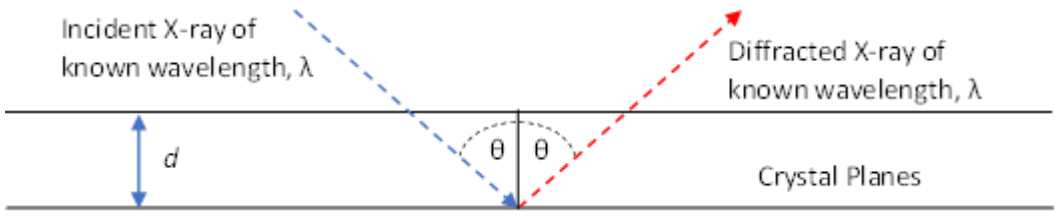

Figure 3.7: *A visual representation of the application of Bragg's law for XRD.*

How this principle is utilised, like most techniques, is a pitch-and-catch set up between a source, sample holder, and detector. There are two main types of XRD measurements –

single crystal XRD and powder XRD, each with their own experimental set up. Single crystal XRD is useful for extracting lattice parameters of a single crystalline phase. The level of detail that can be obtained for the crystal structure is high owing to the discreet diffraction pattern produced from the single crystalline phase, however, the sample preparation is very difficult [26]. The sample must be a single crystalline phase, with low tolerance for impurities and inhomogeneity. Powder XRD is better for samples with multiple crystalline phases [26]. The sample is powdered and placed on a flat sample stage, with the randomly oriented crystal phases creating a continuous diffraction pattern. The disadvantage is that the continuous pattern can be vague and difficult to interpret without supplemental data (for example, compositional data) [26]. In this research, powdered XRD was selected and henceforth, any discussion around XRD is within the context of powder XRD. A visual representation of a powder XRD diffractometer can be seen in **Fig. 3.8**.

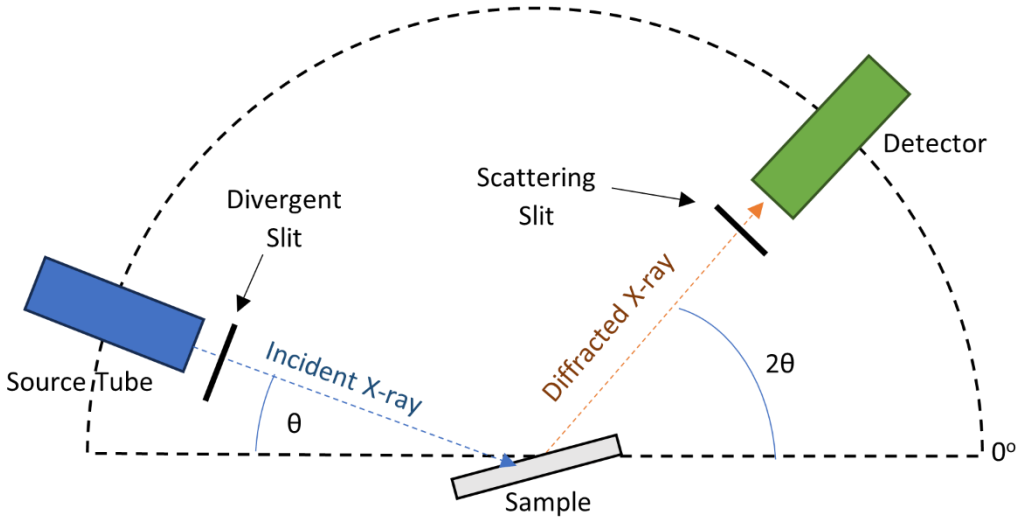

Figure 3.8: *A schematic (not to scale) of an XRD powder diffractometer.*

Within the set-up, the X-ray source tube is fixed while the detector rotates around an axis, with the range and step size being programmable. Divergent and scattering slits are used to reduce the X-ray dispersion along the travelled pathways. In a practical setting, the sample stage would be perfectly horizontal, meaning the zero point of the detectors range would be below the horizontal and the source tube is situated slightly above the horizontal. The detector measures X-ray intensities over a set range of angles, plotting the data as measured intensity against 2θ (see **Fig. 3.7** & **Fig. 3.8**) [26].

The d-spacing and angle of diffraction are characteristics of the well-defined crystalline structure of a material – so how can this be applied to glass? Glass has a distribution of

bond lengths and angles with no isotropic structure [27]. This is reflected in most XRD scans of glass, whereby a fully amorphous silicate glass would manifest itself as a broad diffuse scattering peak commonly referred to as the "amorphous hump", with no discernible Bragg peaks. This is useful however, as XRD can be used to confirm the absence of crystalline phases and can be used as evidence to suggest that all of the components have melted into the amorphous phase. This application has been used extensively in glass science [28 - 39], as well as being used to look at glass samples that phase separate, such as glass ceramics [40 - 42] and ionic conducting media [17, 18, 43, 44]. This use is especially pertinent in the vitrification of radioactive wastes, which typically have complex compositions with components that may be resistant to vitrification that will form separate crystalline phases in the final within the final wasteform [1, 12, 15, 20 – 22, 31 – 33, 45]. In the lattermost example, XRD is used in conjunction with scanning electron microscopy (SEM) with energy dispersive X-ray scattering (EDXS) spectroscopy to identify secondary phases within the glass due to the complex nature of some of secondary phases [45].

Initially, XRD was used to verify that the glasses are fully X-ray amorphous and that any crystalline phases present can be identified and the sources of which explained. In Chapter 7 the use of X-ray diffraction will be expanded upon to include more quantitative analysis of the abundance of secondary phases present and the abundance of the amorphous glass phase relative to a crystalline standard.

To measure the samples, approximately 0.5 g of each powdered sample was loaded onto flat plate sample holders, which were then loaded into a X'Pert Pro X-ray powder diffractometer on a spinner stage, set to spin at 4 revolutions per second. Diffraction patterns were collected using a CuKα radiation source at 40 mA/40 kV power. A mask of 20 mm was used, with the angle range set at 5 – 50 °, at an increment of 0.013 ° with 97.92 seconds per step. Peak identification was performed using PANalytical HighScore Plus software with the International Centre for Diffraction Data (ICDD) database [46]. **Figs. 3.9 – 3.11** show the XRD data acquired for all samples.

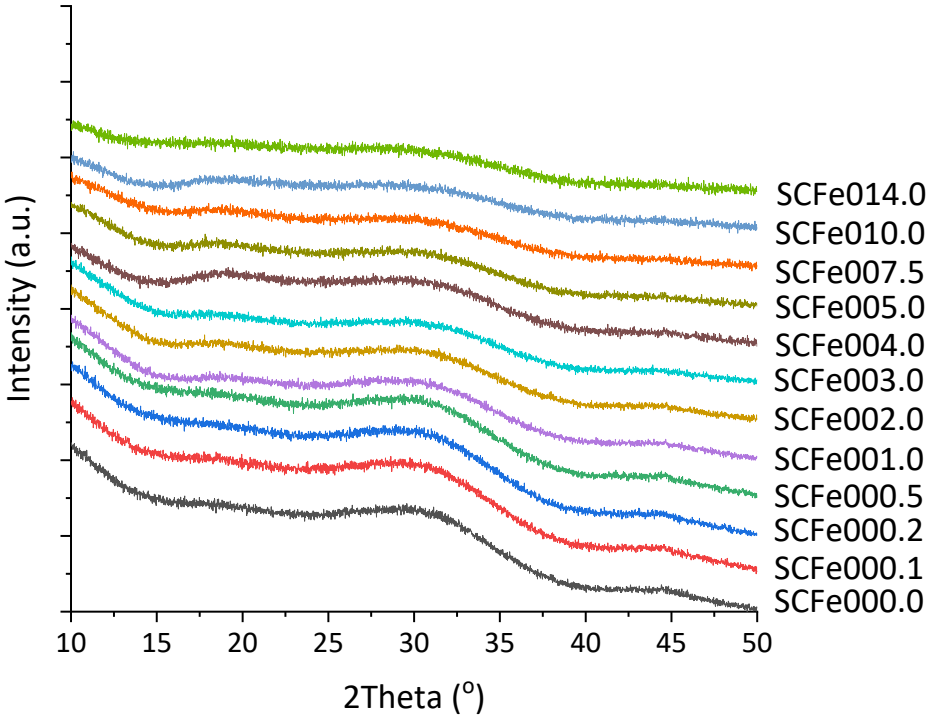

Figure 3.9: *The XRD pattern stack plot for the SCFe series samples.*

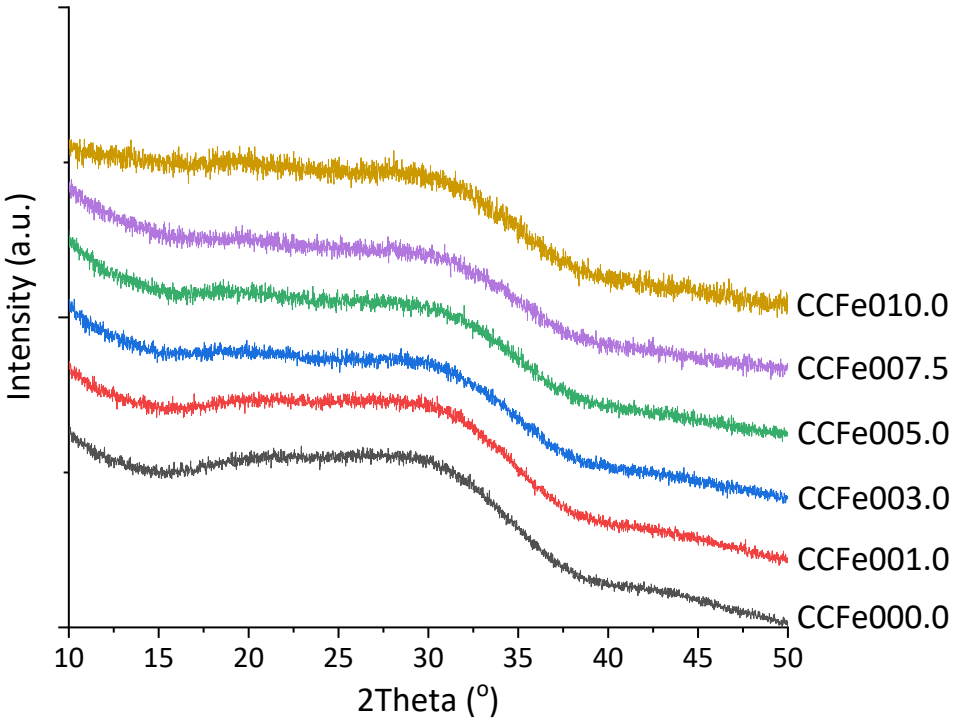

Figure 3.10: *The XRD pattern stack plot for the CCFe series samples.*

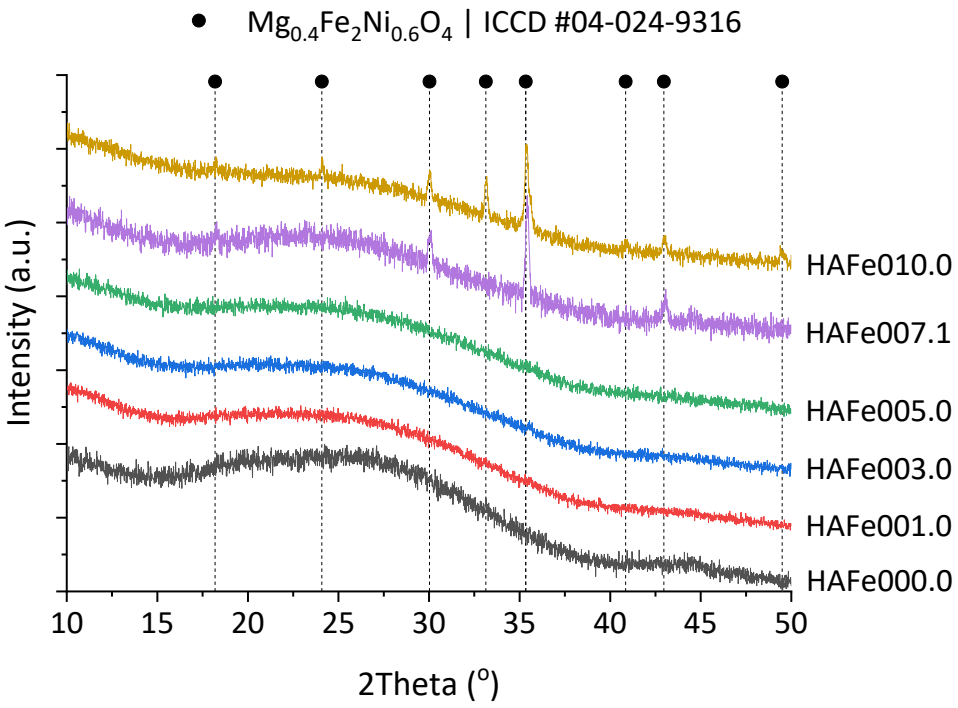

Figure 3.11: *The XRD pattern stack plot for the HAFe series samples.*

The high background in **Figs. 3.9** – **3.11** is likely attributable to fluorescence effects as a result of using a Cu X-ray source. This is a common problem with certain materials, particularly those containing iron [47]. Beyond the high background, the XRD patterns showed no discernible secondary crystalline phases within the glass melt in the SCFe and CCFe series, with both showing the characteristic diffuse scattering pattern indicative of glass (**Figs. 3.9 & 3.10**). The same pattern was seen in the HAFe series too, however, HAFe007.1 and HAFe010.0 both showed a secondary crystalline phase within the glass (**Fig. 3.11**). HighScore Plus software identified this peak pattern as likely being a mixed transitional metal oxide spinel crystal, which is a common crystal phase seen in high-Fe Hanford glasses. The intensity of the detected peaks increases as the iron oxide contents increases which would suggest that between 5 mol% and 7.1 mol% is the solubility limit of iron oxide in the HAFe glass series.

For the HLW-Ng-Fe2 glass from literature [37, 38], there are no spinel crystals in the glass as made, but there are spinel crystals that form at heat treatments at 800, 850, 900, and 950 °C, all of which are only a few percent in abundance as measured by SEM in work done by Matlack et al. [48, 49]. The low intensity of the peaks for the HAFe007.1 (the nearest glass to HLW-Ng-Fe2), would suggest a low abundance that would be in line with findings in the referenced report. These peaks seemingly intensify as the iron content

is further increased to HAFe010.0, which is expected as the primary phase is identified is an iron-bearing spinel phase.

3.4 Methodology

In this section, the methods employed across all the experimental techniques will be documented. The experimental techniques, as outlined in Chapter 2.4, are separated into two areas of interest – structural studies and property studies. For each technique, the samples investigated will be stated, along with any software used. The specific principles of how each technique operates will be covered in specific chapters, with each chapter being mentioned under the relevant technique.

3.5 Structural Studies

3.5.1 ^{57}Fe Mössbauer Spectroscopy

For all measurements, samples were required to be powdered. Bulk samples were placed in a Retsch 250 ml steel disk milling chamber, before being milled in a Retsch RS200 vibratory disk mill, for 1 minute at 700 rpm. The samples were loaded into acrylic sample disks with an area of 1.767 cm^2. Gamma rays of 14.4 keV were supplied by the cascade decay of 25 mCi ^{57}Co in a rhodium matrix source oscillated at a constant acceleration by a SeeCo W304 drive unit. The detector is a SeeCo 45431 Kr proportional counter operating with a bias voltage of 1.720 kV applied to the cathode. For room temperature spectra, only samples containing 5+ mol.% Fe_2O_3 were measured. All spectra were measured at room temperature with a velocity range +/- 4 mm s^{-1} with the exception of HAFe007.1 and HAFe010.0, which were measured at +/- 12 mm s^{-1}, the reason for the difference in velocity for these two samples is elaborated upon in Chapter 4.4.3. Sample HAFe001.0 was measured at 10.0 K to investigate potential hyperfine paramagnetic interactions.

All measurements were calibrated relative to alpha-Fe foil, with all spectral data fitted using the Recoil software package [50], using Lorentzian and xVBF lineshapes. For a breakdown of the principles and limitations of Mössbauer spectroscopy and the results, please see Chapter 4.

3.5.2 X-ray Absorption Spectroscopy

X-ray absorption spectroscopy (XAS) was carried out at two different facilities on two different elemental edges.

3.5.2a Fe K-edge XAS

For Fe *K*-edge XAS measurements, powdered samples and standards (powdered in the same manner outlined in Chapter 3.5.1) were mixed with cellulose acetate ($C_{10}H_{16}O_8$)

flux before being sent to the BM28 beamline at the European Synchrotron Radiation Facility (ESRF) in Grenoble, France [50]. The standards were selected to represent a variety of iron configurations, with the details in **Table 3.8**.

Table 3.8: The selected mineral standards and their respective iron valency and coordination.

Mineral (Formula)	**Oxidation state**	**Coordination number**
Hematite (Fe_2O_3)	3+	6
Aegirine ($NaFeSi_2O_6$)	3+	6
Fe-Berlinite ($FePO_4$)	3+	4
Magnetite (Fe_3O_3)	2+, 3+	6
Wüstite (FeO)	2+	6
Grandidierite $((Mg,Fe)Al_3(BO_3)(SiO_4)O_2)$	2+	5
Staurolite $(Fe_{1.5}Mg_{0.5}Al_9Si_{3.9}Al_{0.1}O_{22}(OH))_2$	2+	4

The ratios of the sample-to-flux, were calculated using XAFSMass software [52], using the pellet dimensions and elemental iron weight percent calculated from the nominal values in **Tables 3.3 – 3.6**. The ratios can be seen in **Table 3.9**.

Table 3.9: The ratio of sample to cellulose acetate flux for each sample and standard.

Sample ID	Sample (mg)	Flux (mg)	Total (mg)	Sample/Flux Ratio
Hematite	10.10	89.90	100.00	0.11
Aegirine	11.56	88.44	100.00	0.13
Fe-Berlinite	7.70	92.30	100.00	0.08
Magnetite	5.20	94.80	100.00	0.05
Wüstite	10.10	89.90	100.00	0.11
Grandidierite	13.88	86.12	100.00	0.16
Staurolite	15.82	84.18	100.00	0.19
SCFe000.1	50.00	50.00	100.00	1.00
SCFe000.2	46.00	54.00	100.00	0.85
SCFe000.5	42.00	58.00	100.00	0.72
SCFe001.0	39.74	60.26	100.00	0.66
SCFe002.0	30.90	69.10	100.00	0.45
SCFe003.0	27.14	72.86	100.00	0.37
SCFe004.0	24.20	75.80	100.00	0.32
SCFe005.0	21.94	78.06	100.00	0.28
SCFe007.5	17.69	82.04	100.00	0.22
SCFe010.0	15.34	84.66	100.00	0.18
SCFe014.0	12.64	87.36	100.00	0.14
CCFe001.0	31.34	68.66	100.00	0.46
CCFe003.0	24.24	75.58	100.00	0.32
CCFe005.0	20.18	79.82	100.00	0.25
CCFe007.5	16.80	83.20	100.00	0.20
CCFe010.0	14.52	85.48	100.00	0.17
HAFe001.0	47.06	52.94	100.00	0.89
HAFe003.0	31.58	64.42	100.00	0.49
HAFe005.0	27.23	72.77	100.00	0.37
HAFe007.1	21.83	78.17	100.00	0.28
HAFe010.0	18.20	81.80	100.00	0.22

The sample and flux ratios were used to make powdered sample-flux mixes of approximately 50 mg which were homogenised using an agate pestle and mortar. These mixes were loaded into uniaxial a 13 mm circular mould, which was loaded into a Specac Manual 15-ton Hydraulic Uniaxial Press. 5 kN of load was applied for 90 seconds to form a pressed pellet. These pellets were sent to the European Synchrotron Radiation Facility (ESRF) in Grenoble, France for measurement.

The fluorescence mode measurements were acquired across the Fe *K*-edge (approximately 7112 eV) between 7000 – 8200 eV for a *k*-range of 15 $Å^{-1}$, with intention of acquiring data for both X-ray Absorption – Near Edge Structure (XANES) and Extended X-ray Absorption – Fine Structure (EXAFS) quality data. From 100 eV below

the edge, up to 200 eV beyond the edge, the photon energy step size was 0.1 eV. The step size outside of this range 0.5 eV, to allow for efficient acquisition of the spectra while also maximising the detail in the areas of interest. For each sample and standard at least two spectra were acquired so that the spectra can be averaged for a higher degree of signal-to-noise ratio. Before any meaningful data processing could begin, the pre-edge peak (contributing the Fe *1s – 3s* transition) of the measured standards, were compared to those in a comprehensive XANES study by Wilke *et al*. [53]. This was carried out by fitting several gaussians (exact number depending on the standard and was guided by Wilke *et al.* [53]), and an average difference between the measured values and the literature values was calculated. This difference was attributed to monochromator drift and was corrected for using Equation 3.4 [54].

$$E_{corrected} = \frac{Eg}{\sqrt{E^2 - g^2}\sin(\Delta\theta) + g\cos(\Delta\theta)} \quad \text{(Eq. 3.4)}$$

Where $E_{corrected}$ is the corrected energy value, E is the detected energy of the photon, g is an energy constant for the Si 111 monochromator of 1977.1 eV [54], and $\Delta\theta$ is the angle drift. The calculated angle drift was corrected for and applied to all measured spectra. The corrected spectra were normalised and averaged using ATHENA software [55], where a proprietary fluorescence correction was applied to each spectrum using the ratios of sample to flux in Table 3.9, as well as the empirical formula for each sample. The pre-edge peak for all corrected and averaged spectra was fitted with gaussian peaks (the amount guided by both Wilke *et al*. [53] and Farges *et al*. [56]). For the results and information on the principles of XAS, please refer to Chapter 5.

3.5.2b B K-edge XAS

For B *K*-edge measurements, powdered samples were also mixed with cellulose acetate flux to form pressed pellets. The measurements were done on the BEAR beamline at the Elettra Synchrotron in Trieste, Italy [57]. For these measurements, only the SCFe and CCFe sample series were measured, due to interfering *L* and *M* edges of heavier elements in the boron *K*-edge region that would be found in measurements of the HAFe sample series.

Alongside the CCFe and SCFe sample series, two mineral standards were measured to provide one standard containing boron that is 100% $^{[3]}$B (ludwigite ($Mg_2Fe^{3+}BO_5$)) and one standard containing boron that is 100% $^{[4]}$B (danburite ($CaB_2Si_2O_8$)). Of all the minerals selected, ludwigite was selected as it is an iron-bearing borate, and danburite

was selected for being a borosilicate mineral, the underlying logic being that these two minerals would provide some spectral similarities to the Fe-bearing borosilicate glass samples. The powdered samples were mixed with cellulose acetate flux one a 1:10 ratio to form 200 mg pellets using the same equipment and methods outlined in Chapter 3.5.2a.

The spectra were acquired around the boron K-edge (approximately 194 eV), with a photon energy range of 170 – 220 eV with an energy step of 0.1 eV. The measurements were performed in fluorescence mode, with the Si *K*-edge and C *K*-edge used to create a first-order energy calibration polynomial to correct for monochromator drift (a method employed successfully at the BEAR beamline by the lab technical specialists). This involves measuring a silicon and carbon standards with known energy values for the primary energy transitions, converting the known and measured energies to a wavelength, and then solving Equation 3.5:

$$\lambda_{NEW,REAL} = a\lambda_{EXP} + b \qquad \text{(Eq. 3.5)}$$

Where *a* and *b* are coefficients that are solved for, and subsequently used to calibrate further measured energy values. Measurements were performed under vacuum conditions due to the X-rays being low energy. For each sample, a minimum of two measurements were performed to improve signal-to-noise statistics for each sample spectrum. For each measured spectrum, measurements for both the measured intensity, *I*, and initial intensity, I_0, were acquired. Equation 3.6 was used to calculate values for μx.

$$ln\frac{I}{I_0} = -\mu x \qquad \text{(Eq. 3.6)}$$

Values for μx were plotted against photon energy in ATHENA [55] to be normalised, fluorescence corrected, and averaged. Analysis of the resulting spectral features for each sample was carried using gaussian peak fitting in OriginPRO [58]. For more information on the nature of the peak fitting as well as the results, please see Chapter 5.

3.5.3 Raman Spectroscopy

Raman spectroscopy measurements were carried out on bulk sample pieces for all samples in this project. Small approximately 10 x 10 x 5 mm bulk sample pieces were sectioned from larger bulk pieces using a Top Tech Preciso CL40 cutting machine with a diamond tipped saw blade. Each piece was buffed to produce a flat surface for the measurements using silicon carbide (SiC) paper ranging from P100 to P600 grit size.

Raman spectra were generated using a Thermo Fisher DX2 Raman spectrometer. The scans were measured using a 532 nm laser at 10 mW power, using a 600 lines mm^{-1} monochromator across a Raman shift range of 50 – 3800 cm^{-1}, with a 50 µm slit, and 10x zoom aperture. For each sample, 200 scans of 10 second exposure time were averaged to produce a single spectrum. This was performed on three separate locations along the buffed surface of the sample, with the resulting three spectra averaged to produce final sample spectrum with good quality signal-to-noise statistics.

The spectra were initially processed using "OMNIC for Dispersive Raman", where a proprietary "polynomial 5" fluorescence correction was applied to all spectra, as all spectra showed signs of fluorescence. From there, the Neuville and Mysen version [59] of the Long correction (Equation 3.7) [60] was applied to all spectra.

$$I = I_{obs} \cdot [v_0^3 \, [1 - exp(-hcv/kT)]v/(v_0 - v)^4] \quad \text{(Eq. 3.7)}$$

Where, h is Planck's constant, k is the Boltzmann constant, c is the speed of light, T is the absolute temperature, v_0 is the wavenumber of the incident laser light and v is the measured Raman shift. The Long-corrected data was then baseline corrected and normalised using vector normalisation (Equation 3.8) [61].

$$x_{norm} = \frac{x_i}{\sqrt{\sum x_i^2}} \quad \text{(Eq. 3.8)}$$

This normalisation method was chosen over the more commonly used min-max normalisation method, due to the apparent shift in the maximum point as the series progresses. While typically not an issue for peak fitting, it is an issue when assess the relative changes in band intensity across a series of glasses. The vector normalisation technique solves this problem by normalising the spectrum in the x-plane instead of the y-plane [61]. For more information on the principles of Raman spectroscopy and for the results of the experiment, please see Chapter 6.

3.5.4 X-Ray Photoelectron Spectroscopy

Due to sample availability at the time of the experiment, only the SCFe and CCFe sample series were measured using X-ray photoelectron spectroscopy (XPS). For the XPS measurements, 10 x 10 x 5 mm bulk sample pieces were sectioned off for all samples measured. The samples were buffed to produce a flat measurement surface using silicon carbide (SiC) paper ranging from grit size P100 to P600. As XPS is very sensitive to surface contaminants, all samples were subjected to sonic baths with surfaces cleaned using household dish soap, followed by deionised water and methylated spirits. Once

rinsed with the methylated spirits, the samples were blown try using a warm air dryer, to prevent any deposits from a slow evaporation of water and spirits.

The samples were measured at the University of Manchester using a Kratos Ultra Hybrid spectrometer, which used a monochromated Al K-alpha X-ray source (1486.6 eV). Each sample was loaded onto a sample changer prior to be loading into the spectrometer. Once in the spectrometer, the sample chamber was placed under vacuum conditions due to the low energy X-rays in use. The samples were aligned such that the oxygen *1s* signal produced a count rate of > 5000 counts per minute. A survey scan across the full energy range of the instrument was carried out for the first five samples, so that they energy regions of interest could be identified and programmed for. This survey scan utilised a pass energy of 50 eV and a dwell time of 500ms, as the data quality was not important at this stage. The energy ranges can be seen in **Table 3.10**.

Table 3.10: The energy ranges measured with the associated number of sweeps within the energy range.

Target Signal(s)	Energy Range (eV)	Number of Sweeps
Na 1s	1064 - 1084	4
Fe 2p	706 - 749	16
O 1s*	524 - 544	4
Ca 2p	342 - 360	16
C 1s*	279 - 299	4
B 1s*	184 - 210	20
Si 2p*	98 - 110	12
Al 2p / Fe 3p / Li 1s	49 - 78	25

**These signals were the original priority signals; the rest were acquired serendipitously*.

For the main scans, the pass energy was lowered to 20 eV and the dwell time was increased to 1000 ms. As the samples were non-conductive and the photoelectron effect is ionising, an electron gun was used to act as a charge neutraliser for the sample, to prevent positive charges from interfering with the spectra.

Initially, the spectra were processed using CasaXPS [62] The spectra for each sample were first corrected for monochromator drift using an offset calculated from the position of the carbon *1s* peak. Given that there is no carbon in the glass itself, the carbon comes from an atmospheric source and has a well-known peak value for the *1s* signal, 284.4 eV. The C *1s* signal was set to 284.4 eV for each sample, and the associated signals for each sample were shifted accordingly. After the calibration was applied, further analysis was carried out in both CasaXPS [62] and OriginPro [58].

3.6 Property Studies

3.6.1 Canister Centreline Cooling Heat Treatments

Canister Centreline Cooling (CCC) heat treatments were carried out on non-active radioactive waste simulant glass series (the HAFe sample series) in order to simulate the slow cooling rate experienced by molten glass poured into a canister. The slower cooling rate within a canister centreline is slow enough to raise legitimate questions as to whether the glass properties will vary between the outermost layer and the centreline. In the context of the Hanford site, there are two CCC profiles to consider, both of which were designed by the Vitreous State Laboratory, Washington D.C., USA [63,64]. As the Hanford analogue glass series is based and derived from HLW glass simulants, only the HLW CCC profile was used. To generate CCC heat treated samples, 15 – 20 g of glass prepared using the methods in Chapter 3.1 were placed in small Pt/Rh crucibles and placed into a static furnace at room temperature. This furnace programmed using the programmable CCC profile outlined in **Table 3.11** [65].

Table 3.11: The temperatures, ramp rates, and dwell times for the HLW CCC programmable furnace profile.

Hours	**Start Temp**	**End Temp.**	**Rate ºC / hr**
N/A*	RT	1004.2	+ 600.0
0.00 – 0.17	1004.2	1050.4	+ 277.2
0.17 – 2.17	1050.4	1002.5	- 24.0
2.17 – 7.00	1002.5	843.7	- 32.9
7.00 – 10.30	843.7	749.2	- 28.6
10.30 – 15.50	749.2	617.4	- 25.4
15.50 – 21.17	617.4	490.8	- 22.4
21.17 – 25.80	490.8	399.8	- 19.7
N/A	399.8	RT	Free Fall**

**Step added to bring temperature up to the start point seen in Smith et al. [14].*
*** Exact Rate dependant on furnace used*

The resulting glass samples were assigned the general nomenclature (see Chapter 2) of "HAFeXXX.X CCC".

3.6.2 X-ray Diffraction with Rietveld Refinement

Similar to the XRD measurements done in Chapter 3.3.2, powder XRD measurements were done using powdered glass samples from the HAFe and HAFe CCC glass sample series. Unlike the XRD done in Chapter 3.3.2, spectroscopic grade silicon powder was added to the powdered sample, to be used as an internal standard, in a 1 : 20 silicon : sample ratio (equates to 5 wt.% of Si powder), before being homogenised using an agate pestle and mortar. While the diffractometer was the same, the operational parameters were

different. These samples were measured across an angle range of 5 – 80 º 2θ, with the same step size 0.0131303 º and a dwell time per step of 4.48545 s.

The Rietveld refinement was carried out on HighScore Plus software [66], with the results presented using OriginPro [58] and can be found in Chapter 7.

3.6.3 Differential Thermal Analysis

Differential Thermal Analysis (DTA) measurements were performed on all HAFe and HAFe CCC series samples. It involved measuring 30 mg of powdered samples into alumina pans. These pans were loaded into a TA Instruments SDT Q600 Simultaneous Thermal Analyser, and then heated from room temperature to 1200 ºC at 10 ºC min^{-1}. The initial data was analysed using TRIOS software. For the analysis, glass transition temperature onset was analysed using the proprietary analysis tool (aptly named "Glass Transition, Onset") in the software. These values were then plotted in OriginPro [58], with the results available in Chapter 7.

3.6.4 Product Consistency Test – Method B

Product Consistency Test – Method B (PCT-B) is a standardised method of measuring the dissolution rates of radioactive waste simulant glasses. The methods are meticulously detailed in the ASTM document [67] for this method. The summary of the methods is as follows:

Density values for all measured samples were used to calculate the sample mass of a particular particle size range required for three measurement pots per sample. The values were calculated using the following principles and assumptions:

1). The surface area-to-volume ratio was kept at 20 cm^{-1}.

2). The sample particles were assumed to be spheres, so the surface area and volumes for a given particle was calculated using the self-same equations used to describe a sphere: $A = 4\pi r^2$ and $V = (^4/_3)\pi r^3$.

3). The radius for the particle "spheres" was calculated using the midpoint of the range specified in the ASTM document, 75 – 150 μm (thereforeee, r = 112.5 μm).

Once the target masses for all samples were identified, bulk samples underwent a series of short mill-sieve combinations until the desired mass threshold was achieved. The mill was the same steel mill used so far, but the mill times were reduced to 3 second bursts as to not grind the sample too fine. After each three second burst, the ground sample was loaded into a sieve tower consisting of a lid, a 150 μm mesh sieve, a 75 μm mesh sieve,

and a receiver. The milled samples were manually sieved for several minutes before the powder collected on the 75 μm sieve was weighed and recorded, while everything collected in the 150 μm sieve was returned to the mill chamber. This process repeated until enough powder was collected to be in excess of the values calculated for each sample.

The sieved powder was then washed using several repeated steps involving mechanical agitation and a series of liquid with decreasing densities starting with deionised water, propanol, and then ethanol. The powder was placed in clean glass beaker, the beaker was filled with the liquid and gently shaken to agitate the powder. The beaker was then placed in a sonic bath to continuously agitate the powder for 90 seconds. The liquid was then left to rest and then carefully drained as to not removed any of the powder. Each liquid was used repeatedly until the liquid upon draining ran clear. After which the powders were dried overnight in a box oven at 110 ºC.

For this experiment, 25 ml high density polyethylene (HDPE) pots were used instead of polytetrafluoroethylene (PTFE) pots. This limited the length of time the experiment could run to 7 days, owing to concerns over the durability of the vessels themselves beyond the 7 days. Beyond this deviation from the ASTM [63], the methodology for loading the samples into the pots, beginning the experiment, and unloading the samples at the end of the experiment was carried out in accordance with the ASTM document [67].

The leachate was sent to the University of Sheffield, where was measured using ICP-OES (the base principles of which were covered in Chapter 3.2.2). The instrument was a Spectrogreen ICP-OES. The plasma power was 1150W with a coolant flow of 13l/min. The auxiliary flow and nebuliser flow were both 0.8l/min, with a sample flow rate of 2ml/min. The leachate was analysed for Al, B, Ca, Cr, Fe, Li, Mg, Mn, Na, Ni, P, S, Si, and Zr. All results from the PCT-B measurements can be seen in Chapter 7.

3.7 Summary

Three series of borosilicate glasses were made in a similar manner to the way lab-scale glass melts are made at Pacific Northwest National Laboratory [1-5], whereby two separate melts are used to make as homogenous a glass as possible while minimising any compositional changes as a result of volatilisation over longer melt times. The compositions of the glasses were then analysed by XRF and ICP-MS, where it was demonstrated that in most cases, the analysed compositions were comparable to the nominal compositions.

The densities for all glasses are in line with borosilicate glasses with the density increasing as the Fe_2O_3 contents within the glass increases, which makes sense due how to much denser Fe_2O_3 is than the iron-free glasses. The X-ray diffraction (XRD) showed that all of the SCFe and CCFe series were fully amorphous, while HAFe series was amorphous up until HAFe007.1 and HAFe010.0 whereby a mixed transition spinel phase was identified. The presence of this phase is in keeping with studies on the nearest analogous Hanford waste glass to the HAFe series, but also in wider high-transition metal Hanford waste glasses. These glasses will then be studied as part of structural studies detailed in the coming chapters.

3.8 References

[1] Rodriguez, C. P., McCloy, J. S., Schweiger, M. J., Crum, J. V., & Winschell, A., Optical Basicity and Nepheline Crystallization in High Alumina Glasses, Pacific Northwest National Laboratory, *PNNL-20184*, 2001.

[2] Kim, D.-S., Crum, J. V., Schweiger, M. J., Vienna, J. D., Rodriguez, C. P., Johnson, F. C., Lepry, W. C., Marra, J. C., Lang, J. B., & Peeler, D. K., Formulation and Characterization of Waste Glasses with Varying Processing Temperature, Pacific Northwest National Laboratory, *PNNL-20774*, 2001.

[3] McCloy, J. S., Schweiger, M. J., Rodriguez, C. P., & Vienna, J. D., Nepheline crystallization in nuclear waste glasses: Progress toward acceptance of high-alumina formulations, *Int. J. Appl. Glass Sci.*, **2**(3), 2011; pp 201 – 214.

[4] Ahmadzadeh, M., Marcial, J., & McCloy, J., Crystallization of iron-containing sodium aluminosilicate glasses in the $NaAlSiO_4$-$NaFeSiO_4$ join, *J. Geophys. Res. Solid*, **122**(4), 2017; pp 2504 – 2524.

[5] McClane, D. L., Amoroso, J. W., Fox, K. M., & Kruger, A. A., Nepheline crystallization behavior in simulated high-level waste glasses, *J. Non-Cryst. Solids*, **505**, 2019; pp 215 - 224.

[6] MarguÍ, E., & Van Grieken, R., X-ray Fluorescence Spectrometry and Related Techniques: An Introduction, Momentum Press LLC, New York, NY, USA. 2013.

[7] Falcone, R., Hreglich, S., Valloto, M., & Verità, M., X-ray fluorescence analysis of raw materials for the glass and ceramic industries, *Glass Technol.*, **43**(1), 2002; pp 39 – 48.

[8] Bell, A. M. T., Backhouse, D. J., Deng, W., Eales, J. D., Kilinc, E., Love, K., Rautiyal, P., Rigby, J. C., Stone, A. H., Vaishnav, S., Wei-Addo, G., & Bingham, P. A., X-ray Fluorescence analysis of feldspars and silicate glass: Effects of melting time on fused bead consistency and volatilisation, *Minerals*, **10**(5), 2020; pp 442 – 458.

[9] Bos, M., Boukamp, B. A., & Vrielink, J. A. M., Determination of diffusion profiles of silver ions in soda-lime-silica glass by X-ray fluorescence spectrometry, *Anal. Chim. Acta*, **459**(2), 2002; pp 305 – 311.

[10] Gazulla, M. F., Gomez, M. P., Barba, A., & Orduña, M., Chemical characterisation of geological raw materials used in traditional ceramics, *Geostand. Geoanal. Res.*, **28**(2), 2004; pp 203 – 212.

[11] Ceglia, A., Nuyts, G., Meulebroeck, W., Cagno, S., Silvestri, A., Zoleo, A., Nys, K., Janssens, K., Thienpont, H., & Terryn, H., Iron speciation in soda-lime-silica glass: a comparison of XANES and UV-vis-NIR spectroscopy, *J. Anal. At. Spectrom.*, **30**(7), 2015; pp 1552 – 1561.

[12] Bingham, P. A., Vaishnav, S., Forder, S. D., Scrimshire, A., Jagnathan, B., Rohini, J., Marra, J. C., Fox, K. M., Pierce, E. M., Workman, P., & Vienna, J. D., Modelling the sulfate capacity of simulated radioactive waste borosilicate glasses, *J. Alloys Compd*, **695**, 2017; pp 656 – 667.

[13] Mary, N., Rebours, M., Castel, E., Vaishnav, S., Deng, W., Bell, A. M. T., Clegg, F., Allsopp, B. L., Scrimshire, A., & Bingham, P. A., Enhanced thermal stability of high-bismuth borate glasses by addition of iron, *J. Non-Cryst. Solids*, **500**, 2018; pp 149 – 157.

[14] Backhouse, D. J., Guilbot, A., Scrimshire, A., Eales, J. D., Deng, W., Bell, A., M. T., Kabir, F., Marshall, M., Ireson, R., & Bingham, P. A., Biomass ashes as potential raw

materials for mineral wool manufacture: initial studies of glass structure and chemistry, *Glass Technol.: Eur. J. Glass Sci. Technol. A*, **63**(1), 2022; pp 19 – 32.

[15] Rigby, J. C., Dixon, D. R., Cutforth, D. A., Marcial, J., Kloužek, J., Pokorný, R., Kruger, A. A., Scrimshrie, A., Bell, A. M. T., & Bingham, P. A., Melting behaviour of simulated radioactive waste as functions of different redox iron-bearing raw materials, *J. Nucl. Mater.*, **569**, 2022.

[16] Thomas, R., Practical Guide to ICP-MS: A Tutorial for Beginners, 3rd Edition, CRC Press, Boca Raton, FL, USA. 2013.

[17] Nuernberg, R. B., Pradel, A., & Rodrigues, A. C. M., A systematic study of glass stability, crystal structure and electrical properties of lithium ion-conducting glass-ceramics of the $Li_{1+x}Cr_x(Ge_yTi_{1-y})_{2-x}(PO_4)_3$ system, *J. Power Sources*, **371**, 2017; pp 167 – 177.

[18] Zakharkin, M. V., Drozhzhin, O. A., Ryazantsev, S. V., Chernyshov, D., Kirsanova, M. A., Mikheev, I. V., Pazhetnov, E. M., Antipov, E. V., & Stevenson, K. J., Electrochemical properties and evolution of the phase transformation behavior in the NASICON-type $Na_{3+x}Mn_xV_{2-x}(PO_4)_3$ ($0 \leq x \leq 1$) cathodes for Na-ion batteries, *J. Power Sources*, **470**, 2020.

[19] Limbach, R., Karlsson, S., Scannell, G., Mathew, R., Edén, M., & Wondraczek, L., The effect of TiO_2 on the structure of Na_2O-CaO-SiO_2 glasses and its implications for thermal and mechanical properties, *J. Non-Cryst. Solids*, **471**, 2017; pp 6 – 18.

[20] Bingham, P. A., Hyatt, N. C., Hand, R. J., & Forder, S. D., Vitrification of UK intermediate level radioactive wastes arising from site decommissioning. Initial laboratory trials, *Glass Technol.: Eur. J. Glass Sci. Technol. A*, **54**(1), 2013; pp 1 – 19.

[21] Hrma, P., Crum, J. V., Bates, D. J., Bredt, P. R., Greenwood, L. R., & Smith H. D., Vitrification and testing of a Hanford high-level waste sample. Part 1: Glass fabrication, and chemical and radiochemical analysis, *J. Nucl. Mater.*, **345**(1), 2005; pp 19 – 30.

[22] Smith, G. L., Schweiger, M. J., Bates, D. J., Smith, H. D., Goles, R. W., Urie, M. W., Greenwood, L. R., Wagner, J. J., Lettau, R. C., & Piepel, G. F., Vitrification and Product Testing of C-104 and AZ-102 Pretreated Sludge Mixed with Flowsheet Quantities of Secondary Wastes, Pacific Northwest National Laboratory, *PNNL-13452*, 2001.

[23] Cantrall, K. J., Wang, G., Snyder, M. M. V., & Buck, E. C., Contaminant Leach Testing of Hanford Tank 241-C-104 Residual Waste, Pacific Northwest National Laboratory, *PNNL-24383*, 2015.

[24] Giles, H. L., Hurley, P. W., & Webster, H. W. M., Simple approach to the analysis of oxides, silicates and carbonates using x-ray fluorescence spectrometry, *X-Ray Spectrom.*, **24**(4), 1995; pp 205 – 218.

[25] Lide, D. R., CRC Handbook of Chemistry and Physics 88th Edition 2007-2008. CRC Press, Taylor & Francis, Boca Raton, FL, USA, 2007.

[26] Waseda, Y., Matsubara, E., & Shinoda, K., X-ray Diffraction Crystallography: Introduction, Examples and Solved Problems, Springer, London, UK. 2011.

[27] Zachariasen, W. H., The atomic arrangement in glass, *J. Am. Chem. Soc.*, **54**(10), 1932; pp 3841 – 3851.

[28] Holland, D., Mekki, A., Gee, I. A., McConville, C. F., Johnson, J. A., Johnson, C. E., Appleyard, P., & Thomas, M., Structure of sodium iron silicate glass - a multi-technique approach, *J. Non-Cryst. Solids*, **253**(1-3), 1999; pp 192 – 202.

[29] Karabulut, M., Marasinghe, G. K., Ray, C. S., Day, D. E., Waddill, G. D., Booth, C. H., Allen, P. G., Bucher, J. J., Caulder, D. L., & Shuh, D. K., An investigation of the local iron environment in iron phosphate glasses having different Fe(II) concentrations, *J. Non-Cryst. Solids*, **306**(2), 2002; 182 – 192.

[30] Al-Hajry, A., Al-Shahrani, A., & El-Desoky, M. M., Structural and other physical properties of barium vanadate glasses, *Mater. Chem. Phys.*, **95**(2-3), 2006; pp 300 – 306.

[31] Bingham, P. A., Hand, R. J., Forder, S. D., Lavaysierre, A., Deloffre, F., Kilcoyne, S. H., & Yasin, I., Structure and properties of borophosphate glasses, *Glass Technol.: Eur. J. Glass Sci. Technol. B*, **47**(4), 2006; pp 313 – 317.

[32] Bingham, P. A., & Hand, R. J., Sulphate incorporation and glass formation in phosphate systems for nuclear and toxic waste immobilization, *Mater. Res. Bull.*, **43**(7), 2008; pp 1679 – 1693.

[33] Karabulut, M., Yuce, B., Bozdogan, O., Ertap, H., & Mammadov, G. M., Effect of boron addition on the structure and properties of iron phosphate glasses, *J. Non-Cryst. Solids*, **357**(5), 2011; pp 1455 – 1462.

[34] Zhu, X., Chengle, M., & Li, M., Effects of B_2O_3 content variation on the Bi ions in Bi_2O_3-B_2O_3-SiO_2 glass structure, *J. Non-Cryst. Solids*, **388**, 2014; pp 55 – 61.

[35] Dahiya, M. S., Khasa, S., & Agarwal, A., Structural, optical and thermal properties of transition metal ions doped bismuth borate glasses, *Glass Technol.: Eur. J. Glass Sci. Technol. B*, **57**(2), 2016; pp 45 – 52.

[36] Hameed, A., Shareefuddin, Md., & Chary, M. N., The mixed alkali effect in the MgO-Li_2O-Na_2O- K_2O-B_2O_3 glass system, *Glass Technol.: Eur. J. Glass Sci. Technol. B*, **57**(5), 2016; pp 227 – 229.

[37] Deng, W., Wright, R., Boden-Hook, C., & Bingham, P. A., Melting behavior of waste glass cullet briquettes in soda-lime-silica container glass batch, *Int. J. Appl. Glass Sci.*, **10**, 2018; pp 125 – 137.

[38] Kaky, K. M., Şakar, E., Akbaba, U., Kasapoğlu, A. E., Sayyed, M. I., Gür, E., Baki, S. O., & Mahdi, M. A., X-ray photoelectron spectroscopy (XPS) and gamma-ray shielding investigation of boro-silicate glasses contained alkali/alkaline modifier, *Results Phys.*, **14**, 2019.

[39] Ratep, A., & Kashif, I., X-ray photoelectron, FTIR, and Mössbauer spectroscopy studied the effect of Fe_2O_3/CuO substitution on structural and electrical properties of lithium borosilicate glasses, *J. Mater. Sci.: Mater. Electon.*, **32**(9), 2021; pp 12340 – 12347.

[40] Deshkar, A., Marcial, J., Southern, S. A., Kobera, L., Bryce, D. L., McCloy, J. S., & Goel, A., Understanding the structural origin of crystalline phase transformations in nepheline ($NaAlSiO_4$)-based glass-ceramics, *J. Am. Ceram. Soc.*, **100**(7), 2017; pp 2859 – 2878.

[41] Suresh, S., Narendrudu, T., Kumar, A. S., Rao, M. V. S., Tirupataiah, C., & Rao, D. K., Assessment of the structural state of vanadium ions in calcium bismuth borophosphate glass-ceramics by means of spectroscopic investigations, *Glass Technol.: Eur. J. Glass Sci. Technol. B*, **58**(2), 2017; pp 49 – 58.

[42] Valderrama, D. M. A., Cuaspud, J. A. G., Roether, J. A., & Boccaccini, A. R., Development and characterization of glass-ceramics from combinations of slag, fly ash, and glass cullet without adding nucleating agents, *Materials*, **12**(12), 2019.

[43] Yadav, P., & Bhatnagar, M. C., Structural studies of NASICON material of different compositions by sol-gel method, *Ceram. Int.*, **38**(2), 2012; pp 1731 – 1735.

[44] Kim, J., Jo, S. H., Bhavaraju, S., Eccleston, A., & Kang, S. O., Low temperature performance of sodium-nickel chloride batteries with NaSICON solid electrolyte, *J. Electroanal. Chem.*, **756**, 2015; pp 201 – 206.

[45] Deshkar, A., Ahmadzadeh, M., Scrimshire, A., Han, E., Bingham, P. A., Guillen, D., McCloy, J., & Goel, A., Crystallization behavior of iron- and boron-containing nepheline ($Na_2O{\cdot}Al_2O_3{\cdot}2SiO_2$) based model high-level nuclear waste glasses, *J. Am. Ceram. Soc.*, **102**(3), 2019; pp 1101 – 1121.

[46] JCPDS – International Centre for Diffraction Data, *International Centre for Diffraction Data*, 2023, Accessed in September 2023, Last Updated 2023 (URL: https://www.icdd.com/).

[47] Mos, Y. M., Vermeulen, A. C., Buisman, C. J. N., & Weijma, J., X-ray diffraction of iron containing samples: The importance of a suitable configuration, *Geomicrobiol. J.,* **35**, 2017; pp 511-517.

[48] Matlack, K. S., Gan, H., Chaudhuri, M., Kot, W., Pegg, I. L., & Joseph, I., Melter Throughput Enhancements for High-Iron HLW, Office of River Protection, *ORP-54002*, 2012.

[49] Matlack, K. S., Viragh, C., Kot, W. K., Pegg, I. L., & Joseph, I., Effect of the Form of Iron on HLW Melt Rate, Vitreous State Laboratory, *VSL-15R3430-1*, 2015.

[50] Lagarec, K., & Rancourt, D. G., Recoil − Mössbauer spectral analysis software for Windows, Department of Physics, University of Ottawa, Ottawa, ON, Canada, 1998, version 1.0, pp. 43.

[51] The University of Warwick, *XMaS: The UK Materials Science Facility at the ESRF: Beamline Details*, Accessed in October 2022, Last Updated June 2021. (URL: https://warwick.ac.uk/fac/cross_fac/xmas/xmasbeamline/description/).

[52] K. V. Klementiev, *XAFSmass*, Updated 2023. (Accessed at freeware: www.cells.es/Beamlines/CLAESS/software/xafsmass.html).

[53] Wilke, M., Farges, F., Petit, P.-E., Brown Jr., G. E., & Martin, F., Oxidation state and coordination of Fe in minerals: An Fe K-XANES spectroscopic study, *Am. Mineral.*, **86**, 2001; pp 714-730.

[54] Bunker, G., An Introduction to EXAFS: A Practical Guide to X-ray Absorption Fine Structure Spectroscopy, Cambridge University Press, Cambridge, UK. 2010.

[55] Ravel, B., & Newville, M., ATHENA, ARTEMIS, HEPHAESTUS: data analysis for X-ray absorption spectroscopy using IFEFFIT, *J. Synchrotron. Radiat.*, **12**, 2005.

[56] Farges, F., Lefrère, Y., Rossano, S., Berthereau, A., Calas, G., & Brown Jr., G. E., The effect of redox state on the local structural environment of iron in silicate glasses: A combined XAFS spectroscopy, molecular dynamics, and bond valence study, *J. Non-Cryst. Solids*, **344**, 2004; pp 176-188.

[57] Nannarone, S., Borgatti, F., DeLuisa, A., Doyle, B. P., Gazzidi, G. C., Giglia, A., Finetti, P., Mahne, N., Pasquali, L., Pedio, M., Selvaggi, G., Naletto, G., Pelizzo, M. G., & Tondello, G., The BEAR beamline at Elettra, *AIP Conf. Proc.*, **705**, 2004; pp 450-453.

[58] Origin(Pro), 2020b. OriginLab Corporation, Northampton, MA, USA.

[59] Neuville, D. R., & Mysen, B. O., Role of aluminium in the silicate network: In situ, high-temperature study of glasses and melts on the join SiO_2-$NaAlO_2$, *Geochim. Cosmochim. Acta*, **60**, 1996; pp 1727-1737.

[60] Long, D. A., Raman Spectroscopy, McGraw-Hill Inc., London, UK, 1977.

[61] Gautam, R., Vanga, S., Ariese, F., & Umapathy, S., Review of multidimensional data processing approaches for Raman and infrared spectroscopy, *EPJ Tech. Instrum.*, **2**, 2015.

[62] Fairly, N., Fernandez, V., Richard-Plouet, M., Guillot-Deudon, C., Walton, J., Smith, E., Flahaut, D., Greiner, M., Biesinger, M., Tougaard, S., Morgan, D., & Baltrusaitis, J., Systematic and collaborative approach to problem solving using X-ray photoelectron spectroscopy, *Appl. Surf. Sci.*, **5**, 2021.

[63] Petkus L. L. "Canister Centerline Cooling Data, Revision 1," RPP-WTP Memorandum to C.A. Musick, CCN#074851, October 29, 2003, River Protection Project, Hanford Tank Waste Treatment and Immobilization Plant, Richland, Washington. 2003.

[64] Petkus, L. L. "LAW Container Centerline Cooling Data," RPP-WTP Memorandum, L. Petkus to C. Musick, CCN# 074181, River Protection Project Waste Treatment Plant, Richland, WA, 2003.

[65] Smith G. L., Schweiger, M. J., Bates, D. J., Smith, H. D., Goles, R. W., Urie, M. W., Greenwood, L. R., Wagner, J. J., Lettau, R. C., & Piepel, G. F., Vitrification and Product testing of C-104 and AZ-102 Pretreated Sludge Mixed with Flowsheet Quantities of Secondary Wastes, Pacific Northwest Naational Laboratory, *WTP-RPT-006*, 2001.

[66] The HighScore suite, T. Degen, M. Sadki, E. Bron, U. König, G. Nénert; Powder Diffraction / Volume 29 / Supplement S2 / December 2014, pp S13-S18.

[67] ASTM Standard C1285, 2021, "Standard Test Methods for Determining Chemical Durability of Nuclear, Hazardous, and Mixed Waste Glasses and Multiphase Glass Ceramics: The Product Consistency Test (PCT)" ASTM International, West Conshohocken, PA, 2021, DOI: 10.1520/C1285-21, www.astm.org

Chapter 4 – ^{57}Fe Mössbauer Spectroscopy

4.1 The Mössbauer effect

The principles of Mössbauer spectroscopy run on the Mössbauer effect. This effect can be described simply as the resonant recoil-free absorption and emission of gamma-ray photons. ^{57}Fe Mössbauer utilises a specific gamma ray from a radioactive ^{57}Co decay into a ^{57}Fe atom, with an energy of 14.14 keV [1,2]. The process that generates this photon, involves an electron capture to cause the ^{57}Co to decay to a ^{57}Fe. This decay results in gamma-rays of three energies being emitted, based on three possible transitions from the 5/2 spin state to the 1/2 spin state. The gamma-ray of interest comes from the cascade transition of 5/2 to 3/2 to 1/2, with the 3/2 to the 1/2 transition generating the photon (see **Fig 4.1** for a visualisation of these transitions) [1,2]. While each transition has a theoretically well-defined energy, in all cases, there is often a distribution around the given energy due to thermal and structural effects. This is known as the theoretical Mössbauer natural linewidth, Γ_M [3].

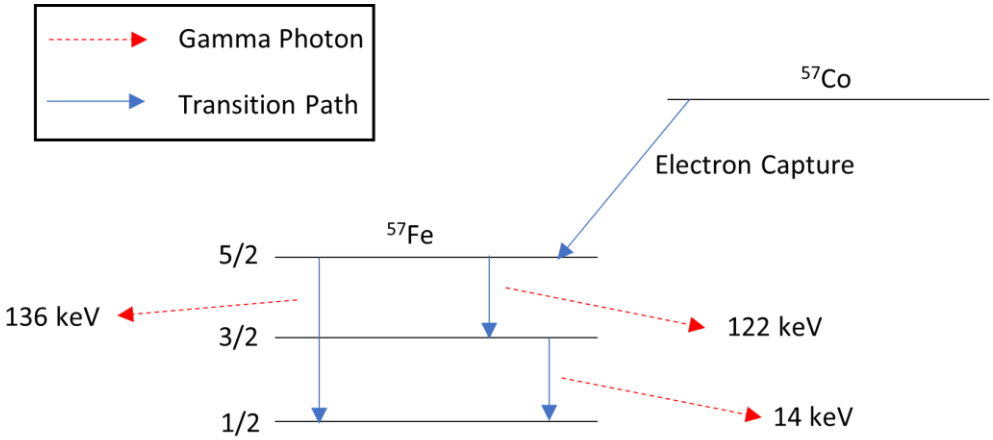

Figure 4.1: *A diagram illustrating the ^{57}Co decay that produces the gamma photon necessary for ^{57}Fe Mössbauer spectroscopy. Diagrams based off similar diagrams found in literature [1,2].*

In free nuclei undergoing the resonant absorption-emission interactions, the recoil interactions can be defined as having a structural component and a thermal component. These energies are significantly larger than the natural linewidth described above, then the resonance effect cannot be observed. As such, the Mössbauer effect cannot provide any meaningful analysis without first addressing the recoil energies involved. When the target nuclei are held in a solid structure, the recoil energies are comparable or lower than the natural linewidth, so the resonant effect can be measured. While this effect cannot be

used to quantify exact properties in isolation, when compared to a known standard, (in the case of ^{57}Fe, natural α-Fe is used), relative changes can be used to describe the chemistry of the target atom [1,2].

4.2 Mössbauer Fit Parameters

The acquisition of Mössbauer data in isolation is not enough. The data must be fit to generate values for certain parameters. It is the value of these parameters which provide the information on the target element chemistry. The key parameters are the total isomer shift, quadrupole shift, linewidth, and hyperfine field.

4.2.1 Total Isomer Shift, δ

The total isomer shift (δ), sometimes referred to as the "Centre Shift" or "Chemical Shift", is the difference in ground state energy between the source and absorber in a given Mössbauer set up, manifests itself as an offset from 0 mm s^{-1} of the fitted symmetrical line shapes (hence the name "Centre Shift"). The differences in the ground state energy are largely due to the density of the s-electron around the nucleus, which will be shielded by higher energy electrons such as the 3d and 4s electrons, depending on the bond configuration of the iron [3]. Since the difference in energy states is measured, the given total isomer shift of any measured calibrated spectrum is the difference between the ground and excited states of the standard and the sample (see **Fig 4.2**), further re-iterating the importance the that the same source is used to measure the standard and sample.

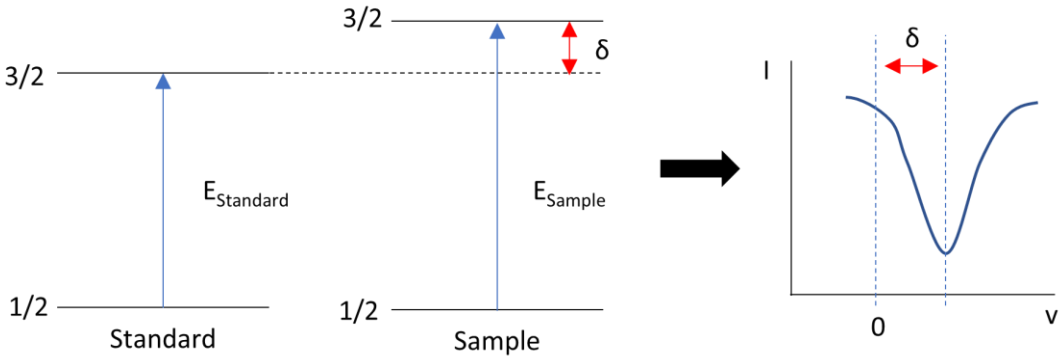

Figure 4.2: *A diagram (not to scale) of the how the total isomer shift manifests on a Mössbauer spectrum [1,2].*

4.2.2 Quadrupole Splitting, Δ

The quadrupole splitting (QS, or Δ) is the peak separation caused by transitions from the ground state to a split excited state. The split comes from interactions between the nuclear quadrupole moment, and the electric field gradient at the nucleus. The ground state ½ has

no nuclear quadrupole moment, whereas the excited state at 3/2 does have a nuclear moment and can exhibit a quadrupole split, as seen in **Fig 4.3**.

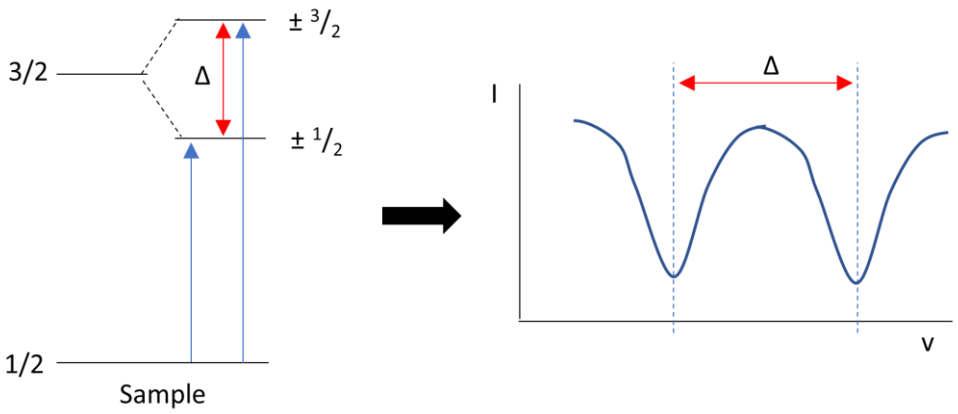

Figure 4.3: *A diagram (not to scale) illustrating where the quadrupole splitting comes from and how it manifests on a Mössbauer spectrum [1,2].*

The electric field gradient at the nucleus is often attributed to the partial filling of inner core orbitals, the bond configurations of the iron, and charges on the ligands.

4.2.3 Magnetic Hyperfine Splitting, hfs

Magnetic hyperfine splitting, or paramagnetic hyperfine splitting (both denoted by hfs, or H, units given in either Tesla (T) or Oersted (Oe)) occurs when the nuclear dipole moment interacts with a magnetic field (internal or external) to produce 6 sublevels between the ground and excited states, denoted by Equations 4.1 – 4.3. **Fig 4.4** shows how these transitions manifest.

$2I + 1$ (Eq. 4.1)

Ground State $(2 * ½ + 1) = 2$ (Eq. 4.2)

Excited State $(2 * {}^{3}/_{2} + 1) = 4$ (Eq. 4.3)

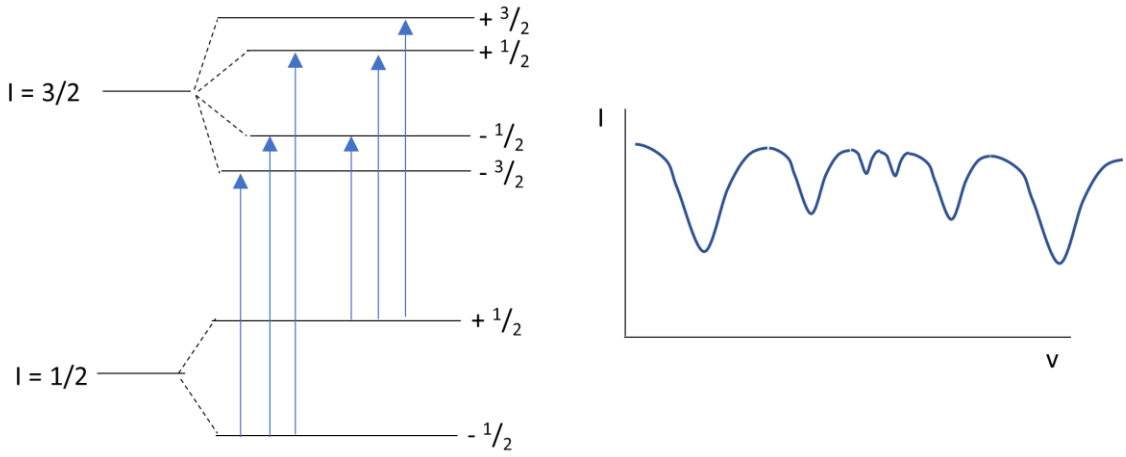

Figure 4.4: *A diagram (not drawn to scale) of the where the magnetic or hyperfine splitting comes from and how it manifests on a Mössbauer spectrum [1,2].*

The 6 transitions seen in **Fig. 4.4** are symmetrical and have an intensity ratio of 3:2:1:1:2:3 for the six peaks. As the nuclear dipole moment is a constant related to the nucleus, the variable parameters are dependent on the magnetic field. As such, fitting this spectral feature can provide information on the magnetic ordering within a material.

At low concentrations of iron within samples (< 4 mol%), paramagnetic sextets due to Fe^{3+} are present in the sample spectra, however, they are not resolvable at room temperature. This is due the relaxation times relative to the Mössbauer sensing time, and the parameters that govern the relaxation time. If the relaxation time is shorter than the Larmor precession time for iron, the hyperfine field is destroyed, and the sample spectrum appears paramagnetic. The relaxation times can be described by Equation 4.4.

$$\frac{1}{\tau_a} = \frac{1}{\tau_1} + \frac{1}{\tau_2} \qquad \text{(Eq. 4.4)}$$

Where τ_a is the resulting relaxation time, τ_1 is the spin-lattice component of relaxation time and τ_2 is the spin-spin component of relaxation time [4]. At low concentrations of iron, the inter-atomic distances are longer and therefore the spin-spin effect component of relaxation time is increased. The spin-lattice component is still too short at room temperature, so the total relaxation time is not long enough to fully resolve the sextet. By cooling the sample to near liquid helium temperatures, the spin-lattice component of relaxation time is much longer, and the hyperfine sextet can be resolved. As the concentration of Fe increases, the interatomic distances between the Fe atoms will decrease, the spin-spin component on the relaxation time becomes so short that the

relaxation time will be shorter than the sensing time at most temperatures and will always present as a paramagnetic doublet in the absence of magnetic ordering within the sample.

For Fe(II), the spin-lattice relaxation time is so short that that the total relaxation time will always be shorter the sensing time at all temperatures and as a result will always manifest as a paramagnetic doublet. Williams *et al*. [4] investigated the nature of the existence of the Fe^{3+} sextet in low abundances of iron in glass. It was found to arise from the disordered nature of glass. In crystals, the spin-spin interactions will be more frequent due to the finite and consistent inter-atomic distances between Fe atoms that govern the spin-spin interactions, though it was noted that the crystal sub-levels having varying relaxation times. In glass, the inter-atomic distances vary to a greater extent, and at low abundances, will manifest in long enough relaxation times that would allow for the sextet to be resolved. This was evidenced by Williams *et al*. [4], when a Mössbauer spectrum of Pilkington's float glass was doped with 1 mol% Fe_2O_3 was measured at 42 K, and showed both a resolved Fe^{3+} doublet and an Fe^{3+} sextet. The existence of both was explained by the varying relaxation times of the iron within the sample whereby some of Fe^{3+} was magnetic, and some of it was paramagnetic.

4.2.4 Linewidth, Γ

The linewidth of a Mössbauer fit refers to the width of the respective lines in a singlet, doublet, or sextet fit. It is given as either a full-width, half-maximum (FWHM) or a half-width, half-maximum (HWHM). As mentioned above, the natural linewidth of the Mössbauer effect, Γ_M, is dominated by the structurally and thermally induced perturbations on the energy of the gamma-ray photon of interest in the cascade decay of ^{57}Co to ^{57}Fe. As such, no measured linewidth will ever be lower than the natural linewidth [3]. When comparing linewidths between materials, linewidths will be narrower if the site in which the target material is situated, places rigid constraints on the bonds of the target material. For crystalline material, the linewidths will be narrower than those of glass/amorphous analogues, due to the variations in bond lengths and angles in the same "sites" in the glass [3].

4.2.5 Recoil-Free Fraction, f

The recoil free fraction is a ratio of the abundance of the detectable gamma-rays re-emitted with no recoil of the nucleus [5]. Kurkijan [3] describes the recoil-free fraction in the context as glass as being influenced by iron valence, coordination, and wider glass composition [3]. It is as important factor when describing the REDOX ratios of the iron within materials, as the ratio of Fe^{3+}/Fe^{2+} in several cases, may not equal 1 [3,6,7].

However, in the case of borosilicate glasses, such as the one studied in this research, published literature has stated that the recoil-free fraction can be assumed to be 1 [8-11], and therefore is assumed as such in this study.

4.2.6 Acquiring Mössbauer Spectra

While the nature of the sample preparation and exact equipment and parameters used are detailed in Chapter 3.5.1, the general acquisition of a Mössbauer spectrum can be simply described as a transmission measurement, i.e. expose a sample to a flux of gamma rays and measure what is able to pass through the sample. It is more complex than this, but the fundamental concept of this being a transmission spectroscopy is accurate. **Fig 4.5** shows a typical equipment set up of a Mössbauer spectrometer.

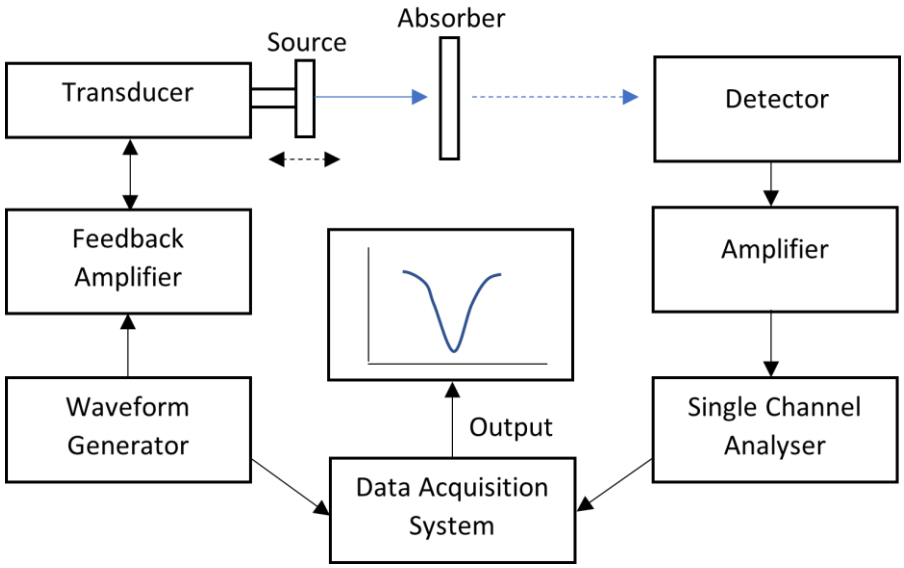

Figure 4.5: *A general set-up of a Mössbauer spectrometer. Recreated from references [1,2].*

This is a similar set up employed in this study. The gamma source is oscillated by the drive motor in order to create a doppler shift of the energy for the necessary gamma ray photon used for the Mössbauer effect [1]. The doppler effect is used to create a spectrum of energies from the lone desirable gamma ray to resolve the sensitive changes of the iron chemistry brought on by the structural environment of the iron within a given material [1]. The velocity of oscillation can be adjusted depending on the structural features present. The resulting spectra are plotted as measured absorption as a function of velocity range.

4.3 Mössbauer studies on glasses

Mössbauer spectroscopy has been used to characterise the environment of iron oxide within a variety of glass matrices in an attempt to elucidate the nature of how iron, a glass network intermediate, integrates within glass networks. There have been several concise reviews that have guided the interpretation of Mössbauer spectra of glasses for many years, including those from Darby-Dyer [6], Nishida [12], Kurkijan [3], and Tomandl [13] to name a few. Primarily, Mössbauer spectra is fitted to determine the oxidation state of the iron, and the coordination number, and to establish whether there are multiple species of iron within the glass (see Chapter 2 for more details). Typically, the centre shift is the primary parameter used to this effect. **Table 4.1** shows the centre shift value interpretations commonly used.

Table 4.1: The centre shift values from select review papers and their associated iron coordination in glass.

[Coordination Number] Oxidation State	**Darby-Dyar [6] (mm s^{-1})***	**Nishida [12] (mm s^{-1})***	**Kurkijan [3] (mm s^{-1})****	**Tomandl [13] (mm s^{-1})***
$^{[4]}Fe^{2+}$	0.90 – 0.95	-	0.60 – 0.77	-
$^{[6]}Fe^{2+}$	1.05 – 1.10	-	0.81 – 1.01	-
$^{[8]}Fe^{2+}$	1.20 – 1.30	-	-	-
$^{[4]}Fe^{3+}$	0.20 – 0.32	< 0.4	0.00 – 0.10	0.2 – 0.4
$^{[6]}Fe^{3+}$	0.35 – 0.55	> 0.4	0.15 – 0.25	0.4 – 0.6

* *Values are relative to a Co source with metallic α-Fe standard.*
** *Values are relative to Co source in a Cu matrix, with a microcline ($KFeSi_3O_8$) standard. These can be compared to an α-Fe standard by adding 0.26 mm s^{-1} [12,14].*

As well as appearing in the reviews above, these values have been used to guide many published papers in recent years [3,4,6-28]. The use of the quadrupole split has been used to characterise the coordination number in Mössbauer spectra of glass but the use of this has yielded some contradictory conclusions in many different papers [3,12,16,25-28]. The contradiction arises from the assignment of higher values of QS, and whether or not a higher QS means 4-coordinated tetrahedral iron structures, or 6-coordination octahedral iron structures. Tomandl [13] stated some rules on how to interpret QS values (see below).

$^{[4]}Fe^{3+}$: 0.7 – 1.0 mm s^{-1}

$^{[6]}Fe^{3+}$: 0.3 – 0.9 mm s^{-1}

Darby-Dyar [6] stated that the use of QS values to determine coordination number is difficult to do, due to the disordered nature of glass and the increased distortion the iron structures will experience as a result. However, in several tables of the reviewed data, it showed that $^{[4]}Fe^{3+}$ in some silicate and borate glasses, had a higher quadrupole split values than that of $^{[6]}Fe^{3+}$ within comparable glass compositions [6]. Further to this, several published works have utilised the approach of defaulting to the centre shift to describe to the coordination of the iron rather than using the quadrupole split when results were ambiguous, with several of these studies being done on borosilicate glasses (for example, references [9,10,25,28]). In the context of borosilicate glasses, Cochain et al. [25] reported that Fe^{3+} in the borosilicate glasses studied all occupied tetrahedral sites, with the reported QS values for Fe^{3+} ranging from 0.46 – 0.96 mm s^{-1}. However, it is worth noting that the justification for this assignment of coordination was made on the low CS values for all Fe^{3+} doublets (0.25 – 0.32 mm s^{-1}). Nishida et al. [19] reported that lower QS values contributed to tetrahedral structures for Fe^{3+} in iron-bearing potassium borosilicate glasses. Ciżman et al. [27] reported tetrahedral Fe^{3+} with QS values ranging from 0.91 – 0.94 mm s^{-1}. In another report Ciżman et al. [28] report a that a low CS doublet of 0.22 – 0.28 mm s^{-1} with QS values of 0.74 mm s^{-1} were attributed to tetrahedral Fe^{3+}, though similarly to Cochain et al. [25], this justification was made on the basis of CS values and it was noted that the low QS value could indicate the presence of distorted octahedral Fe^{3+}. However, Glazkova et al. [31] reported that Fe^{3+} doublets with QS values 0.36 – 0.92 mm s^{-1} corresponded to octahedral Fe^{3+} in Fe-bearing complex HLW glasses. Balasubramanya *et al*. [10] used the centre shift to describe the coordination number of iron in complex borosilicate glasses, in which the iron was found to be predominantly $^{[4]}Fe^{3+}$, with reported CS values ranging between 0.244 – 0.311 mm s^{-1} with associated QS values ranging between 0.711 – 0.914 mm s^{-1} which places the QS values in the overlapping region outlined by Tomandl [13]. Rigby *et al*. [11] used Mössbauer spectroscopy in a stages of melting study on a series of glasses very similar to HAFe sample series in this study. Within the Mössbauer spectral fit interpretations, an assignment of $^{[6]}Fe^{3+}$ was made to a site with CS and QS values of 0.33 mm s^{-1} and 1.12 mm s^{-1} respectively. Further on in the study an assignment of $^{[4]}Fe^{3+}$ was made to a site with CS and QS values of 0.27 mm s^{-1} and 0.79 mm s^{-1} [11]. Wright *et al*. [9] utilised two different peak functions to fit Mössbauer spectra for sodium borosilicate glasses to study the Fe cation environment. In both the xVBF and Lorentzian fits, the Fe^{3+} was assigned to be tetrahedral based both on the CS and QS values. **Table 4.2** shows the CS and QS fit parameters for the $^{[4]}Fe^{3+}$ peaks from Wright *et al*. [9].

Table 4.2: The $^{[4]}Fe^{3+}$ CS and QS fit parameters used in the study published by Wright *et al*. [9].

Peak Type	Peak Shape	Centre Shift (mm s^{-1})	Quadrupole Split (mm s^{-1})
Lorentzian	Doublet	0.13	0.96
	Doublet	0.35	0.96
xVBF	Doublet	0.26	0.94

The parameters in **Table 4.2** show that the QS values for the assignment of $^{[4]}Fe^{3+}$ fit the ranges outlined by Tomandl [13], however within the publication, the centre shift was used as a justification for the assignment [9], which helped rationalise any ambiguity arising from the fit parameters.

Forder et al. [24] discussed the hyperfine parameter ambiguity when investigating glasses using Mössbauer and XANES spectroscopy, in that there is more of tendency to observe distorted structures within glass due to a distribution of Fe-O bond lengths and angles. It is reported that distorted 4-, 5- and 6-coordinated iron structures can have overlapping hyperfine parameters within Mössbauer spectra, which is further noted by several authors [9,10,25,27,28]. The approaches utilised by these authors when dealing with potential ambiguity in interpreting the results were carefully considered in this study.

4.4 Results

For measured samples, the spectra were fit with both Lorentzian functions and extended Voigt-based functions (xVBF). The spectra shown in this Chapter are all fitted with Lorentzian functions as the Lorentzian function provided better fits for all spectra. It is unclear to the author why this is the case. When dealing with highly disordered sites (in which all sites will be disordered in glass), a Voigt or pseudo-Voigt functions should be the appropriate fitting method to account for the normal distribution around a site that would otherwise be described as Lorentzian [29]. The Lorentzian distribution comes from the fact that the photon energy transfer is a not well defined energy matching the energy transition, but rather obeys a Breit-Wigner distribution around the well-defined energy transition [29]. However, in glasses the disordered nature of the network introduces a normal distribution around the otherwise well-defined energy transition, which would necessitate a Gaussian component to the fit function, and therefore, a Voigt-based function should be appropriate [29]. However, attempts to apply a Voigt-based function to the

spectra have yielded either poor fits, fit parameters that are not scientifically justifiable, or fitting methods (such as inconsistent use of force fitting) that are also not scientifically justifiable. When fitting the Mössbauer spectra of any material using Lorentzian fits, multiple Lorentzian functions have been used when there is clear evidence of multiple sites, with each function corresponding to a unique site [29]. It is theorised that this may be the case in this research (with further elaboration in Chapter 4.4.1). As is seen in the results, the multiple sites are somewhat ambiguous and difficult to definitively resolve their physical meaning, which may be a contributing factor as to why the Voigt-based fits proved difficult. The spectra with the xVBF fits can be seen in the Appendix (**Figs A4.1 – A4.10**) with the associated fit parameters also available in the Appendix (**Tables A4.1 – A4.3**).

4.4.1 SCFe Series

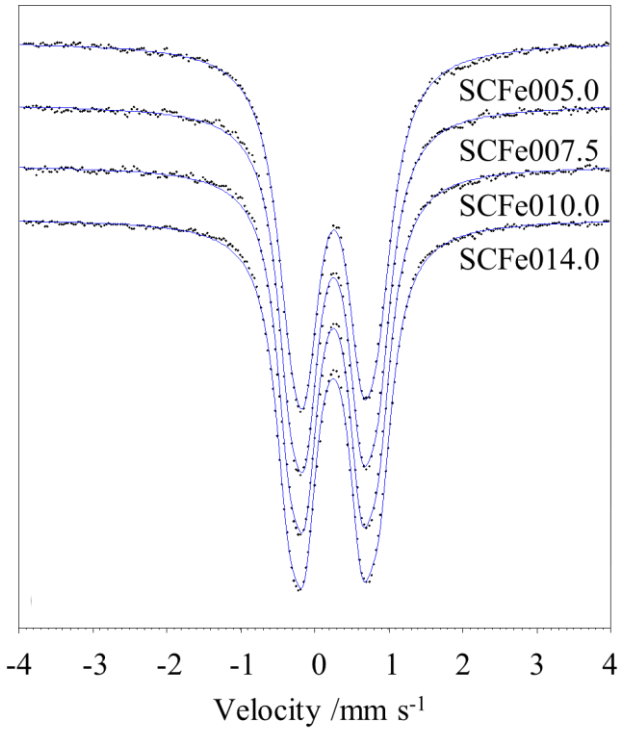

***Figure 4.6**: The stack plot of the SCFe series Mössbauer spectra with Lorentzian fits.*

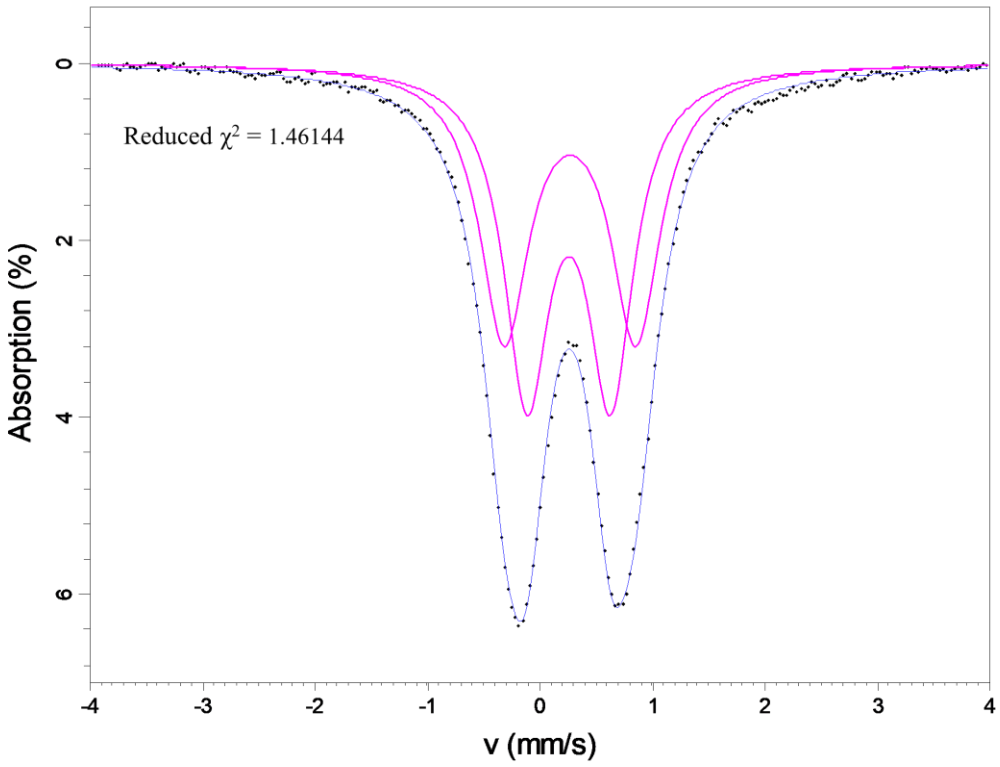

Figure 4.7: *The Mössbauer spectrum of the SCFe005.0 sample fitted with two Lorentzian doublets.*

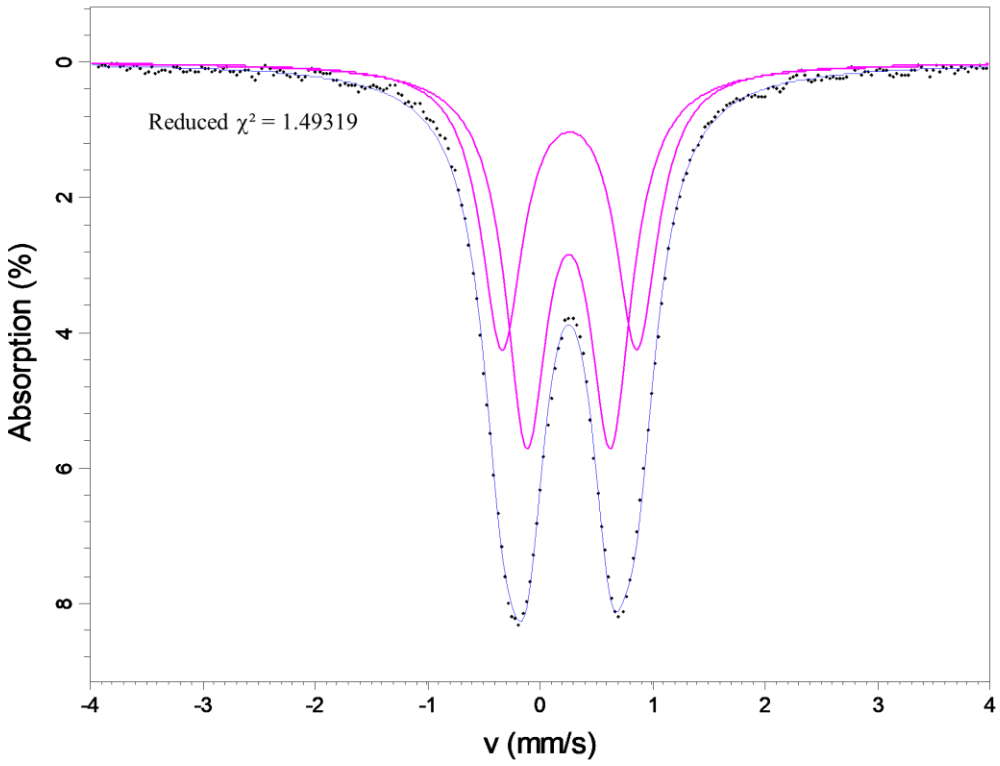

Figure 4.8: *The Mössbauer spectrum for the SCFe007.5 sample fitted with two Lorentzian doublets.*

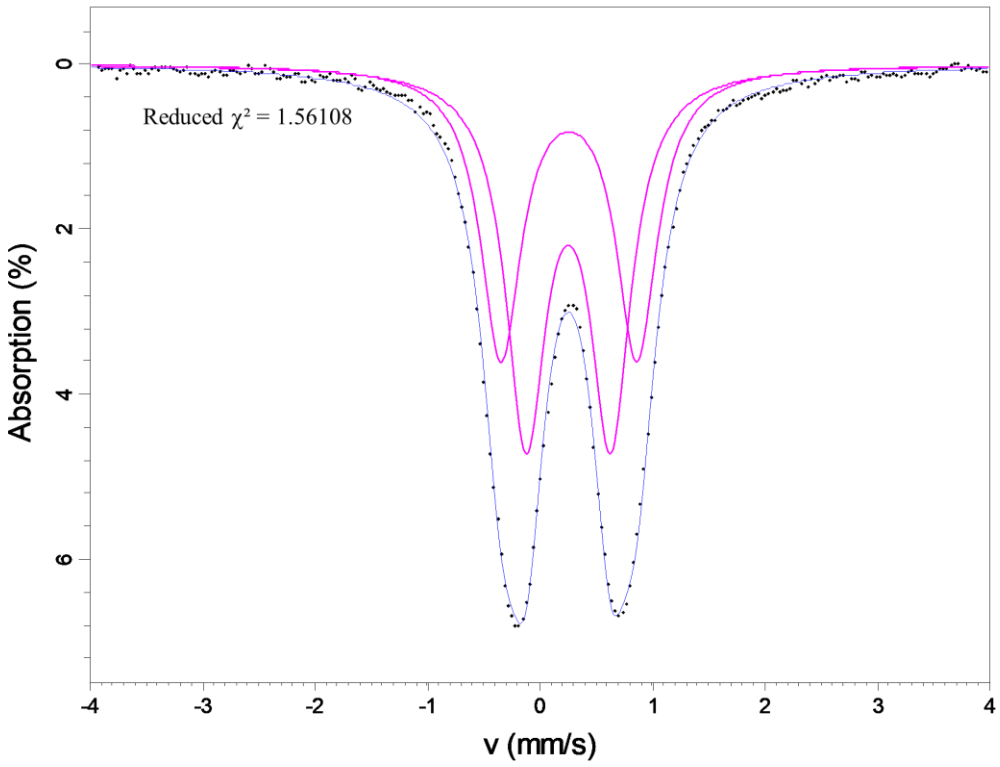

Figure 4.9: *The Mössbauer spectrum for the SCFe010.0 sample fitted with two Lorentzian doublets.*

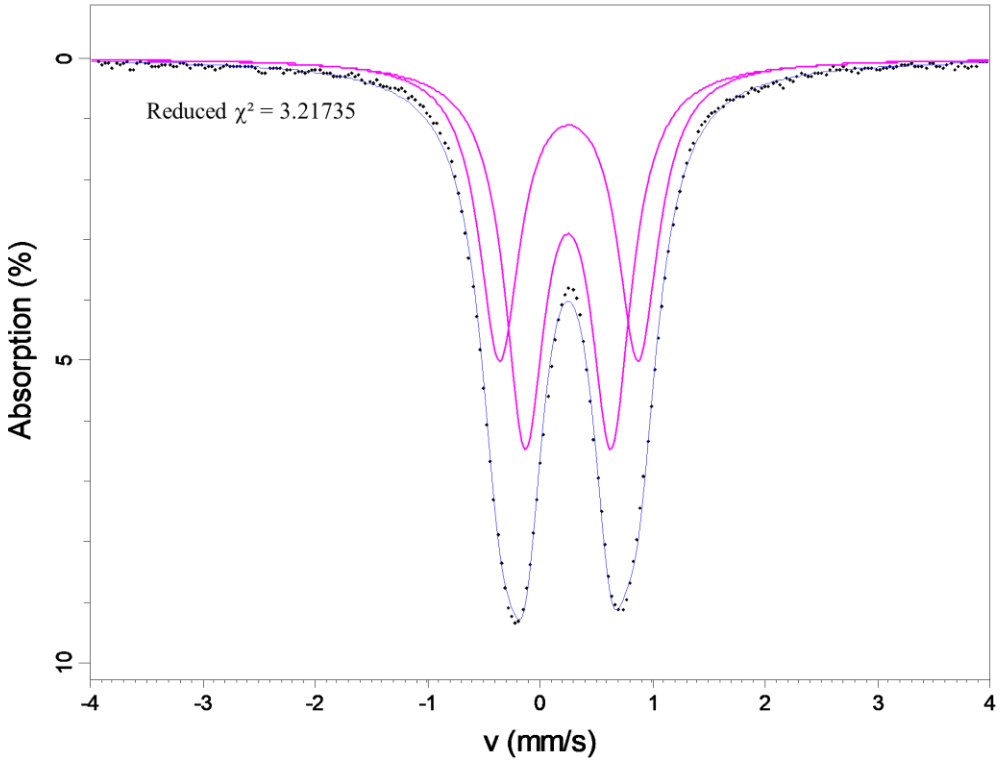

Figure 4.10: *The Mössbauer spectrum for the SCFe014.0 sample fitted with two Lorentzian doublets.*

The Mössbauer spectra for the SCFe sample series can be seen in **Figs 4.6 – 4.10**. The associated fit parameters can be found in **Table 4.3**.

Table 4.3: The Mössbauer fit parameters for the SCFe sample series spectra.

Sample ID	Site Type	Centre Shift (mm s^{-1})	Quadrupole Split (mm s^{-1})	Linewidth (mm s^{-1})	Site Abundance (%)
SCFe005.0	Doublet	0.256 (± 0.002)	0.745 (± 0.022)	0.245 (± 0.008)	52.2 (± 6.7)
	Doublet	0.267 (± 0.002)	1.169 (± 0.029)	0.266 (± 0.008)	47.8 (± 6.9)
SCFe007.5	Doublet	0.265 (± 0.002)	0.758 (± 0.018)	0.227 (± 0.007)	56.2 (± 5.2)
	Doublet	0.262 (±0.002)	1.198 (± 0.022)	0.227 (± 0.009)	43.8 (± 5.3)
SCFe010.0	Doublet	0.252 (± 0.002)	0.751 (± 0.014)	0.216 (± 0.006)	55.2 (± 4.2)
	Doublet	0.257 (± 0.002)	1.211 (± 0.018)	0.220 (± 0.007)	44.8 (± 4.4)
SCFe014.0	Doublet	0.249 (± 0.001)	0.766 (± 0.009)	0.216 (± 0.004)	54.8 (± 2.7)
	Doublet	0.256 (± 0.001)	1.232 (± 0.012)	0.221 (± 0.005)	45.2 (± 2.8)

It can be seen from the parameters in **Table 4.3** that the iron exists exclusively as Fe^{3+} within the simplified series, as denoted by the centre shift values of all doublets in the spectra. For the SCFe005.0 sample spectrum (see **Fig. 4.7**), there is some small evidence of the presence of Fe^{2+} that is manifested in a slightly asymmetrical doublet coupled with a slight underfit of the spectrum at approximately 2 mm s^{-1}. However, when attempting to fit this signal, the site abundance was less than that of the uncertainty ranges of the parameter (± 6.7 - 6.9 %). This evidence of Fe^{2+} is less visible in the remaining spectra for this sample series.

The abundances of the two doublets slightly change as function of the nominal Fe_2O_3 contents within the sample, but when considering the uncertainty of the parameter, it is assumed that the change is insignificant and that abundances are functionally unaffected by the amount of Fe_2O_3. The same can be said for the remaining parameters.

For each spectrum, the two doublets have approximately the same centre shift values which, compared to the values in **Table 4.1**, indicate Fe^{3+} for both doublets. The quadrupole split values for the doublets are significantly different with values of ~ 0.75 and ~ 1.20 mm s^{-1} respectively. As mentioned above in 5.3, the quadrupole splitting has been used to describe the coordination number of iron in glass, but there has been some inconsistency with the assignment of 4-, 5-, and 6-coordinated iron values for quadrupole splitting. The doublet at 0.75 mm s^{-1} is on or around an apparent boundary in literature in

whether or not it is 4- or 6-coordinated iron, so depending on the source of information, the iron can potentially exist as entirely 4-, entirely 6-, or as a mixture of both 4- and 6-coordinated iron within the glass. The presence of two Lorentzian sites would suggest that there are at least two unique sites within the glass samples measured, which lends support to the presence of higher coordinated Fe sites. It is therefore theorised that the presence of two Lorentzian functions in lieu of one Voigt-based function is likely due to a combination of site distortion of the iron sites and the suspected presence of higher-coordinated Fe-sites. Using Mössbauer spectroscopy alone is unlikely to confirm this.

4.4.2 CCFe Series

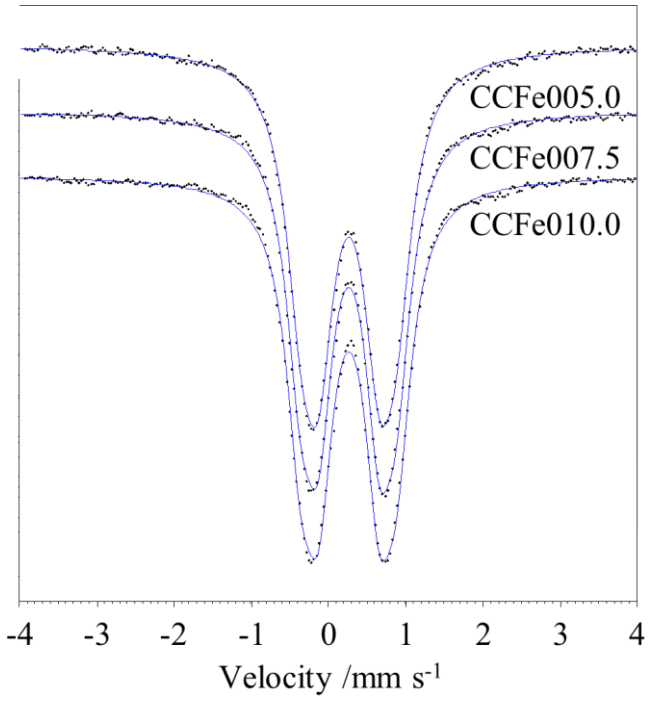

***Figure 4.11**: The stack plot of the CCFe series Mössbauer spectra with Lorentzian fits.*

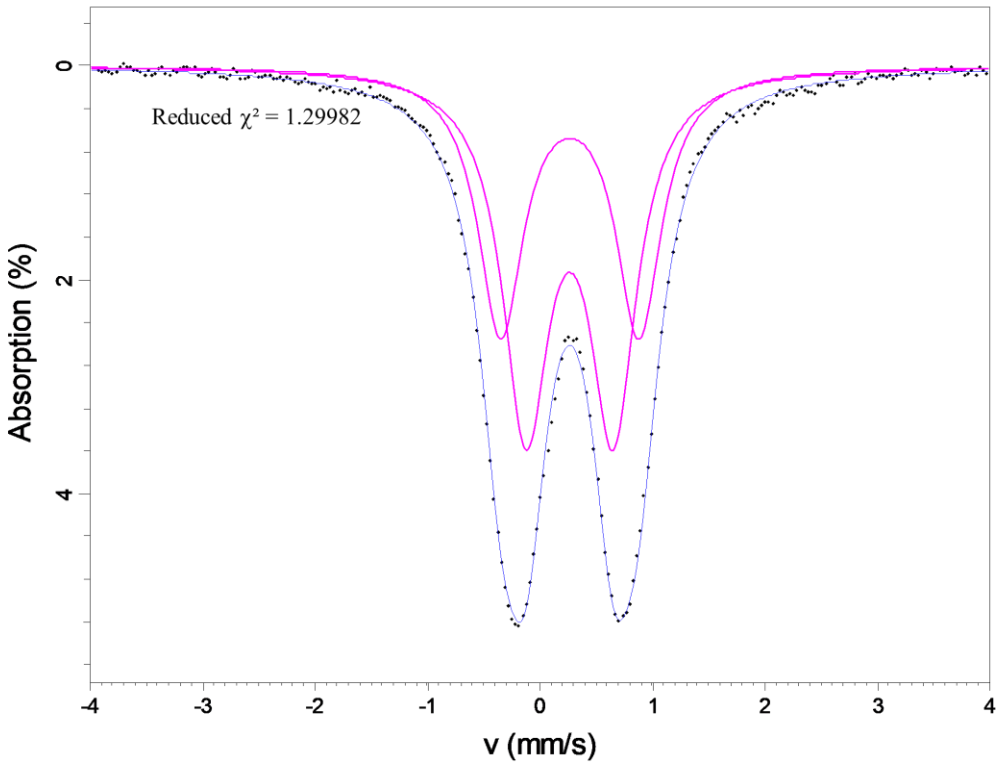

Figure 4.12: *The Mössbauer spectrum for the CCFe005.0 sample fitted with two Lorentzian doublets.*

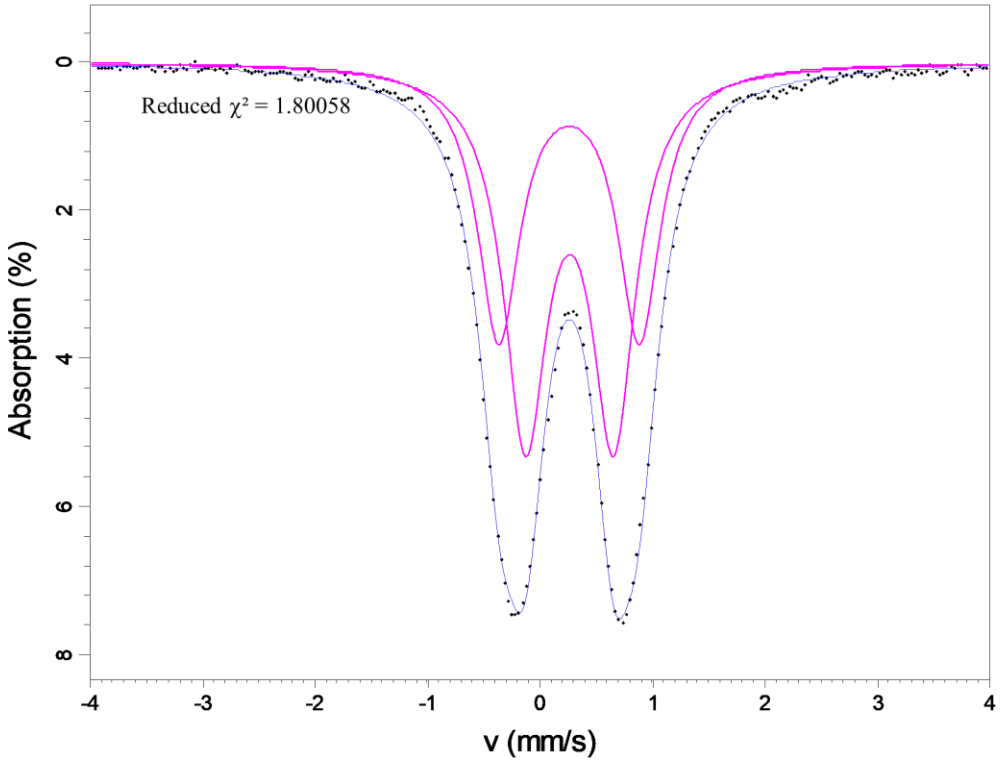

Figure 4.13: *The Mössbauer spectrum for the CCFe007.5 sample fitted with two Lorentzian doublets.*

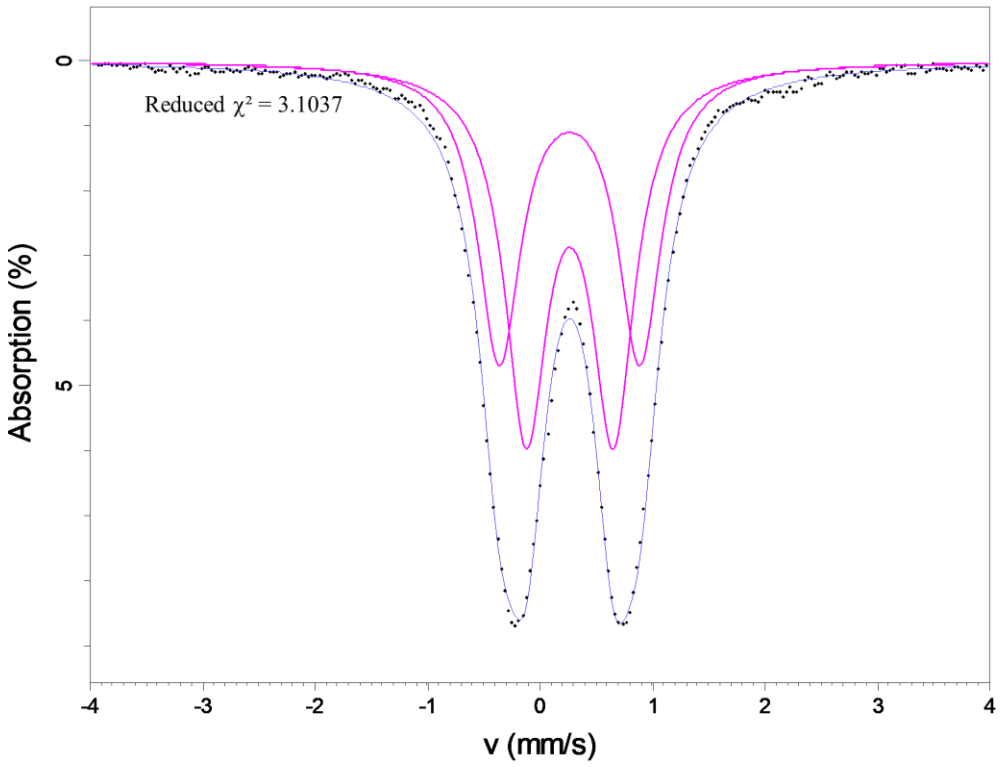

Figure 4.14: *The Mössbauer spectrum for the CCFe010.0 sample fitted with two Lorentzian doublets.*

The Mössbauer spectra for the CCFe sample series can be seen in **Figs 4.11 – 4.14**, with the corresponding fit parameters seen in **Table 4.4**.

Table 4.4: The Mössbauer fit parameters for the CCFe sample series spectra.

Sample ID	Site Type	Centre Shift (mm s^{-1})	Quadrupole Split (mm s^{-1})	Linewidth (mm s^{-1})	Site Abundance (%)
CCFe005.0	Doublet	0.263 (± 0.002)	0.776 (± 0.025)	0.250 (± 0.008)	57.6 (± 7.0)
	Doublet	0.265 (± 0.002)	1.228 (± 0.030)	0.245 (± 0.011)	42.4 (± 7.1)
CCFe007.5	Doublet	0.262 (± 0.002)	0.783 (± 0.016)	0.235 (± 0.006)	57.8 (± 4.5)
	Doublet	0.258 (± 0.002)	1.250 (± 0.020)	0.228 (± 0.008)	42.2 (± 4.6)
CCFe010.0	Doublet	0.265 (± 0.001)	0.775 (± 0.013)	0.229 (± 0.005)	55.0 (± 3.7)
	Doublet	0.262 (± 0.002)	1.248 (± 0.016)	0.231 (± 0.006)	45.0 (± 3.8)

Similarly to SCFe sample series, the spectra in **Figs 4.12 – 4.14** and associated fit parameters in **Table 4.4**, show that the iron exists as Fe^{3+} within the CCFe sample series. The parameters do not exhibit any significant change beyond parameter uncertainty, as a function of changing Fe_2O_3 contents within the glass.

For both doublets the centre shift corresponds to Fe^{3+} (see **Table 4.1**), with comparable quadrupole splitting values seen for the SCFe series, albeit slightly higher. This suggests the iron exists in similarly distorted sites in the CCFe series as it does in the SCFe series, with the possibility of higher-coordinated Fe sites.

4.4.3 HAFe Series

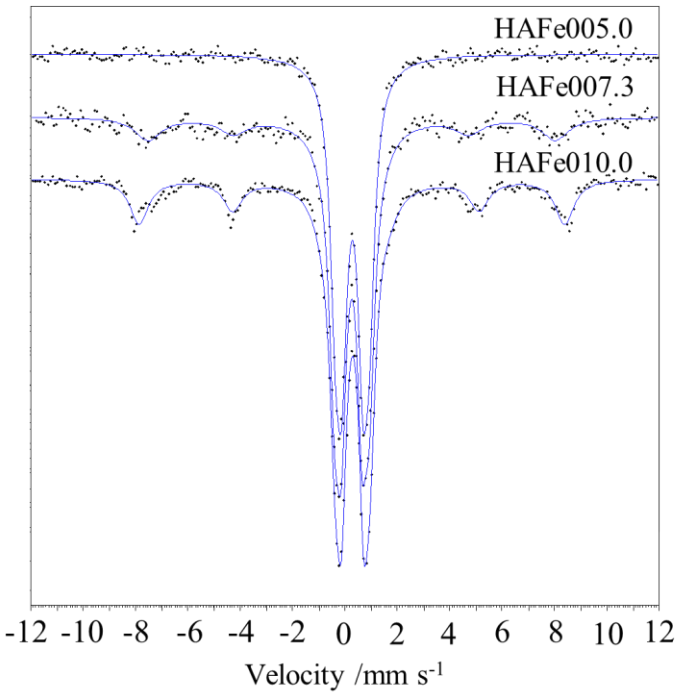

Figure 4.15*: The stack plot for the HAFe series Mössbauer spectra with Lorentzian fits.*

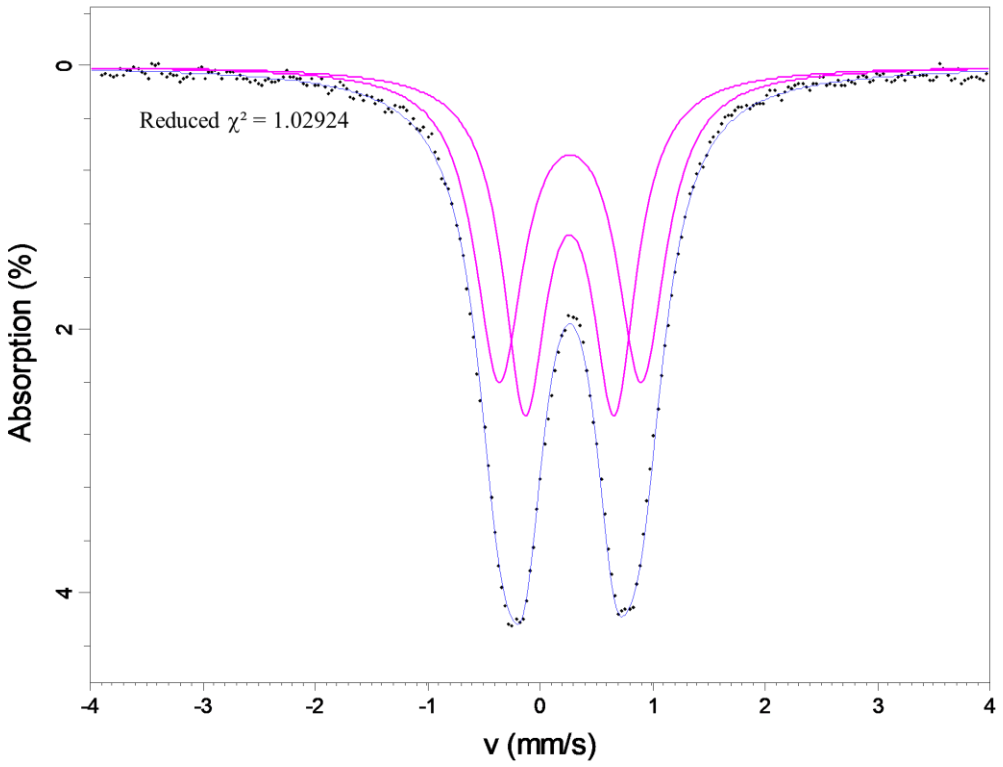

Figure 4.16: *The Mössbauer spectrum for the HAFe005.0 sample fitted with two Lorentzian doublets.*

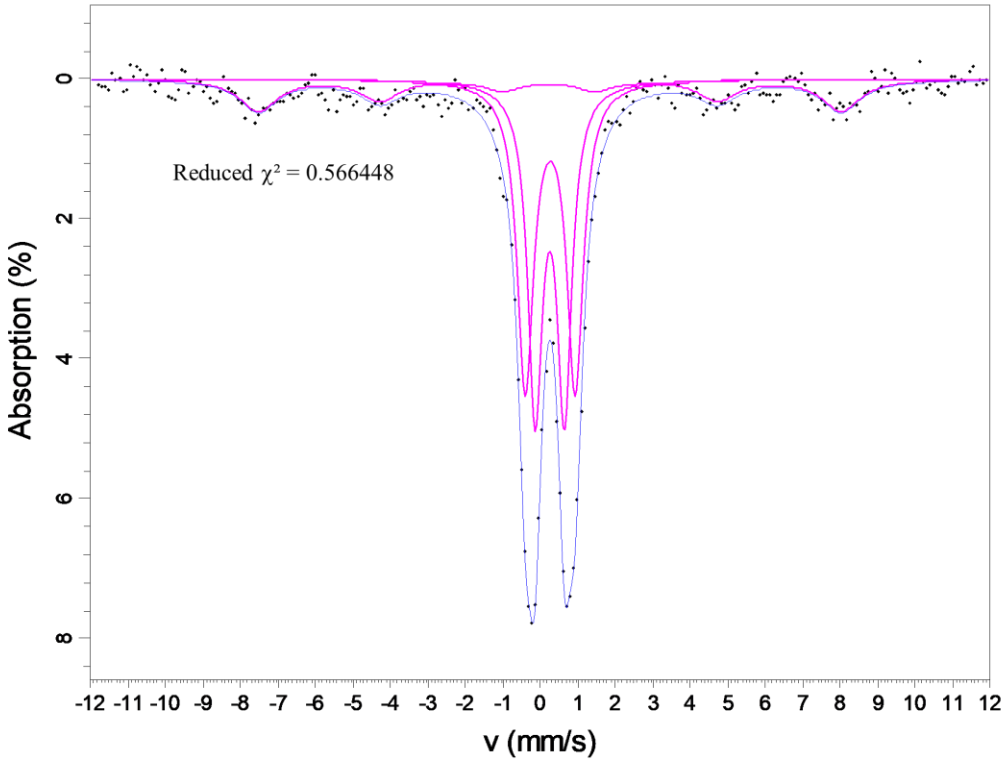

Figure 4.17: *The Mössbauer spectrum for the HAFe007.1 sample fitted with two Lorentzian doublets and one Lorentzian sextet.*

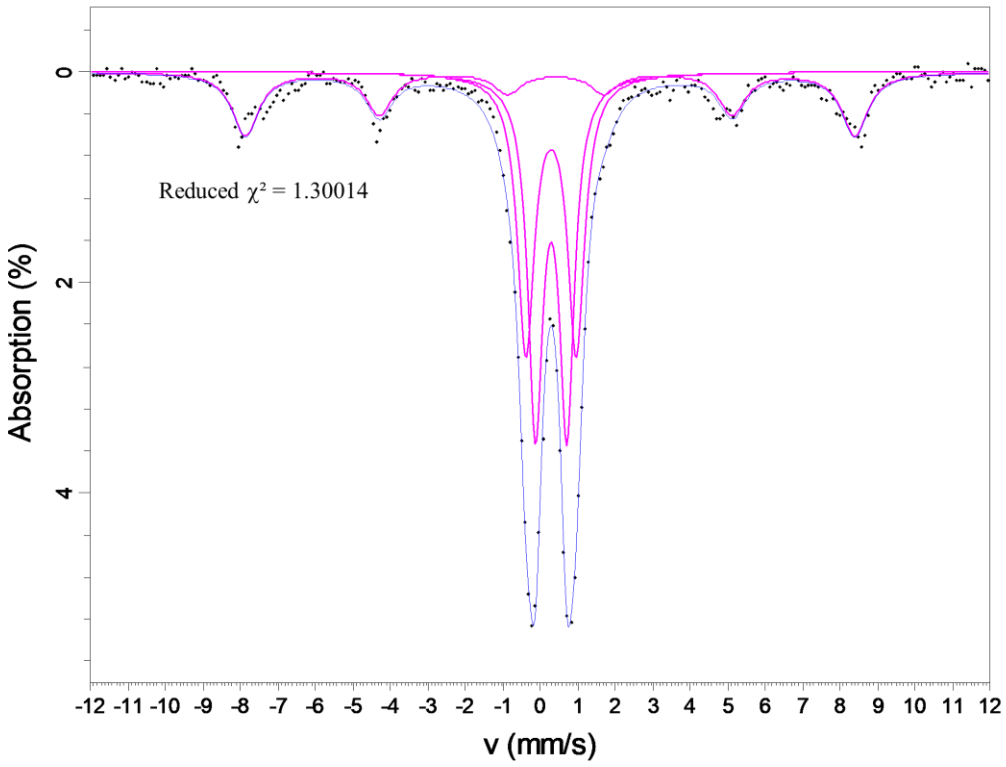

Figure 4.18: *The Mössbauer spectrum for the HAFe010.0 sample fitted with two Lorentzian doublets and one Lorentzian sextet.*

The spectra for the HAFe sample series can be seen in **Figs 4.15 – 4.18**, with the associated fit parameters in **Table 4.5**.

Table 4.5: The Mössbauer fit parameters for the HAFe sample series spectra.

Sample ID	Site Type	Centre Shift (mm s^{-1})	Quadrupole Split (mm s^{-1})	Linewidth (mm s^{-1})	Hyperfine Field (T)	Site Abundance (%)
HAFe005.0	Doublet	0.265 (± 0.003)	0.795 (± 0.027)	0.236 (± 0.011)	-	49.0 (± 7.4)
	Doublet	0.270 (± 0.003)	1.264 (± 0.033)	0.262 (± 0.011)	-	51.0 (± 7.7)
HAFe007.1	Doublet	0.261 (± 0.009)	0.782 (± 0.062)	0.234 (± 0.031)	-	39.0 (± 13.0)
	Doublet	0.273 (± 0.010)	1.330 (± 0.082)	0.262 (± 0.031)	-	41.0 (± 14.0)
	Sextet	0.250 (± 0.130)	0.020 (± 0.120)	0.620 (± 0.220)	48.210 (± 0.840)	20.0 (± 7.1)
HAFe010.0	Doublet	0.297 (± 0.004)	0.838 (± 0.044)	0.239 (± 0.019)	-	39.0 (± 9.5)
	Doublet	0.294 (± 0.006)	1.341 (± 0.068)	0.272 (± 0.022)	-	35.2 (± 9.8)
	Sextet	0.345 (± 0.029)	-0.075 (± 0.028)	0.431 (± 0.050)	50.39 (± 0.20)	25.8 (± 2.8)

Much like the previous sample series, the spectra (**Figs 4.13 – 4.15**) and associated fit parameters (**Table 4.5**) appear to indicate the iron exists as Fe^{3+} within the samples measured as denoted by the centre shift values (see **Table 4.1**). The same trends seen in the SCFe and CCFe sample series are seen in this series.

The primary difference arises in the presence of a sextet at the higher iron content samples in this series. This sextet refers to a form of magnetic ordering at an iron site within the sample, rather than the hyperfine field referred to in 5.2.3, discussed by Williams *et al*. [4]. It is no coincidence that for these two samples, an iron bearing spinel phase was identified within the HAFe007.1 and HAFe010.0 samples in the XRD data from Chapter 3.2.3. The values of hyperfine field in these samples (48.2 and 50.4 T respectively) would correspond to the Fe-rich spinel, when comparing these values to values obtained by Sawatzky *et al*. [30], which was a study on iron-rich spinel phases using Mössbauer spectroscopy, and Oh *et al*. [31] which studied corrosion products on steel using Mössbauer spectroscopy.

4.4.4 HAFe001.0 10 K

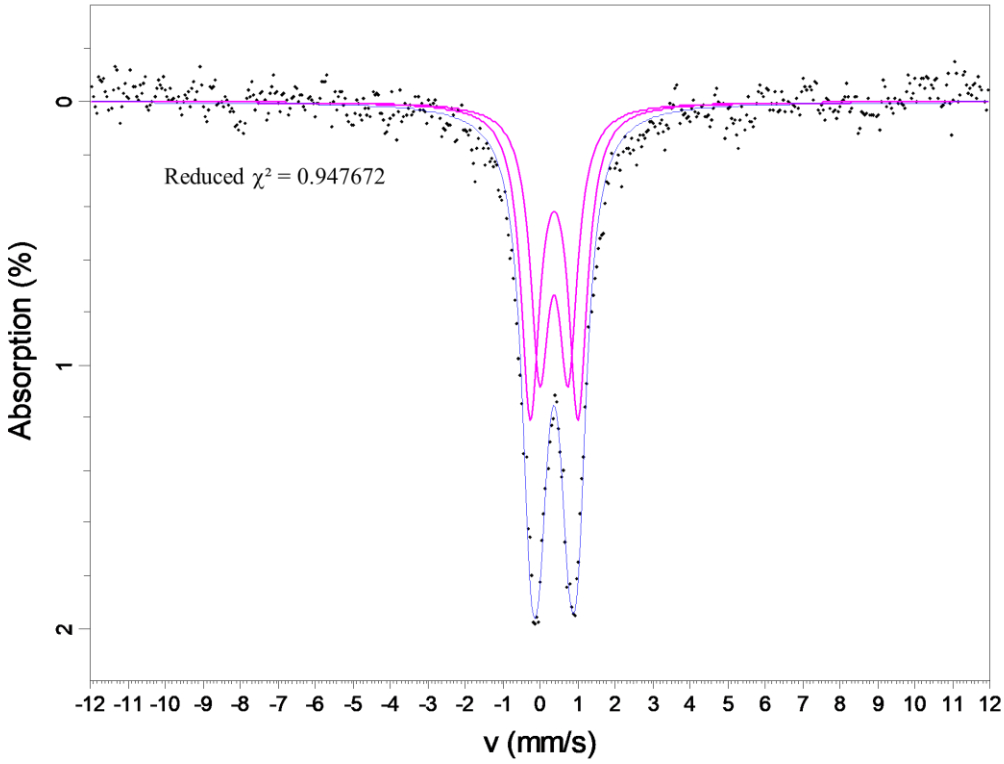

Figure 4.19: *The 10 K Mössbauer spectrum of the HAFe001.0 sample fitted with two Lorentzian doublets.*

The low-temperature spectrum of the HAFe001.0 sample can be seen in **Fig. 4.19**. Despite the absence of a sextet, the spectrum was acquired at +/- 12 mm s^{-1} due to the

expectation that sextet would be present. The associated fit parameters can be seen **Table 4.6**.

Table 4.6: The Mössbauer fit parameters for the 10 K HAFe001.0 sample spectrum.

Sample ID	Site Type	Centre Shift (mm s^{-1})	Quadrupole Split (mm s^{-1})	Linewidth (mm s^{-1})	Site Abundance (%)
HAFe001.0	Doublet	0.373 (± 0.002)	0.759 (± 0.014)	0.291 (± 0.001)	45.4 (± 2.2)
	Doublet	0.377 (± 0.002)	1.271 (± 0.018)	0.376 (± 0.001)	54.6 (± 2.4)

From the site parameters it can be seen that there is no hyperfine splitting evident in the sample, despite the low abundance of iron within the sample. This is contrary to the expectations based on the established theory of Williams *et al*. [4]. This would suggest that the range of inter-atomic distances of the iron is sufficiently close that the relaxation time of the spin-spin contributions is still short enough to prevent the manifestation of hyperfine splitting. Suggesting that the iron does not form isolated units within the HAFe series, even at low abundances. The centre shift values in **Table 4.6** suggests that the iron is all Fe^{3+}.

4.5 Discussion

4.5.1 Iron Chemistry

With all three series, the iron exists as Fe^{3+} with very little evidence to suggest there is any Fe^{2+} within the glass, with no doublets being fit with parameters consistent with Fe^{2+}. Considering the methods and raw materials used to produce the samples (see Chapter 3), the iron comes from Fe_2O_3 and the glasses were melted in a static furnace in ambient conditions, i.e. there was no attempt to influence a reduction of the iron in the making of the samples. This makes the lack of Fe^{2+} within the samples a reasonable finding when compared to previous studies of iron within borosilicate glasses [9,16,25,32-34] (see Chapter 2.3.4).

The coordination of the iron within the glass samples studied here is difficult to determine with Mössbauer spectroscopy in isolation, owing in part to the ambiguity in the use of QS values to describe coordination (see Chapter 4.3), and the QS values from the fits of the samples themselves. If Tomandl's [13] QS ranges were used to describe the coordination, they would suggest that the Fe exists in both octahedral and tetrahedral units. However, the CS values are all in the tetrahedral Fe^{3+} range [3,6,12,13] (see **Table 4.1**), which includes the same review by Tomandl [13]. When confronted with the same discrepancy,

many authors have defaulted to using the centre shift to describe the coordination of the iron [9,10,25,28]. If the same logic is applied to this study, all of the doublets describe 4-coordinated Fe^{3+} in all samples. The distinct differences in quadrupole splitting could be theoretically attributed to a range of distorted sites, with the distortion arising from the intrinsic nature of bonds and groups within a glass network (see Chapter 2.2 for more information). However, given the ambiguity of this approach, coupled with the fact that 6-coordinated iron Fe^{3+} has been frequently seen in borosilicate glasses [9,11,16,25,26,34-36], this conclusion would need further study to elucidate this aspect of the iron chemistry.

While the fit parameters qualitatively show the iron exists as tetrahedral Fe^{3+}, it is important to note that the fit parameters do not deviate significantly between series, nor do they deviate significantly as a function of increasing iron oxide contents within the relative glass series. This would suggest that, despite the lack of quantitative analysis of the coordination number for the iron sites, the sites themselves are broadly comparable across each series. This means that while it is unclear how much, if any, of the iron exists as octahedral Fe^{3+}, it is unlikely that there is a significant difference in the amount of iron in octahedral sites between each of the three series and, by extension, the abundance of tetrahedral Fe^{3+} does not deviate significantly between series. This is key point to note when discussing how this conclusion fits within the discussions in Chapter 8 around the wider glass chemistry.

4.5.2 HAFe001.0 10 K

The low temperature spectrum for the HAFe001.0 sample is interesting for a number of reasons. As discussed earlier in this Chapter, Williams *et al*. [4] demonstrated that at low concentrations of iron within a glass, the spectrum begins to show evidence of hyperfine splitting caused by an increase in relaxation time in isolated Fe^{3+} units. This hyperfine splitting is resolvable at low temperatures by decreasing the relaxation time component dependant on thermal energy (the spin-lattice component). However, as evidenced by **Fig. 4.19**, there is no hyperfine splitting to be seen in the lowest iron Hanford analogue glass, suggesting that the inter-atomic distances between iron atoms is sufficiently low enough that the spin-spin aspect of the relaxation time is sufficiently low (see Equation 4.4). This would suggest that at low concentrations of iron within the glass, there is still evidence that the iron is grouping together within the glass despite the low abundance of iron. Clustering of iron within glass is seen in a wide variety of glass matrices [37-42] and has been linked to the nucleation of Fe-rich crystalline phases in radioactive waste glasses

[36,41]. The phenomenon where the iron seemingly still clusters would make interesting further topic of study, and such a study is elaborated on in Chapter 8.

4.5.3 A Note on Error Analysis

The error values given in **Tables 4.2 – 4.6** are the error values on the fit parameters as given by the fit provided by the Recoil software. It is common within literature to quote specific values that are often more conservative than those provided by various fitting software. Typically these are ± 0.02 on the centre shift (δ), quadrupole splitting (Δ) values, and linewidth (Γ) values, ± 0.5 on the hyperfine field (H), and ± 2.0 on the site abundance (example references that use this [10,11,43]). In the fit parameters in this research, the constant error values would overestimate the fit errors (provided by Recoil) in some spectra while underestimate fit error values in other spectra. It is the author discretion to err on the side of consistency, therefore, rather than picking and choosing with error values to use (some being the commonly quoted values, while some provided by Recoil), all error values given are provided from the fit statistics from the Recoil software.

4.6 References

[1] Cranshaw, T. E., Dale, B. W., Longworth, G. O., & Johnson, C. E., Mössbauer spectroscopy and its applications, Cambridge University Press, Cambridge, UK, 1985.

[2] Dickson, D. P. E., & Berry, F. J., Ch. 1: Principles of Mössbauer spectroscopy, in "Mössbauer Spectroscopy" Ed. Dickson, D. P. E., & Berry, F. J., Cambridge University Press, Cambridge, UK, 1986.

[3] Kurkijan, C. R., Mössbauer spectroscopy in inorganic glasses, *J. Non-Cryst. Solids*, **3**, 1970; pp 157-194.

[4] Williams, K. F. E., Johnson, C. E., & Thomas, M. F., Mössbauer spectroscopy measurement of iron oxidation states in float composition silica glasses, *J. Non-Cryst. Solids*, **226**, 1998; pp 19-23.

[5] Bauminger, E. R., & Nowik, I., Ch. 6: The dynamics of nuclei studied by Mössbauer spectroscopy, in "Mössbauer Spectroscopy" Ed. Dickson, D. P. E., & Berry, F. J., Cambridge University Press, Cambridge, UK, 1986.

[6] Darby-Dyar, M., A review of Mössbauer data on inorganic glasses: The effects of composition on iron valency and coordination, *Am. Mineral.*, **70**, 1985; pp 304-316.

[7] Zhang, H., Advances of ferrous and ferric Mössbauer recoilless fractions in minerals and glasses, *Geosci. Front.*, **13**, 2022.

[8] Bingham, P. A., Vaishnav, S., Forder, S. D., Scrimshire, A., Jaganathan, B., Rohini, J., Marra, J. C., Fox, K. M., Pierce, E. M., Workman, P., & Vienna, J. D., Modelling the sulfate capacity of simulated radioactive waste borosilicate glasses, *J. Alloys Compd.*, **695**, 2017; pp 656-667.

[9] Wright, A. C., Sinclair, R. N., Shaw, J. L., Haworth, R., Bingham, P. A., Forder, S. D., Holland, D., Scales, C. R., Cuello, G. J., & Vedishcheva, N. M., The environment of Fe^{3+}/Fe^{2+} cations in a sodium borosilicate glass, *Phys. Chem. Glasses: Eur. J. Glass Sci. Technol. B*, **58**, 2017; pp 78-91.

[10] Balasubramanya, N., Sun, Z., Ahmadzadeh, M., Kamali, S., Neuville, D. R., McCloy, J. S., & Goel, A., Impact of non-framework cation mixing on the structure and crystallization behavior of model high-level waste glasses, *J. Am. Ceram. Soc.*, **105**, 2022; pp 3967-3985.

[11] Rigby, J. C., Dixon, D. R., Cutforth, D. A., Marcial, J., Kloužek, J., Pokorný, R., Kruger, A. A., Scrimshire, A., Bell, A. M. T., & Bingham, P. A., Melting behaviour of simulated radioactive waste as functions of different redox iron-bearing raw materials, *J. Nucl. Mater.*, **569**, 2022.

[12] Nishida, T., Advances in the Mössbauer effect for the structural study of glasses, *J. Non-Cryst. Solids*, **177**, 1994; pp 257-268.

[13] Tomandl, G., Ch. 5 in "Glass: Science and Technology", vol. 4B, Ed. Uhlmann, D. R., and Kriedl, N. J., Academic Press, New York, USA, 1990.

[14] Benczer-Koller, N., & Herber, R. H., Ch. 1 in "Chemical Applications of Mössbauer Spectroscopy", Ed. Goldanskii, V. I., & Herber, R. H., Academic Press, New York, USA, 1968.

[15] Kurkjian, C. K., & Sigety, E. A., Coordination of Fe^{3+} in glass, *Phys. Chem. Glasses*, **9**, 1968; pp 73-83.

[16] Taragin, M. F., & Eisentein, J. C., Mössbauer effect in some complex borosilicate glasses, *J. Non-Cryst. Solids*, **3**, 1970; pp 311-316.

[17] Bukrey, R. R., Kenealy, P. F., Beard, G. B., & Hooper, H. O., Mössbauer-effect study of the structure and magnetic properties of the $Na_2O{\cdot}Li_2O{\cdot}B_2O_3{\cdot}Fe_2O_3$ glass system, *Phys. Rev. B*, **9**, 1974; pp 1052-1061.

[18] Sekhon, S. S., & Kamal, R., Mössbauer study in the glass system $PbO{\cdot}2B_2O_3{\cdot}Fe_2O_3$, *J. Non-Cryst. Solids*, **28**, 1978; pp 189-192.

[19] Nishida, T., Hirai, T., & Takashima, Y., Mössbauer spectroscopic study of nonbridging oxygen atoms in potassium borosilicate glasses, *Phys. Chem. Glasses*, **22**, 1981; pp 94-98.

[20] Nishida, T., A review of structural studies of supersonic conducting borate and semiconducting vanadate glasses by Mössbauer spectroscopy and DTA, *J. Non-Cryst. Solids*, **108**, 1989; pp 87-98.

[21] Bingham, P. A., Parker, J. M., Searle, T., Williams, J. M., & Fyles K., Redox and clustering of iron in silicate glasses. *J. Non-Cryst. Solids*, **253**, 1999; pp 203-209.

[22] Bingham, P. A., Forder, S. D., Hand, R. J., & Lavaysierre, A., Mössbauer studies of phosphate glasses for the immobilisation of toxic and nuclear wastes, *Hyperfine Interact.*, **165**, 2005; pp 135-140.

[23] Cassingham, N. J., Bingham, P. A., & Hand, R. J., Property modification of a high level nuclear waste borosilicate glass through the addition of Fe_2O_3, *Glass Technol.: Eur. J. Glass Sci. Technol. A*, **49**, 2008; pp 21-26.

[24] Forder S. D., Hannant, O. M., Bingham, P. A., & Hand, R. J., Concerning the use of standards for identifying coordination environments in glasses, *J. Phys.: Conf. Ser.*, **217**, 2010.

[25] Cochain, B., Neuville, D. R., Henderson, G. S., McCammon, C. A., Pinet, O, & Richet, P., Effects of the iron content and redox state on the structure of sodium borosilicate glasses: A Raman, Mössbauer and boron k-edge XANES spectroscopy study, *J. Am. Ceram. Soc.*, **95**, 2012; pp 962-971.

[26] Glazkova Y. S., Kalmykov, S. N., Presnyakov, I. A., Stefanovskaya, O. I., & Stefanovsky, S. V., The structural state of iron in multicomponent aluminum iron borosilicate glass depending on their composition and synthesis conditions, *Glass Phys. Chem.*, **41**, 2015; pp 367-377.

[27] Ciżman, A., Rysiakiewicz-Pasek, E., Krupiński, M., Konon, M., Antropova, T., & Marszałek, M., The effect of Fe on the structure and electrical conductivity of sodium borosilicate glasses, *Phys. Chem. Chem. Phys.*, **19**, 2017; pp 23318-23324.

[28] Ciżman, A. Rysiakiewicz-Pasek, E., Antropova, T., Krupiński, M., Pshenko, O. A., & Zarzycki, A., Effect of the iron content on the structure and electrical properties of sodium borosilicate glasses: XRD, TEM, Mössbauer, FTIR and DIS spectroscopy study, *J. Non-Cryst. Solids*, **531**, 2020.

[29] Darby Dyar, M., Agresti, D. G., Shaefer, M. W., Grant, C. A., & Sklute, E. C., Mössbuaer spectroscopy of Earth and planetary materials, *Annu. Rev. Earth Planet. Sci.*, **34**, 2006; pp 83-125.

[30] Sawatzky, G. A., van der Woude. F., & Morrish, A. H., Mössbauer study of several ferrimagnetic spinels, *Phys. Rev.*, **187**, 1969; pp 747-757.

[31] Oh, S. J., Cook, D. C., & Townsend, H. E., Characterization of iron oxides commonly formed as corrosion products on steel, *Hyperfine Interact.*, **112**, 1998; pp 59-66.

[32] Licheri, G., Paschina, G., Piccaluga, G., Pinna, G., Magini, M., & Cocco, G., On the coordination of iron ions in sodium borosilicate glasses: III. An EXAFS investigation, *J. Non-Cryst. Solids*, **72**, 1985; pp 211-220.

[33] Agostinelli, E., Fiorani, D., & Paparazzo, E., XPS studies of iron sodium borosilicate glasses, *J. Non-Cryst. Solids*, **95** & **96**, 1987; pp 373-379.

[34] Stefanovsky, S. V., Fox, K. M., Marra, J. C., Shiryaev, A. A., & Zubavichus, Y. Z., Structural features of high-Fe_2O_3 and high Al_2O_3/Fe_2O_3 SRS HLW glasses, *Phys. Chem. Glasses: Eur. J. Glass Sci. Technol. B*, **53**, 2012; pp 158–166.

[35] Musić, S., Furić, K., Bajs, Z., & Mohaček, V., Spectroscopic characterization of alkali borosilicate glasses containing iron ions, *J. Mater. Sci.*, **27**, 1992; pp 5269-5275.

[36] Ciżman, A., Rysiakiewicz-Pasek, E., Antropov, T., Krupiński, M., Pshenko, O. A., & Zarzycki, A., Effect of the iron content on the structure and electrical properties of sodium borosilicate glasses: XRD, TEM, Mössbauer, FTIR and DIS spectroscopy study, *J. Non-Cryst. Solids*, **531**, 2020.

[37] Jantzen, C. M., & Brown, K. G., Predicting the spinel-nepheline liquidus for application to nuclear waste glass processing. Part I: Primary phase analysis, liquidus 130easurement, and quasicrystalline approach, *J. Am. Ceram. Soc.*, **90**, 2007; pp 1866-1879.

[38] Vercamer, V., Lelong, G., Hijiya, H., Kondo, Y., Galoisy, L., & Calas, G., Diluted Fe^{3+} in silicate glasses: Structural effects of Fe-redox state and matrix composition. An optical absorption and X-band/Q-band EPR study, *J. Non-Cryst. Solids*, **428**, 2015; pp 138-145.

[39] Bingham, P. A., Hannant, O. M., Reeves-McLaren, N., Stennet, M. C., & Hand, R. J., Selective behaviour of dilute Fe^{3+} ions in silicate glasses: An Fe K-edge EXAFS and XANES study, *J. Non-Cryst. Solids*, **387**, 2014; pp 47-56.

[40] Virgo, D., & Mysen, B. O., The structural state of iron in oxidized vs. reduced glasses at 1 atm: A ^{57}Fe Mössbauer study, *Phys. Chem. Mineral.*, **12**, 1985; pp 65-76.

[41] Wiegal, C., Cormier, L., Calas, G., Galoisy, G., & Bowron D. T., Nature and distribution of iron sites in a sodium silicate glass investigated by neutron diffraction and EPSR simulation, *J. Non-Cryst. Solids*, **354**, 2008; pp 5378-5385.

[42] Dantas, N. O., Ayta, W. E. F., Silva, A. C. A., Cano, N. F., Silva, S. W., & Morais, P. C., Effect of Fe_2O_3 concentration on the structure of the SiO_2–Na_2O–Al_2O_3–B_2O_3 glass system, *Spectrochim. Acta A Mol.*, **81**, 2011; pp 140-143.

[43] Ahmadzadeh, M., Olds, T. A., Scrimshire, A., Bingham, P. A., & McCloy, J. S., Structure and properties of $Na_5FeSi_4O_{12}$ cystalized from $5Na_2O$-Fe_2O_3-$8SiO_2$ glass, *Acta Crysta C*, **74**, 2018; pp 1565-1602.

Chapter 5 – X-Ray Absorption Spectroscopy

XAS spectroscopy has been used to describe the chemistry of a variety of materials, ranging from minerals to glasses. It is an element-specific technique, with very few limits on what elements can be investigated. XAS can be separated into two primary techniques – XANES (X-ray Absorption – Near-Edge Structure) spectroscopy, and EXAFS (Extended X-ray Absorption – Fine Structure) spectroscopy. XANES can provide information on valency on multi-valent species and limited qualitative information of structure and coordination, whereas EXAFS provides quantitative short range structural information. This Chapter will cover the use of two different elemental XANES, Fe K-edge and B K-edge, to study the iron valency and coordination and the boron coordination within the glass samples within this research.

5.1 Overview

As the name might suggest, XAS spectroscopies investigate the absorption of X-rays of specific energies by a given material. The X-rays are typically absorbed by electrons causing an excitation transition within the target material. The energy that causes the transition, the transition itself, and how much absorption occurs, are the primary points of interest in XAS spectroscopies.

5.1.1 X-ray Notation

XAS typically is performed across specific absorption edges, which is named from the sudden increase in absorption of X-rays from no absorption, creating an "edge-like" spectral feature. The names of the edges are given by X-ray notation of the ground state of the target electron. The most common X-ray notations can be found in **Table 5.1**.

Table 5.1: The X-ray notation for each electron orbital up to the $3p^{3/2}$ orbital [1].

Electron	**X-ray Notation**
1s	K
2s	L_1
$2p^{1/2}$	L_2
$2p^{3/2}$	L_3
3s	M_1
$3p^{1/2}$	M_2
$3p^{3/2}$	M_3

If the iron 1s transitions were being investigated using XANES spectroscopy, it would be described as "Fe K-edge XANES spectroscopy". The absorption in this spectrum would

all be electron transitions of 1s electrons of the iron within the sample material. The excited state of the 1s electron does not feature in the name, so for example, if the 1s electron became excited and transitioned to the 3s state, it would not be called "Fe K-M_1 Edge XANES", rather just "Fe K-edge XANES Spectroscopy".

5.1.2 The XAS Spectrum

As mentioned above, XAS involves the absorption of X-rays by electrons to generate a spectrum. The spectrum is presented as a plot of absorption coefficient as a function of X-ray energy. As the absorption is due to the electrons, absorption will only occur at specific energies for different elements [2,3]. As **Fig 5.1** shows, if the photon energy does not match the energy of the electron transition, there will be no absorption of the X-ray photon.

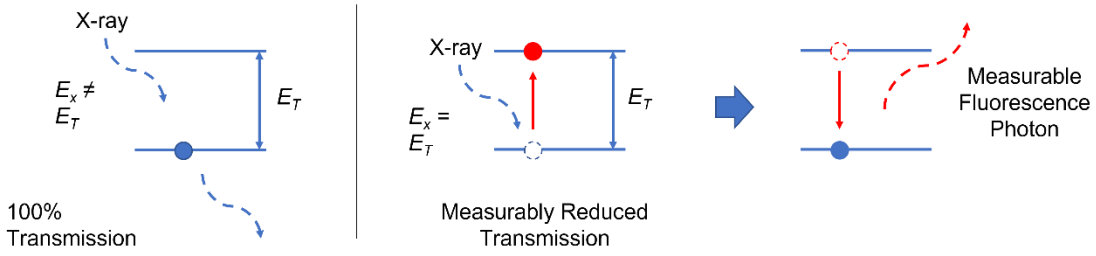

Figure 5.1: *Ac visual representation of X-ray absorption and subsequent fluorescence.*

Fig 5.1 also introduces a visual representation of two different measurement techniques within XAS spectroscopies – transmission mode, and fluorescence mode. Transmission mode is the simplest of the two measurement modes, as it measures the initial X-ray intensity and then the X-ray intensity after it passes through the sample. The absorption at a given energy is described by equation 5.1 [3].

$$I = I_0 e^{-\mu x} \qquad \text{(Eq. 5.1)}$$

Where I is the measured intensity, I_0 is the initial intensity, μ is the attenuation coefficient, and x is the sample thickness. In fluorescence mode, the system detects the energy of the fluorescence photons emitted as the excited electron relaxes back to its ground state. The emitted photons will still be of the same energy as the transitions they correspond to and as such, the spectrum in theory will look identical [2].

Another aspect to consider within an XAS spectrum, are two distinct types of XAS spectroscopy – XANES and EXAFS. The difference between the two can be (over)simplified down to two regions on a given spectrum (see **Fig 5.2**).

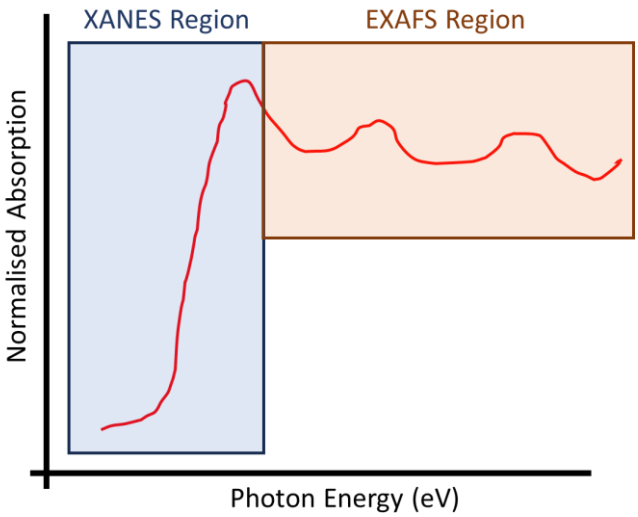

Figure 5.2: *A recreated XAS spectrum (not drawn to scale) with the XANES and EXAFS regions highlighted.*

XANES spectroscopy focuses on the spectrum around the absorption edge itself. This region, depending on the element, can be peak fit to represent different electron transitions and the relative positions/intensities of these transitions will provide information on the chemistry of the material. This will also include "pre-edge" peaks (not shown in **Fig 5.2**), which feature prominently in elements such as iron K-edge XANES [3].

EXAFS spectroscopy is focused on spectra beyond the absorption edge, with the fundamental theory being far more complicated. If the excited electron is considered a wave, the excitation will be scattered by the nearest neighbouring atoms to the target element with the excited electron. These scattering neighbouring atoms will create their own scattering wave patterns. A visual representation of this can be seen in **Figure 5.3**.

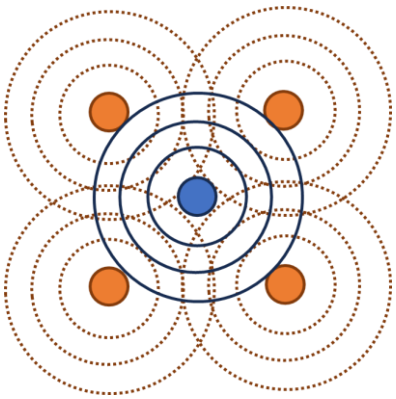

Figure 5.3: *A diagram showing the spherical wave patterns of the target excited atom (blue) and the scattered wave patterns from the nearest neighbouring atoms (orange). Recreated from ref [3].*

These waves constructively and destructively interfere with one another to recreate the oscillating pattern in the rough spectrum diagram seen in **Fig 5.2**. The constructive interference will have a greater photoelectron wave amplitude, so will have a higher absorption coefficient, while the inverse is true for the destructive interference [3]. The patterns of the variations in absorption can be described by a series of equations, that when compared to EXAFS spectra of known materials, with associated known parameters, can be used to generate fits for unknown materials in which valency, coordination, and structural disorder can all be calculated [3]. This makes EXAFS a very useful tool in describing the short-range chemistry of target elements within a given material. However, these equations rely on absorption information of 1000+ eV beyond the absorption edge to be able to accurately fit the EXAFS data. Meaning if the material has any interfering absorption edges from other elements within 1000 eV of the target element, accurate fits of EXAFS spectra are not possible.

5.1.3 Acquiring a Spectrum

The acquisition of an XAS spectrum, requires several key components. An X-ray source, a sample chamber, and several detectors. A schematic of this set up, can be seen in **Fig 5.4**.

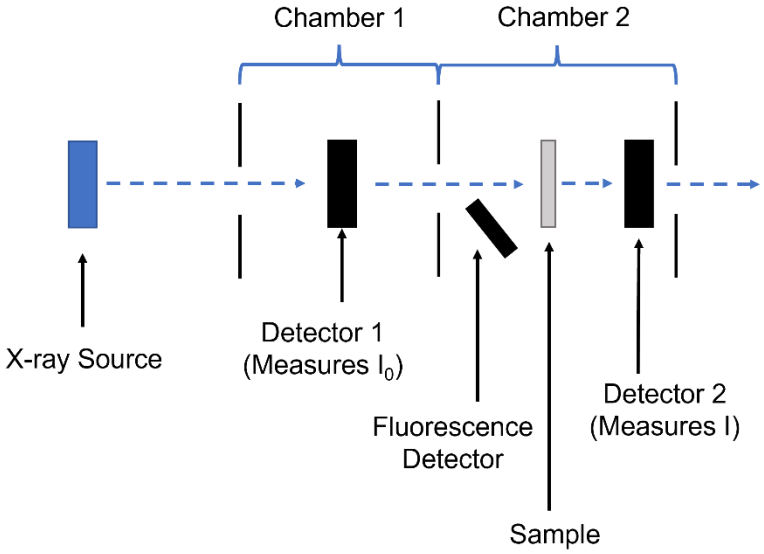

Figure 5.4: *A schematic representation of how XAS data is acquired.*

Detectors 1 & 2 (see **Fig 5.4**) are the key detectors for transmission mode measurements, whereas the fluorescence detector is key for fluorescence mode measurements. However, this does illustrate that both measurement modes in a lot of systems can be done simultaneously.

The X-ray sources in typically come from synchrotron sources, which generate X-rays through particle acceleration, specifically through bremßtrahlung (German for "Breaking Radiation") effects. While X-ray tubes, such as those used in X-ray diffraction, use X-rays from well-defined electron transitions. An example of this would be the CuKα X-ray tube used for XRD in this research (see Chapter 3.3.2). The CuKα X-rays are generated from an electron transitioning from the Cu L orbital to the Cu K orbital, and emitting an X-ray of a narrow energy range in the process. Bremßtrahlung X-rays typically occupy a range of energies allowing for easily tunable X-ray energies across a wide energy range, which is not easily done through the use of X-ray tube sources. Furthermore, synchrotrons are able to produce very high flux of X-rays, that are highly collimated, making it easy to tune the energy range through collimators such as diffraction gratings [2]. This makes synchrotron radiation ideally suited for XAS experiments. However, it is rare that a single synchrotron can provide suitable X-ray energies for all elemental XAS experiments. For example, in Chapter 5.2 a specific beamline was used at the European Synchrotron Radiation Facility (ESRF) to carry out experiments around the Fe K-edge. However, in Chapter 5.3, lower energy X-rays are needed to carry out experiments around the B K-edge, so a different facility was needed as the ESRF could not provide suitably low

enough energy X-rays for the B K-edge, whereas the BEAR beamline at the Elettra Synchrotron could.

5.2 Fe K-Edge XANES

5.2.1 Overview

Iron K-edge XANES has been employed on a wide variety of Fe-bearing materials, ranging from studies on minerals [4-14], through to a variety of glasses [15-33]. XANES specifically has been used to describe the valency of iron and provide some information on the coordination of iron within Fe-bearing minerals and materials. In the case of Fe K-edge XANES, the most important feature of the spectrum is not the absorption edge itself, which occurs at around 7112 eV for ^{56}Fe [34], but the pre-edge peak seen between 7111 – 7114 eV. This particular peak corresponds to the 1s – 3d and 1s – 4p electron transitions [35], the properties of which have been used to describe the valency and coordination of the iron.

This is done by peak fitting the pre-edge feature with gaussian peaks, the exact number depends on the material (see refs [6,10,11,19] for more information on this), and then calculating the average centroid position of the Gaussian peaks to describe the valency. The pre-edge transitions have a slightly higher energy in Fe^{3+} than in Fe^{2+}, which is due to the increased coulombic attraction the nucleus will have on the 1s electron in Fe^{3+} nuclei, resulting in more energy being needed to transition to an orbital further from the nucleus, relative to a lower valence (i.e. Fe^{2+}) cation. The intensity of the absorption of this transition is greater in tetrahedral structures than that of higher coordination numbers, with octahedral being the lowest intensity [6,10,11,19,22]. This is due to the non-centrosymmetric nature of tetrahedral Fe, which allows for some otherwise forbidden 1s – 4d transitions [17].

5.2.2 Fe K-edge XANES on Glass

Within XANES studies around the Fe K-edge on glass, the pre-edge peak remains important. Wu *et al*. [15] measured the XANES pattern around the Fe K-edge in Fe-bearing silicates and compared the spectral patterns to those recreated using molecular dynamic simulations. Based on the patterns produced by the MD simulations, it was concluded that the iron predominantly existed as network forming tetrahedral units with very little 6-coordinated Fe [15]. Galoisy *et al*. [16] used the Fe K-edge XANES spectra of Fe-bearing minerals standards to fit several synthetic and natural Fe-bearing silicate by way of linear combination fitting (LCF). LCF combines the spectral shapes of two or more spectra to recreate a given spectrum. In this case, the spectra of mineral standards

were used to recreate the spectra of Fe-bearing glass. An example from the study by Galoisy *et al*. [16], is the fits of synthetic augite glass. It was shown that the spectrum was best recreated by ferrous standards with no ferric standards used. The conclusions were that the augite glass contains no Fe^{3+} and the Fe^{2+} existed as a mix of $^{[4]}Fe^{2+}$ and $^{[6]}Fe^{2+}$, as a result of the LCF. LCF has been used in further studies, such as those by Magnien *et al*. [18] and Hannant *et al*. [26]. Quartieri *et al*. [17] used fluorescence mode XANES on ancient Roman glass fragments to study both the Fe and Mn K-edge. Gaussian peak fitting was used to describe pre-edge transition, the parameters of which were then compared to literature. This method successfully demonstrated reliable analysis of oxidation state and coordination in a non-destructive manner [17]. Studies by Farges, Wilke, and co-workers [19-23] used XANES and EXAFS to study the Fe K-edge in silicate glasses which utilised the peak fitting of the pre-edge peak. The peak intensity was plotted against centroid energy, with the inclusion of mineral standards to highlight where the various valency and coordination numbers of the iron would lie on the graphs. This form of quantitative analysis has been used extensively in XANES studies [24,25,30-32].

Bingham *et al*. [28] used Fe K-edge XANES and EXAFS spectroscopies to study the Fe^{3+} ions in silicate glasses. In this study, the XANES analysis was purely qualitative, as the presence of the EXAFS analysis rendered the quantitative analysis of the XANES data redundant. As EXAFS spectroscopy can be fit with equations with specific functions regarding valency, structure, and structural distortion, the standard of analysis is considered of a higher, more reliable quality if successfully done. Hence why the XANES analysis was limited to being qualitative, albeit complimentary, to the quantitatively analysis of the EXAFS spectra.

5.2.3 ESRF – BM28/XMaS

Within this research, the Fe K-edge XANES was carried out across two separate measurement periods at the BM28 beamline [36], also known as the X-ray Materials Science (XMaS) facility, at the ESRF in Grenoble, France. The beamline energy ranged from approximately 2 – 40 keV with a 70 x 60 μm spot size, with a liquid nitrogen-cooled Si <111> monochromator [36]. Given the ^{56}Fe K-edge is 7112 eV [34], the energy range for the BM28 was ideally suited to carry out XANES experiments around the Fe K-edge. Furthermore, XANES experiments have been successfully carried out on the BM28, albeit at different edges including the sulphur and nitrogen K-edges on liquid samples [37], and the copper K-edge on glass samples [38], with the lattermost being around a

comparable energy range (Cu K-edge = 8979 eV [34]) to the Fe K-edge. BM28 provided outstanding data quality for this research.

5.3 B K-edge XANES

5.3.1 Overview

Similarly to Fe K-edge XANES, boron K-edge XANES spectroscopy has been used to describe the boron chemistry in a variety of minerals [39-44] and glasses [39,44-48]. B K-edge XANES spectroscopy is often overshadowed by ^{11}B NMR spectroscopy as the top technique in analysing the boron chemistry, however, ^{11}B NMR spectroscopy is not always possible. Yet through comparisons to ^{11}B NMR data, the methods employed in the data analysis of B K-edge XANES data has provided a capable alternative.

Similarly to the Fe K-edge XANES spectroscopy, the data processing involved peak fitting, however, the whole spectrum is typically used (see **Fig 5.5**).

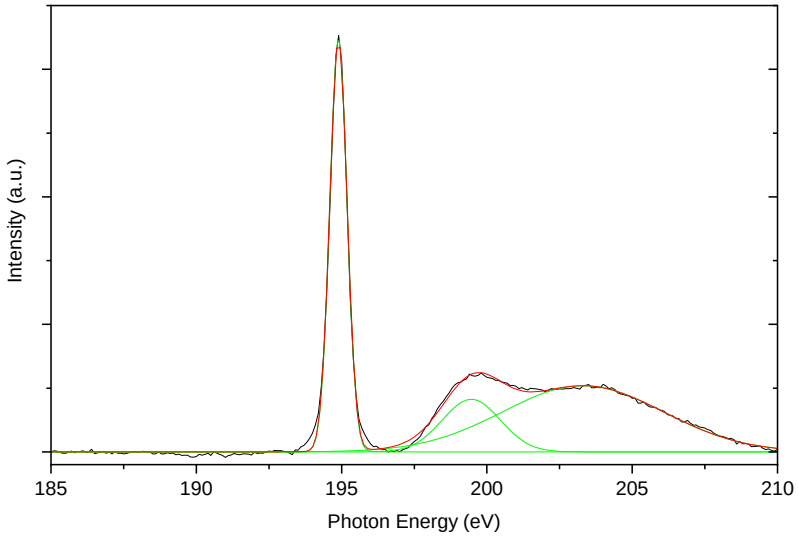

Figure 5.5: *The B K-edge XANES spectrum of ludwigite (Mg_2FeBO_5) with three Gaussian peaks fitted.*

As can be seen in **Fig 5.5**, a minimum three Gaussian peaks are typically used to peak fit the spectrum, with each peak corresponding to different 1s transitions. The sharp peak at around 195 eV (commonly described as “Peak A”) corresponds to the 1s – 2p-like state that is typically only permissible in trigonal boron [41]. The broader peak at around 198 eV (commonly described as “Peak B”), corresponds to a 1s transition to a σ bond transition that is typically only permissible in tetrahedral boron [41]. The broad peak at around 203 eV (commonly described as “Peak C”) is a diffuse mix of contributions from trigonal and tetrahedral boron that is very difficult to deconvolute in materials with mixed $^{[3]}$B and $^{[4]}$B units [41]. It is worth noting, that while in theory the peaks at 195 eV and

198 eV are exclusive to specifically coordinated boron, these peaks are still seen in minerals that in theory should not have these peaks. For example, **Fig 5.5**, shows ludwigite, in which all the boron exists as trigonal boron [41]. There should not be a peak at 198 eV, yet there is. Similarly, danburite is a mineral in which the boron exists exclusively as tetrahedral boron. The boron K-edge XANES spectrum of danburite (see **Fig. 5.6**) should not have a peak at 195 eV, yet it does.

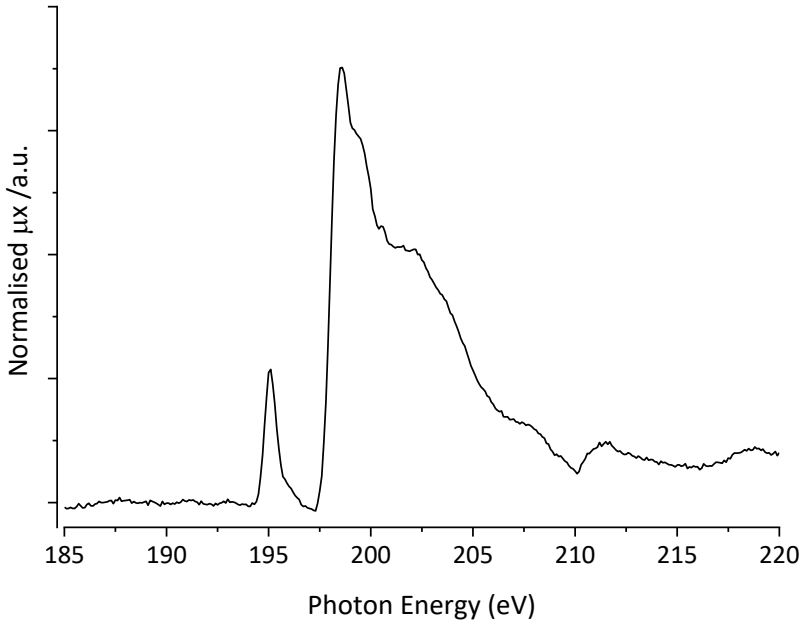

Figure 5.6: *The B K-edge XANES spectrum of the mineral danburite ($CaB_2(SiO_4)_2$).*

Fleet and Muthupari [41] attribute the presence of a trigonal boron in minerals that should not contain trigonal boron (such as danburite) to potential damage caused by the experiment to the boron groups, which results in a minor conversion of tetrahedral boron to trigonal boron. This assignment was based on work by Kasrai *et al*. [40]. Šipr *et al*. [43] suggest that the reason why a peak appears at around 198 eV in minerals in which the boron is solely trigonal, may have something to do with effects brought on by the next nearest neighbouring atoms to the trigonal boron [43]. However, in most research, this peak is broadly ignored in the study of minerals like ludwigite [39-42]. All of this suggests that any use of these peaks to describe the boron chemistry should be aware of potential over and under estimations of $^{[3]}$B and $^{[4]}$B contributions.

5.3.2 B K-edge XANES on Glass

When used to study boron bearing glasses, boron K-edge XANES is typically analysed through peak fitting to provide quantitative analysis on the boron chemistry, particularly the coordination of the boron. Li *et al*. [45] used B K-edge XANES to describe the boron

chemistry in K_2O-SiO_4-B_2O_3-P_2O_5 glasses and compared to the results to electron energy-loss spectroscopy (EELS) and ^{11}B nuclear magnetic resonance (NMR) spectroscopy. The $^{[3]}B$ and $^{[4]}B$ was calculated by using area ratios of peak A and peak B and were in good agreement with the NMR and EELS data available on the same, or comparable glasses. The advantage B K-edge XANES had over EELS is that the destructive interactions between the beam and tetrahedral boron, is less pronounced in XANES than it is in EELS. The advantage over NMR is that it has a potential for quicker data acquisition as well as not been limited by the presence of paramagnetic species, such as iron [45].

Fleet and Muthupari [46] carried out a comprehensive study on alkali borosilicate glasses, in which peak fitting was used to describe the $^{[3]}B$ and $^{[4]}B$ abundances, and also the relative peak positions of the three peaks to describe how the different alkali moderators effect the short-range structure of the borosilicate. Handa, Ide, and co-workers [44,47] used B K-edge XANES (as well as several other edges) to describe barium borate and barium boroaluminate glasses. The boron K-edge was analysed to qualitatively describe trends in the $^{[3]}B$ and $^{[4]}B$ as a function of composition changes but opted against the quantitative analysis seen in Fleet and Muthupari [46] and Li *et al*. [45]. The peak fitting used by Fleet and Muthupari was used by Cochain *et al*. [48] to analyse the trigonal and tetrahedral boron abundances as a function of changing Fe_2O_3 within sodium borosilicate glasses [48]. This is the same way B K-edge XANES will be used in this research.

5.3.3 Elettra – BEAR

The specific beamline used to analyse the boron K-edge, was the BEAR (Bending Magnet for Emission, Absorption, and Reflectivity) beamline at the Elettra Synchrotron in Trieste, Italy. The BEAR beamline covers a low energy range of 2.7 – 1600 eV, with a spot size of 30 x 100 μm, and variety of diffraction grating monochromators available, depending on the desired energy range of interest [49]. While the BEAR beamline has not been noted for research done using B K-edge XANES (there is no mention of B XAS on the research tab of the BEAR beamline website [50]), it has the necessary capabilities of providing high flux of low-energy X-rays as other beam lines such as the Canadian Synchrotron Radiation Facility (CSRF) Grasshopper beamline at the University of Wisconsin-Maddison, which had an energy range of 20 – 1000 eV [51] and was successfully used to study glasses by Fleet & Muthupari [46] and Li *et al*. [39,45].

5.4 Results

5.4.1 Fe K-edge XANES

In order to process the results, all measured spectra must be calibrated for monochromator drift by using data of known mineral standards. As such, the standards must first be processed to determine the monochromator drift. In all cases for both samples and mineral standards, the pre-edge region was fitted with a cubic spline background that used the steep rising region of the primary edge beyond the pre-edge and the flat featureless region before the pre-edge peak as reference zones to apply the background fit

to.

5.4.1a Standards

The measured standards were normalised and corrected for self-absorption using the details highlighted in Chapter 3.5.2a. Each measured standard had the pre-edge feature (see Chapter 5.2 for more information) fitted with a set number of Gaussian peaks. The exact number of peaks was dependent on the mineral and was guided by Wilke *et al*. [11]. The peak fitting can be seen in **Figs 5.7 – 5.11.**

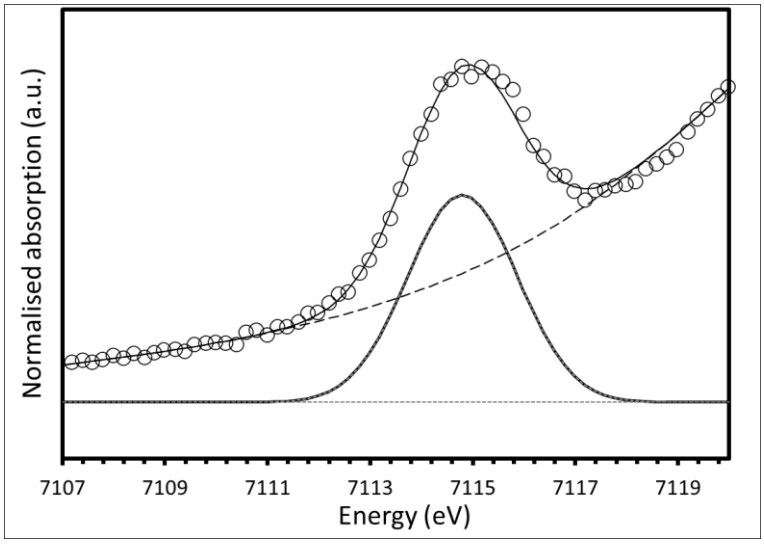

Figure 5.7: *The peak fitted pre-edge spectrum of Fe-berlinite ($FePO_4$) fitted with one Gaussian peak. The R^2 = 0.990366.*

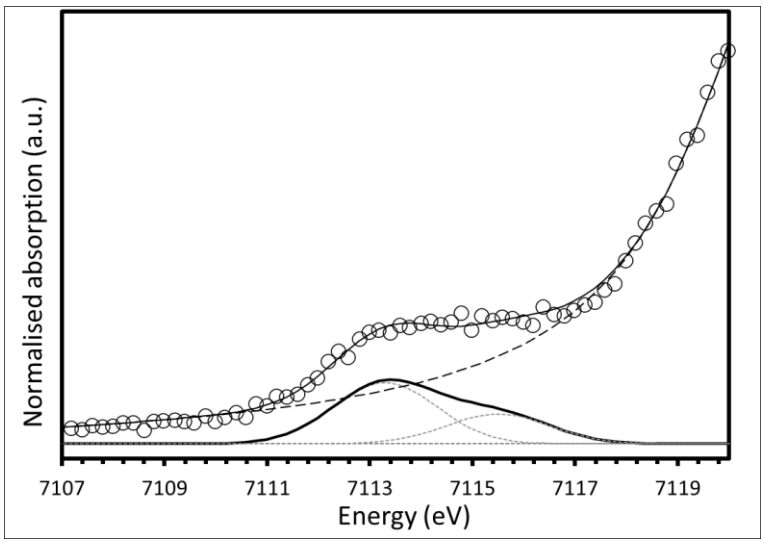

Figure 5.8: *The peak fitted pre-edge spectrum of grandidierite ($(Mg,Fe)Al_3BSiO_9$) fitted with two Gaussian peaks. The $R^2 = 0.998976$.*

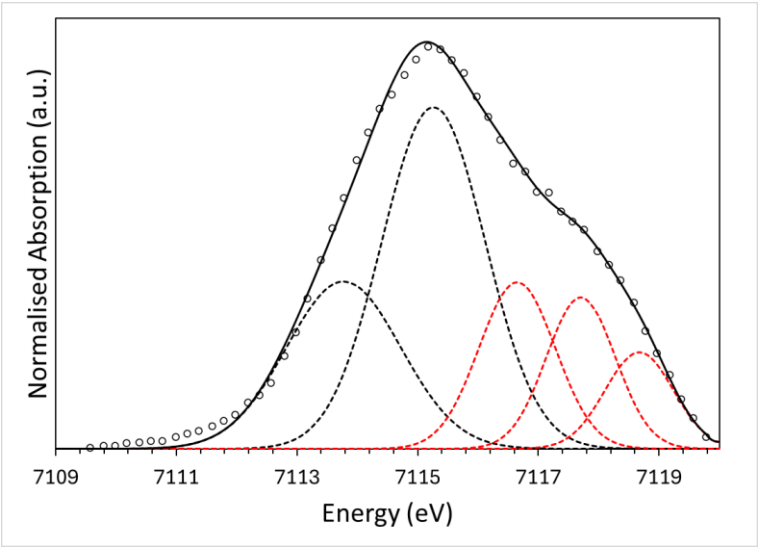

Figure 5.9: *The peak fitted pre-edge spectrum of hematite (α-Fe_2O_3). The $R^2 = 0.998106$. As per Wilke et al. [11], these two Gaussian peaks denoted by the black dash marks are the peaks that pertain to the relevant 1s – 3d/4p transitions. The higher energy Gaussian peaks denoted by the red dash marks are transitions related to clustering. These higher energy transitions were not used by Wilke et al. [11] to calculate the centroid position or intensity and have therefore been omitted in these fits.*

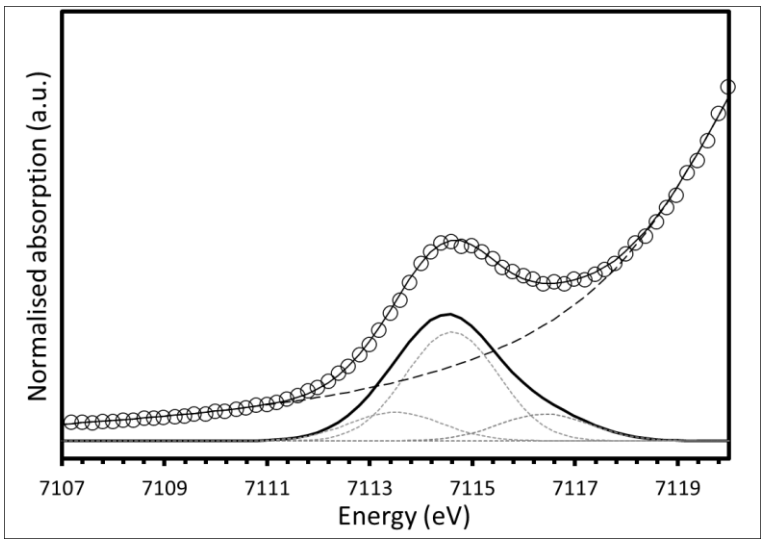

Figure 5.10: *The peak fitted pre-edge spectrum for magnetite (Fe_3O_4) fitted with three Gaussian peaks. The reduced $\chi^2 = 0.998315$.*

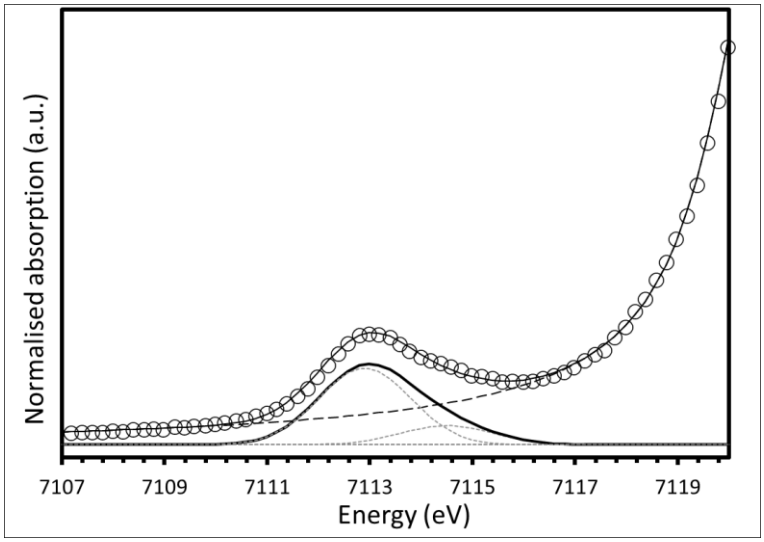

Figure 5.11: *The peak fitted pre-edge spectrum for staurolite ($(Fe,Mg)_2Al_9Si_4O_{23}(OH)$) fitted with two Gaussian peaks. The $R^2 = 0.998845$.*

The average centroid energy for each of the minerals was calculated and compared to the values published in Wilke *et al*. [11]. The difference in the centroid values was then used to calculate an average monochromator drift using equation 3.4 in chapter 3.5.2a.

This monochromator drift value was then used to correct all the spectra acquired in the respective beam line allocations.

5.4.1b SCFe Series

The stack plots for the fully processed and corrected SCFe series can been seen in **Figs 5.12** & **5.13**.

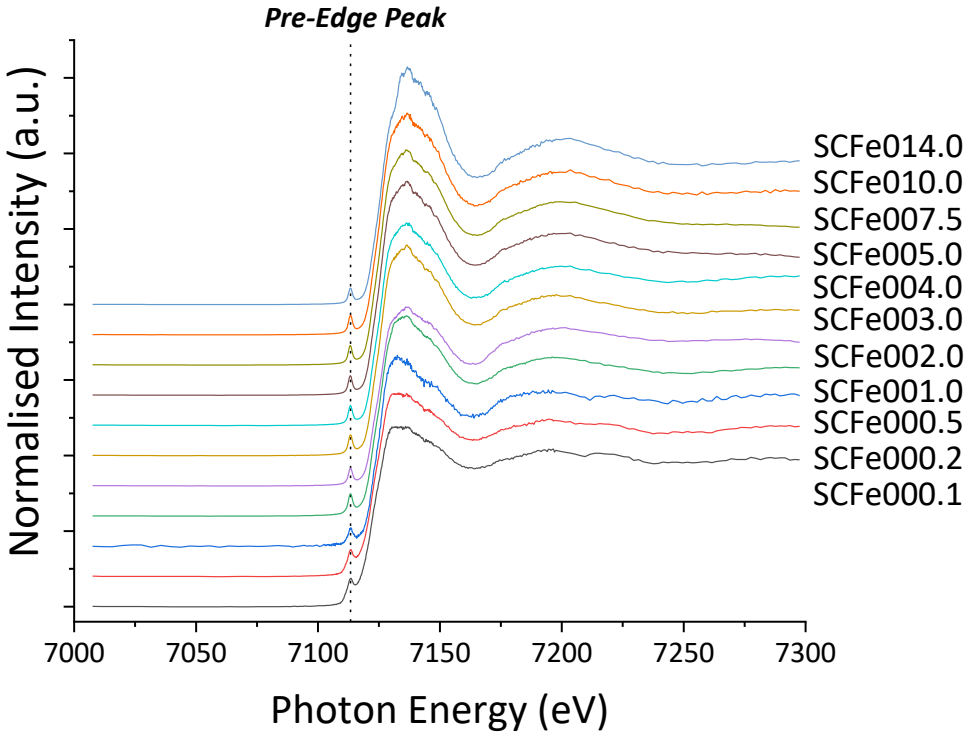

Figure 5.12: *The full-range Fe K-edge XANES stack plot for the SCFe sample series.*

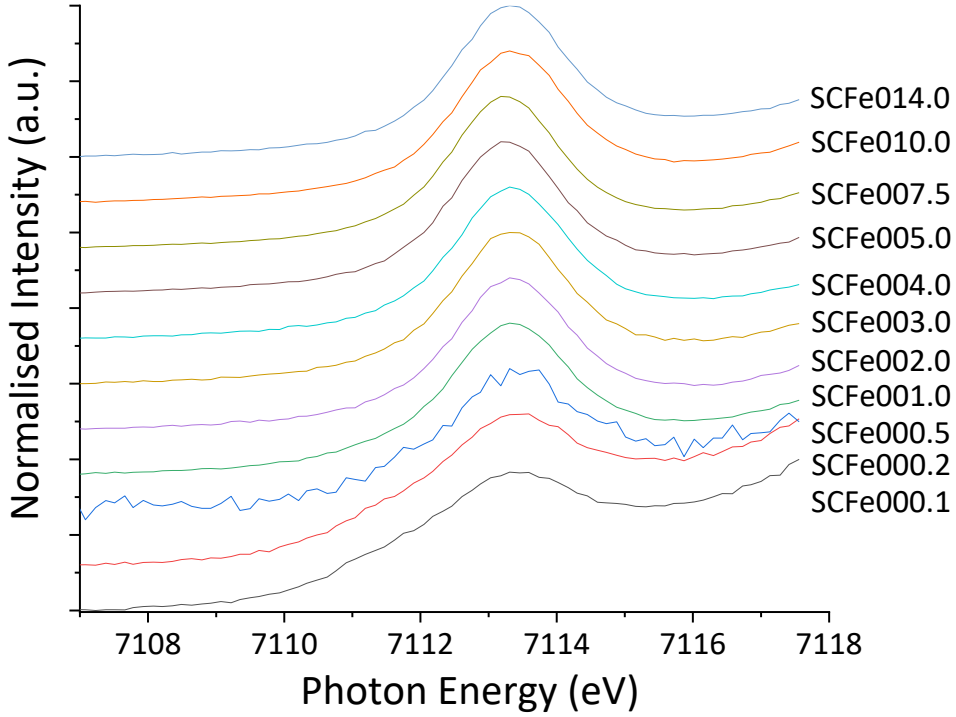

Figure 5.13: *The Fe K-edge XANES stack plot of the pre-edge peak for the SCFe sample series.*

The SCFe000.5 sample spectrum, despite numerous re-processing, is very noisy (this can be clearly seen in **Fig 5.13**). This made peak fitting very-difficult verging on impossible, and as such, this sample was not processed further in this research. The peak fitting of the

pre-edge peaks can be found in **Figs 5.14** – **5.23**. When fitting peaks to the pre-edge region of glass, multiple peaks are used. Wilke *et al*. [22] used two peaks to fit the pre-edge region of iron-silicate glasses, regardless as to whether the iron was predominantly ferrous or ferric. Quartieri *et al*. [17] used three peaks when fitting Roman glass. In both cases it was determined that lower energy peaks were attributable to ferrous iron and higher energy peaks were attributable to ferric iron. In the glasses studied in the current research, it was found to be necessary to fit 3 peaks to accurately describe the shape on the pre-edge feature, as the pre-edge peak resembled that of the glasses studied in Quartieri *et al*. [17].

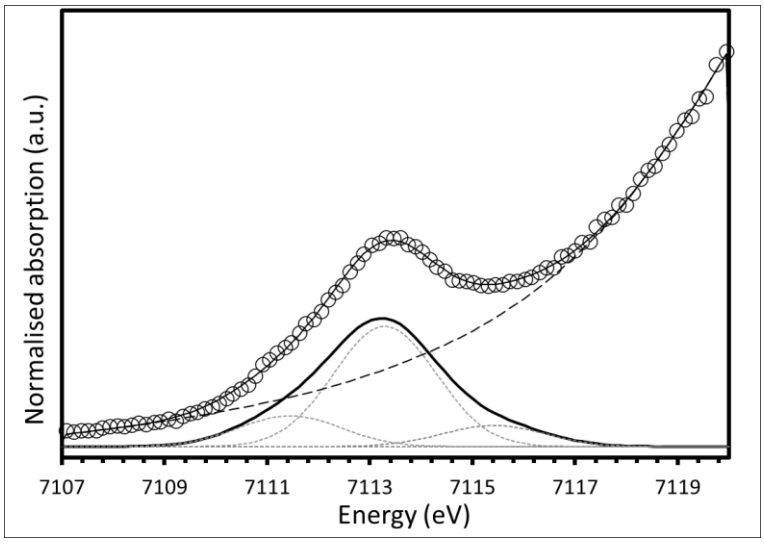

Figure 5.14: *The peak fitted pre-edge spectrum of the SCFe000.1 sample fitted with three Gaussian peaks. The* R^2 *= 0.997289.*

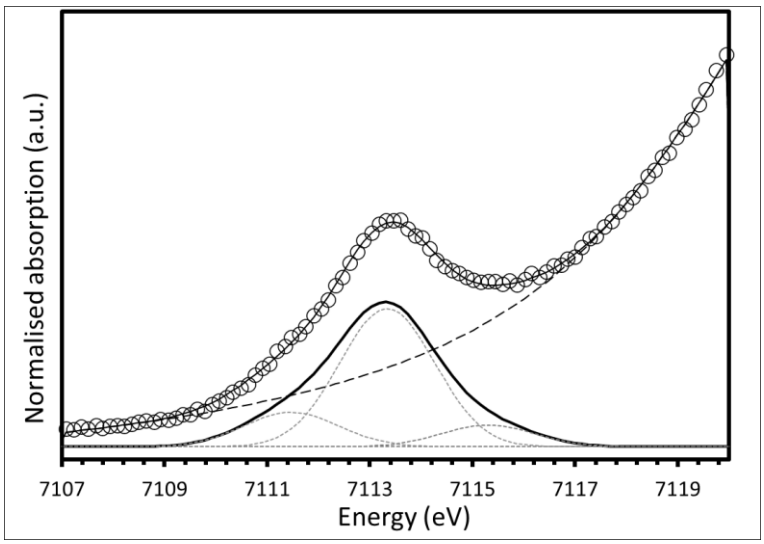

Figure 5.15: *The peak fitted pre-edge spectrum of the SCFe000.2 sample fitted with three Gaussian peaks. The R^2 = 0.998012.*

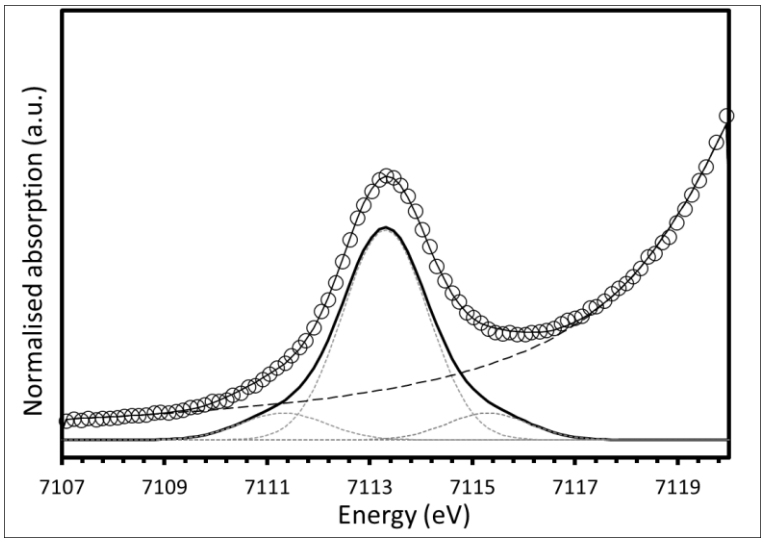

Figure 5.16: *The peak fitted pre-edge spectrum of the SCFe001.0 sample fitted with three Gaussian peaks. The R^2 = 0.998532.*

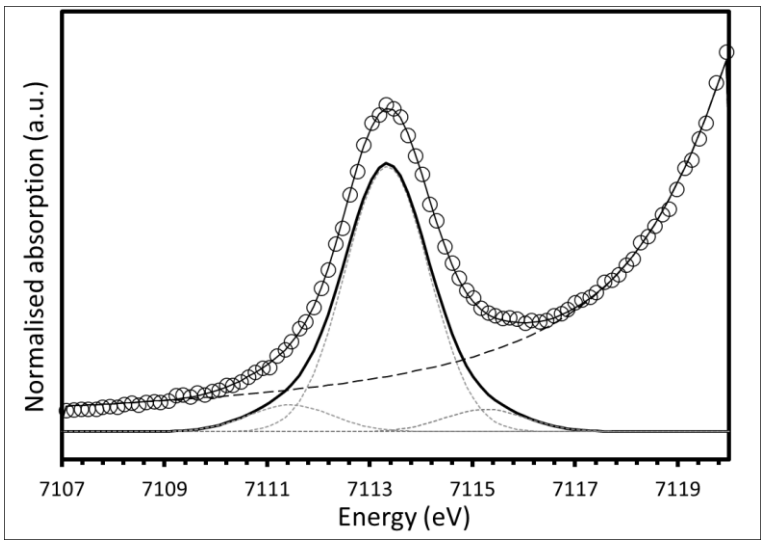

Figure 5.17: *The peak fitted pre-edge spectrum of the SCFe002.0 sample fitted with three Gaussian peaks. The R^2 = 0.998192.*

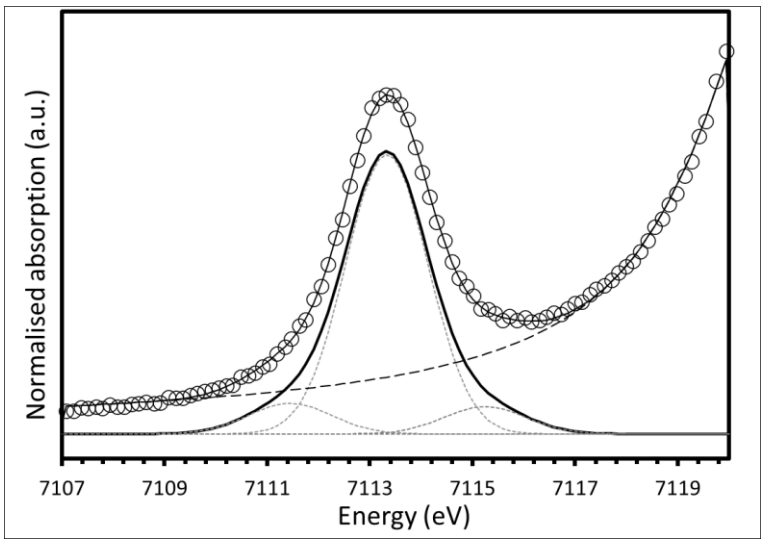

Figure 5.18: *The peak fitted pre-edge spectrum of the SCFe003.0 sample fitted with three Gaussian peaks. The* $R^2 = 0.997998$.

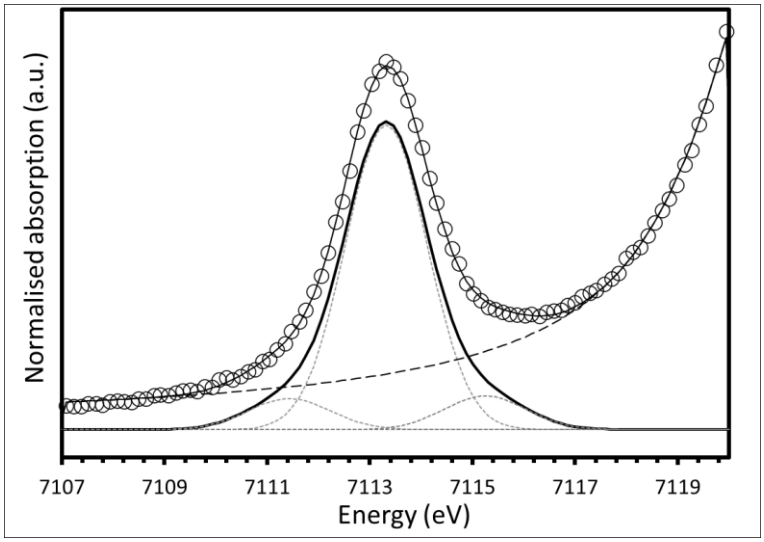

Figure 5.19: *The peak fitted pre-edge spectrum of the SCFe004.0 sample fitted with three Gaussian peaks. The* $R^2 = 0.998162$.

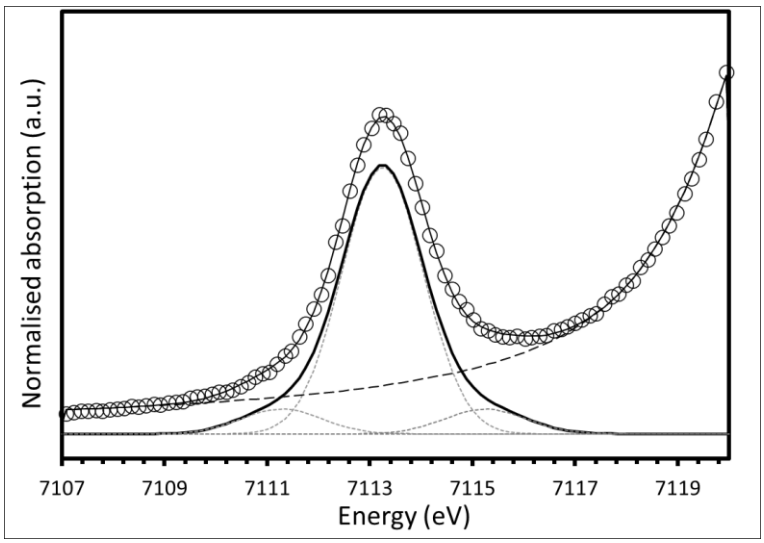

Figure 5.20: *The peak fitted pre-edge spectrum of the SCFe005.0 sample fitted with three Gaussian peaks. The* $R^2 = 0.99875$.

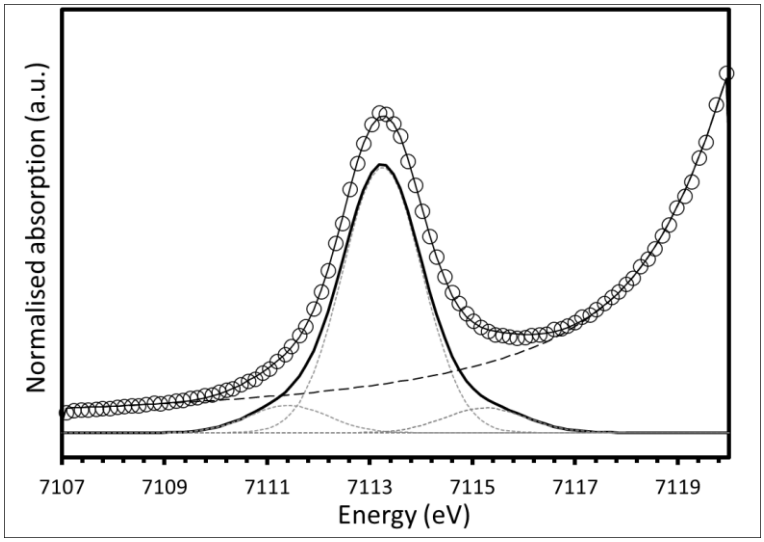

Figure 5.21: *The peak fitted pre-edge spectrum of the SCFe007.5 sample fitted with three Gaussian peaks. The* $R^2 = 0.99875$.

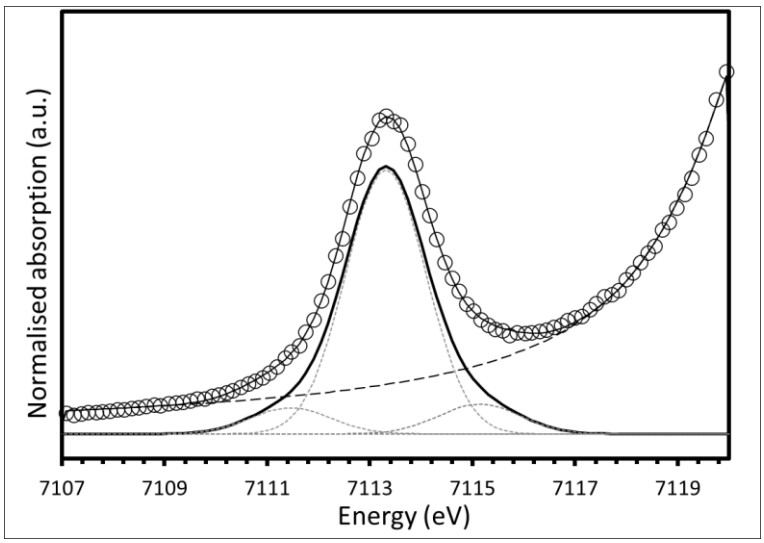

Figure 5.22: *The peak fitted pre-edge spectrum of the SCFe010.0 sample fitted with three Gaussian peaks. The* R^2 *= 0.998194.*

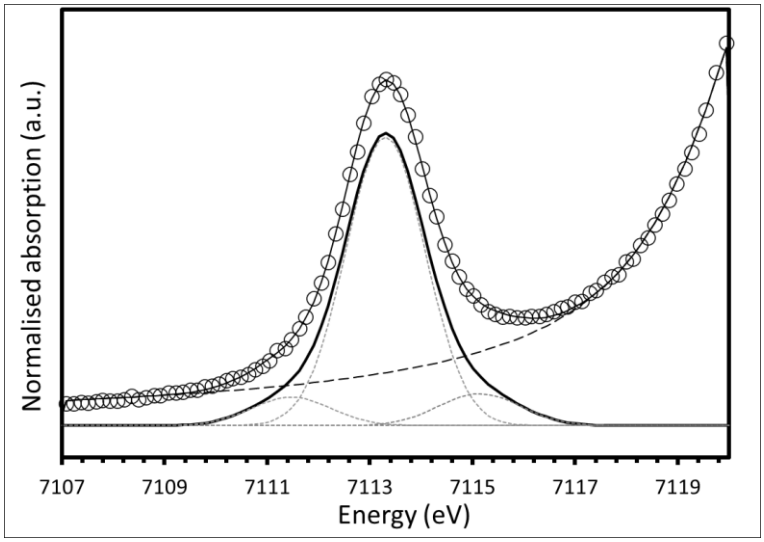

Figure 5.23: *The peak fitted pre-edge spectrum of the SCFe014.0 sample fitted with three Gaussian peaks. The* R^2 *= 0.808903.*

The calculated integrated intensity of the peaks and the average centroid energy for the peaks fitted on the pre-edge, are plotted in **Fig 5.49** & **5.50** in Chapter 5.5.1.

5.4.1c CCFe Series

The fully processed and corrected Fe K-edge XANES spectra for the CCFe sample series can seen in **Figs 5.24** & **5.25**.

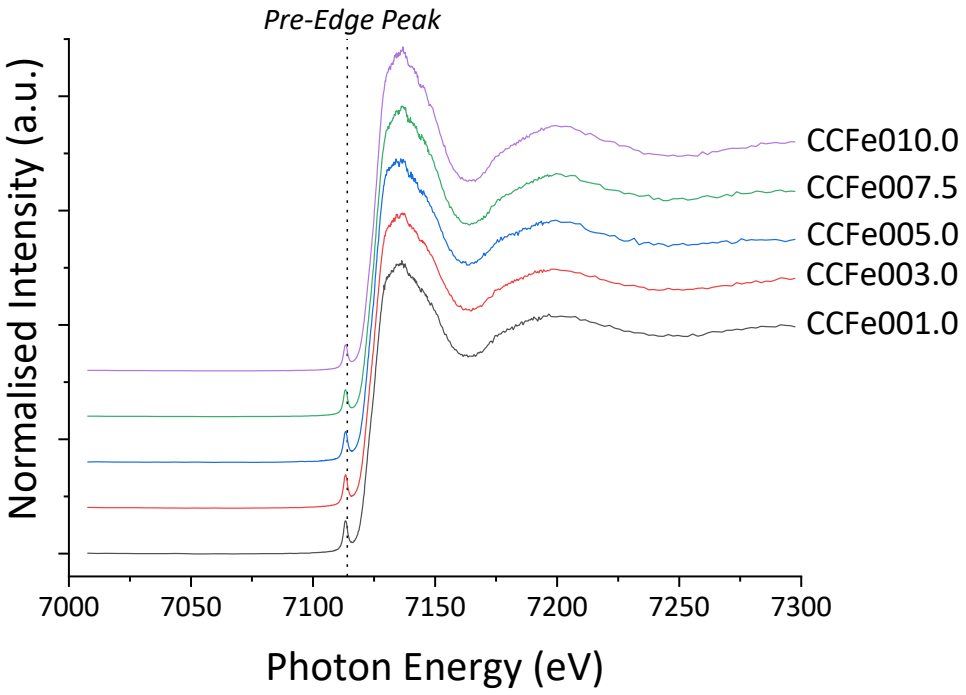

Figure 5.24: *The stack plot of the Fe K-edge XANES spectra for the CCFe sample series.*

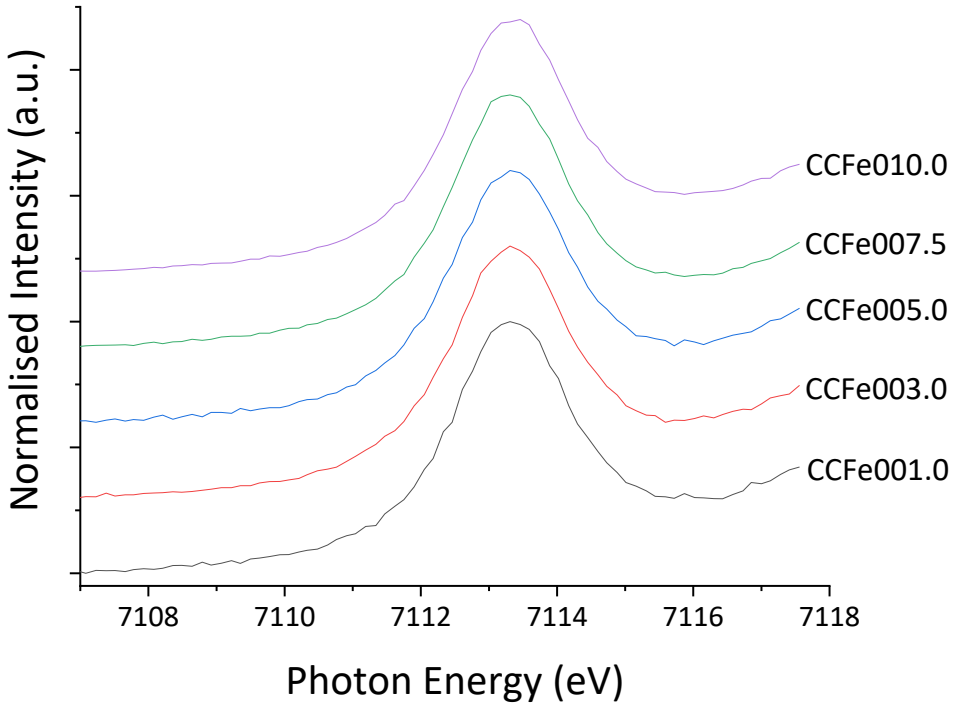

Figure 5.24: *The stack plot of the Fe K-edge XANES spectra of the pre-edge peak for the CCFe sample series.*

The peak fitting for CCFe sample series pre-edge peaks can be seen in **Figs 5.25** – **5.29**. Similar to the SCFe sample series, 3 peaks were used to fit the pre-edge region to

accurately fit the shape of the pre-edge region, similar to the work done by Quartieri *et al.* [17].

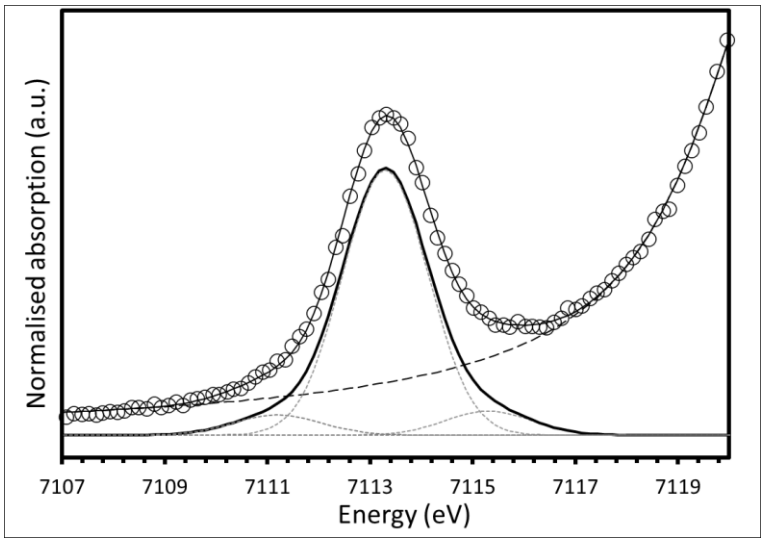

Figure 5.25: *The peak fitted pre-edge spectrum of the CCFe001.0 sample fitted with three Gaussian peaks. The* R^2 *= 0.997918.*

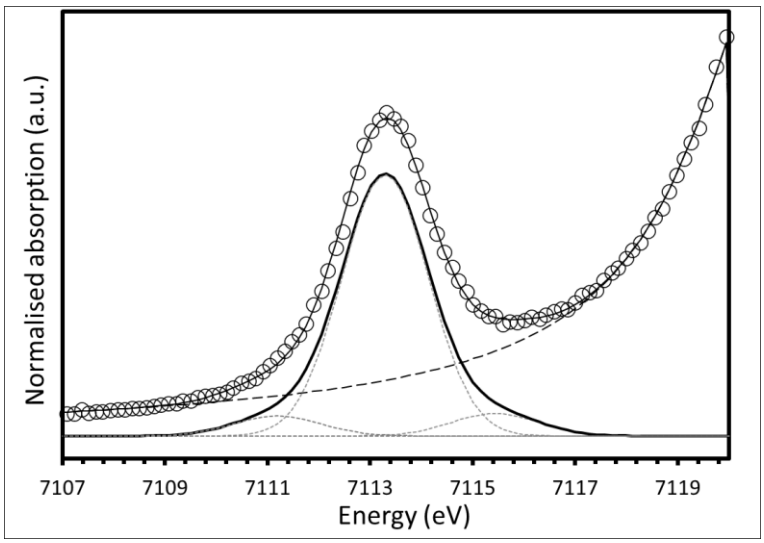

Figure 5.26: *The peak fitted pre-edge spectrum of the CCFe003.0 sample fitted with three Gaussian peaks. The* R^2 *= 0.998411.*

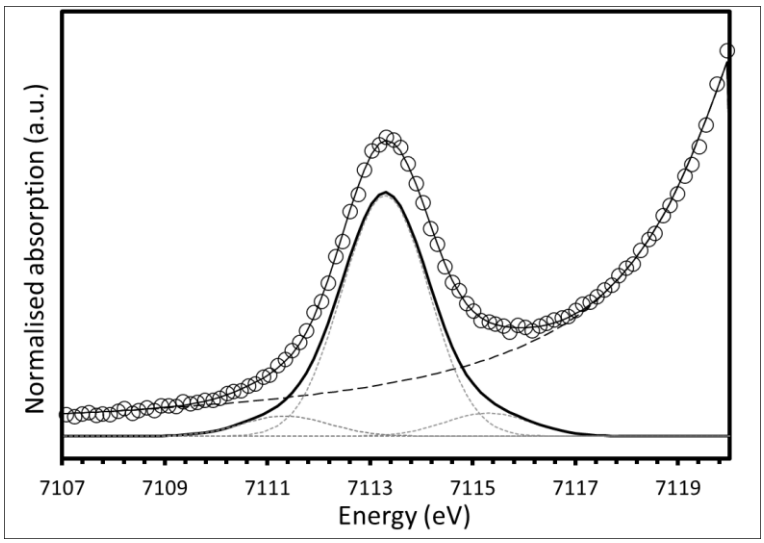

Figure 5.27: *The peak fitted pre-edge spectrum of the CCFe005.0 sample fitted with three Gaussian peaks. The* $R^2 = 0.997962$.

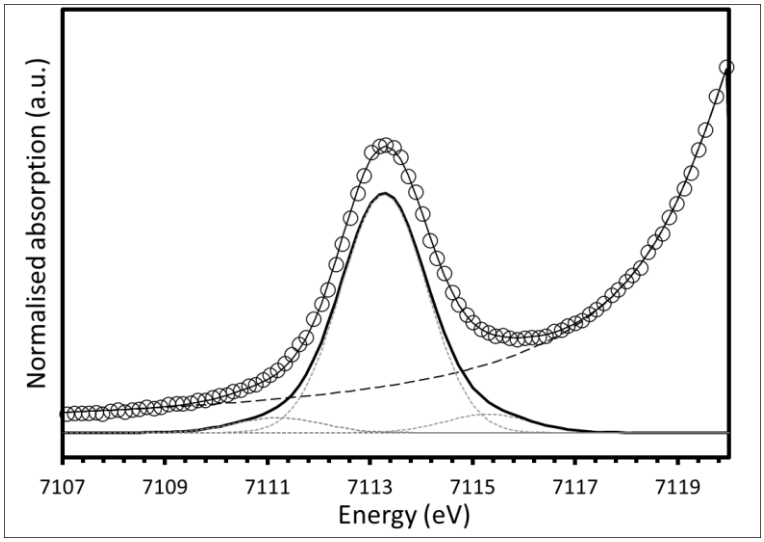

Figure 5.28: *The peak fitted pre-edge spectrum of the CCFe007.5 sample fitted with three Gaussian peaks. The* $R^2 = 0.997903$.

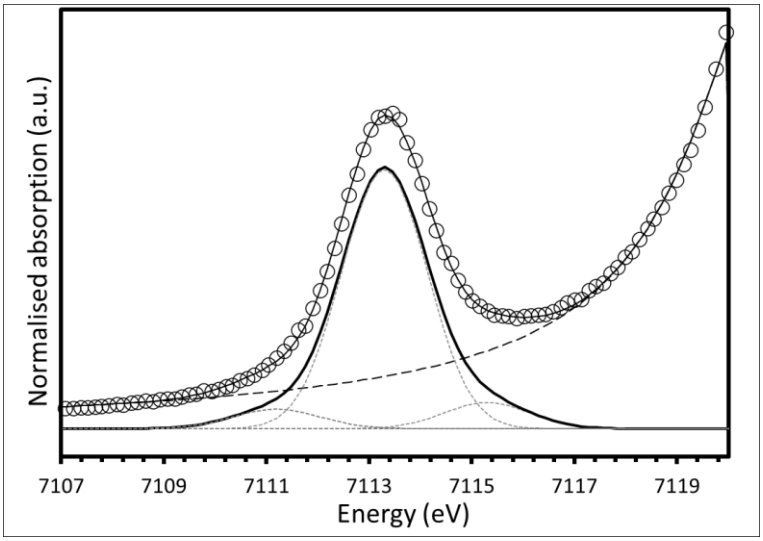

Figure 5.29: *The peak fitted pre-edge spectrum of the CCFe010.0 sample fitted with three Gaussian peaks. The* R^2 *= 0.998293.*

Similarly to the SCFe series, the average centroid energies and the integrated intensities are plotted in **Figures 5.49** & **5.51** to supplement the discussion in Chapter 5.5.1.

5.4.1d HAFe Series

The fully processed and corrected Fe K-edge XANES spectra for the CCFe sample series can be seen in **Figs 5.30** & **5.31**.

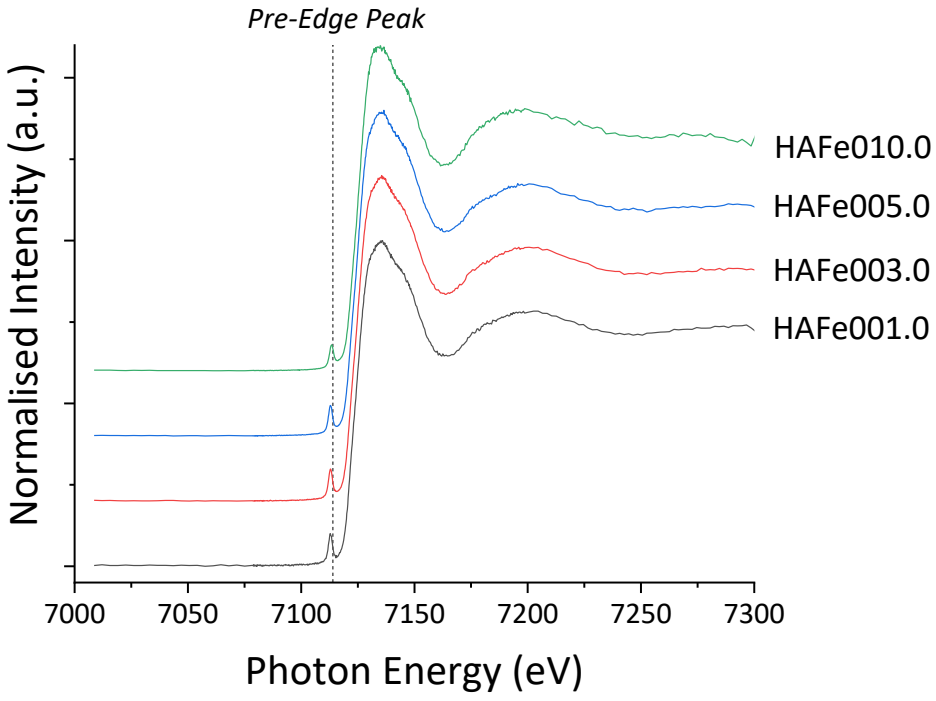

Figure 5.30: *The stack plot of the full range Fe K-edge XANES spectra for the HAFe sample series.*

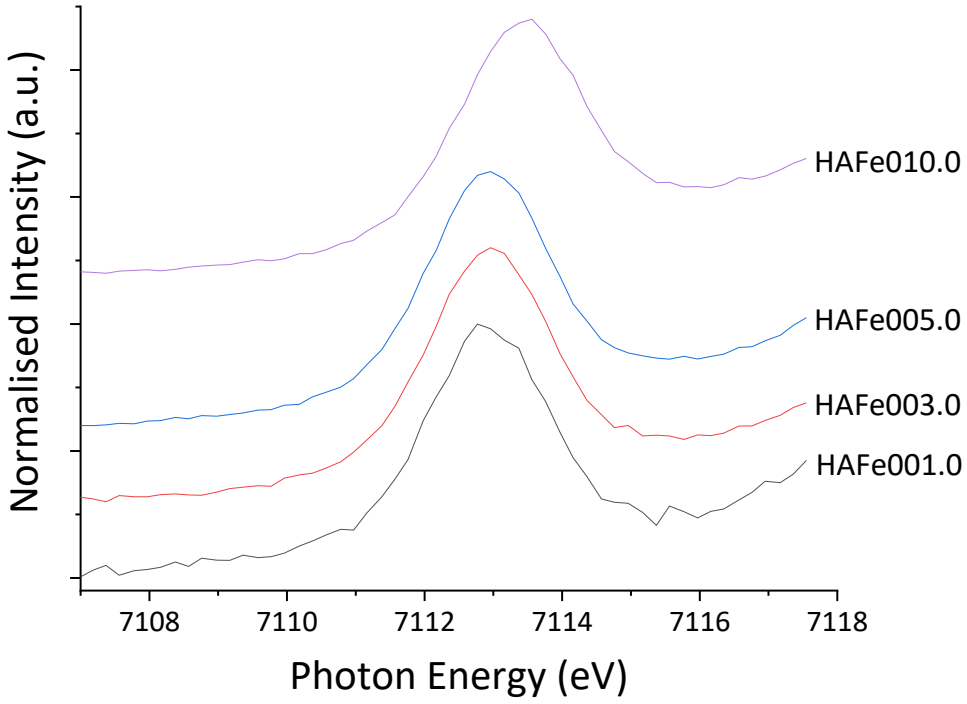

Figure 5.31: *The stack plot for the pre-edge peak spectra for the HAFe sample series.*

The peak fitting for the HAFe sample series can be seen in **Figs 5.32** – **5.35**. The HAFe sample series were also fitted with 3 peaks, in the same manner as the SCFe and CCFe sample series, as per the work by Quartieri *et al.* [17].

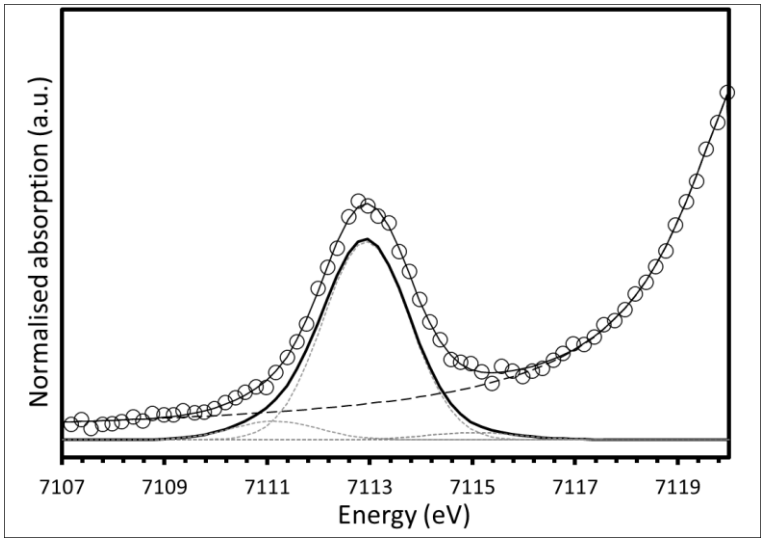

Figure 5.32: *The peak fitting pre-edge spectrum of the HAFe001.0 sample fitted with three Gaussian peaks. The* R^2 *= 0.995977.*

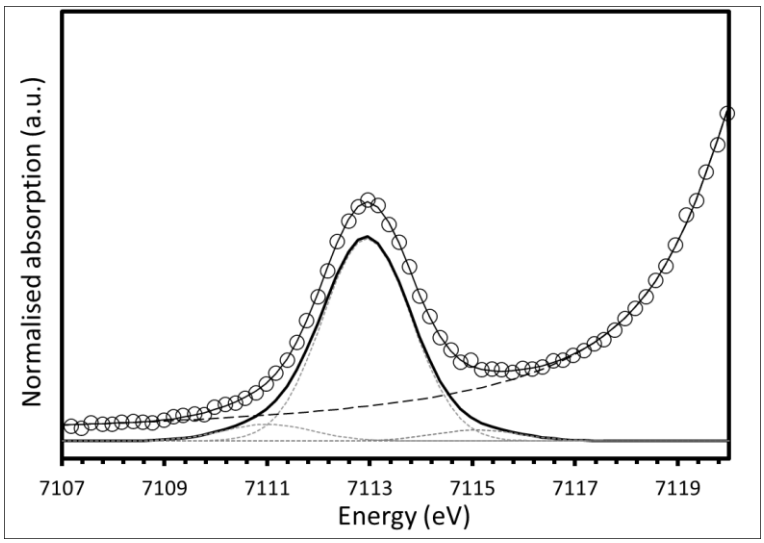

Figure 5.33: *The peak fitting pre-edge spectrum of the HAFe003.0 sample fitted with three Gaussian peaks. The* $R^2 = 0.998519$.

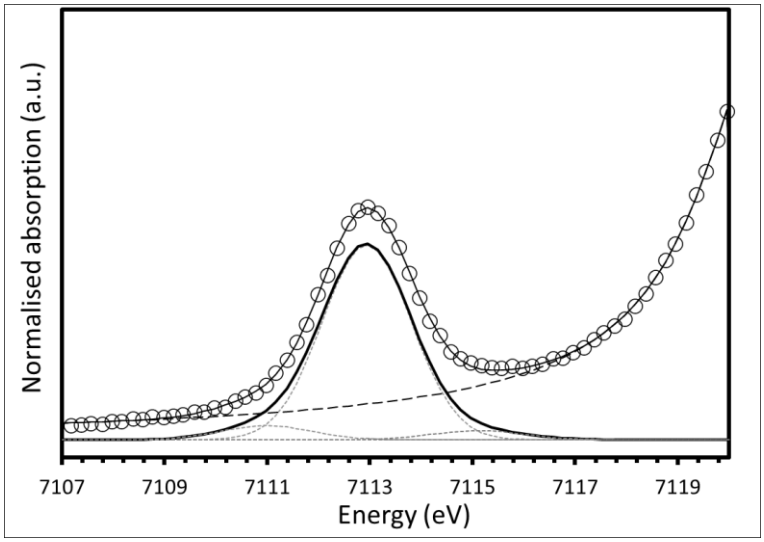

Figure 5.34: *The peak fitting pre-edge spectrum of the HAFe005.0 sample fitted with three Gaussian peaks. The* $R^2 = 0.998217$

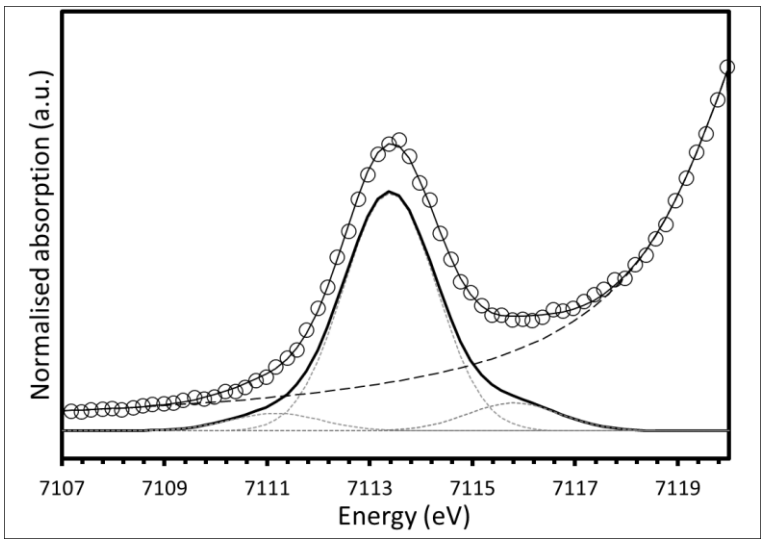

Figure 5.35: *The peak fitting pre-edge spectrum of the HAFe010.0 sample fitted with three Gaussian peaks. The* $R^2 = 0.995284$.

Similarly to the previous two sample series, the integrated intensities and centroid energies are plotted in **Fig 5.49** & **5.52** for discussion in Chapter 5.5.1.

5.4.2 B K-edge XANES

The boron K-edge XANES data were processed for the peak fitting process seen in literature [45,46,48]. This is to analyse the $^{[4]}$B abundance within the glass sample series. Each sample will be fitted with three peaks in the same way to the details outlined in Chapter 5.3. The HAFe series was not investigated using this technique due to the presence of competing L and M edges within the target energy range.

5.4.2a SCFe Series

The stack plots for the corrected SCFe spectra can been seen in **Fig 5.36**. The spectra are baseline corrected and then peak fitted with three Gaussian peaks, that correspond to the three peaks (Peak A, Peak B, & Peak C mentioned in Chapter 5.3).

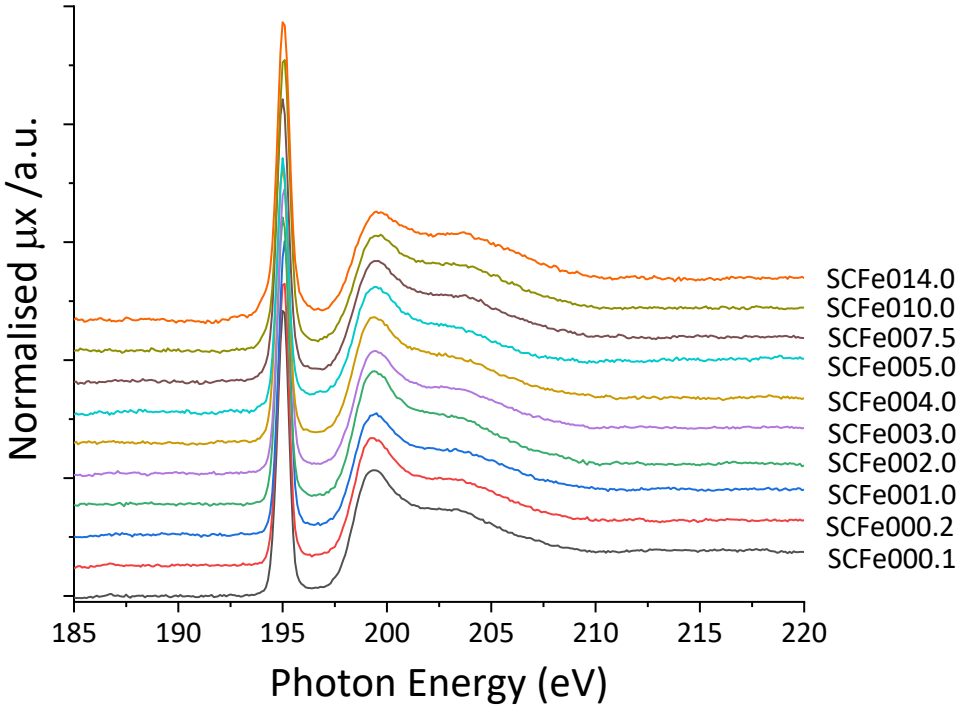

Figure 5.36: *The stack plot of the B K-edge XANES for the SCFe sample series.*

The spectral peak fitting of the baseline corrected SCFe spectra can be seen in **Figs 5.37 – 5.46**.

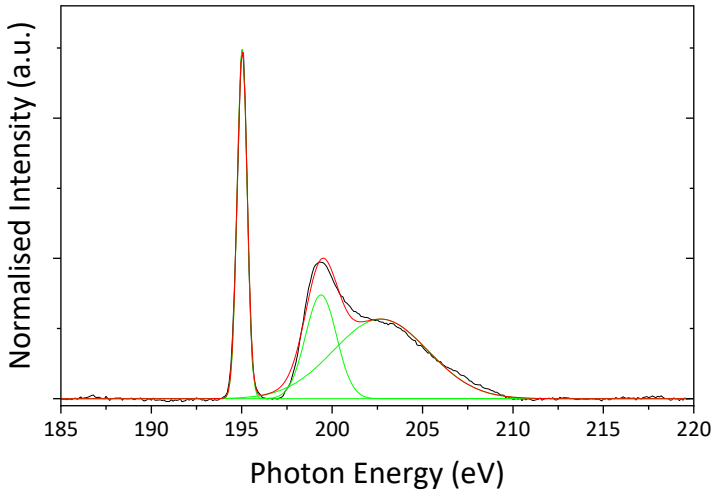

Figure 5.37: *The peak fitted spectrum for SCFe000.1 sample fitted with three Gaussian peaks.*

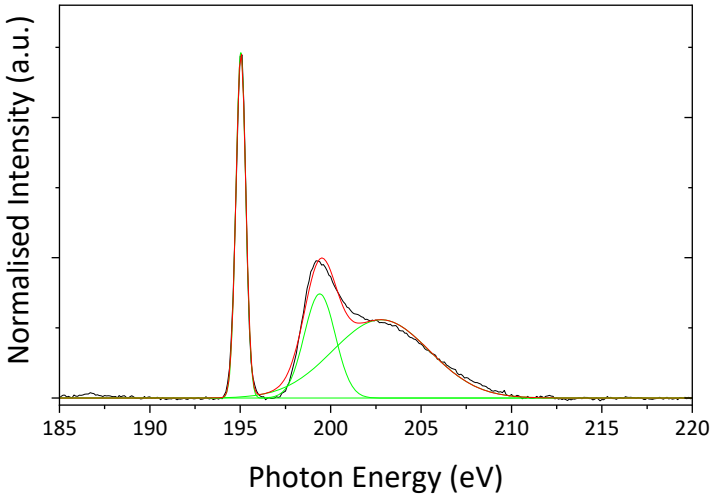

Figure 5.38: *The peak fitted spectrum for SCFe000.2 sample fitted with three Gaussian peaks.*

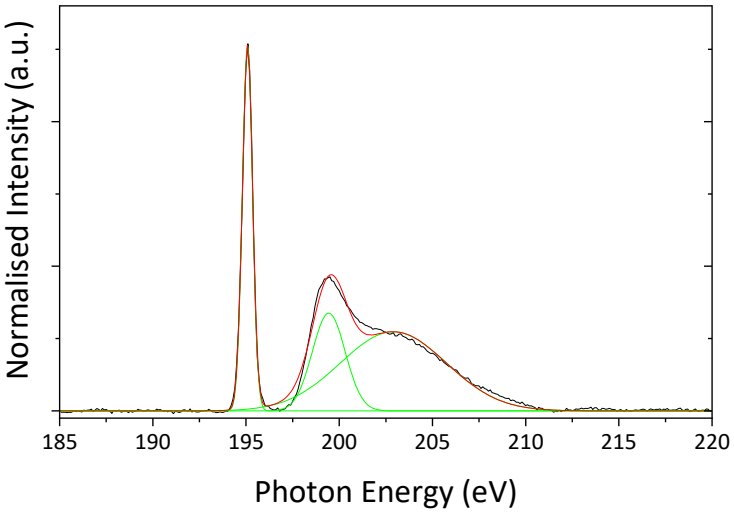

Figure 5.39: *The peak fitted spectrum for SCFe001.0 sample fitted with three Gaussian peaks.*

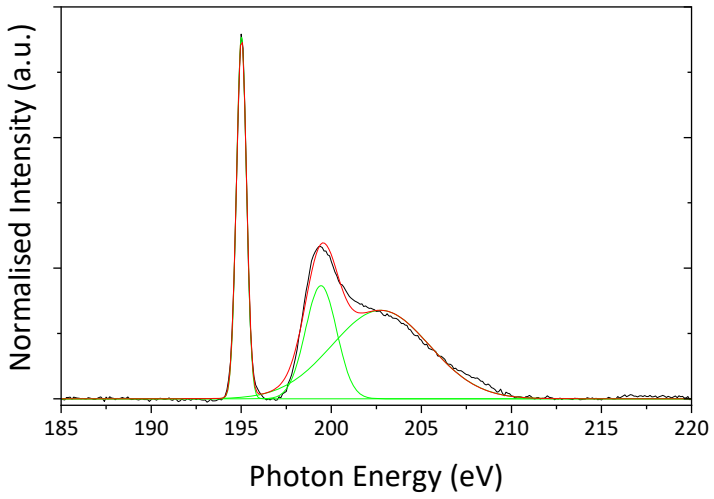

Figure 5.40: *The peak fitted spectrum for SCFe002.0 sample fitted with three Gaussian peaks.*

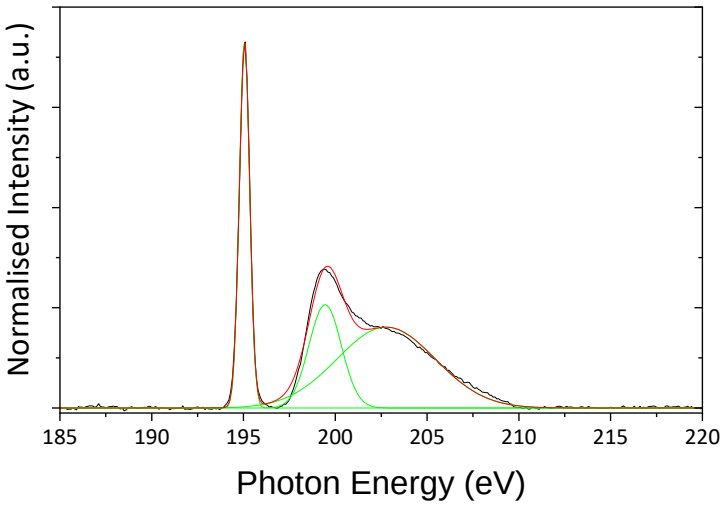

Figure 5.41: *The peak fitted spectrum for SCFe003.0 sample fitted with three Gaussian peaks.*

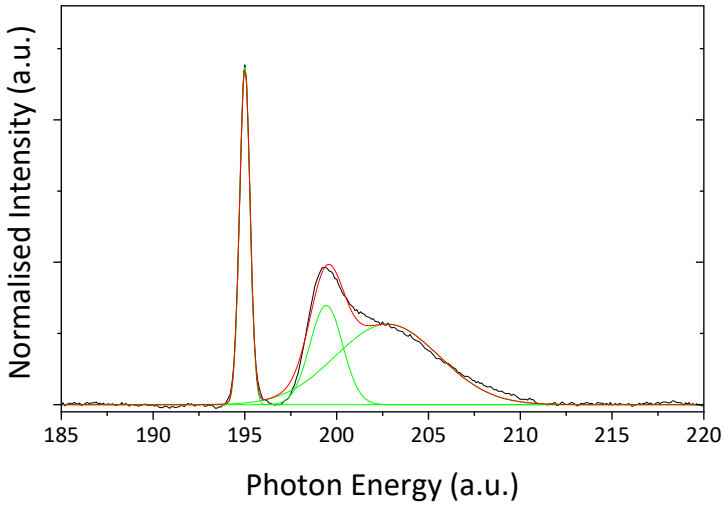

Figure 5.42: *The peak fitted spectrum for SCFe004.0 sample fitted with three Gaussian peaks.*

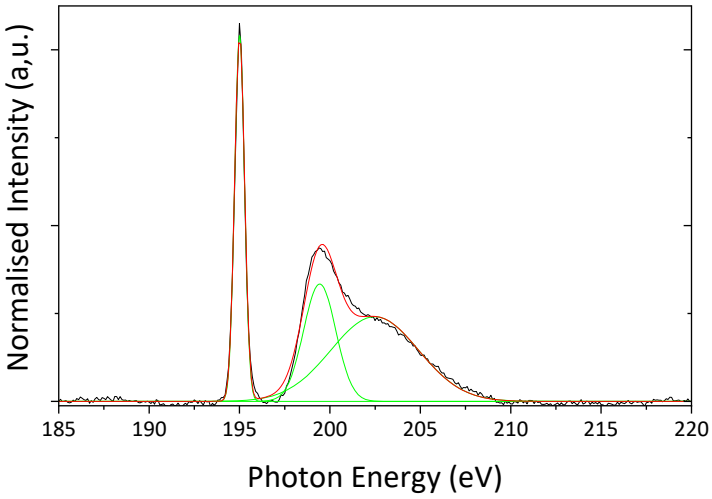

Figure 5.43: *The peak fitted spectrum for SCFe005.0 sample fitted with three Gaussian peaks.*

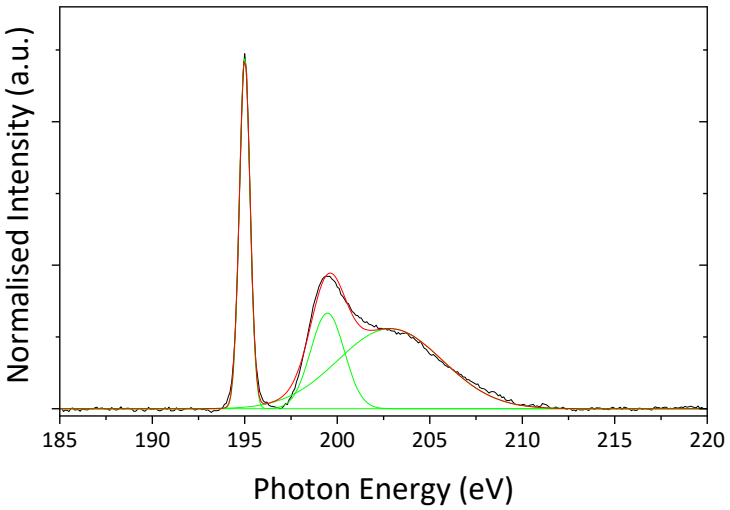

Figure 5.44: *The peak fitted spectrum for SCFe007.5 sample fitted with three Gaussian peaks.*

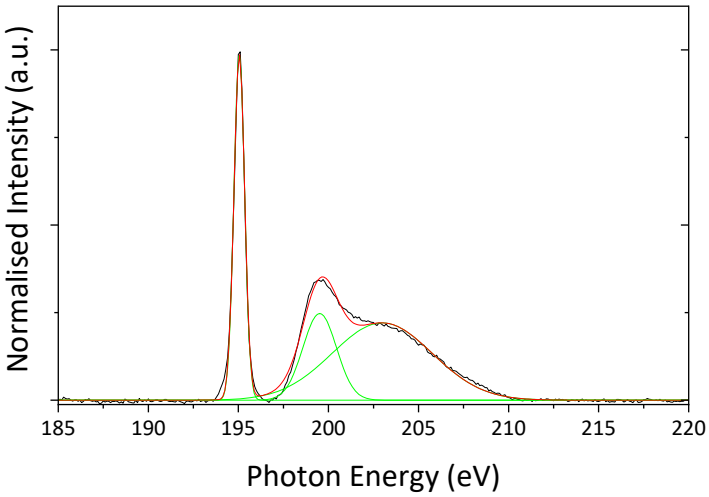

Figure 5.45: *The peak fitted spectrum for SCFe010.0 sample fitted with three Gaussian peaks.*

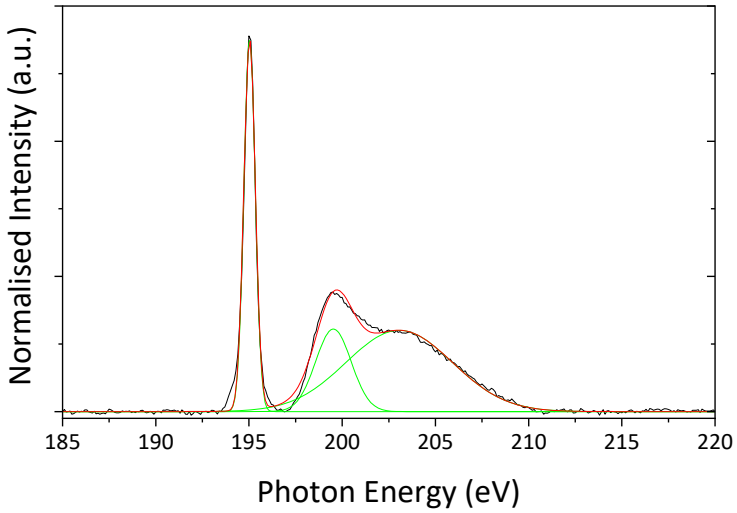

Figure 5.46: *The peak fitted spectrum for SCFe014.0 sample fitted with three Gaussian peaks.*

The $^{[4]}$B abundances are calculated in Chapter 5.5.2 and plotted in **Fig 5.53** for discussion.

5.4.2b CCFe Series

The CCFe sample spectra are processed in the same manner as the SCFe series. The stack plot for the CCFe series can be seen in **Fig 5.47**.

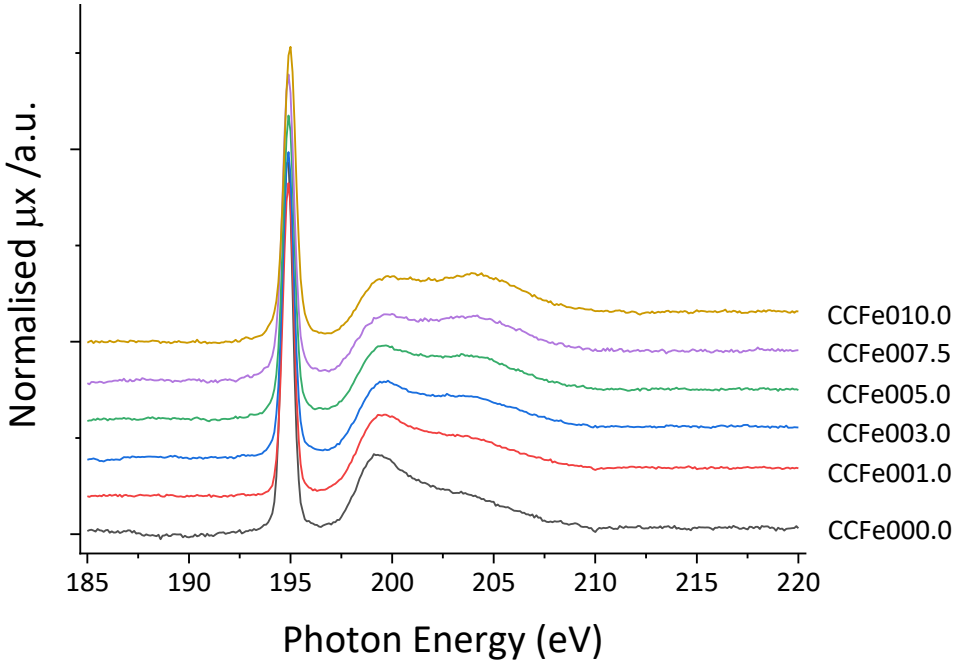

Figure 5.47: *The stack plot for the B K-edge XANES spectra for the CCFe sample series.*

The baseline corrected spectra are peak fitted for the CCFe sample series. They can be seen in **Figs 5.48** – **5.53**.

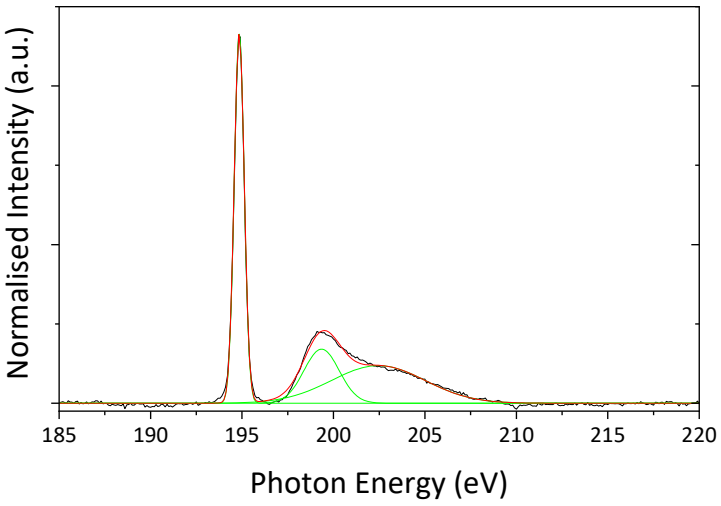

Figure 5.48: *The peak fitted spectrum for the CCFe000.0 spectrum fitted with three Gaussian peaks.*

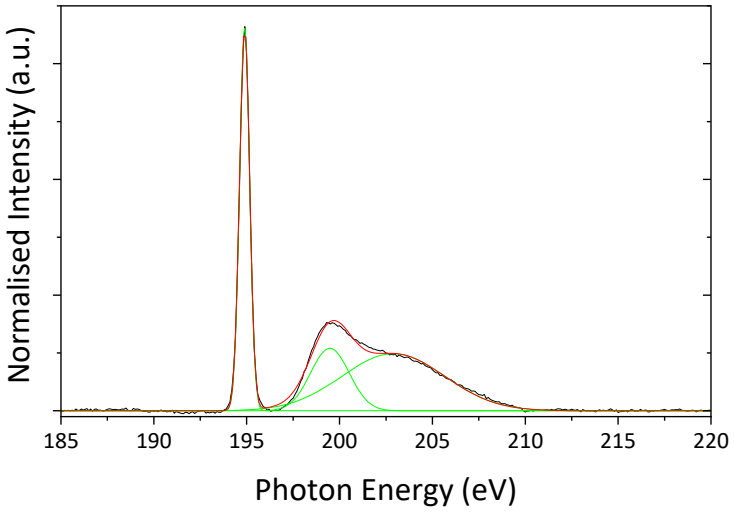

Figure 5.48: *The peak fitted spectrum for the CCFe001.0 spectrum fitted with three Gaussian peaks.*

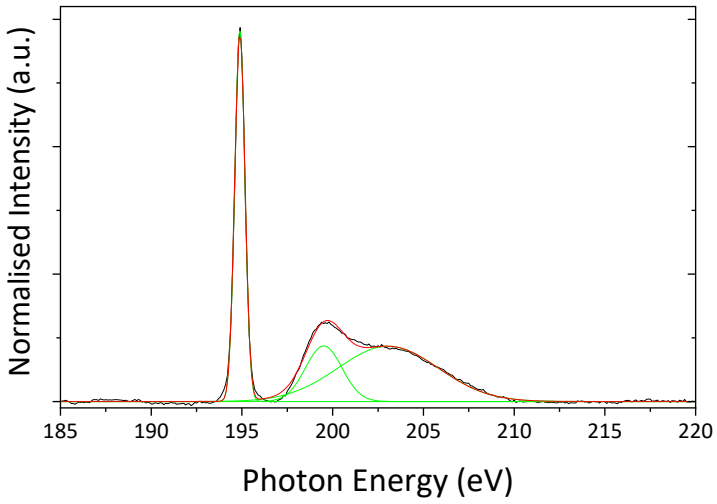

Figure 5.48: *The peak fitted spectrum for the CCFe003.0 spectrum fitted with three Gaussian peaks.*

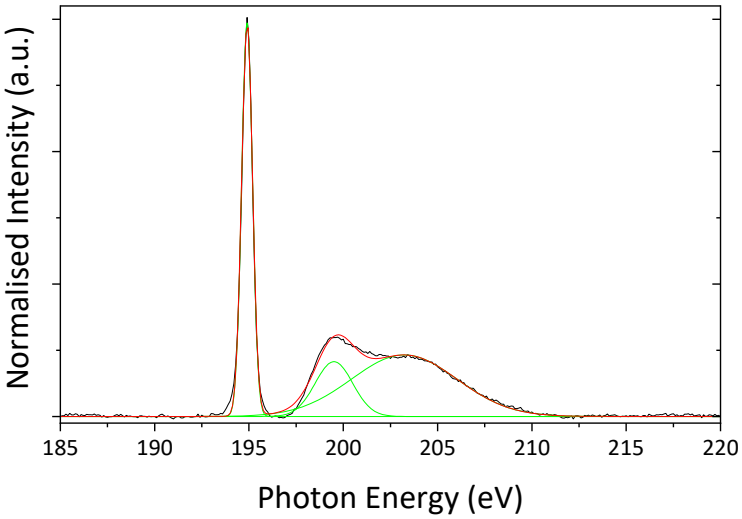

Figure 5.48: *The peak fitted spectrum for the CCFe005.0 spectrum fitted with three Gaussian peaks.*

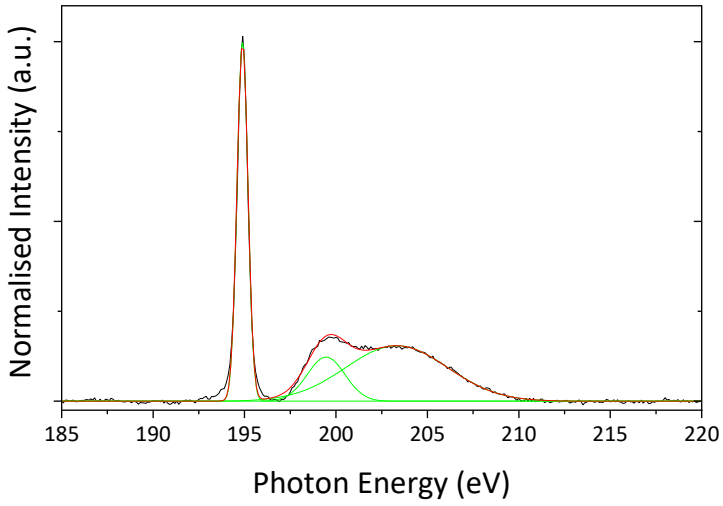

Figure 5.48: *The peak fitted spectrum for the CCFe007.5 spectrum fitted with three Gaussian peaks.*

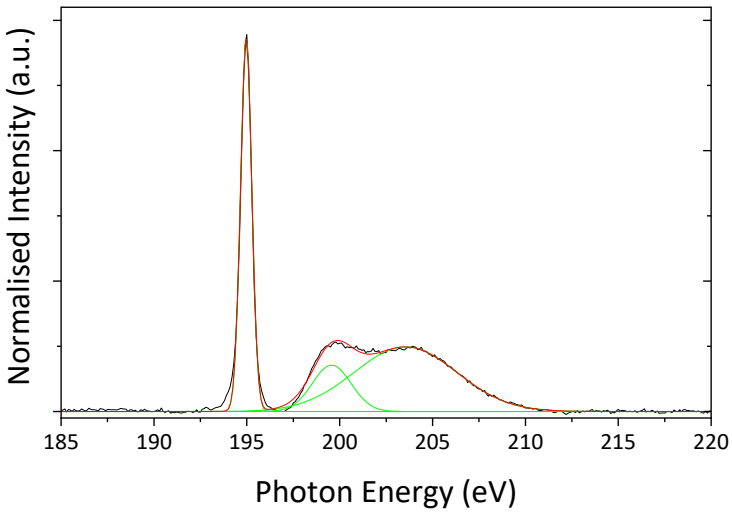

Figure 5.48: *The peak fitted spectrum for the CCFe010.0 spectrum fitted with three Gaussian peaks.*

The $^{[4]}$B abundances are calculated in Chapter 5.5.2 and plotted in **Fig 5.53** for discussion alongside the data from the SCFe sample series.

5.5 Discussion

5.5.1 Fe K-edge XANES

For all sample series, 3 peaks were to the pre-edge region in a similar manner to the methods employed by Quartieri *et al.* [17]. Judging by the relative positions and intensity of the peaks, it can be seen that the iron will be predominantly ferric in the SCFe and CCFe sample series, owing to the position of the peak of the highest intensity in these spectra. These peak positions and relative intensities are similar to “Glass B” published

by Quartieri *et al*. [17], which offered the same conclusion. For the HAFe series however, the samples with the lowest Fe_2O_3 contents, appear have the dominant pre-edge peaks at lower energies, which would suggest the presence of ferrous iron [17,22]. Interestingly, in all three sample series, the pre-edge feature resembles that of magnetite and Fe-berlinite (see **Figs 5.7** & **5.10**), which was also noted by Quartieri *et al*. [17]. This also supports the assessment that the iron is predominantly ferric, while also suggesting the presence of ferrous iron. To illustrate this in a clearer manner, the pre-edge intensities for all measured samples and mineral standards were plotted as a function of average centroid energy on **Figure 5.49**. Included in this plot, are several mineral standards not measured, but included to highlight the positions of different Fe oxidation states and coordination numbers (see **Table 5.2**) for more information.

Table 5.2: The mineral standards plotted in **Figs 5.49** – **5.52**, including the name, composition, Fe valency, Fe coordination, and reference where applicable.

Mineral	**Composition**	**Valency**	**Coordination**	**Reference**
Fe-Berlinite	$FePO_4$	3+	4	*Measured*
Ferriorthoclase	$Fe:KAlSi_3O_8$	3+	4	[7,11]
Yoderite	$(Mg,Fe,Al)_8Si_4(O,OH)_{20}$	3+	5	[4,11]
Hematite	α-Fe_2O_3	3+	6	*Measured*
Aegirine	$NaFeSi_2O_6$	3+	6	[11]
Magnetite	Fe_3O_4	3+ & 2+	-	*Measured*
Franklinite	$(Zn,Mn^{2+},Fe^{2+})(Fe^{3+},Mn^{3+})_2O_4$	3+ & 2+	-	[11]
Staurolite	$(Fe,Mg)_2Al_9Si_4O_{23}(OH)$	2+	4	*Measured*
Grandidierite	$(Mg,Fe)Al_3(BO_3)(SiO_4)O_2$	2+	5	*Measured*
Wüstite	FeO	2+	6	[5,11]

These references will serve as a visual guide on **Figs 5.49** – **5.52** when describing the coordination and valency of the iron oxide within the glass samples.

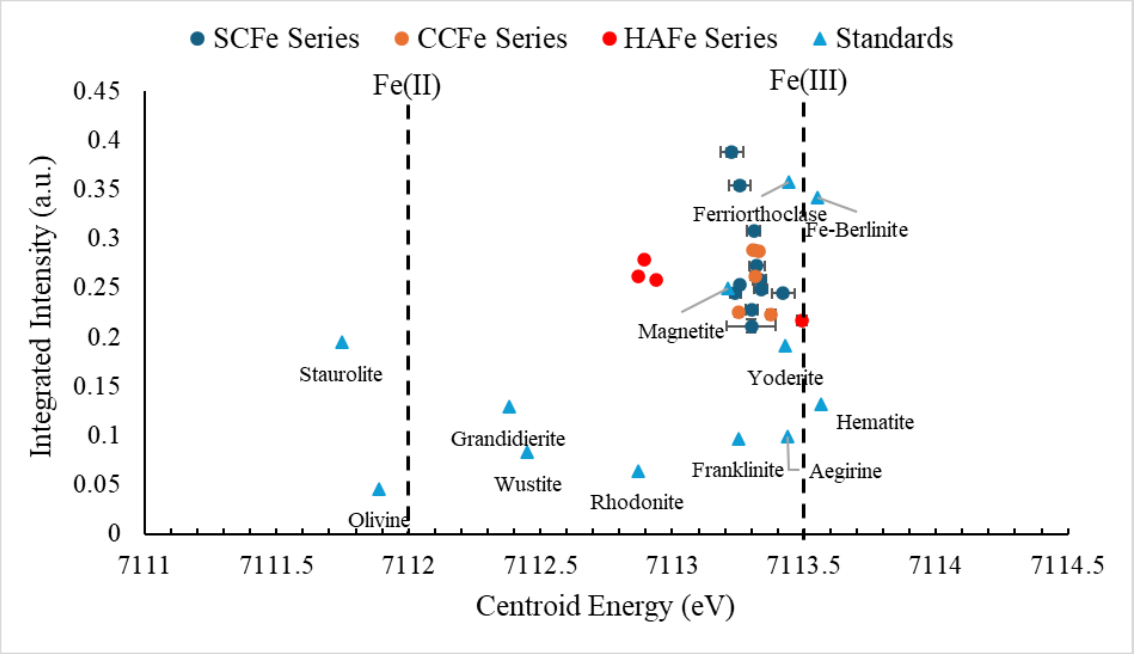

Figure 5.49: *Average Fe K-edge XANES pre-edge centroid energy positions for all samples and standards.*

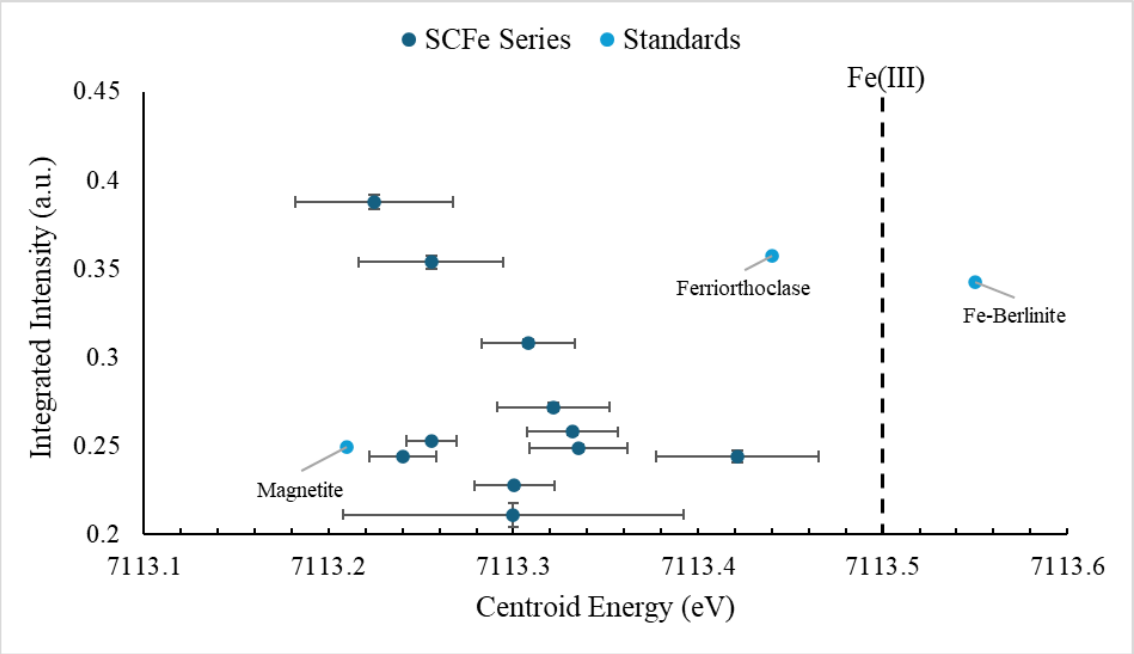

Figure 5.50: *The average centroid energies and integrated intensities of the SCFe sample series.*

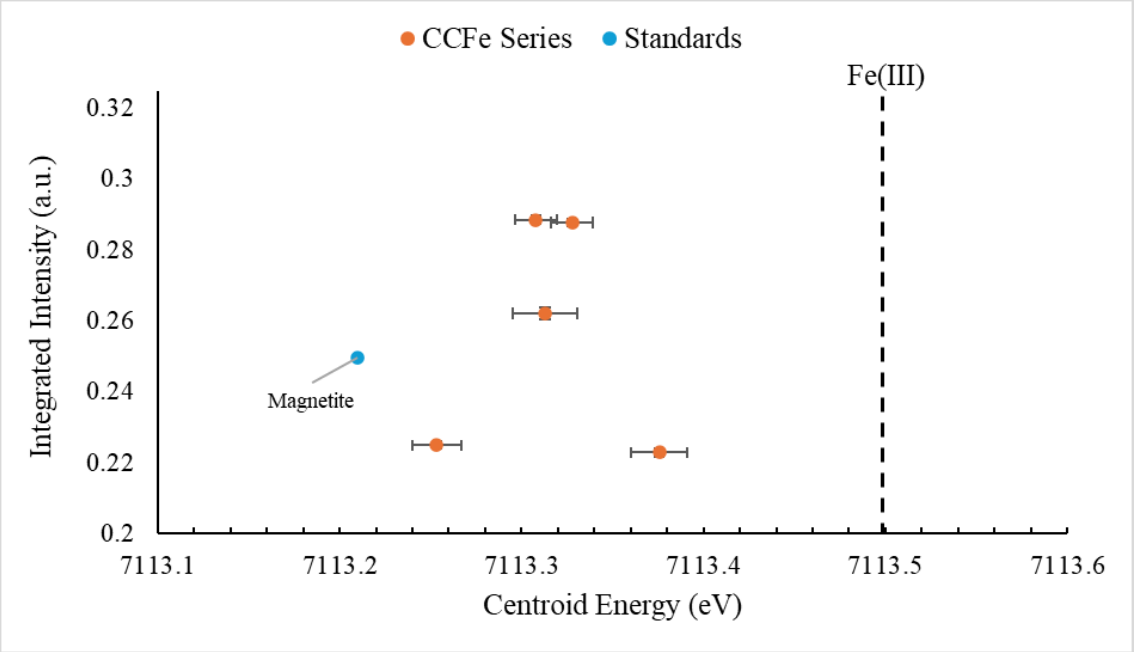

Figure 5.51: *The average centroid energies and integrated intensities of the CCFe sample series.*

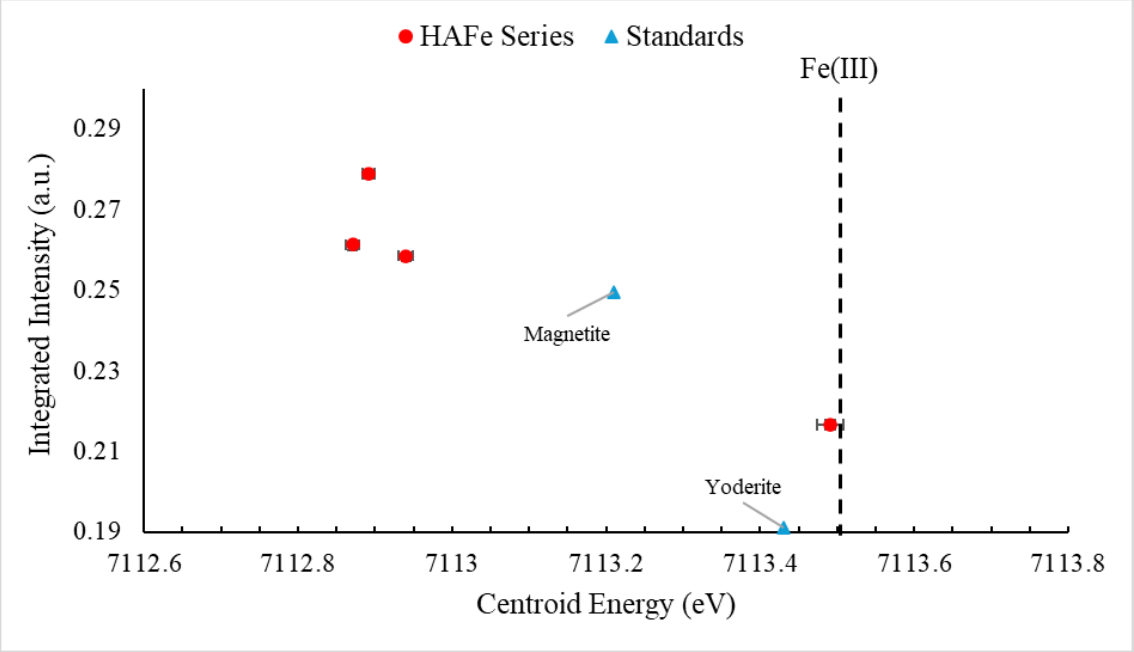

Figure 5.52: *The average centroid energies and integrated intensities of the SCFe sample series.*

The Fe K-edge XANES data shows that the iron within the samples exists predominantly as Fe^{3+} evidenced by the centroid energies of the samples being in close proximity of the Fe^{3+} region of the graphs. However, most samples are in close proximity to magnetite in terms of energy and integrated intensity, which would suggest some presence of Fe^{2+}.

However, the Mössbauer spectra from Chapter 4, do not show any presence of Fe^{2+} within any of the sample therefore it is likely to suggest that the iron is all Fe^{3+} for all of the samples, as the analysis on the oxidation state of iron is considered to be absolute with Mössbauer spectroscopy when compared to Fe K-edge XANES analysis [52]. The obvious outliers to this assumption are the low-Fe HAFe samples (see **Figs 5.49** & **5.52**). These samples have significantly lower centroid energies that majority of the samples measured. The reduced centroid energy is not consistent within the series, with HAFe007.1 and HAFe010.0 showing comparable centroid energies to those seen in the SCFe and CCFe sample series. The source of this discrepancy is unclear. The sample glass batch that produced the samples measured using Mössbauer spectroscopy, produced the samples measured using Fe K-edge XANES, therefore it is unlikely a case of different melt-redox interactions. The same sample preparation methods were used for all sample series and measured standards, so it is unlikely to be as a result of interactions during this process as the same discrepancy would be present in the sample spectra in the other two series. Due to the lack of an obvious source of the discrepancy, the authors will again defer to the Mössbauer spectra for the room temperature HAFe005.0 sample (see **Fig 4.16** and **Table 4.5** for spectrum and fit parameters) and the low temperature HAFe001.0 sample (see **Fig 4.19** and **Table 4.6**), both of which are outliers in **Figs 5.49** & **5.52**, as justification for assigning all of the iron as Fe^{3+} in these samples.

The coordination number within the samples appears to show a mixture of 4 and 6 coordinated Fe, with the possibility of 5 coordinated Fe but very little evidence to suggest any sample has significant quantities of 6 coordinated Fe. This is evidenced by the integrated intensities being relatively high compared to the mineral standards of 6-coordinated Fe and slightly higher than those of 5-coordinated Fe, yet slightly lower than the 4-coordinated Fe mineral standards. Forder *et al*. [27] demonstrated that using mineral standards to describe the coordination of iron within glass, should be done with caution. 5-coordinated Fe in glass will manifest with similar Fe K-edge XANES parameters as a glass with a mixture of 4- and 6-coordinated Fe within glass. On this basis, no quantitative conclusions can be drawn regarding the iron coordination within the glasses. When compared to the conclusions from the Mössbauer spectra in Chapter 4, the two techniques have provided complimentary qualitative conclusions that the iron exists as Fe^{3+} in predominantly four coordinated units with some evidence to support the presence of higher coordinated species.

*A Note on the Error Bars on **Figures 5.49 – 5.52**:*

The error bars seen in ***Figs 5.49 – 5.52*** are error bars provided by the fit statistics of the fitting software used to the fit the Gaussian peaks, with differential calculus used to propagate any error values in the calculation of the average centroid position and integrated areas of the peaks. The authors note that the error bars for the centroid energy in all but one sample are smaller than the energy step size used in the acquisition of the sample spectra. While this should not necessarily impact the error analysis from a statistical standpoint, it has been noted that widely cited literature quote errors that are more conservative than the ones provided by the fit statistics [11,22], which is largely based on statistical analysis of the technique itself, such as the work by Feige *et al*. [22]. The authors have included versions of ***Figs 5.49 – 5.52*** in the appendix (***Figs A5.1 – A5.4***) that contain the more commonly quote error bars in wider literature.

5.5.2 B K-edge XANES

The areas of the peaks fitted to the B K-edge XANES spectra were used to calculate the $^{[4]}$B abundance in each measured sample by using equation 5.2.

$$^{[4]}B = \frac{A_B}{A_A + A_B} \qquad \text{(Eq. 5.2)}$$

The calculated values for $^{[4]}$B abundance for each sample across both measured series were plotted in **Fig 5.53**.

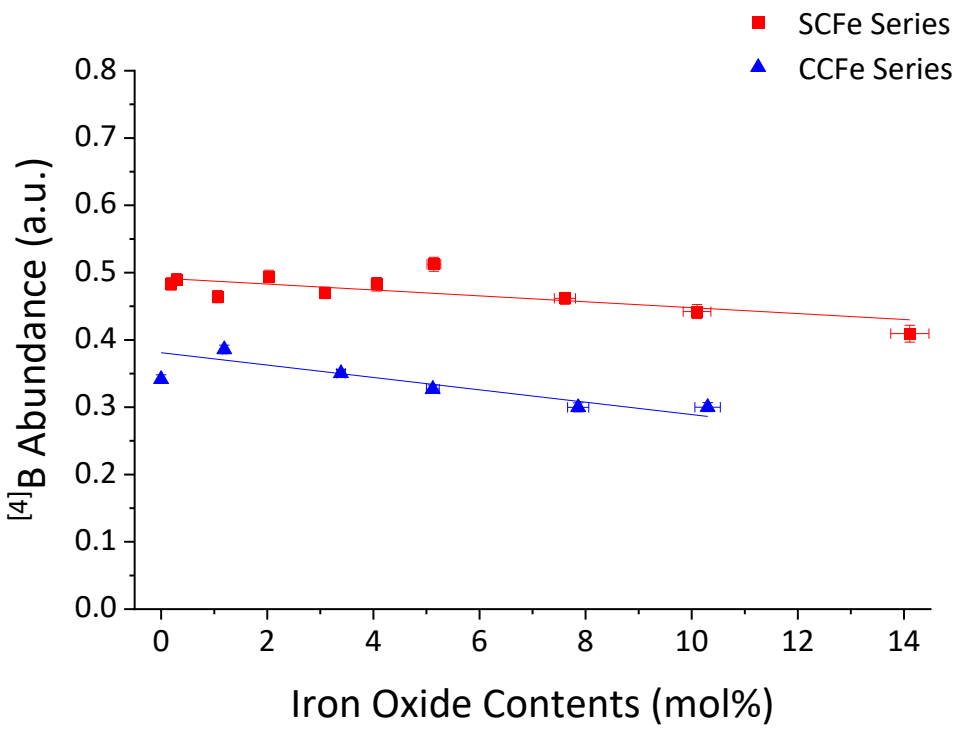

Figure 5.53: *The plotted [4]B abundances for both sample series against analysed Fe_2O_3 contents.*

The data in **Fig 5.53** show that there was very little change in [4]B abundance in either series as a function of increase Fe_2O_3 content within the glass. While the "Pearson's r" correlation factor showed for both series, there was a clear negative correlation (SCFe Series = -0.76914, CCFe Series = -0.8359), the slope of each linear fit was barely above the error range of the of slope value (SCFe Series = -0.00438 ± 0.00151, CCFe Series = - 0.0092 ± 0.0023). This is in accordance with similar findings by Cochain *et al*. [48] and does highlight that at the very least, between $^{[4]}Fe^{3+}$ and [4]B cations, the Fe^{3+} tetrahedra are not charge compensated at the expense of the tetrahedral boron. This interaction has been investigated in literature, but with no clear consensus on which species dominates for the charge compensation [48,53-55]. This research does not offer a definitive verdict on the nature of this hierarchy, but it does show that for these glasses, the Fe^{3+} still forms tetrahedral units but not directly the expense of the boron tetrahedra. The slight decrease in [4]B abundance as a function of changing Fe_2O_3 contents could be linked to how the iron integrates within the borosilicate network. The iron partially integrates into the borate subnetwork and while this change does not cause a large conversion in [4]B to [3]B (~5 % in the SCFe series, ~7.5 % in the CCFe series), it is seen in other spectroscopic techniques that the borate sub-networked is affected. It could be theorised that the conversion of some [4]B to [3]B, may not be a result of charge compensation hierarchies, but may be a

response to the iron integrating into the borate sub-network. This theory was explored in Chapter 6 with the use of Raman and XPS spectroscopies.

The $^{[4]}$B abundance within the SCFe series is approximately 55% based on **Fig 5.53**. is within the expectations set by the Yun, Bray, & Dell model for sodium borosilicate glasses [56-58], when compared with glasses studied in the development of that model that have an R value range (Na_2O / B_2O_3) of 1.58 – 1.70 and a K value range (SiO_2 / B_2O_3) of 3.23 – 3.50, as is the case for the SCFe series [56-58]. This provides a level of confidence in the fit results that can be extrapolated to the CCFe series, for which there are fewer direct comparisons. However, the drop in $^{[4]}$B abundance when compared with the SCFe series is expected, as there is Al_2O_3 within this sample series. Unlike the charge compensation hierarchy between $^{[4]}Fe^{3+}$ and $^{[4]}$B, there is a clear precedent in which $^{[4]}$Al receives preferential charge compensation over $^{[4]}$B and $^{[4]}Fe^{3+}$ [53-55,59] and this is demonstrated in this research with the $^{[4]}$B abundance in the CCFe series being approximately 45%, 10% lower than that of the SCFe series.

5.6 Summary

Fe K-edge XANES was used to support the Mössbauer spectra in describing the chemistry of the iron within the three sample series. The two analytical techniques provided complementary evidence that the iron exists as Fe^{3+} with no evidence of Fe^{2+} within the glass. The average coordination however, also yielded somewhat ambiguous results, with evidence of significant amounts of $^{[4]}Fe^{3+}$ with some evidence of higher coordinated Fe^{3+} with no quantitative evidence around how much each coordination is present.

While the Fe^{3+} has significant quantities of tetrahedral units, B K-edge XANES spectra demonstrated that the $^{[4]}Fe^{3+}$ is not being charge compensated at the expense of $^{[4]}$B. There is little change in the relative abundance of $^{[4]}$B as a function of increasing Fe_2O_3 contents within both measured glass series. This relationship, or lack thereof, will be discussed further in Chapter 8 alongside the results of the XPS and Raman spectroscopy data analysis from Chapter 7.

5.7 References

[1] Jenkins, R., Manne, R., Robin, R., & Senemaud, C., Nomenclature system for X-ray spectroscopy, *Pure & Appl. Chem.*, **63**, 1991; pp 735-746.

[2] Bruker, G., Introduction to XAFS: A Practical Guide to X-Ray Absorption Fine Structure Spectroscopy, Cambridge University Press, Cambridge, UK, 2010.

[3] Vincze, L., Tack, P., Laforce, B., De Pauw, E., Bauters, S., Silversmit, G., & Vekemans, B., Ch. 9 Laboratory and synchrotron X-ray spectroscopy, in "Spectroscopy, Diffraction and Tomography in Art and Heritage Science", Ed. By Adriaens, M., & Dowsett, M., Elsevier, Amsterdam, Netherlands, 2021.

[4] Fleet, S. G., & Megaw, H. D., The crystal structure of yoderite, *Acta Crystallogr.*, **15**, 1962; pp 721-728.

[5] Yamamoto, A., Modulated structure of wustite ($Fe_{1-x}O$) (Three dimensional modulation), *Acta Cryst. B*, **38**, 1982; pp 1451-1456.

[6] Waychunas, G. A., Apted, M. J., & Brown Jr., G. E., X-ray K-edge absorption spectra of Fe minerals and model compounds: Near-edge structure, *Phys. Chem. Minerals*, **10**, 1983; pp 1-9.

[7] White, W. B., Matsumura, M., Linnehan, D. G., Furukawa, T., & Chandrasekhar, B. K., Absorption and luminescence of Fe^{3+} of single-crystal orthoclase, *Am. Mineral.*, **71**, 1986; pp 1415-1419.

[8] Bajt, S., Sutton, S. R., & Delaney, J. S., X-ray microprobe analysis of iron redox states in silicates and oxides using X-ray absorption near edge structure (XANES), *Geochim. Cosmochim. Acta*, **53**, 1994; pp 5209-5214.

[9] Farges, F., Crystal chemistry of iron in natural grandidierites: an X-ray absorption fine-structure spectroscopy study, *Phys. Chem. Minerals*, **28**, 2001; pp 619-629.

[10] Petit, P.-E., Farges, F., Wilke, M., & Solé, V. A., Determination of the iron oxidation state in Earth materials using XANES pre-edge information, *J. Synchrotron Rad.*, **8**, 2001; pp 952-954.

[11] Wilke, M., Farges, F., Petit, P.-E., Brown Jr., G. E., & Martin, F., Oxidation state and coordination of Fe in minerals: An Fe K-XANES spectroscopic study, *Am. Mineral.*, **86**, 2001; pp 714-730.

[12] Canepa, P., Schofield, E., Chadwick, A. V., & Alfredsson, M., Comparison of a calculated and measured XANES spectrum of α-Fe_2O_3, *Phys. Chem. Chem. Phys.*, **13**, 2011; pp 12826-12834.

[13] Okudera, H., Yoshiasa, A., Murai, K.-I., Okube, M., Takeda, T., & Kikkawa, S., Local structure of magnetite and maghemite and chemical shift in Fe K-edge XANES, *J. Mineral. Petrol. Sci.*, **107**, 2012; pp 127-132.

[14] Husain, H., Hariyanto, B., Sulthonul, M., Thamatkeng, P., & Patapa, S., Local structure examination of mineral-derived Fe_2O_3 powder by Fe K-edge EXAFS and XANES, *IOP Conf. Ser.: Mater. Sci.*, **367**, 2018.

[15] Wu, Z., Mosbah-Bonnin, M., Duraud, J. P., Métrich N., & Delaney, J. S., XANES studies of Fe-bearing glasses, *J. Synchrotron Rad.*, **6**, 1999; pp 344-346.

[16] Galoisy, L., Calas, G., & Arrio, M. A., High-resolution XANES spectra of iron in minerals and glasses: structural information from the pre-edge region, *Chem. Geol.*, **174**, 2001; pp 307-319.

[17] Quartieri, S., Triscari, M., Sabatino, G., Boscherini, F., & Sani, A., Fe and Mn K-edge XANES study of ancient Roman glasses, *Eur. J. Mineral.*, **14**, 2002; pp 749-756.

[18] Magnien, V., Neuville, D. R., Cormier, L., Mysen, B. O., Briois, V., Belin, S., Pinet, O., & Richet, P., Kinetics of iron oxidation in silicate melts: A preliminary XANES study, *Chem. Geol.*, **213**, 2004; pp 253-263.

[19] Farges, F., Lefrère, Y., Rossano, S., Berthereau, A., Calas, G., & Brown Jr., G. E., The effect of redox state on the local structural environment of iron in silicate glasses: A combined XAFS spectroscopy, molecular dynamics, and bond valence study, *J. Non-Cryst. Solids*, **344**, 2004; pp 176-188.

[20] Bugaev, L., Farges, F., Rusakova, E., Sokolenko, A., Latokha, Y., & Avakyan, L., Fe-coordination environment in Fe(II)- and Fe(III)-silicate Glasses via the Fourier-transform Analysis of Fe K-XANES, *Phys. Scr.*, **T115**, 2005; pp 215-217.

[21] Farges, F., Rossano, S., Lefrère, Y., Wilke, M., & Brown Jr., G. E., Iron in Silicate Glasses: A Systematic Analysis of Pre-Edge, XANES and EXAFS Features, *Phys. Scr.*, **T115**, 2005; pp 957-959.

[22] Wilke, M., Partzsch, G. M., Bernhardt, R., Lattard, D., Determination of the iron oxidation state in basaltic glasses using XANES at the K-edge, *Chem. Geol.*, **220**, 2005; pp 143-161.

[23] Jackson, W. E., Farges, F., Yeager, M., Mabrouk, P. A., Rossano, S., Waychunas, G. A., Solomon, E. I., & Brown Jr., G. E., Multi-spectroscopic study of Fe(II) in silicate glasses: Implications for the coordination environment of Fe(II) in silicate melts, *Geochim. Cosmochim. Acta*, **69**, 2005; pp 4315-4332.

[24] Pinakidou, F., Katsikini, M., Kavouras, P., Komninou, F., Karakostas, T., & Paloura, E. C., Structural role and coordination environment of Fe in Fe_2O_3-PbO-SiO_2-Na_2O composite glasses, *J. Non-Cryst. Solids*, **354**, 2008; pp 105-111.

[25] Cottrell, E., Kelley, K. A., Lanzirotti, A., & Fischer, R. A., High-precision determination of iron oxidation state in silicate glasses using XANES, *Chem. Geol.*, **268**, 2009; pp 167-179.

[26] Hannant, O. M., Forder, S. D., Bingham, P. A., & Hand, R. J., Structural studies of iron in vitrified toxic wastes, *Hyperfine Interact.*, **192**, 2009; pp 37-42.

[27] Forder, S. D., Hannant, O. M., Bingham, P. A., & Hand, R. J., Concerning the use of standards for identifying coordination environments in glasses, *J. Phys.: Conf. Ser.*, **217**, 2010.

[28] Bingham, P. A., Hannant, O. M., Reeves-McLaren, N., Stennett, M. C., & Hand, R. J., Selective behaviour of dilute Fe^{3+} ions in silicate glasses: An Fe K-edge EXAFS and XANES study, *J. Non-Cryst. Solids*, **387**, 2014; pp 47-56.

[29] Abuín, M., Serrano, A., Chaboy, J., García, M. A., & Carmona, N., XAS study of Mn, Fe and Cu as indicators of historical glass decay, *J. Anal. At. Spectrom.*, **28**, 2013; pp 1118-1124.

[30] Ceglia, A., Nuyts, G., Meulebroeck, W., Cagno, S., Silvestri, A., Zoleo, A., Nys, K., Janssens, K., Thienpont, H., & Terryn, H., Iron speciation in soda-lime-silica glass: a comparison of XANES and UV-vis-NIR spectroscopy, *J. Anal. At. Spectrom.*, **30**, 2015; pp 1552-1561.

[31] Alderman, O. L. G., Wilding, M. C., Tamalonis, A., Sendelbach, S., Heald, S. M., Benmore, C. J., Johnson, C. E., Johnson, J. A., Hah, H.-Y., & Weber, J. K. R., Iron K-edge X-ray absorption near-edge structure spectroscopy of aerodynamically levitated silicate melts and glasses, *Chem. Geol.*, **453**, 2017; 169-185.

[32] Alderman, O. L. G., Lazareva, L., Wilding, M. C., Benmore, C. J., Heald, S. M., Johnson, C. E., Johnson, J. A., Hah, H.-Y., Sendelbach, S., Tamalonis, A., Skinner, L. B., Parise, J. B., & Weber, J. K. R., Local structural variation with oxygen fugacity in Fe_2SiO_{4+x} fayalitic iron silicate melts, *Geochim. Cosmochim. Acta*, **203**, 2017; pp 15-36.

[33] Fiege, A., Ruprecht, P., Simon, A. C., Bell, A. S., Göttlicher, J., Newville, M., Lanzirotti, T., & Moore, G., Calibration of Fe XANES for high-precision determination of Fe oxidation state in glasses: Comparison of new and existing results obtained at different synchrotron radiation sources, *Am. Mineral.*, **102**, 2017; pp 369-380.

[34] Thompson, A., Lindau, I., Attwood, D., Liu, Y., Gullikson, E., Pianetta, P., Howells, M., Robinson, A., Kim, K.-J., Scofield, J., Kirz, J., Underwood, J., Kortright, J., Williams, G., & Winick, H., Center for X-ray optics and advanced light source: X-ray data booklet, Lawrence Berkeley National Laboratory, *LBNL/PUB-490 Rev. 3*, 2009.

[35] Westre, T. E., Kennepohl, P., DeWitt, J. G., Hedman, B., Hodgson, K. O., & Solomon, E. I., A multiplet analysis of Fe K-edge 1s → 3d pre-Edge features of iron complexes, *J. Am. Chem. Soc.*, **119**, 1997; pp 6297-6314.

[36] The University of Warwick, *XMaS: The UK Materials Science Facility at the ESRF: Beamline Details*, Accessed on October 2022, Last Updated June 2021. (URL: https://warwick.ac.uk/fac/cross_fac/xmas/xmasbeamline/description/).

[37] Fogarty, R. M., Matthews, R. P., Clough, M. T., Ashworth, C. R., Brandt-Talbot, A., Corbett, P. J., Palgrave, R. G., Bourne, R. A., Chamberlain, T. W., Hoogerstraete, T. V., Thompson, P. B. J., Hunt, P. A., Besley, N. A., & Lovelock, K. R. J., NEXAFS spectroscopy of ionic liquids: experiments versus calculations, *Phys. Chem. Chem. Phys.*, **19**, 2017.

[38] Yusoff, A. L., Hugtenburg, R. P., & Bradley, D. A., XANES in doped radiosensitive glasses, *Rad. Phys. Chem.*, **71**, 2004; pp 887-888.

[39] Li, D., Bancroft, G. M., & Fleet, M. E., B K-edge XANES of crystalline and amorphous inorganic materials, *J. Electron Spectrosc. Relat. Phenom.*, **79**, 1996; pp 71-73.

[40] Kasrai, M., Fleet, M. E., Muthupari, S., Li, D., & Bancroft, G. M., Surface modification study of borate materials from B K-edge X-ray absorption spectroscopy, *Phys. Chem. Mineral.*, **25**, 1998; pp 268-272.

[41] Fleet, M. E., & Muthupari, S., Boron K-edge XANES of borate and borosilicate minerals, *Am. Mineral.*, **85**, 2000; pp 1009-1021.

[42] Fleet, M. E., & Liu, X., Boron K-edge XANES of boron oxides: Tetrahedral B-O distances and near-surface alteration, *Phys. Chem. Mineral*., **28**, 2001; pp 421-427.

[43] Šipr, O., Šimůnek, A., Vackář, J., Dalba, G., & Rocca, F., Connection between spectral features of B K edge XANES of minerals and the local structure, *Phys. Chem. Glasses: Eur. J. Glass Sci. Technol. B*, **47**, 2006; pp 412-418.

[44] Handa, K., Ide, J., Nishiyama, Y., Ozutsumi, K., Dalba, G., Ohtori, N., & Umesaki, N., XAS study of barium borate glasses and crystals, *Phys. Chem. Glasses: Eur. J. Glass Sci. Technol. B*, **47**, 2006; pp 445-447.

[45] Li, D., Bancroft, G. M., Fleet, M. E., Hess, P. C., & Yin, Z. F., Coordination of B in K_2O-SiO_2-B_2O_3-P_2O_5 glasses using B K-edge XANES, *Am. Mineral.*, **80**, 1995; pp 873-877.

[46] Fleet, M. E., & Muthupari, S., Coordination of boron in alkali borosilicate glasses using XANES, *J. Non-Cryst. Solids*, **255**, 1999; pp 233-241.

[47] Ide, J., Ozutsumi, K., Handa, K., Dalba, G., Ohtori, N., & Umesaki, N., XAS study of barium aluminoborate glasses, *Phys. Chem. Glasses: Eur. J. Glass Sci. Technol. B*, **47**, 2006; pp 521-523.

[48] Cochain, B., Neuville, D. R., Henderson, G. S., McCammon, C. A., Pinet, O., & Richet, P., Effects of the iron content and redox state on the structure of sodium borosilicate glasses: A Raman, Mössbauer and boron K-edge XANES spectroscopy study, *J. Am. Ceram. Soc.*, **95**, 2012; pp 962-971.

[49] Nannarone, S., Borgatti, F., DeLuisa, A., Doyle, B. P., Gazzidi, G. C., Giglia, A., Finetti, P., Mahne, N., Pasquali, L., Pedio, M., Selvaggi, G., Naletto, G., Pelizzo, M. G., & Tondello, G., The BEAR beamline at Elettra, *AIP Conf. Proc.*, **705**, 2004; pp 450-453.

[50] Elettra Sincrotrone Trieste, *BEAR: Research*, Accessed on October 2022, Last Updated May 2012 (URL: https://www.elettra.eu/lightsources/elettra/elettra-beamlines/bear/research/all.html)

[51] NO GIVEN AUTHOR, Synchrotron Radiation Center University of Wisconsin-Madison: Aladdin update, 1983, (URL: https://minds.wisconsin.edu/bitstream/handle/1793/53108/January%201983.pdf?sequence=1&isAllowed=y).

[52] Neuville, D. R., Cicconi, M. R., & Le Losq, C., Chapter 13: How to Measure the Oxidation State of Multivalent Elements in Minerals, Glasses, and Melts?, in Magma REDOX Geochemistry, Geophysical Monograph, **266**, 2021.

[53] Dvornichenko, I. N., & Matsenko, S. V., Structure of glasses in the Na_2O-Fe_2O_3-B_2O_3-SiO_2 system, *Glass Ceram.*, **57**, 2000; pp 11-13.

[54] Deshkar, A., Ahmadzadeh, M., Scrimshire, A., Han, E., Bingham, P. A., Guillen, D., McCloy, J., & Goel, A., Crystallization behavior of iron- and boron-containing nepheline ($Na_2O{\cdot}Al_2O_3{\cdot}2SiO_2$) based model high-level nuclear waste glasses, *J. Am. Ceram. Soc.*, **102**, 2018; pp 1-21.

[55] Balasubramanya, N., Sun, Z., Ahmadzadeh, M., Kamali, S., Neuville, D. R., McCloy, J. S., & Goel, A., Impact of non-framework cation mixing on the structure and crystallization behavior of model high-level waste glasses, *J. Am. Ceram. Soc.*, **105**, 2022; pp 3967-3985.

[56] Yun, Y. H., & Bray, P. J., Nuclear magnetic resonance studies of the glasses in the system Na_2O-B_2O_3-SiO_2, *J. Non-Cryst. Solids*, **27**, 1978; pp 363-380.

[57] Yun, Y. H., Feller, S. A., & Bray, P. J., Correction and addendum to " Nuclear magnetic resonance studies of the glasses in the system Na_2O-B_2O_3-SiO_2", *J. Non-Cryst. Solids*, **33**, 1979; pp 273-277.

[58] Dell, W. J., Bray, P. J., & Xiao, S. Z., 11B NMR studies and structural modeling of NaO-B_2O_3-SiO_2 glasses of high soda content, *J. Non-Cryst. Solids*, **58**, 1983; pp 1-16.

[59] Bouty, O., Delaye, J. M., Beuneu, B., & Charpentier, T., Modelling borosilicate glasses of nuclear interest with the help of RMC, WAXS, neutron diffraction and ^{11}B NMR, *J. Non-Cryst. Solids*, **401**, 2014; pp 27-31.

Chapter 6 – Raman and X-ray Photoelectron Spectroscopy

In spectroscopy studies of glasses, Raman and X-ray Photoelectron spectroscopy are powerful tools in describing the glass network. Both techniques are surface analysis techniques but are highly sensitive to the slightest influences. Both techniques have been used to describe bulk glass chemistry under the assumption that the analysed surface is representative of the bulk, studying various specific properties ranging from Q-species studies, and by extension, the bridging oxygen to the non-bridging oxygen ratios through to the incorporation of certain cations within the glass network. Within this Chapter, the Raman effect, its applications to glass science, and the Raman spectra generated in this research. This is followed by the photoelectron effect, its spectroscopic applications to glass science, and the XPS analysis done to the samples within this research. The complimentary data from both techniques and the common conclusions that emerge are then discussed with some call backs to the previous chapters.

6.1 What is the Raman Effect?

Raman spectroscopy is a vibrational spectroscopy that utilises the Raman effect. The Raman effect describes the inelastic interactions between incident lasers and the vibrations of certain vibrational modes within a given molecule, in which the wavenumber of the incident light changes as a result of these interactions. Raman bands can be broadly separated into two categories of scattering; Stokes and anti-Stokes scattering [1].

Stokes scattering occurs when an incident photon of energy $hc\bar{\upsilon}_0$ (where, h is Planck's constant, c is the speed of light, and $\bar{\upsilon}_0$ is the incident frequency) is annihilated, causing the scattering system to transition to a higher energy state. This results in the creation of a lower energy photon of $hc(\bar{\upsilon}_0 - \bar{\upsilon}_m)$, where $\bar{\upsilon}_m$ is the frequency associated with the energy transition within the scattering system [1]. Anti-Stokes scattering is the same phenomenon, however, the incident photon annihilates causing the scattering system to transition to a lower energy state, resulting in the creation of a higher energy photon of $hc(\bar{\upsilon}_0 + \bar{\upsilon}_m)$ [1] .Typically, Raman spectroscopy focuses on Stokes scattering, as most scattering systems will exist within their ground energy state, and therefore will more readily transition to a higher state. Conversely for anti-Stokes radiation, as the transition energy increases, there is exponential drop-off in how populated the excited energy states are, which would make anti-Stokes scattering less likely to occur and would manifest as

low intensity bands, when compared to the corresponding Stokes band for the same (albeit reverse) transition [1].

For Raman spectroscopy, the spectra are presented as intensity against Raman shift (cm^{-1}), and this Raman shift is typically treated as the absolute magnitude of the of the shift in wavenumber, i.e., $|\bar{\upsilon}_m| = |\bar{\upsilon}_0 - \bar{\upsilon}_F|$. As Stokes scattering is the primary interest in Raman spectroscopy, Stokes scattering is treated as positive when both scattering types are present (see **Fig 6.1**) [1].

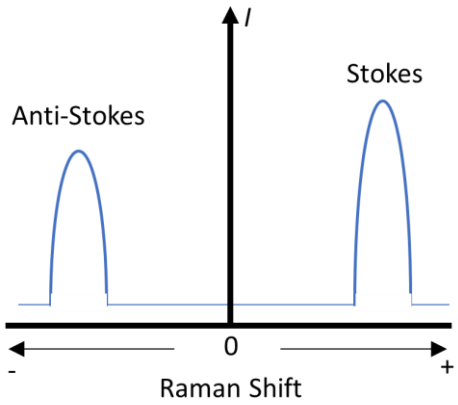

Figure 6.1: *A diagram of a spectrum illustrating the Stokes and anti-Stokes signals on a Raman spectrum. This diagram does not include the large Rayleigh-scattering peak expected at around 0 cm^{-1} on the Raman shift scale.*

When acquiring Raman spectra, there is a general formula of the experimental set up that consists of a source emitter, sample stage, and detection system. This can be seen in **Fig 6.2** [1].

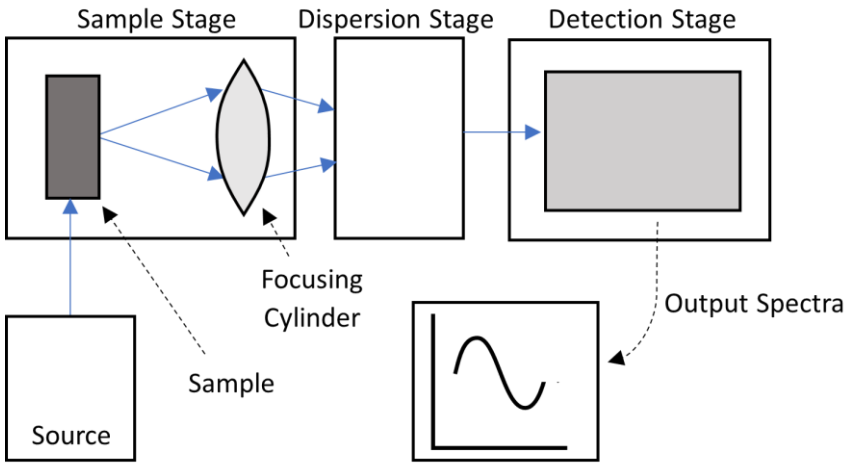

Figure 6.2: *A schematic of a Raman spectrometer set-up. Recreated from ref [1].*

The source will typically be a laser light, which will provide a monochromatic source of self-collimated radiation to be scattered by the sample. From the sample, a dispersion system, typically a diffraction grating, is used to disperse the scattered light on the detection system to increase the resolution of detection. The detection system is typically a variant of photographic plate, which receives the light, and converts it to the spectrographic output that is used for analysis.

The spectrum is presented as intensity against Raman shift (cm^{-1}), and before analysis can take place there are typically some treatment techniques that need to take place before analysis. Given the nature of Stokes scattering causing an excitation from a ground energy state, there is a risk that fluorescence will occur as the scattering medium relaxes back to the ground state. As such, the spectra may show signs of fluorescence (see **Fig 6.3** how this manifests on a spectrum).

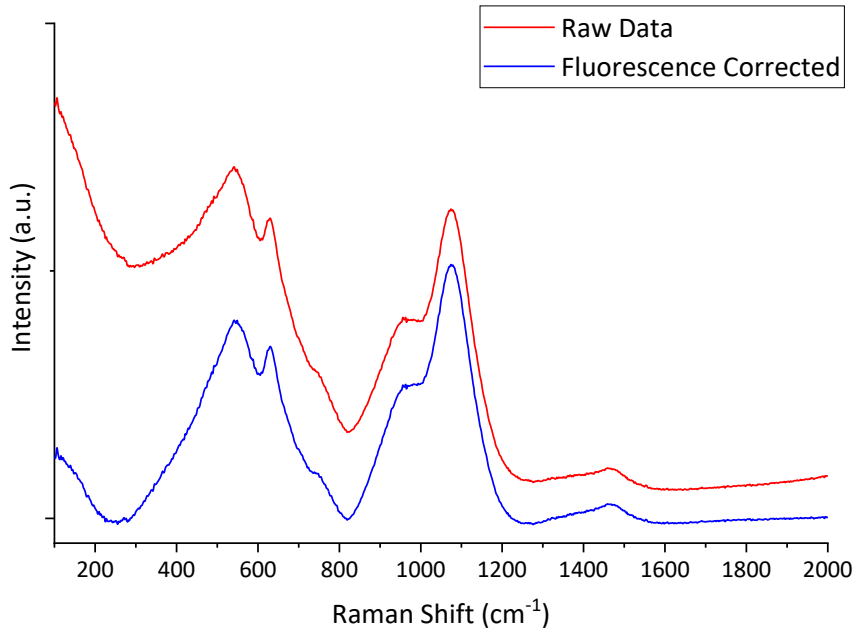

Figure 6.3: *Spectra showing the raw collected spectrum and the same spectrum with Omnic's proprietary 5th Polynomial fluorescence correction applied.*

Furthermore, a temperature and frequency dependant correction is required to resolve lower frequency energy shifts that have spectral contributions from the vibrational density of states. Shuker & Gammon [2] first developed an equation to account for this, that was further developed by Galeener & Sen [3]. The equation (equation 3.6) used can be seen in Chapter 3.5.3 and was taken from Neuville & Mysen [4] and Le Losq *et al*. [5]. The effects on the spectrum can be seen in **Fig 6.4**.

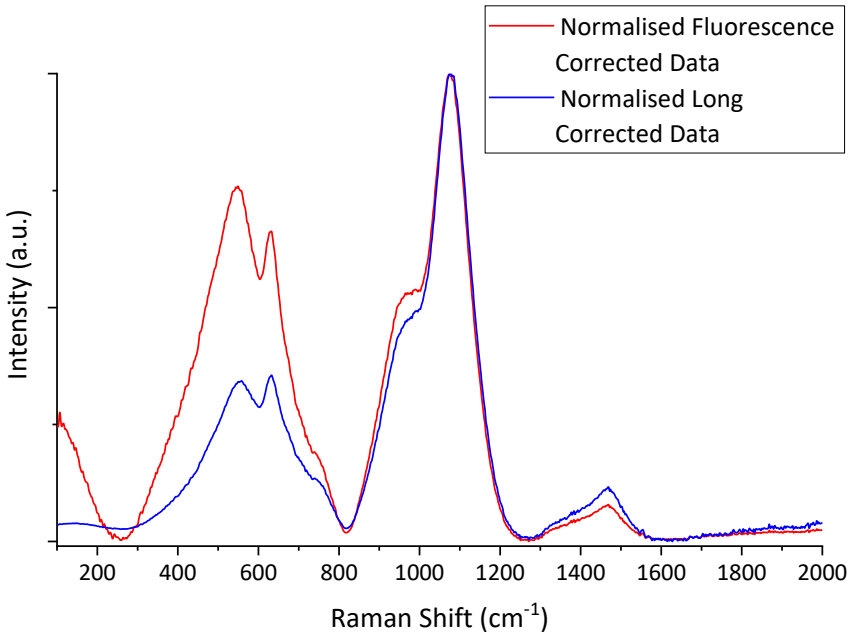

Figure 6.4: *Spectra showing the same spectrum before and after the application of the Long correction.*

Following these two corrections the spectrum is ready to be analysed.

6.2 Raman Spectroscopy on Glass

6.2.1 Overview

Raman spectroscopy has been a key tool in understanding attempting to understand the glass network. While it is a surface analytical technique, if there is sufficient trust the surface is broadly representative of the bulk (i.e. the glass is not phase separated, not showing any crystallinity nucleating on the surface etc.), this technique can be used to describe the bulk chemistry. Raman has been used to describe borate [6-18], silicate [19-39], borosilicate [40-53], and phosphate [54-56] glasses, with several informative reviews compiled on Raman bands within glass and amorphous materials [57-59].

6.2.2 Raman Bands within Glass Spectra

Raman spectra of glasses tend to be investigated across a wavenumber range of 200 – 2000 cm^{-1}. Depending on what glass type is being investigated, this range can be separated into three sub-regions: the low frequency region (200 – 800 cm^{-1}), the mid-frequency region (800 – 1200 cm^{-1}), and high-frequency region (1200 – 2000 cm^{-1}). Within silicate glasses, the mid-frequency region is perhaps the most important region, as this region contains the bands attributed to the various tetrahedral stretching/vibration modes. This range can be peak fit to describe the various contributions in this region by the Q-species of the silicate tetrahedra within silicate (see for example [5,26-30]) and

borosilicate (see for example [43-46]) glass networks. The low-frequency region is dominated by bands associated with the various modes of silicate chain vibrations, as well as larger borosilicate structures. The higher frequency region is typically dominated by borate groups within borate and borosilicate glass.

Table 6.1: Key expected bands the Raman spectra of borate, silicate, and borosilicate glasses, with the inclusion of the Fe^{3+}-O peak.

Band	Components	Description
300 – 500 cm^{-1}	Si-O-Si	Mixed stretching and vibrational modes [26-30]
550 – 850 cm^{-1}	*Mixed*	Borosilicate [46]
850 – 1200 cm^{-1}	*Mixed T-O, where T is a tetrahedral cation*	Tetrahedral vibrational modes [26-30]
980 cm^{-1}	Fe^{3+}-O	Fe^{3+} vibrational modes [27]
1320 cm^{-1}	BO_3	"Loose" BO_3 [11-13]
1410 cm^{-1}	BO_4 – BO_3	BO_4 bonded to BO_3 [11-13]
1480 cm^{-1}	*Mixed BO_3 & BO_4*	Metaborate rings [11-13]
1510 cm^{-1}	BO_3	BO_3 Boroxol rings [11-13]

Table 6.1 provides some of key Raman bands within borate, silicate, and borosilicate glass compositions, but it is by no means a concise list of all Raman bands within glass. Furthermore, the mid-frequency region, the vibrational modes are assigned to the tetrahedral vibrational modes. Le Losq *et al*. [5] demonstrated that these vibrational modes, are not limited to silicate tetrahedral modes. The example given is the presence of aluminate tetrahedral vibrational modes within this region [5]. Magnien *et al*. [27] demonstrated that tetrahedral Fe^{3+} also has a Raman band in this region [27]. This all serves to suggest that Raman spectroscopy in isolation may not provide the best data to analyse complex glasses, due to the sensitivity towards a wide range of structural units found within glass. However, if used in conjunction with other techniques, with a confident understanding of the glass composition, it can be a powerful tool when describing glass networks.

6.2.3 Peak Fitting

On the peak fitting of glasses, there is some disagreement on how this should be done. Careful selection of fitting regime, peak functions, and careful/consistent background selection is important, as failing at any one of those steps runs the risk of propagating fits

and associated conclusions, that are less indicative of the sample itself and more indicative of the mathematics of the fit. This results in over- and underestimation of specific bands or the reporting of trends that may not even exist. A lot of research reference a specific work by Mysen *et al*. [20], in which it was assumed the peaks used to deconvolute the mid-frequency region of Raman spectra of silicate glasses should be Gaussian line shapes. This has been propagated throughout a variety of works since this publication (see for example refs [32,35,44,46,49,60]). However, Kamitsos & Risen [22] suggested that the peak shapes should be Lorentzian line shapes, with Efimov [57] supporting this suggestion. Efimov [57] states that in the mid-frequency region of vibrational spectra, phenomena such a phonon damping cannot be ignored within vibrational spectroscopy. The use of Gaussian peaks ignores this phenomenon, which is best described by Lorentzian distributions, as such any peak fitting should have a Lorentzian function [57]. Bancroft *et al*. [37] further elaborated on this argument by demonstrating that binary silicate glasses can be fit with Lorentzian-dominant Voigt and pseudo-Voigt functions. For reference, Voigt functions are convolutions of Gaussian and Lorentzian functions while pseudo-Voigt functions are linear combinations of Gaussian and Lorentzian functions and can be summed up in equation 6.1.

$$\text{Pseudo-Voigt} = x*\text{Gaussian} + (1-x)*\text{Lorentzian} \qquad \text{(Eq. 6.1)}$$

Using the Lorentzian-dominant Voigt peak shapes, binary alkali and alkali-earth silicate glasses were fit for Q^{1-3} contributions in the 800 – 1200 cm^{-1} to a high standard as verified by ^{29}Si NMR data. The links between the FWHM (Full-Width Half-Maximum) of the fitted peaks was linked to the lifetime of the excited vibrational state within the glass (see Chapter 7.1) and was shown that the FWHM of the fitted peaks could be predicted [37]. O'Shaughnessy *et al*. [39] further developed this work, specifically looking into multiple contributions for each Q^3 species in binary silicates (as fitted described by pseudo-Voigt peaks) within the mid-frequency region as a result of an asymmetry within the Q^3 peak with increasing modifier content. It was suggested that this is due to an increase in negative charge around the Si within the tetrahedron resulting in lower vibrational force constants. This in turn manifests a lower-frequency peak in the Q^3 peak, explaining the asymmetry. These works not only show how sensitive Raman spectroscopy can be as an investigative tool, but also shows that the pseudo-Voigt line shapes can be used effectively in peak fitting.

Gaussian peaks, though not strictly in line with vibrational theory, are still used within Raman studies of glass [39].

6.2.4 Qualitative Analysis

Beyond the peak fitting capabilities, Raman spectroscopy has been used as part of a multi-technique approach in a wide range of studies. While ideally, all analysis would be quantitative, there is real value in qualitative analysis if used in conjunction with more quantitative techniques. Raman spectroscopy is full of bands that are ascribed to a variety of vibrational modes, with specific modes dependant on the glass matrix and wider composition. In the case of complex glasses, a lot of modes may overlap, and deconvolution may not be strictly possible. However, if used to analyse a series of glasses with discrete changes between samples, the apparent and relative change in band intensities has been used to describe potential changes in glass networks [40-42,47,52,53,61]. This need not be limited to studying the glass network, but retention of specific components within a glass network. Bingham *et al*. [61] used Raman spectroscopy as part of a multi-technique approach to study sulphate retention in glasses. Several spectral changes were attributed to changes in analysed amount of sulphate within the glass samples, evidence by qualitative changes in band in tensed that scaled with change in composition, which acted as supporting evidence of sulphate retention that was evidenced by other techniques within the study [61].

Similarly, McKeown *et al*. [53] studied molybdenum retention in borosilicate glasses, in which Raman spectroscopy was qualitatively used alongside X-ray absorption spectroscopy (XAS). Raman bands assigned to Mo tetrahedral vibrations and vanadate tetrahedral vibrations were tracked for shifts in wavenumber and intensity as a function of compositional changes, specifically, modifier content, glass complexity, and amount of Mo and V within the glass. The Raman spectra provided qualitative evidence that the vanadate and molybdate groups compete for modifier cations and will tend to cluster within the glass network. It provided evidence for a mechanism in which vanadium in glass inhibits the formation of water-soluble secondary molybdate phases, and thus increases Mo retention within the glass [53].

6.3 Results

The normalised corrected spectra for all three spectra can be seen in the stack plots in **Figs 6.5** – **6.5**. The stack plots show that in all three series there are significant changes across the entire spectral region of interest (200 – 1600 cm^{-1}).

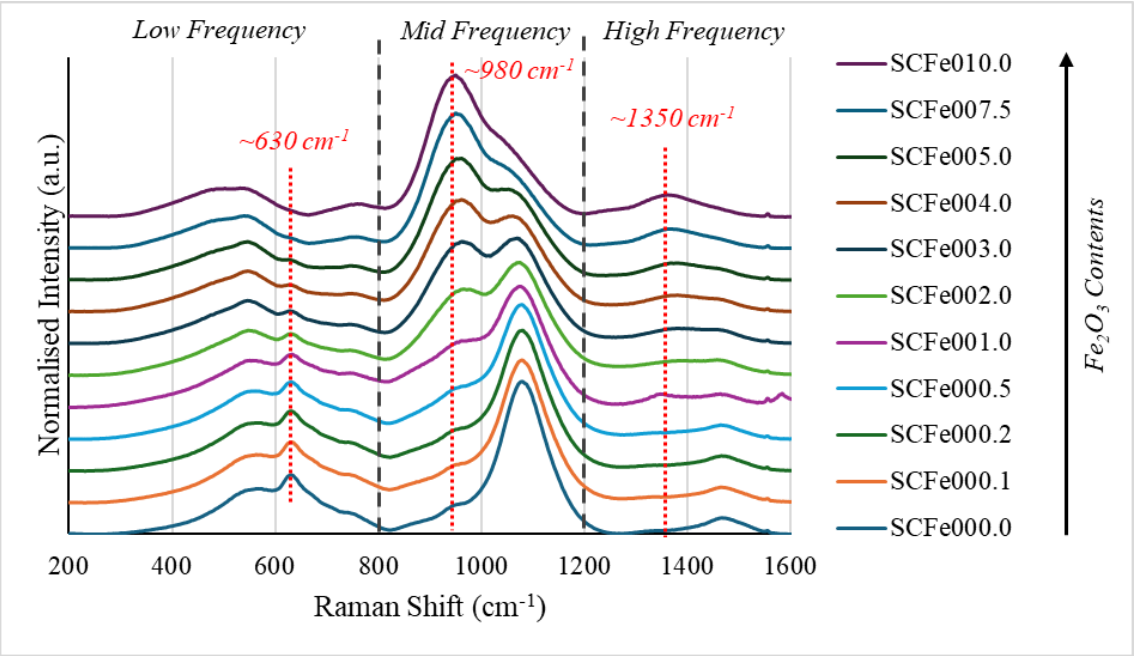

Figure 6.5: *The stack plot of the processed SCFe sample series Raman spectra.*

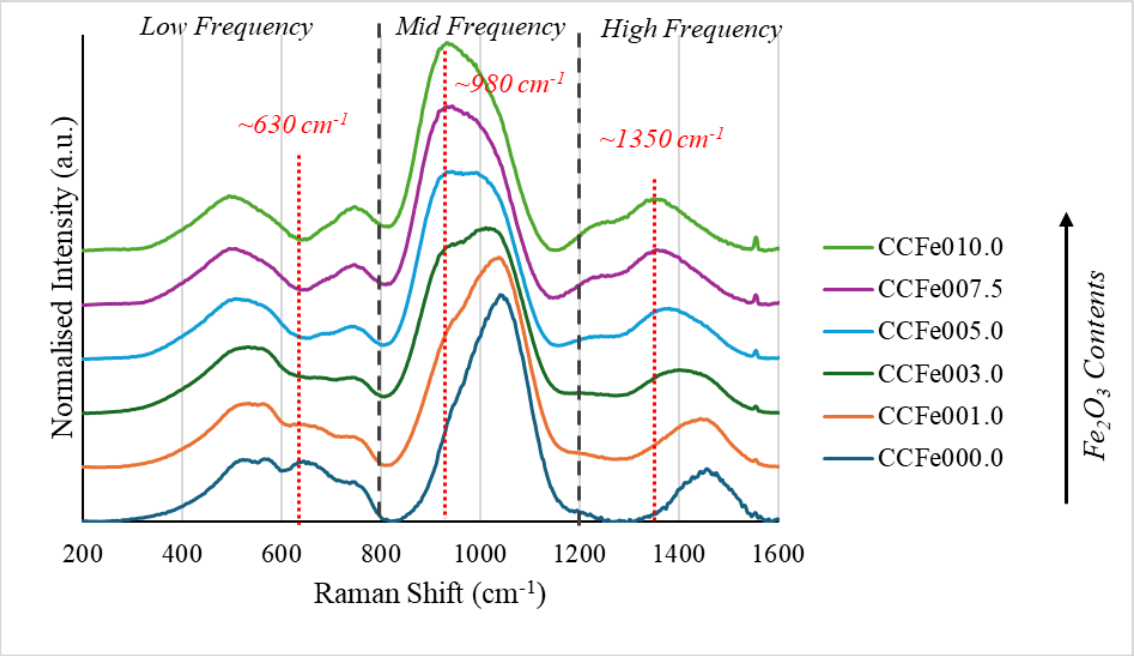

Figure 6.6: *The stack plot of the processed CCFe sample series Raman spectra.*

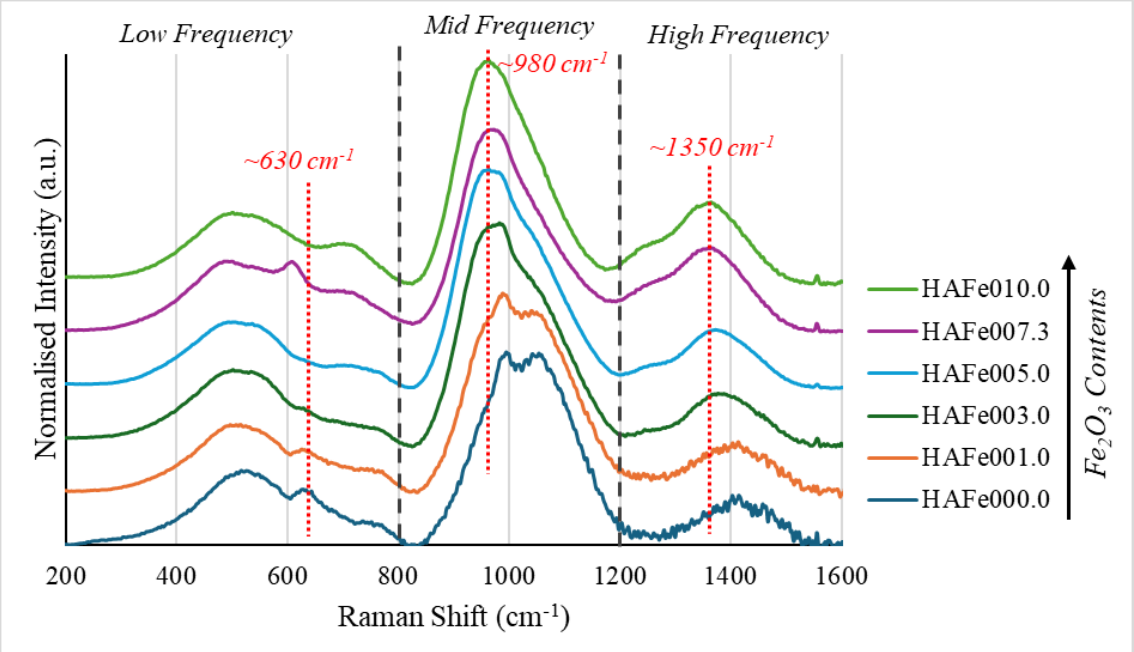

Figure 6.7: *The stack plot of the processed HAFe sample series Raman spectra.*

The spectra seen in **Figs 6.5 – 6.7** are typical of those seen in borosilicate glasses, with the presence of spectral features in each of the three regions. The low-frequency region likely being dominated by silicate and borosilicate groups, the mid region being dominated by tetrahedral vibrational and Fe^{3+} vibrational bands, and high-frequency region being dominated by various borate vibrational modes, such as the metaborate bands [11-13] and "loose" BO_3 [11-13].

Across all three series, there are common trends across all three regions. Within the low-frequency region, the obvious trend is the disappearance of a band located around 630 cm^{-1}, with the exception of the HAFe007.1 sample, which shows an anomalous sharp increase in the band, which is then followed by the continuous disappearance in the following sample, HAFe010.0.

In the mid-frequency region, there is an apparent shift in band intensities as a function of increasing iron contents. The higher frequency bands seemingly decrease in intensity, which is matched by a relative increase in intensity of the lower frequency bands. Furthermore, the bands appear to broaden in width as the composition becomes more complex, i.e. between series. The bands in this region appear to be narrower and more defined in the SCFe series, broaden and far less defined in the CCFe series, with this broadening matched in the HAFe series.

In the high-frequency region, a similar broadening of bands is seen across all series as well as an increase in relative intensity of the borate specific bands in the region. Across

all three series, there is an emergence of a band between 1200 – 1300 cm^{-1} as the Fe_2O_3 content increases, with no obvious corresponding decrease in intensity matched by the higher frequency bands.

These observations are made based on stack plots. To better visualise these relative changes, difference spectra were generated for all three series. The difference spectra were made by subtracting the normalised spectrum of the iron-free sample, from the subsequent spectra. This in theory produces difference spectra that show only the changes as a result of the compositional change (in this case, increasing Fe_2O_3 contents in the glass). These spectra can be seen in **Figs 6.8** – **6.10**.

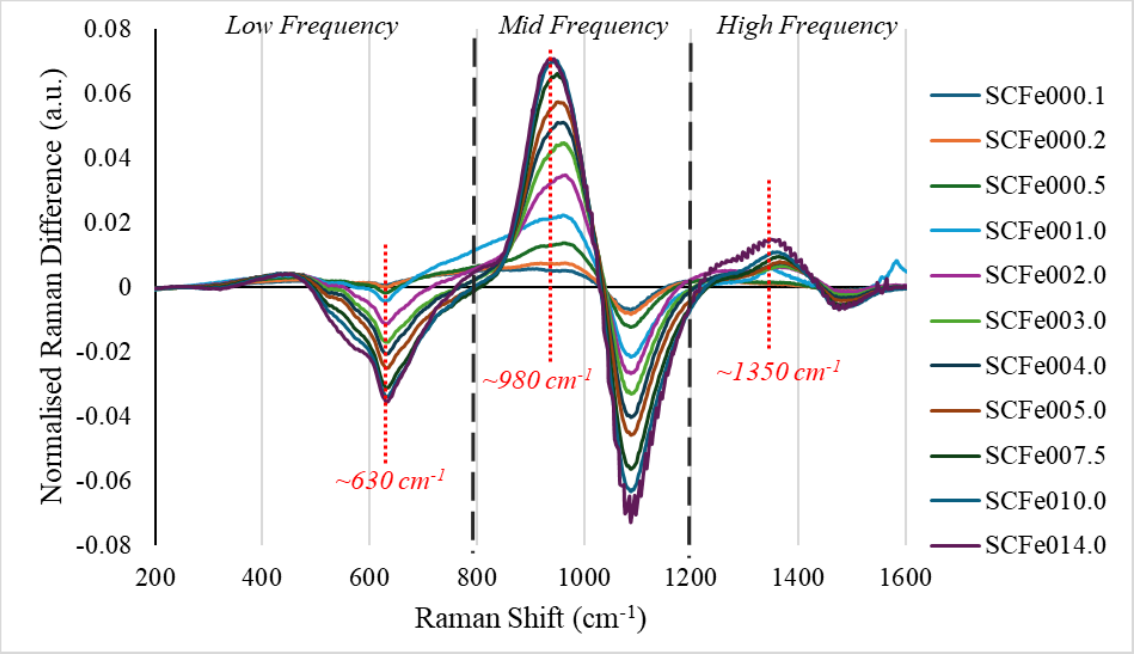

Figure 6.8: *The Raman difference spectra (RDS) for the SCFe series.*

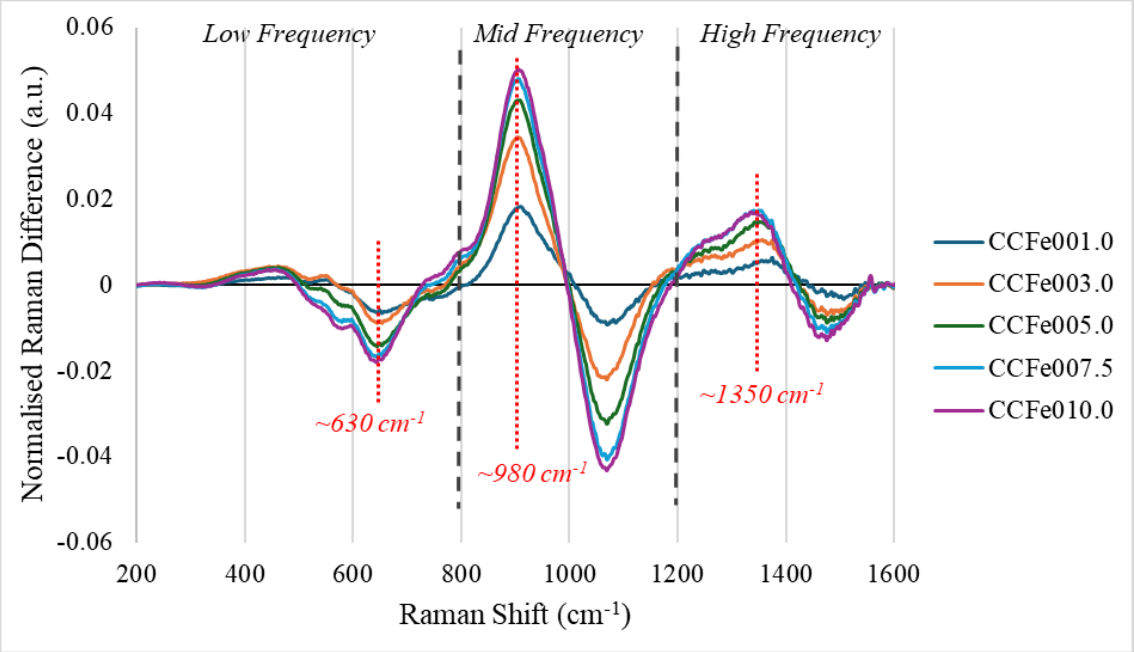

Figure 6.9: *The Raman difference spectra (RDS) for the CCFe series.*

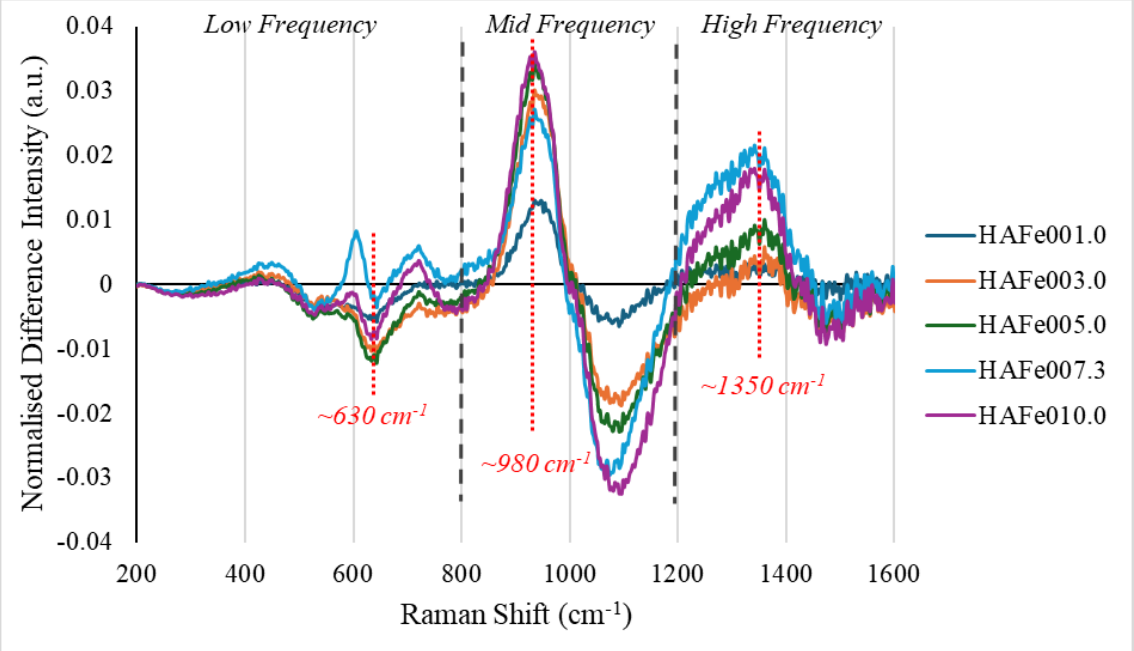

Figure 6.10: *The Raman difference spectra (RDS) for the HAFe series.*

The difference spectra for all three series confirm the original observations made based on the stack plots but provide enhanced visualisation of these observations.

6.4 Discussion

Within the low frequency region, the primary band that appears to change, is the band around 630 cm^{-1} and some associated higher frequency bands around 700 cm^{-1}. Manara *et al*. [46] observed a similar band when studying borosilicate glasses and assigned it to

borosilicate groups of similar composition to danburite or reedmergnerite. Rigby *et al.* [62] observed a similar trend is this band whereby its intensity changed as a function of tetrahedral Fe^{3+} contents within the glass. The theory put forward was that the Fe^{3+} tetrahedra were being preferentially charged compensated over the B^{3+} tetrahedra. This phenomenon results in a conversion from tetrahedral to trigonal B^{3+} in order to remain charge neutral, which results in a break down in the danburite and reedmergnerite structures, in which the boron is tetrahedral [62]. However, the B k-edge XANES data from Chapter 6, shows this theory does not apply to this research, as there is no significant change in the boron coordination as a function of iron oxide contents. Further theories are elaborated upon in Chapter 8.

As mentioned in Chapter 7.2.3, the mid-frequency region can be peak fit to determine the Q-species within various (alumino-, boro-, etc.) silicate glasses (including but not limited to refs [32,35,44,46,49,60]). However, as demonstrated by Bancroft *et al.* [37] and O'Shaughnessy *et al*. [39], Raman spectroscopy is highly sensitive and can detect a variety of different contributions within individual Q^n peaks. This combined with the assertion that this region is not limited to silica tetrahedra but can show alumina tetrahedra [5], an Fe^{3+} band [27,30,62], and some phosphate bands [54-56]. It would make peak fitting this region and being able to compare the findings across the series very difficult, and as such it will not be pursued in this research. However, the band at around 980 cm^{-1} is still of interest as it is the band associated with Fe^{3+} within this region. Across all three series, there is a steady increase in intensity of the band at ~950 cm^{-1}, which is in keeping with this assignment of a $^{[4]}Fe^{3+}$ band – more Fe_2O_3 within the glass, in which Mössbauer spectroscopy has shown to be all Fe^{3+}, corresponds with an increase in intensity of this band. The corresponding decrease in intensity of the higher frequency bands could very well be indicative of a reduction in Q-species, but it could also be a reduction in vibrational energy of these current species as a result of the T-O-Fe (where T = Si, Al, B tetrahedra) having lower energy vibrational states, and therefore will vibrate at a lower Raman shift. Using Raman spectroscopy alone, it will not be possible to conclusively say how much of each theory is contributing to this shift.

The high-frequency region, which is dominated by various borate stretching modes, shows an increasing intensity of a band at around 1350 cm^{-1} with a slight decrease in the higher frequency bands within the region. The band at around 1350 cm^{-1} could likely be the band corresponding to "loose" BO_3 units within borosilicate glasses, which would be expected if the higher frequency bands correspond to metaborate groups that involve BO_4

– BO_3 bonds and BO_3 boroxol rings. The decrease in intensity of bands corresponding to large borate groups coupled with the increase in intensity corresponding to "loose" BO_3, all as a function of increasing Fe_2O_3, would suggest that the iron is influencing the borate sub-network within the glass. Coupled with the decrease in band around 630 cm^{-1} across the three series, it would suggest that the iron, which exists predominantly as $^{[4]}Fe^{3+}$ within the samples, is integrating within the borosilicate network in a manner that is breaking up the borosilicate structures and the metaborate structures.

Further study of the impacts on the silicate and borate sub-networks was carried out through the use of X-ray photoelectron spectroscopy.

6.5 X-Ray Photoelectron Spectroscopy

X-Ray Photoelectron Spectroscopy (XPS) is a technique that investigates electrons liberated from the surface of a sample by way of the photoemission effect. The energies of these electrons (typically 200 – 2000 eV) are analysed to provide information on the chemistry of a target molecule or atom. The electrons analysed are determined by both the standard orbital notation and the electron angular momentum, *l*. These are described in **Table 6.2** [63].

Table 6.2: The standard notation for a variety of electron types.

Orbital Number, *n*	**Angular Momentum number, *l***	**Standard Notation**
1	0	s
2	1	p
3	2	d
4	3	f

The peaks in XPS spectra represent electrons with an angular momentum of greater than 1. These peaks are then typically split between spin values of the electrons within the given orbitals. The electron can be given as nl_j where *n* is the quantum number associated with the orbital, *l* is the quantum number associated with angular momentum and is ranges from 0 to *n*-1, and *j* is the total angular momentum quantum number and is given as $j = l \pm s$, where *s* is the spin value (1/2 or -1/2) [63].

6.6.1 Further theory

As the atom is ionized and needs to relax following the emission of the photoelectron, the atom may emit an X-ray photon know as X-ray fluorescence. An alternative method of relaxation for the ionised atom, is emitted an Auger electron (**Fig 6.11**) [63].

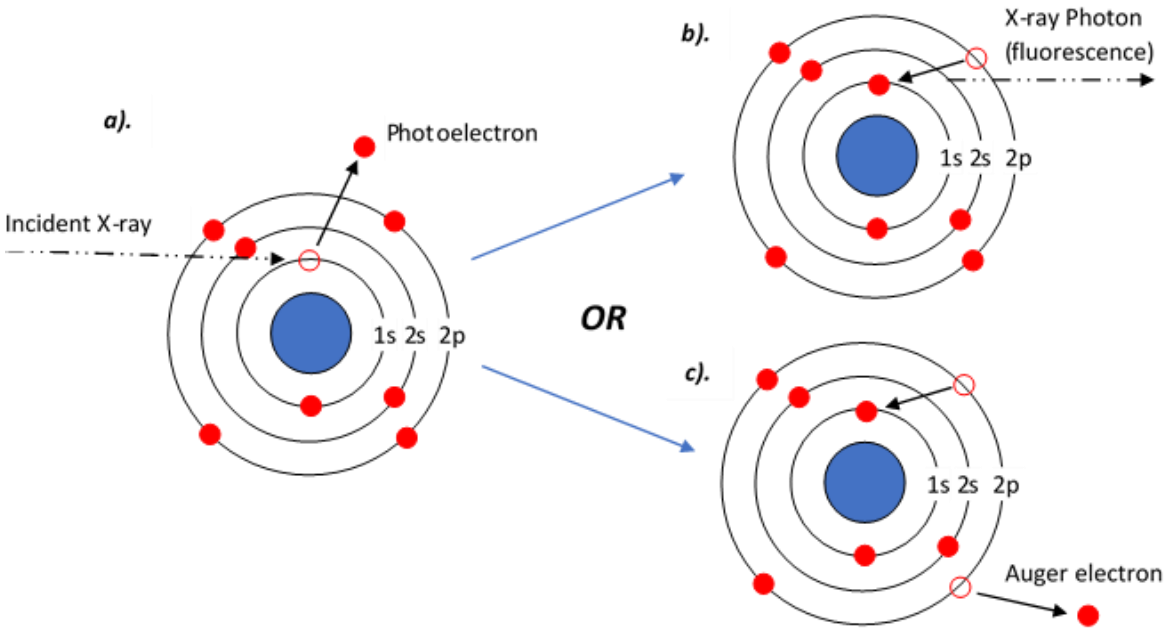

Figure 6.11: *A diagram showing the a). Photoelectron effect b). the X-ray fluorescence effect, and c). the Auger electron effect.*

The Auger electrons will show on the XPS spectrum but can also be used in its own technique known as Auger Electron Spectroscopy (AES), which will not be further elaborated upon in this work.

6.6.2 How are spectra generated?

X-ray photoelectron spectroscopy, like most spectroscopic techniques, can be simplistically reduced to three core components – a wave emitter, the sample, and a signal detector. A simple diagram of an XPS set up can be seen in **Fig 6.12** [63].

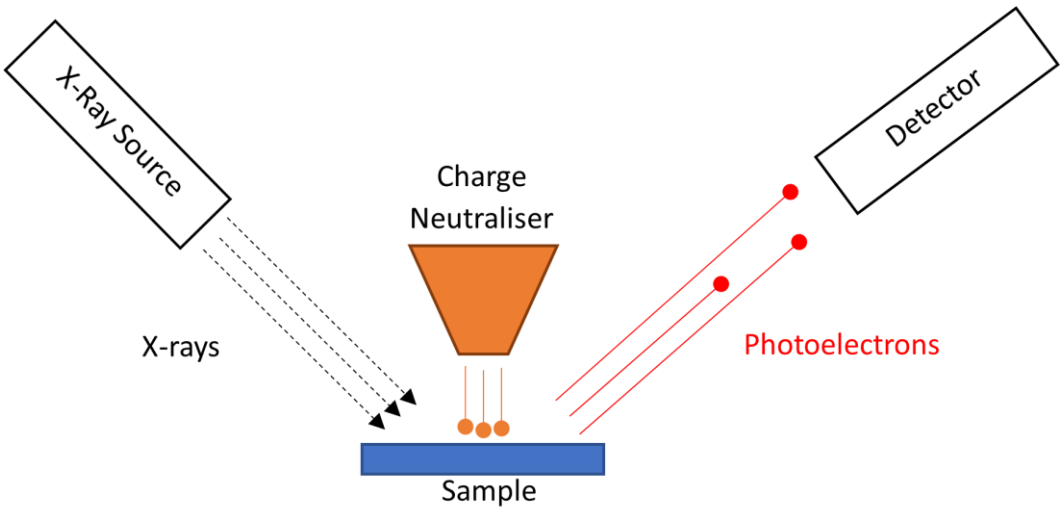

Figure 6.12: *A diagram illustrating a simple diagram of how XPS spectra are generated.*

The reality is always more complex, however. As this sample is investigating electrons liberated from the sample surface, the sample is being ionised by the technique. If the sample is non-conducting and therefore unable to dissipate the consequential build-up of charge, then a neutralising "gun" is required, which bombards the target area with electrons to negate the build-up of positive charge. If the sample is not neutralised, then the energy required to liberate an electron drastically increases with each photoelectron, which causes well defined photoelectron peaks to become broadened or "smeared" on the spectrum. **Fig 6.13** shows a simple diagram of a charge neutraliser gun [63].

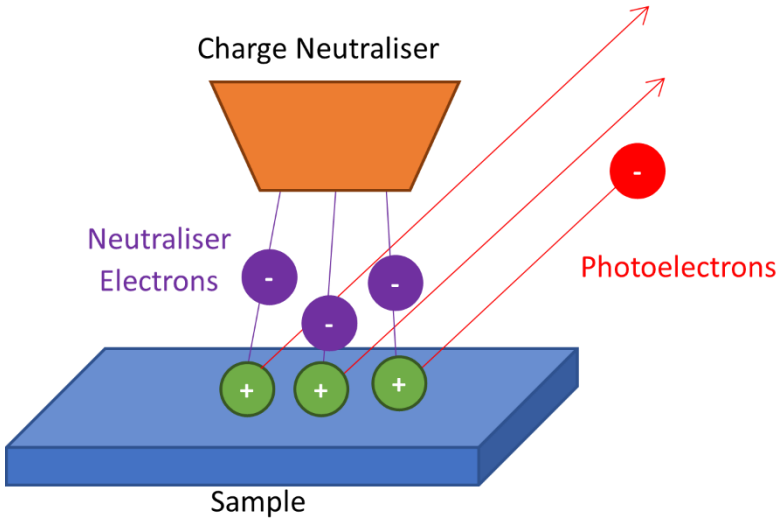

Figure 6.13: *A diagram showing how the charge neutraliser is applied.*

Due to the energy range of a XPS spectrum ranging from 200 – 2000 eV, the measurements must be done under vacuum conditions due to the low energy. Ambient

environmental conditions would attenuate and scatter both the incident X-rays, and the photoelectrons, which would make it very difficult to generate useful spectra [63].

6.6.3 What does the spectrum show?

The electrons are ejected from a core level orbital by an X-ray of energy *hv*. The emitted electrons are analysed by an electron spectrometer with the data presented as intensity (counts or counts/s) against electron energy. While it is the electron kinetic energy that is detected and measured by the spectrometer, it is the binding energy that defines the specific electron property. This is determined using equation 6.2 below.

$$E_B = h\nu - E_K - W \qquad \text{(Eq. 6.2)}$$

E_B = Electron Binding energy

$h\nu$ = Incident X-ray energy

E_K = Electron Kinetic Energy

W = Spectrometer work function

In this technique, all but the binding energy will be known quantities and therefore, the electron binding energy can be calculated. The electron binding energy is the specific property that will provide information on the type of environment the electrons exist in and how this translates to larger atomic structure. All electrons with a binding energy less than that of the incident photon will be liberated and subsequently detected on the spectra, assuming they do not undergo energy loss. Electrons that lose energy via inelastic scattering will contribute to the background of the spectra.

6.6.4 XPS Studies on Glass

XPS has been used to study glass materials in a variety of contexts, ranging from studying glass networks within bulk glass [64-84] through to surface interactions [85-89]. Sprenger *et al*. [65] used XPS in conjunction with Raman and NMR spectroscopies to develop a "Discrete bond model" (DBM) for simple sodium silicate glasses, whereby XPS can be used to differentiate between bond configurations of bridging oxygens and non-bridging oxygens depending on the nearest neighbour and homogeneity of the glass. For example, the O 1s signal contribution from a Q^4-O-Q^4 oxygen would be distinguishable from that of a Q^4-O-Q^3 oxygen, even though both could be described as a bridging oxygen [65]. Such is the sensitivity of this technique. Within borosilicate glasses, XPS has been used a means to describe the bridging oxygen to non-bridging oxygen ratio by peak fitting the O 1s signal [66-69,71,72,75]. This ratio and any relative changes to this ratio as a function of compositional changes, is a commonly used tool to describe the connectivity of the glass network, which in turn can be linked to glass properties. This ratio is often

ascertained through peak fitting of the O 1s spectra. Assuming all oxygen within the samples exists within the glass network (which is not necessarily a strictly valid assumption, for example Nesbitt *et al*. [82] describe the presence of free oxygen in glass), the O 1s spectra can be peak fit with two broad contributions – bridging oxygens and non-bridging oxygens. This can become complicated if the glass is not a single amorphous phase, as other oxygen environments will need to be considered with the fitted area. The BO/NBO ratio is typically calculated by using a peak area ratio for both types of oxygens within the glass network.

Beyond the BO/NBO ratio, XPS has been used to describe the short-range bond configurations in glasses by tying the binding energies of certain glass components, with wider bond theories and rules. Works by Brow and Pantano [85,86] and Hsieh *et al*. [66] linked the binding energies of core glass forming components, with the fractional ionic character of various bonds, and the effective charge on both the anion and cation within the bonds (both stemming from theories developed by Pauling). Hsieh *et al*. [66] used this link to demonstrate that while boron and aluminium cations within silicate glasses are glass network formers, they do form unique bonds owing to differences in electronegativity, ionic radii, and evidenced by binding energy differences in the O 1s spectra [66]. Works by Brow and Pantano [85,86] looked more at the surface interactions of silicon oxynitride thin films [85] and fluorozirconate glasses [86]. The relationship between effective charge and BE of the cations in question was used to detail potential bond configuration and changes in bonds (Si-O to Si-N in ref [85] and ligand substitution from Zr-F to Zr-OH in ref [86]) in semi-quantitative capacities.

Work done by Nesbitt, Sawyer, and co-workers used the sensitivity of XPS to probe binary silicate glasses to better understand the glass network [78,80-82]. Sawyer *et al*. [78] used XPS to investigate potassium silicate glasses to show the existence of three types of oxygen within this system – bridging oxygens, non-bridging oxygens, and free oxygen (O^{2-}). This disagrees with the simple model that suggests every alkaline metal binds to one oxygen in the silicate network, thus leaving no room for free oxygen. Nesbitt *et al*. [80,82] went on to quantitatively analyse the amount of free oxygen in K, Pb, Mg, and Ca binary silicate systems using the O 1s spectra from XPS spectroscopy. This was further supported by O^{17} and Si^{29} NMR spectroscopies, and proved that it is a real component of binary silicates that has implications on melt reaction dynamics. Nesbitt *et al*. [81] also used XPS to describe the electron configuration within the various bonds in sodium silicate glasses. It was shown that the ionic nature of the Na-O bonds causes a

charge distribution across the Si-tetrahedra, which in turn leaves the Si-tetrahedra less stable than it would be in a pure vitreous quartz network. This suggests that the reduction in network connectivity is not the only reason a silicate glass becomes less stable, and that the remaining network forming bonds are weaker as a result of increasing sodium cations [82].

XPS has been demonstrated as a powerful tool to investigate glass networks. For this research, the aim is to use this technique to measure the O 1s signal to describe the bridging oxygen to non-bridging ratio within the SCFe and CCFe glass series, and any relative changes to the ratio as a function of changing Fe_2O_3 contents. Furthermore, changes in binding energy to the boron 1s and silicon 2p signals to determine any changes to the wider glass-forming components as a function of changing Fe_2O_3 contents.

6.6 Results – SCFe Series

6.6.1 Overview

Initially, a survey scan for each sample was taken (see ***Fig 6.14***), so that target regions could be identified. This scan was a low-resolution scan that functioned as a fact-finding scan, in which the energy ranges of the target signals were established, but no further analysis could be done on these particular scans.

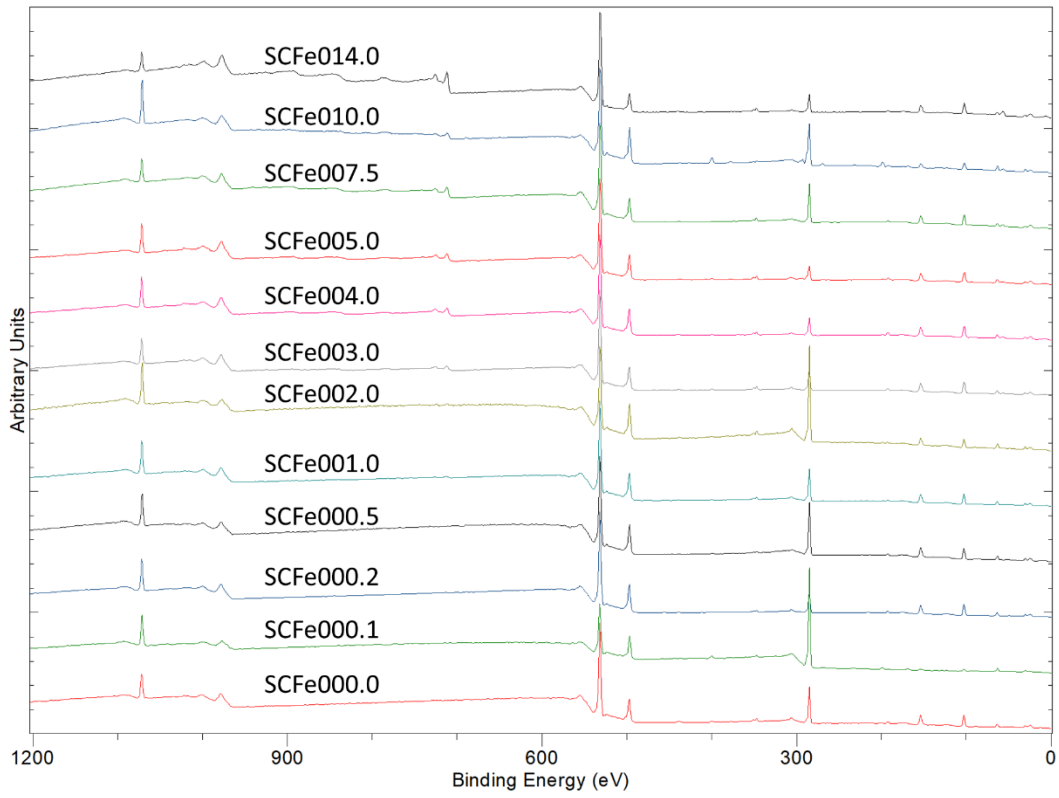

Figure 6.14: *The stack plot of the survey scans for the SCFe sample series.*

Using the survey scan, target regions were selected for higher resolution scans so that the proper analysis could be done. The full details of the survey scan and subsequent regional scans can be found in **Table 3.10** in Chapter 3.5.4. The calibrated (see Chapter 3.5.4) C 1s and O 1s spectra for the SCFe series can be seen in **Figs 6.15** and **6.16** respectively, which subsequent analysis done in Chapter 6.7.2.

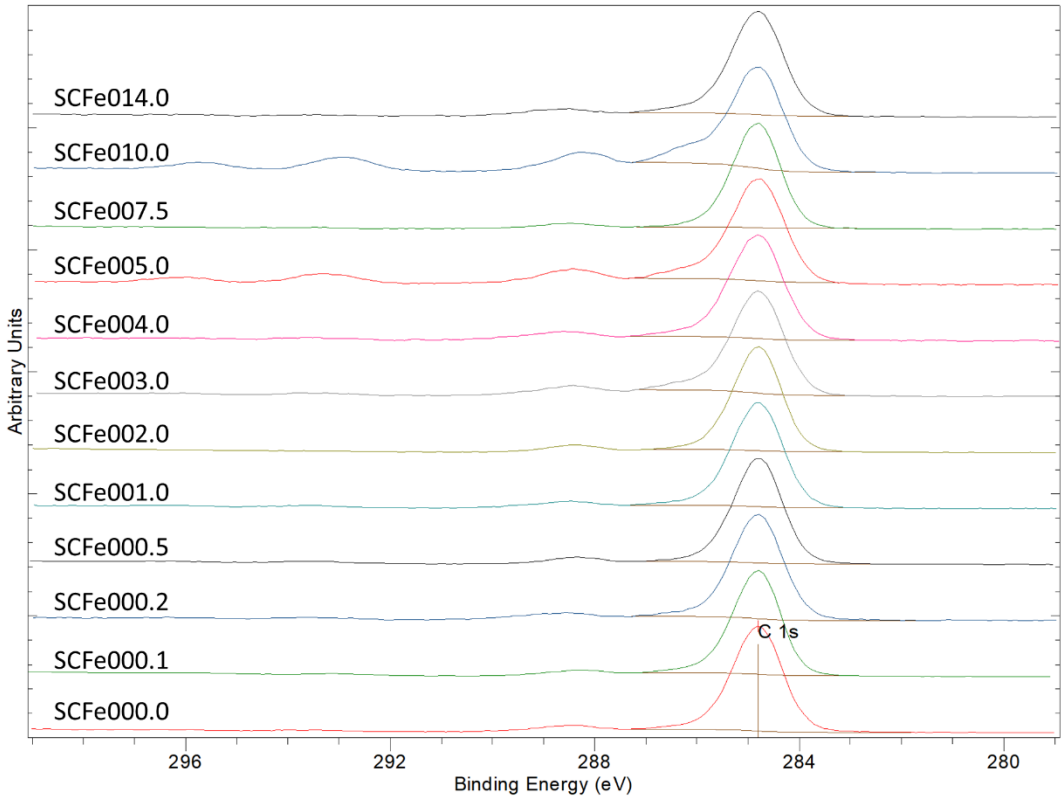

Figure 6.15: *The stack plot for the C 1s spectra of the SCFe series.*

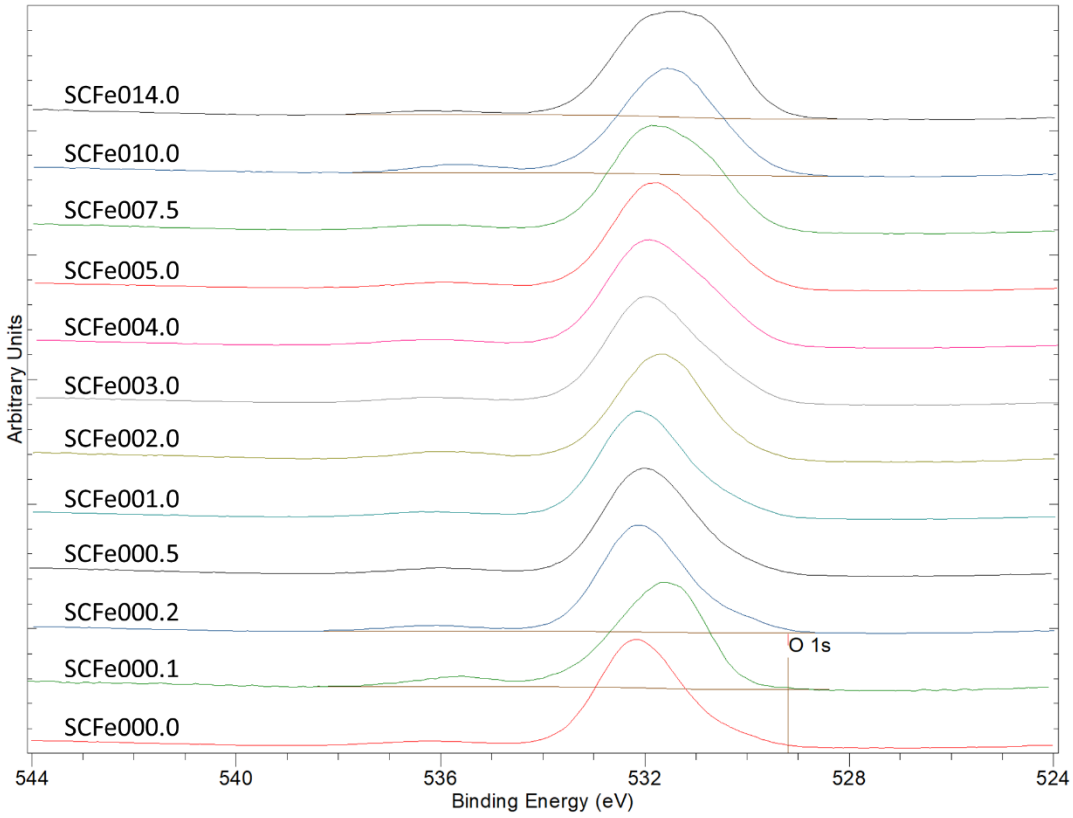

Figure 6.16: *The stack plot for the O 1s spectra of the SCFe series.*

6.6.2 Oxy-Carbon Analysis

With the O 1s and C 1s regions calibrated, each spectrum is fitted with Gaussian-Lorentzian (presumed to be pseudo-Voigt) peak functions, starting with the C 1s spectra.

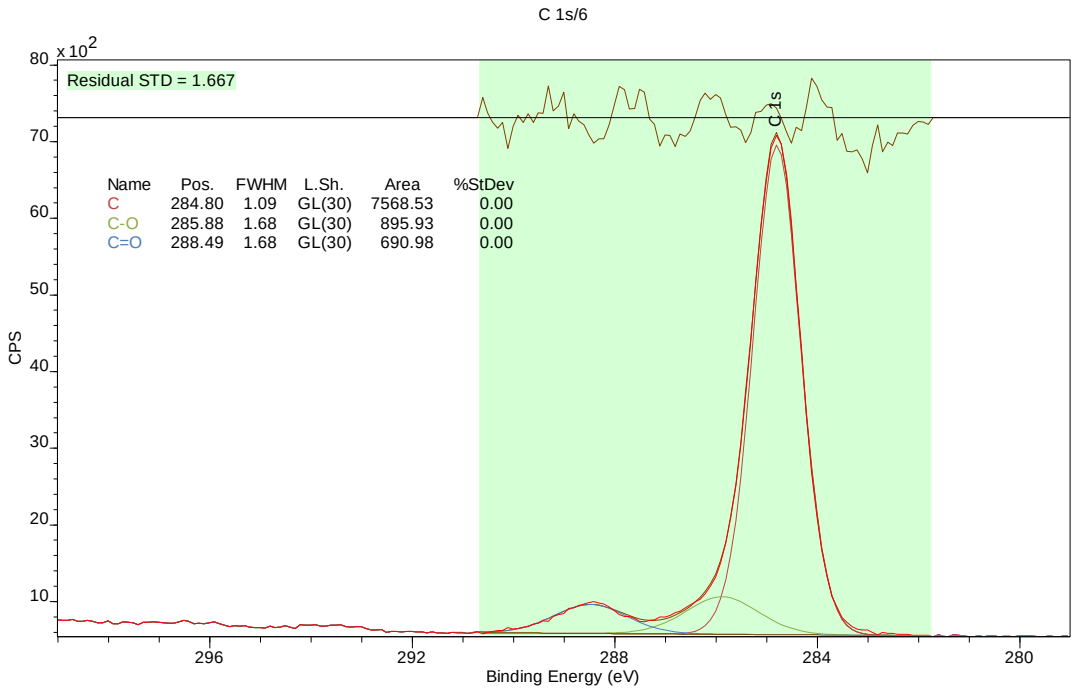

Figure 6.17: *SCFe000.0 C 1s Spectrum showing the presence of the C-C peak used to calibrate the rest of the spectral signals for this sample, but also the presence of two oxy-carbon peaks; C-O and C=O.*

The carbon spectra were fitted with three peaks (example in **Fig. 6.17**). The primary carbon peak relates to the adventitious carbon-carbon peak caused by unavoidable atmospheric carbon contamination (it is this peak used in the calibration method outlined in Chapter 4.2.4). The two secondary peaks are attributed to oxy-carbon bonds, the lower energy peak corresponding to C-O bonds, and the higher energy peak corresponding to C=O. The exact source of these contaminants is currently unknown, but they are external contaminants and therefore not indicative of the bulk sample being investigated. The peaks have the FWHM values to be constrained so that the higher the binding energy, the larger the FWHM of the peak. This is due to the fact that the FWHM of a peak in XPS is tied to the core-hole lifetime from the liberated electron. The higher the energy, the longer the lifetime, and therefore the larger the FWHM [63]. This is difficult to achieve for the C=O peak relative to the C-O peak, so the FWHM values have been constrained as equal.

With all carbon signals for being fitted with three peaks, two of which being oxy-carbon peaks, all of the oxygen 1s signals must contain oxy-carbon contributions that must be considered when fitting peaks for the bridging oxygen and non-bridging oxygen. The component areas for the oxy-carbon contributions were calculated using equation 6.3b. Equations 6.3a and 6.3b were used on the assumption that the atomic ratio between the

oxygen and carbon was assumed to be 1:1 (one oxygen atom and one carbon atom per oxy-carbon bond, regardless of single or double bonding).

$$X = \frac{\left({}^{A_c}/_{R_c}\right)}{\left({}^{A_c}/_{R_c}\right) + \left({}^{A_o}/_{R_o}\right)} \quad \text{(Eq. 6.3a)}$$

Rearranged to:

$$A_o = \frac{R_o(1-X)A_c}{XR_c} \quad \text{(Eq. 6.3b)}$$

Where X is the atomic fraction (which is 0.5 for both oxygen and carbon), A is the peak intensity and R is the relative sensitivity factor (R.S.F.). The subscript o and c denote whether A or R refers to the oxygen or carbon.

The RSF values were taken from the CasaXPS software Kratos database for each of the O 1s and C 1s signals. The A_c values were taken from the peak areas from the C 1s fits. The A_o values were calculated for both bond types and were used to constrain the C-O and C=O component areas for the O 1s signals.

The oxygen 1s signal was ultimately fit with 5 peaks; 1 peak for the bridging oxygens, 1 peak for the non-bridging oxygens (the two primary types of oxygen found in the glass network, see Chapter 2 for more information), 1 peak for a sodium Auger or bonded water (the specific sodium Auger electron signal is seen when using Al Kα sources, example ref [71]), 1 peak for the C-O bonds, and 1 peak for the C=O, both of which must be present in the O 1s spectra, as they are present in the C 1s spectra. The positions of each peak were constrained in accordance with previous work done by the likes of Miura et al. [71], Mekki et al. [77,78], and others [66-69,72,75]. The FWHM values were constrained such that the higher the binding energy of the component, the larger the FWHM, for same reason outlined with the C 1s fits. Area standard deviations were calculated using Monte Carlo error analysis, in which 200 simulations were run using the peak position and FWHM constraints.

When selecting peak binding energy positions, research that specifically investigated the C 1s spectrum in other materials [90-93] suggested that the C=O bond is the higher energy oxy-carbon bond, and therefore has been assigned as such in the fits of the C 1s spectra in this work. The corresponding fitted O 1s spectrum can be seen in **Fig 6.18**.

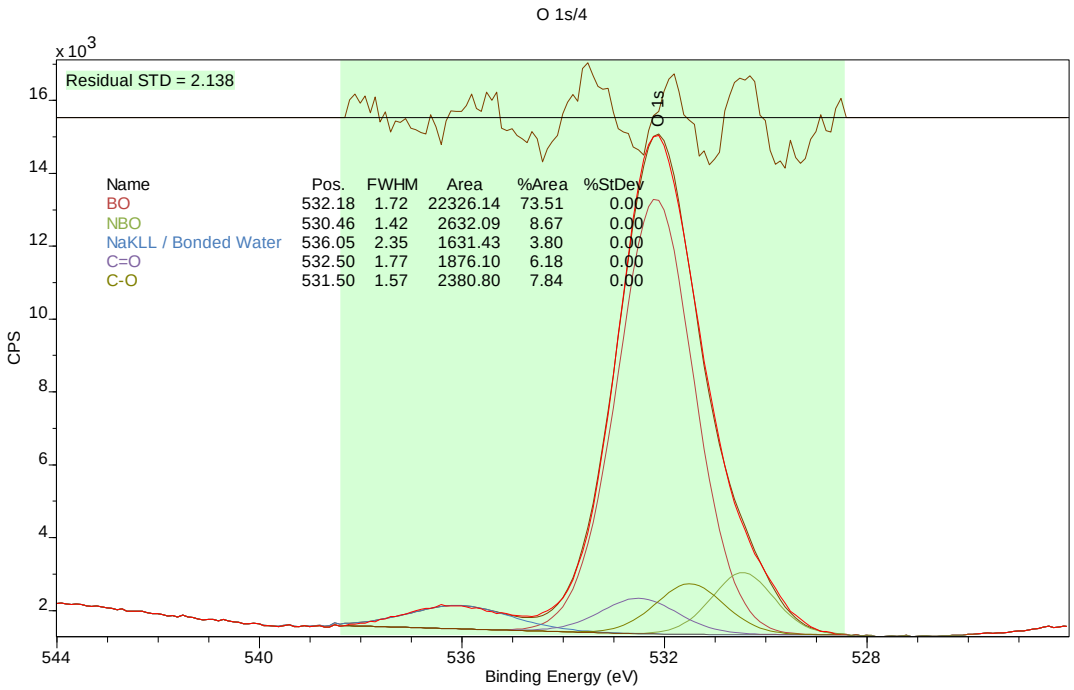

Figure 6.18: *The peak fitted O 1s spectrum for the SCFe000.0 sample. The C-O and C=O peaks can be seen alongside the BO and NBO peaks as well as a sodium Auger peak.*

In this example, the NBO and BO contributions can still be estimated from the spectrum, however, this is not true for all samples.

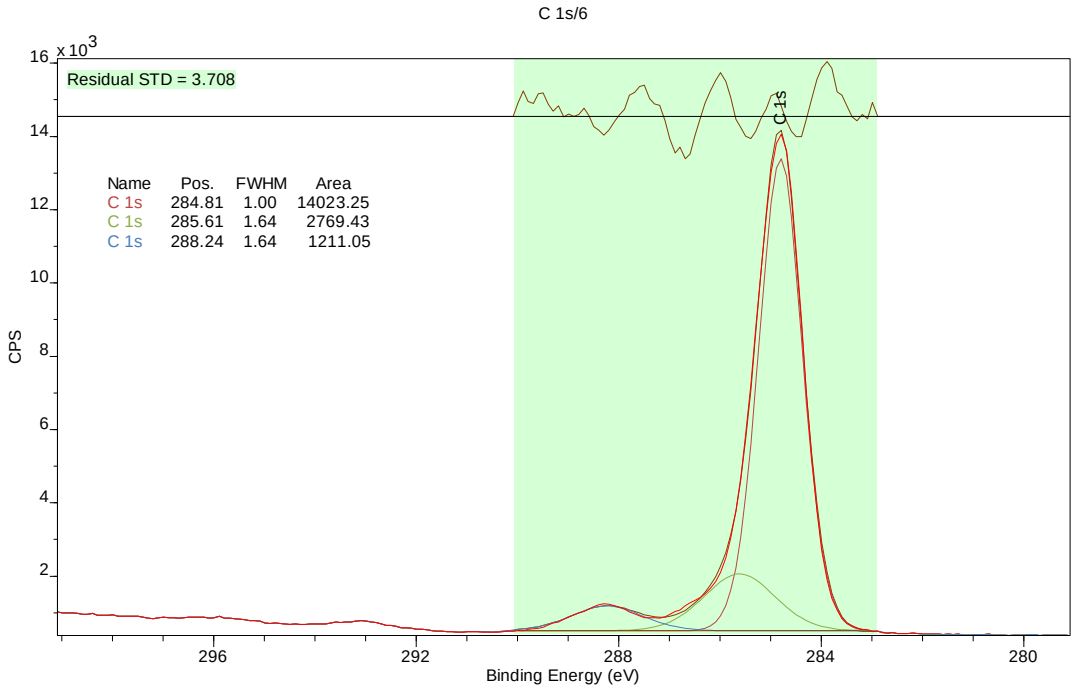

Figure 6.19: *The peak fitted C 1s spectrum for the SCFe000.1 sample showing the C-C, C-O, and C=O peaks.*

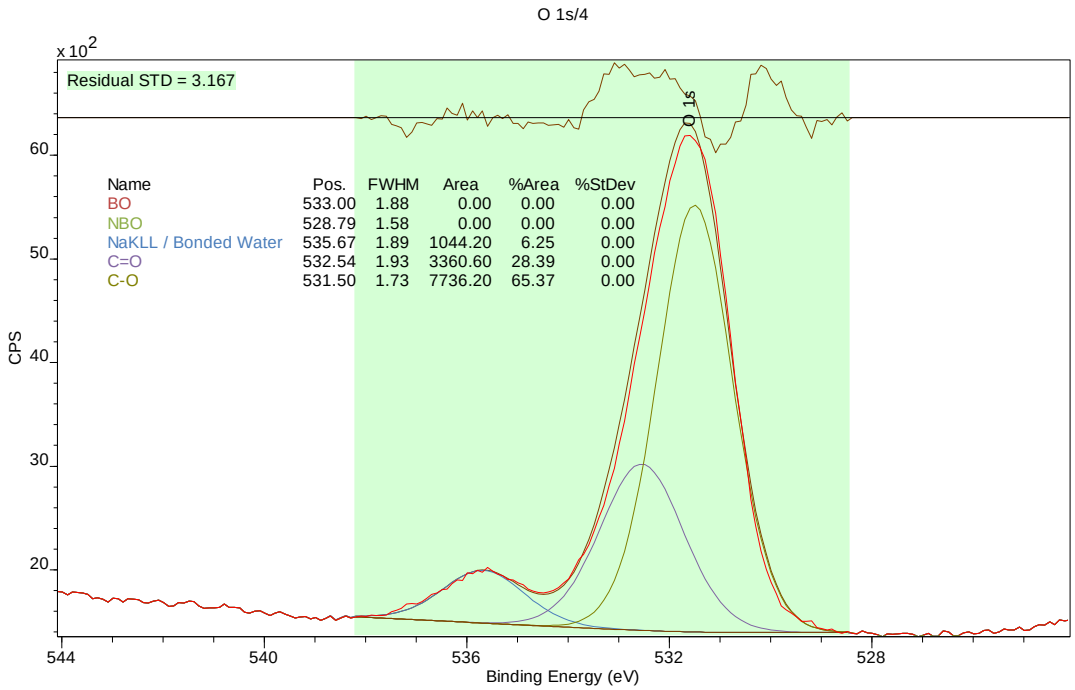

Figure 6.20: *The peak fitted O 1s spectrum for the SCFe000.1 sample. Note that no contributions were possible for the bridging and non-bridging oxygens within the spectrum.*

Figures 6.19 and **6.20** show the C 1s and associated O 1s fits where the C-O and C=O contributions dominate the O 1s spectrum. The relative areas of the NBO and BO oxygen contributions are influenced inconsistently across the series as a result of the oxy-carbon contributions and therefore analysis of the NBO and BO fractions within both the SCFe and CCFe series was not pursued with data presented. The rest of the peak fitted C 1s and O 1s spectra for the SCFe series can be found in the appendix (**Fig A6.1 – A6.10**).

6.6.3 B 1s and Si 2p Analysis

While the O 1s data was influenced by oxy-carbon contributions, the boron and silicon signals were thought to be unaffected by surface contamination (there was no evidence of any boron- or silicon-based surface contaminants). **Figures 6.21** and **6.22** show the stack plots of the B 1s and Si 2p respectively (plotted in OriginPro rather than CasaXPS).

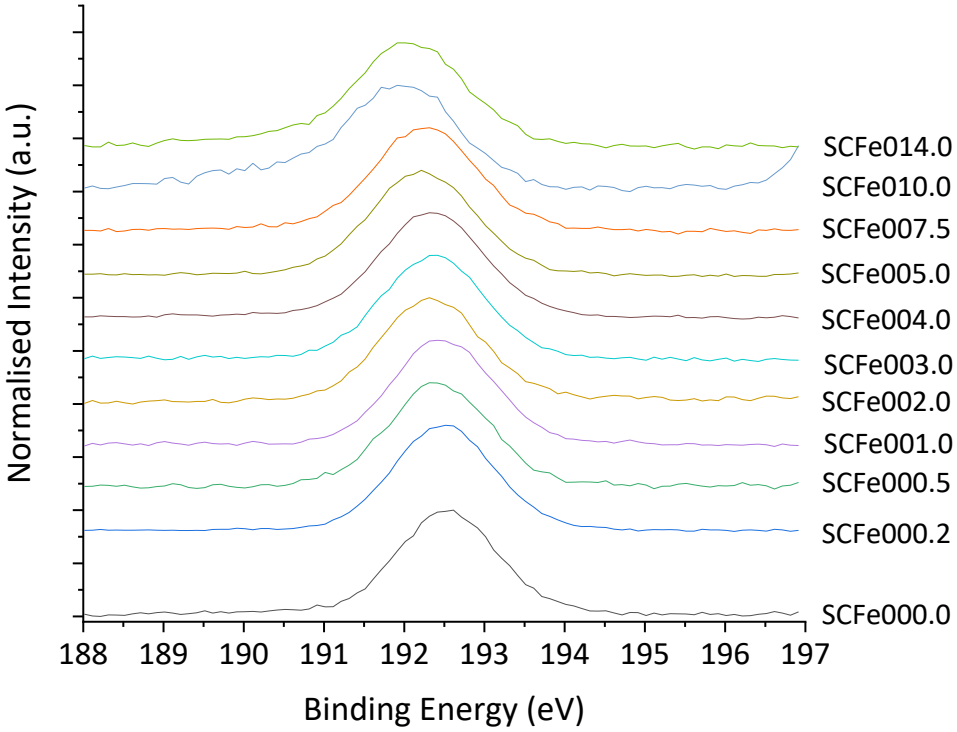

Figure 6.21: *SCFe sample series stack plot of the B 1s spectra.*

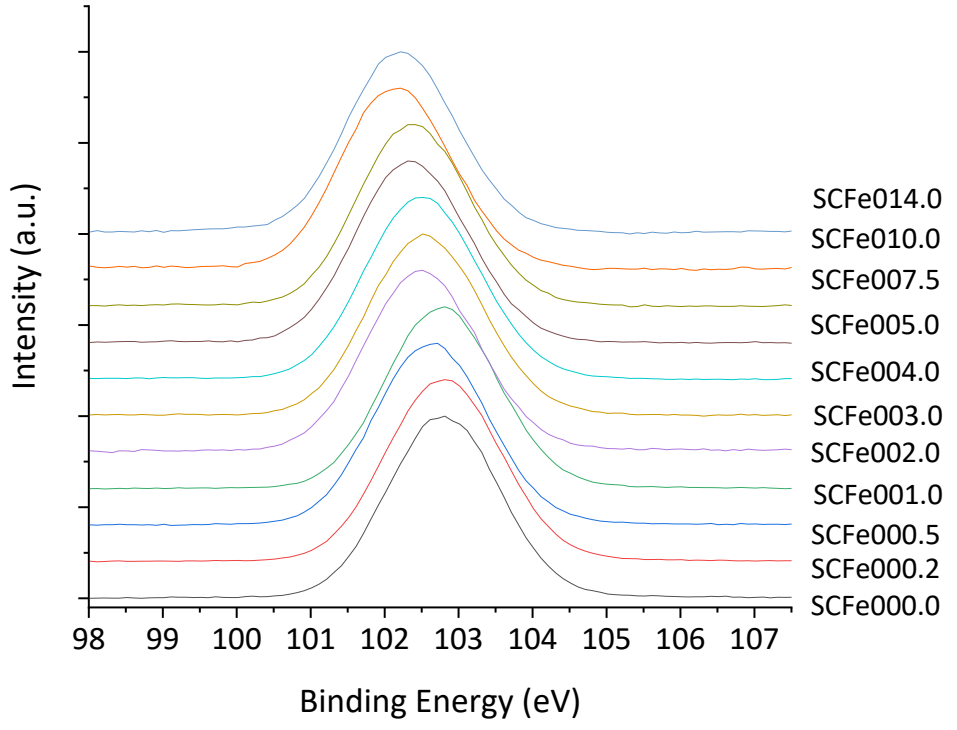

Figure 6.22: *SCFe sample series stack plot of the Si 2p spectra.*

For both the B 1s and Si 2p spectral series, there appears to be a gradual shift to a lower binding energy as the series progresses, essentially, as a function of Fe_2O_3 contents within the glass. This is explored further in Chapter 7.9.2.

6.7 Results - CCFe series

6.7.1 Overview

Similar to the SCFe series, a survey scan was carried out to identify the target energies. This scan be seen in **Fig. 6.23**,

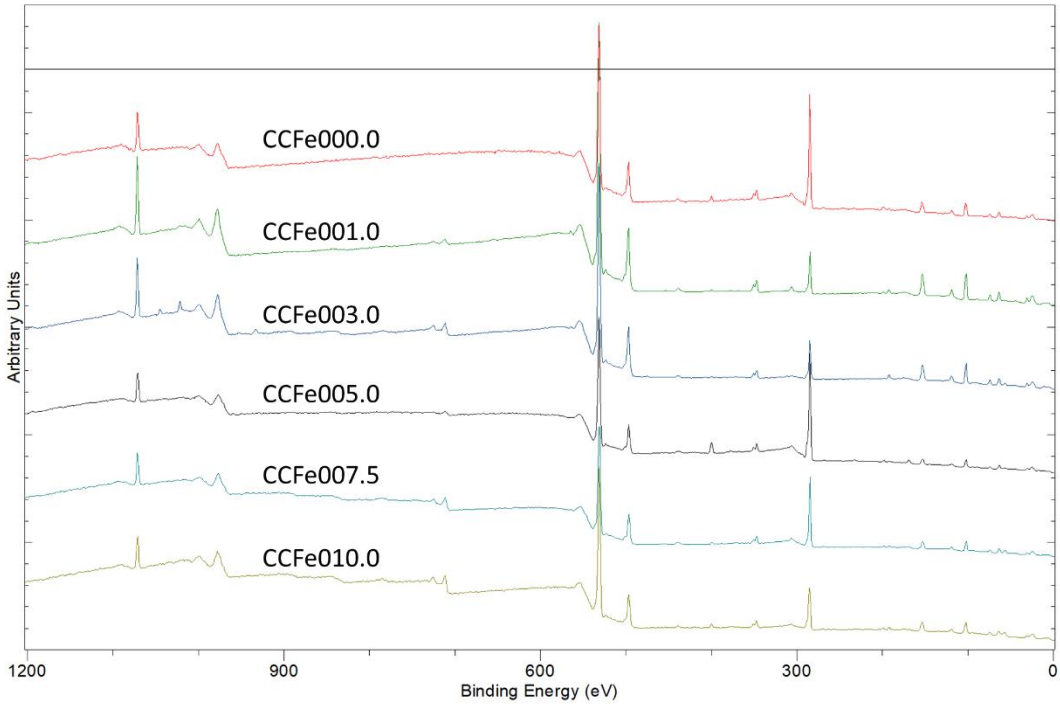

Figure 6.23: *The stack plot of the survey scans for the CCFe sample series.*

The target energy ranges can be found in Chapter 4.2.4 and the method in which the subsequent spectra were calibrated using the C 1s spectra using the details in Chapter 4.2.4.

6.7.2 Oxy-Carbon Analysis

While the peak fitting to the C 1s and O 1s spectra was carried out for the CCFe series, the same issues found in the SCFe series was seen in the CCFe series. Therefore the Oxy-Carbon analysis was not pursued for the CCFe series either. However, all peak fitted O 1s and C 1s spectra for the CCFe series can be found in the appendix (**Figs A6.11 – A6.16**).

6.7.3 B 1s and Si 2p Analysis

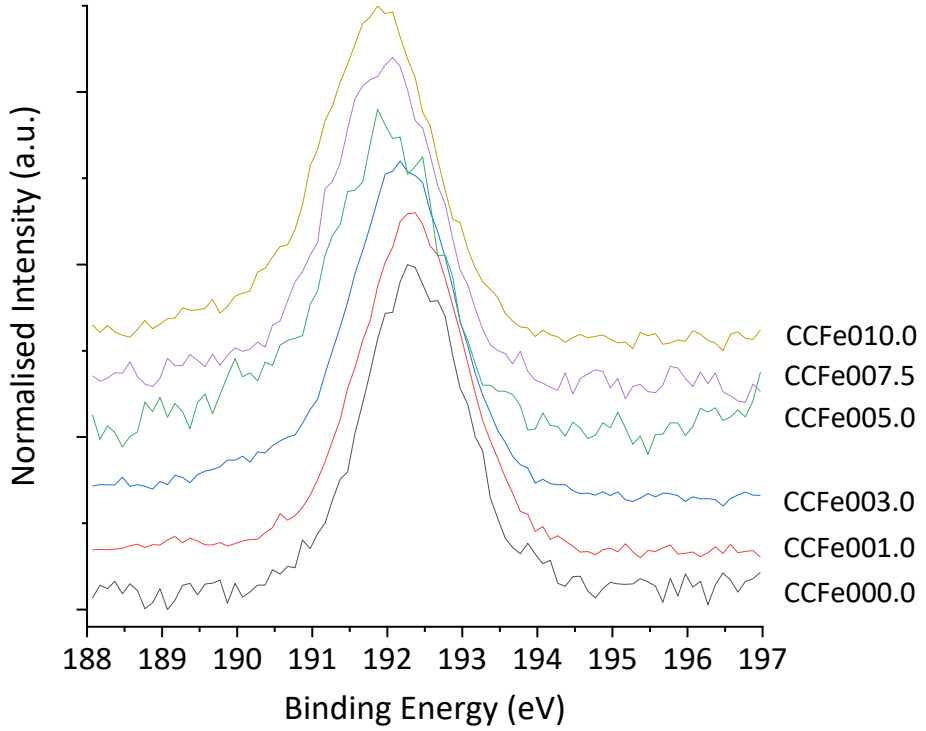

Figure 6.24: *CCFe sample series stack plot of the B 1s spectra.*

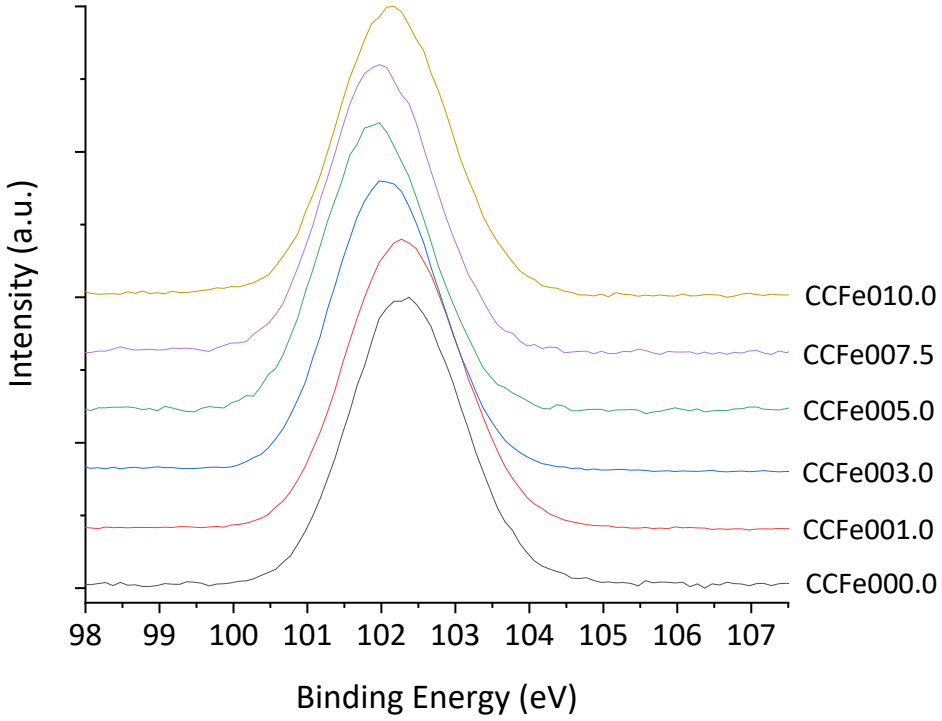

Figure 6.25: *CCFe sample series stack plot of the Si 2p spectra.*

The stack plots for the B 1s and Si 2p can be seen in **Figs 6.24** & **6.25**. Similar to the Si 2p and B 1s spectra for the SCFe series, there is an apparent decrease in binding energy as a function of increasing Fe_2O_3.

6.8 Discussion

6.8.1 XPS - Oxy-Carbon Analysis

The original intention was to use the O 1s spectra to determine values for the BO / NBO ratios for each glass sample for the SCFe and CCFe series. This would have been in line with works by Mekki *et al*. [67,68], Holland *et al*. [69], and Miura *et al*. [71]. However, unlike those works, in the preparation and data acquisition there was a key difference between this research and the referenced research. In previous work on XPS in glass [67-69,71], each sample is fractured in an ultra-high vacuum to produce a fresh surface to analyse that should be free from atmospheric contamination, or at the very least, have less atmospheric surface contamination than a non-freshly exposed surface. This is specifically to reduce the carbon- and oxygen-based contamination that would otherwise interfere with the C 1s and O 1s spectra [67-69,71]. This step was not done in this research, due to the fact that it was not possible to fracture the samples with the set up available. Argon ion etching is another technique considered that has been done to create a measurable surface, but this technique was ultimately not considered due to the potential it has to alter the chemistry of the measured sample [68,94].

In not carrying out this step, the O 1s spectra for all measured samples was inconsistently affected by surface oxy-carbon contaminants, likely through simple atmospheric contamination. Owing to the sensitivity of XPS as a technique, this atmospheric contamination rendered it difficult to acquire reliable BO / NBO ratios for the measured samples across both series. While for most samples, a ratio *could* be calculated (see appendix **Figs A6.1 – A6.16**), they would likely be indefensible under scrutiny and would need to be re-measured as a result. As such, they have not been considered in the conclusions drawn in this research.

6.8.2 XPS – B 1s and Si 2p Analysis

Despite the O 1s spectra showing surface contamination, other target spectra were not showing signs of contamination. The B 1s and Si 2p were selected for further analysis as they represent two of the main glass forming cations within the borosilicate network. The Fe 2p and Fe 3p signals were not selected as the quality of analysis would unlikely surpass that of the Mössbauer and Fe K-edge XANES spectroscopies (see Chapter 5 & 6 for more details).

For the B 1s signal, each sample spectra were fitted with a single Gaussian peak, with the peak centre plotted against analysed Fe_2O_3 content for the sample. This was carried out for both the SCFe and CCFe series, with the resulting plot seen in **Fig 6.26**.

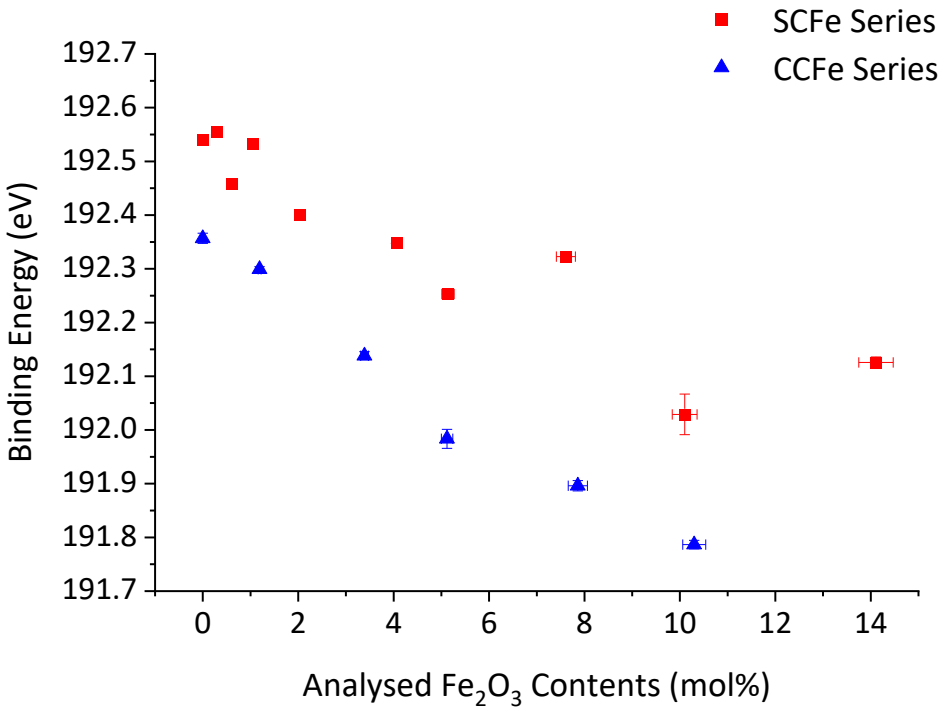

Figure 6.26: *The plot of the B 1s binding energies of the SCFe and CCFe sample series as a function of analysis Fe_2O_3 contents.*

Similarly, this was carried out for the Si 2p spectra. When peak fitting any 2p spectra, it typically requires two peaks to be fitted, for the two separate electron spin configurations, 1/2 and 3/2. The two peaks always have area ratio of 2:1 with the higher spin with the lower area, with a fixed energy difference between the two peaks. The energy difference is directly linked to the target element and in the case of Si 2p, the energy difference is 0.6 eV [95] between the 1/2 and 3/2 peaks in the 2p spectra. In theory, each spectrum should be fit with two peaks with the 1:2 area ratio that are 0.6 eV apart [95]. However, it is often seen in 2p spectra with a low energy separation, that one peak is used to represent the 2p signal [63]. As such, this is what has been done in this research.

As with the B 1s peaks, the peak centre for both series was plotted against analysed Fe_2O_3 contents and can be seen in **Fig 6.27**.

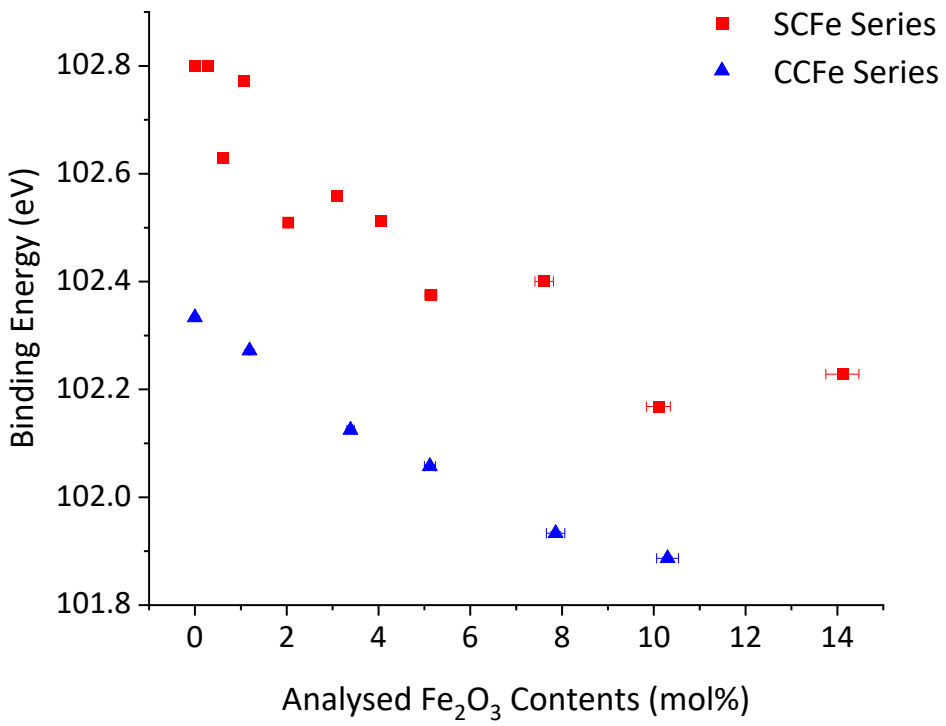

Figure 6.27: *The plot of the Si 2p binding energies of the SCFe and CCFe sample series as a function of analysis Fe_2O_3 contents.*

The plots of both the B 1s and Si 2p binding energies, match up with what the stack plots of the spectra showed – the binding energy decreased as the concentration of Fe_2O_3 increased within the glass.

Table 6.3: The difference in binding energy between the two end members of each series.

XPS Signal	Binding Energy Changes SCFe Series (eV)	Binding Energy Changes CCFe Series (eV)
B 1s	-0.414 (± 0.014)	-0.570 (± 0.018)
Si 2p	-0.571 (± 0.003)	-0.447 (± 0.005)

It can be seen in **Table 6.3**, that within the SCFe series, the Si 2p signal shows a greater reduction in binding energy than the reduction seen in the B 1s signal, whereas the opposite is true for the CCFe series. When considering previous work, such at works by Brow & Pantano [85,86], Clarke & Rizkalla [96], Veal *et al*. [97], and Hsieh *et al*. [66], the binding energy of the target components is linked to the effective charge of the cation. The change in binding energy is proportional to the change in effective charge, which in turn is linked to the change in electronegativity. This change is sensitive to the nearest neighbouring atoms around the target cation. In simpler compositions [66,85,86,96], these changes can be used to calculate change in bond configurations as a function of

compositional changes, however, the glasses studied in this research, are too complex to apply this level quantitative analysis. Mekki *et al*. [67] showed that as iron increased in silicate glasses there was a corresponding decrease in the Si 2p binding energy which was hypothesised to be linked to a reduction in bridging oxygens around the silicate tetrahedra, resulting in fewer covalent bonds and a corresponding reduction in binding energy [67]. Holland *et al*. [69] further developed this by demonstrating that the Si-O-Fe has a contribution in the O 1s spectra, and it was shown to have a higher binding energy than the Si-O-Na contribution, but a lower binding energy than the Si-O-Si contribution. This suggests that the Si-O-Fe has a lower covalent character than the Si-O-Si, which is in line with Stanworth's rules [98] on the covalent character of glass forming bonds when compared to the covalent character of glass network intermediate bonds (see Chapter 2 for more information).

Within the context of this research, it is clear that the binding energy of the B 1s and Si 2p electrons decreases with increasing Fe_2O_3 content, which suggests a decrease in covalent bonds or an increase in ionic bonds around these cations. It is likely due to the increase in Si-O-Fe and B-O-Fe bonds, which are higher in ionic character as shown using equation 6.4 below:

$$f = 1 - \frac{R_i}{M_i}(e^{(-0.25(\Delta\chi^2)}) \qquad \text{(Eq. 6.4)}$$

Where R_i is the cation valency, M_i is the cation coordination, $\Delta\chi$ is the difference in electronegativity between the cation and anion (in this case, oxygen). This version of the equation was taken from Brow and Pantano [85,86], as it includes a coordination factor (R_i / M_i). Using the values found in **Table 6.4**, the fractional ionic character for the Si-O, Fe-O, and B-O bonds are calculated and shown in **Table 6.5**.

Table 6.4: The various values that were used in equation 6.4 that calculated the values for fractional ionic character of the bonds.

Element	**Electronegativity [99]**	**Valency**	**Coordination**
Si	1.90	4+	4
B	2.04	3+	3.45*
Fe	1.83	3+**	4**
O	3.50	N/A***	N/A***

* *Value used derived from B K-edge XANES data for the SCFe series. The data showed the $^{[4]}$B abundance at approximately 45%.*

** *Values derived from Mössbauer and Fe K-edge XANES data. No quantitative analysis available for the coordination number, so far now, it is assumed to be 4.*

*** *Equation 6.4 does not consider the anion valency or coordination.*

Table 6.5: The calculated fractional ionic character of the Si-O, B-O, and Fe-O bonds.

Bond Type	**Fractional ionic character, *f***
Si-O	0.47
B-O	0.47
Fe-O	0.61

The fractional ionic characters of the bonds show the Fe-O bonds to have a higher ionic character. As the oxygen has the greater electronegativity, it would suggest that oxygen has a greater pull of the electrons within that bond. If this view of ionicity is considered and expanded, the hypotheses seen in Holland *et al*. [69] can be applied to this research. A Si-O-Si bond group will have the same ionic character "either side" of the oxygen. If one of the Si cations is replaced by an Fe cation, to make an Si-O-Fe bond group, the overall ionic character is different. If the oxygen is able to attract more electron density towards it in the O-Fe bond, then this will lower its electron attractiveness in the Si-O bond, by virtue of having a greater negative charge density around the oxygen as a result of the Fe-O bond. This means a slight increase in negative charge density around the Si cation, which in turn, would lower the binding energy of the electrons around the Si atom in this system. A visual representation of this can be seen in **Fig 6.28**.

Figure 6.28: *A visual representation of the Si-O-Si and Si-O-Fe bonds. In the Si-O-Si, the oxygen will have the same attractive power on the electrons in bonds "a" and "b". In the Si-O-Fe, if the oxygen has a greater attraction of electrons in the Fe-O bond (bond "b"), then in theory, the electron attractive power of the oxygen in bond "a" will reduce due to the increase in negative charge density around the oxygen from bond "b", causing comparatively more negative charge density around the Si cation.*

When considering the decrease in binding energy of the Si 2p and B 1s electrons in the XPS data as a function of increase Fe_2O_3 contents within the glass, this phenomenon goes some way towards explaining what happens within this research.

However, these are unlikely to be the only metaphorical "moving parts" within these compositional changes, and as such, this analysis approach should be treated as qualitative rather than quantitative. The difference in wider series composition will also provide its own influences within these spectra. Such as the Al-O bonds, and the inclusion of two more network modifiers in CaO and Li_2O, which have been reported to have unique influences within glass compositions, specifically around iron oxide within glass [60,100]. However, the only compositional change that occurs within the series, is the Fe_2O_3 within the series, and at the very least, in a *strictly* qualitative sense, it has been demonstrated that the Fe has a greater influence on the borate sub-network in a more complex composition, while influencing the silicate sub-network in a simpler system.

6.9 Summary

When looking at the Raman and XPS data as a combined entity, there is a common trend in the borate-based data. The Raman spectroscopy shows that as the composition of the series becomes more complex, the relative intensities of the change in borate bands increases. This is reflected in the Si 2p and B 1s data for the two series, where the Si 2p shows the greatest overall decrease in the SCFe series, but in the CCFe series the B 1s shows the greatest overall decrease. The specific borate Raman band that shows the greatest change is the increase in intensity of "loose" BO_3. If the decrease in binding energy is linked to the decrease in covalency around the boron cations, the increase in intensity for the "loose" BO_3 bands would suggest the metaborate structures are being

broken up with the integrate of Fe cations, resulting in more BO_3 units bonded outside of the metaborate structures.

However, for the simpler series, there is a less pronounced impact on the borate groups and more of an impact on the silicate groups. This is in line with a study by Wright *et al*. [101] which studied the environments of Fe^{3+} and Fe^{2+} cations within borosilicate glass. This research found that tetrahedral Fe^{3+} would preferentially bond into the silicate sub-network, which is seen in this research. Octahedral Fe^{3+} would integrate within the borate network with inclusions of Fe^{2+} and potentially $^{[5]}Fe^{3+}$. However, this study by Wright *et al*. [101] also suggests that the iron tetrahedra incorporate into the borosilicate glass network through conversion of BO_4 to BO_3 units. While this is somewhat supported by the Raman bands in the borate group, this not supported by the B K-edge XANES as there is very little conversion from tetrahedral boron to trigonal boron. While there is some evidence to suggest there is octahedral Fe^{3+} within the glass samples, there is more evidence to suggest that the Fe^{3+} exists predominantly as tetrahedral Fe^{3+}. So while the theory put forth by Wright *et al*. [101] on the integration of the Fe cations through both the silicate and borate network being dependant on coordination number, there is evidence in this research to suggest that this does not fully explain what is seen in this chapter. Further elaboration can be found in chapter 8

6.10 References

[1] Long, D. A., Raman Spectroscopy, McGraw-Hill Inc., London, UK, 1977.

[2] Shuker, R., & Gammon, R. W., Raman-scattering selection-rule breaking and the density of states in amorphous materials, *Phys. Rev. Lett.*, **25**, 1970; pp 222-225.

[3] Galeener, S. L., & Sen, N. P., Theory for the first-order vibrational spectra of disordered solids, *Phys. Rev. B*, **17**, 1978; pp 1928-1933.

[4] Neuville, D. R., & Mysen, B. O., Role of aluminium in the silicate network: In situ, high-temperature study of glasses and melts on the join SiO_2-$NaAlO_2$, *Geochim. Cosmochim. Acta*, **60**, 1996; pp 1727-1737.

[5] Le Losq, C., Neuville, D. R., Florian, P., Henderson, G. S., & Massiot, D., The role of Al^{3+} on rheology and structural changes in sodium silicate and aluminosilicate glasses and melts, *Geochim. Cosmochim. Acta*, **126**, 2014; pp 496-517.

[6] Konijnendijk, W. L., & Stevels, J. M., The structure of borate glasses studied by Raman scattering, *J. Non-Cryst. Solids*, **18**, 1975; pp 307-331.

[7] Meera, B. N., Sood, A. K., Chandrabhas, N., & Ramakrishna, J., Raman study of lead borate glasses, *J. Non-Cryst. Solids*, **126**, 1990; pp 224-230.

[8] Meera, B. N., & Ramakrishna, J., Raman spectral studies of borate glasses, *J. Non-Cryst. Solids*, **159**, 1993; pp 1-21.

[9] Yiannopoulas, Y. D., Chryssikos, G. D., & Kamitsos, E. I., Structure and properties of alkaline earth borate glasses, *Phys. Chem. Glasses*, **42**, 2001; pp 164-172.

[10] Akagi, R., Ohtori, N., & Umesaki, N., Raman spectra of K_2O-B_2O_3 glasses and melts, *J. Non-Cryst. Solids*, **293-295**, 2001; pp 471-476.

[11] Yano, T., Kunimine, N., Shibata, S., & Yamane, M., Structural investigation of sodium borate glasses and melts by Raman spectroscopy. I. Quantitative evaluation of structural units, *J. Non-Cryst. Solids*, **321**, 2003; pp 137-146.

[12] Yano, T., Kunimine, N., Shibata, S., & Yamane, M., Structural investigation of sodium borate glasses and melts by Raman spectroscopy. II. Conversion between BO_4 and BO_2O- units at high temperature, *J. Non-Cryst. Solids*, **321**, 2003; pp 147-156.

[13] Yano, T., Kunimine, N., Shibata, S., & Yamane, M., Structural investigation of sodium borate glasses and melts by Raman spectroscopy. III. Relation between the rearrangement of super-structures and the properties of glass, *J. Non-Cryst. Solids*, **321**, 2003; pp 157-168.

[14] Cormier, L., Meneses, D. D. S., Neuville, D. R., & Echegut, P., In situ evolution of the structure of alkali borate glasses and melts by infrared reflectance and Raman spectroscopies, *Phys. Chem. Glasses: Eur. J. Glass Sci. Technol. B*, **47**, 2006; pp 430-434.

[15] Markova, T. S., Yanush, O. V., Polyakova, I. G., & Pevzner, B. Z., Glass property calculations and prediction of new compounds on the basis of raman spectroscopy of borate glasses, *Phys. Chem. Glasses: Eur. J. Glass Sci. Technol. B*, **47**, 2006; pp 476-483.

[16] Vacher, R., Rufflé, B., Hehlen, B., Guimbrètiere, G., Simon, G., & Courtens, E., The vibrational excitations of glasses in the boson-peak region: Application to borates, *Phys. Chem. Glasses: Eur. J. Glass Sci. Technol. B*, **49**, 2008; pp 19-25.

[17] Pascuta, P., Lungu, R., & Ardelean, I., FTIR and Raman spectroscopic investigation of some strontium-borate glasses doped with iron ions, *J. Mater. Sci. Electron.*, **21**, 2010; pp 548-553.

[18] Osipov, A. A., & Osipova, L. M., Low frequency Raman scattering in the $BaO\text{-}B_2O_3$ glasses: The effect of temperature, *Phys. Chem. Glasses: Eur. J. Glass Sci. Technol. B*, **56**, 2015; pp 53-58.

[19] Galeener, S. L., Band limits and the vibrational spectra of tetrahedral glasses, *Phys. Rev. B*, **19**, 1979; pp 4292-4297.

[20] Mysen, B. O., Finger, L. W., Virgo, D., & Seifert, F. A., Curve-fitting of Raman spectra of silicate glasses, *Am. Mineral.*, **67**, 1982; pp 686-695.

[21] Matson, D. W., & Sharma, S. K., & Philpotts, J. A., The structure of high-silica alkali-silicate glasses. A Raman spectroscopic investigation, *J. Non-Cryst. Solids*, **58**, 1983; pp 323-352.

[22] Kamitsos, E. I., & Risen Jr., W. M., Vibrational spectra of single and mixed alkali pentasilicate glasses, *J. Non-Cryst. Solids*, **65**, 1984; pp 333-354.

[23] Luth, R. W., Raman spectroscopic study of the solubility mechanisms of fluorine in glasses in the system $CaO\text{-}CaF_2\text{-}SiO_2$, *Am. Mineral.*, **73**, 1988; pp 297-305.

[24] Fukumi, K., Hayakawa, J., & Komiyama, T., Intensity of Raman band in silicate glasses, *J. Non-Cryst. Solids*, **119**, 1990; pp 297-302.

[25] Wang, Z., Cooney, T. F., & Sharma, S. K., In situ structural investigation of iron-containing silicate liquids and glasses, *Geochim. Cosmochim. Acta*, **59**, 1995; pp 1571-1577.

[26] Soltay, L. G., & Henderson, G. S., Structural differences between lithium silicate and lithium germanate glasses by Raman spectroscopy, *Phys. Chem. Glasses*, **46**, 2005; pp 381-384.

[27] Magnien, V., Neuville, D. R., Cormier, L., Roux, J., Hazemann, J.-L., Pinet, O., & Richet, P., Kinetics of iron redox reactions in silicate liquids: A high-temperature X-ray absorption and Raman spectroscopy study, *J. Nucl. Mater.*, **352**, 2006; pp 190-195.

[28] Neuville, D. R., Viscosity, structure and mixing in (Ca, Na) silicate melts, *Chem. Geol.*, **229**, 2006; pp 28-41.

[29] Manara, D., Grandjean, A., Pinet, O., Dussossoy, J. L., & Neuville, D. R., Sulfur behavior in silicate glasses and melts: Implications for sulfate incorporation in nuclear waste glasses as a function of alkali cation and V_2O_5 content, *J. Non-Cryst. Solids*, **353**, 2007; pp 12-23.

[30] Magnien, V., Neuville, D. R., Cormier, L., Roux, J., Hazemann, J.-L., de Ligny, D., Pascarelli, S., Vickridge, I., Pinet, O., & Richet, P., Kinetics and mechanisms of iron redox reactions in silicate melts: The effects of temperature and alkali cations, *Geochim., Cosmochim. Acta*, **72**, 2008; pp 2157-2168.

[31] Malfait, W. J., & Halter, W. E., Structural relaxation in silicate glasses and melts: High-temperature Raman spectroscopy, *Phys. Rev. B*, **77**, 2008.

[32] Parkinson, B. G., Holland, D., Smith, M. E., Larson, C., Doerr, J., Affatigato, M., Feller, S. A., Howes, A. P., & Scales, C. R., Quantitative measurement of Q^3 species in silicate and borosilicate glasses using Raman spectroscopy, *J. Non-Cryst. Solids*, **354**, 2008; pp 1936-1942.

[33] Koroleva, O. N., Anfilogov, V. N., Shatskiy, A., & Litasov, K. D., Structure of Na_2O-SiO_2 melt as a function of composition: In situ Raman spectroscopic study, *J. Non-Cryst. Solids*, **375**, 2013; pp 62-68.

[34] Hehlen, B., & Neuville, D. R., Raman response of network modifier cations in alumino-silicate glasses, *J. Phys. Chem. B*, **119**, 2015; pp 4093-4098.

[35] Osipov, A., Osipova, L., & Zainullina, R., Raman spectroscopy and statistical a analysis of the silicate species and group connectivity in cesium silicate glass forming system, *Int. J. Spectrosc.*, **2015**, 2015.

[36] Nesbitt, H. W., Henderson, G. S., Bancroft, G. M., & O'Shaughnessy, C., Electron densities over Si and O atoms of tetrahedra and their impact on Raman stretching frequencies and Si-NBO force constants, *Chem. Geol.*, **461**, 2017; pp 65-74.

[37] Bancroft, G. M., Nesbitt, H. W., Henderson, G. S., O'Shaughnessy, C., Withers, A. C., & Neuville, D. R., Lorentzian dominated lineshapes and linewidths for Raman symmetric stretch peaks (800–1200 cm^{-1}) in Q^n (n = 1–3) species of alkali silicate glasses/melts, *J Non-Cryst. Solids*, **484**, 2019; pp 72-83.

[38] Kim, H.-I., & Lee, S. K., The degree of polymerization and structural disorder in $(Mg,Fe)SiO_3$ glasses and melts: Insights from high-resolution ^{29}Si and ^{17}O solid-state NMR, *Geochim. Cosmochim. Acta*, **250**, 2019; pp 268-291.

[39] O'Shaughnessy, C., Henderson, G. S., Nesbitt, H. W., Bancroft, G. M., & Neuville, D. R., The influence of modifier cations on the Raman stretching modes of Q^n species in alkali silicate glasses, *J. Am. Ceram. Soc.*, Special Issue Article, 2020.

[40] McKeown, D. A., Muller, I. S., Buechele, A. C., Pegg, I. L., & Kendziora, C. A., Structural characterization of high-zirconia borosilicate glasses using Raman spectroscopy, *J. Non-Cryst. Solids*, **262**, 2000; pp 126-134.

[41] McKeown, D. A., Muller, I. S., Gan, H., Pegg, I. L., & Kendziora, C. A., Raman studies of sulfur in borosilicate waste glasses: Sulfate environments, *J. Non-Cryst. Solids*, **288**, 2001; pp 191-199.

[42] Raman, S. V., Zareba, A. A., & Czernuszewicz, R. S., Composition dependent analysis of Raman spectra in the modified boroaluminosilicate system: Implications for coupling between structural resonance and relaxation in the glass network, *Phys. Chem. Glasses*, **45**, 2004; pp 328-342.

[43] Grandjean, A., Malki, M., Simonnet, C., Manara, D., & Penelon, B., Correlation between electrical conductivity, viscosity, and structure in borosilicate glass-forming melts, *Phys. Rev. B*, **75**, 2007.

[44] Lenoir, M., Grandjean, A., Linard, Y., Cochain, B., & Neuville, D. R., The influence of Si,B substitution and of the nature of network-modifying cations on the properties and structure of borosilicate glasses and melts, *Chem. Geol.*, **256**, 2008; pp 316-325.

[45] Cochain, B., Neuville, D. R., Henderson, G. S., Pinet, O., & Richet, P., Determination of iron redox ratio in borosilicate glasses and melts from Raman spectra, *Atalante*, 2008.

[46] Manara, D., Grandjean, A., Neuville, D. R., Advances in understanding the structure of borosilicate glasses: A Raman spectroscopy study, *Am. Mineral*., **94**, 2009; pp 777-784.

[47] Möncke, D., Dussauze, M., Kamitsos, E. I., Varsamis, C. P. E., & Ehrt, D., Thermal poling induced structural changes in sodium borosilicate glasses, *Phys. Chem. Glasses: Eur. J. Glass Sci. Technol. B*, **50**, 2009; pp 226-235.

[48] Koroleva, O. N., Shabunina, L. A., & Bykov, V. N., Structure of borosilicate glass according to Raman spectroscopy data, *Glass Ceram. (Translated from Steklo i Keramika)*, **67**, 2011; pp 340-342.

[49] Cochain, B., Neuville, D. R., Henderson, G. S., McCammon, C. A., Pinet, O., & Richet, P., Effects of the iron content and redox state on the structure of sodium borosilicate glasses: A Raman, Mössbauer and boron K-edge XANES spectroscopy study, *J. Am. Ceram. Soc*., **95**, 2012; pp 962-971.

[50] Stefanovsky, S. V., Fox, K. M., Marra, J. C., Shirayaev, A. A., & Zubavichus, Y. V., Structural features of high-Fe_2O_3 and high-Al_2O_3/Fe_2O_3 SRS HLW glasses, *Phys. Chem. Glasses: Eur. J. Glass Sci. Technol. B*, **53**, 2012; pp 158-166.

[51] Koroleva, O. N., & Shabunina, L. A., Effect of the ratio R = [Na_2O]/[B_2O_3] on the structure of glass in the Na_2O-B_2O_3-SiO_2 system, *Rus. J. Gen. Chem.*, **83**, 2013; pp 238-244.

[52] Winterstein-Beckmann, A., Möncke, D., Palles, D., Kamitsos, E. I., & Wondraczek, I., A Raman-spectroscopic study of indentation-induced structural changes in technical alkali-borosilicate glasses with varying silicate network connectivity, *J. Non-Cryst. Solids*, **405**, 2014; pp 196-206.

[53] McKeown, D. A., Gan, H., & Pegg, I. L., X-ray absorption and Raman spectroscopy studies of molybdenum environments in borosilicate waste glasses, *J. Nucl. Mater.*, **488**, 2017; pp 143-149.

[54] Moguš-Milanković, A., Gajović, A., Šantić, A., & Day, D. E., Structure of sodium phosphate glasses containing Al_2O_3 and/or Fe_2O_3. Part I, *J. Non-Cryst. Solids*, **289**, 2001; pp 204-213.

[55] Rivero, C., Richardson, K., Stegeman, R., Stegeman, G., Cardinal, T., Fargin, E., & Couzi, M., Characterisation of the performance parameters of some new broadband glasses for Raman amplification, *Glass Technol.*, **46**, 2005; pp 80-84.

[56] Li, X., Lu, A., & Yang, H., Structure of ZnO-Fe_2O_3-P_2O_5 glasses probed by Raman and IR spectroscopy, *J. Non-Cryst. Solids*, **389**, 2014; pp 21-27.

[57] Efimov, A. M., Vibrational spectra, related properties, and structure of inorganic glasses, *J. Non-Cryst. Solids*, **253**, 1999; pp 95-118.

[58] Yadav, A., & Singh, P., A review of the structures of oxide glasses by Raman spectroscopy, *RSC Advances*, **5**, 2015; pp 67583-67609.

[59] El Mendili, Y., Vaitkus, A., Merkys, A., Gražulis, S., Chateigner, D., Mathevet, F., Gascoin, S., Petit, S., Bardeau, J.-F., Zanatta, M., Secchi, M., Mariotto, G., Kumar, A., Cassetta, M., Lutterotti, L., Borovin, E., Orberger, B., Simon, P., Hehlen, B., & Le Guen, M., Raman Open Database: first interconnected Raman–X-ray diffraction open-access resource for material identification, *J. Appl. Crystallogr.*, **52**, 2019; pp 618-625.

[60] Balasubramanya, N., Sun, Z., Ahmadzadeh, M., Kamili, S., Neuville, D. R., McCloy, J. S., & Goel, A., Impact of non-framework cation mixing on the structure and crystallization behavior of model high-level waste glasses, *J. Am. Ceram. Soc.*, **105**, 2022; pp 3967-3985.

[61] Bingham, P. A., Vaishnav, S., Forder, S. D., Scrimshire, A., Jaganathan, B., Rohini, J., Marra, J. C., Fox, K. M., Pierce, E. M., Workman, P., & Vienna, J. D., Modelling the sulfate capacity of simulated radioactive waste borosilicate glasses, *J. Alloys Compd.*, **656**, 2017; pp 656-667.

[62] Rigby, J. C., Dixon, D. R., Cutforth, D. A., Marcial, J., Kloužek, J., Pokorný, R., Kruger, A. A., Scrimshire, A., Bell, A. M. T., & Bingham, P. A., Melting behaviour of simulated radioactive waste as functions of different redox iron-bearing raw materials, *J. Nucl. Mater.*, **569**, 2022.

[63] Watts, J. F., & Wolstenholme, J., An Introduction to Surface Analysis by XPS and AES 2nd Edition, John Wiley & Sons Ltd., Chichester, UK., 2020.

[64] Agostinelli, E., Fiorani, D., & Paparrazo, E., XPS studies of iron sodium borosilicate glasses, *J. Non-Cryst. Solids*, **95** & **96**, 1987; pp 373-379.

[65] Sprenger, D., Bach, H., Meisel, W., & Gütlich, P., Discrete bond model (DBM) of sodium silicate glasses derived from XPS, Raman and NMR measurements, *J. Non-Cryst. Solids*, **159**, 1993; pp 187-203.

[66] Hsieh, C. H., Jain, H., Miller, A. C., & Kamitsos, E. I., X-ray photoelectron spectroscopy of Al- and B-substituted sodium trisilicate glasses, *J. Non-Cryst. Solids*, **168**, 1994; pp 247-257.

[67] Mekki, A., Holland, D., McConville, C. F., & Salim, M., An XPS study of iron sodium silicate glass surfaces, *J. Non-Cryst. Solids*, **208**, 1996; pp 267-276.

[68] Mekki, A., Holland, D., & McConville, C. F., X-ray photoelectron spectroscopy study of copper sodium silicate glass surfaces, *J. Non-Cryst. Solids*, **215**, 1997; pp 271-282.

[69] Holland, D., Mekki, A., Gee, I. A., McConville, C. F., Johnson, J. A., Johnson, C. E., Appleyard, P., & Thomas, M., Structure of sodium iron silicate glass - a multi-technique approach, *J. Non-Cryst. Solids*, **253**, 1999; pp 192-202.

[70] Ilieva, D., Dimitrov, V., Dimitriev, Y., & Bogachev, G., Infrared, Raman and XPS studies of vanadate glasses containing Ga_2O_3, *Phys. Chem. Glasses*, **40**, 1999; pp 6-11.

[71] Miura, Y., Kusano, H., Nanba, T., & Matsumoto, S., X-ray photoelectron spectroscopy of sodium borosilicate glasses, *J. Non-Cryst. Solids*, **290**, 2001; pp 1-14.

[72] Holland, D., Gee, I. A., Mekki, A., & McConville, C. F., Role of surface science in the determination of glass structure, *Phys. Chem. Glasses*, **42**, 2001; pp 247-254.

[73] Soares Jr., P. C., Nascente, P. A. P., & Zanotto, E. D., XPS study of lithium disilicate glass crystallisation, *Phys. Chem. Glasses*, **43**, 2002; pp 143-146.

[74] Dimitrov, V., & Komatsu, T., Correlation of optical basicity and O1s chemical shift in XPS spectra of oxide glasses, *Phys. Chem. Glasses*, **44**, 2003; pp 357-364.

[75] Nanba, T., & Miura, Y., Alkali distribution in borosilicate glasses, *Phys. Chem. Glasses*, **44**, 2003; pp 244-248.

[76] Shpotyuk, O., Golovchak, R., Jain, H., & Kovalskiy, A., Radiation induced functionality of chalcogenide glasses probed by high resolution XPS, *Phys. Chem. Glasses: Eur. J. Glass Sci. Tech. B*, **49**, 2008; pp 314-316.

[77] Segawa, H., Yano, T., & Shibata, S., An XPS study of the O1s binding energy of sodium borate glasses, *Phys. Chem. Glasses: Eur. J. Glass Sci. Technol. B*, **50**, 2009; pp 79-84.

[78] Sawyer, R., Nesbitt, H. W., & Secco, R. A., High resolution X-ray Photoelectron Spectroscopy (XPS) study of K_2O-SiO_2 glasses: Evidence for three types of O and at least two types of Si, *J. Non-Cryst. Solids*, **358**, 2012; pp 290-302.

[79] Zhu, X., Mai, C., & Li, M., Effects of B_2O_3 content variation on the Bi ions in Bi_2O_3-B_2O_3-SiO_2 glass structure, *J. Non-Cryst. Solids*, **388**, 2014; pp 55-61.

[80] Nesbitt, H. W., Bancroft, G. M., Henderson, G. S., Sawyer, R., & Secco, R. A., Direct and indirect evidence for free oxygen (O^{2-}) in MO-silicate glasses and melts (M = Mg, Ca, Pb), *Am. Mineral.*, **100**, 2015; pp 2566-2578.

[81] Nesbitt, H. W., Bancroft, G. M., & Ho, R., XPS valence band study of Na-silicate glasses: energetics and reactivity, *Surf. Interface Anal.*, **49**, 2017; pp 1298-1308.

[82] Nesbitt, H. W., Henderson, G. S., Bancroft, G. M., Sawyer, R., & Secco, R. A., Bridging oxygen speciation and free oxygen (O^{2-}) in K-silicate glasses: Implications for spectroscopic studies and glass structure, *Chem. Geol.*, **461**, 2017; pp 13-22.

[83] Kaky, K. M., Şakar, E., Akbaba, U., Kasapoğlu, A. E., Sayyed, M. I., Gür, E., Baki, S. O., & Mahdi, M. A., X-ray photoelectron spectroscopy (XPS) and gamma-ray shielding investigation of boro-silicate glasses contained alkali/alkaline modifier, *Results Phys.*, **14**, 2019.

[84] Ratep, A., & Kashif, I., X-ray photoelectron, FTIR, and Mössbauer spectroscopy studied the effect of Fe_2O_3/CuO substitution on structural and electrical properties of lithium borosilicate glasses, *J. Mater. Sci.: Mater. Electron.*, **32**, 2021; pp 12340-12347.

[85] Brow, R. K., & Pantano, C., Compositionally dependent Si 2p binding energy shifts in silicon oxynitride thin films, *J. Am. Ceram. Soc.*, **69**, 1986; pp 314-316.

[86] Pantano, C., & Brow, R. K., Hydrolysis reactions at the surface of fluorozirconate glass, *J. Am. Ceram. Soc.*, **71**, 1988; pp 577-581.

[87] Harrison, P. G., Wood, J. V., & Kelsall, A., An XPS and EXAFS study of the interaction between cerium ions and glass surfaces, *Phys. Chem. Glasses*, **41**, 2000; pp 165-169.

[88] Liu, X., Thomason, J. L., & Jones, F. R., XPS and AFM study of interaction of organosilane and sizing with E-glass fibre surface, *J. Adhes.*, **84**, 2008; pp 322-338.

[89] Reiß, S., Urban, S., Jacob, K., Krischok, S., & Rädlein, E., Investigation of the influence of a commercial glass protector on float glass surfaces by x-ray photoelectron spectroscopy, *Phys. Chem. Glasses: Eur. J. Glass Sci. Technol. B*, **58**, 2017; pp 99-108.

[90] Bou, M., Martin, J. M., & Le Mogne, T., Chemistry of the interface between aluminium and polyethyleneterephthalate by XPS, *Appl. Surf. Sci.*, **47**, 1991; pp 149-161.

[91] Gardner, S. D., Sigamsetty, C. S. K., Booth, G. L., & He, G.-R., Surface characterization of carbon fibers using angle-resolved XPS and ISS, *Carbon*, **33**, 1995; pp 587-595.

[92] Miot, C., Husson, E., Proust, C., Erre, R., & Coutures, J. P., Residual carbon evolution in $BaTiO_3$ ceramics studied by XPS after ion etching, *J. Eur. Ceram. Soc.*, **18**, 1998; pp 339-343.

[93] Yumitori, S., Correlation of C_{1s} chemical state intensities with the O_{1s} intensity in the XPS analysis of anodically oxidized glass-like carbon samples, *J. Mater. Sci.*, **35**, 2000; pp 139-146.

[94] Smets, B. M. J., & Lommen, T. P. A., Ion beam effects on glass surfaces, *J. Am. Ceram. Soc.*, **65**, 1982; pp c80-c81.

[95] Naumkin, A. V., Kraut-Vass, A., Gaarensstroom, S. W., & Powell, C. J., NIST X-ray Photoelectron Spectroscopy Database: NIST Standard Reference Database 20, Version 4.1 (web version), (https://srdata.nist.gov/xps/), 2012.

[96] Clarke, T. A., & Rizkalla, E. N., X-ray photoelectron spectroscopy of some silicates, *Chem. Phys. Lett.*, **37**, 1976; pp 523-526.

[97] Veal, B. W., Lam, D. J., Paulikas, A. P., & Ching, W. Y., XPS study of CaO in sodium-silicate glass, *J. Non-Cryst. Solids*, **49**, 1982; pp 309-320.

[98] Stanworth, J. E., Oxide glass formation from the melt, *J. Am. Ceram. Soc.*, **54**, 1971; pp 61-63.

[99] Pauling, L., The Nature of the Chemical Bond, 3d ed., Cornell University Press, Ithaca, N.Y., 1960.

[100] Bingham, P. A., Hannant, O. M., Reeves-McLaren, N., Stennett, M. C., & Hand, R. J., Selective behaviour of dilute Fe^{3+} ions in silicate glasses: An Fe K-edge EXAFS and XANES study, *J. Non-Cryst. Solids*, **387**, 2014; pp 47-56.

[101] Wright, A. C., Sinclair, R. N., Shaw, J. L., Haworth, R., Bingham, P. A., Forder, S. D., Holland, D., Scales, C. R., Cuello, G. J., Vedishcheva, N. M., The environment of Fe^{3+}/Fe^{2+} cations in a sodium borosilicate glass, *Phys. Chem. Glasses: Eur. J. Glass Sci. Technol. B*, **58**, 2017; pp 78-91.

Chapter 7 – Glass Property Studies

In Chapters 4 – 6, the iron chemistry and the influence on the borosilicate network as a function of iron contents has been studied. However, the influence iron has on the glass properties is also key in this research. Lab scale experimentation on glass properties is a useful tool in assessing a glass compositions fitness for purpose across a variety of applications. Ranging from optical fibres, through to electronic glass, container glass, and radioactive waste glasses. Owing to the timescales of lattermost use, coupled with the logistical challenges with designing true waste analogues that can be safely investigated in most conventional labs, there is some debate around the efficacy of lab scale testing on radioactive waste glass properties. Nevertheless, this chapter will cover three distinct glass properties with an introduction of a sample series that will run parallel to the Hanford analogue (HAFe) sample series.

7.1 Property Studies on Hanford Glass

The property studies around Hanford waste glasses have primarily focused on two areas – secondary phase crystallisation [1-30] and chemical durability [31-41]. This is owing to the significance these properties have around the limiting factors of the waste loading for certain waste types (this is discussed in more detail in Chapter 1.5.4).

7.1.1 Secondary Phases Studies

Secondary phase studies have been of high importance around the Hanford waste glass studies, owing to the problematic nature some of the expected phases. As discussed in Chapter 1.5.4, spinel phases have been linked to shortened lifespan of glass melters at the Savannah River site. The spinel crystals agglomerate as the spout system reduces in temperature the further away it gets from the melt pool, resulting in an increasing likelihood of blockages forming in the pouring system [1-14].

Nepheline crystallisation is also a concern with the expected wastes but for different reasons. Being an alumino-silicate, nepheline crystals remove silica and alumina from the amorphous phase, which results in lower chemical durability [15-30]. Furthermore, nepheline has a significantly different coefficient of thermal expansion, which leads to cracking during cooling. The cracks increase the surface area of the wasteform which further exasperates the chemical durability concerns [15-30]. Nepheline and spinel crystallisation within Hanford wastes is discussed in more detail in Chapter 1.5.4 and the work done to create tolerance models.

7.1.2 Chemical Durability

With every glass composition designed, chemical durability is a key property monitored across the variety of expected waste forms, ranging from LAW (low-activity waste) [37,38] to various HLW wasteforms [32,34-36] and some wasteforms still under investigation, such as glass ceramics [39] and iron phosphate waste glass forms [43]. The chemical durability is typically measured using product consistency testing – method B (PCT-B) [40] and compared to a benchmark standard, which sets the acceptable limits for concentrations of glass components within the analysed leachate. Hanford glasses are measured against the DWPF-EA (Defence Waste Processing Facility – Environmental Assessment) glass [41], where the product waste forms must have comparable or better chemical durability characteristics than the DWPF-EA glass.

7.1.3 Canister Centreline Cooling

Once the melt is ready for pouring, the molten glass will be poured into steel canisters, where it will solidify into glass within the canister. The cooling rates within the canisters will not be uniform throughout, as such, the molten glass will undergo a range of cooling rates dependent on the melts proximity from the centre of the canister. The melt in the centre of the canister will cool far slower than the melt on the outer most edge of the canister. As such, the glass on the outside of the canister may have different properties to that in the middle. As is commonly seen in the study of radioactive waste glasses, samples are subjected to a slow cool heat treatment to replicate the thermal profile expected in the centre of the canister [42,43]. The exact heat treatment parameters vary depending on the canister dimensions and starting temperature of the molten glass. For the Hanford site, the HLW canister centreline cooling (CCC) heat treatment profile can be seen in **Table 3.11** with a visual representation in **Fig 7.1**.

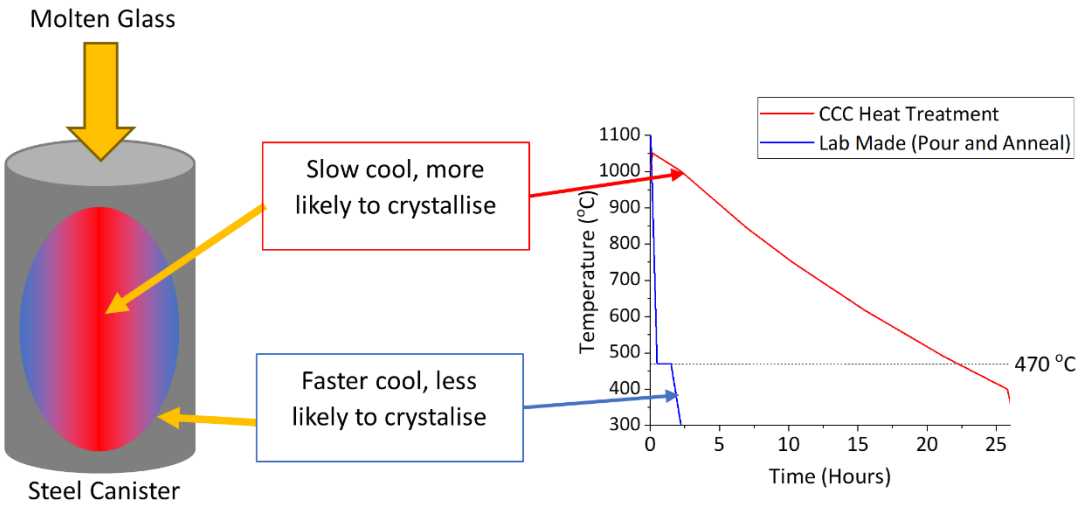

Figure 7.1: *A visual representation of the CCC heat treatment profile used on Hanford HLW glass studies.*

Some of the glass produced for each sample in the HAFe sample series was subjected to this CCC heat treatment profile, and had the properties analysed alongside the HAFe series to study whether or not there is a significant change in glass transition temperature, secondary phase stabilisation, and chemical durability between the samples representing the fast-cooling glass, and the glass in the canister centreline. This Chapter will therefore refer to two sub-series of the HAFe sample series – the laboratory produced (referred to as "Lab Made") sub-series and the canister centreline cooling heat-treated (referred to as "CCC") sub-series.

7.2 Differential Thermal Analysis (DTA)

7.2.1 What is DTA?

Differential thermal analysis (DTA) is used to measure thermal events across a given range of temperatures and heating rates. As the name suggests, it uses the differences in thermal profiles between a standard and a sample to measure sensitive changes in thermal behaviour in samples [44]. This is typically plotted as difference in temperature within the sample against temperature of the system, with troughs in the data representing endothermic events in the sample, and peaks representing exothermic events in the sample [44]. A general schematic of how DTA data is acquired can be seen in **Fig 7.2**.

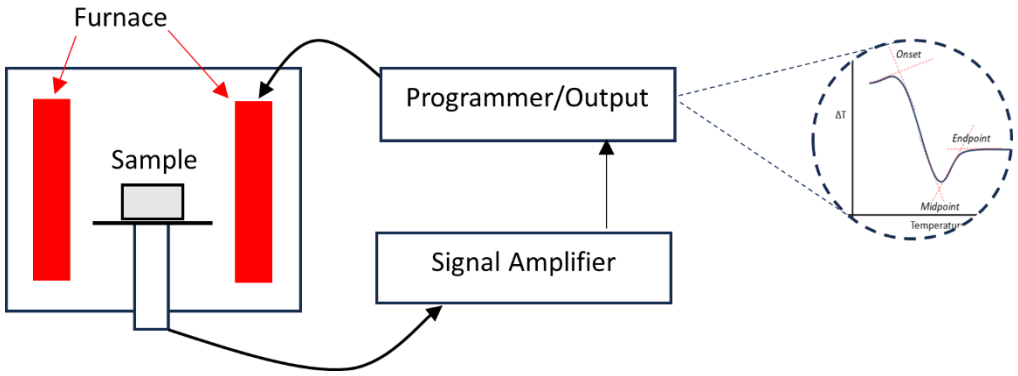

Figure 7.2: *A schematic of how DTA data is acquired. DSC data is acquired in a similar manner [44]. While this diagram only shows a sample being measured, the sample and standard can also be measured simultaneously in some systems.*

The measured standard and the measured sample must undergo the sample thermal program (same heating rates, same dwell times etc.) for the differences between sample and standard to be accurately representative of thermal events within the sample [44].

7.2.2 DTA on Glass

DTA has been used on glass to determine a variety of properties [45-76] linked to the thermal behaviour of glass, including glass transition temperature (T_g), crystallisation temperatures (typically denoted as T_x), and in some cases, thermal stability. Thermal stability looks at the differences in temperatures between the glass transition temperature, crystallisation temperature, and melting temperature with these values being fed into an equation (the exact one depends on which specific model – Hruby, Wennberg, etc.) which provides a coefficient by which glass stability can be compared [71]. This will not be covered in this research owing to the complex nature of the glasses and the fact not all glasses in the HAFe series form fully amorphous glasses (see Chapter 3.3.2 and Chapter 7.3.2), so the entire composition does not fully melt. In this research, the glass transition temperature is the key property of interest (see Chapter 2.1.1 for why glass transition temperature is important) associated with this analytical technique, and this is manifests in an endothermic manner (see **Fig 7.3**).

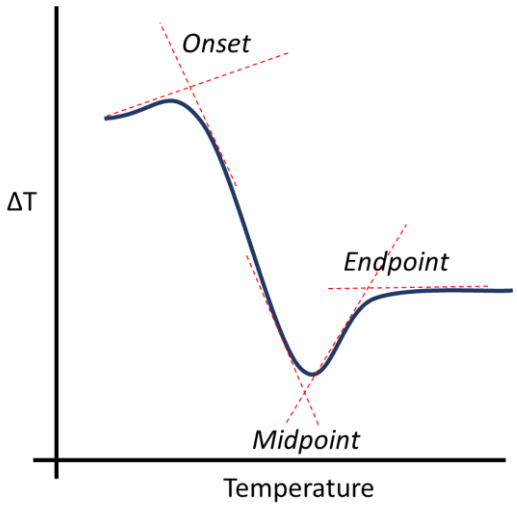

Figure 7.3: *A recreated pattern showing how a glass transition temperature event appears on a DTA scan. The three key glass transition events are labelled.*

The glass transition event has three sub-events within it – the onset, the midpoint, and then endpoint (all highlighted on **Fig 7.3**). Typically, only one of these events in measured and reported as the glass transition temperature for the material and it is usually the onset or the midpoint.

7.2.3 Results

The HAFe and HAFe CCC sample series were measured using DTA to determine the glass transition temperatures of the glass samples. The DTA traces, with annotations on how T_g was derived, can be found in the appendix (**Figs A7.1 – A7.12)**. The glass transition onsets for both sub-series can be seen in **Fig 7.4**.

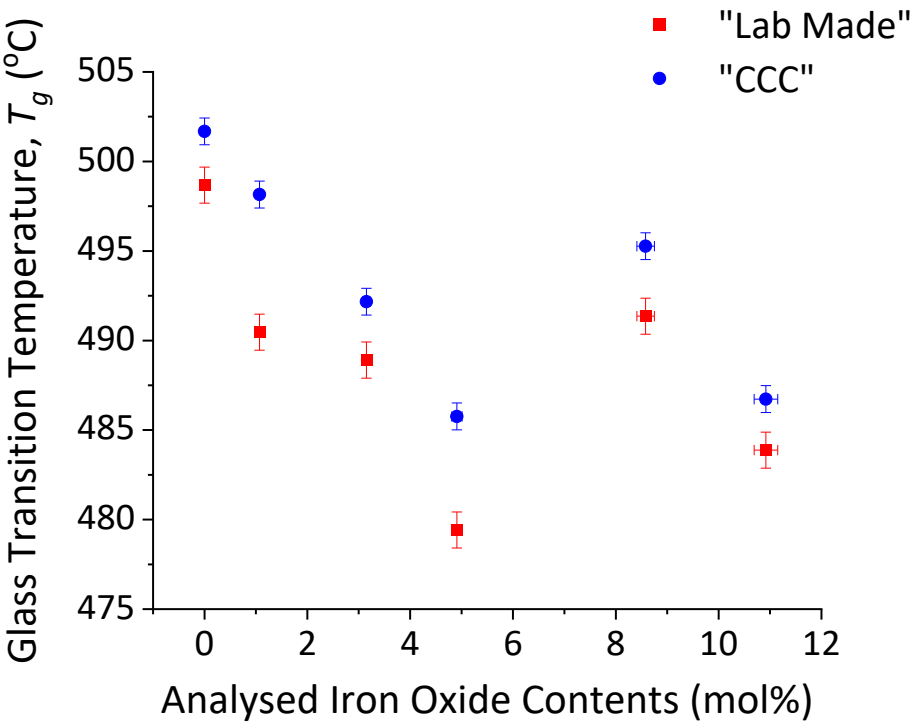

Figure 7.4: *The glass transition temperatures of both HAFe sample sub-series plotted as a function of analysed Fe_2O_3 contents.*

In both sub-series, the glass transition temperature decreases slightly as a function of increasing Fe_2O_3. This is in line with studies on the thermal stability of Fe within glass, such as the study by Cassingham *et al*. [56], which did not comment on the change in glass transition temperature as a function of changing Fe_2O_3 contents within the glass, but the published DTA data did show a slight decrease in the glass transition temperature.

Yang *et al*. [77] noted that glass transition temperatures in lithium aluminosilicate glasses are influenced by the thermal strength of the network forming bonds, Si-O and Al-O. The Al_2O_3 was substituted for Fe_2O_3 and a sharp decrease in glass transition temperature was observed. Yang *et al*. hypothesised that the Fe-O bonds are significantly thermally weaker than the Al-O bonds [77], owing to the fact that the Fe-O bonds are longer than the Al-O, or Si-O bonds, and therefore weaker and require less thermal energy to break, resulting in a lower T_g. This would explain the slight decrease in glass transition temperature seen in **Figs 7.4**. While the Fe_2O_3 is not being substituted for any of the glass forming components, it is introducing more of the weaker Fe-O bonds into the broader glass network at the expense of thermally stronger bonds by way of integrating into the glass network. The slight relative increase in T_g in the highest iron samples can be explained by the presence of Fe-bearing crystalline phases (see Chapter 7.3.2), with the simplest explanation being that the Fe has formed a secondary phase, so there are slightly fewer

Fe-O bonds within the amorphous phase, or at least fewer than the trend would have predicted if all the Fe existed in the amorphous phase. Hence the slight increase between HAFe005.0 and HAFe007.1 in **Fig 7.4**.

7.3 X-Ray Diffraction with Rietveld Refinement

7.3.1 Rietveld Refinement

The principles of X-ray diffraction have been covered in Chapter 3.3.2. The same principles in acquiring the data are used, but where this type of XRD differs, is the quantitative analysis of the diffraction data that will for calculation of the abundances of phases, and the amount of amorphous phase within the glass samples. This is done by mixing known amount of a crystallographic standard and then analysing the abundance of the subsequent phases against this standard. Calculations, alongside a fit of the data, were carried out to calculate the abundance of amorphous phase within the sample [78]. This method is known as the Rietveld refinement method, named after H. M. Rietveld [79]. It is not only used to calculate the amount of phase, but it is also used to analyse the phase structure (assuming an appropriate starting isomorph is used the standard) [78, 80]. In this research, the amount of secondary phase present is the primary interest when using the Rietveld refinement method. This particular use has been utilised in the study of glasses ranging from SLS glasses [81] through to complex aluminosilicates [82-87] and radioactive waste simulants [88-91].

7.3.2 Results

The diffraction patterns for the two HAFe sub-series can be seen in **Figs 7.5** & **7.6**.

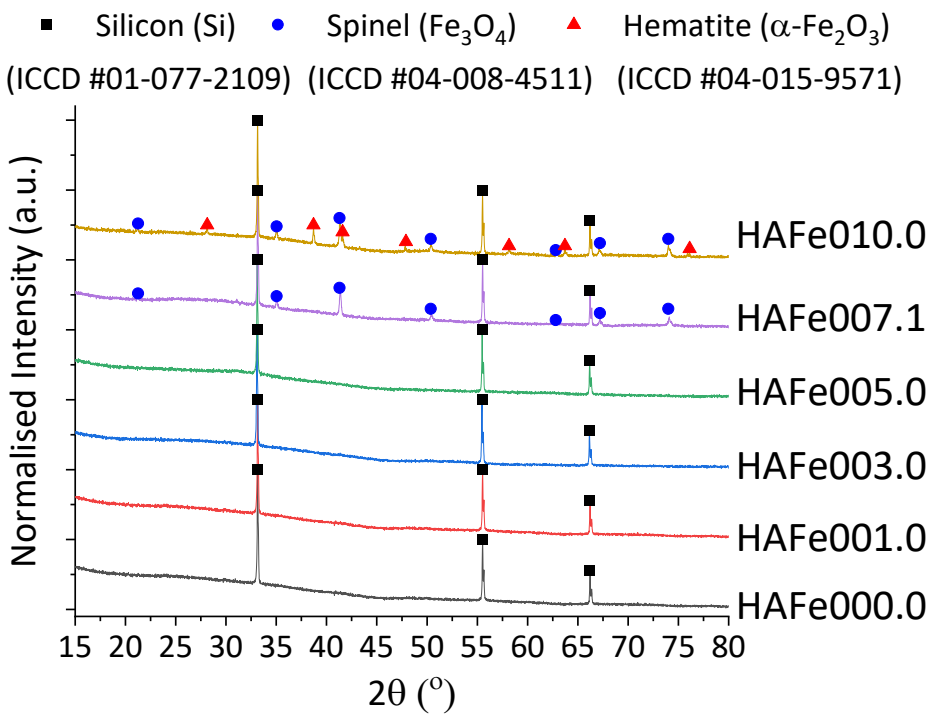

Figure 7.5: *The X-ray diffraction patterns for the "Lab Made" HAFe sample sub-series.*

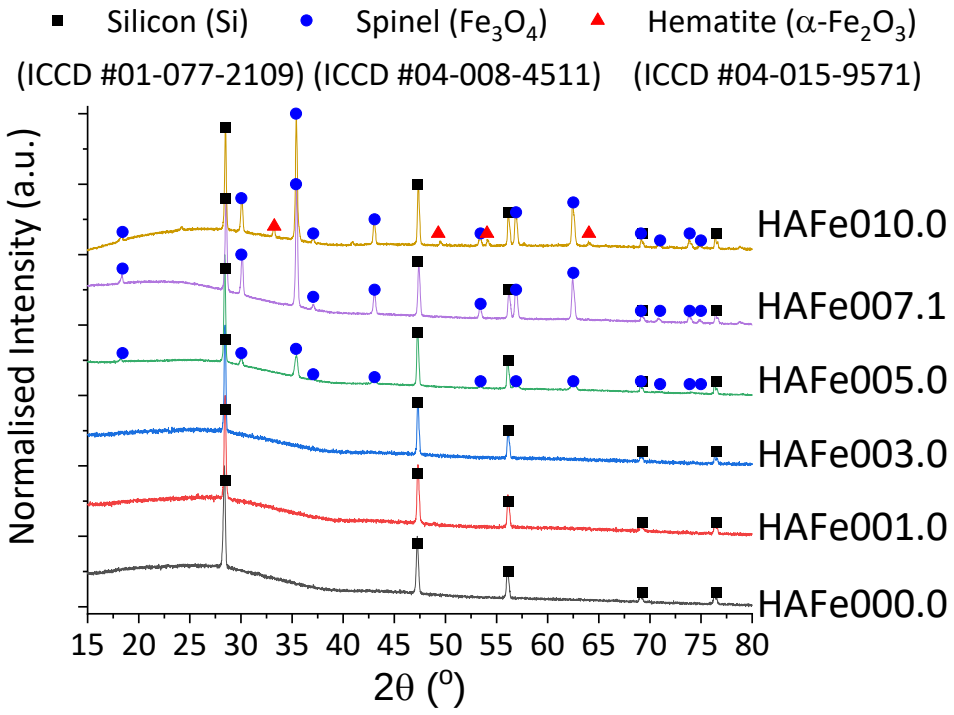

Figure 7.6: *The X-ray diffraction patterns for the "CCC" HAFe sample sub-series.*

The diffraction pattern for silicon (ICCD #01-077-2109) is present in all samples as this was the crystallographic standard used for the Rietveld refinement (see Chapter 3.6.2 for

more information). The spinel phase identified using HighScore Plus was magnetite (Fe_3O_4 ICCD #04-008-4511), however, the general spinel formula is AB_2O_4 and a variety of transition metals can be found in the A and B sites of a spinel crystal. If these inclusions are only minor, they would produce indistinguishable diffraction patterns from the primary spinel phase. While Fe_3O_4 was used for the Rietveld refinement, without further study to demonstrate that this is in fact purely magnetite (for example, scanning electron microscopy with associated energy dispersive X-ray spectroscopy mapping), this phase will be referred to as the "Spinel" phase henceforth. The calculated relative abundances of the two crystalline phases and the amorphous phase can be seen in **Figs 7.7** & **7.8**.

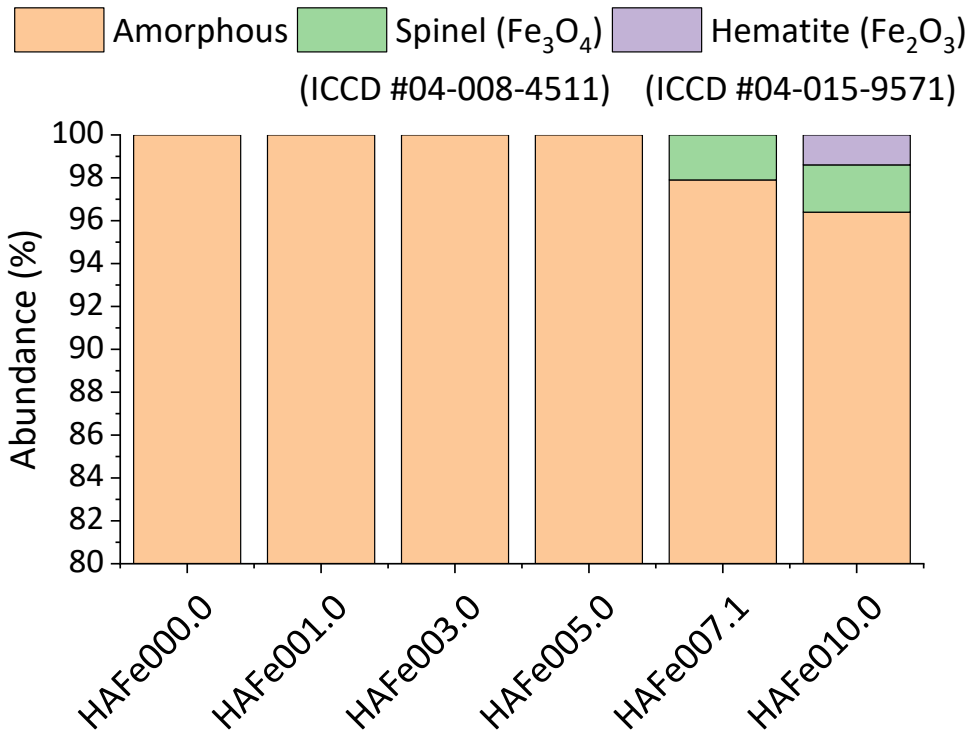

Figure 7.7: *A bar chart showing the relative phase abundances in the "Lab Made" HAFe sample sub-series.*

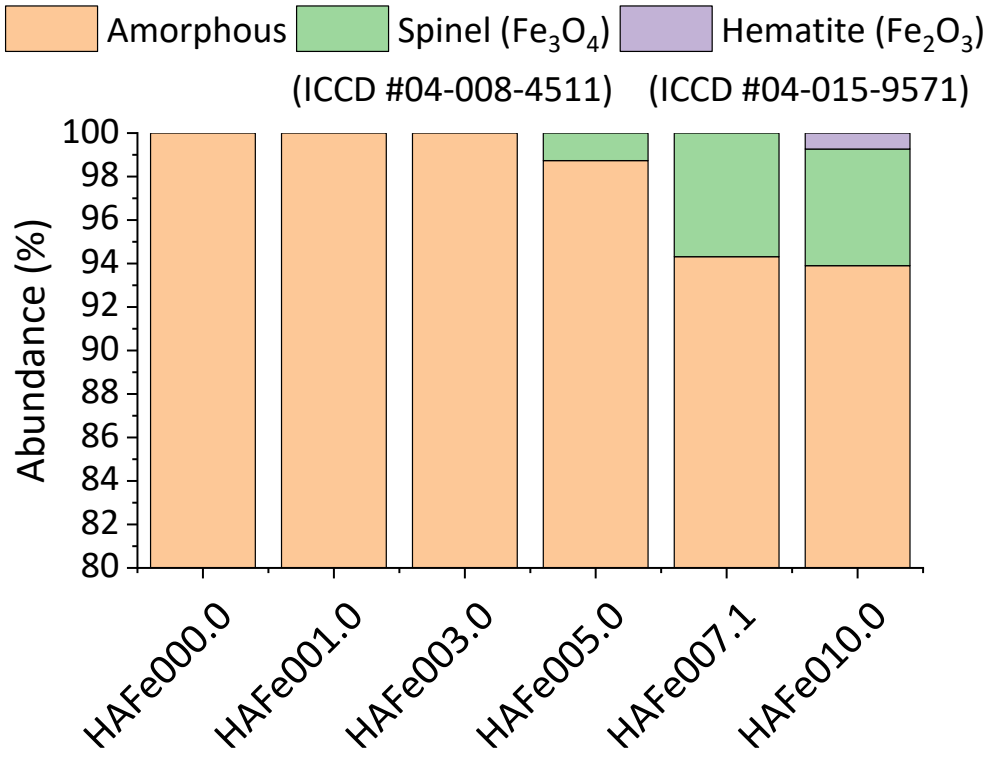

Figure 7.8: *A bar chart showing the relative phase abundances in the "CCC" HAFe sample sub-series.*

Despite the CCC heat treatments, there is no crystalline phase present in the lower iron glass compositions seen in **Figs 7.6** & **7.8**, with < 2% crystallinity seen HAFe005.0 CCC compared with the fully amorphous HAFe0005.0 "Lab Made" sample. In the higher Fe samples, there is a greater abundance of the spinel phase present, but a lower abundance of the hematite phase in the HAFe010.0 CCC sample when compared to the "Lab Made" counterpart. The lattice parameters for the phases can be seen in **Table 7.1**.

Table 7.1 shows the lattice parameters for the phases present in the two HAFe sub-series glass samples. The spinel phase only has one parameter as it is a cubic structure, therefore a = b = c. The hematite phase only has two parameters as it is a trigonal structure, therefore a = b.

Sample ID	Spinel (Å)	Hematite (Å)	
	a	a	c
HAFe007.1 "LM"	8.3999 (± 0.0002)	-	-
HAFe010.0 "LM"	8.4048 (± 0.0002)	5.0354 (± 0.0002)	13.740 (± 0.0002)
HAFe005.0 "CCC"	8.3970 (±0.0010)	-	-
HAFe007.1 "CCC"	8.4158 (± 0.0003)	-	-
HAFe010.0 "CCC"	8.4089 (± 0.0003)	5.0370 (± 0.0030)	13.7330 (± 0.0050)

The lattice parameters for the spinel and hematite phase do not change, which suggests that there are not any significant compositional changes in the spinel phase between the "Lab Made" and "CCC" sample series. As such, the only definitive conclusion on the composition of the spinel phase, is that it is primarily iron, that is likely some derivative of magnetite, with other transition metal inclusions. This is evidenced by the relative abundance of phases increasing with increase Fe_2O_3 contents within the glass. The uncertainty in the specific assignment of the phase can also be inferred by the difference in the assignment of the spinel phase from Chapter 3 (specifically **Fig 3.11**), where HighScore Plus was used to assign the phase as $Mg_{0.4}Fe_2Ni_{0.6}O_4$ (ICCD #04-024-9316), whereas in **Figs 7.5** & **Figs 7.6**, the phase was assigned to Fe_3O_4.

When compared to the HLW Ng-Fe2 glasses studied by Matlack *et al*. [35,36], the crystalline abundance for HAFe007.1 CCC (the sample most similar to HLW Ng-Fe2) is in line with those reported by Matlack after the HLW Ng-Fe2 was subjected to the same CCC heat treatment. Matlack *et al*. reported 4.93 vol.% spinel phase after CCC heat treatment, when compared to the 5.7 (+/- 0.1) wt% abundance seen in **Fig 7.8.** Matlack *et al*. [35] reported no crystallinity in the HLW Ng-Fe2 glass "as melted" ("Lab Made" equivalent) whereas HAFe007.1 "Lab Made" was found to have 2.1 wt.% spinel phase. While the crystallinity is similar there are differences that show that the glasses studied in this research, tend to crystallise slightly more readily than those studied by Matlack *et al*. [35].

7.4 Chemical Durability Analysis - Product Consistency Test – Method B

7.4.1 Overview

Product Consistency Test - Method B (PCT-B) is one of several lab scale techniques used to analyse the chemical durability of radioactive waste glasses and associated analogues across the global nuclear sector. The PCT method was designed to provide a rapid assessment of relative changes in chemical durability through a glass sample series [92]. While PCT-B was designed to assess the chemical durability over longer time scales, it was used in this research to investigate the 7-day durability, which is typically the timescale that the method A (PCT-A) test is done over [92].

Iron oxide has been the subject of study in chemical durability studies, with the overall impacts on chemical durability being best described as "mixed". Unlike silica and alumina, iron oxide does not have a clear trend in whether or not it improves or hinders the chemical durability of a waste glass [93]. Feng *et al*. [94] linked an increase in network forming bonds within a glass network to an increase in chemical durability of a glass. Further to this, Feng *et al*. [94] showed that Fe^{3+} increased the chemical durability of glasses, whereas Fe^{2+} decreased the chemical durability as measured by MCC-3 (Materials Characterisation Center – Test 3). This is supported by Peeler & Edwards [31]. Van Iseghem *et al*. [95] studied the effects on chemical durability as a result of substituting Al_2O_3 for Fe_2O_3. It was found that increasing the Al_2O_3 significantly reduced the leachability of the glass, meaning that Fe_2O_3 has a detrimental effect on chemical durability if it is used as a substitute for Al_2O_3 [95]. Nogues *et al*. [96] studied the effects on chemical durability of substituting ZnO with Fe_2O_3 in alkali borosilicate glasses. It was found that increasing the iron oxide at the expense of ZnO, increased the leach rates of most glass components by a factor of 3, which lead to the conclusion that Fe_2O_3 at the expense of ZnO, negatively impacts the chemical durability. Yangisawa *et al*. [97] incrementally added Fe_2O_3 to a waste glass composition to study the chemical durability, and it was shown that as the concentration of Fe_2O_3 increased, the chemical durability increased. This was linked to the reduction in micro-fissures forming as the Fe_2O_3 increases and the formation of a stable alteration layer, which impedes the leachability of the glass. Cassingham *et al*. [56] showed that as the Fe_2O_3 contents increase within UK MW glasses, the chemical durability increased in the short term (7 - 14 days) for all quantities of Fe_2O_3, however, after 28 days, the normalised released of boron, sodium, lithium, and molybdenum increased in the highest iron samples (10 – 20 wt.%). The increase in chemical durability was linked to the Fe^{3+} cations being tetrahedral, and thus forming network forming bonds that are resistant to hydrolysis reactions. The increase in

the leach rates in higher Fe glasses was hypothesised to be linked to the change in alteration layer behaviour in the longer time scales, however, this was left open for further research [56]. Brossel *et al*. [98] further investigated the influence of Fe cations on corrosion behaviour in simple sodium borosilicate glasses. It was noted that the short-term chemical durability is increased by Fe_2O_3, supporting previous studies [31,56,93,96]. However, the alteration layer that forms as Fe precipitates out of the glass, does not have the same ability to form a barrier that slows the rate of alteration (described as a passivating barrier) as the Al-precipitates, with the extent of the passivating barrier dependent on pH; a lower pH forms octahedral Fe^{3+} resulting in the increase in alkali leach rates and thus an increase in glass alteration [98]. The authors made a careful emphasis on the fact that the glasses studied were highly simplified compared to expected waste glasses studied using these methods.

7.4.2 Results

The raw data from the ICP analysis of the PCT-B leachates can be seen in appendix (**Tables A7.1** & **A7.2**). Due to a Na and Si rich contaminant in the blanks measured with the HAFe "CCC" sub-series samples (sample IDs 7a-c in **Table A7.2**), these blanks were not used in the calculations for the HAFe "CCC" sub-series, instead the blanks samples 0a-c (see **Table A7.1**) which were measured with the HAFe "Lab Made" sub-series samples were used to process the "CCC" sub-series data. The authors acknowledge that this is a significant deviation from standard practice, and acknowledge that these experiments may require re-measuring to verify the results. The processed data in average normalised loss in g m^{-2} and normalised concentration in g L^{-1} (see **Tables A7.3** – **A7.6** for the data and see Chapter 3.6.4 for more information on how PCT-B leachates are processed for data processing). The normalised concentration data for B, Li, Na, Si can be seen in **Figs 7.9** – **7.12**. The data points for the "As Made" (i.e. not CCC heat treated) HLW Ng-Fe2 PCT-B analysis published by Matlack *et al*. [35] is included in **Figs 7.9** – **7.12**.

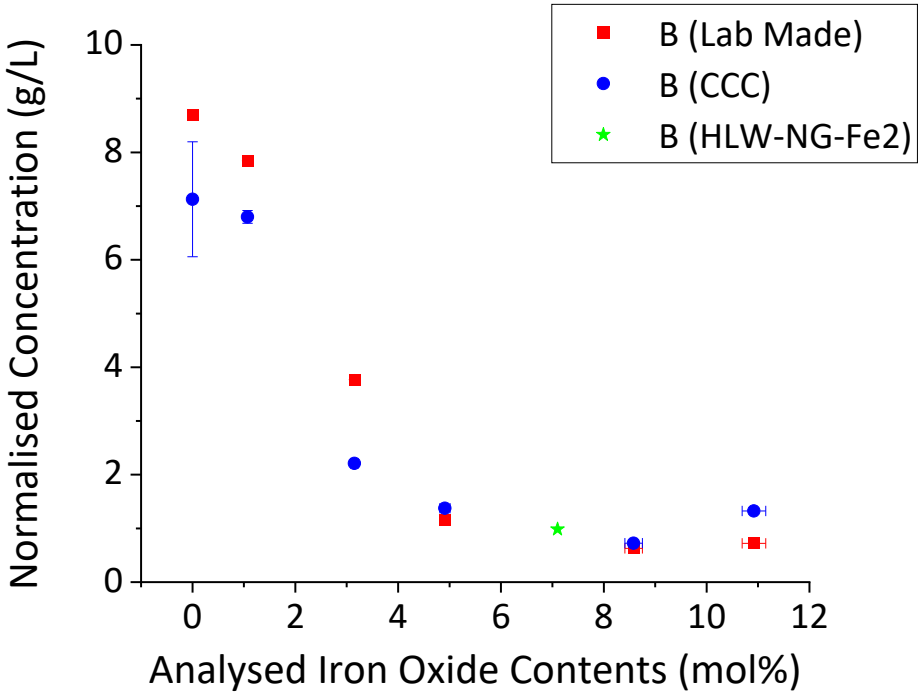

Figure 7.9: *The normalised concentration of boron in the PCT-B leachates as a function of Fe_2O_3 contents in both HAFe sample sub-series.*

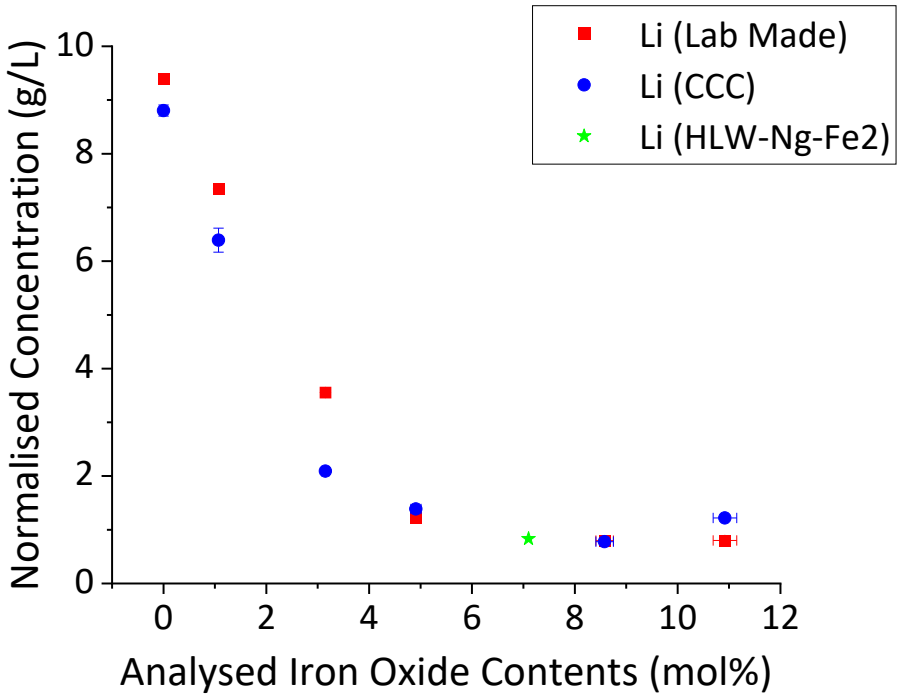

Figure 7.10: *The normalised concentration of lithium in the PCT-B leachates as a function of Fe_2O_3 contents in both HAFe sample sub-series.*

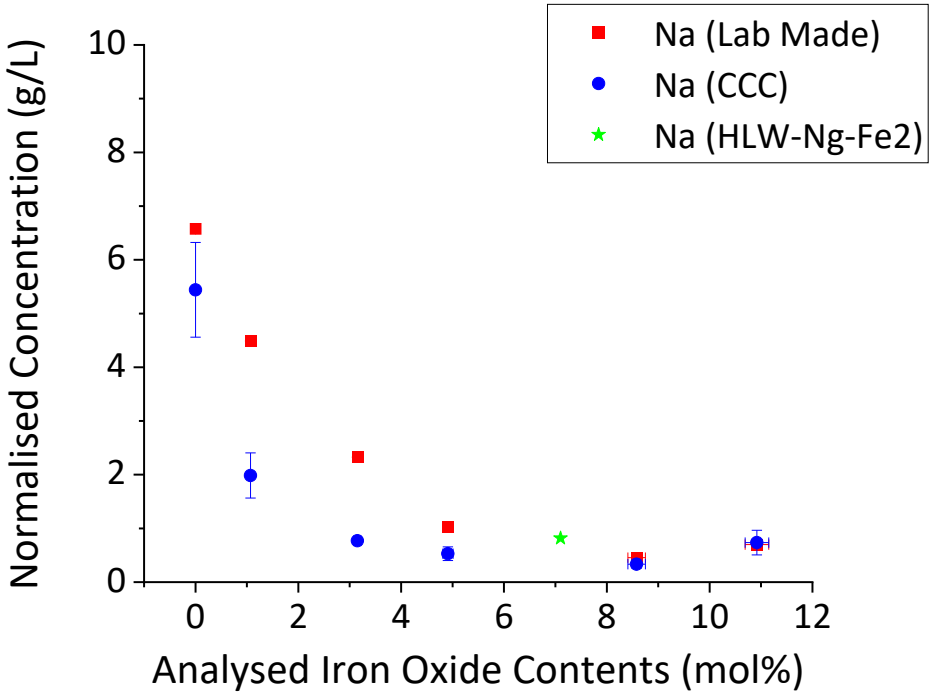

Figure 7.11: *The normalised concentration of sodium in the PCT-B leachates as a function of Fe_2O_3 contents in both HAFe sample sub-series.*

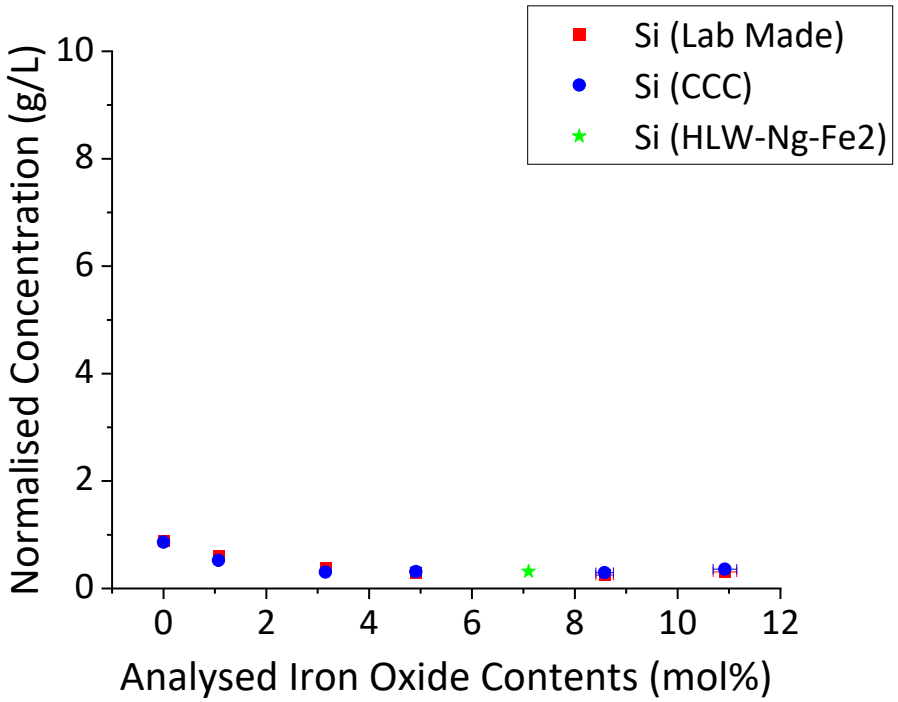

Figure 7.12: *The normalised concentration of silicon in the PCT-B leachates as a function of Fe_2O_3 contents in both HAFe sample sub-series.*

The data in **Figs 7.9** – **7.12** show that as the iron contents increases within the glass, the normalised mass loss of elements decreases, which is supported by the findings in literature where the Fe_2O_3 is the only variable (i.e. the iron is not substituted for another component) [31,56,94,97]. The data points for the HAFe007.1 samples very similar to the those in Matlack *et al*. [35]. There is not a significant difference between the two sub-series, suggesting that the CCC heat treatments do not significantly influence the chemical durability in this particular glass series. This distinction is important, as a Hanford waste with a tendency to form nepheline crystals (for example a high-alumina waste), may show significant differences in the chemical durability between the "CCC" and "Lab Made" samples.

Considering the studies on the iron chemistry done in Chapters 4 and 5, the amorphous iron in these samples exist predominantly as $^{[4]}Fe^{3+}$, which has been shown to form network forming bonds. These network forming bonds have been suggested to be resistant to hydrolysis reactions and therefore will inhibit leach rates of key glass components [56,94], which would explain the decreasing normalised concentrations seen in the leachates as evidenced by **Figs 7.9** – **7.12**.

The values seen in this PCT study are compared to the benchmarks set for Hanford glasses by the DWPF-EA glass in **Tables 7.2a** & **7.2b**.

Table 7.2a: The normalised concentration of the "Lab Made" HAFe sample sub-series and the DWPF-EA standard reference glass for B, Li, Na, and Si.

Element	Normalised Concentration of the "Lab Made" samples (g L^{-1})						
	DWPF-EA [35]	**HAFe 000.0**	**HAFe 001.0**	**HAFe 003.0**	**HAFe 005.0**	**HAFe 007.1**	**HAFe 010.0**
B	16.695	8.6982 (± 0.0483)	7.8420 (± 0.0699)	3.7706 (± 0.0737)	1.1580 (± 0.0425)	0.6283 (± 0.0068)	0.7221 (± 0.0085)
Li	9.565	9.3867 (± 0.0760)	7.3457 (± 0.0745)	3.5544 (± 0.0639)	1.2154 (± 0.0300)	0.7994 (± 0.0223)	0.8015 (± 0.0101)
Na	13.346	6.5768 (± 0.0606)	4.4897 (± 0.0679)	2.3269 (± 0.0624)	1.0275 (± 0.0217)	0.4549 (± 0.0121)	0.6994 (± 0.0073)
Si	3.922	0.8916 (± 0.0173)	0.6089 (± 0.0033)	0.3875 (± 0.0187)	0.2874 (± 0.0024)	0.2488 (± 0.0014)	0.3082 (± 0.0007)

Table 7.2b: The normalised concentration of the "CCC" HAFe sample sub-series and the DWPF-EA standard reference glass for B, Li, Na, and Si.

Element	Normalised Concentration of the "CCC" samples (g L^{-1})						
	DWPF-EA [35]	**HAFe 000.0**	**HAFe 001.0**	**HAFe 003.0**	**HAFe 005.0**	**HAFe 007.1**	**HAFe 010.0**
B	16.695	7.1268 (± 1.0693)	6.7981 (± 0.1181)	2.2095 (± 0.0319)	1.3759 (± 0.0096)	0.7237 (± 0.0110)	1.3248 (± 0.0206)
Li	9.565	8.8040 (± 0.1033)	6.3912 (± 0.2248)	2.0908 (± 0.0451)	1.3864 (± 0.0425)	0.7780 (± 0.0183)	1.2197 (± 0.0095)
Na	13.346	5.4407 (± 0.8820)	1.9854 (± 0.4192)	0.7702 (± 0.0199)	0.5284 (± 0.1271)	0.3345 (± 0.0780)	0.7364 (± 0.2292)
Si	3.922	0.8621 (± 0.0078)	0.5236 (± 0.014)	0.3056 (± 0.0079)	0.3134 (± 0.0243)	0.2934 (± 0.0215)	0.3587 (± 0.0065)

While the data in **Tables 7.2a** & **7.2b** show that all glasses have normalised concentrations that are below the limits set by the DWPF-EA, it is worth noting that the data for the DWPF-EA comes from Matlack *et al*. [35] and was not investigated alongside the HAFe sample series. While the sample data is significantly lower than the DWPF-EA data for the boron, sodium, and silicon values, both HAFe000.0 lithium values are close to the limit set by the DWPF-EA standard. While there is justification to suggest the glasses are all likely within the limits, it would be necessary to remeasure all samples alongside the standard reference glass to suggest this with full confidence.

7.5 Discussion

The secondary phase and chemical durability properties all demonstrated a clear dependence on concentration of Fe_2O_3 within the glass, with increasing Fe_2O_3 demonstrating an increase in short-term chemical durability but also an increase in spinel crystallisation. The values for both the "Lab Made" and "CCC" HAFe007.1 sample were broadly comparable to the HLW-Ng-Fe2 data published by Matlack *et al*. [35], which provides confidence in the data for the rest of the samples which do not have a clear comparable analogue to measure against.

The glass transition temperature decreases as function of increase Fe_2O_3 content, which agrees with a trend seen in a similar study by Cassingham *et al*. [56]. Yang *et al*. [77] has suggested that the Fe-O bonds are thermally weaker than Si-O and Al-O bonds when studying lithium aluminosilicate glasses, and this theory would explain this trend and why it is only a slight decrease (approximately 25 ºC from 0 – 10 mol.% Fe_2O_3 based on **Fig. 7.4**) and not significant decrease. The weaker Fe-O bonds are not directly replacing

thermally stronger bonds, but more being increased and dispersed throughout the glass network. If the Fe_2O_3 was substituted in for SiO_2, (i.e. the active removal of Si-O bonds, rather than diluting them by increasing the Fe-O bonds) the decrease in glass transition temperature would have been significant. The slight increase in glass transition temperature is likely due to some of the weaker Fe-O bonds being removed from the amorphous phase into crystalline phase, resulting in a slight increase in T_g between HAFe005.0 and HAFe007.1 in both sub-series.

The 7-day PCT tests showed that increasing the Fe_2O_3 within the glass significantly reduced the leachability of some of the key glass components in boron, silicon, lithium, sodium. Previous studies [31,56,94,97] have linked this to $^{[4]}Fe^{3+}$ forming network forming bonds that are resistant to hydrolysis reactions which inhibits the leachability of these components. Given that the iron within these samples have been shown to exist predominantly as tetrahedral Fe^{3+} (see Chapters 4 & 5), it is likely that this theory explains the trends seen in this research. However, based on the short timescales of the PCT experiment, it is not appropriate to state that the iron is a net positive on the chemical durability of the glass. Studies by Brossel *et al*. [98] showed that the alteration layer formed during corrosion is influenced by the environment created by the leachate and the conditions of the experiment. It was demonstrated in simpler glasses that the alteration may not inhibit further dissolution as affectively as it could if the layer is iron-rich, and the environment (such as pH) meets certain criteria. This was also hypothesised by Cassingham *et al*. [56] to explain the increase in leach rate in longer timescales (14 – 28 days) for high-Fe (10 – 20 wt.%) samples. While the short-term chemical durability is clearly enhanced by higher Fe_2O_3 contents, further dedicated study is required to determine irons net-influence on chemical durability across longer timescales.

7.6 References

[1] Vienna, J. D., Hrma, P., Crum, J. V., & Mika, M., Liquidus temperature-composition model for multi-component glasses in the Fe, Cr, Ni, and Mn spinel primary phase field, *J. Non-Cryst. Solids*, **292**, 2001; pp 1-24.

[2] Jiricka, M., Hrma, P., & Vienna, J. D., The effect of composition on spinel crystals equilibrium in low-silica high-level waste glasses, *J. Non-Cryst. Solids*, **319**, 2003; pp 280-288.

[3] Jantzen, C. M., & Brown, K. G., Predicting the spinel-nepheline liquidus for application to nuclear waste glass processing. Part I: Primary phase analysis, liquidus measurement, and quasicrystalline approach, *J. Am. Ceram. Soc.*, **90**, 2007; pp 1866-1879.

[4] Hrma, P., Crystallization during processing of nuclear waste glass, *J. Non-Cryst. Solids*, **356**, 2010; pp 3019-3025.

[5] Fox, K. M., Crystallization in High Level Waste (HLW) Glass Melters: Operational Experience from the Savannah River Site, Savannah River National Laboratory, *SRNL-STI-2013-00724*, 2014.

[6] Hrma, P., Riley, B. J., Crum, J. V., & Matyas, J., The effect of high-level waste glass composition on spinel liquidus temperature, *J. Non-Cryst. Solids*, **384**, 2014; pp 32-40.

[7] Fox, K. M., & Fowley, M. D., Crystal Accumulation in the Hanford Waste Treatment Plant High Level Waste Melter: Summary of 2017 Experiments, Savannah River National Laboratory, *SRNL-STI-2017-00730 Revision 0*, 2018.

[8] Matyáš, J., Crum, J., Vienna, J., Arrigoni, A., Schaible, M., Tate, R., & Rodriguez, C., Development of crystal-tolerant high-level waste glasses, Pacific Northwest National Laboratory, *PNNL-20072*, 2010.

[9] Kim, D.-S., Schweiger, M. J., Rodriguez, C. P., Lepry, W. C., Lang, J. B., Crum, J. V., Vienna, J. D., Johnson, F., Marra, J. C., & Peeler, D. K., Formulation and characterization of waste glass with varying processing temperatures, Pacific Northwest National Laboratory, *PNNL-20774*, 2011.

[10] Matyáš, J., Huckleberry, A. R., Rodriguez, C. P., Lang, J. B., Owen, A. T., & Kruger, A. A., Crystal-tolerant glass approach for mitigation of crystal accumulation in continuous melters processing radioactive waste, Office of River Protection, *ORP-52717*, 2013.

[11] Matyáš, J., Schaible, M. J., & Vienna, J., Determination of Stokes Shape Factor for Single Particles and Agglomerates, *Ceram. Trans.*, **227**, 2011; pp 195-202.

[12] Vienna, J. D., Skorski, D. C., Kim, D.-S., & Matyas, J., Glass property models and constraints for estimating the glass to be produced at Hanford by implementing current advanced glass formulation efforts, Pacific Northwest National Laboratory, *PNNL-22631 Rev. 1*, 2013.

[13] Matyáš, J., Vienna, J. D., Peeler, D. K., Fox, K. M., Herman, C. C., & Kruger, A. A., Road map for development of crystal-tolerant high level waste glasses, Pacific Northwest National Laboratory, *PNNL-23363*, 2014.

[14] Marra, J. C., & Kim, D.-S., Towards increased waste loading in high level waste glasses: developing a better understanding of crystallization behavior, *Proc. Mater. Sci.*, **7**, 2014; pp 87-92

[15] Li, H., Hrma, P., Vienna, J. D., Qian, M., Su, Y., & Smith, D. E., Effects of Al_2O_3, B_2O_3, Na_2O, and SiO_2 on nepheline formation in borosilicate glasses: Chemical and physical correlations, *J. Non-Cryst. Solids*, **331**, 2003; pp 202-216.

[16] Jantzen, C. M., & Brown, K. G., Predicting the spinel-nepheline liquidus for application to nuclear waste glass processing. Part II: Quasicrystalline freezing point depression model, *J. Am. Ceram. Soc*., **90**, 2007; pp 1880-1891.

[17] Fox, K. M., Edwards, T. B., & Peeler, D. K., Control of nepheline crystallization in nuclear waste glass, *Int. J. Appl. Ceram. Technol.*, **5**, 2008; pp 666-673.

[18] McCloy, J. S., Schweiger, M. J., Rodriguez, C. P., & Vienna, J. D., Nepheline crystallization in nuclear waste glasses: Progress toward acceptance of high-alumina formulations, *Int. J. Appl. Glass Sci.*, **2**, 2011; pp 201-214.

[19] Rodriguez, C. P., McCloy, J. S., Schweiger, M. J., Crum, J. V. & Winschell, A., Optical Basicity and Nepheline Crystallization in High Alumina Glasses, Pacific Northwest National Laboratory, *PNNL-20184*, 2011.

[20] Pareizs, J. M., Sludge batch 7b qualification activities with SRS tank farm sludge, Savannah River National Laboratory, *SRNL-STI-2011-00548 Revision 0*, 2011.

[21] Vienna, J. D., Kim, D.-S., Schweiger, M. J., Piepel, G. F., & Kruger, A. A., Glass Formulation and Testing for U.S. High-Level Tank Wastes Project 17210 Year 1 Status Report: October 15, 2014, Pacific Northwest National Laboratory, *PNNL-SA-84872*, 2014.

[22] Marcial, J., Crum, J., Neill, O., & McCloy, J., Nepheline structural and chemical dependence on melt composition, *Am. Mineral.*, **101**, 2016; pp 266-276.

[23] Fox, K. M., Edwards, T. B., & McClane, D. L., Chemical composition analysis and product consistency tests supporting refinement of the nepheline model for the high aluminum Hanford glass composition region, Savannah River National Laboratory, *SRNL-STI-2016-00028 Revision 0*, 2016.

[24] Ahmadzadeh, M., Marcial, J., & McCloy, J., Crystallization of iron-containing sodium aluminosilicate glasses in the $NaAlSiO_4$-$NaFeSiO_4$ join, *J. Geophys. Res. Solid Earth*, **122**, 2017;

[25] Vienna, J. D., Kroll, J. O., Hrma, P. R., Lang, J. B., & Crum, J. V., Submixture model to predict nepheline precipitation in waste glasses, *Int. J. Appl. Glass Sci.*, **8**, 2017; pp 143-157.

[27] Ahmadzadeh, M., Olds, T. A., Scrimshire, A., Bingham, P. A., McCloy, J. S., Structure and properties of $Na_5FeSi_4O_{12}$ crystallized from $5Na_2O–Fe_2O_3–8SiO_2$ glass, *Acta. Cryst.*, **C74**, 2018; pp 1595-1602.

[29] McClane, D. L., Amoroso, J. W., Fox, K. M., & Kruger, A. A., Nepheline crystallization behavior in simulated high-level waste glasses, *J. Non-Cryst. Solids*, **505**, 2019; pp 215-224.

[30] Amoroso, J. W., McClane, D. L., & Fox, K. M., Nucleation and crystal growth behavior of nepheline in simulated high-level waste glasses, Savannah River National Laboratory, *SRNL-STI-2017-00517 Revision 0*, 2017.

[31] Peeler, D. K., & Edwards, T. B., Impact of REDOX on glass durability: The glass selection process, Savannah River Technology Center, *WSRC-TR-2004-00135 Revision 0*, 2004.

[32] Crawford, C. L., Marra, J. C., & Bibler, N. E., Glass fabrication and product consistency testing of lanthanide borosilicate glass for plutonium disposition, Savannah River National Laboratory, *WSRC-STI-2007-00079 Revision 0*, 2007.

[33] Neeway, J. J., Rieke, P. C., Parruzot, B. P., Ryan, J. V., & Asmussen, R. M., The dissolution behavior of borosilicate glasses in far-from equilibrium conditions, *Geochim. Cosmochim. Acta*, **226**, 2018; pp 132-148.

[34] Matlack, K. S., Gan, H., Chaudhuri, M., Kot, W., Gong, W., Bardacki, T., Pegg, I. L., & Joseph, I., Melt rate enhancement for high aluminum HLW glass formulations, Office of River Protection, *VSL-08R1360-1*, 2008.

[35] Matlack, K. S., Gan, H., Chaudhuri, M., Kot, W., Pegg, I. L., & Joseph, I., Melter throughput enhancements for high-iron HLW, Office of River Protection, *VSL-12R2490-1*, 2012.

[36] Matlack, K. S., Kot, W. K., Pegg, I. L., & Joseph, I., Support for HLW direct feed – Phase 2, Office of River Protection, *VSL-15R3440-1*, 2015.

[37] Muller, I. S., Matlack, K. S., Gan, H., Joseph, I., & Pegg, I. L., Waste loading enhancements for Hanford LAW glasses, Office of River Protection, *VSL-10R1790-1*, 2010.

[38] Matlack, K. S., Muller, I. S., Callow, R. A., D'Angelo, N., Bardacki, T., Joseph, I., & Pegg, I. L., Improving technetium retention in Hanford LAW glass – Phase 2, Office of River Protection, *VSL- 11R2260-1*, 2011.

[39] Vienna, J. D., Crum, J. V., Sevigny, G. J., & Smith, G. L., Preliminary technology maturation plan for immobilization of high-level waste glass-ceramics, Pacific Northwest National Laboratory, *PNNL-21714 Revision 0*, 2012.

[40] ASTM Standard C1285, 2021, "Standard Test Methods for Determining Chemical Durability of Nuclear, Hazardous, and Mixed Waste Glasses and Multiphase Glass Ceramics: The Product Consistency Test (PCT)" ASTM International, West Conshohocken, PA, 2021, DOI: 10.1520/C1285-21, www.astm.org.

[41] Jantzen, C. M., Bibler, N. E., Beam, D. C., Crawford, C. L., & Pickett, M. A., Characterization of the Defence Waste Processing Facility (DWPF) Environmental Assessment (EA) glass standard reference material (U), Savannah River Site, *WSRC-TR-92-346 Revision 1*, 1993.

[42] Smith, G. L., Schweiger, M. J., Bates, D. J., Smith, H. D., Goles, R. W., Urie, M. W., Greenwood, L. R., Wagner, J. J., Lettau, R. C., & Piepel, G. F., Vitrification and product testing of C-104 and AZ-102 pretreated sludge mixed with flowsheet quantities of secondary wastes, Pacific Northwest National Laboratory, *WTP-RPT-006 Revision 0*, 2001.

[43] Riley, B. J., & Chong, S., Effects of composition and canister centerline cooling on microstructure, phase distribution, and chemical durability of dehalogenated iron phosphate waste forms, *J. Non-Cryst. Solids*, **579**, 2021.

[44] Haines, P. J., & Wilbur F. W., Ch 3. Differential thermal analysis and differential scanning calorimetry, in Thermal Methods of Analysis: Principles, Applications, and Problems, Edited by Haines, P. J., Springer, Netherlands, 1994.

[45] Moguš-Milanković, A., Rajić, M., Drašner, A., Trojko, R., & Day, D. E., Crystallization of iron phosphate glasses, *J. Therm. Anal.*, **22**, 1981; pp 213-219.

[46] Ray, C. S., Fang, X., Karabulut, M., Marasinghe, G. K., & Day, D. E., Effect of melting temperature and time on iron valence and crystallization of iron phosphate glasses, *J. Non-Cryst. Solids*, **249**, 1999; pp 1-16.

[47] Karamanov, A., Di Gioacchino, R., Pisciella, P., & Pelino, M., Glass transformation range of iron rich glass and glass ceramics determined by different methods, *Glass Technol*., **42**, 2001; pp 126-129.

[48] Metcalfe, B. L., Fong, S. K., & Donald, I. W., Preparation, thermal characterisation and chemical durability of calcium iron phosphate glasses, *Glass Technol.*, **46**, 2005; pp 130-133.

[49] Natrup, F. V., & Bracht, H., Correlation between the cation radii and the glass transition in mixed cation silicate glasses, *Phys. Chem. Glasses*, **46**, 2005; pp 95-98.

[50] Cramer, C., & Gao, Y., & Funke, K., Mixed cation effects in glasses with three types of alkali ions, *Phys. Chem. Glasses*, **46**, 2005; pp 2279-2284.

[51] Bingham, P. A., Hand, R. J., Forder, S. D., & Lavaysierre, A., Vitrified metal finishing wastes: II. Thermal and structural characterisation, *J. Hazard. Mater.*, **122**, 2005; pp 129-138.

[52] Al-Hajry, A., Al-Shahrani, A., & El-Desoky, M. M., Structural and other physical properties of barium vanadate glasses, *Mater. Chem. Phys.*, **95**, 2006; pp 300-306.

[53] Aitken, B. G., & Youngman, R. E., Borophosphosilicate glasses: Properties and structure, *Phys. Chem. Glasses: Eur. J. Glass Sci. Technol. B*, **47**, 2006; pp 381-387.

[54] Bingham, P. A., Hand, R. J., Forder, S. D., Lavaysierre, A., Deloffre, F., Kilcoyne, S. H., & Yasin, I., Structure and properties of borophosphate glasses, *Phys. Chem. Glasses: Eur. J. Glass Sci. Technol. B*, **47**, 2006; pp 313-317.

[55] Kodana, M., Ono, A., Kojima, S., Feller, S. A., & Affatigato, M., Borate anomaly and anharmonicity in sodium borate glasses, *Phys. Chem. Glasses: Eur. J. Glass Sci. Technol. B*, **47**, 2006; pp 465-470.

[56] Cassingham, N. J., Bingham, P. A., Hand, R. J., & Forder, S. D., Property modification of a high level nuclear waste borosilicate glass through the addition of Fe_2O_3, *Glass Technol.: Eur. J. Glass Sci. Technol. A*, **49**, 2008; pp 21-26.

[57] Ferreira, E. B., Lima, M. L., & Zanotto, E. D., DSC method for determining the liquidus temperature of glass-forming systems, *J. Am. Ceram. Soc.*, **93**, 2010; pp 3757-3763.

[58] Kumar, V., Kaur, G., Pandey, O. P., & Singh, K., Chemical interaction and thermal studies of calcium borosilicate glass sealants, *Phys. Chem. Glasses: Eur. J. Glass Sci. Technol. B*, **52**, 2011; pp 212-220.

[59] Karabulut, M., Yuce, B., Bozdogan, O., Ertap, H., & Mammadov, G. M., Effect of boron addition on the structure and properties of iron phosphate glasses, *J. Non-Cryst. Solids*, **357**, 2011; pp 1455-1462.

[60] Liu, H., Yang, R., Wang, Y., & Liu, S., Influence of alumina additions on the physical and chemical properties of lithium-iron-phosphate glasses, *Phys. Proc.*, **48**, 2013; pp 17-22.

[61] Chavoutier, M., Caurant, D., Majérus, O., Boulesteix, R., Loiseau, P., Jousseaume, C., Brunet, E., & Lecomte, E., Effect of TiO_2 content on the crystallization and the color of (ZrO_2,TiO_2)-doped Li_2O-Al_2O_3-SiO_2 glasses, *J. Non-Cryst. Solids*, **384**, 2014; pp 15-24.

[62] Dalal, S., Khasa, S., Dahiya, M. S., Yadav, A., Agarwal, A., & Dahiya, S., Optical and thermal investigations on vanadyl doped zinc lithium borate glasses, *J. Asian Ceram. Soc.*, **3**, 2015; pp 234-239.

[63] Chromčková, M., Teplanová, M., Plško, A., Lissová, M., & Liška, M., Crystallization kinetics of borosilicate glasses for CHROMPIC nuclear waste vitrification, *Phys. Chem. Glasses: Eur. J. Glasses Sci. Technol. B*, **56**, 2015; pp 49-52.

[64] Michalski, P. P., Pietrzak, T. K., Nowiński, J. L., Wasiucionek, M., & Garbarczyk, J. E., Dependence of a glass transition temperature on a heating rate in DTA experiments for glasses containing transition metal oxides, *J. Non-Cryst. Solids*, **443**, 2016; pp 155-161.

[65] Vassilev, T., Penkov, I., Tzvetkova, C., & Pascova, R., Glass transition temperatures and structures of multicomponent borate glasses: Influence of modifier cation field strengths, *J. Non-Cryst. Solids*, **438**, 2016; pp 1-6.

[66] Dahiya, M. S., Khasa, S., & Agarwal, A., Structural, optical and thermal properties of transition metal ions doped bismuth borate glasses, *Phys. Chem. Glasses: Eur. J. Glass Sci. Technol. B*, **57**, 2016; pp 45-52.

[67] Suresh, S., Narendrudu, T., Kumar, A. S., Rao, M. V. S., Tirupataiah, C., & Rao, D. K., Assessment of the structural state of vanadium ions in calcium bismuth borophosphate glass-ceramics by means of spectroscopic investigations, *Phys. Chem. Glasses: Eur. J. Glass Sci. Technol. B*, **58**, 2017; pp 49-58.

[68] Jospeh, K., Stennett, M. C., Hyatt, N. C., Asvathraman, R., Dube, C. L., Gandy, A. S., Kutty, K. V. G., Jolley, K., Rao, P. R. V., & Smith, R., Iron phosphate glasses: Bulk properties and atomic scale structure, *J. Nucl. Mater.*, **494**, 2017; pp 342-353.

[69] Rodriguez, C. P., Chun, J., Crum, J. V., Canfield, N. L., Rönnebro, E. C. E., Vienna, J. D., & Kruger, A. A., Thermal properties of simulated Hanford waste glasses, *J. Am. Ceram. Soc.*, **100**, 2017; pp 2533-2542.

[70] Mary, N., Rebours, M., Castel, E., Vaishnav, S., Deng, W., Bell, A. M. T., Clegg, F., Allsopp, B. L., Scrimshire, A., & Bingham, P. A., Enhanced thermal stability of high-bismuth borate glasses by addition of iron, *J. Non-Cryst. Solids*, **500**, 2018; pp 149-157.

[71] Polyakova, I. G., The criterion for the crystallization ability assessment as applied to borate glass powders and monoliths, *Entropy*, **21**, 2019.

[72] Valderrama, D. M. A., Cuaspud, J. A. G., Roether, J. A., & Boccaccini, A. R., Development and characterization of glass-ceramics from combinations of slag, fly ash, and glass cullet without adding nucleating agents, *Mater.*, **12**, 2019.

[73] Zheng, Q., Zheng, J., Solvang, M., Yue, Y., & Mauro, J. C., Determining the liquidus viscosity of glass-forming liquids through differential scanning calorimetry, *J. Am. Ceram. Soc.*, 2020; pp 1-5.

[74] Iordanova, R., Milanova, M., Aleksandrov, L., & Shinozaki, K., Structural study of WO_3-La_2O_3-B_2O_3-Nb_2O_5 glasses, *J. Non-Cryst. Solids*, **543**, 2020.

[75] Dutta, D. P., Roy, M., Mishra, R. K., Meena, S. S., Yadav, A., Kaushik, C. P., & Tyagi, A. K., Structural investigations on Mo, Cs and Ba ions-loaded iron phosphate glass for nuclear waste storage application, *J. Alloys. Compd.*, **850**, 2021.

[76] Nishida, T., Kubuki, S., & Oka, N., Local structure, glass transition, structural relaxation, and crystallization of functional oxide glasses investigated by Mössbauer spectroscopy and DTA, *J. Mater. Sci.: Mater. Electron.*, 2021.

[77] Yang, Z., Wang, B., & Cormack, A. N., The local structure of Fe in Li(Al, Fe)Si_2O_6 glasses from molecular dynamics simulations, *J. Non-Cryst. Solids*, **444**, 2016; pp 16-22.

[78] Bell, A. M. T., Structural studies using synchrotron X-ray powder diffraction and other techniques, 1999. (Available at: https://www.repository.cam.ac.uk/handle/1810/294545).

[79] Rietveld, H. M., A profile refinement method for nuclear and magnetic structures, *J. Appl. Cryst.*, **2**, 1969; pp 65-71.

[80] Li, W., Liang, X., An, P., Feng, X., Tan, W., Qui, G., Yin, H., & Liu, F., Mechanisms on the morphology variation of hematite crystals by Al substitution: The modification of Fe and O reticular densities, *Sci. Rep.*, **6**, 2016; pp 1-10.

[81] Kilinc, E., Bell, A. M. T., Bingham, P. A., & Hand, R. J., Effects of composition and phase relations on mechanical properties and crystallization of silicate glasses, *J. Am. Ceram. Soc.*, **104**, 2021; pp 3921-3946.

[82] Deshkar, A., Ahmadzadeh, M., Scrimshire, A., Han, E., Bingham, P. A., Guillen, D., McCloy, J., & Goel, A., Crystallization behavior of iron- and boron-containing nepheline ($Na_2O{\cdot}Al_2O_3{\cdot}2SiO_2$) based model high-level nuclear waste glasses, *J. Am. Ceram. Soc.*, **102**, 2019; pp 1101-1121.

[83] Marcial, J., Kabel, J., Saleh, M., Washton, N., Shaharyar, Y., Goel, A., & McCloy, J. S., Structural dependence of crystallization in glasses along the nepheline ($NaAlSiO_4$) - eucryptite ($LiAlSiO_4$) join, *J. Am. Ceram. Soc.*, **101**, 2018; pp 2840-2855.

[84] Deshkar, A., Parruzot, B., Youngman, R. E., Gulbiten, O., Vienna, J. D., & Goel, A., Compositional dependence of crystallization and chemical durability in alkali aluminoborosilicate glasses, *J. Non-Cryst. Solids*, **590**, 2022.

[85] Ahmadzadeh, M., Marcial, J., & McCloy, J., Crystallization of iron-containing sodium aluminosilicate glasses in the $NaAlSiO_4$-$NaFeSiO_4$ join, *J. Geophys. Res. Solid*, **122**, 2017; pp 2504-2524.

[86] Shaharyar, Y., Cheng, J. Y., Han, E., Maron, A., Weaver, J., Marcial, J., McCloy, J. S., & Goel, A., Elucidating the effect of iron speciation (Fe^{2+}/Fe^{3+}) on crystallization kinetics of sodium aluminosilicate glasses, *J. Am. Ceram. Soc.*, **99**, 2016; pp 2306-2315.

[87] Deshkar, A., Marcial, J., Southern, S. A., Kobera, L., Bryce, D. L., McCloy, J. S., & Goel, A., Understanding the structural origin of crystalline phase transformations in nepheline ($NaAlSiO_4$)-based glass-ceramics, *J. Am. Ceram. Soc.*, **100**, 2017; pp 2859-2878.

[88] Rigby, J. C., Dixon, D. R., Kloužek, J., Pokorný, R., Thompson, P. B. J., Scrimshire, A., Kruger, A. A., Bell, A. M. T., & Bingham, P. A., Alternative reductants for foam control during vitrification of high-iron High Level Waste (HLW) feeds, *J. Non-Cryst. Solids*, **608**, 2023.

[89] Gorelova, L. A., Filatov, S. K., Krzhizhanovskaya, M. G., & Bubnova, R. S., High temperature behaviour of danburite-like borosilicates $MB_2Si_2O_8$ (M = Ca, Sr, Ba), *Phys. Chem. Glasses: Eur. J. Glass Sci. Technol. B*, **56**, 2015; pp 189-196.

[90] Rigby, J. C., Dixon, D. R., Cutforth, D. A., Marcial, J., Kloužek, J., Pokorný, R., Kruger, A. A., Scrimshire, A., Bell, A. M. T., & Bingham, P. A., Melting behaviour of simulated radioactive waste as functions of different redox iron-bearing raw materials, *J. Nucl. Mater.*, **569**, 2022.

[91] Balasubramanya, N., Sun, Z., Ahmadzadeh, M., Kamali, S., Neuville, D. R., McCloy, J. S., & Goel, A., Impact of non-framework cation mixing on the structure and crystallization behavior of model high-level waste glasses, *J. Am. Ceram. Soc.*, **105**, 2022; pp 3967-3985.

[92] Thorpe, C. L., Neeway, J. J., Pearce, C. L., Hand, R. J., Fisher, A. J., Walling, S. A., Hyatt, N. C., Kruger, A. A., Schweiger, M., Kosson, D. S., Arendt, C. L., Marcial, J., & Corkhill, C. L., Forty years of durability assessment of nuclear waste glasses by standard methods, *npj Mater. Degrad.*, **61**, 2021.

[93] Cunnane, J. C., Bates, J. K., Bradley, C. R., Buck, E. C., Ebert, W. L., Feng, X., Mazer, J. J., Wronkiewicz, D. J., Sproull, J., McGraill, B. P., & Altenhofen, M. K., High-Level Waste Borosilicate Glass: A Compendium of Corrosion Characteristics, Volume II, US DoE Office of Waste Management, 1994.

[94] Feng, X., Pegg, I. L., Barkatt, A. A., Macedo, P. B., Cucinell, S, J., & Lai, S., Correlation between composition effects on glass durability and the structural role of the constituent oxides, *Nucl. Technol.*, **85**, 1989; pp 334-345.

[95] Van Iseghem, P., Timmermans, W., & De Batist, R., Corrosion behavior of TRUW base and reference glasses, *Mat. Res. Soc. Symp. Proc.*, **26**, 1984; pp 527-534.

[96] Nogues, J. L., & Hench, L. L., Effect of Fe_2O_3/ZnO on two glass compositions for solidification of Swedish nuclear wastes, *Mat. Res. Soc. Symp. Proc.*, **11**, 1982; pp 273-278.

[97] Yangisawa, F., & Sakai, H., Effect of iron and potassium contents in a simulated borosilicate glass on its leaching behavior at hydrothermal conditions, *Geochem J.*, **21**, 1987; pp 209-217.

[98] Brossel, M., Marchetti, L., Jollivet, P., & Schlegel, M. L., About the role of iron on the alteration of simplified nuclear glasses in deaerated at 50 °C, *J. Nucl. Mater.*, **567**, 2022.

Chapter 8 – Summary, Conclusions, & Future Work

8.1 Summary & Conclusions

8.1.1 Iron Chemistry & Structure

The ^{57}Fe Mössbauer spectra from Chapter 4 showed that the iron within the glass exists entirely as Fe^{3+} with no detectable amounts of Fe^{2+} within any sample across all three series. This was supported by the Fe K-edge XANES data in Chapter 5, which showed that the majority of samples consisted of Fe^{3+} with some evidence of Fe^{2+}, this included three samples in the HAFe series, which appeared to show significant amounts of Fe^{2+} in the lower-Fe samples, despite the lack of corresponding evidence in the Mössbauer spectra. When determining the oxidation state in materials, Neuville *et al*. [1] describes Mössbauer spectroscopy as a precise absolute technique in determining oxidation state, and notes that XANES data (especially XANES spectra of the 1s – 3s pre-edge transition) can be difficult to accurately determine redox ratios in complex amorphous materials [1]. For this reason, the Mössbauer spectra will be weighted more when discussing the oxidation state of the iron within the samples, which shows 100% Fe^{3+} in all glass samples, including the low-Fe HAFe sample outliers seen in **Fig 5.49**.

The coordination of the Fe within the samples is somewhat ambiguous in the Mössbauer spectra. As discussed in Chapter 4.3, the quadrupole split values are typically used to describe the coordination of the iron, however there is some ambiguity and overlap between tetrahedral and octahedral Fe^{3+} (see Chapter 4.3 for more details). Each sample was fit with two Lorentzian doublets, with the quadrupole split values lying within or close to the overlap region between tetrahedral and octahedral Fe^{3+}, leading to multiple, yet distinctly different justifiable assignments of the average coordination number based on the quadrupole split alone. However, the centre shift values for all samples corresponded to tetrahedral Fe^{3+} with no ambiguity relative to the centre shift values of octahedral Fe^{3+}. In many publications containing ^{57}Fe Mössbauer spectra on glasses, the centre shift values have been used to assign the coordination number in the event of ambiguous quadrupole split values [2-5]. If this approach was used in this research, then the Mössbauer spectra would show that the iron exists predominantly as tetrahedral Fe^{3+}. This assignment is supported by the integrated intensity of the XANES data, which shows an average coordination between 4-5 for all samples (see **Fig 5.49**). While it would be desirable to extract more quantitative analysis from the two techniques regarding the iron coordination, Forder *et al*. [6] argues against doing so based on ^{57}Fe Mössbauer and Fe K-edge XANES data when compared to mineral standards. Forder *et al*. [6] demonstrated

that due to the distribution of bond angles and lengths a given structural unit can occupy within the amorphous phase, the distortion of tetrahedral and octahedral units produces spectral fit data that overlap significantly. For example, a glass with 5-coordinated Fe will have spectral fit parameters that are very similar, if not indistinguishable from a glass that has a mix of 4- and 6-coordinated Fe [6].

When collating the conclusions from the data available, the conclusions that can be drawn suggest that the iron exists as Fe^{3+} in predominantly tetrahedral structures, with significant evidence of some amount of higher coordinated Fe^{3+}. Further work would be needed to provide more quantitative results on the iron coordination within the glasses studied in this research, with examples of further work given in Chapter 8.2.

8.1.2 Glass Chemistry & Structure

The increasing contents of Fe_2O_3 within the glass series had a varied impact on the wider glass chemistry. The Raman spectra (see Chapter 6) showed very similar spectral changes in the difference spectra (see **Figs 6.8** – **6.10**) for all three series. Most notably, there was a decrease in a band located at around 630 cm^{-1} in all three series, that has been assigned to borosilicate structures comparable to danburite- and reedmergnerite-like structures [7]. Furthermore, there were significant changes in higher frequency bands that corresponded to "loose" BO_3 and metaborate groups and BO_3 – BO_4 [8-10]. The band corresponding to the larger BO_3 – BO_4 metaborate groups decreased, while the band corresponding to "loose" BO_3 increased.

This led to an early hypothesis that the tetrahedral Fe^{3+} was being preferentially charge compensated over the tetrahedral B. This would result in the breakdown of danburite- and reedmergnerite-like borosilicate structures (as the boron exists as $^{[4]}B$) and the breakdown of BO_3-BO_4 metaborate structures, with a corresponding increase in "loose" BO_3. This hypothesis was used as a potential explanation for similar trends in Raman spectra for glasses similar to the HAFe series by Rigby *et al*. [11]. However, the boron K-edge XANES data (see **Fig 5.53**) showed that there were no significant changes to the boron coordination in either of the SCFe or CCFe sample series as a function of increasing Fe_2O_3 contents. Thereforeee, an alternative hypothesis was needed to explain these trends.

The B 1s and Si 2p XPS spectra showed that for both electron signals, the binding energy decreases as a function of Fe_2O_3 contents within the glass. For the SCFe series, it shows the Si 2p undergoes more of a decrease in binding energy than the B 1s, yet the opposite is true for the CCFe series. A similar trend is seen in the higher frequency Raman bands

corresponding to the borate groups, where the relative intensity of the change in boron bands is higher in the CCFe samples than it is the SCFe samples. In Chapter 6.9.2, this was linked to change in the average covalent character of the bonds around the silicate and borate groups, likely linked to the introduction of Si-O-Fe and B-O-Fe bonds, which could account for the change in covalent character of the bonds. This suggests that in the SCFe series, the iron preferentially integrates into the silicate sub-network more so than the borate sub-network, whereas in the CCFe series, the iron preferentially integrates into the borate sub-network.

Wright *et al*. [2] demonstrated that in sodium borosilicate glasses, tetrahedral Fe^{3+} preferentially bonds to the silicate sub-network whereas octahedral Fe^{3+} preferentially bonds to the borate sub-network. This theory explains why the Si 2p binding energy shows a greater change than the B 1s binding energy for the SCFe series, and anecdotally suggests that iron exists as tetrahedral Fe^{3+} more so than octahedral Fe^{3+} as per the conclusions from Chapter 8.1.1. However, in order for this theory to fully explain what happens in the CCFe series, one would expect a significant change in the centre shift and quadrupole split values in Mössbauer spectral fits between the SCFe and CCFe series, coupled with a significantly different integrated intensity of the 1s - 3s pre-edge fits in the Fe K-edge XANES. Neither of these changes are observed when comparing the SCFe and CCFe spectral fit parameters for either technique.

One hypothesis that may explain the changes is the tetrahedral avoidance theory. Du and Stebbins [12] studied alkali aluminoborosilicate glasses and demonstrated that alumina tetrahedra avoid boron tetrahedra [12]. Zhang *et al*. [13] observed tetrahedral avoidance between alumina and iron tetrahedra in phosphate and phosphate-free alkali aluminoborosilicate glasses. It could be hypothesised that the within the CCFe series (and by extension, the HAFe series) that the alumina and boron tetrahedra avoid each other as per Du and Stebbins [12] which results in more alumina in the silicate sub-network. The iron tetrahedra are then forced into the borate sub-network through avoiding the alumina tetrahedra as per Zhang *et al*. [13]. This would explain why there is a significant relative increase in changes to borate related bands in the Raman spectra, coupled with the evidence of the boron being more impacted by the iron in XPS data, in the CCFe series than the SCFe series. It would also explain why the theory of Fe environments in borosilicate glasses put forth by Wright *et al*. [2] does not fully explain the spectral changes in the CCFe series, as the glasses studied by Wright *et al*. [2] did not contain alumina.

The tetrahedral avoidance theory is not the only factor to consider. The addition of alumina is not the only compositional difference between the SCFe and CCFe series – the CCFe series also contains Li_2O and CaO within the glass. Bingham et al. [14] studied the selective behaviour of dilute Fe^{3+} cations in silicate glasses and found that depending on the alkali or alkaline earth cation type providing charge compensation or bonding with the Fe^{3+} cation, the Fe-O coordination and bond length would change. Qualitatively, it was shown that the lower the ionic radii ratios of the modifier parings (examples given in ref [14]: Li-Ba & Na-Ba), the higher the coordination of the Fe, while the higher the ionic radii ratios (examples given in ref [14]: K-Ca, K-Mg, Na-Mg) the coordination of the Fe was lower [14]. This qualitatively supported findings by Farges et al. [15], which used Fe K-edge XANES and molecular dynamic simulations to study the changes in Fe-coordination and valency as a function of changing modifier cations, which included Ca, Na, Mg, K. Balasubramanya et al. [16] studied the effects of Na, Li, and Ca network modifiers on the spinel crystallisation within complex borosilicate glasses. It was shown that the higher the cation field strength, the greater the depolymerisation, greater the increase in Fe^{2+}, and more likely to promote secondary crystallisation through clustering of Fe, or even LiAl (which forms spodumene). Furthermore, Wiegel et al. [17] used neutron diffraction and Empirical Potential Structure Refinement (EPSR) simulations to show that within $NaFeSi_2O_6$ (NFS) glasses, that while the iron exists predominantly as $^{[4]}Fe^{3+}$, there is also $^{[5]}Fe^{3+}$ and $^{[5]}Fe^{2+}$ species that can form edge-sharing clusters in higher concentrations of Fe within the glass.

The leading hypothesis as to why the borate sub-network is affected more by the iron oxide in complex borosilicate glasses is likely a combination of the tetrahedral avoidance theory [12,13] and the effects different modifier cations have on the iron oxide [14-17]. To fully understand these complex interactions, further dedicated study is required.

8.1.3 Glass Properties

The glass property studies in Chapter 7, demonstrated that iron oxide has clear influence on glass properties but nothing from these studies demonstrated anything that was not already known through previous studies. With the phase study, it was shown that long cooling resulted in more crystallisation, with the amount of Fe-bearing crystal phase increasing with increasing Fe_2O_3 contents within the glass. The type of phase, an Fe-bearing spinel phase, is a phase commonly seen in high-Fe Hanford waste glass analogues [18-28].

The iron has a slightly detrimental effect on the glass transition temperature of both HAFe sub-series, which was theorised by Yang *et al*. [29] to be due the Fe-O bonds being thermally weaker bonds that those of Si-O and Al-O. The overall decrease was slight (approximately a 25 ^{o}C between 0 – 10 mol% Fe_2O_3), but it is a trend that was seen in a similar study by Cassingham *et al*. [30].

Furthermore, Cassingham *et al*. [30] reported that Fe_2O_3 had a positive impact on chemical durability in the short term (0 – 14 days). This trend was also seen in this research (see **Figs 7.9** – **7.12**). This was linked to tetrahedral Fe^{3+} polymerising the glass network with hydrolysis resistant bonds. This provides further anecdotal evidence that iron does exist in predominantly tetrahedral units (see Chapter 8.1.1), and while it does not rule out the higher coordinated Fe, it does at least show that there is a significant amount of $^{[4]}Fe^{3+}$. The normalised concentration of glass components in the leachate was presented against the values for the DWPF-EA standard reference glass [31] measured by Matlack *et al*. [27] and it showed all components had a lower concentration in the two HAFe sub-series and would suggest that across all concentrations of iron, the chemical durability passes that form of benchmark testing. However, the values for DWPF-EA were not measured in this research, so this particular finding would require a repeat of the experiment with samples of the DWPF-EA being measured at the same time, in order to confirm this finding.

8.1.4 Relevance to Hanford Site

While the SCFe and CCFe glass sample series are highly simplified when compared to expected waste forms at the Hanford site, the data and associated conclusions can be linked back to the Hanford analogues. In the Raman spectra, the relative changes in band intensity for the HAFe series are very similar to those found in the CCFe series (see **Figs 6.9** & **6.10**), particularly the higher frequency borate bands. Within the CCFe series, these were linked to XPS spectra and changes in binding energy of the Si 2p and B 1s, which qualitatively showed that in the more complex composition, the borate sub-network is more affected by the increase in Fe_2O_3 contents and it is likely that the iron is preferentially integrating into the borate sub-network over the silicate sub-network (see Chapter 8.1.2). It is likely that the same phenomenon is occurring in the HAFe series, especially as the HAFe series has alumina and multiple network modifying cations. Further study would be required to confirm these links, such as measuring the HAFe series using XPS to confirm whether similar binding energy changes are seen in the HAFe series.

The property studies were done exclusively on the Hanford analogue HAFe-series, with a sub-series developed using the Hanford HLW CCC heat treatment profile. The data was compared with the same reference standard (DWPF-EA) used in Hanford studies, which results in data that can be directly linked to the Hanford site. As mentioned in Chapter 8.1.3, the data did not yield any unexpected results and were in line with established research on comparable Hanford analogue glasses, and with wider similar studies.

Where the data and conclusions need to be compared with caution, is the production methods used to generate the samples. Every sample was made with lab-grade reagents, with standard lab practices, in static furnaces. The Hanford wastes will not be vitrified in such a manner. Research by Rigby *et al*. [11,32] studied a common glass composition, but with the waste feed pre-made into a sludge prior to melting and with additional reducing agents in order to study the melt-foaming behaviour resulting from the "cold-cap". Furthermore, these studies were done simulant waste-feeds with different iron-bearing raw materials. Rigby *et al*. [32] demonstrated that the use of reducing agents with different raw materials can result in quantities of Fe^{2+} within the glass. This is not seen in this research. Furthermore, the chemical reaction stages within the cold cap, also has an influence on phase development and propagation into the final waste form [33-44]. The change in iron valency and secondary phases would also influence the glass properties (see for example refs [11,32,45]). These factors have not been considered within this research.

While the conclusions from this research have some qualitive conclusions on how the iron integrates with complex borosilicate networks that are useful in the scientific studies on the potential waste forms, there are definite caveats on direct comparisons and further study would be needed to appropriately address these caveats.

8.2 Suggested Future Work

Throughout this research project, several key areas have been identified for further study, that would both contribute to and enhance the findings from this study. Ranging from redoing certain experiments to correct mistakes made in this research (e.g. O 1s XPS) through to following up on interesting results, for example, the low temperature ^{57}Fe Mössbauer spectrum for the HAFe001.0 sample (see **Fig 4.19** in Chapter 4.4.4). This future work, the desired outcomes, and the hypothesised benefits to this research are detailed in this section.

8.2.1 Fe K-edge EXAFS

The ^{57}Fe Mössbauer and Fe K-edge XANES spectral data qualitative suggested that the iron exists predominantly as $^{[4]}Fe^{3+}$ with some evidence of higher coordinated iron. However, beyond this qualitative assessment, no quantitative analysis on the coordination was possible from this data. Fe K-edge EXAFS (see Chapter 5.1.2 for more details on EXAFS) has been used to quantitatively analyse iron coordination in a variety of materials, including minerals [46-49] and glasses [6,14,50-53]. While it is not expected to provide exact amounts of each coordinating of iron within the samples, it is expected that it would provide an average coordination for each sample and from there relative changes (if any) could be analysed.

For example, if the SCFe001.0 sample EXAFS spectrum was processed and fitted with a resulting average coordination of 4.5, and the SCFe010.0 sample EXAFS spectrum was processed and fitted with a resulting average coordination of 4.9, it can be said that both have significant amounts of tetrahedral iron but the SCFe010.0 has an increased amount of higher coordinated Fe than the SCFe001.0 sample. While this analysis is still not fully quantitative, it provides an increased layer of depth when comparing the Fe coordination of samples both within and across the three investigated series. This extra context would have been very useful when interpreting the Fe K-edge XANES and ^{57}Fe Mössbauer spectroscopy data for the analysis on the Fe coordination.

8.2.2 Low-Temperature ^{57}Fe Mössbauer Spectroscopy

When acquiring the ^{57}Fe Mössbauer spectra, a low-temperature spectrum was acquired for the HAFe001.0 sample. The expectation was that there would be a sextet in the spectrum indicative of hyperfine splitting (HFS) due to the increased relaxation times as a result of isolated Fe cations within the sample (see **Fig 4.19** and Chapter 4.5.2 for more information, with further context provided by Willliams *et al*. [54]). However, as can be seen in **Fig 4.19**, there is no sextet. This would suggest that the Fe within the glass is not isolated enough to cause an increase in relaxation times that would result in the presence of hyperfine splitting.

While the study by Williams *et al*. [54] researched silicate and not borosilicate glass, research by Cornwall *et al*. [55] showed that there is hyperfine splitting seen in the SCFe001.0 sample, which rules out the theory that the lack of hyperfine splitting is a result of a different glass matrix. Further work on low-temperature ^{57}Fe Mössbauer spectroscopy would first start with acquiring a low-temperature spectrum of the CCFe001.0 sample and seeing if the HFS sextet is present in this sample. If the sextet is

present, then there is a significant influence on iron grouping within the HAFe composition that merits further research, as iron grouping (or clustering) has been linked to crystallisation which is a big concern for the Hanford waste vitrification efforts. If there is not a HFS sextet in the CCFe001.0 sample, then the iron grouping is influenced by the addition of Al_2O_3, Li_2O, and/or CaO. Which would also warrant further study as these components are commonly used glass additives in both radioactive waste glasses and the wider glass industry.

8.2.3 O 1s XPS

The primary aim for the XPS study was to quantitatively analyse the non-bridging oxygen to oxygen ratio. However, as outlined in Chapter 6.6.2, this was unsuccessful due to a limitation in the sample preparation/loading capabilities, which resulted in the O 1s spectra containing oxy-carbon surface contamination. When acquired properly, the O 1s spectra has been used successfully to describe the bridging and non-bridging oxygens within the glass [56-62], which is a key property when describing the connectivity of the glass network. The conclusions from the chemical durability study show a link between the $^{[4]}Fe^{3+}$ forming network forming bonds within the glass network and an increase in chemical durability, therefore it would be beneficial to this research to have some form of analysis on this key glass property.

8.2.4 Chemical Durability

Further elaborating on the chemical durability, there are two distinct chemical durability studies that would be beneficial to this research. The first study would be an extension on the PCT study done in this research. This would include measuring the DWPF-EA standard reference and measuring all samples and standards across a range of time intervals between 0 – 28 days. This would also include re-measurement of the of the HAFe “CCC” sub-series at 7-days due to the Na and Si rich contaminant found in the blanks measured alongside these samples.

Parallel to this elaboration on the PCT study, a Vapour Hydration Test (VHT) would be done in parallel across the same time periods. Where PCT studied the dissolution rates of glass powders, VHT is a study on glass monoliths and will provide samples that would allow for the study of how the glass surface alteration propagates through time (see Thorpe *et al*. [63] for an overview and the ASTM [64] for measurement protocol). This would be achieved by combination of Scanning Electron Microscopy (SEM) and potentially X-ray Diffraction (XRD). A successful VHT study could go some ways to

addressing the question marks raised on the alteration layer efficacy on reducing the leachability of the key glass components.

8.2.5 Scanning Electron Microscopy

As well as being used in the VHT study, SEM would be used in the study of the secondary phase formation within the two HAFe sub-series. The Rietveld refinement studies (see Chapter 7.3) allowed for quantitative analysis on the abundance of phases within the glass samples and how much of the amorphous phase is presence. The limitation of XRD and the Rietveld refinements, were the exact composition of the spinel phase. The ICCD database labelled the spinel phases as either magnetite (Fe_3O_4) or a zinc-iron oxide spinel phase. However, due to the presence of other transition metal oxides, there is a chance that other transition metal inclusions could not be ruled out. SEM with associated Energy Dispersive X-ray Spectroscopy (EDXS) mapping would be used to determine if some transition metals have a predisposition to be included within the spinel phase more than others.

8.3 Thesis Summary

This research has qualitatively shown that iron oxide within the glass exists entirely of Fe^{3+} in predominantly tetrahedral units, with some evidence of higher coordinated structures. This finding was anecdotally supported by 7-day chemical durability studies with showed the iron oxide increases the chemical durability, a trend seen in previous studies which have linked this to $^{[4]}Fe^{3+}$ polymerising the glass network with hydrolysis resistant bonds [30].

Studies on the wider glass chemistry have shown that in the SCFe series, the iron preferentially bonds into the silicate sub-network whereas in the CCFe series, the iron preferentially bonds into the borate sub-network. Similarities in the Raman spectra between the CCFe and HAFe series, alongside some common glass components such as Al_2O_3, CaO, and Li_2O, have suggested that the iron preferentially bonds into the borate sub-network in the HAFe series. The hypothesis as to why this occurs, is led by the tetrahedral avoidance theory which suggests complex tetrahedral avoidance hierarchies between the AlO_4^-, BO_4^-, and FeO_4^- units within the glass [12,13]. There are likely significant impacts to the glass due to the different modifiers included within the glass, such as CaO, and Li_2O as reported in previous studies [14-17].

The property studies showed very few differences between the “Lab Made” and “CCC” sample sub-series, with the most pronounced difference being the expected increase in secondary phase abundance in the “CCC” samples, however, the low-Fe “CCC” sample

series were still fully amorphous. While the data and conclusions from both the spectroscopic and property studies have clear and useful links to the wider Hanford research, there are still some caveats and research questions that would need to be addressed through further dedicated study to further enhance the outputs from this study.

8.4 References

[1] Neuville, D. R., Cicconi, M. R., & Le Losq, C., Ch.13 How to Measure the Oxidation State of Multivalent Elements in Minerals, Glasses, and Melts?, in Magma Redox Geochemistry, Geophysical Monograph, 266, 2021.

[2] Wright, A. C., Sinclair, R. N., Shaw, J. L., Haworth, R., Bingham, P. A., Forder, S. D., Holland, D., Scales, C. R., Cuello, G. J., & Vedishcheva, N. M., The environment of Fe^{3+}/Fe^{2+} cations in a sodium borosilicate glass, *Phys. Chem. Glasses: Eur. J. Glass Sci. Technol. B*, **58**, 2017; pp 78-91.

[3] Balasubramanya, N., Sun, Z., Ahmadzadeh, M., Kamali, S., Neuville, D. R., McCloy, J. S., & Goel, A., Impact of non-framework cation mixing on the structure and crystallization behavior of model high-level waste glasses, *J. Am. Ceram. Soc.*, **105**, 2022; pp 3967-3985.

[4] Cochain, B., Neuville, D. R., Henderson, G. S., McCammon, C. A., Pinet, O, & Richet, P., Effects of the iron content and redox state on the structure of sodium borosilicate glasses: A Raman, Mössbauer and boron k-edge XANES spectroscopy study, *J. Am. Ceram. Soc.*, **95**, 2012; pp 962-971.

[5] Ciżman, A. Rysiakiewicz-Pasek, E., Antropova, T., Krupiński, M., Pshenko, O. A., & Zarzycki, A., Effect of the iron content on the structure and electrical properties of sodium borosilicate glasses: XRD, TEM, Mössbauer, FTIR and DIS spectroscopy study, *J. Non-Cryst. Solids*, **531**, 2020.

[6] Forder S. D., Hannant, O. M., Bingham, P. A., & Hand, R. J., Concerning the use of standards for identifying coordination environments in glasses, *J. Phys.: Conf. Ser.*, **217**, 2010.

[7] Manara, D., Grandjean, A., Neuville, D. R., Advances in understanding the structure of borosilicate glasses: A Raman spectroscopy study, *Am. Mineral*., **94**, 2009; pp 777-784.

[8] Yano, T., Kunimine, N., Shibata, S., & Yamane, M., Structural investigation of sodium borate glasses and melts by Raman spectroscopy. I. Quantitative evaluation of structural units, *J. Non-Cryst. Solids*, **321**, 2003; pp 137-146.

[9] Yano, T., Kunimine, N., Shibata, S., & Yamane, M., Structural investigation of sodium borate glasses and melts by Raman spectroscopy. II. Conversion between BO_4 and BO_2O-units at high temperature, *J. Non-Cryst. Solids*, **321**, 2003; pp 147-156.

[10] Yano, T., Kunimine, N., Shibata, S., & Yamane, M., Structural investigation of sodium borate glasses and melts by Raman spectroscopy. III. Relation between the rearrangement of super-structures and the properties of glass, *J. Non-Cryst. Solids*, **321**, 2003; pp 157-168.

[11] Rigby, J. C., Dixon, D. R., Cutforth, D. A., Marcial, J., Kloužek, J., Pokorný, R., Kruger, A. A., Scrimshire, A., Bell, A. M. T., & Bingham, P. A., Melting behaviour of simulated radioactive waste as functions of different redox iron-bearing raw materials, *J. Nucl. Mater.*, **569**, 2022.

[12] Du, L.-S., & Stebbins, J. F., Network connectivity in aluminoborosilicate glasses: A high-resolution ^{11}B, ^{27}Al and ^{17}O NMR study, *J. Non-Cryst. Solids*, **351**, 2005; pp 3508-3520.

[13] Zhang, Y., Balasubramanya, N., Stone-Weiss, N., Kamali, S., Youngman, R. E., Florian, P., & Goel, A., Insights into the iron- and phosphorus-induced structural rearrangements in sodium aluminoborosilicate glasses and their impact on melt rheology and crystallization behavior, *J. Phys. Chem. C*, **126**, 2022; pp 21771-21792.

[14] Bingham, P. A., Hannant, O. M., Reeves-McLaren, N., Stennett, M. C., & Hand, R. J., Selective behaviour of dilute Fe^{3+} ions in silicate glasses: An Fe K-edge EXAFS and XANES study. *J. Non-Cryst. Solids*, **387**, 2014; pp 47-56.

[15] Farges, F., Lefrère, Y., Rossano, S., Berthereau, A., Calas, G., & Brown Jr., G. E., The effect of redox state on the local structural environment of iron in silicate glasses: A combined XAFS spectroscopy, molecular dynamics, and bond valence study, *J. Non-Cryst. Solids*, **344**, 2004; pp 176-188.

[16] Balasubramanya, N., Sun, Z., Ahmadzadeh, M., Kamali, S., Neuville, D. R., McCloy, J, S., & Goel, A., Impact of non-framework cation mixing on the structure and crystallization behavior of model high-level waste glasses, *J. Am. Ceram. Soc.*, **105**, 2022; pp 3967-3985.

[17] Wiegel, C., Cormier, L., Calas, G., Galoisy, L., & Bowron, D. T., Nature and distribution of iron sites in a sodium silicate glass investigated by neutron diffraction and EPSR simulation, *J. Non-Cryst. Solids*, **354**, 2008; pp 5378-5385.

[18] Vienna, J. D., Hrma, P., Crum, J. V., & Mika, M., Liquidus temperature-composition model for multi-component glasses in the Fe, Cr, Ni, and Mn spinel primary phase field, *J. Non-Cryst. Solids*, **292**, 2001; pp 1-24.

[19] Jiricka, M., Hrma, P., & Vienna, J. D., The effect of composition on spinel crystals equilibrium in low-silica high-level waste glasses, *J. Non-Cryst. Solids*, **319**, 2003; pp 280-288.

[20] Jantzen, C. M., & Brown, K. G., Predicting the spinel-nepheline liquidus for application to nuclear waste glass processing. Part I: Primary phase analysis, liquidus measurement, and quasicrystalline approach, *J. Am. Ceram. Soc.*, **90**, 2007; pp 1866-1879.

[21] Hrma, P., Crystallization during processing of nuclear waste glass, *J. Non-Cryst. Solids*, **356**, 2010; pp 3019-3025.

[22] Fox, K. M., Crystallization in High Level Waste (HLW) Glass Melters: Operational Experience from the Savannah River Site, Savannah River National Laboratory, *SRNL-STI-2013-00724*, 2014.

[23] Hrma, P., Riley, B. J., Crum, J. V., & Matyas, J., The effect of high-level waste glass composition on spinel liquidus temperature, *J. Non-Cryst. Solids*, **384**, 2014; pp 32-40.

[24] Kim, D.-S., Schweiger, M. J., Rodriguez, C. P., Lepry, W. C., Lang, J. B., Crum, J. V., Vienna, J. D., Johnson, F., Marra, J. C., & Peeler, D. K., Formulation and characterization of waste glass with varying processing temperatures, Pacific Northwest National Laboratory, *PNNL-20774*, 2011.

[25] Matyáš, J., Vienna, J. D., Peeler, D. K., Fox, K. M., Herman, C. C., & Kruger, A. A., Road map for development of crystal-tolerant high level waste glasses, Pacific Northwest National Laboratory, *PNNL-23363*, 2014.

[26] Marra, J. C., & Kim, D.-S., Towards increased waste loading in high level waste glasses: developing a better understanding of crystallization behavior, *Proc. Mater. Sci.*, **7**, 2014; pp 87-92.

[27] Matlack, K. S., Gan, H., Chaudhuri, M., Kot, W., Pegg, I. L., & Joseph, I., Melter throughput enhancements for high-iron HLW, Office of River Protection, *VSL-12R2490-1*, 2012.

[28] Matlack, K. S., Kot, W. K., Pegg, I. L., & Joseph, I., Support for HLW direct feed – Phase 2, Office of River Protection, *VSL-15R3440-1*, 2015.

[29] Yang, Z., Wang, B., & Cormack, A. N., The local structure of Fe in Li(Al, Fe)Si_2O_6 glasses from molecular dynamics simulations, *J. Non-Cryst. Solids*, **444**, 2016; pp 16-22.

[30] Cassingham, N. J., Bingham, P. A., Hand, R. J., & Forder, S. D., Property modification of a high level nuclear waste borosilicate glass through the addition of Fe_2O_3, *Glass Technol.: Eur. J. Glass Sci. Technol. A*, **49**, 2008; pp 21-26.

[31] Jantzen, C. M., Bibler, N. E., Beam, D. C., Crawford, C. L., & Pickett, M. A., Characterization of the Defence Waste Processing Facility (DWPF) Environmental Assessment (EA) glass standard reference material (U), Savannah River Site, *WSRC-TR-92-346 Revision 1*, 1993.

[32] Rigby, J. C., Dixon, D. R., Kloužek, J., Pokorný, R., Thompson, P. B. J., Scrimshire, A., Kruger, A. A., Bell, A. M. T., & Bingham, P. A., Alternative reductants for foam control during vitrification of high-iron High Level Waste (HLW) feeds, *J. Non-Cryst. Solids*, **608**, 2023.

[33] Tan, S., Chapter 26: Glass-based stabilization/solidification of radioactive waste, in 'Low Carbon Stabilization and Solidification of Hazardous Wastes' Ed. By Tsang, D. & Wang, L., Elsevier, Amsterdam, Netherlands, 2022.

[34] Blair, H. T., & Lukacs, J. M., Investigation of foaming during nuclear defense-waste solidification by electric melting, Pacific Northwest Laboratory, *PNL-3552*, 1980.

[35] Lee, S.-M., Hrma, P., Pokorný, R., Klouzek, J., VanderVeer, B. J., Dixon, D. R., Luksic, S. A., Rodriguez, C. P., Chun, J., Schweiger, M. J., & Kruger, A. A., Effect of melter feed foaming on heat flux to the cold cap, *J. Nucl. Mater.*, **496**, 2017; pp 54-65.

[36] Lee, S.-M., Hrma, P., Pokorný, R., Klouzek, J., Eaton, W. C., & Kruger, A. A., Glass production rate in electric furnaces for radioactive waste vitrification, *J. Am. Ceram. Soc.*, **102**, 2019; pp 5828-5842.

[37] Pokorny, R., & Hrma, P., Model for the conversion of nuclear waste melter feed to glass, *J. Nucl. Mater.*, **445**, 2014; pp 190-199.

[38] Dixon, D. R., Schweiger, M. J., Riley, B. J., Pokorny, R., & Hrma, P., Temperature distribution within a cold cap during nuclear waste vitrification, *Environ. Sci. Technol.*, **49**, 2015; pp 8856-8863.

[39] Guillen, D. P., Abboud, A. W., Pokorny, R., Eaton, W. C., Dixon, D. Fox, K., & Kruger, A. A., Development of a validation approach for an integrated waste glass melter model, *Nucl. Technol.*, **203**, 2018; pp 244-260.

[40] Hrma, P., Pokorny, R., Lee, S.-M., & Kruger, A. A., Heat transfer from glass melt to cold cap: Melting rate correlation equation, *Int. J. Appl. Glass Sci.*, **10**, 2019; pp 143-150.

[41] Beerkens, R. D. C., & van der Schaaf, J., Gas release and foam formation during melting and fining of glass, *J. Am. Ceram. Soc.*, **89**, 2006; pp 24-35.

[42] Goldman, D. S., Melt foaming, foam stability and redox in nuclear waste vitrification, *J. Non-Cryst. Solids*, **84**, 1986; pp 292-298.

[43] Jin, T., Chun, J., Dixon, D. R., Kim, D.-S., Crum, J. V., Bonham, C. C., VanderVeer, B. J., Rodriguez, C. P., Weese, B. L., Schweiger, M. J., Kruger, A. A., & Hrma, P., Melter feed viscosity during conversion to glass: Comparison between low-activity waste and high-level waste feeds, *J. Am. Ceram. Soc.*, **101**, 2018; pp 1880-1891.

[44] McCarthy, B. P., George J. L., Dixon, D. R., Wheeler, M., Cutforth, D. A., Hrma, P., Linn, D., Chun, J., Hujova, M., Kruger, A. A., & Pokorny, R., Rheology of simulated radioactive waste slurry and cold cap during vitrification, *J. Am. Ceram. Soc.*, **101**, 2018; pp 5020-5029.

[45] Peeler, D. K., & Edwards, T. B., Impact of REDOX on glass durability: The glass selection process, Savannah River Technology Center, *WSRC-TR-2004-00135 Revision 0*, 2004.

[46] Husain, H., Hariyanto, B., Sulthonul, M., Thamatkeng, P., & Patapa, S., Local structure examination of mineral-derived Fe_2O_3 powder by Fe K-edge EXAFS and XANES, *IOP Conf. Ser.: Mater. Sci.*, **367**, 2018.

[47] Combes, J. M., Manceau, A., & Calas, G., XAS study of the evolution of local order around Fe(III) in the solution to gel to α-Fe_2O_3 transformation, *Phys. B: Condens.*, **158**, 1989; pp 419-420.

[48] Farges, F., Crystal chemistry of iron in natural grandidierites: An X-ray absorption fine-structured spectroscopy study, *Phys. Chem. Minerals*, **28**, 2001; pp 619-629.

[49] Okudera, H., Yoshiasa, A., Murai, K.-I., Okube, M., Takeda, T., & Kikkawa, S., Local structure of magnetite and maghemite and chemical shift in Fe K-edge XANES, *J. Mineral. Petrol. Sci.*, **107**, 2012; pp 127-132.

[50] Greaves, G. N., EXAFS and the structure of glass, *J. Non-Cryst. Solids*, **71**, 1985; pp 203-217.

[51] Lichieri, G., Paschina, G., Piccaluga, G., Pinna, G., Magini, M., & Cocco, G., On the coordination of iron ions in sodium borosilicate glasses: III. An EXAFS investigation, *J. Non-Cryst. Solids*, **72**, 1985; pp 211-220.

[52] Farges, F., Rossano, S., Lefrère, Y., Wilke, M., & Brown Jr., G. E., Iron in Silicate Glasses: A Systematic Analysis of Pre-Edge, XANES and EXAFS Features, *Phys. Scr.*, **T115**, 2005; pp 957-959.

[53] Pinakidou, F., Katsikini, M., Kavouras, P., Komninou, F., Karakostas, T., & Paloura, E. C., Structural role and coordination environment of Fe in Fe_2O_3-PbO-SiO_2-Na_2O composite glasses, *J. Non-Cryst. Solids*, **354**, 2008; pp 105-111.

[54] Williams, K. F. E., Johnson, C. E., & Thomas, M. F., Mössbauer spectroscopy measurement of iron oxidation states in float composition silica glasses, *J. Non-Cryst. Solids*, **226**, 1998; pp 19-23.

[55] Cornwall, J., Eales, J. D., Scrimshire, A., & Bingham, P. A., *Manuscript in Preparation*.

[56] Hsieh, C. H., Jain, H., Miller, A. C., & Kamitsos, E. I., X-ray photoelectron spectroscopy of Al- and B-substituted sodium trisilicate glasses, *J. Non-Cryst. Solids*, **168**, 1994; pp 247-257.

[57] Mekki, A., Holland, D., McConville, C. F., & Salim, M., An XPS study of iron sodium silicate glass surfaces, *J. Non-Cryst. Solids*, **208**, 1996; pp 267-276.

[58] Mekki, A., Holland, D., & McConville, C. F., X-ray photoelectron spectroscopy study of copper sodium silicate glass surfaces, *J. Non-Cryst. Solids*, **215**, 1997; pp 271-282.

[59] Holland, D., Mekki, A., Gee, I. A., McConville, C. F., Johnson, J. A., Johnson, C. E., Appleyard, P., & Thomas, M., Structure of sodium iron silicate glass - a multi-technique approach, *J. Non-Cryst. Solids*, **253**, 1999; pp 192-202.

[60] Miura, Y., Kusano, H., Nanba, T., & Matsumoto, S., X-ray photoelectron spectroscopy of sodium borosilicate glasses, *J. Non-Cryst. Solids*, **290**, 2001; pp 1-14.

[61] Holland, D., Gee, I. A., Mekki, A., & McConville, C. F., Role of surface science in the determination of glass structure, *Phys. Chem. Glasses*, **42**, 2001; pp 247-254.

[62] Nanba, T., & Miura, Y., Alkali distribution in borosilicate glasses, *Phys. Chem. Glasses*, **44**, 2003; pp 244-248.

[63] Thorpe, C. L., Neeway, J. J., Pearce, C. L., Hand, R. J., Fisher, A. J., Walling, S. A., Hyatt, N. C., Kruger, A. A., Schweiger, M., Kosson, D. S., Arendt, C. L., Marcial, J., & Corkhill, C. L., Forty years of durability assessment of nuclear waste glasses by standard methods, *npj Mater. Degrad.*, **61**, 2021.

[64] ASTM Standard C1663-18, 2019, "Standard Test Method for Measuring Waste Glass or Glass Ceramic Durability by Vapor Hydration Test" ASTM International, West Conshohocken, PA, 2019, DOI: 10.1520/*C1663-18*, www.astm.org.

Appendix

Chapter 4

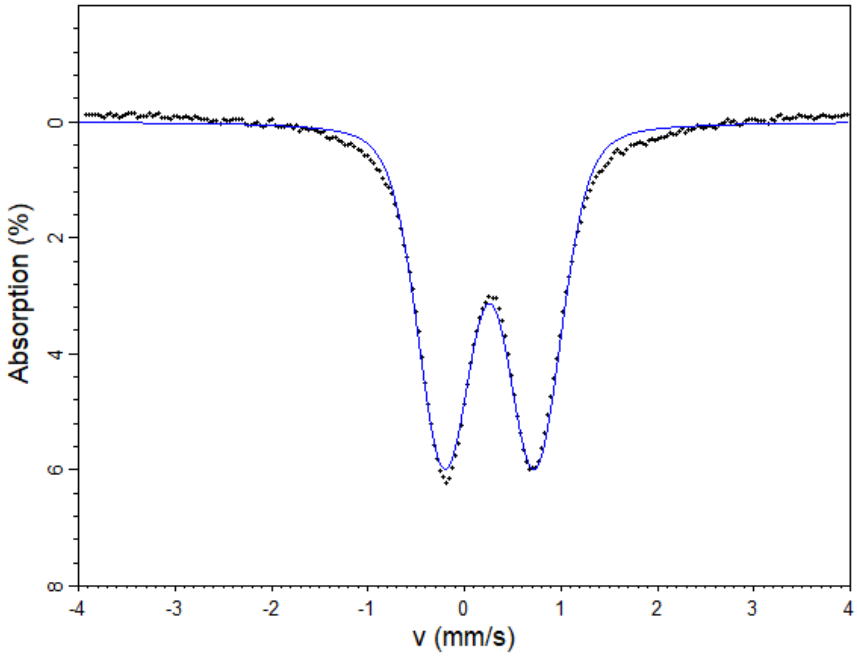

Figure A4.1: *The Mössbauer Spectrum for the SCFe005.0 sample fitted using xVBF function. Note the under-fitting on the shoulders that is not seen in the Lorentzian function fits. The reduced* $\chi^2 = 10.8334$.

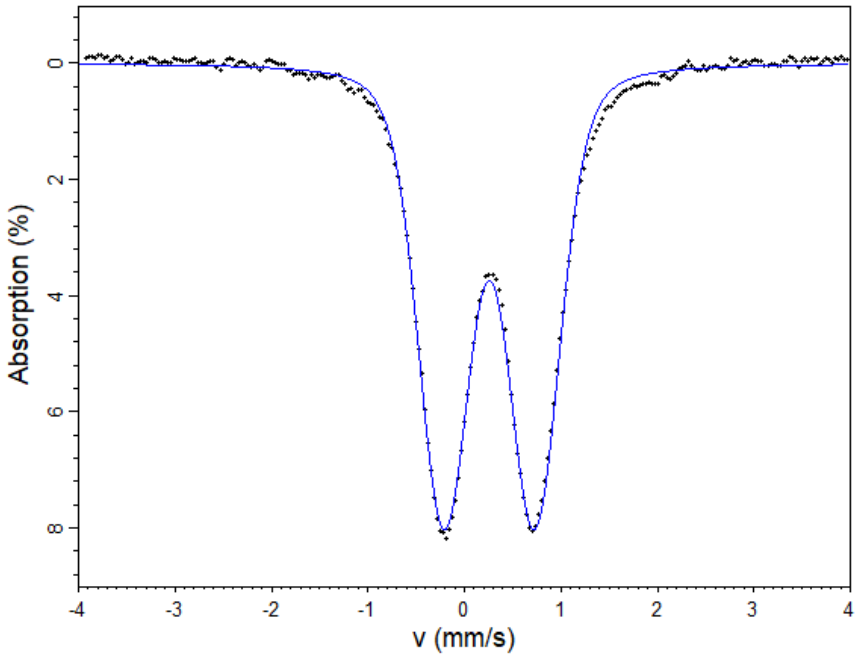

Figure A4.2: *The Mössbauer Spectrum for the SCFe007.5 sample fitted using xVBF function. Note the under-fitting on the shoulders that is not seen in the Lorentzian function fits. The reduced* $\chi^2 = 3.5403$.

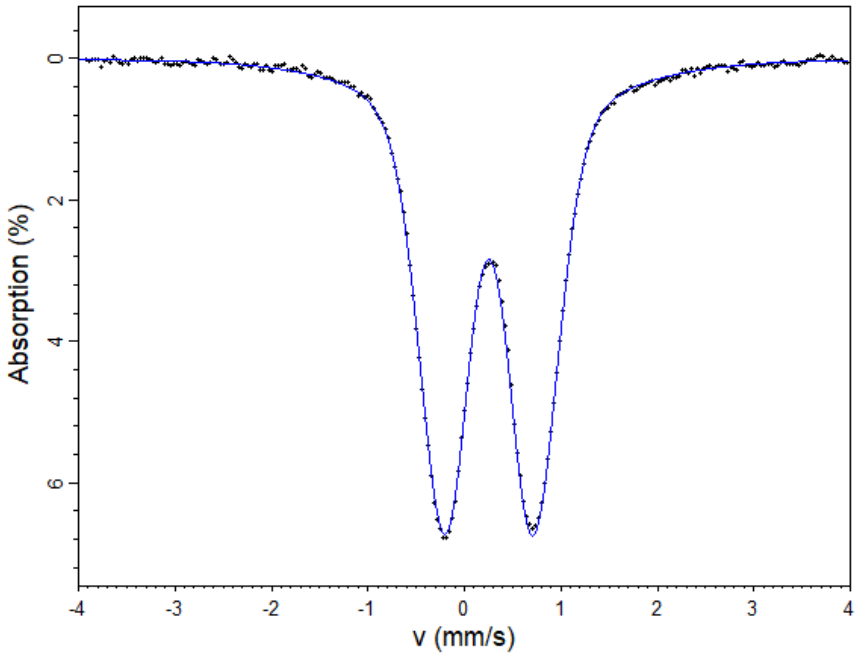

Figure A4.3: *The Mössbauer Spectrum for the SCFe010.0 sample fitted using xVBF function. The reduced* $\chi^2 = 0.917195$.

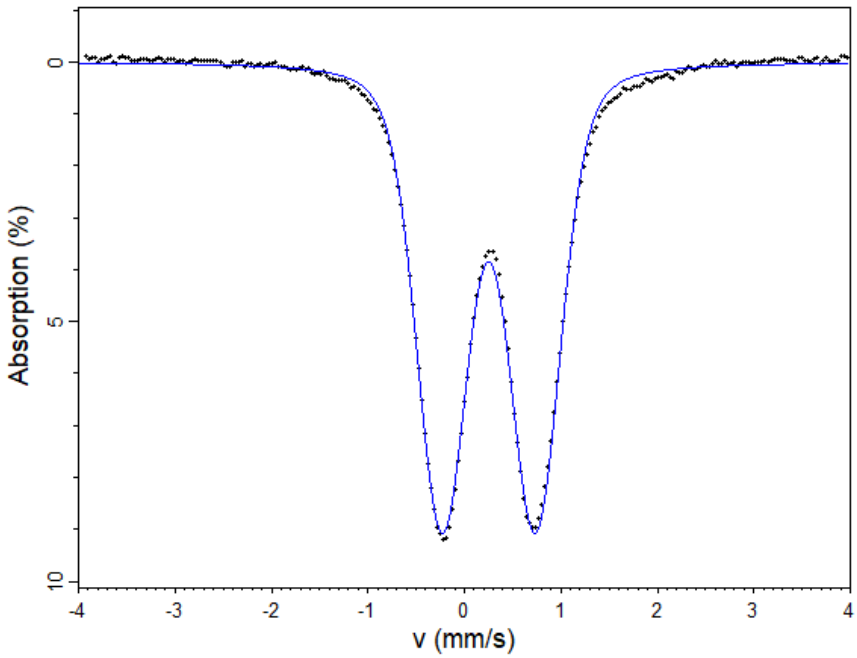

Figure A4.4: *The Mössbauer Spectrum for the SCFe014.0 sample fitted using xVBF function. The reduced* $\chi^2 = 6.47125$.

Table A4.1: The xVBF fit parameters for the RT ^{57}Fe Mössbauer spectrum for the SCFe sample series.

Sample ID	CS (mm s^{-1})	QS (mm s^{-1})	ΔQS (mm s^{-1})	Skew (mm s^{-1})
SCFe005.0	0.261437	0.935226	0.273522	0.00525714
SCFe007.5	0.258267	0.939667	0.177461	1.71478e-06
SCFe010.0	0.26304	0.954257	0.275611	0.455326
SCFe014.0	0.252227	0.967454	0.247229	0.000905724

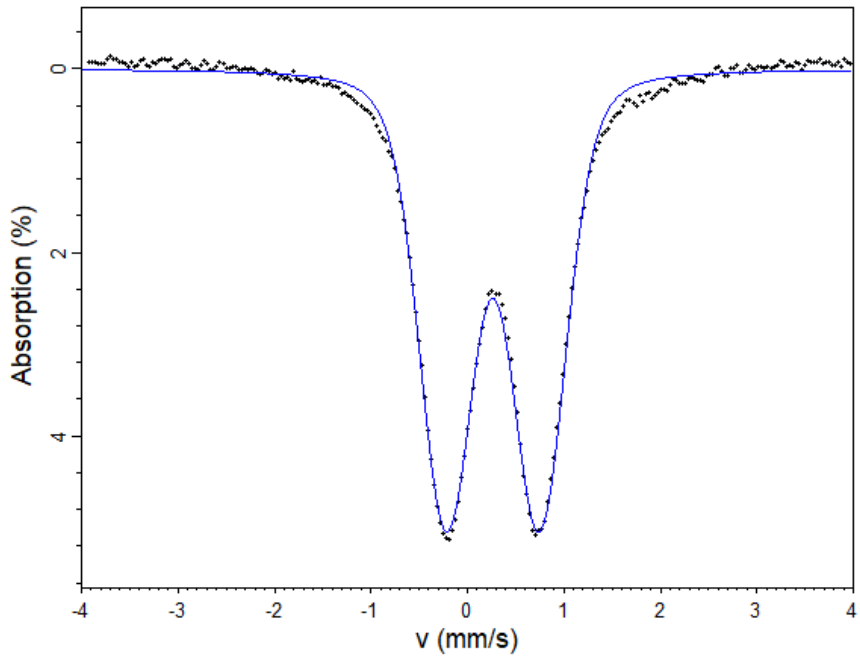

Figure A4.5: *The Mössbauer Spectrum for the CCFe005.0 sample fitted using xVBF function. The reduced* $\chi^2 = 5.05127$.

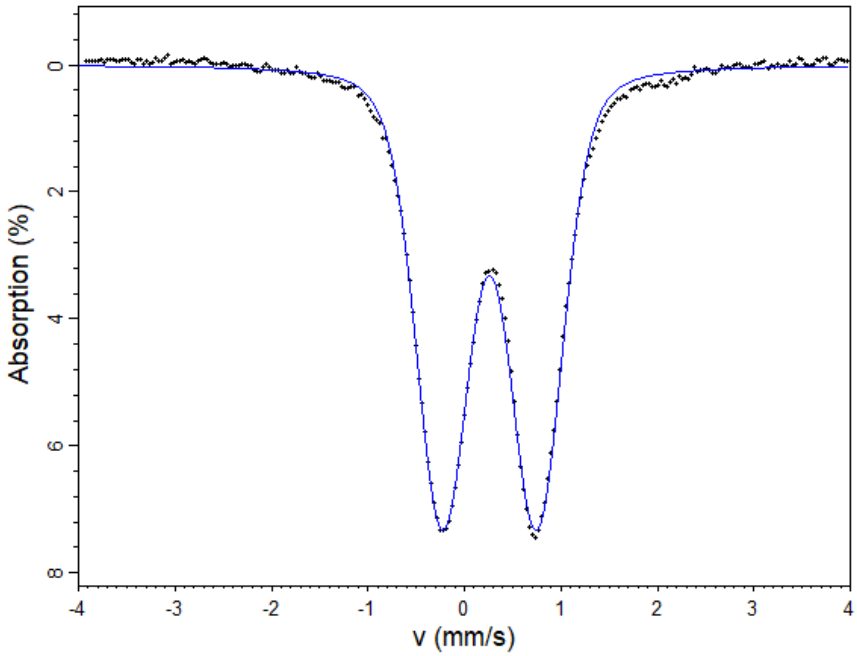

Figure A4.6: *The Mössbauer Spectrum for the CCFe007.5 sample fitted using xVBF function. The reduced* χ^2 *= 3.92309.*

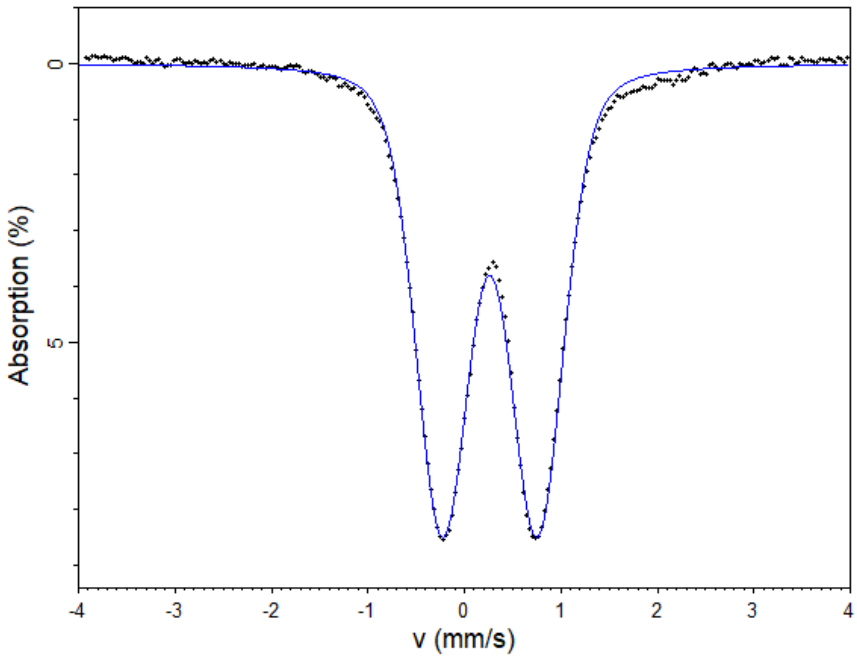

Figure A4.7: *The Mössbauer Spectrum for the CCFe010.0 sample fitted using xVBF function. The reduced* χ^2 *= 4.93576.*

Table A4.2: The xVBF fit parameters for the RT ^{57}Fe Mössbauer spectrum for the CCFe sample series.

Sample ID	**CS (mm s^{-1})**	**QS (mm s^{-1})**	**ΔQS (mm s^{-1})**	**Skew (mm s^{-1})**
CCFe005.0	0.263955	0.964439	0.262214	0.00215927
CCFe007.5	0.260705	0.976176	0.263959	0.00200887
CCFe010.0	0.2637	0.982561	0.265052	0.00194603

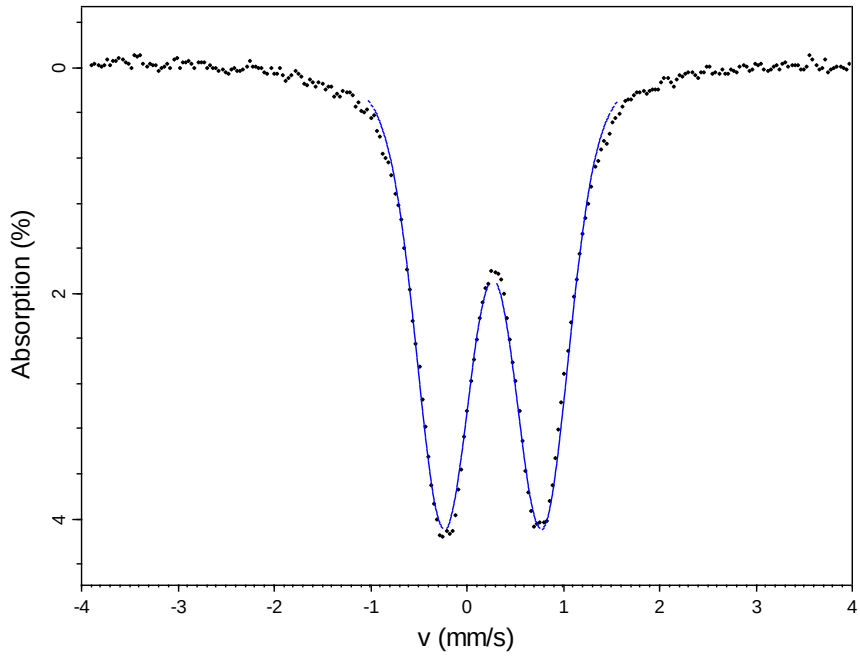

Figure A4.8: *The Mössbauer Spectrum for the HAFe005.0 sample fitted using xVBF function. The reduced* $\chi^2 = 2.97419$.

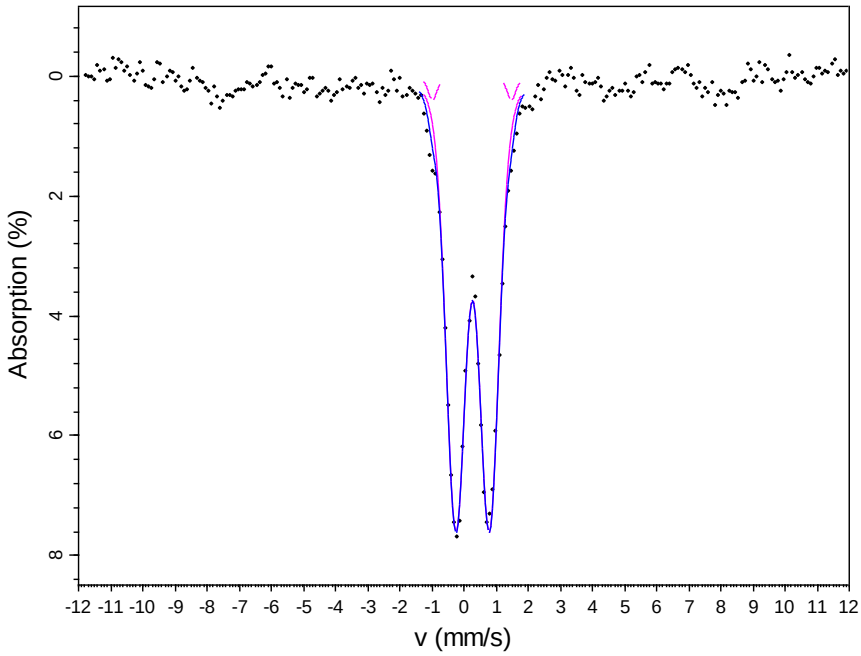

Figure A4.9: *The Mössbauer Spectrum for the HAFe007.1 sample fitted using xVBF function. The reduced* χ^2 *= 0.784248.*

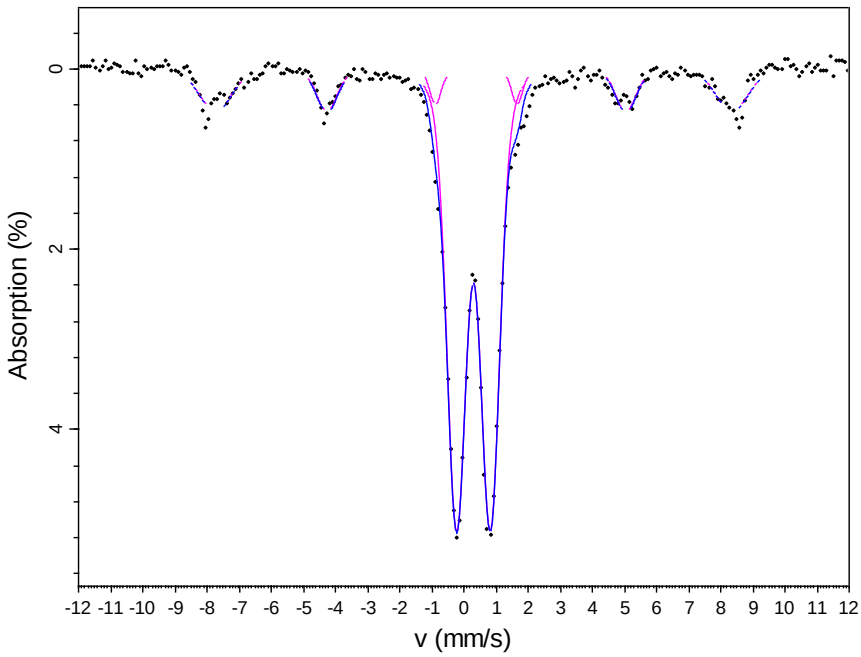

Figure A4.10: *The Mössbauer Spectrum for the HAFe010.0 sample fitted using xVBF function. The reduced* χ^2 *= 1.81177.*

Table A4.3: The xVBF fit parameters for the RT ^{57}Fe Mössbauer spectrum for the HAFe sample series.

Sample ID	Site Type	CS (mm s^{-1})	QS (mm s^{-1})	ΔQS (mm s^{-1})	Skew (mm s^{-1})	H (T)	ΔH (T)
HAFe005.0	Doublet	0.267	1.018	0.028	2.1e^{-3}	-	-
HAFe007.1	Doublet	0.267	1.047	0.127	-8.2e^{-14}	-	-
	Sextet	0.249	0.006	-	2.1e^{-13}	48.219	3.607
HAFe010.0	Doublet	0.296	1.055	0.028	9.3e^{-12}	-	-
	Sextet	0.338	-0.043	-	2.7e^{-12}	49.876	2.773

Chapter 5

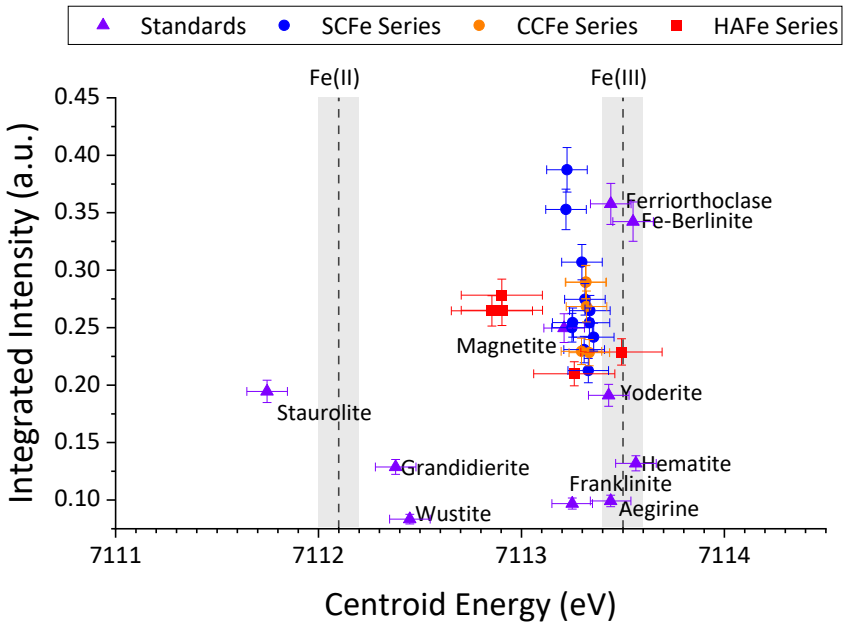

***Figure A5.1**: The "Wilke" plot for all measured samples and standards. X-axis error bars are +/- 0.1 eV on the centroid energy (per Feige et al. [reference Chapter 5 ref 33) for the SCFe and CCFe series but +/- 0.2 eV for the HAFe series due to the larger step size used in acquiring the data. Y-axis error bars +/- 5% of the value on the integrated intensity (per Wilke et al. [reference Chapter 5 ref 22]). Grey regions around the Fe^{2+} and Fe^{3+} lines indicate the +/- 0.1 eV uncertainty on these positions.*

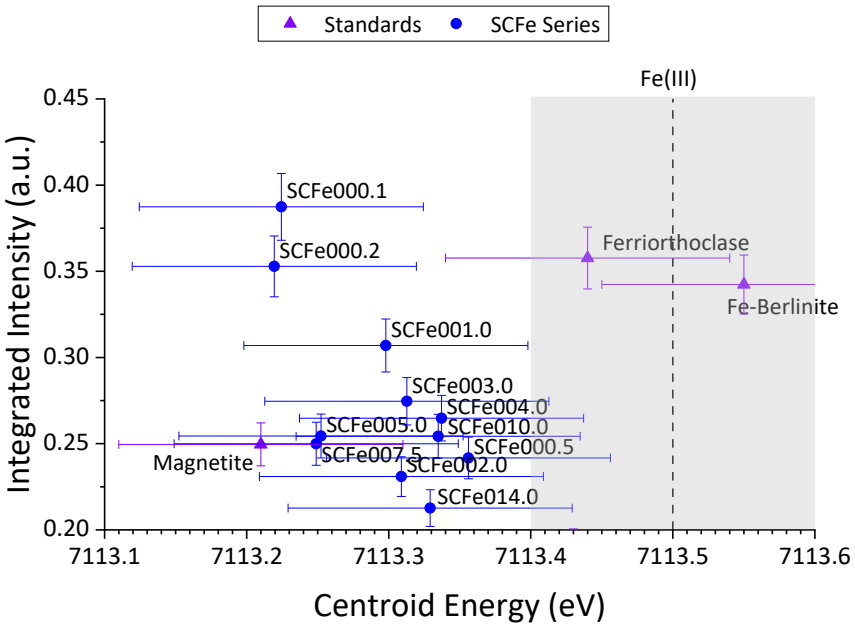

***Figure A5.2**: The "Wilke" plot for all measured SCFe samples and select standards that appear in this region. The error bars are the same as those seen in **Fig A5.1**.*

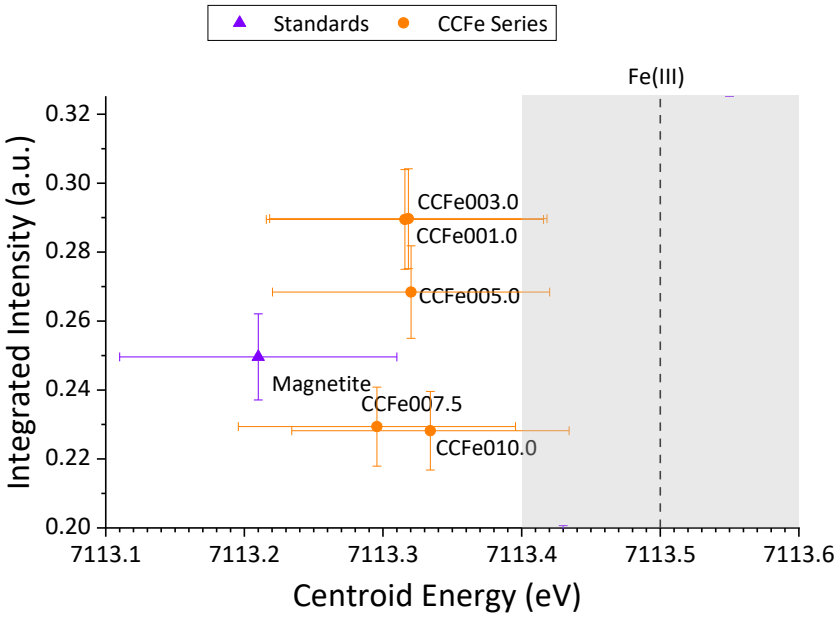

***Figure A5.3**: The "Wilke" plot for all measured CCFe samples and select standards that appear in this region. The error bars are the same as those seen in **Fig A5.1**.*

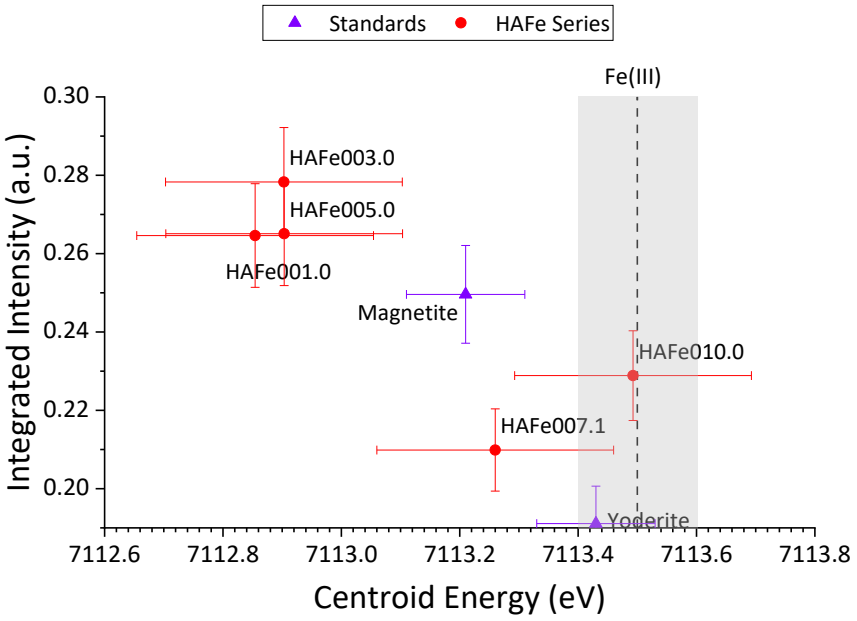

***Figure A5.4**: The "Wilke" plot for all measured HAFe samples and select standards that appear in this region. The error bars are the same as those seen in **Fig A5.1**.*

Chapter 6

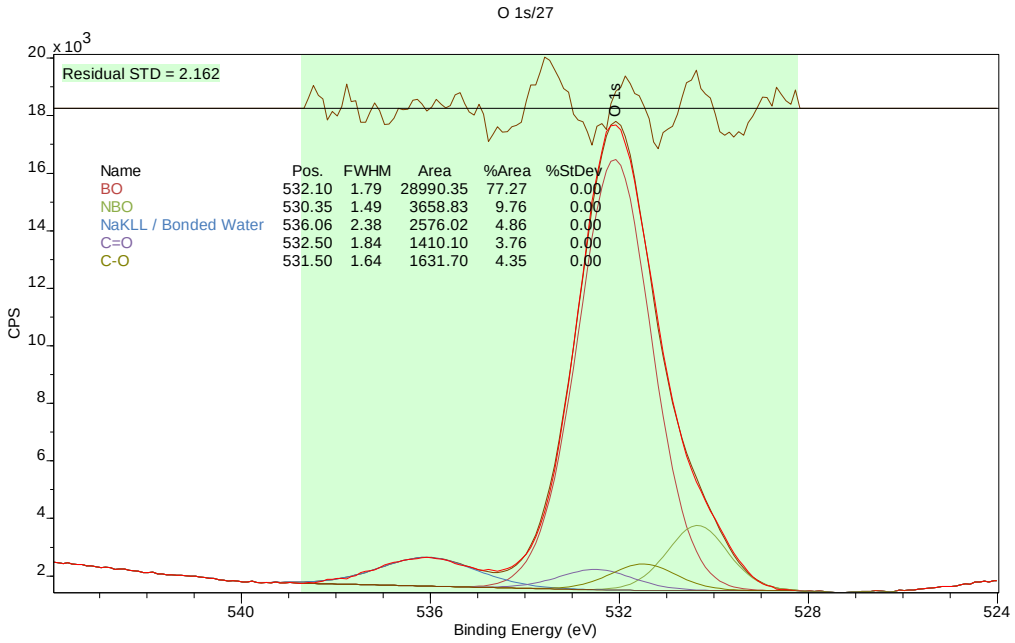

***Figure A6.1:** The peak fitted O 1s spectrum of the SCFe000.2 sample.*

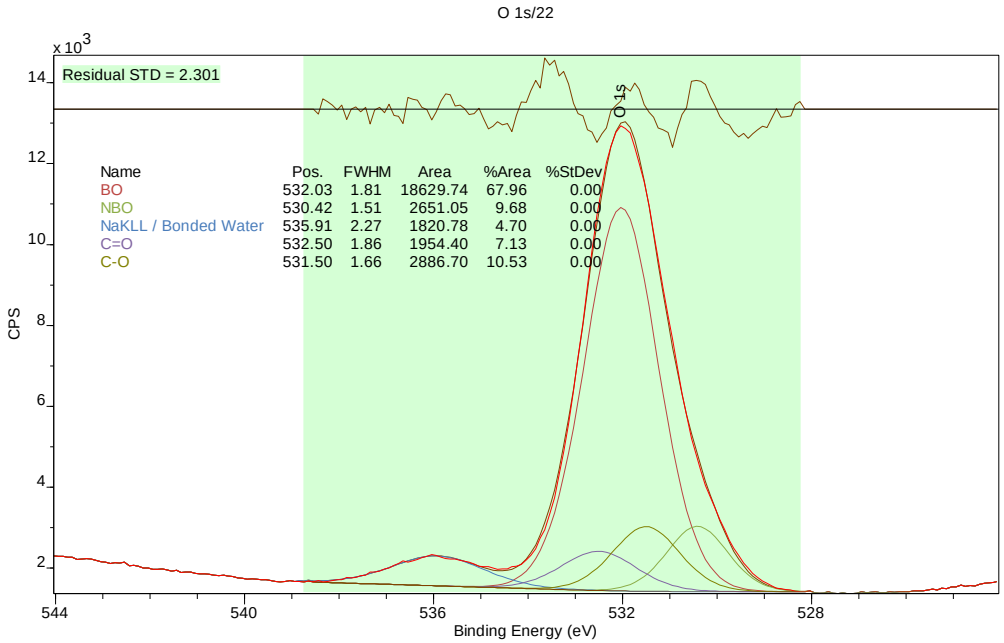

Figure A6.2: *The peak fitted O 1s spectrum of the SCFe000.5 sample.*

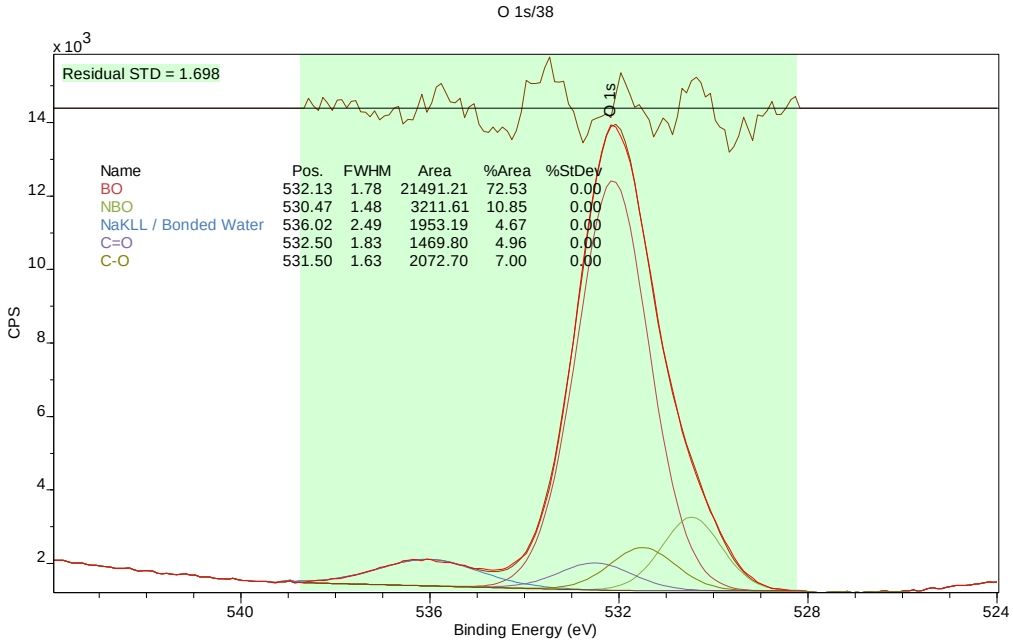

Figure A6.3: *The peak fitted O 1s spectrum of the SCFe001.0 sample.*

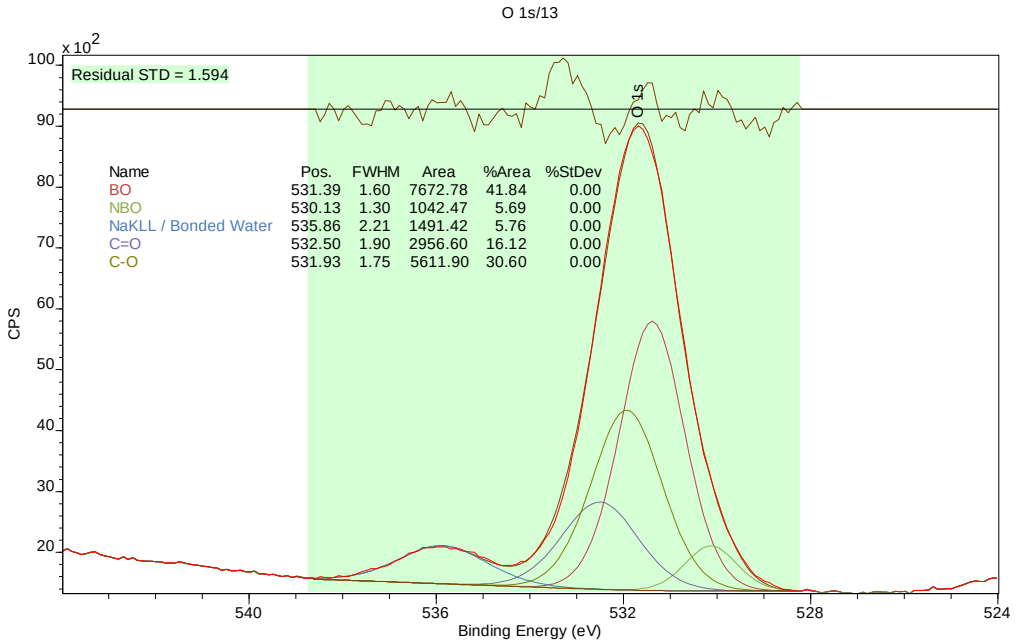

Figure A6.4: *The peak fitted O 1s spectrum of the SCFe002.0 sample.*

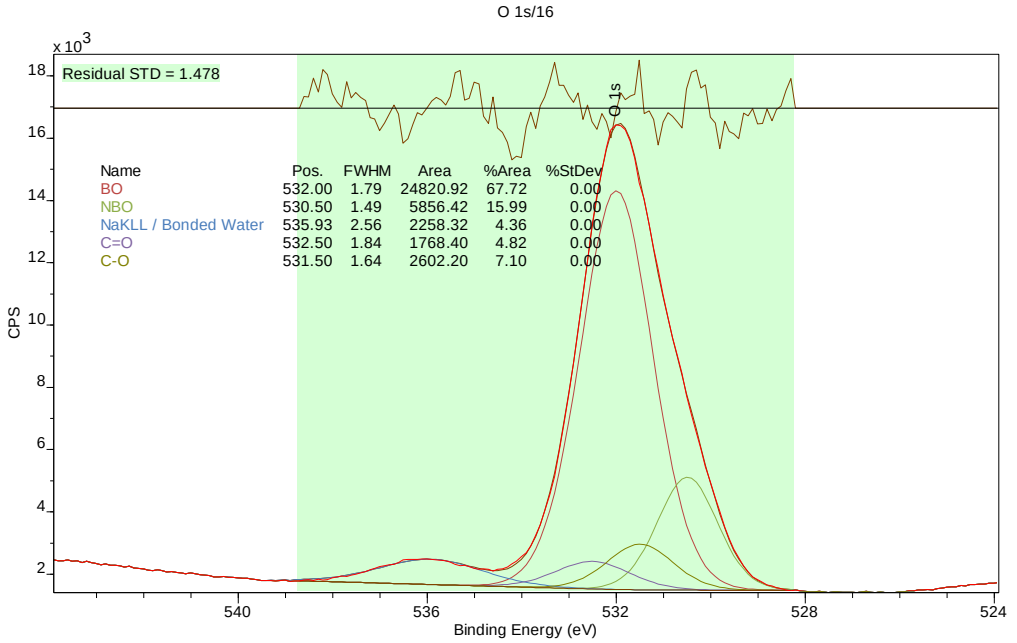

Figure A6.5: *The peak fitted O 1s spectrum of the SCFe003.0 sample.*

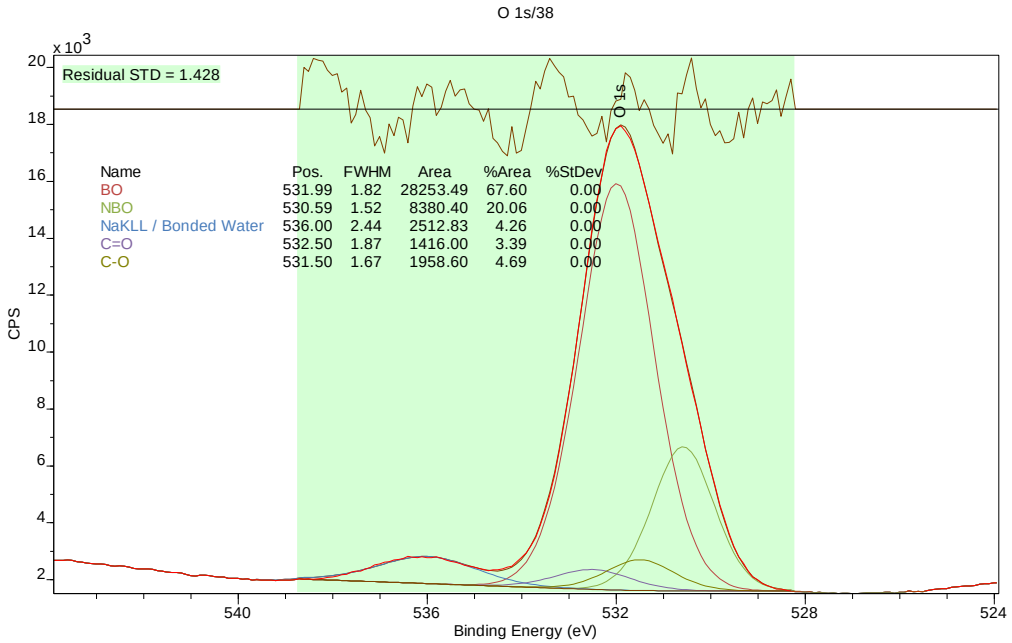

Figure A6.6: *The peak fitted O 1s spectrum of the SCFe004.0 sample.*

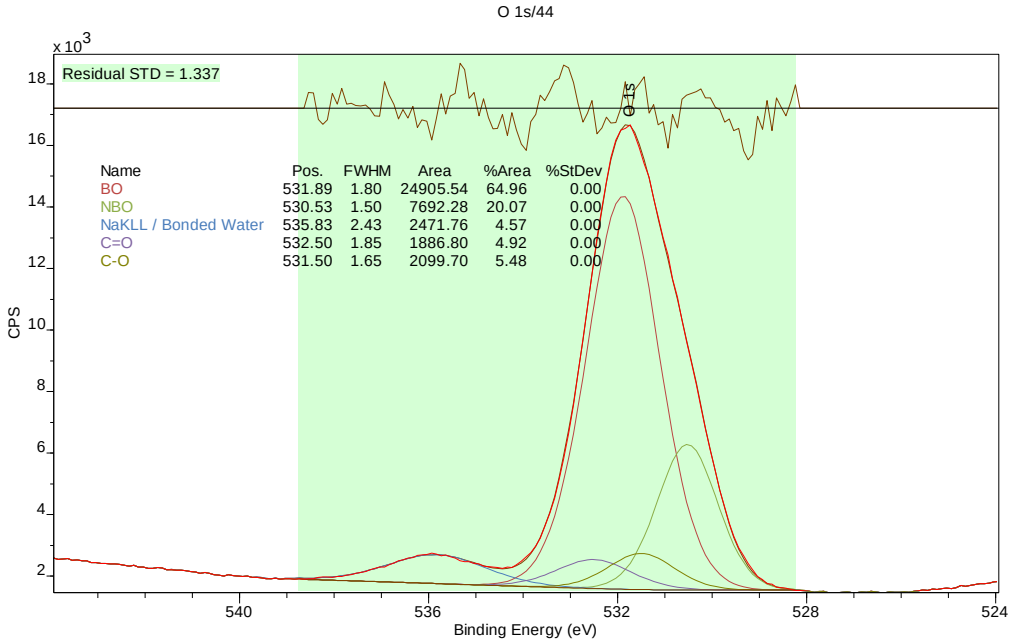

Figure A6.7: *The peak fitted O 1s spectrum of the SCFe005.0 sample.*

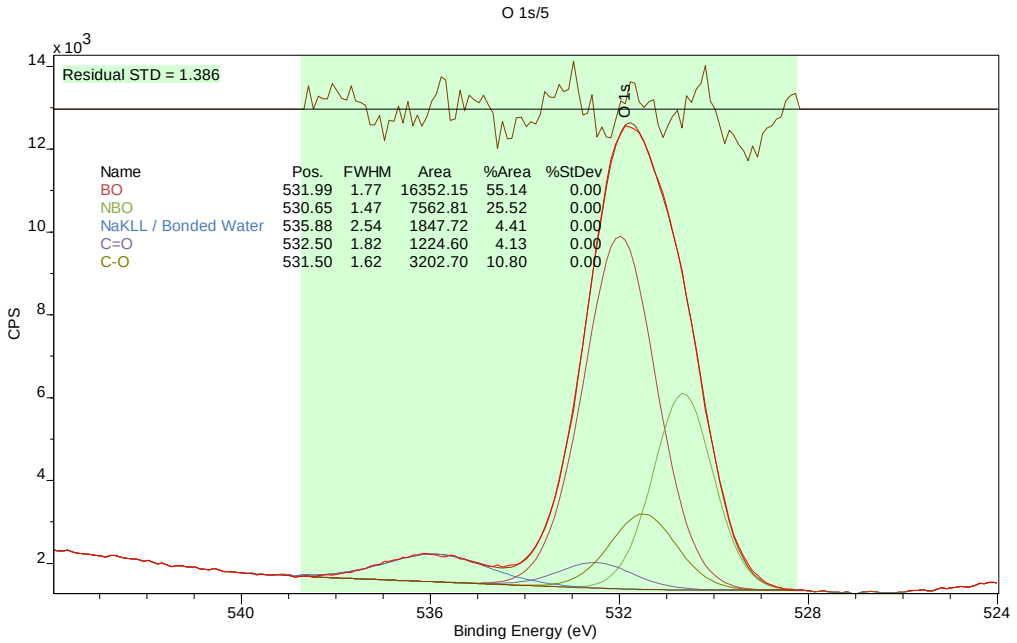

Figure A6.8: *The peak fitted O 1s spectrum of the SCFe007.5 sample.*

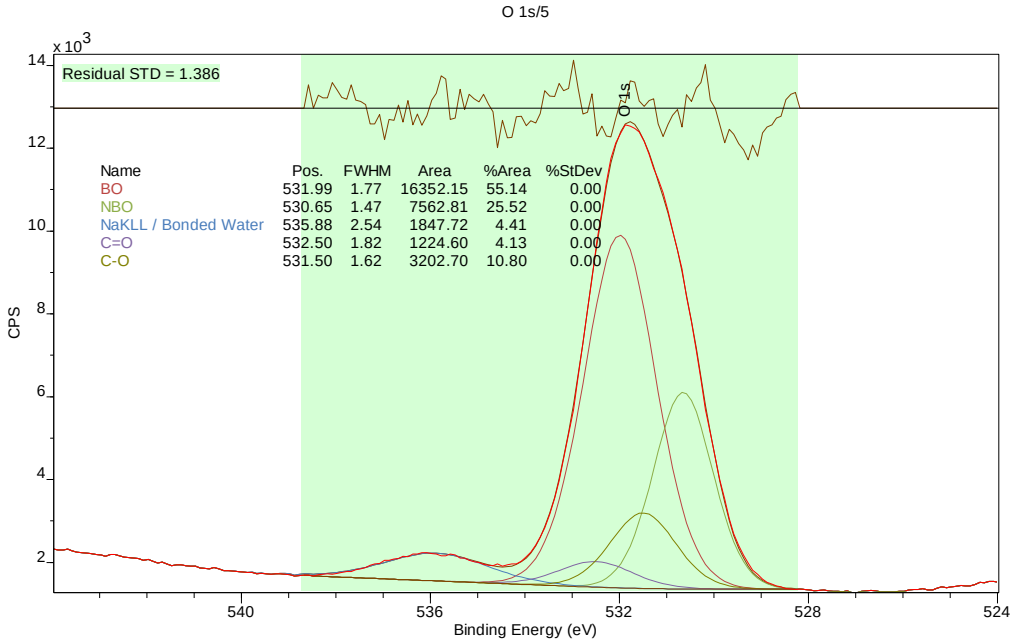

Figure A6.9: *The peak fitted O 1s spectrum of the SCFe010.0 sample.*

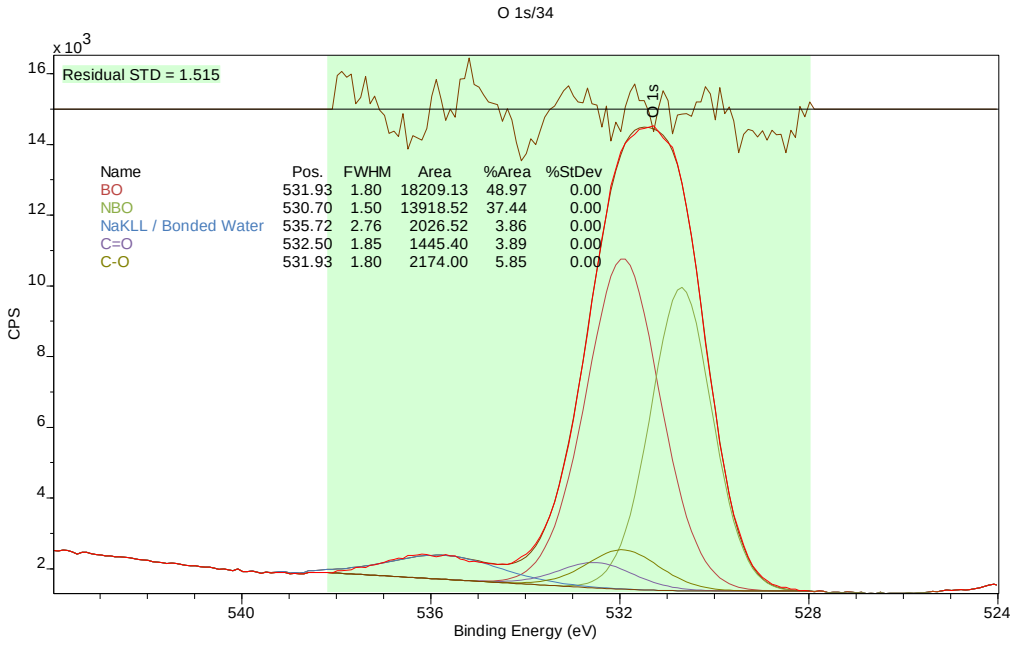

Figure A6.10: *The peak fitted O 1s spectrum of the SCFe014.0 sample.*

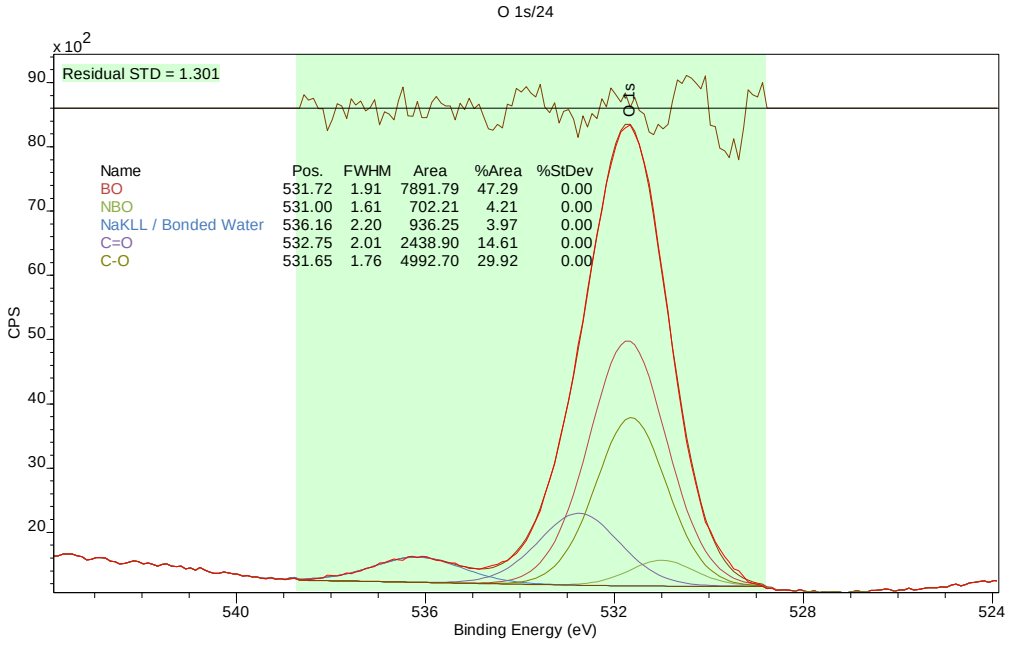

Figure A6.11: *The peak fitted O 1s spectrum of the CCFe000.0 sample.*

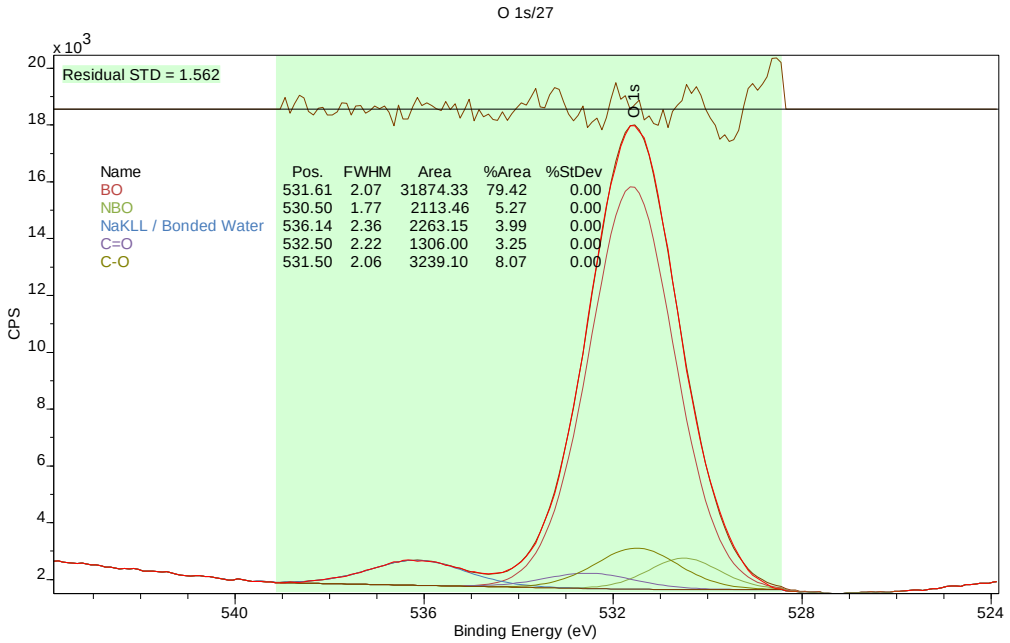

Figure A6.12: *The peak fitted O 1s spectrum of the CCFe001.0 sample.*

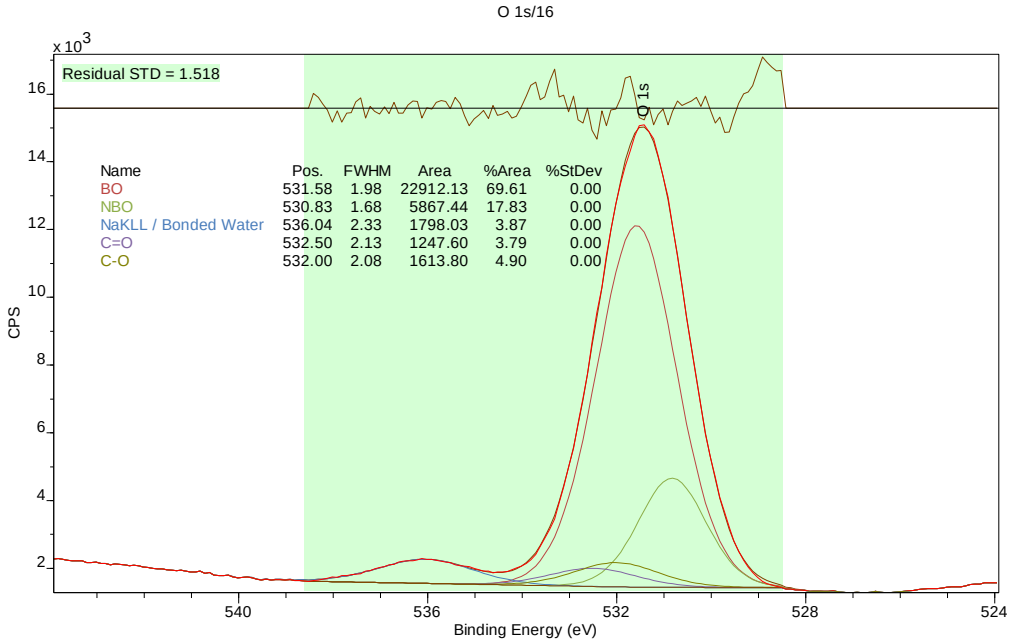

Figure A6.13: *The peak fitted O 1s spectrum of the CCFe003.0 sample.*

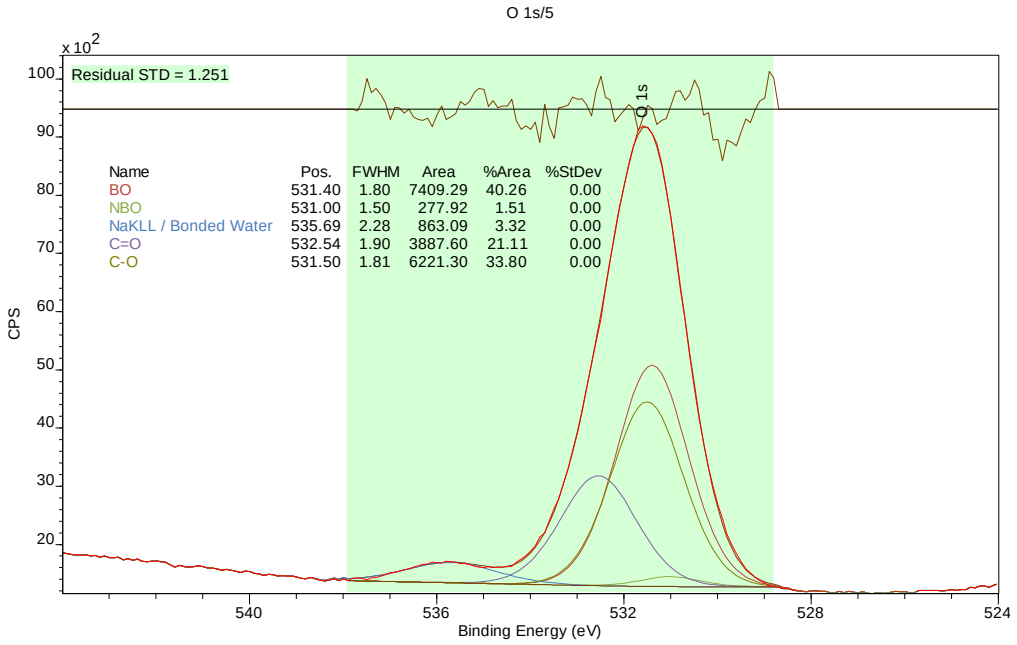

Figure A6.14: *The peak fitted O 1s spectrum of the CCFe005.0 sample.*

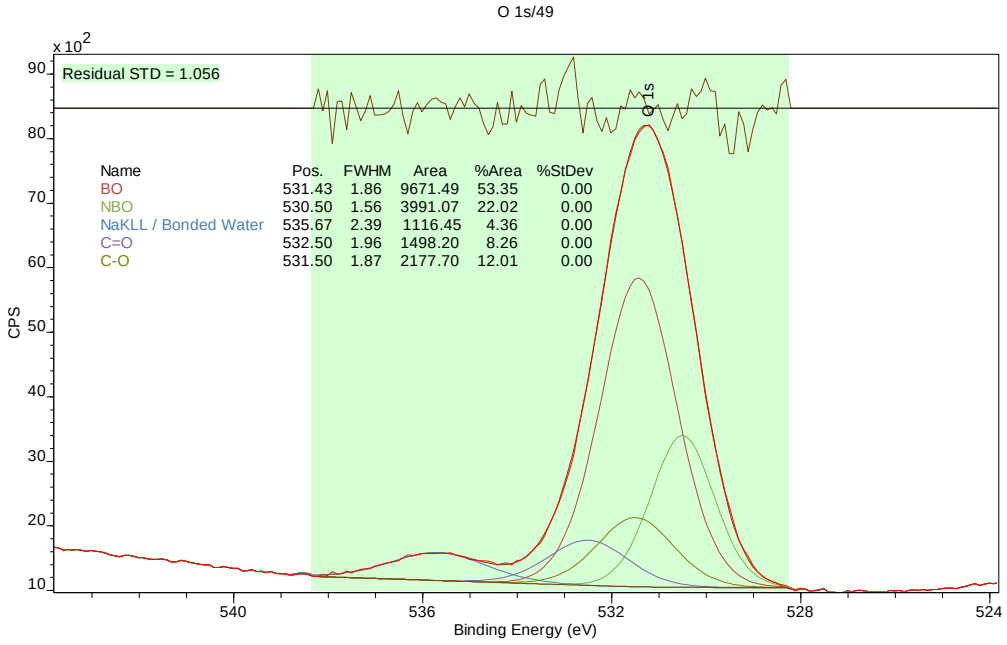

Figure A6.15: *The peak fitted O 1s spectrum of the CCFe007.5 sample.*

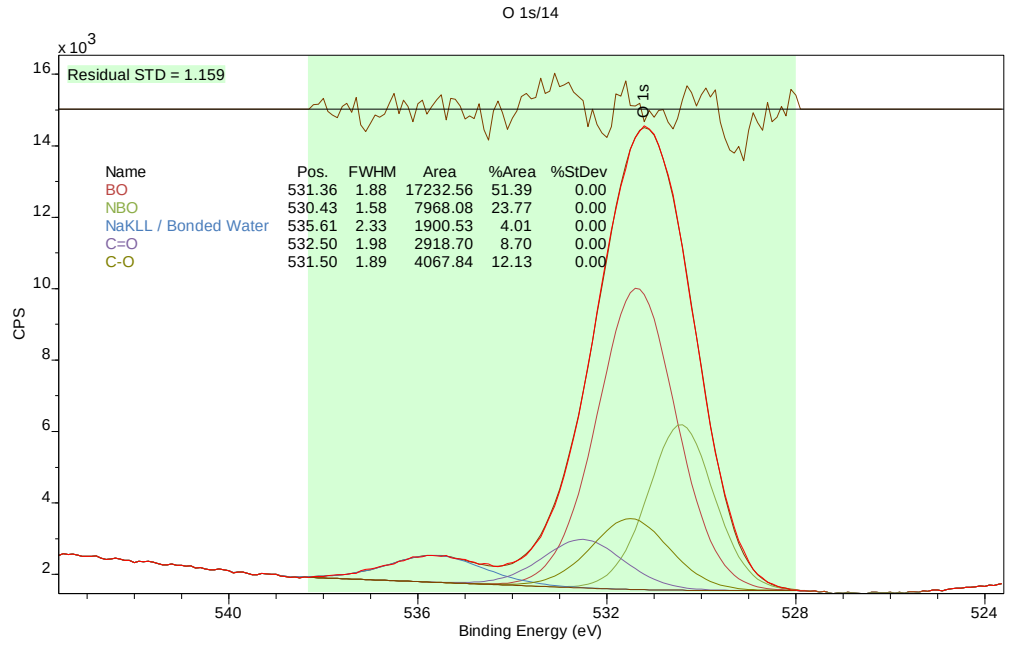

Figure A6.16: *The peak fitted O 1s spectrum of the CCFe010.0 sample.*

Chapter 7

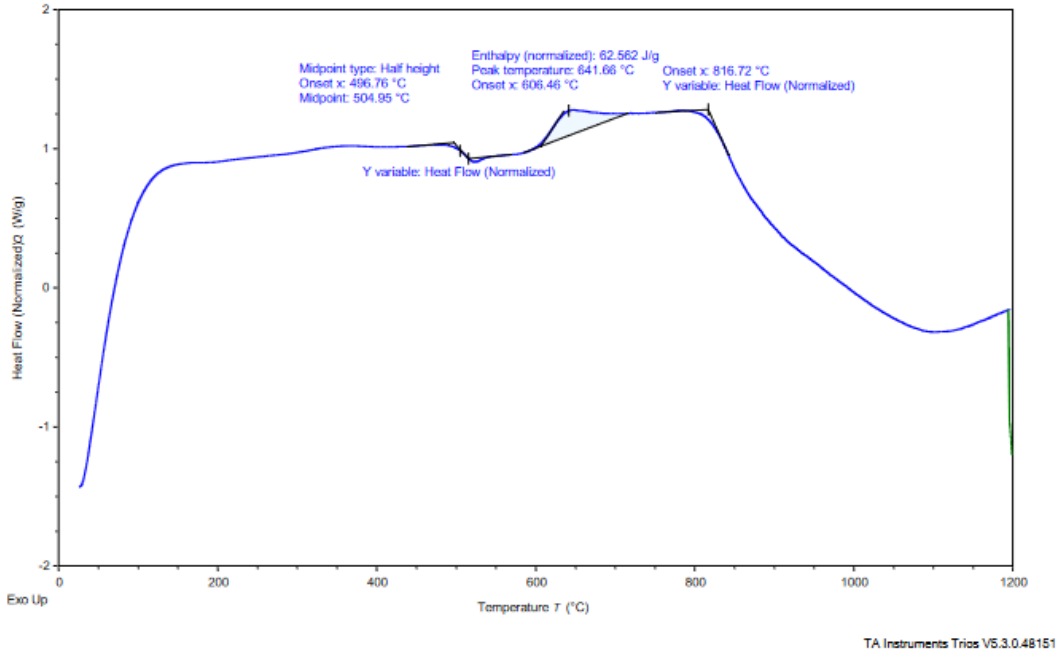

Figure A7.1: *The DTA trace for the "Lab Made" HAFe000.0 sample.*

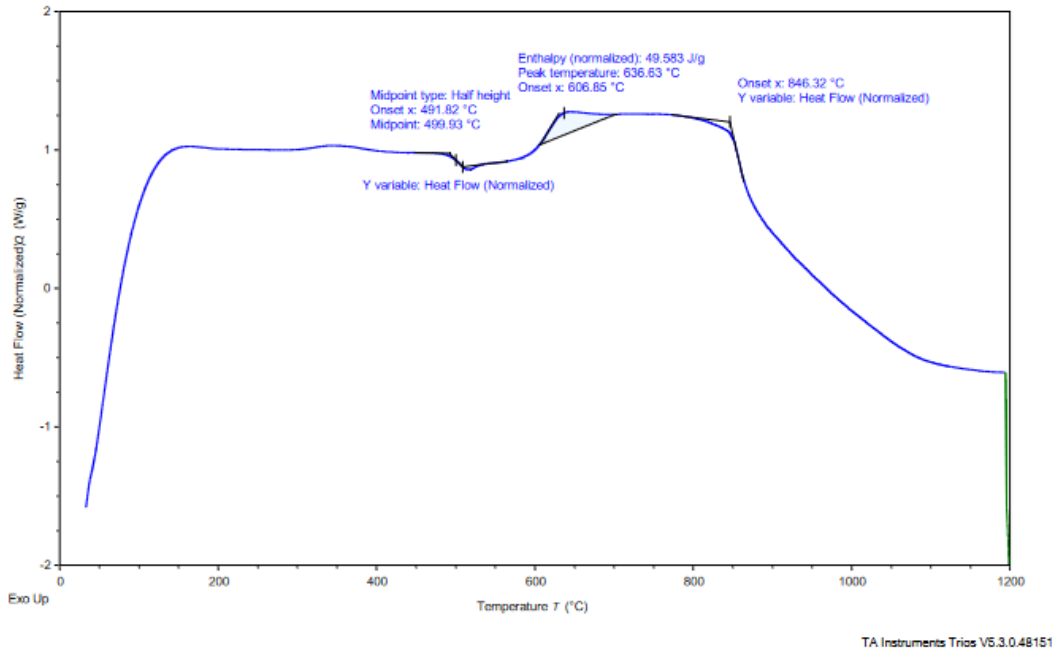

Figure A7.2: *The DTA trace for the "Lab Made" HAFe001.0 sample.*

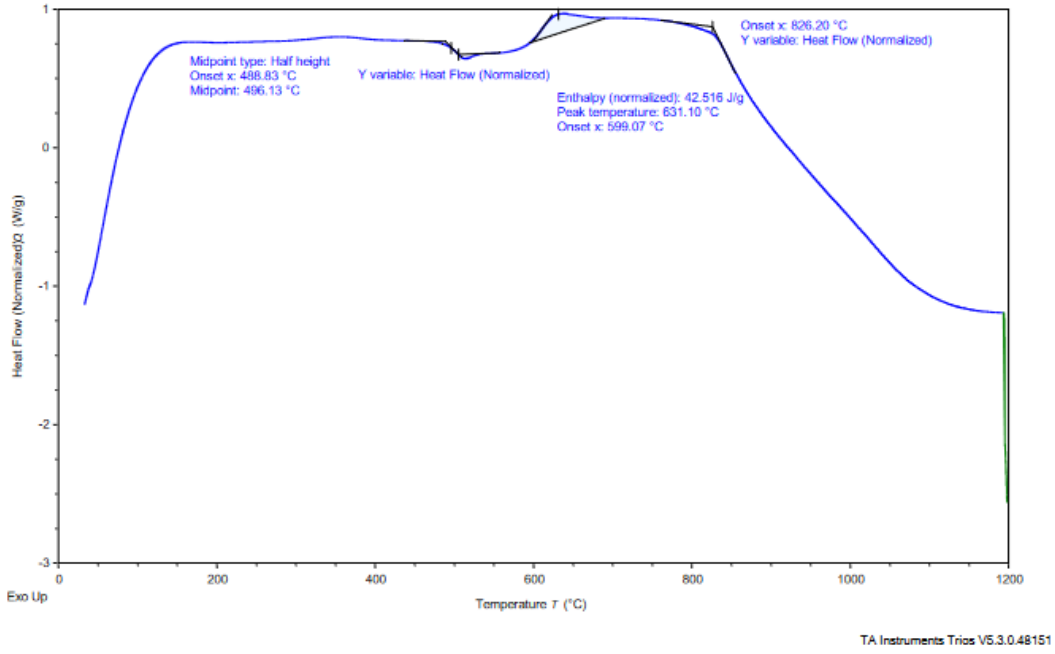

Figure A7.3: *The DTA trace for the "Lab Made" HAFe003.0 sample.*

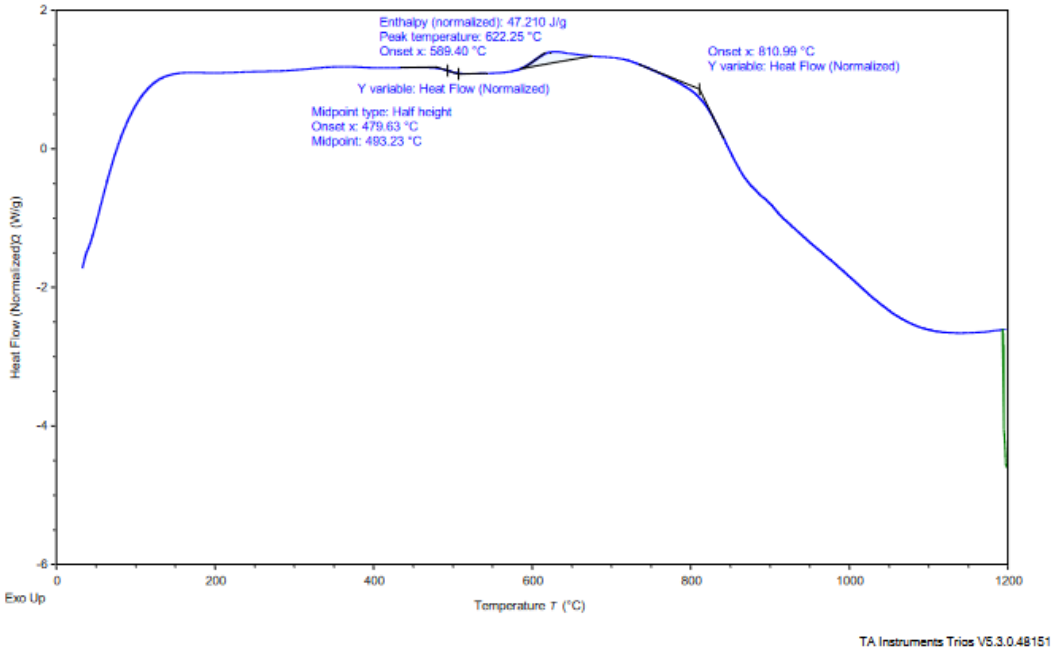

Figure A7.4: *The DTA trace for the "Lab Made" HAFe005.0 sample.*

7.3

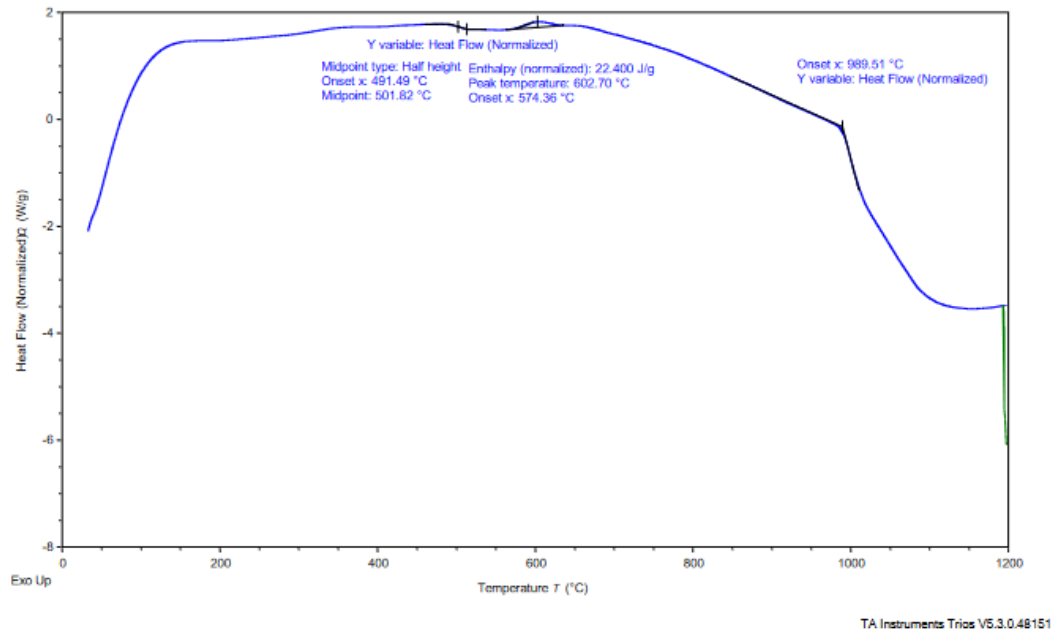

Figure A7.5: *The DTA trace for the "Lab Made" HAFe007.1 sample.*

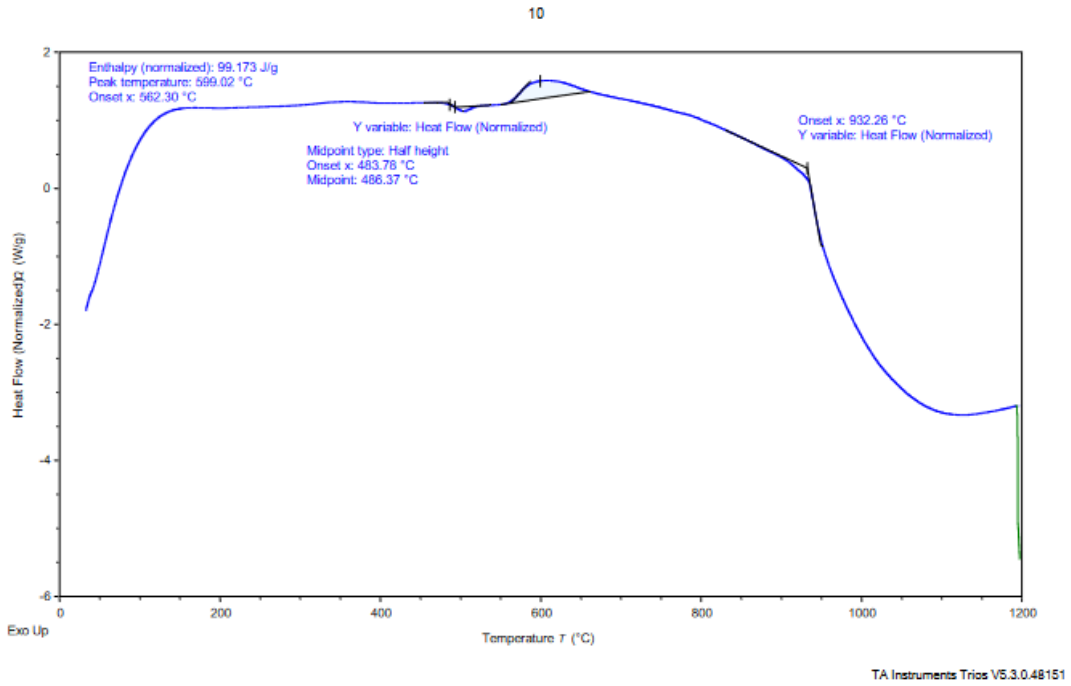

Figure A7.6: *The DTA trace for the "Lab Made" HAFe010.0 sample.*

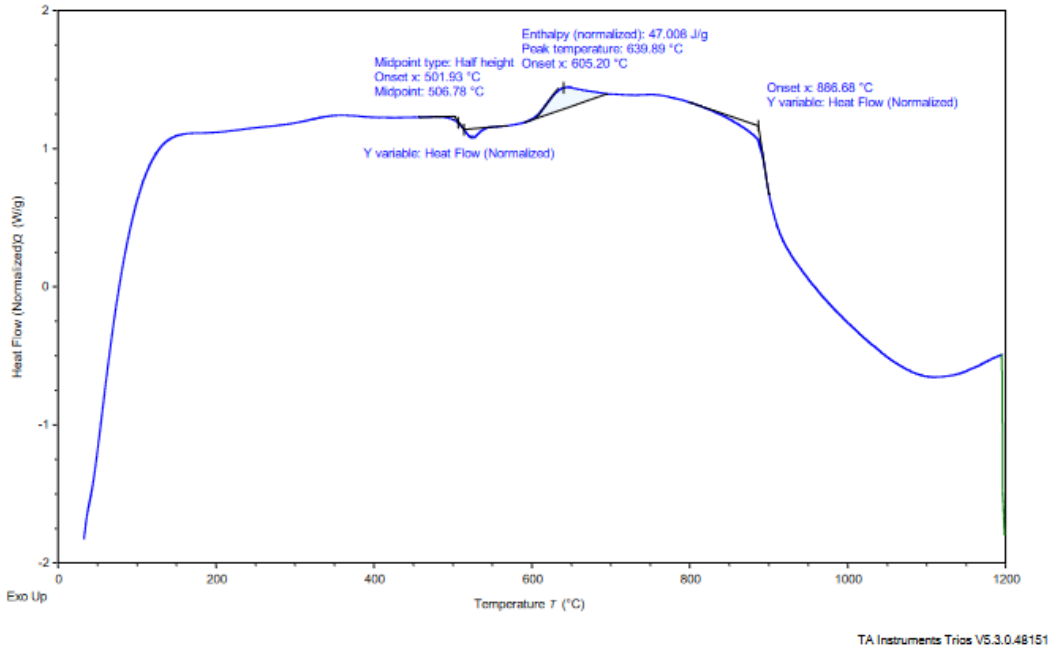

Figure A7.7: *The DTA trace for the "CCC" HAFe000.0 sample.*

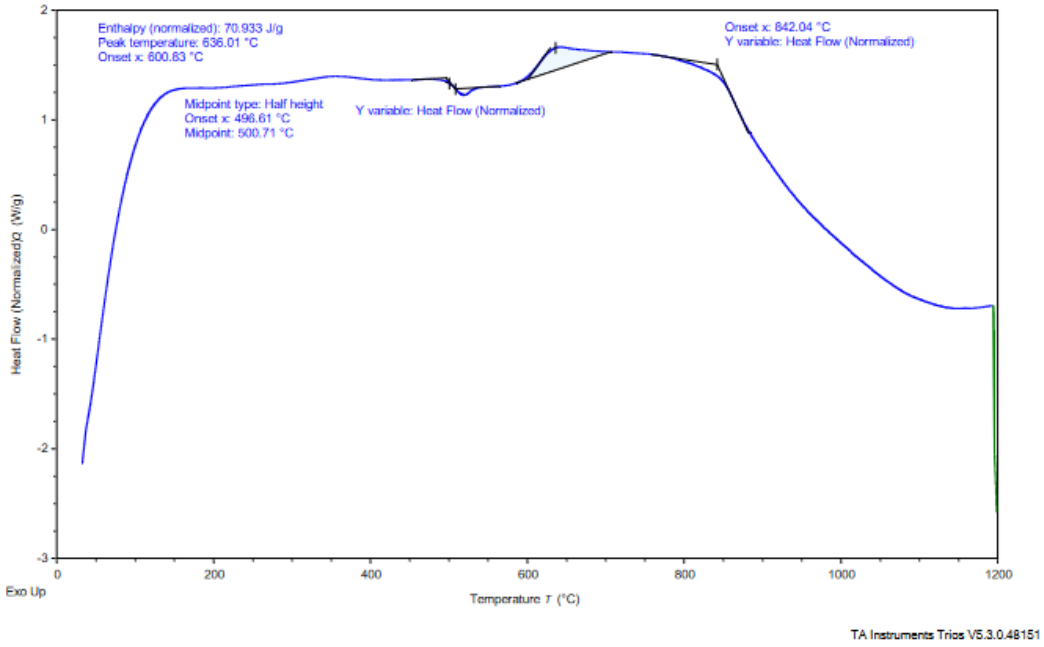

Figure A7.8: *The DTA trace for the "CCC" HAFe001.0 sample.*

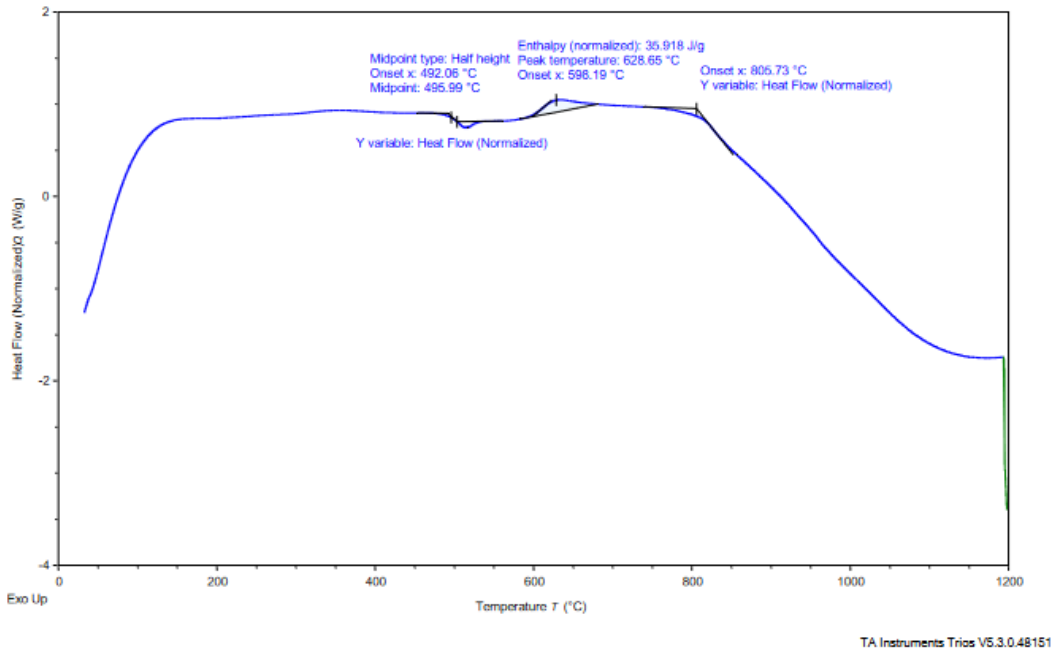

Figure A7.9: *The DTA trace for the "CCC" HAFe003.0 sample.*

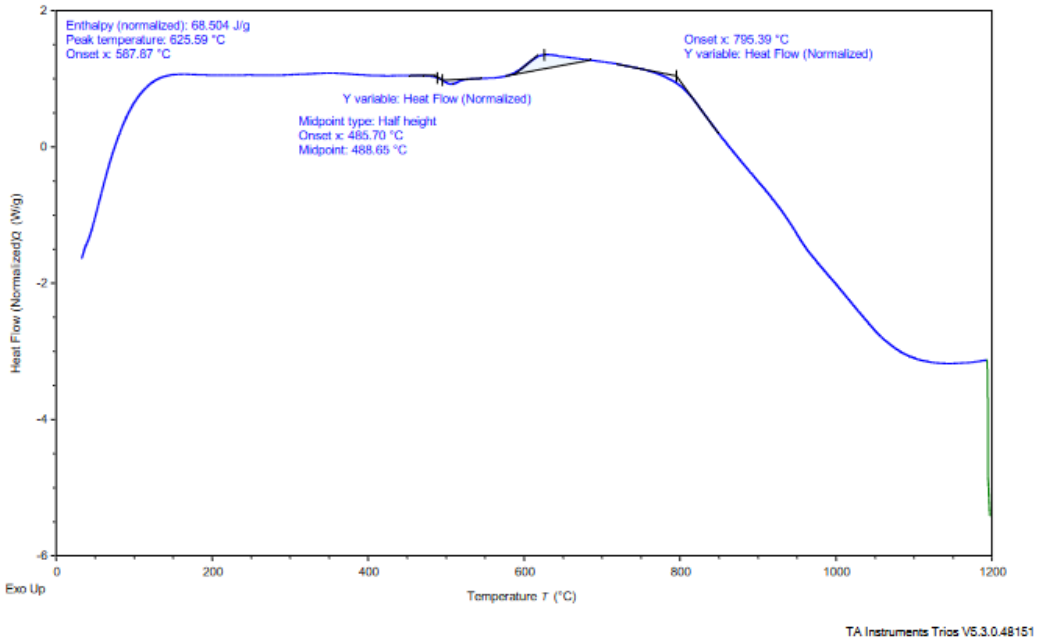

Figure A7.10: *The DTA trace for the "CCC" HAFe005.0 sample.*

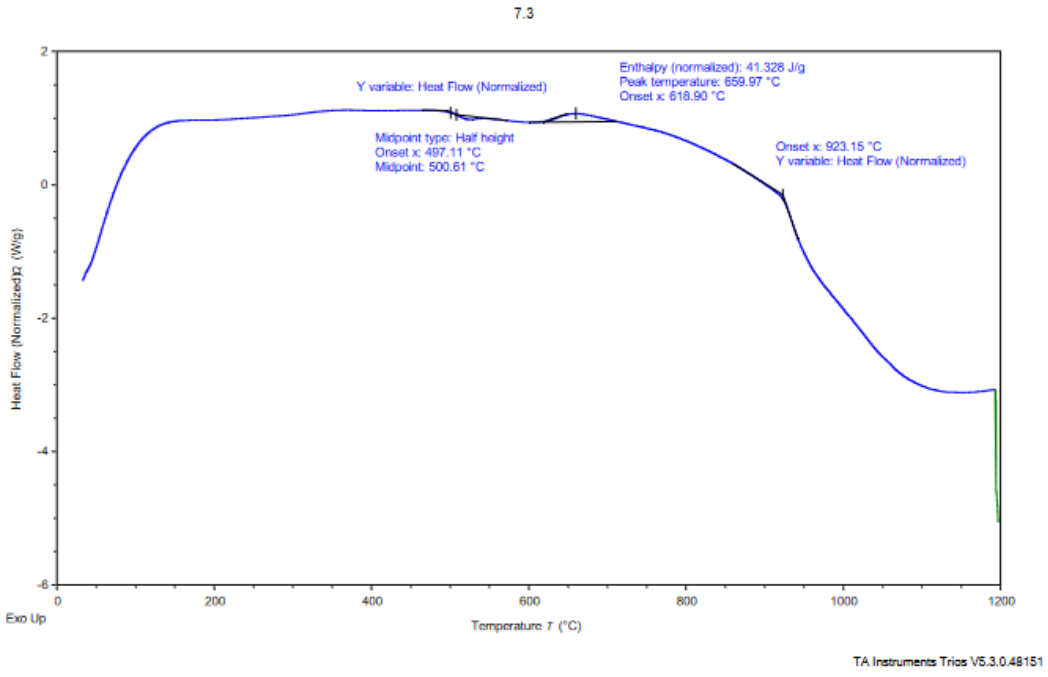

Figure A7.11: *The DTA trace for the "CCC" HAFe007.1 sample.*

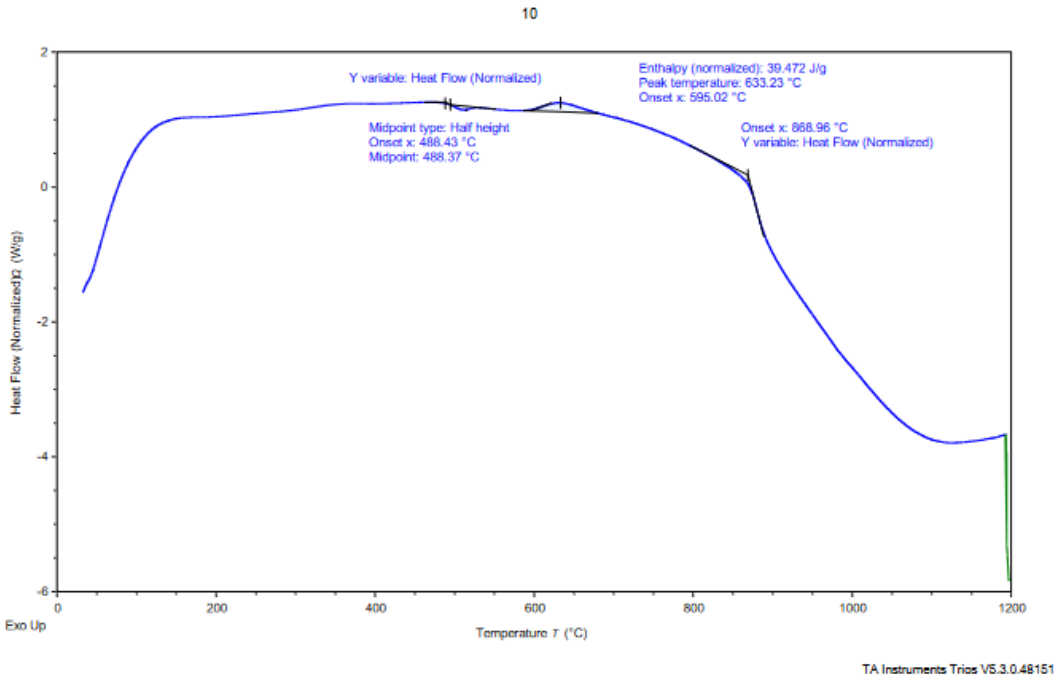

Figure A7.12: *The DTA trace for the "CCC" HAFe010.0 sample.*

Appendix

Table A7.1: The analysed concentrations of selected elements in the leachate of the HAFe “Lab Made” sample sub-series.

Sample ID	Sample Number	The analysed concentrations within the leachate (mg L^{-1})													
		Al	**B**	**Ca**	**Cr**	**Fe**	**Li**	**Mg**	**Mn**	**Na**	**Ni**	**P**	**S**	**Si**	**Zr**
Blanks	0a	0.116	0.014	0.793	<0.004	0.005	<0.002	0.338	<0.001	1.52	<0.003	0.099	0.315	0.091	<0.002
	0b	0.011	0.275	0.733	<0.004	0.005	0.067	0.319	<0.001	1.40	<0.003	0.100	0.297	0.072	<0.002
	0c	<0.001	<0.001	0.99	<0.004	<0.003	<0.002	0.368	<0.001	1.62	<0.003	0.100	0.339	0.096	<0.002
HAFe 000.0	1a	0.360	434	6.72	0.773	<0.015	63.3	2.65	0.388	743	<0.015	12.6	4.63	192	<0.01
	1b	0.434	434	8.07	0.773	<0.015	63.0	3.11	0.740	736	<0.015	12.4	4.68	186	<0.01
	1c	0.332	432	6.70	0.813	<0.015	62.2	2.55	0.301	730	<0.015	12.6	4.62	190	<0.01
HAFe 001.0	2a	1.31	301	7.54	0.446	0.821	44.6	3.17	6.59	499	0.336	9.32	3.30	130	<0.01
	2b	1.28	295	7.06	0.429	0.803	43.4	2.99	6.91	504	0.371	8.98	3.22	130	<0.01
	2c	1.18	297	7.36	0.442	0.749	44.3	3.05	6.02	491	0.311	9.16	3.20	130	<0.01
HAFe 003.0	3a	2.78	139	6.35	0.267	0.837	20.5	2.60	0.878	236	<0.015	2.71	1.31	79.2	<0.01
	3b	2.90	140	5.71	0.289	1.01	20.8	2.28	1.22	234	<0.015	2.61	1.13	74.3	<0.01
	3c	2.77	143	6.29	0.259	0.783	21.6	2.36	0.804	239	<0.015	2.72	1.30	78.5	<0.01
HAFe 005.0	4a	6.11	52.7	3.98	0.124	0.457	7.85	1.59	0.237	95.4	<0.015	1.44	0.577	54.4	<0.01
	4b	6.19	51.9	3.66	0.124	0.466	7.99	1.49	0.237	96.7	<0.015	1.35	0.531	54.0	<0.01
	4c	5.91	48.2	3.56	0.111	0.533	7.52	1.46	0.266	91.8	<0.015	1.35	0.596	53.1	<0.01
HAFe 007.1	5a	7.62	20.1	1.82	<0.02	0.322	3.52	0.779	<0.005	33.7	<0.015	1.00	0.669	47.1	<0.01
	5b	7.57	20.0	1.49	<0.02	0.313	3.62	0.697	<0.005	34.0	<0.015	1.02	0.651	46.8	<0.01
	5c	7.56	19.5	2.18	<0.02	0.421	3.37	0.956	<0.005	31.9	<0.015	0.998	0.702	46.3	<0.01
HAFe 010.0	6a	6.06	27.6	2.48	<0.02	0.116	4.60	1.02	<0.005	55.7	<0.015	1.35	0.504	49.7	<0.01
	6b	6.11	26.9	2.69	<0.02	0.116	4.44	1.11	<0.005	54.1	<0.015	1.35	0.485	49.3	<0.01
	6c	6.05	27.7	2.68	<0.02	0.148	4.56	1.10	<0.005	55.3	<0.015	1.37	0.573	49.8	<0.01

Appendix

Table A7.2: The analysed concentrations of selected elements in the leachate of the HAFe “CCC” sample sub-series.

Sample ID	Sample Number	The analysed concentrations within the leachate (mg L^{-1})													
		Al	**B**	**Ca**	**Cr**	**Fe**	**Li**	**Mg**	**Mn**	**Na**	**Ni**	**P**	**S**	**Si**	**Zr**
Blanks	7a	0.204	0.397	0.944	< 0.004	< 0.003	<0.002	0.224	<0.001	44.1	< 0.003	0.067	0.200	5.91	<0.002
	7b	0.26	0.376	0.989	< 0.004	< 0.003	<0.002	0.262	<0.001	45.7	< 0.003	0.063	0.170	6.99	<0.002
	7c	0.194	0.318	0.907	< 0.004	< 0.003	<0.002	0.208	<0.001	45.4	< 0.003	0.062	0.166	5.74	<0.002
HAFe 000.0 CCC	8a	0.321	389	4.11	0.846	0.012	58.7	0.348	1.18	675	0.078	14.4	3.56	180	0.006
	8b	0.319	393	4.46	0.879	0.006	59.6	0.423	1.2	680	0.083	14.6	3.67	184	0.008
	8c	0.439	278	3.76	0.831	0.02	57.8	0.544	1.76	468	0.111	14.5	3.54	182	0.011
HAFe 001.0 CCC	9a	1.33	262	2.63	0.559	0.826	37.7	0.499	5.51	266	0.313	8.18	2	115	0.041
	9b	1.25	251	2.89	0.559	0.817	36.8	0.372	5.61	157	0.298	8.33	2.01	109	0.038
	9c	1.27	258	0.365	0.612	0.774	40.1	0.05	4.81	239	0.289	8.72	2.11	109	0.033
HAFe 003.0 CCC	10a	4.75	81.8	2.39	0.182	0.48	12.2	0.261	0.327	82.7	0.042	1.44	0.414	60.5	0.035
	10b	4.77	83.3	1.85	0.177	0.479	12.3	0.171	0.316	80.7	0.043	1.44	0.404	60.5	0.038
	10c	5.05	84.7	2.18	0.19	0.542	12.8	0.372	0.374	77.7	0.049	1.47	0.43	63.8	0.041
HAFe 005.0 CCC	11a	6.17	61.1	2.11	0.009	0.431	9.28	0.393	0.145	41.8	< 0.003	1.12	0.27	59.4	0.039
	11b	6.39	60.5	3.56	0.009	0.427	8.57	0.787	0.135	42.7	< 0.003	1.14	0.363	64.7	0.045
	11c	5.88	61.9	1.74	0.009	0.434	9.12	0.08	0.15	67.5	< 0.003	1.12	0.28	53.9	0.035
HAFe 007.1 CCC	12a	8.1	23.3	1.12	< 0.004	1.6	3.52	0.078	0.147	18.8	< 0.003	0.807	0.38	49.7	0.059
	12b	8.36	23	2.64	< 0.004	1.66	3.34	0.814	0.161	32.8	< 0.003	0.835	0.512	59.7	0.089
	12c	8.27	22.6	2.04	< 0.004	1.67	3.42	0.508	0.155	26.1	< 0.003	0.787	0.381	56.1	0.078
HAFe 010.0 CCC	13a	6.63	49.9	1.76	< 0.004	1.05	6.90	0.291	0.119	68.6	< 0.003	1.01	0.186	56.4	0.046
	13b	6.73	49.7	2.14	< 0.004	1.1	6.87	0.511	0.124	34.3	< 0.003	1.04	0.21	58.8	0.055
	13c	6.73	51.4	2.31	< 0.004	1.11	6.99	0.462	0.125	75.6	< 0.003	1.03	0.234	58.3	0.053

Appendix

Table A7.3: The average normalised loss of each of the analysed components for the "Lab Made" HAFe sample sub-series.

Sample ID	Average Normalised Loss (g m^{-2})													
	Al	**B**	**Ca**	**Cr**	**Fe**	**Li**	**Mg**	**Mn**	**Na**	**Ni**	**P**	**S**	**Si**	**Zr**
HAFe 000.0	0.0052 (± 0.0015)	4.3502 (± 0.0241)	0.8260 (± 0.0682)	0.1986 (± 0.0055)	N/A	4.6946 (± 0.0380)	0.9940 (± 0.0803)	0.0084 (± 0.0033)	3.2894 (± 0.0303)	0.0018 (± 0.0001)	2.0533 (± 0.0247)	1.8679 (± 0.0013)	0.4459 (± 0.0087)	0.0005 (± 0.0001)
HAFe 001.0	0.0176 (± 0.0017)	3.9204 (± 0.0349)	0.9318 (± 0.0240)	0.1075 (± 0.0017)	0.0234 (± 0.0010)	3.6723 (± 0.0372)	N/A*	0.0918 (± 0.0056)	2.2446 (± 0.0339)	0.0401 (± 0.0031)	1.5077 (± 0.0227)	1.2505 (± 0.0205)	0.3044 (± 0.0016)	0.0005 (± 0.0001)
HAFe 003.0	0.0422 (± 0.0042)	1.8853 (± 0.0372)	0.7874 (± 0.0511)	0.0628 (± 0.030)	0.0092 (± 0.0010)	1.7772 (± 0.0323)	0.8203 (± 0.0674)	0.0182 (± 0.0033)	1.1635 (± 0.0312)	0.0018 (± 0.0001)	0.4415 (± 0.0165)	0.4932 (± 0.0404)	0.1937 (± 0.0094)	0.0005 (± 0.0001)
HAFe 005.0	0.0937 (± 0.0188)	0.5791 (± 0.0212)	0.5787 (± 0.0256)	0.0329 (± 0.0016)	0.0033 (± 0.0002)	0.6078 (± 0.0149)	N/A*	0.0040 (± 0.0002)	0.5140 (± 0.0107)	0.0020 (± 0.0001)	0.2524 (± 0.0070)	0.2330 (± 0.0109)	0.1437 (± 0.0012)	0.0006 (± 0.0001)
HAFe 007.1	0.1138 (± 0.0042)	0.3143 (± 0.0034)	0.2220 (± 0.0332)	0.0060 (± 0.0001)	0.0014 (± 0.0002)	0.3999 (± 0.0113)	0.2068 (± 0.0274)	0.0001 (± 0.0001)	0.2278 (± 0.0061)	0.0022 (± 0.0001)	0.1866 (± 0.0020)	0.2792 (± 0.0089)	0.1245 (± 0.0007)	0.0007 (± 0.0001)
HAFe 010.0	0.1063 (± 0.0191)	0.3612 (± 0.0042)	0.4708 (± 0.0172)	0.0047 (± 0.0001)	0.0004 (± 0.0001)	0.4009 (± 0.0050)	N/A*	0.0001 (± 0.0001)	0.3500 (± 0.0037)	0.0018 (± 0.0001)	0.3041 (± 0.0022)	0.2103 (± 0.0144)	0.1542 (± 0.0003)	0.0007 (± 0.0001)

***** *No average normalised loss calculated as the compositional analysis did not detect MgO within the samples*

Table A7.4: The average normalised loss of each of the analysed components for the "CCC" HAFe sample sub-series.

Sample ID	Average Normalised Loss (g m^{-2})													
	Al	**B**	**Ca**	**Cr**	**Fe**	**Li**	**Mg**	**Mn**	**Na**	**Ni**	**P**	**S**	**Si**	**Zr**
HAFe 000.0	0.0099 (± 0.0019)	7.1268 (± 1.0694)	0.7638 (± 0.0648)	0.4301 (± 0.0099)	N/A	8.8040 (± 0.1033)	0.0738 (± 0.0583)	0.0489 (± 0.0096)	5.4407 (± 0.8820)	0.0206 (± 0.0034)	4.7378 (± 0.0275)	2.6424 (± 0.0445)	0.8621 (± 0.0078)	0.0006 (± 0.0002)
HAFe 001.0	0.0175 (± 0.0013)	3.3989 (± 0.0591)	0.1521 (± 0.1438)	0.1411 (± 0.0060)	0.0239 (± 0.0007)	3.1955 (± 0.1124)	N/A*	0.0753 (± 0.0051)	0.9928 (± 0.2096)	0.0353 (± 0.0012)	1.3756 (± 0.0360)	0.6702 (± 0.0183)	0.2618 (± 0.0068)	0.0017 (± 0.0002)
HAFe 003.0	0.0715 (± 0.0037)	1.1047 (± 0.0159)	0.1736 (± 0.0281)	0.0410 (± 0.0013)	0.0052 (± 0.0003)	1.0453 (± 0.0225)	N/A**	0.0063 (± 0.0005)	0.3852 (± 0.0099)	0.0050 (± 0.0004)	0.2204 (± 0.0024)	0.0428 (± 0.0042)	0.1528 (± 0039)	0.0019 (± 0.0001)
HAFe 005.0	0.0927 (± 0.0191)	0.6836 (± 0.0195)	0.2560 (± 0.1214)	0.0014 (± 0.0001)	0.0029 (± 0.0001)	0.6885 (± 0.0176)	N/A*	0.0023 (± 0.0001)	0.2637 (± 0.0679)	N/A**	0.1849 (± 0.0059)	N/A**	0.1557 (± 0.0125)	0.0021 (± 0.0003)
HAFe 007.1	0.1231 (± 0.0049)	0.3618 (± 0.0055)	0.1363 (± 0.0728)	N/A**	0.0068 (± 0.0001)	0.3890 (± 0.0091)	0.0346 (± 0.0759)	0.0032 (± 0.0001)	0.1675 (± 0.0390)	N/A**	0.1315 (± 0.0038)	0.0483 (± 0.0253)	0.1467 (± 0.0108)	0.0055 (± 0.0009)
HAFe 010.0	0.1174 (± 0.0184)	0.6709 (± 0.0221)	0.2321 (± 0.0439)	N/A**	0.0037 (± 0.0001)	0.6177 (± 0.0155)	N/A*	0.0022 (± 0.0001)	0.3743 (± 0.1200)	N/A**	0.2101 (± 0.0051)	N/A**	0.1816 (± 0.0053)	0.0033 (± 0.0003)

** No average normalised loss calculated as the compositional analysis did not detect MgO within the samples*

*** After normalisation and blank correction, average normalised loss was calculated to be zero at 4 d.p.*

Table A7.5: The average normalised concentration of each component in the analysed leachate for the "Lab Made" HAFe sample sub-series.

Sample ID	Average Normalised Concentration (g L^{-1})													
	Al	**B**	**Ca**	**Cr**	**Fe**	**Li**	**Mg**	**Mn**	**Na**	**Ni**	**P**	**S**	**Si**	**Zr**
HAFe 000.0	0.0117 (± 0.0013)	8.6982 (± 0.0483)	1.6469 (0.1354)	0.3970 (± 0.0109)	N/A	9.3867 (± 0.0760)	1.9812 (± 0.1592)	0.0168 (± 0.0066)	6.5768 (± 0.0606)	0.0035 (± 0.0001)	4.1047 (± 0.0496	3.7283 (± 0.0039)	0.8916 (± 0.0173)	0.0009 (± 0.0001)
HAFe 001.0	0.0365 (± 0.0017)	7.8420 (± 0.0699)	1.8589 (± 0.0479)	0.2150 (± 0.0033)	0.0469 (± 0.0020)	7.3457 (± 0.0745)	N/A*	0.1837 (± 0.0113)	4.4897 (± 0.0679)	0.0802 (± 0.0062)	3.0151 (± 0.0418)	2.4952 (± 0.0418)	0.6089 (± 0.0033)	0.0010 (± 0.0001)
HAFe 003.0	0.0888 (± 0.0022)	3.7706 (± 0.0738)	1.5727 (± 0.1060)	0.1255 (± 0.0060)	0.0185 (± 0.0019)	3.5544 (± 0.0639)	1.6381 (± 0.1403)	0.0364 (± 0.0065)	2.3269 (± 0.0624)	0.0036 (± 0.0001)	0.8826 (± 0.0335)	0.9839 (± 0.0854)	0.3875 (± 0.0187)	0.0010 (± 0.0001)
HAFe 005.0	0.2113 (± 0.0041)	1.1580 (± 0.0426)	1.1521 (± 0.0507)	0.0658 (± 0.0033)	0.0066 (± 0.0005)	1.2154 (± 0.0300)	N/A*	0.0081 (± 0.0005)	1.0275 (± 0.0217)	0.0040 (± 0.0001)	0.5039 (± 0.0140)	0.4603 (± 0.0217)	0.2874 (± 0.0024)	0.0012 (± 0.0001)
HAFe 007.1	0.2213 (± 0.0001)	0.6283 (± 0.0068)	0.4393 (± 0.0666)	0.0120 (± 0.0001)	0.0029 (± 0.0004)	0.7994 (± 0.0223)	0.4091 (± 0.0551)	0.0002 (± 0.0001)	0.4549 (± 0.0121)	0.0043 (± 0.0001)	0.3721 (± 0.0040)	0.5518 (± 0.0183)	0.2488 (± 0.0014)	0.0015 (± 0.0001)
HAFe 010.0	0.2386 (± 0.0017)	0.7221 (± 0.0085)	0.9352 (± 0.0346)	0.0094 (± 0.0001)	0.0008 (± 0.0001)	0.8015 (± 0.0101)	N/A*	0.0002 (± 0.0001)	0.6994 (± 0.0073)	0.0036 (± 0.0001)	0.6070 (± 0.0043)	0.4147 (± 0.0283)	0.3082 (± 0.0007)	0.0013 (± 0.0001)

***** *No average normalised concentration calculated as the compositional analysis did not detect MgO within the samples*

Appendix

Table A7.6: The average normalised concentration of each component in the analysed leachate for the "CCC" HAFe sample sub-series.

Sample ID	Average Normalised Concentration (g L^{-1})													
	Al	**B**	**Ca**	**Cr**	**Fe**	**Li**	**Mg**	**Mn**	**Na**	**Ni**	**P**	**S**	**Si**	**Zr**
HAFe 000.0	0.0041 (± 0.0002)	3.5643 (± 0.5348)	0.3839 (± 0.0325)	0.2151 (0.0049)	N/A	4.4031 (± 0.0516)	0.0395 (± 0.0291)	0.0245 (± 0.0048)	2.7211 (± 0.4411)	0.0103 (± 0.0017)	2.3698 (± 0.0138)	1.3242 (± 0.0223)	0.4312 (± 0.0039)	0.0003 (± 0.0001)
HAFe 001.0	0.0362 (± 0.0010)	6.7981 (± 0.1181)	0.3001 (± 0.2878)	0.2821 (± 0.0119)	0.0477 (± 0.0014)	6.3912 (± 0.2248)	N/A*	0.1506 (± 0.0103)	1.9854 (± 0.4192)	0.0706 (± 0.0024)	2.7507 (± 0.0720)	1.3354 (± 0.0364)	0.5236 (± 0.0136)	0.0034 (± 0.0003)
HAFe 003.0	0.1512 (± 0.0044)	2.2095 (± 0.0319)	0.3435 (± 0.0563)	0.0820 (± 0.0025)	0.0104 (± 0.0006)	2.0908 (± 0.0450)	N/A**	0.0126 (± 0.0009)	0.7702 (± 0.0007)	0.0100 (± 0.0007)	0.4403 (± 0.0048)	0.0811 (± 0.0085)	0.3056 (± 0.0079)	0.0037 (± 0.0003)
HAFe 005.0	0.2104 (± 0.0078)	1.3759 (± 0.0096)	0.5066 (± 0.2392)	0.0026 (± 0.0001)	0.0058 (± 0.0001)	1.3864 (± 0.0425)	N/A*	0.0046 (± 0.0002)	0.5284 (± 0.1271)	N/A**	0.3710 (± 0.0048)	N/A**	0.3134 (± 0.0243)	0.0043 (± 0.0005)
HAFe 007.1	0.2397 (± 0.0028)	0.7237 (± 0.0110)	0.2682 (± 0.1452)	N/A**	0.0135 (± 0.0002)	0.7780 (± 0.0183)	0.0650 (± 0.1515)	0.0064 (± 0.0002)	0.3345 (± 0.0780)	N/A**	0.2621 (± 0.0076)	0.0903 (± 0.0505)	0.2934 (± 0.0215)	0.0109 (± 0.0018)
HAFe 010.0	0.2631 (± 0.0032)	1.3248 (± 0.0206)	0.6332 (± 0.2072)	0.0012 (± 0.0009)	0.0072 (± 0.0002)	1.2197 (± 0.0095)	N/A*	0.0043 (± 0.0001)	0.7363 (± 0.2292)	0.0005 (± 0.0004)	0.4444 (± 0.0270)	0.0835 (± 0.1305)	0.3587 (± 0.0065)	0.0066 (± 0.0006)

** No average normalised concentration calculated as the compositional analysis did not detect MgO within the samples*

*** After normalisation and blank correction, average normalised concentration was calculated to be zero at 4 d.p.*